DYNAMIC BEHAVIOR OF WRAP-FACED REINFORCED SOIL RETAINING WALL ON SOFT CLAY

by

Ripon Hore

DOCTOR OF PHILOSOPHY

Department of Civil Engineering

BANGLADESH UNIVERSITY OF ENGINEERING AND TECHNOLOGY

2020

DYNAMIC BEHAVIOR OF WRAP-FACED REINFORCED SOIL RETAINING WALL ON SOFT CLAY

by

Ripon Hore

Student No: 1014044004

A Thesis Presented in Partial Fulfillment of the Requirements for the Degree of Doctor of Philosophy

Department of Civil Engineering

Bangladesh University of Engineering and Technology

2020

The thesis titled "**DYNAMIC BEHAVIOR OF WRAP-FACED REINFORCED SOIL RETAINING WALL ON SOFT CLAY**" submitted by Ripon Hore, Student No. 1014044004P, and Session: October, 2014 has been accepted as satisfactory in partial fulfillment of the requirement for the degree of DOCTOR OF PHILOSOPHY on 26th September, 2020.

BOARD OF EXAMINERS

Dr. Mehedi Ahmed Ansary Professor, Department of Civil Engineering, BUET, Dhaka, Bangladesh.	Chairman (Supervisor)
Dr. Md. Habibur Rahman Professor & Head, Department of Civil Engineering, BUET, Dhaka, Bangladesh.	Member (Ex-officio)
Dr. Abu Siddique Professor, Department of Civil Engineering, BUET, Dhaka, Bangladesh.	Member
Dr. Tahmeed Malik Al-Hussaini Professor, Department of Civil Engineering, BUET, Dhaka, Bangladesh	Member
Dr. Md. Mahmudur Rahman Professor, Department of Civil Engineering, AUST, Dhaka, Bangladesh	Member (External)
Dr. Md. Abu Taiyab Professor, Department of Civil Engineering, DUET, Gazipur, Bangladesh	Member (External)

CANDIDATES DECLARATION

It is hereby declared that this thesis or any part of it has not been submitted elsewhere for the award of any degree or diploma.

Ripon Hore

Ripon Hore

TABLE OF CONTENTS

LIST OF TABLES

LIST OF FIGURES

LIST OF ABBREVIATIONS OF TECHNICAL SYMBOLS

a_{max}	Peak ground acceleration
C	Cohesion
C_c	coefficient of curvature
C_u	uniformity coefficient
C_k	Change of permeability
D_r	relative density of sand
D_{50}	mean particle diameter
d	Displacement
E	Young Modulus
E_{50}^{ref}	Secant stiffness in standard drained
E_{oed}^{ref}	Tangent stiffness for primary oedometer loading
E_{ur}^{ref}	Unloading / reloading stiffness
F	Force
e	Void ratio
e_{max}	maximum void ratio
e_{min}	minimum void ratio
f	Frequency
g	acceleration due to gravity
H	height of the wall
δh	horizontal displacements
G_s	specific gravity of soil
K*	Modified swelling index
k_x	Horizontal permeability (x-direction)
k_y	Horizontal permeability (y-direction)
K_z	Vertical permeability
L	Length
M	Power for stress-level dependency of stiffness
n	porosity of soil
S	Height of Clay Layer
T	Total height of the Model
t	Time
V_s	Shear Wave velocity
z	Elevation

σ	Stress
ε	Strain
Φ	Friction angle
Ψ	Dilatancy angle
γ_{sat}	Saturated unit weight
υ	Poisson’s ratio
λ^*	Modified compression index
σ_t	Tensile strength
ψ_{max}	Dilatancy angle

ACKNOWLEDGEMENT

All praises to God, the merciful and the kind.

The author wishes to express his deepest gratitude to Dr. Mehedi Ahmed Ansary, Professor, Department of Civil Engineering, BUET for his continuous guidance, invaluable suggestions and affectionate encouragement at every stage of this study. The author also wishes to express his deepest gratitude to Dr. Md. Habibur Rahman, Professor and Head, Department of Civil Engineering, BUET, Dr. Abu Siddique, Professor. Department of Civil Engineering, BUET, Dr. Tahmeed Malik Al-Hussaini, Professor, Department of Civil Engineering, BUET, Dhaka, Bangladesh, Dr. Md. Mahmudur Rahman, Professor, Department of Civil Engineering, AUST, Dhaka, Bangladesh and Dr. Md. Abu Taiyab, Professor, Department of Civil Engineering, DUET, Gazipur, Bangladesh for their invaluable suggestions and encouragement of this research.

The author wishes to express his gratitude and appreciation to his parents and wife for their inspiration and encouragement.

ABSTRACT

This research aimed to understand the dynamic behavior (acceleration amplification, displacement, strain, and pore water pressure) of wrap-faced reinforced soil retaining wall resting on soft clayey soil. It also investigated the response of wrap faced reinforced soil retaining wall with respect to sand types (Sylhet and Local), surcharge loads, and relative densities under dynamic loading. For these purposes, experimental study and numerical simulations were carried out.

The experimental study was basically a model study using a shake table. The test scheme included a succession of 1D Shake Table Tests (STT) with 0.05g to 0.2g base acceleration on 0.4 m high wrap faced reinforced-soil wall model, which was placed over 0.3 m high soft clayey soil foundation. To assess the seismic behavior, the model was subjected to harmonic sinusoidal input motions at frequencies of 1 Hz, 2 Hz, 3 Hz, and 5 Hz. The model was also subjected to earthquake loadings (1995 Kobe earthquake, Japan and 1989 Loma Prieta earthquake, USA). In order to incorporate the influences of soil, a laminar box was used to contain the soil during the experiments. The base excitations, frequencies, and surcharge pressures were varied in several shake table tests with different relative densities (48%, 64%, and 80% for Sylhet sand and 27%, 41%, and 55% for local sand). A total of 576 (Five hundred and seventy-six) shaking table tests for harmonic sinusoidal wave and 144 (One hundred and forty-four) for earthquake wave (Kobe and Loma Prieta) were carried out on this model embankment. The levels of base acceleration, intensities of frequency and magnitude of surcharge loads had a significant influence on the model wall and varied along the elevation. The acceleration amplification, faced displacement, pore water pressure, and strain were also influenced by the base excitation, frequency, surcharge pressure and relative density.

The response of wrap faced reinforced soil retaining wall was also compared with a similar model developed by a numerical model using PLAXIS3D software. After defining soil stratigraphy, the embankment and wrap faced retaining wall was defined. In the next step, the mesh was generated. After assigning the loadings, the calculation was performed. The results obtained from PLAXIS 3D were compared with the results obtained from model shake table tests.

The results of this study revealed that input accelerations, frequency, and surcharge load had significantly influenced the acceleration amplification, faced displacement, excess pore water pressure, and strain changes along the elevation. Acceleration response was increased with the increase in base acceleration, the difference being more perceptible at higher elevations. The displacement, pore water pressures, and strain were found to be high for high base shaking and low surcharge pressures at higher elevations. The strains of the bottom-layer were the smallest, and the strains of the top-layer were the largest, which indicated that the geotextiles located in the top layers play important roles in the seismic stability of the wrap faced reinforced retaining walls. The walls constructed with higher backfill relative density had shown lesser face displacements, strain and acceleration amplification compared to the walls constructed with lower densities when tested at higher base excitation. The experimental result was found to be lower than the numerical result, the deviation was less than 15%. These results are helpful to observe the dynamic behavior of the wrap faced soil retaining wall on the soft clay layer, which is useful for the design process of this type of retaining wall considering the dynamic loading conditions in Bangladesh.

CHAPTER 1
INTRODUCTION

1.1 General

Wrap faced reinforced soil retaining wall on soft Clay is accessible all over the world because wrap faced layer consumes less space in both sides of the wall, which is economical and less susceptible to dynamic loading. It is essential to consider dynamic loading in the design phase. But none of the implemented projects in Bangladesh consider dynamic loading in the design phases. Typically, in railway or road embankment projects of Bangladesh, a sand embankment is generally constructed on top of soft Clay. Sometimes these soft Clay layers are improved and sometimes not. In the current research, it has been proposed to use wrap faced geotextile layers, which will be put on top of a reconstituted soft Clay layer. These models will be subjected to dynamic loading through the shake table. Reinforced soil retaining walls offer competitive solutions to earth retaining problems associated with less space and more loads posed by the tremendous growth in infrastructure in recent times.

According to worldwide experiences, the reinforced soil walls show a flexible behavior and considerable displacement under seismic loads (Edgar et al. 1989; Collin et al. 1992; Ho and Rowe 1996; White and Holtz 1997; Tatsuoka et al. 1995, 1997; Ling et al. 2001). Reinforced soil walls show a better performance level compared to traditional retaining walls under seismic load (Roessing and Sitar (1998)). Moreover, the cost of constructions of reinforced soil wall is less than a conventional retaining wall, as stated by Latha and Krishna (2006). Many researchers (e.g., Murata et al. 1994, Matsuo et al. 1998, Bathurst et al. 2002a, Nimbalkar et al. 2006) have studied full scale rigid retaining walls and segmental retaining walls (Nova-Roessig and Sitar 1999, Huang et al. 2003, Ling et al. 2005, Huang and Wu 2006). The practice of wrap-faced reinforced soil walls has increased rapidly worldwide due to its better seismic performance. Despite its importance, very few studies (e.g., Sakaguchi et al. 1992, Koerner 1999, Perez and Holtz 2004, Benjamim et al. 2007) are available in this regard.

Richardson and Lee (1975) attempted first small-scale shaking table tests on reinforced soil walls with metallic reinforcement. Sakaguchi et al. (1992) and Sakaguchi (1996) carried out shaking table tests on 1.5m high reinforced model walls and discussed the influence of various parameters. Parameters like the relative density of soil, frequency and amplitude of the motion, reinforcement's types, and spacing between the reinforcements, tensile strength, and soil interaction, friction angle between reinforcements, facing material, surcharge pressure, and others have an influence on displacements of the reinforced soil walls under seismic load (Roessing and Sitar 1998, Paulsen 2002). The seismic performance of reinforced soil walls using different reinforcing materials and facing systems was inspected through experimentations and numerical analyses conducted under various conditions (Richardson et al. 1977, Ling et al. 1997, Matsuo et al. 1998, Koseki et al. 2006).

Several shaking table studies carried out on wrap-faced reinforced soil retaining walls to gain insight into their behavior under dynamic loads by Latha and Krishna (2006; 2008), Krishna and Latha (2007), and Sabermahani et al. (2009). Moreover, a series of laboratory shaking table tests were performed for observing the performance of unreinforced and reinforced soil slopes [Srilatha et al. (2013; 2014) and Latha and Nandhi (2014)]. Two different slope angles and reinforcement were used in their tests. A reduced-scale shake table test investigating the seismic response of a slurry wall and sandy soil were presented by Xiao et al. (2014). Moreover, shaking table tests were performed effectively to investigate the behavior of excess pore water pressure in different soft soil-foundations of soil-structure interaction (SSI) system (Zhang, et al. 2009). The performance of geo-cell retaining walls inside a laminar box, under seismic shaking conditions, was described by Latha and Manju (2016). Moreover, a series of shaking table tests on 0.9 m high reinforced-soil wall models with different steel strip lengths were performed by Yazdandoust (2017).

Zhou et al. (2019) presented shaking table tests on three aeolian sand high embankment models. Moreover, shaking is an effective technique to study the seismic response of underground structures embedded in soft soil sites. Goktepeet al. (2019) observed that the local soil properties have considerably amplified the earthquake response of the structures in comparison to the fixed base structure. Çelebi et al. (2019) specified a realistic geometric scaling coefficient for the test model to be used in a small-capacity shaking table. The scaling factor addressed in this study involves not only geometric similarity but also the kinematic and dynamic similarity with the real system. The dynamic parameters for a scaled model of a single layer soil are restricted with base-rock, which have been compared numerically with the proposed laminar soil container to provide a good agreement. Many researchers (Ye et al.

2018 and Cai et al. 2019) performed shaking table test, to study the seismic responses of different structures embedded in soft soil. Moreover, it is necessary to consider the influence of pore pressure in soft soil sites.

Seismic influence on soil structures has occupied an important, for research in the area of earthquake geotechnical engineering. Two aspects of model testing were given importance, namely a rigid box, and a laminar box. A laminar box is a sophisticated container than a rigid box, which can enhance the accuracy in assessing the ground behavior. In this research, a wrap reinforced soil wall was fabricated on Clayey soil enclosed by a laminar box and subjected to sinusoidal and earthquake input motions through the shake table. Moreover, the spacing between the reinforcements was kept constant in all shaking table tests. Based on shaking table tests, this paper attempts to investigate the effect of the frequency and acceleration of the base sinusoidal motion, surcharge pressure and pore water pressure, horizontal face displacements, and soil pressures in wrap-faced retaining walls under simulated seismic conditions. Wrap faced reinforced soil retaining wall on soft Clay is popular in all over the world because wrap faced layer consumes less space in both sides of the wall, which is economical and less susceptible to dynamic loading.

This study focuses on the seismic design of roadway or railway embankment on soft Clayey soil. A scale model testing platform was developed for a single degree of freedom shaking table tests that symbolize the dynamic free-field conditions of Clayey soil where a wrapped geotextile-sand retaining wall was erected on Clayey soil subjected to seismic loading. A total of 576 (Five hundred and seventy-six) shaking table tests for harmonic sinusoidal wave and 144 (One hundred and forty-four) for earthquake wave (Kobe and Loma) were carried out on this model embankment. To explore the possible influence of the impact on the soil, the test implements repeated loading and unloading process. The Acceleration amplification, displacement, pore water pressure, and strain along the different elevations were observed in this study.

The response of wrap faced reinforced soil retaining wall was also compared with a similar model developed by PLAXIS3D software. Firstly, soil stratigraphy was defined. In the second step, the embankment and wrap faced retaining wall was defined. In the third step, the mesh was generated. After assigning the loadings, the calculation was performed. The results obtained from PLAXIS3D were compared with the results obtained from model shake table tests.

A scale model on soft Clay will be developed for shaking table tests. In order to explore the possible influence of the dynamic loading on the soil, the test will implement repeated loading and unloading process. The effect of frequency, acceleration, surcharge, pore water pressure, and displacement along the different elevations will be observed by physical and numerical modeling. The outcome of the research subject to dynamic loading on wrap faced reinforced soil retaining wall will aid the design process of similar structures in Bangladesh. The results obtained from this study will also be helpful in understanding the relative performance of reinforced soil retaining wall under different test conditions resting on soft Clay.

1.2 Geology of Bangladesh

Bangladesh is the largest delta in the world. Huge alluvium is opened on the surface. The oldest deposit is the Plio-Pleistocene Barend Clay, Madhapur Clay, and Lamaic region Clay. Sediment deposited is not evenly distributed throughout the country. In the northern part, it is about 128 m thick where granite is extracting for construction purposes. But thickness is gradually increased towards the south. At the center, the capital city Dhaka of Bangladesh, where sediment is covering more than 22 km.

About 250 large and small rivers are flowing through the country. River born sediment was deposited from these rives system. From north to south Bangladesh was classified into three tectonic zones namely; a) Stable platform or Indian platform (consisting of Himalayan foredeep, Rangpur Saddle, Dinajpur Shield, Bangura platform and Hinge zone); b) Bengal Basin (consisting of Faridpur Trough, Hatiya Trough, Barisal Trough, Surma Basin); and c) the Chittagong Hill tract.

Sedimentary covers are not uniform throughout the country. Massive drilling, geophysical survey viz. electromagnetic survey, seismic survey, resistivity survey etc. are revealing the depositional and basin history of the country. Various deposit such as Natural hydrocarbon deposit such as Coal deposit at the Northern part of Dinajpur district; gas at the south and eastern part, Bijoypur Clay of Netrokona district, Heavy minerals of Cox's Bazar Inane beach with the radiometric element, glass sand, limestone, etc. are major resources of the country. A geological map of Bangladesh is shown in Figure 1.1. Three types of soil [a) Alluvial Clay and Silt b) Alluvial Silt and c) Madhupur Clay residuum] were described in this map.

Alluvial Silt and Clay: Medium to dark grey Silt to Clay; Colour is darker as the number of organic materials increases. The map unit is a combination of alluvial and paludal deposits, includes flood–basin Silt, backs wamp silty Clay, and organic-rich Clay in sag ponds and large depressions. Some depressions contain peat. Large areas underlain by this unit are dry only a few months of the years; the deeper part of depressions and bills contains water throughout the year.

Alluvial Silt: Light to medium grey, Fine sandy to Clayey silt. Commonly poorly stratified, average grain size decreases away from main channels. Chiefly deposited in flood basins and inter stream areas. Units include small backs wamp deposits and varying episodic or unusually large floods. Illite is the most abundant Clay mineral. Most areas were flooded annually. Included in this unit are thin veneers of sand spread by large episodic floods over flood plain silts. Historic pottery, artifact, and charcoal were found in the upper 4 m.

Madhupur Clay residuum: light yellowish-grey, orange, light to brick red and grayish-white, a micaceous silty Clay to sandy Clay; plastic and abundantly matted in upper 8 m, contains small clusters of organic matter. Sand fraction dominantly quartz; minor feldspar and mica; sand content increases with depth. Dominant Clay minerals are kaolinite and Illite. Iron manganese oxide modules rare.

Figure 1.2 shows the soft soil thickness map of Bangladesh. The SPT value less than 5 consider as soft soil. The figure found that the Dhaka region comply for soft soil layer. For this reason, we selected BUET soil center part of Dhaka for the preparation of the reconstituting soil sample.

Dhaka city which is a metropolis as well as the capital city of Bangladesh lies between latitude 23°40' N to 23°54' N and longitude from 90°20' E to 90°30' E and covers an area of about 470 km^2 having the altitude of 6.5 to 9 m above mean sea level. Geologically, it is an integral part of the southern tip of the Madhupur tract, an uplifted block in the Bengal Basin, with many depressions of recent origin in it. It is bounded by the Tongi Khal (Small River) in the north, the Bariganga river in the south and southeast, the Balu river in the East, and Turag river in the West.

The subsurface geology of Dhaka city shows that upper formation is the Madhupur Clay, and termed as aquitard, and it is 6 to 12 m thick in most parts of the city. The Madhupur Clay mainly consists of Kaolinite (27~53%) and Illite (14~33%) with a very small amount of Illite smectite (2~13%) down to 5m depth (Zahid et al., 2004). However, below the Clay layer, medium to coarse-grained formation exists.

Kamal and Midorikawa (2004) delineated the geomorphology of the Dhaka city area, differentiating the ground of the city into seventeen geomorphic units using aerial photographs. These geomorphic units represent the soil conditions. surface geology of Dhaka with minor anthropogenic modifications. It is observed that the city has been expanding rapidly even in the low-lying geomorphic units by fill practices for urban growth since 1960. They also classified the fill-sites into four classes based on the thickness of fills. In order to collect the fill-thickness, the boreholes and old topographic maps prepared in 1961 are used. Later on, the classified fills were integrated with the pre-urban geomorphic-soil units.

1.3 Objective

a) To develop a wrap faced reinforced soil retaining wall on soft Clay.

b) To measure the dynamic response (acceleration, displacement, strain, and pore water pressure) of wrap faced reinforced soil retaining wall on soft Clay subjected to dynamic loading through shake table.

c) To investigate the acceleration amplification with respect to the effect of base acceleration, frequency, and surcharge of wrap faced reinforced soil retaining wall on soft Clay.

d) To compare the experimental results with the predicted results obtained using PLAXIS 3D model.

1.4 Outline of the Thesis

The thesis consists of seven chapters from Chapter 1 to Chapter 7.

Chapter 1 provides a brief introduction to the subject and states the major objectives. Chapter 2 is devoted to the review of past researches on wrap-faced reinforced soil retaining wall on shaking table test. Details of experimental and numerical modeling are also reviewed in this Chapter.

Chapter 3 describes the detail methodology of this research. The procedure of the shake table test and preparation of the reconstituted soil sample will be presented in Chapter 4.

Chapter 5 discusses PLAXIS 3D modeling in details. Chapter 6 presents the results obtained from shake table test and PLAXIS 3D modeling. Chapter 7 summarizes the conclusions and has put forward recommendations for future research.

CHAPTER 2
LITERATURE REVIEW

2.1 General

The objective of this Chapter is to review past researches related to the shake table test. In addition to that detail, theoretical aspects of experimental and numerical methods are also discussed.

2.2 Seismicity in Bangladesh and problem hazards

Significant damaging historical earthquakes have occurred in and around Bangladesh, and damaging moderate magnitude earthquakes occurred every few years. The country's position adjacent to the very active Himalayan front and ongoing displacement in nearby parts of southeast Asia expose it to strong shaking from a variety of earthquake sources that can produce tremors of magnitude eight or greater. The potential for magnitude eight or greater earthquake on the nearby Himalayan front is very high, and the effects of strong shaking from such an Earthquake directly affect much of the country. In addition, historical seismicity within Bangladesh indicates that potential for damaging moderate to strong Earthquake exist throughout most of the country.

Large earthquakes occur less frequently than serious floods, but they can affect much larger areas and can have long-lasting economic, social, and political effects. Bangladesh covers one of the largest deltas and one of the thickest sedimentary basins in the world. According to the report on time, predictable fault modeling CDMP (2009), earthquake, and tsunami preparedness component of CDMP have identified five tectonic fault zones that may produce damaging earthquakes in Bangladesh. These are:

a) Madhupur fault zone
b) Dauki fault zone.
c) Plate boundary fault zone-1
d) Plate boundary fault zone-2
e) Plate boundary fault zone-3

Considering fault length, fault characteristics, earthquake records etc, the maximum magnitude of earthquakes that can be produced in different tectonic blocks are given in Table 2.1.

In the generalized tectonic map of Bangladesh, as shown in Figure 2.1, the distribution of epicenters is found to be linear along with the Dauki fault system and random in other regions of Bangladesh. The investigation of the map demonstrates that the epicenters are lying in the weak zones comprising surface or subsurface faults. Most of the events are of moderate rank (magnitude 4~6) and lie at a shallow depth, which suggests that the recent movements occurred in the sediments overlying the basement rocks. In the northeastern region (Surma basin), major events are controlled by the Dauki fault system. The events located in and around the Madhupur tract also indicate shallow displacement in the faults separating the block from the alluvium. Figure 2.2 shows the major fault lines which affect seismicity in Bangladesh.

Information of earthquakes in and around Bangladesh is available for the last 250 years. Among these, during the last 150 years, seven major earthquakes have affected Bangladesh.The characteristics of some recent earthquakes are also shown in Table 2.2. The surface wave magnitude, maximum intensity according to the European Macroseismic Scale (EMS), and epicentral distance from Dhaka is presented in Table 2.3.

Based on the above, the probable hazard scenario for an earthquake to a scale of $M_w = 6.5$ or above in Dhaka city could cause:

a) Panic among the city dwellers and no knowledge of what is to be done during and immediately after earthquake occurrence.

b) Possible sinking of many of the buildings on filled earth with shallow foundations due to the liquefaction effect.

c) If the earthquake occurs during monsoon time possible damage of the Dhaka flood protection embankment due to liquefaction effect causing sudden submergence of a large area.

d) Large scale damage and some collapse of poorly constructed and /or old building.

e) Possible outbreak of fire in most of the building from the gas lines.

f) Possible damage of power installation and power cut off for identifying period.

g) Water supply failure as almost all the deep tube wells are run by power, and possible water line damage.

h) Damage of roads and blockage of traffic due to falling of debris from collapsed buildings and other installations on or near roads.

i) Some of the hospital buildings may collapse killing a large number of inmates and stopping medical for the disaster victims.

j) Some of the school buildings may collapse killing and injuring a large number of students.

k) An aftershock may cause the further collapse of many of the already damaged buildings.

l) A few rescue equipment, whatever is available, cannot be operated due to the lack of guidance, availability of operators, some cannot find access to rescue sports due to road blockage, etc.

m) Limited access from outside as most of the highways/bridges, the airport may not be functional.

Although, during the last decade much advancement is achieved in earthquake engineering, modern science has yet to invent any technology that can predict earthquake. But some earthquake-induced damages like liquefaction susceptibility can be evaluated beforehand. Therefore, liquefaction susceptibility of Dhaka soil demands extensive research in order to mitigate and reduce earthquake-induced hazards to the most populated city in the world.

Table 2.1 Maximum estimated earthquake magnitude in different tectonic faults (CDMP, 2009)

Fault zone	Earthquake events	Estimated magnitude, $_{MW}$
Madhupur fault zone	AD 1885	7.5
Dauki fault zone	AD 1897. AD 1500 to 1630 (AD 1548)	8.0
Plate Boundary-1	AD 1762, AD 680 to 980, BC 150 to AD 60, BC 395 to 740	8.5
Plate Boundary-2	Before 16th century	8.0
Plate Boundary-3	Before 16th century	8.3

Table 2.2 Recent earthquakes in Bangladesh

Date	Place of earthquake	Magnitude	Destructions
13 November,1997	Chittagong	6.0	It caused minor damage around Chittagong town.
12 July,1999	Maheshkhali Island	5.2	Severely felt around maheshali island and the adjoining sea.
7 July,2003	Kolabunia union of barkal upazila, rangamati district	5.1	Houses cracks and landslides.

2.2.1 Seismic zoning map of Bangladesh

The seismicity zones and the zone coefficients may be determined from the earthquake magnitude for various return periods and the acceleration attention relationship. It was required that for design or ordinary structures, the seismic ground motion having 10%

probability of being exceeded in the design life of a structure (50 years) considered critical. An earthquake having 200 years return period originating in the sub-Dauki zone has the epicentral acceleration of more than 1.0g, but at 50 kilometers, the acceleration shall be reduced to as low as 0.3g.

Table 2.3 List of major earthquakes affecting Bangladesh during last 150 years (Ms>7) (Sabri, 2002)

Date	Name of earthquake	Surface wave magnitude (m_s)	Maximum intensity (EMS)	Epicentral distance from Dhaka (km)	Basis
10 January, 1869	Cachar earthquake	7.5	IX	250	Back calculation from intensity
14 July,1885	Bengal earthquake	7.0	VII to IX	170	Directly from seismograph
12 June, 1897	Great Indian earthquake	8.7	X	230	
8 July,1918	Srimongal earthquake	7.0	VII to IX	150	
2 July,1930	Dhubri earthquake	7.1	IX	250	
15 January,1934	Bihar-nepal earthquake	8.3	X	510	
15 August,1950	Assum earthquake	8.5	X	780	

Ali (1998) presented the earthquake base and seismic zoning map of Bangladesh. Tectonic framework of Bangladesh adjoining areas indicates that Bangladesh was situated adjacent to the plate margins of India and Eurasia where devastating earthquake have occurred in the past. Non-availability of earthquake, geology and tectonic data posed the great problems in earthquake hazard mapping of Bangladesh in the past. The first seismic map which was prepared in 1979 was developed considering only the epicentral location of the past earthquake and isoseismic map of very few of them. During the preparation of the National Building Code of Bangladesh in 1993, substantial effort was given in revising the existing seismic zoning map using geophysical and tectonic data, earthquake data, ground motion attenuation data, and strong motion data available from within as well as outside of the country. Geophysical and tectonic data were available from the Geological Survey of Bangladesh. Earthquake data were collected from NOAA data files and geodetic survey, US Dept. of commerce.

The Seismic zoning map for Bangladesh was presented in Bangladesh National Building code (BNBC) published in 1993. The pattern of ground surface acceleration contours having 200-year return period from the basis of this seismic zoning map. There are three zones in the map zone 1, zone 2, zone 3. The seismic coefficients of the zones are 0.075g, 0.15g, and 0.250g for zone 1, zone 2 and zone 3 respectively. Bangladesh National Building Code (1993) placed the Dhaka city area in seismic zone 2, as shown in Figure 2.3. However, the seismic zones in the code were not based on the analytical assessment of seismic hazard and mainly based on the location of historic data.

The first seismic zoning map of the subcontinent was compiled by the Geological Survey of India in 1935. The Bangladesh Meteorological Department adopted a seismic zoning map in 1972. In 1977, the Government of Bangladesh constituted a Committee of Experts to examine the seismic problem and make appropriate recommendations. The Committee proposed a zoning map of Bangladesh in the same year. Figure 2.4 shows the proposed Seismic Zoning Map of Bangladesh.

According to the Bangladesh National Building Code (BNBC, 1993), Bangladesh was divided into 3 earthquake zones (Figure 2.3).

Zone-3 comprising the northern and eastern regions of Bangladesh with the presence of the Dauki Fault system of eastern Sylhet and the deep seated Sylhet Fault, and proximity to the highly disturbed southeastern Assam region with the Jaflong thrust, Naga thrust and Disang thrust, is a zone of high seismic risk with a basic seismic zoning co-efficient of 0.25. Northern Bangladesh comprising greater Rangpur and Dinajpur districts is also a region of high seismicity because of the presence of the Jamuna Fault and the proximity to the active east-west running fault and the Main Boundary Fault to the north in India. The Chittagong-Tripura Folded Belt experiences frequent earthquakes, as just to its east is the Burmese Arc where a large number of shallow depth earthquakes originate.

Zone-2 comprising the central part of Bangladesh represents the regions of recent uplifted Pleistocene blocks of the Barend and Madhupur Tracts, and the western extension of the folded belt. The zone extends to the south covering Chittagong and Cox's Bazar. Seismic zoning coefficient for Zone II is 0.15.

Zone-1 comprising the southwestern part of Bangladesh is seismically quiet, with an estimated basic seismic zoning co-efficient of 0.075.

2.2.2 Major source of earthquake in Bangladesh

Bangladesh is one of the most earthquake prone countries in the world. Specialists are expecting a severe earthquake in this area in the near future, which will cause serious human casualty, damages of infrastructure and other losses.

Although Bangladesh is extremely vulnerable to seismic activity, the nature and the level of this activity is yet to be defined. In Bangladesh, complete earthquake monitoring facilities are not available. The Meteorological Department of Bangladesh established a seismic observatory at Chittagong in 1954. This remains the only observatory in the country. Since the whole Indian subcontinent is situated on the junction of the Indo-Australian plate and the Eurasian plate, the tectonic evaluation of Bangladesh can be explained as a result of the collision of the north moving Indo-Australian plate with the Eurasian plate. Figure 2.5 shows the Tectonic plates.

2.2.3 Example of significant earthquake in the world

Two significant earthquake name Kobe and Loma is described as follow:

KOBE Earthquake

Kobe earthquake of 1995, also called Great Hanshin earthquake, Japanese in full Hanshin-Awaji Daishinsai ("Great Hanshin-Awaji Earthquake Disaster"), (Jan. 17, 1995) large-scale earthquake in the Ōsaka-Kōbe (Hanshin) metropolitan area of western Japan that was among the strongest, deadliest, and costliest to ever strike that country.

The earthquake hit at 5:46 am on Tuesday, Jan. 17, 1995, in the southern part of Hyōgo prefecture, west-central Honshu. It lasted about 20 seconds and registered as a magnitude 6.9 (7.3 on the Richter scale). Its epicenter was the northern part of Awaji Island in the Inland Sea, 12.5 miles (20 km) off the coast of the port city of Kobe; the quake's focus was about 10 miles (16 km) below the earth's surface. The Hanshin region (the name is derived from the characters used to write Ōsaka and Kobe) is Japan's second largest urban area, with more than 11 million inhabitants; with the earthquake's epicenter located as close as it was to such a densely populated area, the effects were overwhelming. Its estimated death toll of 6,400 made it the worst earthquake to hit Japan since the Tokyo-Yokohama (Great Kanto) earthquake of 1923, which had killed more than 140,000. The Kobe quake's devastation included 40,000 injured, more than 300,000 homeless residents, and in excess of 240,000 damaged homes, with millions of homes in the region losing electric or water service. Kobe was the hardest hit city with 4,571 fatalities, more than 14,000 injured, and more than 120,000 damaged structures, more than half of which was fully collapsed. Portions of the Hanshin Expressway linking Kobe and Osaka also collapsed or were heavily damaged during the earthquake.

The earthquake was notable for exposing the vulnerability of the infrastructure. Authorities who had proclaimed the superior earthquake-resistance capabilities of Japanese construction were quickly proved wrong by the collapse of numerous supposedly earthquake-resistant buildings, rail lines, elevated highways, and port facilities in the Kobe area. Although most of the buildings that had been constructed according to new building codes withstood the earthquake, many others, particularly older wood-frame houses, did not. The transportation network was completely paralyzed, and the inadequacy of national disaster preparedness was also exposed. Figure 2.6 shows the damage of different infrastructures due to Kobe earthquake.

Loma Prieta Earthquake

San Francisco earthquake of 1989, also called Loma Prieta earthquake, major earthquake that struck the San Francisco Bay Area, California, U.S., on October 17, 1989, and caused 63 deaths, nearly 3,800 injuries, and an estimated $6 billion in property damage. It was the strongest earthquake to hit the area since the San Francisco earthquake of 1906. The earthquake was triggered by a slip along the San Andreas Fault. Its epicenter was in the Forest of Nisene Marks State Park, near Loma Prieta peak in the Santa Cruz mountains, northeast of Santa Cruz and approximately 60 miles (100 km) south of San Francisco. It struck just after 5:00 pm local time and lasted approximately 15 seconds, with a moment magnitude of 6.9. The most severe damage was suffered by San Francisco and Oakland, but communities throughout the region, including Alameda, Santa Clara, Santa Cruz, and Monterey, also were affected. San Francisco's Marina district was particularly hard hit because it had been built on filled land (comprising loose, sandy soil), and the unreinforced masonry buildings in Santa Cruz (many of which were 50 to 100 years old) failed completely. The earthquake significantly damaged the transportation system of the Bay Area. The collapse of the Cypress Street Viaduct (Nimitz Freeway) caused most of the earthquake-related deaths. The San Francisco–Oakland Bay Bridge was also damaged when a span of the top deck collapsed. In the aftermath, all bridges in the area underwent seismic retrofitting to make them more resistant to earthquakes. Figure 2.7 shows the damage of different infrastructures due to Loma Prieta earthquake.

2.3 Past Experimental Studies

This section presents a brief literature review for academic and commercial research related to shake table testing. Included herein are previous efforts related to shake table control, use of shake tables, Real-Time Hybrid Simulation (RTHS) and substructure shake table testing.

2.3.1 Shake table testing

Shake table testing has gained a lot of attention from the experimental earthquake engineering community since the development of the first hand-powered shake table in the late 19th century Severn (2011), see Figure 2.8. A modern shake table consists of hydraulic actuators that drive a large platform to which a structure can be attached, Figure 2.9. The inherent true-rate dynamic nature of shake table tests, which include all inertial effects of the test structure, is ideal for seismic performance evaluation of structures. Shake tables have become a staple in many of the earthquake engineering laboratories (Conte et al., 2004; Ogawa et al., 2001; Reinhorn et al., 2004) and results from shake table tests continue to serve for the improvement of the design specifications on today's new and existing buildings (Deierlein et al., 2011; Elwood and Moehle, 2003; Filiatrault et al., 2001; Jacobsen, 1930).

While shake table testing is now accepted as a structural testing technique, recent developments are allowing researchers to explore new applications of shake table testing. However, shake table testing presents some unique challenges which need to be overcome to allow shake table testing to reach its full potential. Some of the challenges are due to practical matters and economic constraints. For example, although full-scale shake table tests with multi-directional loading might be desirable, such tests are rarely possible because of limited access to experimental facilities and lack of funds. Such practical and economic challenges are often beyond the engineer's control. However, some of the other challenges in shake table testing are technical issues that should be addressed by Engineers.

Technical challenges in shake table testing range from actuator control to efficient post-processing of test results: reproduction of desired table accelerations; shake table nonlinearities; control of multiple actuators for multi-dimensional loading and asynchronous ground motions; instrumentations to capture structural responses of interest; boundary conditions such as soil-structure interaction and interaction with surrounding members that are omitted in shake table testing; difficulties in incorporate substructure techniques; extrapolation of scale effects; interpretation, implication, and generalization of test results; and so on. While all of these challenges require attention and consideration, accurate acceleration control of shake tables is the focus of the work presented in this research.

The challenge in acceleration control of shake tables is mainly due to the inherent dynamics of the control system (i.e., servo hydraulic actuators) and its interaction with the test structures, often referred to as control-structure interaction (Dyke et al., 1995). In general, the hydraulic actuators used in shake tables are displacement controlled with proportional-integral-differential (PID) controllers; where reference displacements are determined a priori by integrating the acceleration time history and removing drifting components. In some cases, velocity and acceleration feedback are added to the displacement controller (e.g., three-variable controller by MTS (Nowak et al., 2000; Tagawa and Kajiwara, 2007). Iterative approaches are often incorporated in commercial shake table controllers to compensate for the dynamics of the control system by modifying the reference displacement outside the servo control loops (Spencer and Yang, 1998). Displacement control in shake tables provides reasonable performance in the low frequency range if evaluated in the frequency domain (e.g., performance spectrum often used in manufacturer specifications). However, displacement control generally produces poor acceleration tracking in the time domain and does not provide adequate repeatability in generated accelerations (Nakata, 2010).

Efforts to improve acceleration control accuracy of shake tables over the conventional displacement control strategies can be found in the literature. Stoten and Gomez (2001) proposed adaptive control using the minimal control synthesis (MCS) algorithm for shake tables. The MCS algorithm improves the control of shake tables when using the first-order strategy of displacement control in the low-medium frequency range. Kuehn et al. (1999) developed a feedback/feed-forward control strategy based on receding horizon control (RHC). Experimental results showed that the RHC based controller had better phase characteristics in the acceleration transfer function than a feedback control using the linear quadratic regulator control. Other approaches adopt feed-forward/feedback control using additional reference signals (Nowak et al., 2000; Phillips et al., 2013; Tagawa and Kajiwara, 2007). Some studies utilize advanced feedback controllers for improvement of shake table acceleration control with heavy test structures, Stehman and Nakata (2013). Trombetti and Conte (2002) employed a method that combines displacement feedback, velocity feed-forward and differential pressure feedback control in a test-analysis comparison study. Their sensitivity analysis showed the effectiveness of the velocity feed-forward term in the magnitude characteristics of the displacement transfer function. Nakata (2010) developed an acceleration trajectory tracking control strategy that combines acceleration feed-forward, displacement feedback, command shaping, and a Kalman filter for the displacement measurement. Experimental results showed superior performance and repeatability of the acceleration trajectory tracking control over the conventional displacement control. While those methods improve control accuracy of shake tables to some extent, acceleration tracking in a wide range of frequencies, particularly in high-frequency range, is still a challenging problem.

2.3.2 Real time hybrid simulation

While shake table testing is the preferred experimental testing technique, size constraints typically limit researchers to the use of scaled experiments. Real-time hybrid simulation (RTHS) is a promising new experimental technique that enables systems level performance assessment of structures at the true dynamic loading rate. In RTHS, responses of entire structural systems are simulated combining computational models (computational substructures) and physical tests (experimental substructures); in general, only structural members of which responses are difficult to model are experimentally tested. It was expanded upon from pseudo-dynamic testing incorporating real-time computational processes and an experimental substructure using hydraulic actuators to apply boundary forces, (Mahin and Shing, 1985; Nakashima et al., 1992), see Figure 2.10. Pseudo-dynamic testing allows for testing of restoring members and does not include inertial components in the experiment; thus, tests are run at slow speed and the system dynamics are simulated. RTHS offers a cost-effective means for performance assessment of entire structural systems with fully incorporated physical tests of structural members. In particular, RTHS is advantageous for simulations of systems with rate-dependent structural members that are not accurately evaluated by conventional slow-speed pseudo-dynamic testing. Those structural members include dampers (Carrion et al., 2009; Christenson et al., 2008; Zapateiro et al., 2010), Figure 2.11 depicts a traditional RTHS partitioning scheme, and bearings (Igarashi et al., 2009; Pan et al., 2005). Although the advantages of RTHS were recognized by many earthquake engineers, research efforts on RTHS are still limited to date. Challenges in RTHS that have yet to be addressed by the community include but are not limited to tests where the experimental substructure has a significant influence on the computational substructure and tests where experimental substructures include all inertial components. Further advances in methodologies and more applications are needed to promote this emerging experimental technique. One of the main challenges in RTHS is the ability of the experimental loading system (typically hydraulic actuators) to impose the boundary conditions accurately. Since both experimental and computational substructures form a closed loop, any errors introduced by the experimental loading system are propagated through the system. Depending on the system configuration and parameters, the added energy from such errors may not be dissipated fast enough, resulting in an unstable simulation. Such challenges typically limit RTHS to applications where the experimental substructure is simple and includes significant damping. Recent research has made steps toward RTHS implementations with more challenging experimental conditions. Some of the most notable advancements in this area include the use of shake tables in RTHS implementations.

2.3.3 Substructure shake table testing

One of the more recent and promising advancements in the use of shake tables is the incorporation of shake tables into the real-time hybrid simulation, known as substructure shake table testing (some refer to it as real-time substructure systems, Neild et al. (2005), or hybrid shake table testing, Schellenberg et al. (2013).

Substructure shake table testing combines the fully dynamic nature of shake table testing with the effective computational modeling in hybrid simulation. Substructure shake table testing in an active research area because most shake tables can be upgraded to enable RTHS, and a number of researchers have investigated substructure shake table testing to date. Igarashi et al. (2000) introduced a substructure shake table test method that allows for tuned mass dampers to be tested on the top floor of a computational substructure represented by a shake table, Figure 2.12. Lee et al. (2007) introduced a method where the shake table included the upper stories of the test structure while the lower stories were computational. Shao et al. (2011) and Nakata and Stehman (2012) investigated substructure shake table testing where the experimental substructure and shake table represented the lower floors of the test structure. Recently Mosalam and Gu¨nay (2013) have used substructure shake table testing to examine the performance of large-scale electrical equipment. Nakata and Stehman (2014a) introduced an array of compensation techniques that can be added to existing substructure shake table systems to increase accuracy and ensure the stability of the tests. Like any RTHS, substructure shake table testing is very sensitive to time delays introduced by hydraulic actuators. Actuator delay compensation was a major research topic for the stabilization and improvement of RTHS methods. Many new delay compensation techniques were developed and implemented since the topic was first addressed (Horiuchi et al., 1999; Horiuchi and Konno, 2001; Nakashima and Masaoka, 1999). Many of the delay compensation techniques use models of the test structure or actuator dynamics. Carrion and Spencer (2007) introduced two model-based delay compensation techniques: the first uses computational models of the RTHS substructures to predict future actuator commands from the iterative simulation. The second technique uses an inverse model of the actuator to compensate for the closed-loop actuator dynamics (including magnitude roll-off and phase/time delay). Chen and Ricles (2009) have completed comparative studies to analyze the performance of popular delay compensation techniques. Gao et al. (2013) proposed an $H\infty$ approach for actuator control and delay compensation that handles uncertainties in the experimental system. Phillips and Spencer (2011) expanded on Carrion and Spencer's second method by realizing the actuator inverse model as a weighted series of derivatives of the reference signal. While delay compensation techniques are widely studied for RTHS applications, most implementations have been limited to experimental substructures with little to no inertial effects (i.e., single dampers and structures with negligible mass). Substructure shake table testing often includes test structures with substantial floor mass and delay compensation techniques need to be studied for such cases with significant inertial components.

The presence of inertial components (e.g., the mass of experimental substructures) as well as restoring members affects the dynamics of the actuator (known as Control-Structure-Interaction (CSI), Dyke et al. (1995). Several studies in shake table control have addressed the adverse effects of CSI and actuator dynamics. While approaches that can compensate for CSI are available for shake table control, their primary objective is the improvement of the magnitude characteristics. Compensation techniques for shake tables that focus on phase characteristics (equivalently time delay), are necessary to fully enable substructure shake table testing due to the challenging experimental conditions.

2.4 Shake Table Dynamics

The work presented throughout this dissertation relies on the use of shake tables. This Chapter provides a basic introduction to the dynamic relations for shake tables, including electro-hydraulic actuators, table platform, test structure and standard feedback control system. The purpose of this Chapter is to familiarize the reader with the dynamics of a shake table system as well as the challenges that arise due to said dynamics. The contents of this

Chapter were previously published in Stehman and Nakata (2014). The schematic of a uniaxial shake table with a linear structure is shown in Figure 2.13.

2.5 Scaling of Shake Table Test

The model size in this present study was fixed according to the facilities obtainable for this test. Considering the stress-dependent behavior of the soil and boundary conditions, precise scaling of soil wall and reinforcement properties are mandatory. 1-g or N-g type of testing was performed to satisfy the similitude requirements between model and prototype, consequently, the behavior of the prototype structure can be predicted accurately.

Shaking table tests are often conducted in the 1 g gravitational field in order to understand the behavior of soil structures and foundations during earthquakes. On some occasions, the shaking table tests are conducted for the very complex models, the saturated soil-structure-fluid models under earthquake loadings. The necessity for such model tests is increasing nowadays because offshore, waterfront and other development are urgently requested in the seismically active areas in the world. In general, the similitude is necessary to interpret the results of the model tests. There is another study on the similitude of nonlinear dynamic responses of grounds by using Buckingham's theorem (Kokusho and Iwatate, 1979). Both of the studies resulted in the same similitude. However, the result of their studies is applicable only to the shear displacement of soil structures. There is a need to extend their similitude to a more general form in order to interpret the dynamic model tests of the saturated soil-structure-fluid system. In what follows, such similitude was shown by using basic equations that govern the dynamic behavior of the saturated soil-structure-fluid system.

Among the basic equations which govern the behavior of saturated soil-structure-fluid system, the constitutive law of soil is one of the most important equations. Although the constitutive law of soil was extensively studied as one of the main subjects in the soil mechanics, it is still under controversy. Therefore, in a strict sense, the basic equations on the behavior of the soil were not fully established. However, except for the constitutive law of the soil, basic equations such as those for equilibrium and mass balance of soil skeleton, pore water, etc. were well established for the dynamic behavior of the saturated soil-structure-fluid system. First of all, let us regard the saturated soil as a porous material composed of two phases: a solid phase formed by the particles of soil and a liquid phase that fills the pore of the solid phase, as shown in Figure 2.14. Figure 2.15 shows displacements u, effective stresses σ' and pressures of pore water and external water p in the model and the prototype. Figure 2.16 shows the Stress-strain relations of soils in the model and the prototype.

Even if the model is properly scaled to achieve similitude with the prototype wall, in low stress limiting 1-g shake table tests is not possible to guess the accurate behavior of the prototype with compare to the reinforced model wall (Sabermahani et al., 2009; Latha and Krishna, 2008 and Krishna and Latha, 2007). Scaling of tensile strength-strain behavior and modeling of the bond between soil and geotextile these two similitude requirements have to be fulfilled as addressed by Viswanadham and Mahajan (2007). Table 2.4 presents the scaling factors for this study assuming, $\alpha = 0.5$ for sand (Kokusho, 1980; Yu and Richart, 1984) and considering the prototype to model scale being $N = 10$.

Table 2.4 Scale factors of selected engineering variables (Kokusho, 1980; Yu and Richart, 1984)

Description	Parameter	Scale factor	Scale factor M/P	Scale factor P/M
Acceleration	a	1	1	1
Density	ρ	1	1	1
Length	L	1/N	0.10	10
Stress	σ	1/N	0.10	10
Strain	ε	$1/N^{1-\alpha}$	0.32	3.125
Stiffness	G	$1/N^{\alpha}$	0.32	3.125
Displacement	d	$1/N^{2-\alpha}$	0.031	32.25
Frequency	f	$N^{1-\alpha/2}$	5.62	0.18
Force	F	$1/N^{3}$	0.001	1000
Force/L	F/L	$1/N^{2}$	0.01	100
Shear Wave velocity	V_s	$1/N^{\alpha/2}$	0.56	1.785
Time	t	$1/N^{1-\alpha/2}$	0.178	5.62
*P-Prototype; M-Model				

2.6 Wrap Faced Embankment

Reinforced soil retaining walls offer competitive solutions to earth retaining problems associated with less space and more loads posed by the tremendous growth in infrastructure in recent times. Wrap faced reinforced soil retaining wall on soft Clay is accessible all over the world because wrap faced layer consumes less space in both sides of the wall, which is economical and less susceptible to dynamic loading.

Wrap faced reinforced soil retaining wall on soft Clay is popular in all over the world because wrap faced layer consumes less space in both sides of the wall, which is economical and less susceptible to dynamic loading. It is important to consider dynamic loading in the design phase. But none of the implemented projects in Bangladesh consider dynamic loading in design phases. Some implementing project in Bangladesh is shown in Figure 2.17. A real Picture of Wrap Faced Reinforced Soil Retaining Wall is shown in Figure 2.18.

Several shaking table studies carried out on wrap-faced reinforced soil retaining walls to gain insight into their behavior under dynamic loads by Latha and Krishna (2006; 2008), Krishna and Latha (2007), and Sabermahani et al. (2009). The response of the wrap-faced soil-retaining walls is significantly affected by the base acceleration levels, frequency of shaking, quantity of reinforcement and magnitude of surcharge pressure on the crest. The effects of these different parameters on acceleration response at different elevations of the retaining wall, horizontal soil pressures and face deformations are also presented by Krishna and Latha (2007). A total of nine model tests with variations in acceleration and frequency of base motion, surcharge pressure on the crest and number of layers of reinforcement were described, along with the model preparation, testing methodology and results. It is observed that the seismic response of the retaining walls is significantly affected by the variations in base motion parameters, reinforcement configuration and surcharge pressure. According to Krishna and Latha (2007), accelerations are amplified at higher elevations and with low surcharge pressures and lower number of reinforcing layers for a given height of the wall. On the other hand, the face deformations are high for low-frequency shaking, low surcharge pressures, fewer reinforcing layers and high base accelerations. The rigid box instead of laminar box was used in the research of Sabermahani et al. (2009).

Moreover, a series of laboratory shaking table tests were performed for observing the performance of unreinforced and reinforced soil slopes [Srilatha et al. (2013; 2014) and Latha and Nandhi (2014)]. The effect of frequency of base shaking on the dynamic response of unreinforced and reinforced soil slopes through a series of shaking table testshas been presented by Srilatha et al. (2013). Two different slope angles 45° and 60° were used in tests and the quantity and location of reinforcement is varied in different tests. Acceleration of shaking was kept constant as 0.3 g in all the tests to maximize the response and the frequency of shaking was 2 Hz, 5 Hz and 7 Hz in different tests. The displacements at all elevations increased with increase in frequency for all slopes, whereas the effect of frequency on acceleration amplifications is not significant for reinforced slopes. The acceleration and displacement response is not increasing proportionately with the increase in the frequency.

2.7 Numerical Modeling

PLAXIS is a finite element package that was developed specifically for the analysis of displacement, stability and flow in geotechnical engineering projects. The simple graphical input procedures enable a quick generation of complex finite element models, and the enhanced output facilities provide a detailed presentation of computational results. The calculation itself is fully automated and based on robust numerical procedures. Users are expected to have a basic understanding of soil mechanics and should be able to work in a Windows environment.

PLAXIS 2D is a two-dimensional finite element program, developed for the analysis of displacement, stability and groundwater flow in geotechnical engineering. It is a part of the PLAXIS product range, a suite of finite element programs that are used Worldwide for geotechnical engineering and design. The development of PLAXIS began in 1987 at Delft University of Technology as an initiative of the Dutch Ministry of Public Works and Water Management (Rijkswaterstaat). The initial purpose was to develop an easy-to-use 2D finite element code for the analysis of river embankments on the soft soils of the lowlands of Holland. In subsequent years, PLAXIS was extended to cover most other areas of geotechnical engineering. Because of continuously growing activities, the PLAXIS company (Plaxis bv) was formed in 1993. In 1998, the first PLAXIS 2D for Windows was released. In the meantime, a calculation kernel for 3D finite element calculations was developed which resulted in the release of the 3DTunnel program in 2001.

3D Foundation was the second three-dimensional PLAXIS program, and was developed in cooperation with TNO. The 3DFoundation program was released in 2004. However, in neither 3DTunnel nor 3DFoundation, it is possible to define arbitrary 3D geometries, because of their geometrical limitations. PLAXIS 3D is a full three-dimensional PLAXIS program that combines an easy-to-use interface with full 3D modeling facilities. The PLAXIS 3D program was released in 2010.

PLAXIS is intended to provide a tool for practical analysis to be used by geotechnical engineers who are not necessarily numerical specialists. Quite often, practicing engineers consider nonlinear finite element computations cumbersome and time-consuming. The PLAXIS research and development team has addressed this issue by designing robust and theoretically sound computational procedures, which are encapsulated in a logical and easy-to-use shell. As a result, many geotechnical engineers worldwide have adopted the product and are using it for engineering purposes.

Research and development of the PLAXIS software are supported by the Plaxis Development Community (PDC), in which a consortium of more than 30 international companies participate. The consortium contributes financially to the PLAXIS developments and checks the efficiency and quality of the resulting software products. The consortium provides a valuable link with engineering practice. Future developments are discussed within the consortium and feedback is provided after new releases. The PLAXIS company and its employees are member of various institutions on civil and geotechnical engineering throughout the world. The PLAXIS company is member of NAFEMS, a non-profit organization with the goal of stimulate the use of the finite element method in various types of engineering. The development of the PLAXIS products would not be possible without world-wide research at universities and research institutes. To ensure that the high technical standard of PLAXIS is maintained and that new technology is adopted, the development team is in contact with a large network of researchers in the field of geomechanics and numerical methods.

2.7.1 Different model

The mechanical behavior of soils may be modeled at various degrees of accuracy. Hooke's law of linear, isotropic elasticity, for example, maybe thought of as the simplest available stress-strain relationship. As it involves only two input parameters, i.e. Young's modulus, E, and Poisson's ratio, u, it is generally too crude to capture essential features of soil and rock behavior. For modeling massive structural elements and bedrock layers, however, linear elasticity tends to be appropriate.

Linear Elastic Perfectly Plastic Model (Mohr-Coulomb Model)

Soils behave rather non-linear when subjected to changes of stress or strain. In reality, the stiffness of soil depends at least on the stress level, the stress path and the strain level. Some such features are included in the advanced soil models in PLAXIS. The Mohr-Coulomb model however, is a simple and well-known linear elastic perfectly plastic model, which can be used as a first approximation of soil behavior. The linear elastic part of the Mohr-Coulomb model is based on Hooke's law of isotropic elasticity. The perfectly plastic part is based on the Mohr-Coulomb failure criterion, formulated in a non-associated plasticity framework.

Plasticity involves the development of irreversible strains. In order to evaluate whether or not plasticity occurs in a calculation, a yield function, f, is introduced as a function of stress and strain. Plastic yielding is related with the condition $f = 0$. This condition can often be presented as a surface in principal stress space. A perfectly-plastic model is a constitutive model with a fixed yield surface, i.e. a yield surface that is fully defined by model parameters and not affected by (plastic) straining. For stress states represented by points within the yield surface, the behavior is purely elastic and all strains are reversible.

The linear elastic perfectly-plastic Mohr-Coulomb model requires a total of five parameters, which are generally familiar to most geotechnical engineers and which can be obtained from basic tests on soil samples. The parameter tab sheet for Mohr-Coulomb model is shown in Figure 2.19.

The Hoek-Brown Model (Rock Behavior)

The material behavior of rock differs from the behavior of soils in the sense that it is generally stiffer and stronger. The dependency of the stiffness on the stress level is almost negligible, so the stiffness of rocks can be considered constant. On the other hand, the dependency of the (shear) strength on the stress level is significant. In this respect, heavily jointed or weathered rock can be regarded as a frictional material. A first approach is to model the shear strength of rock by means of the Mohr-Coulomb failure criterion. However, considering the large range of stress levels where rock may be subjected to, a linear stress-dependency, as obtained from the Mohr-Coulomb model, is generally not sufficient. Furthermore, rock may also show significant tensile strength. The Hoek-Brown failure criterion is a better non-linear approximation of the strength of rocks. It involves shear strength as well as tensile strength in a continuous formulation. Together with Hooke's law of isotropic linear elastic behavior it forms the Hoek-Brown model for rock behavior. The 2002 edition of this model (Hoek, Carranza-Torres & Corkum, 2002) has been implemented in PLAXIS to simulate the isotropic behavior of rock-type materials. The implementation of the model, including the material strength factorization, is based on Benz, Schwab, Vermeer & Kauther (2007). More background information on the Hoek-Brown model and the selection of model parameters can be found in Hoek (2006). The Hoek-Brown failure contour in principal stress space is shown in Figure 2.20.

The Hoek-Brown model involves a total of 8 parameters, which are generally familiar to geologists and mining engineers. These parameters with their standard units are listed below:

E	:	Young's modulus	[kN/m^2]
ν	:	Poisson's ratio	[-]
σ_{ci}	:	Uni-axial compressive strength of the intact rock (>0)	[kN/m^2]
m_i	:	Intact rock parameter	[-]
GSI	:	Geological Strength Index	[-]
D	:	Disturbance factor	[-]
ψ_{max}	:	Dilatancy angle (at $\sigma'_3 = 0$)	[°]
σ_ψ	:	Absolute value of confining pressure σ'_3 at which $\psi = 0°$	[kN/m^2]

<u>The Jointed Rock Model (ANISOTROPY)</u>

Materials may have different properties in different directions. As a result, they may respond differently when subjected to particular conditions in one direction or another. This aspect of material behavior is called anisotropy. When modeling anisotropy, distinction can be made between elastic anisotropy and plastic anisotropy. Elastic anisotropy refers to the use of different elastic stiffness properties in different directions. Plastic anisotropy may involve the use of different strength properties in different directions, as considered in the Jointed Rock model. Another form of plastic anisotropy is kinematic hardening. The latter is not considered in PLAXIS. Visualization of the concept behind the Jointed Rock model is shown in Figure 2.21.

The Jointed Rock model is an anisotropic elastic perfectly-plastic model, especially meant to simulate the behavior of stratified and jointed rock layers. In this model it is assumed that there is intact rock with an optional stratification direction and major joint directions. The intact rock is considered to behave as a transversely anisotropic elastic material, quantified by five parameters and a direction. The anisotropy may result from stratification or from other phenomena. In the major joint directions, it is assumed that shear stresses are limited according to Coulomb's criterion. Upon reaching the maximum shear stress in such a direction, plastic sliding will occur.

A maximum of three sliding directions (’planes') can be defined, of which the first plane is assumed to coincide with the direction of elastic anisotropy. Each plane may have different shear strength properties. In addition to plastic shearing, the tensile stresses perpendicular to the three planes are limited according to a predefined tensile strength (tension cut-off).

The Hardening Soil Model (Isotropic Hardening)

In contrast to an elastic perfectly-plastic model, the yield surface of a hardening plasticity model is not fixed in principal stress space, but it can expand due to plastic straining. The distinction can be made between two main types of hardening, namely shear hardening and compression hardening. Shear hardening is used to model irreversible strains due to primary deviatoric loading. Compression hardening is used to model irreversible plastic strains due to primary compression in oedometer loading and isotropic loading. Both types of hardening are contained in the present model.

The Hardening Soil model is an advanced model for simulating the behavior of different types of soil, both soft soils and stiff soils, Schanz (1998). When subjected to primary deviatoric loading, soil shows a decreasing stiffness and simultaneously irreversible plastic strains develop. In the special case of a drained triaxial test, the observed relationship between the axial strain and the deviatoric stress can be well approximated by a hyperbola. Such a relationship was first formulated by Kondner (1963) and later used in the well-known hyperbolic model (Duncan & Chang, 1970). The Hardening Soil model, however, supersedes the hyperbolic model by far: Firstly, by using the theory of plasticity rather than the theory of elasticity, secondly by including soil dilatancy and hardly by introducing a yield cap.

<u>The Hardening Soil Model with Small-Strain Stiffness (HSSMALL)</u>

The original Hardening Soil model assumes elastic material behavior during unloading and reloading. However, the strain range in which soils can be considered truly elastic, i.e. where they recover from applied straining almost completely, is very small. With increasing strain amplitude, soil stiffness decays nonlinearly. Plotting soil stiffness against log(strain) yields characteristic S-shaped stiffness reduction curves. It also outlines the characteristic shear strains that can be measured near geotechnical structures and the applicable strain ranges of laboratory tests. It turns out that at the minimum strain which can be reliably measured in classical laboratory tests, i.e. triaxial tests and oedometer tests without special instrumentation, soil stiffness is often decreased to less than half its initial value. The soil stiffness that should be used in the analysis of geotechnical structures is not the one that relates to the strain range at the end of construction, according to Figure 2.22. Instead, very small-strain soil stiffness and its nonlinear dependency on strain amplitude should be properly taken into account. In addition to all features of the Hardening Soil model, the Hardening Soil model with small-strain stiffness offers the possibility to do so.

The Hardening Soil model with small-strain stiffness implemented in PLAXIS is based on the Hardening Soil model and uses almost entirely the same parameters. In fact, only two additional parameters are needed to describe the variation of stiffness with strain:

- the initial or very small-strain shear modulus G_o
- the shear strain level 70.7 at which the secant shear modulus G_s is reduced to about 70% of G_0

<u>The Soft Soil Model</u>

As soft soils, we consider near-normally consolidated Clays, Clayey silts and peat. A special feature of such materials is their high degree of compressibility. This is best demonstrated by oedometer test data as reported, for instance by Janbu in his Rankine lecture (1985).

Considering tangent stiffness moduli at a reference oedometer pressure of 100 kPa, he reports for normally consolidated Clays E_{oed} = 1 to 4 MPa, depending on the particular type of Clay considered. The differences between these values and stiffnesses for NC-sands are considerable as here we have values in the range of 10 to 50 MPa, at least for non-cemented laboratory samples. Hence, in oedometer testing normally consolidated Clays behave ten times softer than normally consolidated sands. This illustrates the extreme compressibility of soft soils.

The parameters of the Soft Soil model include compression and swelling indices, which are typical for soft soils, as well as the Mohr-Coulomb model failure parameters. In total, the Soft Soil model requires the following parameters to be determined:

Basic parameters:

λ^*	:	Modified compression index	[-]
κ^*	:	Modified swelling index	[-]
c	:	Effective cohesion	[kN/m^2]
φ	:	Friction angle	[°]
ψ	:	Dilatancy angle	[°]
σ_t	:	Tensile strength	[kN/m^2]

Advanced parameters (use default settings):

ν_{ur}	:	Poisson's ratio for unloading / reloading	[-]
K_0^{nc}	:	Coefficient of lateral stress in normal consolidation	[-]
M	:	K_0^{nc}-parameter	[-]

<u>Soft Soil Creep Model (Time Dependent Behaviour)</u>

Both the Hardening Soil model and the Soft Soil model can be used to model the behavior of compressible soft soils, but none of these models are suitable when considering creep, i.e., secondary compression. All soils exhibit some creep, and primary compression is thus always followed by a certain amount of secondary compression. Assuming the secondary compression (for instance, during a period of 10 or 30 years) to be a certain percentage of the primary compression, it is clear that creep is important for problems involving large primary compression. This is for instance the case when constructing embankments on soft soils. Indeed, large primary settlements of footings and embankments are usually followed by substantial creep settlements in later years. In such cases, it is desirable to estimate the creep from FEM-computations.

Foundations may also be founded on initially overconsolidated soil layers that yield relatively small primary settlements. Then, as a consequence of the loading, a state of normal consolidation may be reached and significant creep may follow. This is a treacherous situation as considerable secondary compression is not preceded by the warning sign of large primary compression. Again, computations with a creep model are desirable.
Buisman (1936) was probably the first to propose a creep law for Clay after observing that soft-soil settlements could not be fully explained by classical consolidation theory. This work on 1 D-secondary compression was continued by other researchers including, for example, Bjerrum (1967), Garlanger (1972), Mesri & Godlewski (1977) and Leroueil (1977). More mathematical lines of research on creep were followed by, for example, Sekiguchi (1977), Adachi & Oka (1982) and Borja & Kavaznjian (1985). This mathematical 3D-creep modeling was influenced by the more experimental line of 1 D-creep modeling, but conflicts exist.

3D-creep should be a straight forward extension of 1 D-creep, but this is hampered by the fact that present 1 D-models have not been formulated as differential equations. For the presentation of the Soft Soil Creep model we will first complete the line of 1 D-modeling by conversion to a differential form. From this 1 D differential equation an extension was made to a 3D-model. This chapter gives a full description of the formulation of the Soft Soil Creep model. In addition, attention is focused on the model parameters. Finally, a validation of the 3D model is presented by considering both model predictions and data from triaxial tests. Here, attention is focused on constant strain rate triaxial tests and undrained triaxial creep tests. For more applications of the model the reader is referred to Vermeer, Stolle & Bonnier (1998), Vermeer & Neher (1999) and Brinkgreve (2004).

Some basic characteristics of the Soft Soil Creep model are:

- Stress-dependent stiffness (logarithmic compression behavior)
- Distinction between primary loading and unloading-reloading
- Secondary (time-dependent) compression
- Ageing of pre-consolidation stress
- Failure behavior according to the Mohr-Coulomb criterion

The Sekiguchi-Ohta Model

The Sekiguchi-Ohta model has been developed to formulate a constitutive law for normally consolidated Clay. Particular emphasis is placed on taking the effect of time and stress-induced anisotropy into consideration. A complete description of the model has been presented in Sekiguchi & Ohta (1977) and lizuka & Ohta (1987).

The Sekiguchi-Ohta model combines the concepts lying behind the well-known Cam Clay model (Roscoe, Schofield & Thurairajah (1963)) and the rheological model developed by Murayama & Shibata (1966). The Cam Clay model was further developed by Ohta & Hata (1973) counting for the stress induced anisotropy for anisotropic ally consolidated Clays. However due to the fact that this model deals with the stress-strain behavior of the soil in equilibrium, the time effect is not considered. The rheological model is further developed by Sekiguchi (1977) to describe the time-dependent and elastoplastic behavior for normally consolidated Clays.

2.8 Summary

In this Chapter, past researches related to the shake table test and wrap faced embankment model was presented. Different models related to PLAXIS 3D analysis was also discussed. These discussions will be helpful in understanding the procedure of the shake table test and also analyzing the shake table and numerical data.

CHAPTER 3
METHODOLOGY

3.1 General

The shake table model tests and the numerical modeling of wrap faced embankment are performed in this study. These experimental test and numerical modeling were intended to understand the dynamic behaviour of wrap faced embankment. The model studies conducted by different researchers are briefly discussed in the literature review of the previous chapter. The detailed description of experimental and numerical procedures of the model studies are outlined later in Chapter 4 and Chapter 5. Figure 3.1 shows a flow diagram of the methodology followed in this study.

3.2 Experimental Modeling

To fulfill the objectives and possible outcomes of the study for the experimental study, the following steps were followed.

<u>Setting up the Shake Table</u>

A computer-controlled servo-hydraulic single degree of freedom shaking table facility available in the Department of Civil Engineering, BUET were used to simulate the horizontal shaking action. The shaking table operated over an acceleration range of 0.05g to 0.2g and frequency between 1 to 5 Hz with a maximum amplitude of ±200 mm. The maximum velocities were 0.3 m/s.

<u>Arrangement of Laminar Box</u>

In this study, embankment with soft Clay was constructed in a laminar box to reduce boundary effects as far as practicable. The laminar box was designed according to the following criteria: the layers and the inside membrane should have a minimum stiffness to horizontal shear; offers little resistance to the vertical settlement of soil; the height of each layer is small which increases the flexibility for the displacement of the soil inside; it is fairly large to better simulate field behavior; possesses the capability to increase confining pressure; maintains its horizontal cross-section during shaking and it develops shear stress on the interface between the soil and the vertical wall equal to that on the horizontal plane. The laminar shear box was composed of 24 hollow aluminum layers of frames. Each layer consists of an inner frame with inside dimensions of 915 mm × 1220 mm × 1220 mm. The aluminum alloy were adopted for its sufficient strength and rigidity, and it's lightweight to minimize the effect of the inertia of the frame on the soil movements. The gap between the successive layers was 2 mm, and the most bottom layer was rigidly connected to the solid aluminum baseplate of size 915 mm x 1220 mm in plan and 15 mm thickness.

<u>Preparation of Reconstituted Clay Soil</u>

Clay soil sample was collected from a suitable location of Dhaka (BUET Campus). The homogeneous, reddish-brown samples were at first oven-dried; subsequently, the dry lumps was then powdered gently by using a wooden hammer; and finally sieved through #200 standard sieve to obtain clean Clay powder. Dhaka Clay was reconstituted by thoroughly mixing the oven-dried Clay powder with an initial water content equal to the Liquid Limit (LL). The thorough mixing of the slurry was attained with the aid of a 'Hobart' rotary mixer. With this slurry, a 300 mm reconstituted Clay layer constructed in the laminar shear box; and then consolidated under the drained isotropic condition at loads: 15kPa, 20kPa, 25kPa, 30kPa, 40kPa, 60kPa, 80kPa and 100kPa. The consolidation process was observed through the settlement of Clay versus time graph, plotted with the aid of calibrated mechanical dial gauges, instrumented on either side of the laminar shear box. Once the consolidation process was ceased, three undisturbed cylindrical samples were collected from the soil cake from three different locations. From these cylindrical samples, 38 mm by 76 mm samples were then trimmed before being shifted to the triaxial cell. For determination of the shear strength parameters, Unconsolidated Undrained triaxial shear tests were performed.

<u>Setting of the Height of Clay Layer and Scale Factor</u>

A 300 mm thick Clay layer foundation was constructed first. Above which, a 50 cm sand blanket was provided. This Clay layer reflected the height limitation of the laminar box and the total weight of the model. Approximately 1 m^2 geotextile was placed between the Clay foundation and the sand blanket. A non-woven polypropylene multifilament geotextile used for reinforcing the sand in the tests. Based on the model height of 300 mm, a prototype height of 3 m was considered. So, the considered scale factor was 10.

Preparation of Embankment and Wrap Face Retaining Wall

A 400 mm high wrap faced geotextile model was fabricated for this current study. The sand wall consists of 4 layers, each layer of 100 mm high. A portable traveling pluviator was used for achieving the desired relative density. By changing the height of the fall, an exact relative density was achieved. This portable pluviator comprised of hopper, reducer, orifice plate, flexible pipe, rigid tube, and diffuser sieves.

Sensor Arrangement

The accelerations and lateral displacement were measured using accelerometers and displacement transducers (LVDT sensors), respectively, at different locations within the Clay layer, geotextile wrapped face wall, and backfill soil. An accelerometer has to attach to the shake table base to measure base acceleration. Six accelerometers, two pore water pressure sensors, four strain gauges, and 3 LVDTs were used in this model test. All the sensors were positioned at predefined locations during the layer by layer construction of the physical model.

Surcharge Load and Relative Density

According to Hossain and Ansary [2018] a portable pluviator was used in this study to achieve a uniform density of the backfill material. Relative density for Sylhet sand 48%, 64%, and 80% and for local sand 27%, 41%, and 55% were achieved by maintaining the height of fall. The sand which used for backfill material was passed ASTM standard sieve number 4 (4.75 mm) and retained at 200 number sieve (0.075 mm).

Input Motions

Results obtained from several shaking table tests on the embankment on soft Clay. The parameters varied in tests are base acceleration, frequency, surcharge pressure, and pore water pressure. The base acceleration kept between 0.05g to 0.2g with frequency between 1 to 5 Hz in different tests. The surcharge pressure were 0.70, 1.12, and 1.72 kPa.

3.3 Numerical Modeling

The PLAXIS 3D software (Brinkgreve and Broere, 2006) which uses quadratic tetrahedral 10-node elements was used for performing the current analyses. In the initial step, the geometry of the model was created in the software. The 0.4 m height wrap faced embankment with a length of 2.6 m was modeled. Detailed description of the numerical model are presented in chapter-5.

CHAPTER 4: EXPERIMENTAL STUDY

4.1 General

Seismic influence on soil structures has occupied an important field, for research in the area of earthquake geotechnical engineering and was found considerable development in the recent past. Two aspects of model testing are given importance, namely a rigid box, and a laminar box. A laminar box is a sophisticated container than a rigid box, which can enhance the accuracy in assessing the ground behavior. In this research, a wrap reinforced soil wall was fabricated on Clayey soil enclosed by a laminar box and subjected to sinusoidal and Earthquake input motions through the shake table. Moreover, the spacing between the reinforcements was kept constant in all shaking table tests. Based on shaking table tests, this thesis attempts to investigate the effect of the frequency and acceleration of the base sinusoidal motion, surcharge pressure, pore water pressure, and horizontal face displacements and strain in wrap-faced retaining walls under simulated seismic conditions. A total of 576 (Five hundred and seventy-six) shaking table tests for harmonic sinusoidal wave and 144 (One hundred and forty-four) for earthquake wave (Kobe and Loma Prieta) were carried out on this model embankment. The model embankment was made by Sylhet and Local sand. The effect of frequency, acceleration amplification, surcharge, and relative density on acceleration amplification, face displacement, pore water pressure, and strain at the different elevations were observed.

4.2. Equipment and Materials

4.2.1 Shaking table

A computer-controlled servo-hydraulic single degree of freedom shaking table facility was used to simulate the horizontal shaking action, associated with seismic and other vibration conditions. The testing platform was a square 2 m by 2 m dimension and an approximate payload capacity of 1500 kg, which was made from steel plates, as shown in Figure 4.1 (a) Shaking was provided by a digitally controlled servo-hydraulic actuator with ±200 mm stroke and 30 KN force rating. Figure 4.1 (b) shows a dedicated control room housing, where the control system included a host computer to facilitate testing under both constant amplitude and pseudo-random conditions. The shaking table can be operated over an acceleration range of 0.05g to 2g and frequency range 0.05 to 50 Hz with a maximum amplitude of ±200 mm.

The maximum velocities are 0.3 m/s. The total operating system was controlled in a dedicated room.

4.2.2 Laminar box

The ideal container is one that gives a seismic response of the soil model identical to that obtained in the prototype. The boundary conditions created by the model container walls have to be considered carefully, otherwise the field conditions cannot be simulated properly. In this study, embankment with soft Clay soil models was constructed in a laminar box to reduce boundary effects as far as practicable. The boundary conditions for physical modeling in problems of earthquake geotechnical engineering have a significant influence on the test results. In order to reduce the undesirable effects of boundaries on the model responses, the laminar shear boxes are used. In laminar shear boxes, the stiffness of the walls is proportional to the stiffness of soil. For increasing the flexibility of the box walls, depending on soil type, model dimensions and the studied phenomena, setting each layer on the other, within the frame made of rigid light material which can easily move on each other. The laminar box was designed according to some criteria such as, the layers and the inside membrane should have a minimum stiffness to horizontal shear; offers little resistance to the vertical settlement of soil; the height of each layer is small which increases the flexibility for the displacement of the soil inside; it is fairly large to better simulate field behavior; possesses the capability to increase confining pressure; maintains its horizontal cross-section during shaking and it develops shear stress on the interface between the soil and the vertical wall equal to that on the horizontal plane. The laminar shear box developed at Bangladesh University of Engineering Technology (BUET) is composed of 24 hollow aluminum layers of frames. Each layer consists of an inner frame with inside dimensions of 915 mm × 1220 mm × 1220 mm. The aluminum alloy was adopted for its sufficient strength and rigidity, and it's lightweight to minimize the effect of the inertia of the frame on the soil movements. The gap between the successive layers was 2 mm, and the most bottom layer was rigidly connected to the solid aluminum baseplate of size 915 mm x 1220 mm in plan and 15 mm thickness. The layers were separated by linear roller bearings arranged to permit relative movement between the layers in the longitudinal direction with minimum friction. The laminar box mounted on the shake table was presented in Figure 4.2 (a).

The Layers

Each layer was a rectangular frame with 1.22 m X 0.92 m X 0.05 m internal dimension, which was made from the hollow aluminum profiles with 50 mm X 50 mm section and 1.5 mm thickness. The whole system was composed of 24 layers, each being set directly on the other making the total height of 1.22 m. In order to minimize the friction between the layers, transfer ball bearings were used so that the two-dimensional motion in the horizontal plane is possible. This ball bearing consists of one main ball having a diameter of 16 mm which was put in a hemispherical space full of fine balls. These balls are designed in a way that they can be simply and without additional devices installed on the surface of the layer, and the base is alighted on the lower wall of the hollow aluminum profile. This makes the balls act as a column between the lower and upper hollow aluminum sections and prevents the surface from being deformed, by the point contact stress between the ball bearing and the surface of the aluminum profile. In order to make the distribution uniform, 12 rotating ball bearing was used in each layer and the gap between the two adjacent layers was 2 mm.

Base Plate and Saturation and Drainage Systems

The lowest layer was fixed on a steel base, which in turn, is fixed on a steel plate with the same dimension of laminar layers. In addition to preserving the upper layers, the base was some space for watering and dewatering via four valves.

Membrane

The third key module of the laminar box is the membrane that lines the inside of the box, as presented in Figure 4.2 (b). The fabric was designed to fold or unfold as the sand moves against it rather than to stretch like a conformist silicone rubber membrane. In the current investigation, a 2 mm thick rubber membrane was placed inside the container for the hydraulic cut-off system and for the protection of the ball bearings.

Portable Pluviator

Many researchers (e.g., Fretti et al. 1995, Zhao et al. 2006, Choi et al. 2010) attempted in developing methods to control uniformity and to achieve desired relative density (Dr) of the sand specimen (Miura and Toki 1982, Rad and Tumey 1987, Lo Presti et al. 1993, Choi et al. 2010, Dave and Dasaka 2012, Srinivasan et al. 2016, Gade et al. 2016). Among these techniques, air pluviation method is preferable because of its advantage to reconstitute uniform sand bed for laboratory testing.

In this study, a portable traveling pluviator developed by Hossain and Ansary (2018), was operated to maintain the different height to obtain the corresponding relative density of sand layer. Relative density for Sylhet sand 48%, 64%, and 80% and for local sand 27%, 41%, and 55% were achieved by maintaining height of fall. The components of the pluviator are shown in Figure 4.2 c). The physical model was prepared with two soil layers—Clayey soil as the lower layer and sandy soil as the upper layer.

4.2.3 Materials used in this study

Clay Soil

Dhaka Clay soil sample was collected from within the premise of BUET campus, from a depth of 5 ft (1.5 m) below the existing ground level. These homogeneous, stiff, reddish-brown samples were at first oven-dried; subsequently, the dry lumps were then powdered gently by using a wooden hammer; and finally sieved through #200 standard sieve to obtain clean Clay powder. Figure 4.3 a) represents the particle size distribution of the clean Clay. The specific gravity G_s of the soil was determined, from the laboratory test, to be 2.72. To identify the mineral composition of Dhaka Clay, X-ray diffraction tests (XRD) were performed, at a scanning speed of 8° (2θ) min-1 by using Ni filtered CuKα radiation. XRD test results were summarized in Figure 4.3 b) and Table 4.1. A careful examination of these data reveals that the predominant mineralogical composition of Dhaka Clay is Kaolinite (75%), followed by Illite (25%). Atterberg limit tests were performed on five representative samples. The average liquid limit (LL) and plastic limit (PL) were established to be 41% and 16% respectively. It was observed that the PL points located above the A-line are defined by PI = 0.73(LL-20), where PI is the plasticity index. The soil was defined as Lean Clay (CL), as per as USCS.

Reconstituted Clay Soil

Burland (1990) was demonstrated that the essential engineering properties of reconstituted Clay—shear strength and compressibility—provides a basis to interpret the corresponding properties of the in-situ natural Clay soil (regardless of it being normally consolidated or overconsolidated).

Table 4.1 Brief description of XRD test

Compound Name	Percent (%) by atomic weight
SiO_2	67.1747
Al_2O_3	15.8718
Fe_2O_3	7.7982
K_2O	3.8247
MgO	1.9221
TiO_2	1.4624
CaO	0.7423
Na_2O	0.6149
P_2O_5	0.1960
SO_3	0.1568
MnO	0.0960
ZrO_2	0.0439
Cr_2O_3	0.0339
Rb_2O	0.0246
ZnO	0.0205
SrO	0.0171

Consequently, in this study, Dhaka Clay was reconstituted by thoroughly mixing the oven-dried Clay powder with an initial water content equal to the LL—a procedure described by Burland (1990). The thorough mixing of the slurry was attained with the aid of a 'Hobart' rotary mixer, as presented in Figure 4.4 a). With this slurry, a 300 mm thick reconstituted Clay layer was constructed in the laminar shear box; and then one-dimensional consolidations were taken place under the drained condition at loads: 15 kPa, 20 kPa, 25 kPa, 30 kPa, 40 kPa, 60 kPa, 80 kPa, and 100 kPa. The consolidation process was observed through the settlement of Clay versus time graph, plotted with the aid of calibrated mechanical dial gauges, instrumented on either side of the laminar shear box. The isotropic condition at loads with sensor arrangement is shown in Figure 4.4 b) and c). The average settlement curve is shown in Figure 4.4 d). This curve shows progressive soil structure collapse, a kind of time-dependent bond weakening in the soil. Moreover, pore water pressure dissipates slowly then due to quicker dissipation settlement increases.

Once the consolidation process was ceased, three undisturbed cylindrical samples were collected from the soil cake from three different locations—it are ensured that the disturbed region does not interfere with the region of collected sample location. From these cylindrical samples, 1.5" by 3" samples were then trimmed before being shifted to the triaxial cell. In addition, the water content (w %) of the collected reconstituted Clay samples were determined to be 27%.

UU triaxial test is suitable for saturated Clay, silt, peat in both undisturbed and remolded or reconstituted sample for providing the actual field conditions. UU triaxial test was performed on the collected soil sample with a shear rate of 1.5 mm/min for each test. The applied confining stresses for the reconstituted Clayey soil samples were 50 kPa and 100 kPa. The value of undrained strength (S_u) was 28 kPa shown in Figure 4.4 (e).

Sandy Soil

The sand was utilized in the construction of the 0.4 m (16") high reinforced soil zone and backfill soil. To investigate its properties, the representative sample was oven-dried and sieved through ASTM standard sieves (Passing sieve #4 and retaining on #200). The resulting particle size distribution (Sylhet and local sand) is shown in Figure 4.5 a) and 4.5 c). From this curve 4.5 a), Coefficient of uniformity Cu, coefficient of curvature Cz, was estimated to be at 3.08 and 0.88 respectively—results indicating a poorly graded, medium to fine sand (SP). Moreover, fineness modulus was determined to be at 2.031 and 0.933 for Sylhet and local sand respectively. Other physical parameters such as Gs and maximum dry density were determined to be 2.65 and 16.6 kN/m^3 respectively. The minimum dry density were determined to be 13.8 KN/m^3. For controlling this density of sand (in the layer by layer staged-construction of the single-tiered geotextile reinforced sand mass), a portable travelling pluviator was developed by Hossain and Ansary (2018), to maintain the different height to obtain corresponding relative density. Relative density for Sylhet sand 48%, 64%, and 80% and for local sand 27%, 41%, and 55% were achieved by maintaining the height of fall. This was achieved by ensuring that sand falls from the pluviator at a predetermined constant height for each layer laterally and longitudinally. The strength parameters were determined using the direct shear test, as seen in Figure 4.5 b) and 4.5 d). The test establishes an internal angle of friction ϕ of 34 and 31° for Sylhet and local sand respectively. Figure 4.5. e) & f) shows Shear Stress versus shear displacement curve of Sylhet and local sand.

Reinforcement

A non-woven polypropylene multifilament geotextile (DF50) was used for reinforcing the sand in the tests as shown in Figure 4.6. The individual multifilament is woven together so as to provide dimensional stability relative to each other. The properties of the geotextile were given in Table 4.2.

Table 4.2: Geotextile specification

Details	DF 50
1. Reinforcement type	mechanically bonded needle punched
2. Yarn material (staple Fibre)	Polypropylene
3. Mass/unit area (gsm)	322
4. Aperture Size , O_{95} (μm)	130
5. Thickness (mm)	2.54
6. Ultimate Tensile Strength (KN/m)	15.5
Ultimate Tensile Strength at 2% strain (KN/m)	15.97
Ultimate Tensile Strength at 5% strain (KN/m)	16.57

The tensile properties of geotextile were determined by using a universal tensile testing machine. Picture of testing machine and clamps used in wide width test are shown in Fig. 4.6 (a). 500 mm × 200 mm sized geotextile sample has been taken for this test as shown in Figure 4.6 (b). The gage length is 100 mm as presented in Figure 4.6 (c). For each X and Y direction, three samples were collected. The test samples were taken from the Supplied Specimen by cutting into the desired size. The clamps were sufficiently wide to grip the entire width of the geotextile sample. The testing machine had two load scales, i.e. 1500 and 600 scales. For wide-width strip, tensile test (ASTM D4595) 1500 scale was used. Elongation of specimens with respect to gradually increased load was measured manually. The load-elongation response of the geotextile was obtained from the wide-width tensile strength test that was conducted in the wrap direction in both X and Y direction is shown in Figure 4.7.

The Average initial modulus (Ei) and secant modulus (Es) in both directions (X and Y) were 0.039, 0.1407 kPa and 0.0467, 0.1230 kPa respectively.

4.3. Model Geometry

4.3.1 Height of clay layer

The present study was conducted with a thickness of 300 mm (12 inches) Clayey soil layer foundation above which a 50 mm (2 inches) sand blanket was provided, as shown in Figure 4.8. This Clayey soil layer reflects the height limitation of the laminar box and the total weight of the model. Approximately 1 m^2 geotextile was placed between the Clayey soil foundation and sand blanket. The toe boundary of the wall can be horizontally free sliding due to the wall was constructed on the surface of the foundation and none of the reinforced-soil layers was concealed in the foundation layer. The height of the Clayey soil layer of 300 mm (12 inches) was made in three 100 mm (4 inches) layers. Considering the prototype to model scale being N=10 and scale factor 1/N, the height of the prototype was 3 m (10 ft). After the Clay model has been placed, a CPT test was conducted as shown in Figure 4.9 to ascertain its properties. The placement of the third layer of Clayey soil is shown in Figure 4.10.

4.3.2 Wall height and layers

Wall height is a significant factor governing scale effects and the reaction of the model in contrast with the prototype. Better results were found with the higher height of the sand wall. The average height of traditional walls usually ranges from 4.5 to 5 m (Sabermahani et al. 2009). A 400 mm (16 inches) high model with a scale factor of 10 was fabricated for this current study.

Many shake table tests, on the different height of the sand wall, such as 1.5 m (Sakaguchi et al. 1992; Sakaguchi 1996), 1 m (Matsuo et al. 1998; El-Emam and Bathurst 2007), 0.6 m (Krishna and Latha 2007), 0.33 m (Richardson and Lee 1975) were performed at a various time. The schematic geometry of the experimental model for this study is shown in Figure 4.8. The sand wall consisted of 4 layers and each layer was 100 mm (4 inches) high. A concrete block was placed at the top of the upper layer of the wall after the full construction of four layers as shown in Figure 4.11.

4.3.3 Facing type

Wrap-around type wall facing was used with flexible geotextile as shown in Figure 4.11. It allowed free movement of the reinforcing enclosure and had no interaction with the rigid bottom. As per Koerner (1999), each individual facing was formed by wrapping each layer with soft flexible geotextile element. The extended geotextile was anchored by partial burial at the end by backfill material as shown in Figure 4.8. Approximately 1 m^2 geotextile was placed between the Clayey soil foundation and sand blanket. The total length of the geotextiles wrap-around is 1.10 meters.

4.3.4. Sensor arrangement

The accelerations and lateral displacement were measured using accelerometers and displacement transducers (LVDT sensors), respectively at different locations within the Clayey soil layer, geotextile wrapped face wall and backfill soil. An accelerometer was attached to the shake table base to measure base acceleration. Six accelerometers (A1, A2, A3, A4, A5, and A6), two pore water pressure sensors (P1 and P2), four strain gauges (Sg1, Sg2, Sg3 and Sg4), and three linear variable differential transformers (LVDT1, LVDT2 and LVDT3) were used in this model test. All the sensors were positioned at predefined locations during the layer by layer construction of the physical model. One accelerometer, A1, is fixed to the shake table to record the base acceleration. Moreover, the other five accelerometers A2, A3, A4, A5, and A6 were placed at elevations 457 mm (18 inches), 710mm (28 inches), 810 mm (32 inches), 915mm (36 inches), and 1015mm (40 inches) mm, respectively, from the base, are shown in Figure 4.8. A3, A4, A5, and A6 were positioned at a constant distance of 100 mm (4 inches) from the middle of each sand slice. Two pore water pressure sensors; P1 and P2, where P1 was set at the base of the Clayey soil layer and P2 was positioned at elevation 457 mm (18 inches) from the base is presented in Figure 4.8. The pore water pressure sensor (P2) was placed at the height of 457 mm (18 inches) from the base. However, it was placed to maintain 254 mm (10 inches) horizontal distance from the left face of the laminar box is shown in Figure 4.12. Strain gauges were attached with geotextile. Sg1 was placed at the bottom of the first layer which was just above the sand blanket. However, other three strain gauges Sg2, Sg3 and Sg4 were placed at elevation 100 mm (4 inches), 200 mm (8 inches), 300 mm (12 inches), respectively from the sand blanket at a constant distance of 100 mm (4 inches) from the bottom facing of each layer is depicted in Figure 4.8. The wire that was attached with strain gauges finally was connected to the board which was directly linked to the digital data logger, as shown in Figure 4.13. Three displacement transducers (LVDT1, LVDT2, and LVDT3) were placed at elevations 150 mm (6 inches), 250 mm (10 inches) and 350 mm (14 inches), respectively from the sand blanket along the facing is depicted in Figure 4.14 to measure horizontal displacement. LVDTs were positioned in place using a T-shaped bracket and it can be seen from Figure 4.15 that it was rigidly connected to the laminar box frame and base.

4.3.5. Surcharge load and relative density

Three different types-0.7, 1.12, and 1.72 kPa surcharge loads were employed in this study. The surcharge load was made in the form of a concrete slab as shown in Figure 4.16. The dimension and weight of each surcharge were 24"×18"×3" (61 cm×46 cm×7.5 cm), 24"×18"×2" (61 cm×46 cm×5 cm) and 24"×18"×1" (61 cm×46 cm×2.5 cm) and 49, 34 and 19.9 kg respectively. After completion of all the layer construction and sensor arrangement in predefined location 0.05g, 0.1g, 0.15g, and 0.2g acceleration-based sinusoidal waves were applied to the model for each surcharge load.

A portable pluviator was used in this study to achieve uniform density of the backfill material as described in Hossain and Ansary (2018). Relative density for Sylhet sand 48%, 64%, and 80% and for local sand 27%, 41%, and 55% were achieved by maintaining height of fall. Relative density was achieved by maintaining 20 cm height of fall as presented in Figure 4.17 and 4.18. The sand used for backfill material was passed ASTM standard sieve number 4 (4.75 mm) and was retained at 200 number sieve (0.075 mm).

4.4. Prototype-Model Similitude

The model size in this present study was fixed according to the facilities obtainable for this test. Considering the stress-dependent behavior of the soil and boundary conditions, precise scaling of soil wall and reinforcement properties was mandatory. 1-g Shake table type of testing was performed to satisfy the similitude requirements between model and prototype, consequently the behavior of the prototype structure can be predicted accurately. Even if the model is properly scaled to achieve similitude with the prototype wall, in low stress limiting 1-g shake table tests is not possible to guess the accurate behavior of the prototype with compare to the reinforced model wall (Sabermahani et al., 2009; Latha and Krishna, 2008 and Krishna and Latha, 2007). Scaling of tensile strength-strain behavior and modeling of the bond between soil and geotextile these two similitude requirements have to be fulfilled as addressed by Viswanadham and Mahajan (2007). Table 4.3 presents the scaling factors for this study assuming, $\alpha = 0.5$ for sand (Kokusho, 1980; Yu and Richart, 1984) and considering the prototype to model scale being N = 10.

Table 4.3: Scale factors for Prototype-Model Similitude (Kokusho, 1980; Yu and Richart, 1984)

Description	Parameter	Scale factor	Scale factor M/P	Scale factor P/M
Acceleration	a	1	1	1
Density	ρ	1	1	1
Length	L	1/N	0.10	10
Stress	σ	1/N	0.10	10
Strain	ε	$1/N^{1-\alpha}$	0.32	3.125
Stiffness	G	$1/N^{\alpha}$	0.32	3.125
Displacement	d	$1/N^{2-\alpha}$	0.031	32.25
Frequency	f	$N^{1-\alpha/2}$	5.62	0.18
Force	F	$1/N^3$	0.001	1000
Force/L	F/L	$1/N^2$	0.01	100
Shear Wave velocity	V_s	$1/N^{\alpha/2}$	0.56	1.785
Time	t	$1/N^{1-\alpha/2}$	0.178	5.62
***P-Prototype; M-Model**				

4.5. Fundamental Frequency

As physical models are shorter versions of prototype walls, the frequency of induced input motions should be scaled accurately to produce similar effects to those of earthquakes on prototype walls. It is an essential phase in the seismic design to determine the natural frequencies of the structure. Reinforced-soil retaining walls of typical heights (e.g., H > 10 m) and backfill material is generally considered as short-period structures as addressed by

Sabermahani et al. (2009). Therefore, the response of the wall to ground motion is dominated by the fundamental frequency of the structure (Hatami and Bathurst, 2000). In the present study, the fundamental frequency of wall models was calculated based on impact tests performed before the first shaking of actual tests. Latha and Krishna (2008) stated that the resonant frequency of the walls changes significantly with the height of the wall.

4.6. Input Motions

Sabermahani et al. (2009) cited from different researchers, (El-Emam and Bathurst, 2007; Bathurst and Hatami, 1998 and Matsuo et al., 1998) that this harmonic sinusoidal base acceleration has more aggressiveness than an archetypal earthquake with the same predominant frequency and amplitude. Harmonic sinusoidal type of base acceleration was used for this current parametric study. Sabermahani et al. (2009) has quoted according to Kramer (1996) and Bathurst and Hatami (1998) that wall response is critically dependent on the base frequency of the structure and the range of the applied frequencies should be kept in a range distant from the fundamental frequency of the walls to avoid resonance. As the fundamental frequency of the model wall was 16 Hz, physical models were subjected to 1, 2, 3, 5, 8, 10, 12, and 15 Hz frequency as input motions. Based on the scale factor of frequency was demonstrated in Table 4.3, these values were corresponding to 0.18, 0.36, 0.54, 0.89, 1.42, 1.78, 2.14, and 2.67 Hz frequencies for the prototype. Since frequencies of 2–3 Hz are representative of typical medium to high-frequency earthquakes (Bathurst and Hatami, 1998), the 5 to 15 Hz were applied frequencies fall within the realistic range. The duration of each shaking was employed for at least 5 seconds. Exactly 576 numbers of harmonic sinusoidal shaking were applied for this research as presented in Table 4.4 and Table 4.5. The embankment model was subjected to several different excitations from 0.05g (low amplitude) to 0.2g (high amplitude) peak base accelerations, each being applied after the termination of the previous motion. For each frequency (1-5 Hz) and surcharge pressures (0.70, 1.12, and 1.72 kPa), a specific base acceleration was achieved through changing the input amplitude. In the case of a sinusoidal wave, total of 288 nos. of the test have been performed for Sylhet sand as shown in Table 4.4. on the other hand, total of 288 nos. of the test are performed for local sand as shown in Table 4.5. In the case of earthquake wave (Kobe and Loma Prieta), a total 144 (36*4) nos. of the test are performed for Sylhet and Local sand as shown in Table 4.6, 4.7, 4.8 and 4.9.

Table 4.4 Brief description of two 288 tests- Sylhet sand

Name of Tests	Base Acceleration a_{max} (g)	Frequency (Hz)	Relative Density (%)	Surcharge (kPa)	Remarks
ST1*-ST8*	0.05	1, 2, 3, 5, 8, 10, 12 and 15	48	1.72	
ST9*-ST18	0.10	1, 2, 3, 5, 8, 10, 12 and 15			
ST19*-ST26	0.15	1, 2, 3, 5, 8, 10, 12 and 15			
ST27*-ST34	0.20	1, 2, 3, 5, 8, 10, 12 and 15			ST32*
ST35*-ST42	0.05	1, 2, 3, 5, 8, 10, 12 and 15	48	1.12	
ST43-ST50	0.10	1, 2, 3, 5, 8, 10, 12 and 15			ST47*
ST51-ST58	0.15	1, 2, 3, 5, 8, 10, 12 and 15			
ST59-ST66	0.20	1, 2, 3, 5, 8, 10, 12 and 15			ST64*
ST67*-ST74	0.05	1, 2, 3, 5, 8, 10, 12 and 15	48	0.70	ST72*
ST75-ST82	0.10	1, 2, 3, 5, 8, 10, 12 and 15			ST 80*
ST83-ST90	0.15	1, 2, 3, 5, 8, 10, 12 and 15			ST88*
ST91*-ST98*	0.20	1, 2, 3, 5, 8, 10, 12 and 15			
ST99-ST106	0.05	1, 2, 3, 5, 8, 10, 12 and 15	64	1.72	ST102*
ST107-ST114	0.10	1, 2, 3, 5, 8, 10, 12 and 15			

Name of Tests	Base Acceleration a_{max} (g)	Frequency (Hz)	Relative Density (%)	Surcharge (kPa)	Remarks
ST115-ST122	0.15	1, 2, 3, 5, 8, 10, 12 and 15			
ST123-ST130	0.20	1, 2, 3, 5, 8, 10, 12 and 15			
ST131-ST138	0.05	1, 2, 3, 5, 8, 10, 12 and 15	64	1.12	
ST139-ST146	0.10	1, 2, 3, 5, 8, 10, 12 and 15			ST143*
ST147-ST152	0.15	1, 2, 3, 5, 8, 10, 12 and 15			
ST153-ST160	0.20	1, 2, 3, 5, 8, 10, 12 and 15			
ST161-ST168	0.05	1, 2, 3, 5, 8, 10, 12 and 15	64	0.70	
ST169-ST176	0.10	1, 2, 3, 5, 8, 10, 12 and 15			
ST177-ST184	0.15	1, 2, 3, 5, 8, 10, 12 and 15			
ST185-ST192	0.20	1, 2, 3, 5, 8, 10, 12 and 15			ST190*
ST193*-ST200*	0.05	1, 2, 3, 5, 8, 10, 12 and 15	80	1.72	
ST201*-ST208	0.10	1, 2, 3, 5, 8, 10, 12 and 15			
ST209*-ST216	0.15	1, 2, 3, 5, 8, 10, 12 and 15			
ST217*-ST224	0.20	1, 2, 3, 5, 8, 10, 12 and 15			
ST225*-ST232	0.05	1, 2, 3, 5, 8, 10, 12 and 15	80	1.12	

Name of Tests	Base Acceleration a_{max} (g)	Frequency (Hz)	Relative Density (%)	Surcharge (kPa)	Remarks
ST233-ST240	0.10	1, 2, 3, 5, 8, 10, 12 and 15			ST237*
ST241-ST248	0.15	1, 2, 3, 5, 8, 10, 12 and 15			
ST249-ST256	0.20	1, 2, 3, 5, 8, 10, 12 and 15			
ST257*-ST264	0.05	1, 2, 3, 5, 8, 10, 12 and 15	80	0.70	
ST265-ST272	0.10	1, 2, 3, 5, 8, 10, 12 and 15			
ST273-ST280	0.15	1, 2, 3, 5, 8, 10, 12 and 15			
ST281-ST288	0.20	1, 2, 3, 5, 8, 10, 12 and 15			ST286*

*PLAXIS 3D Analysis

Table 4.5 Brief description of two 288 tests- Local sand

Name of Test	Base Acceleration a_{max} (g)	Frequency (Hz)	Relative Density (%)	Surcharge (kPa)	Remarks
LT1*-LT8*	0.05	1, 2, 3, 5, 8, 10, 12 and 15	27	1.72	
LT9*-LT18	0.10	1, 2, 3, 5, 8, 10, 12 and 15			
LT19*-LT26	0.15	1, 2, 3, 5, 8, 10, 12 and 15			
LT27*-LT34	0.20	1, 2, 3, 5, 8, 10, 12 and 15			LT32*

Name of Test	Base Acceleration a_{max} (g)	Frequency (Hz)	Relative Density (%)	Surcharge (kPa)	Remarks
LT35*-LT42	0.05	1, 2, 3, 5, 8, 10, 12 and 15	27	1.12	
LT43-LT50	0.10	1, 2, 3, 5, 8, 10, 12 and 15			LT47*
LT51-LT58	0.15	1, 2, 3, 5, 8, 10, 12 and 15			
LT59-LT66	0.20	1, 2, 3, 5, 8, 10, 12 and 15			LT64*
LT67*-LT74	0.05	1, 2, 3, 5, 8, 10, 12 and 15	27	0.70	LT72*
LT75-LT82	0.10	1, 2, 3, 5, 8, 10, 12 and 15			LT 80*
LT83-LT90	0.15	1, 2, 3, 5, 8, 10, 12 and 15			LT88*
LT91*-LT98*	0.20	1, 2, 3, 5, 8, 10, 12 and 15			LT96*
LT99-LT106	0.05	1, 2, 3, 5, 8, 10, 12 and 15	41	1.72	LT102*
LT107-LT114	0.10	1, 2, 3, 5, 8, 10, 12 and 15			
LT115-LT122	0.15	1, 2, 3, 5, 8, 10, 12 and 15			
LT123-LT130	0.20	1, 2, 3, 5, 8, 10, 12 and 15			
LT131-LT138	0.05	1, 2, 3, 5, 8, 10, 12 and 15	41	1.12	
LT139-LT146	0.10	1, 2, 3, 5, 8, 10, 12 and 15			LT143*
LT147-LT152	0.15	1, 2, 3, 5, 8, 10, 12 and 15			

Name of Test	Base Acceleration a_{max} (g)	Frequency (Hz)	Relative Density (%)	Surcharge (kPa)	Remarks
LT153-LT160	0.20	1, 2, 3, 5, 8, 10, 12 and 15			
LT161-LT168	0.05	1, 2, 3, 5, 8, 10, 12 and 15	41	0.70	
LT169-LT176	0.10	1, 2, 3, 5, 8, 10, 12 and 15			
LT177-LT184	0.15	1, 2, 3, 5, 8, 10, 12 and 15			
LT185-LT192	0.20	1, 2, 3, 5, 8, 10, 12 and 15			LT190*
LT193*-LT200*	0.05	1, 2, 3, 5, 8, 10, 12 and 15	55	1.72	
LT201*-LT208	0.10	1, 2, 3, 5, 8, 10, 12 and 15			
LT209*-LT216	0.15	1, 2, 3, 5, 8, 10, 12 and 15			
LT217*-LT224	0.20	1, 2, 3, 5, 8, 10, 12 and 15			
LT225*-LT232	0.05	1, 2, 3, 5, 8, 10, 12 and 15	55	1.12	
LT233-LT240	0.10	1, 2, 3, 5, 8, 10, 12 and 15			LT237*
LT241-LT248	0.15	1, 2, 3, 5, 8, 10, 12 and 15			
LT249-LT256	0.20	1, 2, 3, 5, 8, 10, 12 and 15			
LT257*-LT264	0.05	1, 2, 3, 5, 8, 10, 12 and 15	55	0.70	
LT265-LT272	0.10	1, 2, 3, 5, 8, 10, 12 and 15			

Name of Test	Base Acceleration a_{max} (g)	Frequency (Hz)	Relative Density (%)	Surcharge (kPa)	Remarks
LT273-LT280	0.15	1, 2, 3, 5, 8, 10, 12 and 15			
LT281-LT288	0.20	1, 2, 3, 5, 8, 10, 12 and 15			LT286*

*PLAXIS 3D Analysis

Table 4.6 Kobe earthquake for Sylhet sand

Name of Tests	Base Acceleration $a_{max}(g)$	Relative Density (%)	Surcharge (kPa)
KST1*	0.05	48	1.72
KST2*	0.10		
KST3*	0.15		
KST4*	0.20		
KST5*	0.05	48	1.12
KST6	0.10		
KST7	0.15		
KST8	0.20		
KST9*	0.05	48	0.70
KST10	0.10		
KST11	0.15		
KST12	0.20		
KST13	0.05	64	1.72
KST14*	0.10		
KST15	0.15		
KST16	0.20		
KST17	0.05	64	1.12
KST18	0.10		
KST19	0.15		

Name of Tests	Base Acceleration $a_{max}(g)$	Relative Density (%)	Surcharge (kPa)
KST20	0.20		
KST21	0.05	64	0.70
KST22	0.10		
KST23	0.15		
KST24	0.20		
KST25	0.05	80	1.72
KST26*	0.10		
KST27	0.15		
KST28	0.20		
KST29	0.05	80	1.12
KST30	0.10		
KST31	0.15		
KST32	0.20		
KST33	0.05	80	0.70
KST34	0.10		
KST35	0.15		
KST36	0.20		

* PLAXIS 3D Analysis

Table 4.7 Kobe earthquake for Local sand

Name of Test	Base Acceleration $a_{max}(g)$	Relative Density (%)	Surcharge (kPa)
KLT1*	0.05	27	1.72
KLT2*	0.10		
KLT3*	0.15		
KLT4*	0.20		
KLT5*	0.05	27	1.12
KLT6	0.10		
KLT7	0.15		

Name of Test	Base Acceleration $a_{max}(g)$	Relative Density (%)	Surcharge (kPa)
KLT8	0.20		
KLT9*	0.05	27	0.70
KLT10	0.10		
KLT11	0.15		
KLT12	0.20		
KLT13	0.05	41	1.72
KLT14*	0.10		
KLT15	0.15		
KLT16	0.20		
KLT17	0.05	41	1.12
KLT18	0.10		
KLT19	0.15		
KLT20	0.20		
KLT21	0.05	41	0.70
KLT22	0.10		
KLT23	0.15		
KLT24	0.20		
KLT25	0.05	55	1.72
KLT26*	0.10		
KLT27	0.15		
KLT28	0.20		
KLT29	0.05	55	1.12
KLT30	0.10		
KLT31	0.15		
KLT32	0.20		
KLT33	0.05	55	0.70
KLT34	0.10		
KLT35	0.15		
KLT36	0.20		

*PLAXIS 3D Analysis

Table 4.8 Loma Prieta earthquake for Sylhet sand

Name of Tests	Base Acceleration $a_{max}(g)$	Relative Density (%)	Surcharge (kPa)
LST1*	0.05	48	1.72
LST2*	0.10		
LST3*	0.15		
LST4*	0.20		
LST5*	0.05	48	1.12
LST6	0.10		
LST7	0.15		
LST8	0.20		
LST9*	0.05	48	0.70
LST10	0.10		
LST11	0.15		
LST12	0.20		
LST13	0.05	64	1.72
LST14*	0.10		
LST15	0.15		
LST16	0.20		
LST17	0.05	64	1.12
LST18	0.10		
LST19	0.15		
LST20	0.20		
LST21	0.05	64	0.70
LST22	0.10		
LST23	0.15		
LST24	0.20		
LST25	0.05	80	1.72
LST26*	0.10		
LST27	0.15		
LST28	0.20		

Name of Tests	Base Acceleration $a_{max}(g)$	Relative Density (%)	Surcharge (kPa)
LST29	0.05	80	1.12
LST30	0.10		
LST31	0.15		
LST32	0.20		
LST33	0.05	80	0.70
LST34	0.10		
LST35	0.15		
LST36	0.20		

*PLAXIS 3D Analysis

Table 4.9 Loma Prieta earthquake for local sand

Name of Test	Base Acceleration $a_{max}(g)$	Relative Density (%)	Surcharge (kPa)
LLT1*	0.05	27	1.72
LLT2*	0.10		
LLT3*	0.15		
LLT4*	0.20		
LLT5*	0.05	27	1.12
LLT6	0.10		
LLT7	0.15		
LLT8	0.20		
LLT9*	0.05	27	0.70
LLT10	0.10		
LLT11	0.15		
LLT12	0.20		
LLT13	0.05	41	1.72
LLT14*	0.10		
LLT15	0.15		

Name of Test	Base Acceleration $a_{max}(g)$	Relative Density (%)	Surcharge (kPa)
LLT16	0.20		
LLT17	0.05	41	1.12
LLT18	0.10		
LLT19	0.15		
LLT20	0.20		
LLT21	0.05	41	0.70
LLT22	0.10		
LLT23	0.15		
LLT24	0.20		
LLT25	0.05	55	1.72
LLT26*	0.10		
LLT27	0.15		
LLT28	0.20		
LLT29	0.05	55	1.12
LLT30	0.10		
LLT31	0.15		
LLT32	0.20		
LLT33	0.05	55	0.70
LLT34	0.10		
LLT35	0.15		
LLT36	0.20		

*PLAXIS 3D Analysis

4.7 Summary

The procedure of shake table test was described in this chapter. The dynamic response like acceleration, displacement, strain and pore water pressure of wrap-faced reinforced soil retaining wall on soft Clay were estimated using the shake table test. The test results were verified through numerical modeling (PLAXIS 3D) in the next chapter.

CHAPTER 5
NUMERICAL ANALYSIS

5.1 General

The numerical analysis is the design and analysis of techniques to give approximate but accurate solutions to critical problems. PLAXIS is a finite element package that was developed specifically for the analysis of displacement, stability, and flow in geotechnical engineering projects. The PLAXIS 3D software (Brinkgreve and Broere, 2006) which uses quadratic tetrahedral 10-node elements, was used for performing the current analyses. The simple graphical input procedures enable a quick generation of complex finite element models, and the enhanced output facilities provide a detailed presentation of computational results. The calculation itself is fully automated and based on robust numerical procedures.

5.2 Construction of a Wrap Faced Embankment

The construction of an embankment on soft soil with a high groundwater level leads to an increase in pore pressure. As a result of this undrained behavior, the effective stress remains low and intermediate consolidation periods have to be adopted in order to construct the embankment safely. During consolidation, the excess pore pressures dissipate so that the soil can obtain the necessary shear strength to continue the construction process.

This research concerns the construction of a wrap faced embankment in which the mechanism of physical modeling described in the previous chapter is analyzed in detail.

Numerical analysis of wrap faced embankment was carried out in this chapter.

Modeling sequences are as follows:

1. Definition of soil stratigraphy
2. Definition of the embankment
3. Mesh generation
4. Performing calculation

5.3 Geometry

The embankment was 0.9 m wide. The wrap faced embankment was totally vertical. The problem was symmetric, so only one half is modeled (in this case, the right half is chosen). A representative section of 0.2 m width was considered in this research. The embankment itself was composed of sandy soil on top of the soft Clay soil. The subsoil consists of 0.3 m of soft soil. The 0.3 m of this soft soil layer was modeled as Clay. The phreatic level was located 0.35 m below the original ground surface. An title as wrap faced embankment model was set from the Quick select dialog box. Model dimension was set as follows $x_{min} = 0$, $x_{max} = 2.6$, $y_{min} = 0$ and $y_{max} = 0.2$. Boundary condition of the model are shown in Table 5.1 (a). Figure 5.1 shows the model tabsheet of the project properties window.

5.4 Definition of Soil Stratigraphy

The soil layers comprising the embankment foundation were defined using a borehole. The wrap embankment layers were defined in the Structures mode. A borehole was created by clicking at (0 0 0). Two soil layers were defined as shown in Figure 5.2. Soil material data sets were created according to Table 5.1 (b) and assigned them to the corresponding layers in the borehole (Figure 5.2). Also, the geotextile property was set according to Figure 5.3 and 5.4. The water level was located at z = -0.35 m. In the borehole, the column specifies a value of -0.35 to Head.

5.5 Definition of Structural Elements

In this section, the structure element was defined. The geotextile layer was modeled and defined their properties. To model geotextile, initially a poly curve was drawn. To draw poly curve, four-segment were created separately. The segment type and properties are shown in Table 5.2.

After creating the polyline, polyline was selected for extrusion assign value 0.2. Then the extrude object button was the click. The geotextile layer is shown in Figure 5.3. After creating a geotextile layer, this layer was selected and provided geotextile properties. In PLAXIS the geotextile was introduced as a tensile element. In the software structural element is selected for introducing the geotextile layer. The axial stiffness of the geotextile reinforcement used is 1000 kN/m.

Table 5.1 (a) Boundary condition of the model

Location	Boundary Limits	$X_{min.}$	$X_{max.}$	$Y_{min.}$	$Y_{max.}$	$Z_{min.}$	$Z_{max.}$
Clay layer	X=0 to 2.6 m Y=0 to 0.2 m Z=-0.35 to -0.05 m	Free	Free	Fixed	Fixed	Fixed	Free
Sand layer	X=0 to 2.6 m Y=0 to 0.2 m Z=-0.05 m to 0	Free	Free	Fixed	Fixed	Free	Free
Bottom (Wrap faced)	X=0 to 0.45 m Y=0 to 0.2 m Z=0 to 0.1 m	Free	Free	Fixed	Fixed	Free	Free
Middle 1 (Wrap faced)	X=0 to 0.45 m Y=0 to 0.2 m Z=0.1 to 0.2 m	Free	Free	Fixed	Fixed	Free	Free
Middle 2 (Wrap faced)	X=0 to 0.45 m Y=0 to 0.2 m Z=0.2 to 0.3 m	Free	Free	Fixed	Fixed	Free	Free
Top (Wrap faced)	X=0 to 0.45 m Y=0 to 0.2 m Z=0.3 to 0.4 m	Free	Free	Fixed	Fixed	Free	Free

The interface element was used to model the interaction of sand-geotextile layers. The properties of the geotextile layer are shown in Figure 5.4. A surface was created as boundary of surface as (0, 0, 0) (0.45, 0, 0) (0.45, 0.2, 0) (0, 0.2, 0). The extraction vector of the surface was 0.1 meter. After extraction, set the materials properties as a sand layer.

Table 5.1 (b) Material properties of the road embankment and subsoil

Parameter	Name	Sylhet Sand	Clay	Unit
General				
Material model	*Model*	Hardening soil	Soft soil	-
Drainage type	*Type*	Drained	Under.	-
Soil unit weight above the phreatic level	γ_{unsat}	15.0, 15.5 and 16.0	15	kN/m^3
Initial void ratio	e_o	0.63, 0.68 and 0.73	0.71	-
Parameters				
Secant stiffness in standard drained	E_{50}^{ref}	25.0* 10^3	-	kN/m^2
Tangent stiffness for primary oedometer loading	E_{oed}^{ref}	25.0* 10^3	-	kN/m^2
Unloading / reloading stiffness	E_{ur}^{ref}	75.0* 10^3	-	kN/m^2
Power for stress-level dependency of stiffness	*m*	0.5	-	-
Modified compression index	λ	-	0.16	-
Modified swelling index	*K*	-	0.03	-
Cohesion	*C*	2.0	28.0	kN/m^2
Friction angle	*Φ*	30, 34 and 38	1.0	O
Dilatancy angle	Ψ	4.0	0.0	0
Advanced: Set to	-	Yes	Yes	-
Groundwater				
Data set	-	USDA	USDA	-
Model	-	Van Genuchten	Van Genuchten	-
Soil type	-	Sand	Clay	-
< 0.002mm	-	0.0	49.0	%
0.002 – 0.05mm	-	0.0	18.0	%
0.05 - 2mm	-	100.0	33.0	%
Set to default	-	Yes	Yes	-
Horizontal permeability (x-direction)	k_x	25.92	0.07	m/day
Horizontal permeability (y-direction)	k_y	25.92	0.07	m/day
Vertical permeability	K_z	25.92	0.07	m/day

Parameter	Name	Sylhet Sand	Clay	Unit
Change of permeability	C_k	1- 10^{15}	0.2	-
Interfaces				
Interface strength	-	Rigid	Rigid	-
Strength reduction factor		1.0	1.0	-
Initial				
Ko determination	-	Automatic	Automatic	-
Over-consolidation	*OCR*	1.0	1.0	-
Pre-overburden	*POP*	0.0	0.0	kN/m^2

Table 5.2 Segments composing the poly curve

Segment	Segment-1	Segment-2	Segment-3	Segment-4
Segment Type	Line	Arc	Line	Line
Segment properties	Relative start angle= 0° Length=0.35 m	Relative start angle= 0° Radius=0.05 m Segment angle= 180°	Relative start angle= 30° Length=0.025 m	Relative start angle= 30° Length=0.35 m

After completing the geotextile layer and soil layer, another three-layer of wrap faced were created using the array option. The process of the array is shown in Figure 5.5. Then Create Surface tab was a click. From the command tab, put the value the boundary of surface Another surface was created as (0, 0, 0.4) (0.45, 0, 0.4) (0.45, 0.2, 0.4) (0, 0.2, 0.4) and provided the corresponding surface load. Then geotextile layer, 0.05 m below the embankment was provided. The coordinate of the geotextile layer was (0, 0, -0.05) (2.6, 0, -0.05) (2.6, 0.2, -0.05) (0, 0.2, -0.05) by applying create surface tab. After selecting the individual geotextile layer, a negative and positive interface was provided. The material mode was also selected as adjacent soil & permeable. Another new surface was created as (0, 0, -0.35) (0.45, 0, -0.35) (0.45, 0.2, -0.35) (0, 0.2, -0.35) for defining the dynamic multipliers. Figure 5.6 shows whole structural element.

Definition of Dynamic Multipliers

Dynamic loads were defined on the basis of input values of loads or prescribed displacements and corresponding time-dependent multipliers. The load multipliers tab was selected for providing different dynamic parameters such as amplitude, phase and frequency. Harmonic signal with a suitable Amplitude a Frequency and a Phase of 0° were defined as shown in Figure 5.7.

5.6 Mesh Generation

For the mesh generation, proceed to the Mesh mode. Total volumes of the structure were selected, including the embankment. The Coarseness factor was 0.3. Mash options are shown in Figure 5.8 The resulting mesh was found by applying to generate the mesh. The element distribution was Coarse. The resulting mesh is shown in Figure 5.9. The resulting mesh is also shown in Figure 5.10.

5.7 Performing Calculations

The initial phase and seven different phases were defined for performing the calculation. Phase 7 was in a dynamic condition. Construction profile is shown in Figure 5.11.

5.7.1 Initial phase

In the initial situation, the embankment was not present. Therefore, the corresponding soil volumes were deactivated in the initial phase. The K_O procedure was used to calculate the initial stresses. The initial water pressures were fully hydrostatic and based on a general phreatic level defined by the head value assigned to the boreholes. For the initial phase, the Phreatic option was selected for the pore pressure calculation type and the Global water level has been set to BoreholeWaterlevel_1 corresponding to the water level defined by the heads specified for the boreholes. The boundary conditions for flow as specified in the Model conditions subtree in the Model Explorer. In the current situation, the left vertical boundary (Xmin) was closed because of symmetry, so horizontal flow has not occurred. The bottom was opened as the excess pore pressures freely flow into the deep and permeable sand layer. The upper boundary was opened. Defining the initial phase was given in Figure 5.12.

Phase 1

A new phase was added. The default setting of the added phase was used for this calculation phase. The calculation type was selected as plastic. Reset displacement to zero was selected for the displacement control parameters. Defining phase 1 is shown in figure 5.13. In the stage construction mode, the Clay layer and first layer of sand were activated as shown in Figure 5.14. The static and dynamic load was not activated in this phase.

Phase 2

Parameters inputting of Phase 2 was the same as phase 1. In the stage construction mode, the Clay layer, 0.05 m sand layer and also first layer of wrap faced embankment were activated as shown in Figure 5.15. The static and dynamic loads were not activated in this phase.

Phase 3

In the stage construction mode, the Clay layer, 0.05 m sand layer and also first & second layer of wrap faced embankment were activated as shown in Figure 5.16. The static and dynamic loads were activated.

Phase 4

In the stage construction mode, the Clay layer, 0.05 m sand layer and also first to the third layer of wrap faced embankment were activated as shown in Figure 5.17. The static and dynamic loads were not activated.

Phase 5

In the stage construction mode, the Clay layer, 0.05 m sand layer and also first to the fourth layer of wrap faced embankment was activated (Figure 5.18). The static and dynamic loads were not activated.

Phase 6

In the stage construction mode, the Clay layer, 0.05 m sand layer and also first to the fourth layer of wrap faced embankment were activated as shown in Figure 5.19. The static surface was also activated. On the other hand, the dynamic load was not activated.

Phase 7

In the stage construction mode, the Clay layer, 0.05 m sand layer and also first to the fourth layer of wrap faced embankment were activated as shown in Figure 5.20. The static surface and dynamic loads were also activated. Defining phase 7 is shown in Figure 5.21 (a).

After defining the phase 1 to phase 7, The definition of the calculation phases was completed. Before starting the calculation, the following points: (0.4, 0.1, 0.05) (0.4, 0.1, 0.15) (0.4, 0.1, 0.25) (0.4, 0.1, 0.35) were selected. The calculation progress displayed is shown in Figure 5.21 (b) in the active tasks window.

5.8 Viewing the Results

After the calculation finished, the seventh phase was selected. The output window showed the deformed mesh after the undrained construction of the final part of the embankment, as shown in Figure 5.22. Considering the results of the seventh phase, the deformed mesh showed the uplift of the embankment toe and hinterland due to undrained behavior.

In the displacement's menu, the incremental displacement was selected. On the evaluation of the total displacement increments, a failure mechanism is shown in Figure 5.23. The different output results are shown in Figure 5.24 & 5.25.

The curves manager button in the toolbar was selected. For the X-axis, the project option from the drop-down menu and dynamic time in the tree was selected. For the Y axis, the point from the drop-down menu was selected. In the tree, displacement/stress/pore water pressure/ acceleration was selected. The phases 1 to 7 in the appearing window were also selected. The curve generation process was shown in Figure 5.26 & 5.27.

5.9 Summary

Currently, the seismic designs of the highway or railway embankment rely on little to no empirical data for calibrating numerical simulations. This research is working towards filling that empirical data gap. By applying numerical analysis (PLAXIS 3D) will be able to validate the shake table data.

CHAPTER 6

RESULTS AND DISCUSSION

6.1 General

In this chapter, the results obtained from the experiments (Shaking table test) and numerical analysis (PLAXIS 3D) were studied and compared. Results obtained from several shaking table tests (576 nos.) on the embankment with soft Clayey soil model were discussed in this section. The parameters varied in the tests were base acceleration, frequency, and surcharge pressure. The base acceleration was kept as 0.05g, 0.1g, 0.15g and 0.2g in different tests. The range of frequency was varied from 1 Hz to 5 Hz. The surcharge pressure was kept as 0.70 kPa, 1.12 kPa, and 1.72 kPa. The relative density of wrap faced embankment were 48%, 64% and 80% for Sylhet sand and 27%, 41%, and 55% for Local sand. The unconfined compressive strength of the soft Clayey soil layer was estimated from the Undrained Triaxial Test to be 28 kPa. Wrap faced reinforced-soil wall was constructed using sand upon the Clayey soil layer in equal lifts (Sv) of 100 mm (4 inches) to achieve a total wall height (H) of 400 mm (16 inches). The full model height was 750 mm, including the height of the Clayey soil (300 mm), sand blanket (50 mm) and wrap faced reinforced wall (400 mm). The model wall was subjected to 20 cycles of sinusoidal shaking. The model was also subjected to earthquake load (Kobe and Loma Prieta). The model used in the shake table was analyzed numerically using the software PLAXIS 3D.

6.2 Analysis of the Dynamic Response of Sylhet Sand

Various dynamic soil parameters like acceleration amplification, displacement, pore water pressure and strain for Sylhet sand for sinusoidal wave, Kobe and Loma Prieta earthquakes were estimated and presented in this section.

6.2.1 Sinusoidal wave

The variation of the different soil parameters like acceleration amplification, displacement, pore water pressure and strain with respect to height for various sinusoidal waves are presented in this section.

6.2.1.1 Acceleration response

Acceleration amplification was utilized to rearrange the introduction of acceleration response at various elevations of the wall. Acceleration amplification is the proportion of maximum peak to peak acceleration value in the soil to that of the corresponding value of the base motion. The acceleration amplification profile, along with the height of the wall for various inputs of base motion after each test of 20 cycles of sinusoidal motion. However, the elevation (z) was represented in a non-dimensional shape subsequent to normalizing by the full height (T) of the model. The acceleration time histories of the shake table tests ST1-ST4, ST9, ST19, ST27, ST35, ST67, ST99 and ST193 with 1.72 kPa, 1.12 kPa ans 0.7 kPa surcharge, 0.05g, 0.1g, 0.15g, and 0.2g base acceleration and 1 Hz-5 Hz frequency of base sinusoidal motion at same elevation are shown throughout Figures 6.1 (a) to 6.1 (k). Maximum acceleration amplification was observed at the top of the wall in all the tests.

<u>Effect of Input Acceleration</u>

The acceleration amplifications from along the height of the wall for different base accelerations of 0.05g, 0.10g, 0.15g, and 0.2g from ST1, ST9, ST19, and ST27 tests, respectively, which was conducted at 1 Hz frequency and 1.72 kPa surcharge pressure is presented in Figure 6.2. Acceleration amplifications were increased with increased base accelerations. However, from the tests was conducted, later it was observed that acceleration amplifications shake table testing (ST1, ST9, ST19, and ST27) at the top of the wall (z/T = 0.93) for 0.05g base accelerations were very close to 1.38, whereas it was 1.42, 1.48 and 1.58 for 0.1g, 0.15g and 0.20g base acceleration, respectively. From the same figure, it can also be observed that the maximum acceleration amplification was 1.58 at an acceleration of 0.2g, whereas it decreased to 1.38 at an acceleration of 0.05g (values can be seen in Table 6.1). Acceleration amplification was higher at the top of the wall. At the top of the wall, overburden pressure was lower compared to the bottom of the wall. For this reason, at the bottom of the wall, the amplification was less due to higher overburden pressure [surcharge and wrap faced embankment (4 layers)]. Acceleration amplifications were increased with increased base accelerations. Increasing the base accelerations creates shaking of the soil embankment and amplification was also increased. Results from By PLAXIS 3D analysis showed that acceleration amplification [Profile for tests ST1(P), ST9 (P), ST19(P), and

ST27(P)] also at all elevations increased with an increase in Acceleration as can be seen from Figure 6.2. From the same figure, it can also be observed that the maximum acceleration amplification was 1.71 at an acceleration of 0.2g, whereas it decreased to 1.49 at an acceleration of 0.05g. The present study was also compared with the study of Krishna and Latha (2007) as shown in Figure 6.2. The acceleration amplifications along with the height of the wall for different base accelerations of 0.1g, 0.15g, and 0.2g from T4, T6, and T7 model tests (Krishna and Latha, 2007) was compared with the present study. Acceleration amplifications were increased with increased base accelerations for all the curves. The maximum and minimum acceleration amplification from PLAXIS 3D was 8.23% and 7.97% higher than the shake table model test respectively.

Effect of Surcharge

Acceleration response against different surcharge pressures was presented from tests ST1, ST35 and ST67 are depicted in Figure 6.3. These tests were conducted with 1.72 kPa, 1.12 kPa and 0.7 kPa surcharge pressures at 1 Hz frequency and 0.05g base acceleration. Accelerations at the top of the wall were inversely proportional to the surcharge pressures from the range of tests that were conducted. It is observed from the figure that, the acceleration amplification values were 1.38, 1.50, and 1.58 for 1.72 kPa, 1.12 kPa, and 0.7 kPa, surcharge pressures, respectively. From the same figure, it can also be observed that the maximum acceleration amplification was 1.58 at a surcharge of 0.7 kPa, whereas it decreased to 1.38 at a surcharge of 1.72 kPa (values can be seen in Table 6.1). Acceleration amplification at the top of the wall was inversely proportional to the surcharge pressure. Increasing of the surcharge pressure, overburden pressure increases. So, the soil will be less amplified. Results from By PLAXIS 3D analysis showed that acceleration amplification [Profile for tests ST1(P), ST35(P), and ST67(P)] also at all elevations decreased with an increase in surcharge as can be seen from Figure 6.3. From the same figure, it can also be observed that the maximum acceleration amplification was 1.65 at a surcharge of 0.7 kPa, whereas it decreased to 1.49 at a surcharge of 1.72 kPa. A comparison of the present study with the study of Krishna and Latha (2007) is shown in Figure 6.3. The acceleration amplifications along with the height of the wall for different surcharge pressures of 0.5 kPa, 1.0 kPa and 2.0 kPa from T1, T2, and T3 model tests Krishna and Latha (2007) was compared with the present study. The maximum and minimum acceleration amplification from PLAXIS 3D was 4.43% and 7.97% higher than the shake table model test respectively.

Effect of Input Frequency

The effect of frequency on the acceleration response along the height of the wall for tests ST1, ST2, ST3, and ST4 with frequencies of 1Hz, 2Hz, 3Hz, and 5Hz which were conducted at 0.05g base acceleration and 1.7 kPa surcharge pressure is shown in Figure 6.4. From the figure, it is observed that the acceleration response against frequency variation was not directly proportional. In fact, within the range of tests was conducted accelerations were amplified less for 1Hz, 2Hz, and 3Hz and more for 5Hz frequencies at all elevations. Moreover, accelerations at normalized elevations of 0.53, 0.67, 0.80, and 0.93 were amplified closer or slightly more than 1 for the frequency 1 Hz. The differences in acceleration amplification for various frequencies were increased with an increase in wall height. At a normalized height of 0.93, for 1Hz, 2Hz, 3Hz, and 5Hz frequency, the values of acceleration amplification were 1.38, 2.40, 2.30, and 2.54 respectively. Moreover, the acceleration amplification values were 1.20, 1.58, 1.48, and 1.66 for 1Hz, 2Hz, 3Hz, and 5Hz, respectively at a normalized height of 0.53. From the same figure, it can also be observed that the maximum acceleration amplification was 2.54 at a frequency of 5Hz, whereas it decreased to 1.38 at a frequency of 1 Hz (values can be seen in Table 6.1). Results from By PLAXIS 3D analysis showed that acceleration amplification [Profile for tests ST1(P), ST2(P), ST3(P), ST4(P), and ST5 (P)] also at all elevations the displacement against Acceleration variation was not directly proportional as can be seen from Figure 6.4. From the same figure, it can also be observed that the maximum acceleration amplification was 2.72 at a frequency of 5 Hz, whereas it decreased to 1.49 at a frequency of 1 Hz. Figure 6.4 also compares the present study with the study of Krishna and Latha (2007). The acceleration amplifications along with the height of the wall for the different Frequency of 1Hz, 2Hz and 3 Hz from T1, T4, and T5 model tests Krishna and Latha (2007) was compared with the present study. The maximum and minimum acceleration amplification from PLAXIS 3D was 7.09% and 7.97% higher than the shake table model test respectively.

6.2.1.2 Displacement response

Horizontal face displacement along the height of the wall was monitored using three LVDTs positioned is shown in Figure 5.1. The displacement time histories of the shake table tests

ST1-ST4, ST9, ST19, ST27, ST35, ST67, ST99 and ST193 with 1.72 kPa, 1.12 kPa ans 0.7 kPa surcharge, 0.05g, 0.1g, 0.15g, and 0.2g base acceleration and 1 Hz-5 Hz frequency of base sinusoidal motion at same elevation are shown throughout Figures 6.5 (a) to 6.5 (k). The displaced face profiles from various tests after 20 cycles of sinusoidal motion are presented in Figures 6.6 to 6.8. Here elevation (z) and horizontal displacements (δh) are presented in non-dimensional form after normalizing them by the height of the wall (H).

Table 6.1: Experimental and Numerical results for each layer of the model retaining Wall of Sylhet sand (Acceleration amplification)

Test Name	Parameters	Layer of sand layer/Location	Experimental Results	Numerical results	Variation of Results (%)
ST1	Acceleration	A3	1.20	1.29	7.50
		A6	1.38	1.49	7.97
ST9		A3	1.25	1.30	4.00
		A6	1.42	1.54	8.45
ST19		A3	1.34	1.43	6.72
		A6	1.48	1.62	9.46
ST27		A3	1.38	1.45	5.07
		A6	1.58	1.71	8.23
ST1	Surcharge	A3	1.20	1.29	7.50
		A6	1.38	1.49	7.97
ST35		A3	1.30	1.35	3.85
		A6	1.50	1.61	7.33
ST67		A3	1.35	1.46	8.15
		A6	1.58	1.65	4.43
ST1	Frequency	A3	1.20	1.29	7.50
		A6	1.38	1.49	7.97
ST2		A3	1.58	1.75	10.76
		A6	2.40	2.62	9.17
ST3		A3	1.48	1.62	9.46
		A6	2.30	2.53	10.00
ST4		A3	1.66	1.86	12.05
		A6	2.54	2.72	7.09

<u>Effect of Input Acceleration</u>

Figure 6.6 depicts the normalized displacement profile for different base accelerations of 0.05g, 0.10g, 0.15g and 0.20g from tests ST1, ST9, ST19, and ST27 respectively. From the figure, it was observed that the normalized displacements were relatively high at higher base

accelerations at the normalized elevation of z/H= 0.875. This phenomenon had similarities to the test results of Sakaguchi et al. (1992) and Krishna and Latha (2007). From the Figure, a maximum horizontal displacement of 2.98% of the total wall height (H), for 0.20g, was observed compared with 1.70% for 0.05g base accelerations. From the same figure, it can also be observed that the maximum displacement was 1.19 mm at an acceleration of 0.2g, whereas it decreased to 0.68 mm at an acceleration of 0.05g (values can be seen in Table 6.2). Displacement was higher at the top of the wall. At the top of the wall, overburden pressure was lower compared to the bottom of the wall. For this reason, at the bottom of the wall, displacement was less due to higher overburden pressure [surcharge and wrap faced embankment (4 layers)] and less lateral movement soil. Displacement was increased with increased base accelerations. Increasing the base accelerations creates shaking of the soil embankment and amplification was also increased (Higher lateral movement). Results from By PLAXIS 3D analysis showed that displacement [Profile for tests ST1(P), ST9(P), ST19(P), and ST27(P)] also at all elevations Acceleration variation was directly proportional as can be seen from Figure 6.6. From the same figure, it can also be observed that the maximum displacement was 1.28 mm at an acceleration of 0.20 g, whereas it decreased to 0.76 mm at an acceleration of 0.05 g. The maximum and minimum displacements from PLAXIS 3D were 7.56% and 11.76% higher than the shake table model test respectively. The displacements at the end of the dynamic load were less at both sides of the boundary and high at the middle of the Clay model for different input time. The results of the graphical representation of the model were shown in this section. It can be seen that the displacement for 1 sec vibration was larger than the 0.33 and 0.67 sec vibration. This clearly showed that with increasing of input motion time the displacement was increased.

Effect of Surcharge

The normalized displacement profile for tests ST1, ST35, and ST67 which were conducted at 0.05g base acceleration and 1 Hz frequency, were providing an insight into the effect of different surcharge loadings of 1.72 kPa, 1.12 kPa, and 0.7 kPa as shown in Figure 6.7. It was observed that the displacement response against surcharge variation was inversely proportional at all elevations. Moreover, this observation was concurrent with the test performed by Krishna and Latha (2007). The maximum displacement of the wall was (δh/H=3.5%) at a surcharge pressure of 0.7 kPa, whereas it was decreased to (δh/H=1.70%) at a surcharge pressure of 1.72 kPa. From the same figure, it can also be observed that the maximum displacement was 1.40 mm at a surcharge of 0.7 kPa, whereas it decreased to 0.68 mm at a surcharge of 1.72 kPa (values can be seen in Table 6.2). Displacement at the top of the wall was inversely proportional to the surcharge pressure. Increasing the surcharge pressure, overburden pressure will be increased. So, the soil will be less displaced due to less lateral movement. Results from By PLAXIS 3D analysis showed that displacement [Profile for tests ST1(P), ST35(P), and ST67(P)] also at all elevations Acceleration variation is inversely proportional as can be seen from Figure 6.7. From the same figure, it can also be observed that the maximum displacement was 1.52 mm at a surcharge of 0.7 kPa, whereas it decreased to 0.76 mm at a surcharge of 1.72 kPa. The maximum and minimum displacements from PLAXIS 3D were 8.57% and 11.76% higher than the shake table model test respectively.

Effect of Input Frequency

According to Figure 6.8. it can be said that the displacement response against frequency variation was inversely proportional. The normalized displacement profile observed for tests ST1, ST2, ST3, and ST4 with frequencies 1 Hz, 2 Hz, 3 Hz, and 5 Hz, respectively, which were conducted at 0.05g base acceleration and 1.72 kPa surcharge pressure as presented in Figure 6.8. The displacement had occurred more at z/H=0.875 from the range of tests that were conducted. The maximum displacement of 1.7% was observed for 1 Hz frequency at z/H=0.875. From the same figure, it can also be observed that the maximum displacement was 0.68 mm at a frequency of 1 Hz, whereas it decreased to 0.24 mm at a frequency of 5 Hz (values can be seen in Table 6.2). This phenomenon had similarities to the test results of Latha and Krishna (2006). Results from By PLAXIS 3D analysis showed that displacement [Profile for tests ST1(P), ST2(P), ST3(P), and ST4(P) also at all elevations Acceleration variation was inversely proportional with frequency as can be seen from Figure 6.8. From the same figure, it can also be observed that the maximum displacement was 0.76 mm at a frequency of 1 Hz, whereas it decreased to 0.26 mm at a frequency of 5 Hz. The maximum and minimum displacements from PLAXIS 3D were 11.76% and 8.33% higher than the shake table model test respectively.

Table 6.2: Experimental and Numerical results for each layer of the model retaining wall of Sylhet sand (Displacement)

Test Name	Parameters	Layer of sand layer/Location	Experimental Results (mm)	Numerical results (mm)	Variation of Results (%)
ST1	Acceleration	2nd Layer (2nd Bottom)	0.44	0.49	11.36
		3rd Layer (Mid)	0.49	0.53	8.16
		4th Layer (Top)	0.68	0.76	11.76
ST9		2nd Layer (2nd Bottom)	0.67	0.72	7.46
		3rd Layer (Mid)	0.80	0.88	10.00
		4th Layer (Top)	1.00	1.06	6.00
ST19		2nd Layer (2nd Bottom)	0.70	0.79	12.86
		3rd Layer (Mid)	0.90	0.96	6.67
		4th Layer (Top)	1.10	1.17	6.36
ST27		2nd Layer (2nd Bottom)	0.84	0.88	4.76
		3rd Layer (Mid)	0.98	1.10	12.24
		4th Layer (Top)	1.19	1.28	7.56
ST1	Surcharge	2nd Layer (2nd Bottom)	0.44	0.49	11.36
		3rd Layer (Mid)	0.49	0.53	8.16
		4th Layer (Top)	0.68	0.76	11.76
ST35		2nd Layer (2nd Bottom)	0.94	1.05	11.70
		3rd Layer (Mid)	0.93	1.06	13.98
		4th Layer (Top)	1.25	1.30	4.00
ST67		2nd Layer (2nd Bottom)	1.10	1.15	4.55
		3rd Layer (Mid)	1.22	1.40	14.75
		4th Layer (Top)	1.40	1.52	8.57
ST1	Frequency	2nd Layer (2nd Bottom)	0.44	0.49	11.36
		3rd Layer (Mid)	0.49	0.53	8.16
		4th Layer (Top)	0.68	0.76	11.76
ST2		2nd Layer (2nd Bottom)	0.20	0.21	5.00
		3rd Layer (Mid)	0.25	0.28	12.00
		4th Layer (Top)	0.47	0.50	6.38
ST3		2nd Layer (2nd	0.20	0.22	10.00

Test Name	Parameters	Layer of sand layer/Location	Experimental Results (mm)	Numerical results (mm)	Variation of Results (%)
		Bottom)			
		3rd Layer (Mid)	0.22	0.23	4.55
		4th Layer (Top)	0.37	0.42	13.51
ST4		2nd Layer (2nd Bottom)	0.12	0.13	8.33
		3rd Layer (Mid)	0.14	0.15	7.14
		4th Layer (Top)	0.24	0.26	8.33

6.2.1.3 Pore water pressure response

The pore water pressure time histories of the shake table tests ST1-ST4, ST9, ST19, ST27, ST35, ST67, ST99 and ST193 with 1.72 kPa, 1.12 kPa ans 0.7 kPa surcharge, 0.05g, 0.1g, 0.15g, and 0.2g base acceleration and 1 Hz-5 Hz frequency of base sinusoidal motion at same elevation are shown throughout the Figures 6.9 (a) to 6.9 (k). Typical pore water pressure variations obtained from the tests are presented in Figures 6.10, 6.11 and 6.12. The height of Clayey soil layer (S) was taken as 300 mm in the case of pore water pressure.

<u>Effect of Input Acceleration</u>

The variations of the pore water pressure from model tests ST1, ST9, ST19, and ST27 with base accelerations 0.05g, 0.10g, 0.15g and 0.20g, respectively for 1Hz frequency and surcharge load of 1.72 kPa is shown in Figure 6.10. The pore water pressure response against base acceleration variation was directly proportional at z/S=0.84 it can be seen from the figure. The maximum pore water pressure was 0.390 kPa at a base acceleration of 0.20g. The maximum pore water pressure for model tests ST1, ST9, ST19, and ST27 was 0.110 kPa, 0.260 kPa, 0.320 kPa, and 0.390 kPa, respectively. From the same figure, it can also be observed that the pore water pressure was 0.390 kPa at an acceleration of 0.2g, whereas it decreased to 0.110 kPa at an acceleration of 0.05g (values can be seen in Table 6.3). Pore water pressure was increased with increased base accelerations. Increasing the base accelerations creates shaking of the soil embankment and amplification was also increased (Higher lateral movement). Results from By PLAXIS 3D analysis showed that pore water pressure [Profile for tests ST1(P), ST9(P), ST19(P), and ST27(P)] also at all elevations pore water pressure was directly proportional as can be seen from Figure 6.10. From the same figure, it can also be observed that the maximum pore water pressure was 0.420 kPa at an acceleration of 0.20 g, whereas it decreased to 0.122 kPa at an acceleration of 0.05 g. The maximum and minimum pore water pressure from PLAXIS 3D was 7.69% and 10.91% higher than the shake table model test respectively. Figure 6.13 shows the PLAXIS 3D output results of the porewater pressure response.

Effect of Surcharge

Variations of the pore pressure from model tests ST1, ST35, and ST67 with of surcharge 1.72kPa, 1.12 kPa, and 0.7 kPa, respectively for 1Hz frequency and base acceleration of 0.20g is presented in Figure 6.11. From the figure, it is observed that pore water pressure response against surcharge variation was inversely proportional at all elevations. The maximum pore water pressure was 0.310 kPa at a surcharge load of 0.7 kPa. The maximum pore water pressure for model tests ST1, ST35, and ST67 were 0.110 kPa, 0.220 kPa, and 0.310 kPa respectively. From the same figure, it can also be observed that the maximum pore water pressure was 0.310 kPa at a surcharge of 0.7 kPa, whereas it decreased to 0.110 kPa at a surcharge of 1.72 kPa (values can be seen in Table 6.3). Pore water pressure at the top of the wall was inversely proportional to the surcharge pressure. Increasing the surcharge pressure, water was dissipated from the pore. So, the pore pressure was decreased due to a large surcharge. Results from By PLAXIS 3D analysis showed that pore water pressure [Profile for tests ST1(P), ST35(P), and ST67(P)] also at all elevations pore water pressure variation was inversely proportional as can be seen from Figure 6.11. From the same figure, it can also be observed that the maximum pore water pressure was 0.330 kPa at a surcharge of 0.7 kPa, whereas it decreased to 0.122 kPa at a surcharge of 1.72 kPa. The maximum and minimum pore water pressure from PLAXIS 3D was 6.45% and 10.91% higher than the shake table model test respectively.

Effect of Input Frequency

The effect of frequency for a given base acceleration and surcharge load on pore water pressure for tests ST1, ST2, ST3, and ST4 with the frequency of 1 Hz, 2 Hz, 3 Hz, and 5 Hz for 0.1g base accelerations and 1.72 kPa surcharge is shown in Figure 6.12. From the figure, it is observed that pore water pressures response against frequency variation was directly proportional. The highest pore water pressure was 0.220 kPa at 5 Hz frequency. From the same figure, it can also be observed that the maximum pore water pressure was 0.220 at a frequency of 5 Hz, whereas it decreased to 0.110 kPa at a frequency of 1 Hz (values can be seen in Table 6.3). Results from By PLAXIS 3D analysis showed that pore water pressure [Profile for tests ST1(P), ST2(P), ST3(P), and ST4(P)] also at all elevations pore water pressure variation was not directly proportional with frequency as can be seen from Figure 6.12. From the same figure, it can also be observed that the maximum pore water pressure was 0.247 kPa at a frequency of 5 Hz, whereas it decreased to 0.122 kPa at a frequency of 1 Hz. The maximum and minimum pore water pressure from PLAXIS 3D was 12.27% and 10.91% higher than the shake table model test respectively.

Table 6.3: Experimental and Numerical results for each layer of the model retaining wall of Sylhet sand (Pore water pressure)

Test Name	Parameters	Layer of sand layer/Location	Experimental Results (kPa)	Numerical results (kPa)	Variation of Results (%)
ST1	Acceleration	P2 Location	0.110	0.122	10.91
ST9		P2 Location	0.260	0.270	3.85
ST19		P2 Location	0.320	0.350	9.37
ST27		P2 Location	0.390	0.420	7.69
ST1	Surcharge	P2 Location	0.110	0.122	10.91
ST35		P2 Location	0.220	0.240	9.09
ST67		P2 Location	0.310	0.330	6.45
ST1	Frequency	P2 Location	0.110	0.122	10.91
ST2		P2 Location	0.150	0.160	6.67
ST3		P2 Location	0.190	0.210	10.53
ST4		P2 Location	0.220	0.247	12.27

6.2.1.4 Strain response

The strain time histories of the shake table tests ST1-ST4, ST9, ST19, ST27, ST35, ST67, ST99 and ST193 with 1.72 kPa, 1.12 kPa ans 0.7 kPa surcharge, 0.05g, 0.1g, 0.15g, and 0.2g base acceleration and 1 Hz-5 Hz frequency of base sinusoidal motion at same elevation are shown throughout Figures 6.14 (a) to 6.14 (k). The Strain profiles from various tests after 20 cycles of sinusoidal motion are presented in Figures 6.15 to 6.17.

Effect of Input Acceleration

Figure 6.15 depicts the strain (%) profile for different base accelerations of 0.05g, 0.10g, 0.15g and 0.20g from tests ST1, ST9, ST19, and ST27 respectively. From the figure, it was observed that the strain (%) was relatively high at higher base accelerations at the normalized elevation of z/H= 0.75. From the Figure, a maximum strain (%) of 3.45 of the total wall height (H), for 0.20g, was observed compared with 2.85 for 0.05g base accelerations. From the same figure, it can also be observed that the maximum strain (%) was 3.45 at an acceleration of 0.2g, whereas it decreased to 2.85 at an acceleration of 0.05g (values can be seen in Table 6.4). The strains of the bottom-layer were the smallest, and the strains of the top-layer were the largest, which indicated that the geotextiles located in the top layers play important roles in the seismic stability of the wrap faced reinforced retaining walls. Strain was higher at the top of the wall. At the top of the wall, overburden pressure was lower compared to the bottom of the wall. For this reason, at the bottom of the wall, percentage deformation was less due to higher overburden pressure [surcharge and wrap faced embankment (4 layers)] and less lateral movement soil. Strain was increased with increased base accelerations. Increasing the base accelerations creates shaking of the soil embankment and amplification was also increased (Higher lateral movement). The strains obtained in the present study are in close agreement with the results presented by Wang et al. (2015). Results from By PLAXIS 3D analysis showed that strain (%) [Profile for tests ST1(P), ST9(P), ST19(P), and ST27(P)] also at all elevations strain (%) variation was directly proportional as can be seen from Figure 6.15. From the same figure, it can also be observed that the maximum strain (%) was 3.60 at an acceleration of 0.20 g, whereas it decreased to 3.06 at an acceleration of 0.05 g. The maximum and minimum Strain (%) from PLAXIS 3D was 4.35% and 7.37% higher than the shake table model test respectively. Figure 6.18 shows the strain contour from PLAXIS 3D output results at end program of strain response.

Effect of Surcharge

The strain (%) profile for tests ST1, ST35, and ST67 which were conducted at 0.05g base acceleration and 1Hz frequency, were providing an insight into the effect of different surcharge loadings of 1.72 kPa, 1.12kPa, and 0.7kPa as shown in Figure 6.16. It was observed that the strain (%) response against surcharge variation was inversely proportional at all elevations. The maximum strain (%) of the wall was 3.55 at a surcharge pressure of 0.7 kPa, whereas it decreased to 2.00 at a surcharge pressure of 1.72 kPa. From the same figure, it can also be observed that the maximum strain (%) was 3.55 at a surcharge of 0.7 kPa, whereas it decreased to 2.00 at a surcharge of 1.72 kPa (values can be seen in Table 6.4). Strain at the top of the wall was inversely proportional to the surcharge pressure. Increasing the surcharge pressure, overburden pressure will be increased. So, the soil will be less deformed due to less lateral movement. Results from By PLAXIS 3D analysis showed that strain (%) [Profile for tests ST1(P), ST35(P), and ST67(P)] also at all elevations strain (%) variation was inversely proportional as can be seen from Figure 6.16. From the same figure, it can also be observed that the maximum strain (%) was 3.81 at a surcharge of 0.7 kPa, whereas it decreased to 2.14 at a surcharge of 1.72 kPa. The maximum and minimum Strain (%) from PLAXIS 3D was 7.32% and 7.37% higher than the shake table model test respectively.

<u>Effect of Input Frequency</u>

According to Figure 6.17. it can be said that the strain (%) response against frequency variation was inversely proportional. The normalized strain (%) profile observed for tests ST1, ST2, ST3, and ST4 with frequencies 1 Hz, 2 Hz, 3 Hz, and 5 Hz, respectively, which were conducted at 0.05g base acceleration and 1.72 kPa surcharge pressure as presented in Figure 6.17. The strain (%) had occurred more at z/H=0.75 from the range of tests that were conducted. The maximum strain (%) of 2.85 was observed for 1 Hz frequency at z/H=0.75. From the same figure, it can also be observed that the maximum strain (%) was 2.85 at a frequency of 1 Hz, whereas it decreased to 2.35 at a frequency of 5 Hz (values can be seen in Table 6.4). Results from By PLAXIS 3D analysis showed that strain (%) [Profile for tests ST1(P), ST2(P), ST3(P), ST4(P), ST5(P), ST6(P), ST7(P), and ST8(P)] also at all elevations strain (%) variation was inversely proportional with frequency as can be seen from Figure 6.17. From the same figure, it can also be observed that the maximum strain (%) was 3.06 at a frequency of 1 Hz, whereas it decreased to 2.64 at a frequency of 5 Hz. The maximum and minimum strain (%) from PLAXIS 3D were 12.34 and 7.37 higher than the shake table model test respectively.

Table 6.4: Experimental and Numerical results for each layer of the model retaining wall of Sylhet sand (Strain)

Test Name	Parameters	Layer of sand layer/Location	Experimental Results (%)	Numerical results (%)	Variation of Results (%)
ST1	Acceleration	Sg1 (Bottom)	2.00	2.14	7.00
		Sg4(Top)	2.85	3.06	7.37
ST9		Sg1 (Bottom)	2.20	2.37	7.73
		Sg4(Top)	3.10	3.44	10.97
ST19		Sg1 (Bottom)	2.35	2.49	5.96
		Sg4(Top)	3.30	3.58	8.48
ST27		Sg1 (Bottom)	2.41	2.56	6.22
		Sg4(Top)	3.45	3.60	4.35
ST1	Surcharge	Sg1 (Bottom)	2.00	2.14	7.00
		Sg4(Top)	2.85	3.06	7.37
ST35		Sg1 (Bottom)	2.80	3.16	12.86
		Sg4(Top)	3.30	3.52	6.67
ST67		Sg1 (Bottom)	3.10	3.24	4.52
		Sg4(Top)	3.55	3.81	7.32
ST1	Frequency	Sg1 (Bottom)	2.00	2.14	7.00
		Sg4(Top)	2.85	3.06	7.37
ST2		Sg1 (Bottom)	1.80	2.06	14.44
		Sg4(Top)	2.71	2.86	5.54
ST3		Sg1 (Bottom)	1.40	1.56	11.43
		Sg4(Top)	2.68	2.83	5.60
ST4		Sg1 (Bottom)	0.90	0.98	8.89
		Sg4(Top)	2.35	2.64	12.34

6.2.1.5 Effect of relative density within the geotextile sand filling

In this section, the effect of backfill densities has been discussed for Sylhet Sand. The backfill relative densities are 48%, 64%, and 80% with fixed frequency (1 Hz), base acceleration (0.05g) and surcharge (1.72 kPa). The face displacement, pore water pressure, strain and acceleration amplification responses were described in Figures 6.19 to 6.22.

<u>Face Displacement Response</u>

Figure 6.19 presents the displacement profile for tests ST1, ST99, and ST193 providing an insight into the effect of surcharge loading of 1.72kPa, frequency of 1 Hz and acceleration of 0.05g with different relative densities (48%, 64% and 80%). Displacements at all elevations

decreased with an increase in relative densities. From the same figure/Table 6.5, it can also be observed that the maximum displacement of the wall was 0.68 mm (δh/H = 1.7%) at a relative density 48%, whereas it decreased to 0.31 mm (δh/H = 0.93%) at a relative density 80% (values can be seen in Table 6.5). The displacements obtained in the present study are in close agreement with the results presented by Latha et al. (2008), corresponding to the relative density levels used in the present study. Results from PLAXIS 3D analysis showed that displacements [Profile for tests ST1 (P), ST99 (P), and ST193 (P)] at all elevations decreased with an increase in relative density as can be seen from Figure 6.19. From the same figure/Table, it can be observed that the maximum displacement of the wall was 0.76 mm (δh/H = 1.9%) at a relative density 48%, whereas it decreased to 0.35 mm (δh/H = 0.88%) at a relative density 80%. The maximum and minimum displacement from PLAXIS 3D was 11.76% and 12.90% higher than the shake table model test. Table 6.5 shows the Experimental and Numerical results for each layer of the model retaining Wall.

<u>Porewater Pressure Response</u>

Figure 6.20 presents the pore water pressure profile for tests ST1, ST99, and ST193 providing an insight into the effect of surcharge loading of 1.72 kPa, frequency of 1 Hz and acceleration of 0.05g with different relative densities (48%, 64% and 80%). Pore water pressure at all elevations decreased with an increase in relative densities. From the same figure/Table 6.5 it can also be observed that the maximum pore water pressure of the wall was 0.11 kPa at a relative density of 48%, whereas it decreased to 0.07 kPa at a relative density of 80% (values can be seen in Table 6.5). Results from PLAXIS 3D analysis showed that pore water pressure [Profile for tests ST1 (P), ST99(P), and ST193(P)] at all elevations decreased with an increase in relative densities as can be seen from Figure 6.20. From the same figure/Table, it can also be observed that the maximum pore water pressure was 0.12 kPa at a relative density of 48%, whereas it decreased to 0.08 kPa at a relative density of 80%. The maximum and minimum pore water pressure from PLAXIS 3D was 10.91% and 14.29% higher than the shake table model test respectively.

<u>Strain Response</u>

Figure 6.21 presents the Strain profile for tests ST1, ST99, and ST193 providing an insight into the effect of surcharge loadings of 1.72 kPa, frequency of 1 Hz and acceleration of 0.05g

with different relative densities (48%, 64%, and 80%). Strain at all elevations decreased with an increase in relative densities. From the same figure/Table 6.5, it can also be observed that the maximum Strain (%) was 2.85 at a relative density of 48%, whereas it decreased to 2.10 at a relative density of 80% (values can be seen in Table 6.5). The strains of the bottom-layer were the smallest, and the strains of the top-layer were the largest, which indicated that the geotextiles located in the top layers play important roles in the seismic stability of the wrap faced reinforced retaining walls. The strains obtained in the present study are in close agreement with the results presented by Wang et al. (2015). Results from PLAXIS 3D analysis showed that Strain [Profile for tests ST1 (P), ST99 (P), and ST193 (P)] at all elevations decreased with an increase in relative densities as can be seen from Figure 6.21. From the same figure, it can also be observed that the maximum Strain (%) was 3.06 at a relative density of 48%, whereas it decreased to 2.33 at a relative density of 80%. The maximum and minimum Strain (%) from PLAXIS 3D was 7.37% and 10.95% higher than the shake table model test respectively.

Acceleration Amplification Response

Figure 6.22 presents the Acceleration amplification for tests ST1, ST99, and ST193 providing an insight into the effect of surcharge loadings of 1.72 kPa, frequency of 1 Hz and acceleration of 0.05g with different relative densities (48%, 64%, and 80%). Acceleration amplification at all elevations decreased with an increase in relative densities. From the same figure/Table 6.5 it can also be observed that the maximum Acceleration amplification was 1.38 at a relative density of 48%, whereas it decreased to 1.24 at a relative density of 80% (values can be seen in Table 6.5). The Acceleration amplification obtained in the present study is in close agreement with the results presented by Latha et al. (2008) corresponding to the relative density levels used in the present study. Results from PLAXIS 3D analysis showed that Acceleration amplification [Profile for tests ST1 (P.), ST99(P.), and ST193(P.)] at all elevations decreased with an increase in relative densities as can be seen from Figure 6.22. From the same figure/Table, it can also be observed that the maximum Acceleration amplification of the wall was 1.49 at a relative density of 48%, whereas it decreased to 1.35 at a relative density of 80%. The maximum and minimum acceleration amplification from PLAXIS 3D was 7.97% and 8.87% higher than the shake table model test respectively.

Table 6.5: Experimental and Numerical results of the model wall (Relative density)

Test Name (Dr)	Dynamic properties	Layer of sand layer/Location	Experimental Results	Numerical results	Variation of Results (%)
ST1 (48%)	Deformation (mm)	2^{nd} Layer (2^{nd} Bottom)	0.44	0.49	11.36
		3^{rd} Layer (Mid)	0.49	0.53	8.16
		4^{th} Layer (Top)	0.68	0.76	11.76
ST99 (64%)		2^{nd} Layer (2^{nd} Bottom)	0.27	0.28	3.70
		3^{rd} Layer (Mid)	0.35	0.39	11.43
		4^{th} Layer (Top)	0.45	0.47	4.44
ST193 (80%)		2^{nd} Layer (2^{nd} Bottom)	0.12	0.13	8.33
		3^{rd} Layer (Mid)	0.20	0.21	5.00
		4^{th} Layer (Top)	0.31	0.35	12.90
ST1 (48%)	Pore water Pressure (kPa)	P2 location	0.11	0.12	10.91
ST99 (64%)			0.10	0.11	14.00
ST193 (80%)			0.07	0.08	14.29
ST1 (48%)	Strain (%)	Sg1 (Bottom)	2.00	2.14	7.00
		Sg4(Top)	2.85	3.06	7.37
ST99 (64%)		Sg1 (Bottom)	1.80	1.89	5.00
		Sg4(Top)	2.35	2.52	7.23
ST193 (80%)		Sg1 (Bottom)	0.90	0.97	7.78
		Sg4(Top)	2.10	2.33	10.95
ST1 (48%)	Acceleration Amplification	A3	1.20	1.29	7.50
		A6	1.38	1.49	7.97
ST99 (64%)		A3	1.10	1.22	10.91
		A6	1.26	1.38	9.52
ST193 (80%)		A3	1.04	1.14	9.62
		A6	1.24	1.35	8.87

6.2.2 Kobe earthquake

The variation of the different soil parameters like acceleration amplification, displacement, pore water pressure and strain (KST1, KST2, KST3, KST4, KST5 and KST9) with respect to height for various Kobe earthquake are presented in this section.

6.2.2.1 Acceleration response

Acceleration amplification for earthquake excitation was utilized to rearrange the introduction of acceleration response at various elevations of the wall. Acceleration amplification is the proportion of maximum peak to peak acceleration value in the soil to that of the corresponding value of the base motion. The acceleration amplification profile along with the height of the wall for various inputs of base motion after each test of 20 cycles of sinusoidal motion. However, the elevation (z) was represented in a non-dimensional shape subsequent to normalizing by the full height (T) of the model. Maximum acceleration amplification was observed at the top of the wall in all the tests.

Effect of Input Acceleration

The acceleration amplifications from along the height of the wall for different base accelerations of 0.05g, 0.10g, 0.15g, and 0.2g from KST1, KST2, KST3 and KST4 tests, respectively, which was conducted at 1.72 kPa surcharge pressure and 48% relative density is presented in Figure 6.23. Acceleration amplifications were increased with increased base accelerations. However, from the tests was conducted, later it was observed that acceleration amplifications shake table testing (KST1, KST2, KST3 and KST4) at the top of the wall (z/T = 0.93) for 0.05g base accelerations were very close to 1.28, whereas it was 1.30, 1.36 and 1.60 for 0.1g, 0.15g, and 0.20g base acceleration, respectively. From the same figure, it can also be observed that the maximum acceleration amplification was 1.60 at an acceleration of 0.2g, whereas it decreased to 1.28 at an acceleration of 0.05g (values can be seen in the Table 6.6). Results from By PLAXIS 3D analysis showed that acceleration amplification [Profile for tests KST1(P), KST2 (P), KST3(P), and KST4(P)] also at all elevations increased with an increase in Acceleration as can be seen from Figure 6.23. From the same figure, it can also be observed that the maximum acceleration amplification was 1.65 at an acceleration of 0.2g, whereas it decreased to 1.39 at an acceleration of 0.05g. The present study was also compared with the study of Krishna and Latha (2007) as shown in Figure 6.23. The acceleration amplifications along with the height of the wall for different base accelerations of 0.1g, 0.15g, and 0.2g from T4, T6, and T7 model tests (Krishna and Latha, 2007) was compared with the present study. Acceleration amplifications were increased with increased base accelerations for all the curves. The maximum and minimum acceleration amplification from PLAXIS 3D was 3.12% and 8.59% higher than the shake table model test respectively.

Effect of Surcharge

Acceleration response against different surcharge pressures was presented from tests KST1, KST5 and KST9 are depicted in Figure 6.24. These tests were conducted with 1.72 kPa, 1.12 kPa and 0.7 kPa surcharge pressures at 0.05g base acceleration. Accelerations at the top of the wall were inversely proportional to the surcharge pressures from the range of tests that were conducted. It is observed from the figure that, the acceleration amplification values were 1.28, 1.36 and 1.66 for 1.72 kPa, 1.12 kPa and 0.7 kPa, surcharge pressures, respectively. From the same figure, it can also be observed that the maximum acceleration amplification was 1.66 at a surcharge of 0.7 kPa, whereas it decreased to 1.28 at a surcharge of 1.72 kPa (values can be seen in the Table 6.6). Results from By PLAXIS 3D analysis showed that acceleration amplification [Profile for tests KST1(P), KST5(P) and KST9(P)] also at all elevations decreased with an increase in surcharge as can be seen from Figure 6.24. From the same figure, it can also be observed that the maximum acceleration amplification was 1.73 at a surcharge of 0.7 kPa, whereas it decreased to 1.39 at a surcharge of 1.72 kPa. A comparison of the present study with the study of Krishna and Latha (2007) is shown in Figure 6.24. The acceleration amplifications along with the height of the wall for different surcharge pressures of 0.5 kPa, 1.0 kPa and 2.0 kPa from T1, T2, and T3 model tests Krishna and Latha (2007) was compared with the present study. The maximum and minimum acceleration amplification from PLAXIS 3D was 4.22% and 8.59% higher than the shake table model test respectively.

6.2.2.2 Displacement response

Horizontal face displacement along the height of the wall was monitored using three LVDTs positioned is shown in Figure 5.1. The displaced face profiles from various tests after 20 cycles of sinusoidal motion are presented in Figures 6.25 to 6.26. Here elevation (z) and horizontal displacements (δh) are presented in non-dimensional form after normalizing them by the height of the wall (H).

Table 6.6: Experimental and Numerical results for each layer of the model retaining wall of Sylhet sand (Kobe-Acceleration amplification)

Test Name	**Parameters**	**Layer of sand layer/Location**	**Experimental Results**	**Numerical results**	**Variation of Results (%)**
KST1	Acceleration	A3	1.10	1.18	7.27
		A6	1.28	1.39	8.59
KST2		A3	1.17	1.28	9.40
		A6	1.30	1.41	8.46
KST3		A3	1.25	1.35	8.00
		A6	1.36	1.47	8.09
KST4		A3	1.41	1.53	8.51
		A6	1.60	1.65	3.12
KST1	Surcharge	A3	1.10	1.18	7.27
		A6	1.28	1.39	8.59
KST5		A3	1.21	1.29	6.61
		A6	1.36	1.48	8.82
KST9		A3	1.42	1.55	9.15
		A6	1.66	1.73	4.22

Effect of Input Acceleration

Figure 6.25 depicts the normalized displacement profile for different base accelerations of 0.05g, 0.10g, 0.15g and 0.20g from tests KST1, KST2, KST3 and KST4 respectively. From the figure, it was observed that the normalized displacements were relatively high at higher base accelerations at the normalized elevation of z/H=0.875. This phenomenon had similarities to the test results of Sakaguchi et al. (1992) and Krishna and Latha (2007). From the Figure, a maximum horizontal displacement of 1.27% of the total wall height (H), for 0.20g, was observed compared with 0.35% for 0.05g base accelerations. From the same figure, it can also be observed that the maximum displacement was 0.510 mm at an acceleration of 0.2g, whereas it decreased to 0.140 mm at an acceleration of 0.05g (values can be seen in the Table 6.7). Results from By PLAXIS 3D analysis showed that displacement [Profile for tests KST1(P), KST2(P), KST3(P), and KST4(P)] also at all elevations acceleration variation was directly proportional as can be seen from Figure 6.25. From the same figure, it can also be observed that the maximum displacement was 0.540 mm at an acceleration of 0.20 g, whereas it decreased to 0.153 mm at an acceleration of 0.05 g. The maximum and minimum displacements from PLAXIS 3D were 5.88% and 9.29% higher than the shake table model test respectively.

Effect of Surcharge

The normalized displacement profile for tests KST1, KST5 and KST9 which were conducted at 0.05g base acceleration were providing an insight into the effect of different surcharge loadings of 1.72 kPa, 1.12 kPa and 0.7 kPa as shown in Figure 6.26. It was observed that the displacement response against surcharge variation was inversely proportional at all elevations. Moreover, this observation was concurrent with the test performed by Krishna and Latha (2007). The maximum displacement of the wall was ($\delta h/H$=1.03%) at a surcharge pressure of 0.7 kPa, whereas it decreased to ($\delta h/H$=0.35%) at a surcharge pressure of 1.72 kPa. From the same figure, it can also be observed that the maximum displacement was 0.410 mm at a surcharge of 0.7 kPa, whereas it decreased to 0.140 mm at a surcharge of 1.72 kPa (values can be seen in the Table 6.7). Results from By PLAXIS 3D analysis showed that displacement [Profile for tests KST1(P), KST5(P), and KST9(P)] also at all elevations acceleration variation was inversely proportional as can be seen from Figure 6.26. From the same figure, it can also be observed that the maximum displacement was 0.440 mm at a surcharge of 0.7 kPa, whereas it decreased to 0.153 mm at a surcharge of 1.72 kPa. The maximum and minimum displacements from PLAXIS 3D were 7.32% and 9.29% higher than the shake table model test respectively.

6.2.2.3 Pore water pressure response

Typical pore water pressure variations obtained from the tests are presented in Figures 6.27 and 6.28. The height of Clayey soil layer (S) was taken as 300 mm in the case of pore water pressure.

Table 6.7: Experimental and Numerical results for each layer of the model retaining wall of Sylhet sand (Kobe-Displacement)

Test Name	Parameters	Layer of sand layer/Location	Experimental Results (mm)	Numerical results (mm)	Variation of Results (%)
KST1	Acceleration	2nd Layer (2nd Bottom)	0.038	0.042	10.53
		3rd Layer (Mid)	0.021	0.022	4.76
		4th Layer (Top)	0.140	0.153	9.29
KST2		2nd Layer (2nd Bottom)	0.071	0.076	7.34
		3rd Layer (Mid)	0.067	0.073	8.96
		4th Layer (Top)	0.150	0.166	10.67
KST3		2nd Layer (2nd Bottom)	0.200	0.216	8.00
		3rd Layer (Mid)	0.180	0.190	5.56
		4th Layer (Top)	0.360	0.390	8.33
KST4		2nd Layer (2nd Bottom)	0.380	0.400	5.26
		3rd Layer (Mid)	0.300	0.330	10.00
		4th Layer (Top)	0.510	0.540	5.88
KST1	Surcharge	2nd Layer (2nd Bottom)	0.038	0.042	10.53
		3rd Layer (Mid)	0.021	0.022	4.76
		4th Layer (Top)	0.140	0.153	9.29
KST5		2nd Layer (2nd Bottom)	0.150	0.160	6.67
		3rd Layer (Mid)	0.200	0.230	15.00
		4th Layer (Top)	0.250	0.280	12.00
KST9		2nd Layer (2nd Bottom)	0.200	0.210	5.00
		3rd Layer (Mid)	0.310	0.350	12.90
		4th Layer (Top)	0.410	0.440	7.32

Effect of Input Acceleration

The variations of the pore water pressure from model tests KST1, KST2, KST3, and KST4 with base accelerations 0.05g, 0.10g, 0.15g and 0.20g, respectively for surcharge load of 1.72 kPa is shown in Figure 6.27. The pore water pressure response against base acceleration variation was directly proportional at z/S=0.84 it can be seen from the figure. The maximum pore water pressure was 0.147 kPa at a base acceleration of 0.20g. The maximum pore water pressure for model tests KST1, KST2, KST3, and KST4 was 0.083 kPa, 0.210 kPa, 0.430 kPa, and 0.960 kPa, respectively. From the same figure, it can also be observed that the pore water pressure was 0.960 kPa at an acceleration of 0.2g, whereas it decreased to 0.083 kPa at an acceleration of 0.05g (values can be seen in the Table 6.8). Results from By PLAXIS 3D analysis showed that pore water pressure [Profile for tests KST1(P), KST2(P), KST3(P), and KST4(P)] also at all elevations pore water pressure was directly proportional as can be seen from Figure 6.27. From the same figure, it can also be observed that the maximum pore water pressure was 1.050 kPa at an acceleration of 0.20 g, whereas it decreased to 0.090 kPa at an acceleration of 0.05 g. The maximum and minimum pore water pressure from PLAXIS 3D was 9.38% and 8.43% higher than the shake table model test respectively.

Effect of Surcharge

Variations of the pore pressure from model tests KST1, KST5 and KST9 with of surcharge 1.72kPa, 1.12 kPa and 0.7 kPa, respectively for the base acceleration of 0.05g is presented in Figure 6.28. From the figure, it is observed that pore water pressure response against surcharge variation was inversely proportional at all elevations. The maximum pore water pressure was 0.310 kPa at a surcharge load of 0.7 kPa. The maximum pore water pressure for model tests KST1, KST5 and KST9 was 0.083 kPa, 0.150 kPa and 0.310 kPa respectively. From the same figure, it can also be observed that the maximum pore water pressure was 0.310 kPa at a surcharge of 0.7 kPa, whereas it decreased to 0.083 kPa at a surcharge of 1.72 kPa (values can be seen in the Table 6.8). Results from By PLAXIS 3D analysis showed that pore water pressure [Profile for tests KST1(P), KST5(P), and KST9(P)] also at all elevations pore water pressure variation was inversely proportional as can be seen from Figure 6.28. From the same figure, it can also be observed that the maximum pore water pressure was 0.320 kPa at a surcharge of 0.7 kPa, whereas it decreased to 0.090 kPa at a surcharge of 1.72 kPa. The maximum and minimum pore water pressure from PLAXIS 3D was 3.23% and 8.43% higher than the shake table model test respectively.

6.2.2.4 Strain response

The Strain profiles from various tests after 20 cycles of sinusoidal motion are presented in Figures 6.29 to 6.30.

Table 6.8: Experimental and Numerical results for each layer of the model retaining wall of Sylhet sand (Kobe-Pore water pressure)

Test Name	**Parameters**	**Layer of sand layer/Location**	**Experimental Results (kPa)**	**Numerical results (kPa)**	**Variation of Results (%)**
KST1	Accelaration	P2 Location	0.083	0.090	8.43
KST2		P2 Location	0.210	0.224	6.67
KST3		P2 Location	0.430	0.470	9.30
KST4		P2 Location	0.960	1.050	9.38
KST1	Surcharge	P2 Location	0.083	0.090	8.43
KST5		P2 Location	0.150	0.162	8.00
KST9		P2 Location	0.310	0.320	3.23

Effect of Input Acceleration

Figure 6.29 depicts the strain (%) profile for different base accelerations of 0.05g, 0.10g, 0.15g and 0.20g from tests KST1, KST2, KST3, and KST4 respectively. From the figure, it was observed that the strain (%) was relatively high at higher base accelerations at the normalized elevation of z/H= 0.75. From the Figure, a maximum strain (%) of 3.31 of the total wall height (H), for 0.20g, was observed compared with 2.71 for 0.05g base accelerations. From the same figure, it can also be observed that the maximum strain (%) was 3.31 at an acceleration of 0.2g, whereas it decreased to 2.71 at an acceleration of 0.05g (values can be seen in the Table 6.9). The strains of the bottom-layer were the smallest, and the strains of the top-layer were the largest, which indicates that the geotextiles located in the top layers play important roles in the seismic stability of the wrap faced reinforced retaining walls. The strains obtained in the present study are in close agreement with the results presented by Wang et al. (2015). Results from By PLAXIS 3D analysis showed that strain (%) [Profile for tests KST1(P), KST2(P), KST3(P), and KST4(P)] also at all elevations strain (%) variation was directly proportional as can be seen from Figure 6.29. From the same figure, it can also be observed that the maximum strain (%) was 3.55 at an acceleration of 0.20 g, whereas it decreased to 3.00 at an acceleration of 0.05 g. The maximum and minimum Strain (%) from PLAXIS 3D was 7.25% and 10.70% higher than the shake table model test respectively.

Effect of Surcharge

The strain (%) profile for tests KST1, KST5 and KST9 which were conducted at 0.05g base acceleration, where providing an insight into the effect of different surcharge loadings of 1.72 kPa, 1.12kPa and 0.7kPa as shown in Figure 6.30. It was observed that the strain (%) response against surcharge variation was inversely proportional at all elevations. The maximum strain (%) of the wall was 3.40 at a surcharge pressure of 0.7 kPa, whereas it was decreased to 2.71 at a surcharge pressure of 1.72 kPa. From the same figure, it can also be observed that the maximum strain (%) was 3.40 at a surcharge of 0.7 kPa, whereas it decreased to 2.71 at a surcharge of 1.72 kPa (values can be seen in the Table 6.9). Results from By PLAXIS 3D analysis showed that strain (%) [Profile for tests KST1 (P), KST5(P), and KST9(P)] also at all elevations strain (%) variation was inversely proportional as can be seen from Figure 6.30. From the same figure, it can also be observed that the maximum strain (%) was 3.71 at a surcharge of 0.7 kPa, whereas it decreased to 3.00 at a surcharge of 1.72 kPa. The maximum and minimum Strain (%) from PLAXIS 3D was 9.12% and 10.70% higher than the shake table model test respectively.

6.2.2.5 Effect of relative density within the geotextile sand filling

In this section, the effect of backfill densities has been discussed for Sylhet Sand. The backfill relative densities are 48%, 64% and 80% earthquake loading (Kobe) with base acceleration (0.1g) and surcharge (1.72 kPa). The face displacement, pore water pressure, strain and acceleration amplification responses have been described in Figures 6.31 to 6.34.

Face Displacement Response

Figure 6.31 presents the displacement profile for tests KST2, KST14 and KST26 providing an insight into the effect of surcharge loading of 1.72kPa and acceleration of 0.1g with different relative densities (48%, 64% and 80%). Displacements at all elevations decreased with an increase in relative densities. From the same figure/Table, it can also be observed that the maximum displacement of the wall was 0.140 mm ($\delta h/H$ = 0.35%) at a relative density 48%, whereas it decreased to 0.10 mm ($\delta h/H$ = 0.25%) at a relative density 80% (values can be seen in the Table 6.10). The displacements obtained in the present study are in close agreement with the results presented by Latha et al. (2008) corresponding to the relative density levels used in the present study. Results from PLAXIS 3D analysis showed that displacements [Profile for tests KST2 (P), KST14 (P) and KST26 (P)] at all elevations decreased with an increase in relative density as can be seen from Figure 6.31. From the same figure/Table, it can be observed that the maximum displacement of the wall was 0.153 mm ($\delta h/H$ = 0.38%) at a relative density 48%, whereas it decreased to 0.110 mm ($\delta h/H$ = 0.28%) at a relative density 80%. The maximum and minimum displacement from PLAXIS 3D was 9.29% and 10.00% higher than the shake table model test. Table 6.10 shows the Experimental and Numerical results for each layer of the model retaining Wall.

Table 6.9: Experimental and Numerical results for each layer of the model retaining wall of Sylhet sand (Kobe-Strain)

Test Name	Parameters	Layer of sand layer/Location	Experimental Results (%)	Numerical results (%)	Variation of Results (%)
KST1	Accelaration	Sg1 (Bottom)	1.80	1.88	4.44
		Sg4(Top)	2.71	3.00	10.70
KST2		Sg1 (Bottom)	2.20	2.33	5.91
		Sg4(Top)	2.87	3.10	8.01
KST3		Sg1 (Bottom)	2.21	2.35	6.33
		Sg4(Top)	2.97	3.13	5.39
KST4		Sg1 (Bottom)	2.81	2.95	4.98
		Sg4(Top)	3.31	3.55	7.25
KST1	Surcharge	Sg1 (Bottom)	1.80	1.88	4.44
		Sg4(Top)	2.71	3.00	10.70
KST5		Sg1 (Bottom)	2.40	2.51	4.58
		Sg4(Top)	3.20	3.60	12.50
KST9		Sg1 (Bottom)	2.47	2.54	2.83
		Sg4(Top)	3.40	3.71	9.12

Porewater Pressure Response

Figure 6.32 presents the pore water pressure profile for tests KST2, KST14 and KST26 providing an insight into the effect of surcharge loading of 1.72 kPa and acceleration of 0.1g with different relative densities (48%, 64% and 80%). Pore water pressure at all elevations decreased with an increase in relative densities. From the same figure/Table it can also be observed that the maximum pore water pressure of the wall was 0.08 kPa at a relative density of 48%, whereas it decreased to 0.04 kPa at a relative density of 80% (values can be seen in the Table 6.10). Results from PLAXIS 3D analysis showed that pore water pressure [Profile for tests KST2 (P), KST14(P) and KST26(P)] at all elevations decreased with an increase in relative densities as can be seen from Figure 6.32. From the same figure/Table, it can also be observed that the maximum pore water pressure was 0.04 kPa at a relative density of 48%, whereas it decreased to 0.09 kPa at a relative density of 80%. The maximum and minimum pore water pressure from PLAXIS 3D was 8.43% and 4.76% higher than the shake table model test respectively.

Strain Response

Figure 6.33 presents the Strain profile for tests KST2, KST14 and KST26 providing an insight into the effect of surcharge loadings of 1.72 kPa and acceleration of 0.10g with different relative densities (48%, 64% and 80%). Strain at all elevations decreased with an increase in relative densities. From the same figure/Table, it can also be observed that the maximum Strain (%) was 2.71 at a relative density of 48%, whereas it decreased to 1.61 at a relative density of 80% (values can be seen in the Table 6.10). The strains of the bottom-layer were the smallest, and the strains of the top-layer were the largest, which indicated that the geotextiles located in the top layers play important roles in the seismic stability of the wrap faced reinforced retaining walls. The strains obtained in the present study are in close agreement with the results presented by Wang et al. (2015). Results from PLAXIS 3D analysis showed that Strain [Profile for tests KST2 (P), KST14 (P) and KST26 (P)] at all elevations decreased with an increase in relative densities as can be seen from Figure 6.33. From the same figure, it can also be observed that the maximum Strain (%) was 3.00 at a relative density of 48%, whereas it decreased to 1.82 at a relative density of 80%. The maximum and minimum Strain (%) from PLAXIS 3D was 10.70% and 13.04% higher than the shake table model test respectively.

Acceleration Amplification Response

Figure 6.34 presents the Acceleration amplification for tests KST2, KST14 and KST26 providing an insight into the effect of surcharge loadings of 1.72 kPa and acceleration of 0.10g with different relative densities (48%, 64% and 80%). Acceleration amplification at all elevations decreased with an increase in relative densities. From the same figure/Table, it can also be observed that the maximum Acceleration amplification was 1.28 at a relative density of 48%, whereas it decreased to 1.10 at a relative density of 80% (values can be seen in the Table 6.10). The Acceleration amplification obtained in the present study is in close agreement with the results presented by Latha et al. (2008) corresponding to the relative density levels used in the present study. Results from PLAXIS 3D analysis showed that Acceleration amplification [Profile for tests KST2 (P.), KST14(P.) and KST26(P.)] at all elevations decreased with an increase in relative densities as can be seen from Figure 6.34. From the same figure/Table, it can also be observed that the maximum Acceleration amplification of the wall was 1.39 at a relative density of 48%, whereas it decreased to 1.26 at a relative density of 80%. The maximum and minimum Acceleration amplification from PLAXIS 3D was 8.59% and 14.55% higher than the shake table model test respectively.

6.2.3 Loma Prieta earthquake

The variation of the different soil parameters like acceleration amplification, displacement, pore water pressure and strain (LST1, LST2, LST3, LST4, LST5 and LST9) with respect to height for various Loma Prieta earthquake are presented in this section.

6.2.3.1 Acceleration response

Acceleration amplification for earthquake excitation was utilized to rearrange the introduction of acceleration response at various elevations of the wall. Acceleration amplification is the proportion of maximum peak to peak acceleration value in the soil to that of the corresponding value of the base motion. The acceleration amplification profile along with the height of the wall for various inputs of base motion after each test of 20 cycles of sinusoidal motion. However, the elevation (z) was represented in a non-dimensional shape subsequent to normalizing by the full height (T) of the model. Maximum acceleration amplification was observed at the top of the wall in all the tests.

Table 6.10: Experimental and Numerical results of the model wall (Kobe- Relative density)

Test Name (Dr)	Dynamic properties	Layer of sand layer/Location	Experimental Results (mm)	Numerical results (mm)	Variation of Results (%)
KST1 (48%)	Deformation (mm)	2nd Layer (2nd Bottom)	0.038	0.042	10.53
		3rd Layer (Mid)	0.021	0.022	4.76
		4th Layer (Top)	0.140	0.153	9.29
KST13 (64%)		2nd Layer (2nd Bottom)	0.011	0.012	9.09
		3rd Layer (Mid)	0.018	0.019	5.56
		4th Layer (Top)	0.120	0.125	4.17
KST25 (80%)		2nd Layer (2nd Bottom)	0.010	0.011	10.00
		3rd Layer (Mid)	0.012	0.013	8.33
		4th Layer (Top)	0.100	0.110	10.00
KST1 (48%)	Pore water Pressure (kPa)	P2 location	0.08	0.09	8.43
KST13 (64%)			0.06	0.07	6.56
KST25 (80%)			0.04	0.04	4.76
KST1 (48%)	Strain (%)	Sg1 (Bottom)	1.80	1.88	4.44
		Sg4(Top)	2.71	3.00	10.70
KST13 (64%)		Sg1 (Bottom)	1.20	1.29	7.50
		Sg4(Top)	2.10	2.28	8.57
KST25 (80%)		Sg1 (Bottom)	1.05	1.10	4.76
		Sg4(Top)	1.61	1.82	13.04
KST1 (48%)	Accelaration Amplification	A3	1.10	1.18	7.27
		A6	1.28	1.39	8.59
KST13 (64%)		A3	1.04	1.15	10.58
		A6	1.14	1.30	14.04
KST25 (80%)		A3	1.05	1.10	4.76
		A6	1.10	1.26	14.55

Effect of Input Acceleration

The acceleration amplifications from along the height of the wall for different base accelerations of 0.05g, 0.10g, 0.15g, and 0.2g from LST1, LST2, LST3 and LST4 tests, respectively, which was conducted at 1.72 kPa surcharge pressure and 48% relative density is presented in Figure 6.35. Acceleration amplifications were increased with increased base accelerations. However, from the tests was conducted, later it was observed that acceleration amplifications shake table testing (LST1, LST2, LST3 and LST4) at the top of the wall (z/H = 0.93) for 0.05g base accelerations were very close to 1.28, whereas it was 1.34, 1.39 and 1.52 for 0.1g, 0.15g, and 0.20g base acceleration, respectively. From the same figure, it can also be observed that the maximum acceleration amplification was 1.52 at an acceleration of 0.2g, whereas it decreased to 1.28 at an acceleration of 0.05g (values can be seen in the Table 6.11). Results from By PLAXIS 3D analysis showed that acceleration amplification [Profile for tests LST1(P), LST2 (P), LST3(P), and LST4(P)] also at all elevations increased with an increase in Acceleration as can be seen from Figure 6.35. From the same figure, it can also be observed that the maximum acceleration amplification was 1.69 at an acceleration of 0.2g, whereas it decreased to 1.44 at an acceleration of 0.05g. The present study was also compared with the study of Krishna and Latha (2007) as shown in Figure 6.35. The acceleration amplifications along with the height of the wall for different base accelerations of 0.1g, 0.15g, and 0.2g from T4, T6, and T7 model tests (Krishna and Latha, 2007) was compared with the present study. Acceleration amplifications were increased with increased base accelerations for all the curves. The maximum and minimum acceleration amplification from PLAXIS 3D was 11.18% and 12.50% higher than the shake table model test respectively.

Effect of Surcharge

Acceleration response against different surcharge pressures was presented from tests LST1, LST5 and LST9 are depicted in Figure 6.36. These tests were conducted with 1.72 kPa, 1.12 kPa and 0.7 kPa surcharge pressures at 0.05g base acceleration. Accelerations at the top of the wall were inversely proportional to the surcharge pressures from the range of tests that were conducted. It is observed from the figure that, the acceleration amplification values were 1.28, 1.43 and 1.64 for 1.72 kPa, 1.12 kPa and 0.7 kPa, surcharge pressures, respectively. From the same figure, it can also be observed that the maximum acceleration amplification was 1.64 at a surcharge of 0.7 kPa, whereas it decreased to 1.28 at a surcharge of 1.72 kPa (values can be seen in the Table 6.11). Results from By PLAXIS 3D analysis showed that acceleration amplification [Profile for tests LST1(P), LST5(P) and LST9(P)] also at all elevations decreased with an increase in surcharge as can be seen from Figure 6.36. From the same figure, it can also be observed that the maximum acceleration amplification was 1.71 at a surcharge of 0.7 kPa, whereas it decreased to 1.44 at a surcharge of 1.72 kPa. A comparison of the present study with the study of Krishna and Latha (2007) is shown in Figure 6.36. The acceleration amplifications along with the height of the wall for different surcharge pressures of 0.5 kPa, 1.0 kPa and 2.0 kPa from T1, T2, and T3 model tests Krishna and Latha (2007) was compared with the present study. The maximum and minimum acceleration amplification from PLAXIS 3D was 4.27% and 12.50% higher than the shake table model test respectively.

6.2.3.2 Displacement response

Horizontal face displacement along the height of the wall was monitored using three LVDTs positioned is shown in Figure 5.1. The displaced face profiles from various tests after 20 cycles of sinusoidal motion are presented in Figures 6.37 to 6.38. Here elevation (z) and horizontal displacements (δh) are presented in non-dimensional form after normalizing them by the height of the wall (H).

Table 6.11: Experimental and Numerical results for each layer of the model retaining wall of Sylhet sand (Loma Prieta-Acceleration amplification)

Test Name	Parameters	Layer of sand layer/Location	Experimental Results	Numerical results	Variation of Results (%)
LST1	Acceleration	A3	1.22	1.29	5.74
		A6	1.28	1.44	12.50
LST2		A3	1.28	1.39	8.59
		A6	1.34	1.49	11.19
LST3		A3	1.29	1.41	9.30
		A6	1.39	1.52	9.35
LST4		A3	1.35	1.49	10.37
		A6	1.52	1.69	11.18
LST1	Surcharge	A3	1.22	1.29	5.74
		A6	1.28	1.44	12.50
LST5		A3	1.32	1.46	10.61
		A6	1.43	1.56	9.09
LST9		A3	1.39	1.50	7.91
		A6	1.64	1.71	4.27

Effect of Input Acceleration

Figure 6.37 depicts the normalized displacement profile for different base accelerations of 0.05g, 0.10g, 0.15g and 0.20g from tests LST1, LST2, LST3 and LST4 respectively. From the figure, it was observed that the normalized displacements were relatively high at higher base accelerations at the normalized elevation of z/H= 0.875. This phenomenon had similarities to the test results of Sakaguchi et al. (1992) and Krishna and Latha (2007). From the Figure, a maximum horizontal displacement of 0.63% of the total wall height (H), for 0.20g, was observed compared with 0.2% for 0.05g base accelerations. From the same figure, it can also be observed that the maximum displacement was 0.250 mm at an acceleration of 0.2g, whereas it decreased to 0.080 mm at an acceleration of 0.05g (values can be seen in the Table 6.12). Results from By PLAXIS 3D analysis showed that displacement [Profile for tests LST1(P), LST2(P), LST3(P), and LST4(P)] also at all elevations acceleration variation was directly proportional as can be seen from Figure 6.37. From the same figure, it can also be observed that the maximum displacement was 0.280 mm at an acceleration of 0.20 g, whereas it decreased to 0.088 mm at an acceleration of 0.05 g. The maximum and minimum displacements from PLAXIS 3D were 12.00% and 10.00% higher than the shake table model test respectively.

Effect of Surcharge

The normalized displacement profile for tests LST1, LST5 and LST9 which were conducted at 0.05g base acceleration were providing an insight into the effect of different surcharge loadings of 1.72 kPa, 1.12kPa and 0.7kPa as shown in Figure 6.38. It was observed that the displacement response against surcharge variation was inversely proportional at all elevations. Moreover, this observation was concurrent with the test performed by Krishna and Latha (2007). The maximum displacement of the wall was (δh/H=0.78%) at a surcharge pressure of 0.7 kPa, whereas it decreased to (δh/H=0.2%) at a surcharge pressure of 1.72 kPa. From the same figure, it can also be observed that the maximum displacement was 0.310 mm at a surcharge of 0.7 kPa, whereas it decreased to 0.080 mm at a surcharge of 1.72 kPa (values can be seen in the Table 6.12). Results from By PLAXIS 3D analysis showed that displacement [Profile for tests LST1(P), LST5(P), and LST9(P)] also at all elevations acceleration variation was inversely proportional as can be seen from Figure 6.38. From the same figure, it can also be observed that the maximum displacement was 0.340 mm at a surcharge of 0.7 kPa, whereas it decreased to 0.088 mm at a surcharge of 1.72 kPa. The maximum and minimum displacements from PLAXIS 3D were 9.68% and 10.00% higher than the shake table model test respectively.

Table 6.12: Experimental and Numerical results for each layer of the model retaining wall of Sylhet sand (Loma Prieta-Displacement)

Test Name	Parameters	Layer of sand layer/Location	Experimental Results (mm)	Numerical results (mm)	Variation of Results (%)
LST1	Acceleration	2^{nd} Layer (2^{nd} Bottom)	0.037	0.040	8.11
		3^{rd} Layer (Mid)	0.056	0.061	8.93
		4^{th} Layer (Top)	0.080	0.088	10.00
LST2		2^{nd} Layer (2^{nd} Bottom)	0.041	0.042	2.44
		3^{rd} Layer (Mid)	0.074	0.080	8.11
		4^{th} Layer (Top)	0.092	0.103	11.96
LST3		2^{nd} Layer (2^{nd} Bottom)	0.085	0.091	7.06
		3^{rd} Layer (Mid)	0.110	0.116	5.45
		4^{th} Layer (Top)	0.150	0.163	8.67
LST4		2^{nd} Layer (2^{nd} Bottom)	0.150	0.165	10.00
		3^{rd} Layer (Mid)	0.200	0.213	6.50
		4^{th} Layer (Top)	0.250	0.280	12.00
LST1	Surcharge	2^{nd} Layer (2^{nd} Bottom)	0.037	0.040	8.11
		3^{rd} Layer (Mid)	0.056	0.061	8.93
		4^{th} Layer (Top)	0.080	0.088	10.00
LST5		2^{nd} Layer (2^{nd} Bottom)	0.090	0.096	6.67
		3^{rd} Layer (Mid)	0.130	0.140	7.69
		4^{th} Layer (Top)	0.190	0.210	10.53
LST9		2^{nd} Layer (2^{nd} Bottom)	0.195	0.210	7.69
		3^{rd} Layer (Mid)	0.240	0.270	12.50
		4^{th} Layer (Top)	0.310	0.340	9.68

6.2.3.3 Pore water pressure response

Typical pore water pressure variations obtained from the tests are presented in Figures 6.39 and 6.40. The height of Clayey soil layer (S) was taken as 300 mm in the case of pore water pressure.

Effect of Input Acceleration

The variations of the pore water pressure from model tests LST1, LST2, LST3, and LST4 with base accelerations 0.05g, 0.10g, 0.15g and 0.20g, respectively for surcharge load of 1.72 kPa is shown in Figure 6.39. The pore water pressure response against base acceleration variation was directly proportional at z/S=0.84 it can be seen from the figure. The maximum pore water pressure was 0.350 kPa at a base acceleration of 0.20g. The maximum pore water pressure for model tests LST1, LST2, LST3, and LST4 was 0.120 kPa, 0.200 kPa, 0.250 kPa, and 0.350 kPa, respectively. From the same figure, it can also be observed that the pore water pressure was 0.350 kPa at an acceleration of 0.2g, whereas it decreased to 0.120 kPa at an acceleration of 0.05g (values can be seen in the Table 6.13). Results from By PLAXIS 3D analysis showed that pore water pressure [Profile for tests LST1(P), LST2(P), LST3(P), and LST4(P)] also at all elevations pore water pressure was directly proportional as can be seen from Figure 6.39. From the same figure, it can also be observed that the maximum pore water pressure was 0.370 kPa at an acceleration of 0.20 g, whereas it decreased to 0.130 kPa at an acceleration of 0.05 g. The maximum and minimum pore water pressure from PLAXIS 3D was 5.71% and 8.33% higher than the shake table model test respectively.

Effect of Surcharge

Variations of the pore pressure from model tests LST1, LST5 and LST9 with of surcharge 1.72kPa, 1.12 kPa and 0.7 kPa, respectively for the base acceleration of 0.05g is presented in Figure 6.40. From the figure, it is observed that pore water pressure response against surcharge variation was inversely proportional at all elevations. The maximum pore water pressure was 0.410 kPa at a surcharge load of 0.7 kPa. The maximum pore water pressure for model tests KST1, KST5 and KST9 was 0.120 kPa, 0.350 kPa and 0.410 kPa respectively. From the same figure, it can also be observed that the maximum pore water pressure was

0.410 kPa at a surcharge of 0.7 kPa, whereas it decreased to 0.120 kPa at a surcharge of 1.72 kPa (values can be seen in the Table 6.13). Results from By PLAXIS 3D analysis showed that pore water pressure [Profile for tests LST1(P), LST5(P), and LST9(P)] also at all elevations pore water pressure variation was inversely proportional as can be seen from Figure 6.40. From the same figure, it can also be observed that the maximum pore water pressure was 0.450 kPa at a surcharge of 0.7 kPa, whereas it decreased to 0.130 kPa at a surcharge of 1.72 kPa. The maximum and minimum pore water pressure from PLAXIS 3D was 9.76% and 8.33% higher than the shake table model test respectively.

Table 6.13: Experimental and Numerical results for each layer of the model retaining wall of Sylhet sand (Loma Prieta-Pore water pressure)

Test Name	Parameters	Layer of sand layer/Location	Experimental Results (kPa)	Numerical results (kPa)	Variation of Results (%)
LST1	Acceleration	P2 Location	0.120	0.130	8.33
LST2		P2 Location	0.200	0.228	14.00
LST3		P2 Location	0.250	0.270	8.00
LST4		P2 Location	0.350	0.370	5.71
LST1	Surcharge	P2 Location	0.120	0.130	8.33
LST5		P2 Location	0.350	0.390	11.43
LST9		P2 Location	0.410	0.450	9.76

6.2.3.4 Strain response

The Strain profiles from various tests after 20 cycles of sinusoidal motion are presented in Figures 6.41 to 6.42.

Effect of Input Acceleration

Figure 6.41 depicts the strain (%) profile for different base accelerations of 0.05g, 0.10g, 0.15g and 0.20g from tests LST1, LST2, LST3, and LST4 respectively. From the figure, it was observed that the strain (%) was relatively high at higher base accelerations at the normalized elevation of z/H= 0.75. From the Figure, a maximum strain (%) of 4.97 of the total wall height (H), for 0.20g, was observed compared with 2.51 for 0.05g base accelerations. From the same figure, it can also be observed that the maximum strain (%) was

4.97 at an acceleration of 0.2g, whereas it decreased to 2.51 at an acceleration of 0.05g (values can be seen in the Table 6.14). The strains of the bottom-layer were the smallest, and the strains of the top-layer were the largest, which indicated that the geotextiles located in the top layers play important roles in the seismic stability of the wrap faced reinforced retaining walls. The strains obtained in the present study are in close agreement with the results presented by Wang et al. (2015). Results from By PLAXIS 3D analysis showed that strain (%) [Profile for tests LST1(P), LST2(P), LST3(P), and LST4(P)] also at all elevations strain (%) variation was directly proportional as can be seen from Figure 6.41. From the same figure, it can also be observed that the maximum strain (%) was 5.20 at an acceleration of 0.20 g, whereas it decreased to 2.59 at an acceleration of 0.05 g. The maximum and minimum Strain (%) from PLAXIS 3D was 4.63% and 3.19% higher than the shake table model test respectively.

Effect of Surcharge

The strain (%) profile for tests LST1, LST5 and LST9 which were conducted at 0.05g base acceleration, were providing an insight into the effect of different surcharge loadings of 1.72 kPa, 1.12kPa and 0.7kPa as shown in Figure 6.42. It was observed that the strain (%) response against surcharge variation was inversely proportional at all elevations. The maximum strain (%) of the wall was 3.09 at a surcharge pressure of 0.7 kPa, whereas it was decreased to 2.51 at a surcharge pressure of 1.72 kPa. From the same figure, it can also be observed that the maximum strain (%) was 3.09 at a surcharge of 0.7 kPa, whereas it decreased to 2.51 at a surcharge of 1.72 kPa (values can be seen in the Table 6.14). Results from By PLAXIS 3D analysis showed that strain (%) [Profile for tests LST1 (P), LST5(P), and LST9(P)] also at all elevations strain (%) variation was inversely proportional as can be seen from Figure 6.42. From the same figure, it can also be observed that the maximum strain (%) was 3.33 at a surcharge of 0.7 kPa, whereas it decreased to 2.59 at a surcharge of 1.72 kPa. The maximum and minimum Strain (%) from PLAXIS 3D was 7.77% and 3.19% higher than the shake table model test respectively.

6.2.3.5 Effect of relative density within the geotextile sand filling

In this section, the effect of backfill densities has been discussed for Sylhet Sand. The backfill relative densities are 48%, 64% and 80% earthquake loading (Loma Prieta) with base acceleration (0.1g) and surcharge (1.72 kPa). The face displacement, pore water pressure, strain and acceleration amplification responses have been described in Figures 6.43 to 6.46.

Face Displacement Response

Figure 6.43 presents the displacement profile for tests LST2, LST14 and LST26 providing an insight into the effect of surcharge loading of 1.72kPa and acceleration of 0.1g with different relative densities (48%, 64% and 80%). Displacements at all elevations decreased with an increase in relative densities. From the same figure/Table, it can also be observed that the maximum displacement of the wall was 0.080 mm ($\delta h/H$ = 0.20%) at a relative density 48%, whereas it decreased to 0.037 mm ($\delta h/H$ = 0.09%) at a relative density 80% (values can be seen in the Table 6.15). The displacements obtained in the present study are in close agreement with the results presented by Latha et al. (2008) corresponding to the relative density levels used in the present study. Results from PLAXIS 3D analysis showed that displacements [Profile for tests LST2 (P), LST14 (P) and LST26 (P)] at all elevations decreased with an increase in relative density as can be seen from Figure 6.43. From the same figure/Table, it can be observed that the maximum displacement of the wall was 0.088 mm ($\delta h/H$ = 0.22%) at a relative density 48%, whereas it decreased to 0.040 mm ($\delta h/H$ = 0.1%) at a relative density 80%. The maximum and minimum displacement from PLAXIS 3D was 10.00% and 8.11% higher than the shake table model test. Table 6.15 shows the Experimental and Numerical results for each layer of the model retaining Wall.

Porewater Pressure Response

Figure 6.44 presents the pore water pressure profile for tests LST2, LST14 and LST26 providing an insight into the effect of surcharge loading of 1.72 kPa and acceleration of 0.1g with different relative densities (48%, 64% and 80%). Pore water pressure at all elevations decreased with an increase in relative densities. From the same figure/Table, it can also be observed that the maximum pore water pressure of the wall was 0.120 kPa at a relative density of 48%, whereas it decreased to 0.058 kPa at a relative density of 80% (values can be seen in the Table 6.15). Results from PLAXIS 3D analysis showed that pore water pressure [Profile for tests LST2 (P), LST14 (P) and LST26 (P)] at all elevations decreased with an increase in relative densities as can be seen from Figure 6.44. From the same figure/Table, it can also be observed that the maximum pore water pressure was 0.130 kPa at a relative density of 48%, whereas it decreased to 0.063 kPa at a relative density of 80%. The maximum and minimum pore water pressure from PLAXIS 3D was 8.33% and 8.62% higher than the shake table model test respectively.

Table 6.14: Experimental and Numerical results for each layer of the model retaining wall of Sylhet sand (Loma Prieta-Strain)

Test Name	Parameters	Layer of sand layer/Location	Experimental Results (%)	Numerical results (%)	Variation of results (%)
LST1	Acceleration	Sg1 (Bottom)	1.70	1.79	5.29
		Sg4(Top)	2.51	2.59	3.19
LST2		Sg1 (Bottom)	2.06	2.19	6.31
		Sg4(Top)	2.87	2.94	2.44
LST3		Sg1 (Bottom)	3.50	3.74	6.86
		Sg4(Top)	4.10	4.61	12.44
LST4		Sg1 (Bottom)	3.90	4.20	7.69
		Sg4(Top)	4.97	5.20	4.63
LST1	Surcharge	Sg1 (Bottom)	1.70	1.79	5.29
		Sg4(Top)	2.51	2.59	3.19
LST5		Sg1 (Bottom)	1.87	2.00	6.95
		Sg4(Top)	2.81	3.21	14.23
LST9		Sg1 (Bottom)	2.05	2.24	9.27
		Sg4(Top)	3.09	3.33	7.77

Strain Response

Figure 6.45 presents the Strain profile for tests LST2, LST14 and LST26 providing an insight into the effect of surcharge loadings of 1.72 kPa and acceleration of 0.10g with different relative densities (48%, 64% and 80%). Strain at all elevations decreased with an increase in relative densities. From the same figure/Table, it can also be observed that the maximum Strain (%) was 2.51 at a relative density of 48%, whereas it decreased to 1.77 at a relative density of 80% (values can be seen in the Table 6.15). The strains of the bottom-layer were the smallest, and the strains of the top-layer were the largest, which indicated that the geotextiles located in the top layers play important roles in the seismic stability of the wrap faced reinforced retaining walls. The strains obtained in the present study are in close agreement with the results presented by Wang et al. (2015). Results from PLAXIS 3D analysis showed that Strain [Profile for tests LST2 (P), LST14 (P) and LST26 (P)] at all elevations decreased with an increase in relative densities as can be seen from Figure 6.45.

From the same figure, it can also be observed that the maximum Strain (%) was 2.59 at a relative density of 48%, whereas it decreased to 1.97 at a relative density of 80%. The maximum and minimum Strain (%) from PLAXIS 3D was 3.19% and 11.30% higher than the shake table model test respectively.

Acceleration Amplification Response

Figure 6.46 presents the Acceleration amplification for tests LST2, LST14 and LST26 providing an insight into the effect of surcharge loadings of 1.72 kPa and acceleration of 0.10g with different relative densities (48%, 64% and 80%). Acceleration amplification at all elevations decreased with an increase in relative densities. From the same figure/Table, it can also be observed that the maximum Acceleration amplification was 1.28 at a relative density of 48%, whereas it decreased to 1.03 at a relative density of 80% (values can be seen in the Table 6.15). The Acceleration amplification obtained in the present study is in close agreement with the results presented by Latha et al. (2008) corresponding to the relative density levels used in the present study. Results from PLAXIS 3D analysis showed that Acceleration amplification [Profile for tests LST2 (P), LST14 (P) and LST26 (P)] at all elevations decreased with an increase in relative densities as can be seen from Figure 6.46. From the same figure/Table, it can also be observed that the maximum Acceleration amplification of the wall was 1.44 at a relative density of 48%, whereas it decreased to 1.18 at a relative density of 80%. The maximum and minimum Acceleration amplification from PLAXIS 3D was 12.50% and 14.56% higher than the shake table model test respectively.

6.3 Analysis of Dynamic Response of Local Sand

Various dynamic soil parameters like acceleration amplification, displacement, pore water pressure and strain for local sand were estimated and presented in this section.

6.3.1 Sinusoidal wave

The variation of the different soil parameters like acceleration amplification, displacement, pore water pressure and strain with respect to height for various sinusoidal waves are presented in this section.

Table 6.15: Experimental and Numerical results of the model wall (Loma Prieta-Relative density)

Test Name (Dr)	Dynamic properties	Layer of sand layer/Location	Experimental Results	Numerical results	Variation of Results (%)
LST1 (48%)	Deformation (mm)	2nd Layer (2nd Bottom)	0.037	0.040	8.11
		3rd Layer (Mid)	0.056	0.061	8.93
		4th Layer (Top)	0.080	0.088	10.00
LST13 (64%)		2nd Layer (2nd Bottom)	0.020	0.022	10.00
		3rd Layer (Mid)	0.026	0.029	12.50
		4th Layer (Top)	0.050	0.057	14.00
LST25 (80%)		2nd Layer (2nd Bottom)	0.017	0.019	10.00
		3rd Layer (Mid)	0.021	0.023	9.52
		4th Layer (Top)	0.037	0.040	8.11
LST1 (48%)	Pore water Pressure (kPa)	P2 location	0.120	0.130	8.33
LST13 (64%)			0.070	0.080	14.29
LST25 (80%)			0.058	0.063	8.62
LST1 (48%)	Strain (%)	Sg1 (Bottom)	1.70	1.79	5.29
		Sg4(Top)	2.51	2.59	3.19
LST13 (64%)		Sg1 (Bottom)	1.44	1.59	10.42
		Sg4(Top)	2.37	2.42	2.11
LST25 (80%)		Sg1 (Bottom)	1.31	1.43	9.16
		Sg4(Top)	1.77	1.97	11.30
LST1 (48%)	Accelaration Amplification	A3	1.22	1.29	5.74
		A6	1.28	1.44	12.50
LST13 (64%)		A3	1.08	1.17	8.84
		A6	1.16	1.23	6.03
LST25 (80%)		A3	0.95	1.09	14.74
		A6	1.03	1.18	14.56

6.3.1.1 Acceleration response

Acceleration amplification was utilized to rearrange the introduction of acceleration response at various elevations of the wall. Acceleration amplification is the proportion of maximum peak to peak acceleration value in the soil to that of the corresponding value of the base motion. The acceleration amplification profile along with the height of the wall for various inputs of base motion after each test of 20 cycles of sinusoidal motion. However, the elevation (z) was represented in a non-dimensional shape subsequent to normalizing by the full height (T) of the model. Maximum acceleration amplification was observed at the top of the wall in all the tests.

<u>Effect of Input Acceleration</u>

The acceleration amplifications from along the height of the wall for different base accelerations of 0.05g, 0.10g, 0.15g, and 0.2g from LT1, LT9, LT19, and LT27 tests, respectively, which was conducted at 1 Hz frequency and 1.72 kPa surcharge pressure and 27% relative density for local sand is presented in Figure 6.47. Acceleration amplifications were increased with increased base accelerations. However, from the tests was conducted, later it was observed that acceleration amplifications shake table testing (LT1, LT9, LT19, and LT27) at the top of the wall (z/T = 0.93) for 0.05g base accelerations were very close to 1.43, whereas it was 1.52, 1.73 and 2.10 for 0.1g, 0.15g, and 0.20g base acceleration, respectively. From the same figure, it can also be observed that the maximum acceleration amplification was 2.10 at an acceleration of 0.2g, whereas it decreased to 1.43 at an acceleration of 0.05g (values can be seen in the Table 6.16). The present study was also compared with the study of Krishna and Latha (2007). The acceleration amplifications along with the height of the wall for different base accelerations of 0.1g, 0.15g, and 0.2g from the model tests (Krishna and Latha, 2007) was compared with the present study. Acceleration amplifications were increased with increased base accelerations for all the curves. This observation was concurrent with the test performed by Krishna and Latha (2007).

<u>Effect of Surcharge</u>

Acceleration response against different surcharge pressures was presented from tests LT1, LT35 and LT67 are depicted in Figure 6.48. These tests were conducted with 1.72 kPa, 1.12

kPa and 0.7 kPa surcharge pressures at 1 Hz frequency and 0.05g base acceleration. Accelerations at the top of the wall were inversely proportional to the surcharge pressures from the range of tests that were conducted. It is observed from the figure that, the acceleration amplification values were 1.43, 1.57 and 1.63 for 1.72 kPa, 1.12 kPa and 0.7 kPa, surcharge pressures, respectively. From the same figure, it can also be observed that the maximum acceleration amplification was 1.63 at a surcharge of 0.7 kPa, whereas it decreased to 1.43 at a surcharge of 1.72 kPa (values can be seen in the Table 6.16). A comparison of the present study with the study of Krishna and Latha (2007). The acceleration amplifications along with the height of the wall for different surcharge pressures of 0.5 kPa, 1.0 kPa and 2.0 kPa from the model tests Krishna and Latha (2007) was compared with the present study. Accelerations at the top of the wall were inversely proportional to the surcharge pressures. This observation was concurrent with the test performed by Krishna and Latha (2007).

Effect of Input Frequency

The effect of frequency on the acceleration response along the height of the wall for tests LT1, LT2, LT3, and LT4 with frequencies of 1Hz, 2Hz, 3Hz, and 5Hz which were conducted at 0.05g base acceleration and 1.7 kPa surcharge pressure is shown in Figure 6.49. From the figure, it observed that the acceleration response against frequency variation was not directly proportional. Moreover, accelerations at normalized elevations of 0.52, 0.65, 0.80 and 0.92 were amplified closer or slightly more than 1 for the frequency 1 Hz. The differences in acceleration amplification for various frequencies were increased with an increase in wall height. At a normalized height of 0.93, for 1Hz, 2Hz, 3Hz, and 5Hz frequency, the values of acceleration amplification were 1.43, 2.30, 2.20, and 2.61, respectively. Moreover, the acceleration amplification values were 1.29, 1.59, 1.32, and 1.70 for 1Hz, 2Hz, 3Hz, and 5Hz, respectively at a normalized height of 0.53. From the same figure, it can also be observed that the maximum acceleration amplification was 2.61 at a frequency of 5 Hz, whereas it decreased to 1.43 at a Frequency of 1 Hz (values can be seen in the Table 6.16). The acceleration amplifications along with the height of the wall for the different frequency of 1Hz, 2Hz and 3 Hz from the model tests Krishna and Latha (2007) was compared with the present study. The acceleration response against frequency variation is not directly proportional. This observation was concurrent with the test performed by Krishna and Latha (2007).

Table 6.16: Experimental results for each layer of the model retaining wall of Local sand (Acceleration amplification)

Test Name	Parameters	Layer of sand layer/Location	Experimental Results
LT1	Accelaration	A3	1.29
		A6	1.43
LT9		A3	1.39
		A6	1.52
LT19		A3	1.48
		A6	1.73
LT27		A3	1.72
		A6	2.10
LT1	Surcharge	A3	1.29
		A6	1.43
LT35		A3	1.33
		A6	1.57
LT67		A3	1.42
		A6	1.63
LT1	Frequency	A3	1.29
		A6	1.43
LT2		A3	1.59
		A6	2.30
LT3		A3	1.32
		A6	2.20
LT4		A3	1.70
		A6	2.61

6.3.1.2 Displacement response

Horizontal face displacement along the height of the wall was monitored using three LVDTs positioned is shown in Figure 5.1. The displaced face profiles from various tests after 20 cycles of sinusoidal motion are presented in Figures 6.50 to 6.52. Here elevation (z) and horizontal displacements (δh) are presented in non-dimensional form after normalizing them by the height of the wall (H).

Effect of Input Acceleration

Figure 6.50 depicts the normalized displacement profile for different base accelerations of 0.05g, 0.10g, 0.15g and 0.20g from tests LT1, LT9, LT19, and LT27 respectively. From the figure, it was observed that the normalized displacements were relatively high at higher base accelerations at the normalized elevation of z/H= 0.875. This phenomenon had similarities to the test results of Sakaguchi et al. (1992) and Krishna and Latha (2007). From the Figure, a maximum horizontal displacement of 3.53% of the total wall height (H), for 0.20g, was observed compared with 1.75% for 0.05g base accelerations. From the same figure, it can also be observed that the maximum displacement was 1.41 mm at an acceleration of 0.2g, whereas it decreased to 0.70 mm at an acceleration of 0.05g (values can be seen in the Table 6.17).

Effect of Surcharge

The normalized displacement profile for tests LT1, LT35, and LT67 which were conducted at 0.05g base acceleration and 1Hz frequency, were providing an insight into the effect of different surcharge loadings of 1.72 kPa, 1.12 kPa and 0.7 kPa as shown in Figure 6.51. It was observed that the displacement response against surcharge variation was inversely proportional at all elevations. Moreover, this observation was concurrent with the test performed by Krishna and Latha (2007). The maximum displacement of the wall was ($\delta h/H$=3.68%) at a surcharge pressure of 0.7 kPa, whereas it was decreased to ($\delta h/H$=1.75%) at a surcharge pressure of 1.72 kPa. From the same figure, it can also be observed that the maximum displacement was 1.47 mm at a surcharge of 0.7 kPa, whereas it decreased to 0.70 mm at a surcharge of 1.72 kPa (values can be seen in the Table 6.17).

Effect of Input Frequency

According to Figure 6.52. it can be said that the displacement response against frequency variation was not directly proportional. The normalized displacement profile observed for tests LT1, LT2, LT3, and LT4 with frequencies 1 Hz, 2 Hz, 3 Hz, and 5 Hz which were conducted at 0.05g base acceleration and 1.72 kPa surcharge pressure as presented in Figure 6.52. The displacement had occurred more at z/H=0.875 from the range of tests that were conducted. The maximum displacement of 1.75% was observed for 1 Hz frequency at z/H=0.875. From the same figure, it can also be observed that the maximum displacement was 0.70 mm at a frequency of 1 Hz, whereas it decreased to 0.29 mm at a frequency of 5 Hz (values can be seen in the Table 6.17).

6.3.1.3 Pore water pressure response

Typical pore water pressure variations obtained from the tests are presented in Figures 6.53, 6.54 and 6.55. The height of Clayey soil layer (S) was taken as 300 mm in the case of pore water pressure.

<u>Effect of Input Acceleration</u>

The variations of the pore water pressure from model tests LT1, LT9, LT19, and LT27 with base accelerations 0.05g, 0.10g, 0.15g and 0.20g, respectively for 1 Hz frequency and surcharge load of 1.72 kPa is shown in Figure 6.53. The pore water pressure response against base acceleration variation was directly proportional at z/S=0.84 it can be seen from the figure. The maximum pore water pressure was 0.410 kPa at a base acceleration of 0.20g. The maximum pore water pressure for model tests LT1, LT9, LT19, and LT27 was 0.120 kPa, 0.310 kPa, 0.370 kPa, and 0.410 kPa, respectively. From the same figure, it can also be observed that the pore water pressure was 0.410 kPa at an acceleration of 0.2g, whereas it decreased to 0.120 kPa at an acceleration of 0.05g (values can be seen in the Table 6.18).

<u>Effect of Surcharge</u>

Variations of the pore pressure from model tests LT1, LT35 and LT67 with of surcharge 1.72kPa, 1.12 kPa and 0.7 kPa, respectively for 1 Hz frequency and base acceleration of 0.20g is presented in Figure 6.54. From the figure, it was observed that pore water pressure response against surcharge variation was inversely proportional at all elevations. The maximum pore water pressure was 0.370 kPa at a surcharge load of 0.7 kPa. The maximum pore water pressure for model tests LT1, LT35 and LT67 was 0.120 kPa, 0.280 kPa and 0.370 kPa respectively. From the same figure, it can also be observed that the maximum pore water pressure was 0.370 kPa at a surcharge of 0.7 kPa, whereas it decreased to 0.120 kPa at a surcharge of 1.72 kPa (values can be seen in the Table 6.18).

Table 6.17: Experimental results for each layer of the model retaining Wall of Local sand (Displacement)

Test Name	Parameters	Layer of sand layer/Location	Experimental Results (mm)
LT1	Accelaration	2^{nd} Layer (2^{nd} Bottom)	0.49
		3^{rd} Layer (Mid)	0.54
		4^{th} Layer (Top)	0.70
LT9		2^{nd} Layer (2^{nd} Bottom)	0.70
		3^{rd} Layer (Mid)	0.88
		4^{th} Layer (Top)	1.20
LT19		2^{nd} Layer (2^{nd} Bottom)	0.77
		3^{rd} Layer (Mid)	0.94
		4^{th} Layer (Top)	1.31
LT27		2^{nd} Layer (2^{nd} Bottom)	0.90
		3^{rd} Layer (Mid)	1.10
		4^{th} Layer (Top)	1.41
LT1	Surcharge	2^{nd} Layer (2^{nd} Bottom)	0.49
		3^{rd} Layer (Mid)	0.54
		4^{th} Layer (Top)	0.70
LT35		2^{nd} Layer (2^{nd} Bottom)	0.97
		3^{rd} Layer (Mid)	0.99
		4^{th} Layer (Top)	1.33
LT67		2^{nd} Layer (2^{nd} Bottom)	1.19
		3^{rd} Layer (Mid)	1.31
		4^{th} Layer (Top)	1.47
LT1	Frequency	2^{nd} Layer (2^{nd} Bottom)	0.49
		3^{rd} Layer (Mid)	0.54
		4^{th} Layer (Top)	0.70
LT2		2^{nd} Layer (2^{nd} Bottom)	0.23
		3^{rd} Layer (Mid)	0.29
		4^{th} Layer (Top)	0.57
LT3		2^{nd} Layer (2^{nd} Bottom)	0.21
		3^{rd} Layer (Mid)	0.25
		4^{th} Layer (Top)	0.44
LT4		2^{nd} Layer (2^{nd} Bottom)	0.16

Test Name	Parameters	Layer of sand layer/Location	Experimental Results (mm)
		3rd Layer (Mid)	0.15
		4th Layer (Top)	0.29

<u>Effect of Input Frequency</u>

The effect of frequency for a given base acceleration and surcharge load on pore water pressure for tests LT1, LT2, LT3, and LT4 with the frequency of 1 Hz, 2 Hz, 3 Hz, and 5 Hz for 0.1g base accelerations and 1.72 kPa surcharge is shown in Figure 6.55. From the figure, it was observed that pore water pressures response against frequency variation was directly proportional. The highest pore water pressure was 0.270 kPa at 5 Hz frequency. From the same figure, it can also be observed that the maximum pore water pressure was 0.270 at a frequency of 5 Hz, whereas it decreased to 0.120 kPa at a frequency of 1 Hz (values can be seen in the Table 6.18).

Table 6.18: Experimental results for each layer of the model retaining Wall of Local sand (Pore water pressure)

Test Name	Parameters	Layer of sand layer/Location	Experimental Results (kPa)
LT1	Acceleration	P2 Location	0.120
LT9		P2 Location	0.310
LT19		P2 Location	0.370
LT27		P2 Location	0.410
LT1	Surcharge	P2 Location	0.120
LT35		P2 Location	0.280
LT67		P2 Location	0.370
LT1	Frequency	P2 Location	0.120
LT2		P2 Location	0.180
LT3		P2 Location	0.210
LT4		P2 Location	0.270

6.3.1.4 Strain response

The Strain profiles from various tests after 20 cycles of sinusoidal motion are presented in Figures 6.56 to 6.58.

Effect of Input Acceleration

Figure 6.56 depicts the strain (%) profile for different base accelerations of 0.05g, 0.10g, 0.15g and 0.20g from tests LT1, LT9, LT19, and LT27 respectively. From the figure, it was observed that the strain (%) was relatively high at higher base accelerations at the normalized elevation of z/H= 0.75. From the Figure, a maximum strain (%) of 3.57 of the total wall height (H), for 0.20g, was observed compared with 3.10 for 0.05g base accelerations. From the same figure, it can also be observed that the maximum strain (%) was 3.57 at an acceleration of 0.2g, whereas it decreased to 3.10 at an acceleration of 0.05g (values can be seen in the Table 6.19). The strains of the bottom-layer were the smallest, and the strains of the top-layer were the largest, which indicated that the geotextiles located in the top layers play important roles in the seismic stability of the wrap faced reinforced retaining walls. The strains obtained in the present study are in close agreement with the results presented by Wang et al. (2015).

Effect of Surcharge

The strain (%) profile for tests LT1, LT35, and LT67 which were conducted at 0.05g base acceleration and 1 Hz frequency, were providing an insight into the effect of different surcharge loadings of 1.72 kPa, 1.12 kPa and 0.7 kPa as shown in Figure 6.57. It was observed that the strain (%) response against surcharge variation was inversely proportional at all elevations. The maximum strain (%) of the wall was 3.63 at a surcharge pressure of 0.7 kPa, whereas it was decreased to 3.10 at a surcharge pressure of 1.72 kPa. From the same figure, it can also be observed that the maximum strain (%) was 3.63 at a surcharge of 0.7 kPa, whereas it decreased to 3.10 at a surcharge of 1.72 kPa (values can be seen in the Table 6.19).

Effect of Input Frequency

According to Figure 6.58. it can be said that the strain (%) response against frequency variation was inversely proportional. The normalized strain (%) profile observed for tests LT1, LT2, LT3, and LT4 with frequencies 1 Hz, 2 Hz, 3 Hz, and 5 Hz, respectively, which were conducted at 0.05g base acceleration and 1.72 kPa surcharge pressure as presented in

Figure 5.58. The strain (%) had occurred more at z/H=0.75 from the range of tests that were conducted. The maximum strain (%) of 3.10 was observed for 1 Hz frequency at z/H=0.75. From the same figure, it can also be observed that the maximum strain (%) was 3.10 at a frequency of 1 Hz, whereas it decreased to 2.59 at a frequency of 5 Hz (values can be seen in the Table 6.19).

6.3.1.5 Effect of relative density within the geotextile sand filling

In this section, the effect of backfill densities has been discussed for Local Sand. The backfill relative densities are 27%, 41%, and 55% with fixed frequency (1 Hz), base acceleration (0.05g) and surcharge (1.72 kPa). The face displacement, pore water pressure, strain and acceleration amplification responses have been described in Figures 6.59 to 6.62.

<u>Face Displacement Response</u>

Figure 6.59 presents the displacement profile for tests LT1, LT99 and LT193 providing an insight into the effect of surcharge loading of 1.72 kPa, frequency of 5 Hz and acceleration of 0.05g with different relative densities (27%, 41% and 55%). Displacements at all elevations decreased with an increase in relative densities. From the same figure/Table, it can also be observed that the maximum displacement of the wall was 0.70 mm ($\delta h/H$ = 1.75%) at a relative density 27%, whereas it decreased to 0.33 mm ($\delta h/H$ = 0.83%) at a relative density 55% (values can be seen in the Table 6.20). The displacements obtained in the present study are in close agreement with the results presented by Latha et al. (2008) corresponding to the relative density levels used in the present study. Table 5.20 shows the Experimental and Numerical results for each layer of the model retaining Wall.

<u>Porewater Pressure Response</u>

Figure 6.60 presents the pore water pressure profile for tests LT1, LT99 and LT193 providing an insight into the effect of surcharge loading of 1.72 kPa, frequency of 5 Hz and acceleration of 0.05g with different relative densities (27%, 41% and 55%). Pore water pressure at all elevations decreased with an increase in relative densities. From the same figure/Table, it can also be observed that the maximum pore water pressure of the wall was 0.12 kPa at a relative

density of 27%, whereas it decreased to 0.08 kPa at a relative density of 55% (values can be seen in the Table 6.20).

Table 6.19: Experimental results for each layer of the model retaining wall of Local sand (Strain)

Test Name	Parameters	Layer of sand layer/Location	Experimental Results (%)
LT1	Acceleration	Sg1 (Bottom)	1.70
		Sg4(Top)	3.10
LT9		Sg1 (Bottom)	2.29
		Sg4(Top)	3.13
LT19		Sg1 (Bottom)	2.32
		Sg4(Top)	3.36
LT27		Sg1 (Bottom)	2.42
		Sg4(Top)	3.57
LT1	Surcharge	Sg1 (Bottom)	1.70
		Sg4(Top)	3.10
LT35		Sg1 (Bottom)	2.90
		Sg4(Top)	3.40
LT67		Sg1 (Bottom)	3.10
		Sg4(Top)	3.63
LT1	Frequency	Sg1 (Bottom)	1.70
		Sg4(Top)	3.10
LT2		Sg1 (Bottom)	1.62
		Sg4(Top)	2.84
LT3		Sg1 (Bottom)	1.42
		Sg4(Top)	2.73
LT4		Sg1 (Bottom)	1.05
		Sg4(Top)	2.59

<u>Strain Response</u>

Figure 6.61 presents the Strain profile for tests LT1, LT99 and LT193 providing an insight into the effect of surcharge loadings of 1.72 kPa, frequency of 5 Hz and acceleration of 0.05g with different relative densities (27%, 41% and 55%). Strain at all elevations decreased with an increase in relative densities. From the same figure/Table, it can also be observed that the maximum Strain (%) was 3.10 at a relative density of 27%, whereas it decreased to 2.10 at a relative density of 55% (values can be seen in the Table 6.20). The strains of the bottom-layer

were the smallest, and the strains of the top-layer were the largest, which indicated that the geotextiles located in the top layers play important roles in the seismic stability of the wrap faced reinforced retaining walls. The strains obtained in the present study are in close agreement with the results presented by Wang et al. (2015).

Acceleration Amplification Response

Figure 6.62 presents the Acceleration amplification for tests LT1, LT99 and LT193 providing an insight into the effect of surcharge loadings of 1.72 kPa, frequency of 5 Hz and acceleration of 0.05g with different relative densities (27%, 41% and 55%). Acceleration amplification at all elevations decreased with an increase in relative densities. From the same figure/Table, it can also be observed that the maximum Acceleration amplification was 1.43 at a relative density of 27%, whereas it decreased to 1.25 at a relative density of 55% (values can be seen in the Table 6.20). The Acceleration amplification obtained in the present study is in close agreement with the results presented by Latha et al. (2008) corresponding to the relative density levels used in the present study.

6.3.2 Kobe earthquake

The variation of the different soil parameters like acceleration amplification, displacement, pore water pressure and strain (KLT1, KLT2, KLT3, KLT4, KLT5 and KLT9) with respect to height for various Kobe Earthquakes are presented in this section.

6.3.2.1 Acceleration response

Acceleration amplification for earthquake excitation was utilized to rearrange the introduction of acceleration response at various elevations of the wall. Acceleration amplification is the proportion of maximum peak to peak acceleration value in the soil to that of the corresponding value of the base motion. The acceleration amplification profile along with the height of the wall for various inputs of base motion after each test of 20 cycles of sinusoidal motion. However, the elevation (z) was represented in a non-dimensional shape subsequent to normalizing by the full height (T) of the model. Maximum acceleration amplification was observed at the top of the wall in all the tests.

Table 6.20: Experimental results of the model wall of Local Sand (Relative density)

Test Name (Dr)	Dynamic properties	Layer of sand layer/Location	Experimental Results
LT1 (27%)	Deformation (mm)	2nd Layer (2nd Bottom)	0.49
		3rd Layer (Mid)	0.54
		4th Layer (Top)	0.70
LT99 (41%)		2nd Layer (2nd Bottom)	0.29
		3rd Layer (Mid)	0.37
		4th Layer (Top)	0.47
LT193 (55%)		2nd Layer (2nd Bottom)	0.13
		3rd Layer (Mid)	0.22
		4th Layer (Top)	0.33
LT1 (27%)	Pore water Pressure (kPa)	P2 location	0.12
LT99 (41%)			0.10
LT193 (55%)			0.08
LT1 (27%)	Strain (%)	Sg1 (Bottom)	1.70
		Sg4(Top)	3.10
LT99 (41%)		Sg1 (Bottom)	1.62
		Sg4(Top)	2.50
LT193 (55%)		Sg1 (Bottom)	0.90
		Sg4(Top)	2.10
LT1 (27%)	Accelaration Amplification	A3	1.29
		A6	1.43
LT99 (41%)		A3	1.12
		A6	1.31
LT193 (55%)		A3	1.10
		A6	1.25

<u>Effect of Input Acceleration</u>

The acceleration amplifications from along the height of the wall for different base accelerations of 0.05g, 0.10g, 0.15g, and 0.2g from KLT1, KLT2, KLT3 and KLT4 tests, respectively, which was conducted at 1.72 kPa surcharge pressure and 48% relative density is presented in Figure 6.63. Acceleration amplifications were increased with increased base accelerations. However, from the tests was conducted, later it was observed that acceleration amplifications shake table testing (KLT1, KLT2, KLT3 and KLT4) at the top of the wall (z/T = 0.93) for 0.05g base accelerations were very close to 1.37, whereas it was 1.51, 1.57 and 1.71 for 0.1g, 0.15g, and 0.20g base acceleration, respectively. From the same figure, it can also be observed that the maximum acceleration amplification was 1.71 at an acceleration of 0.2g, whereas it decreased to 1.37 at an acceleration of 0.05g (values can be seen in the Table 6.21).

Effect of Surcharge

Acceleration response against different surcharge pressures was presented from tests KLT1, KLT5 and KLT9 are depicted in Figure 6.64. These tests were conducted with 1.72 kPa, 1.12 kPa and 0.7 kPa surcharge pressures at 0.05g base acceleration. Accelerations at the top of the wall were inversely proportional to the surcharge pressures from the range of tests that were conducted. It is observed from the figure that, the acceleration amplification values were 1.37, 1.47 and 1.56 for 1.72 kPa, 1.12 kPa and 0.7 kPa, surcharge pressures, respectively. From the same figure, it can also be observed that the maximum acceleration amplification was 1.56 at a surcharge of 0.7 kPa, whereas it decreased to 1.37 at a surcharge of 1.72 kPa (values can be seen in the Table 6.21).

6.3.2.2 Displacement response

Horizontal face displacement along the height of the wall was monitored using three LVDTs positioned is shown in Figure 5.1. The displaced face profiles from various tests after 20 cycles of sinusoidal motion are presented in Figures 6.65 to 6.66. Here elevation (z) and horizontal displacements (δh) are presented in non-dimensional form after normalizing them by the height of the wall (H).

Effect of Input Acceleration

Figure 6.65 depicts the normalized displacement profile for different base accelerations of 0.05g, 0.10g, 0.15g and 0.20g from tests KLT1, KLT2, KLT3 and KLT4 respectively. From the figure, it was observed that the normalized displacements were relatively high at higher base accelerations at the normalized elevation of z/H=0.875. This phenomenon had similarities to the test results of Sakaguchi et al. (1992) and Krishna and Latha (2007). From the Figure, a maximum horizontal displacement of 1.25% of the total wall height (H), for 0.20g, was observed compared with 0.43% for 0.05g base accelerations. From the same figure, it can also be observed that the maximum displacement was 0.50 mm at an acceleration of 0.2g, whereas it decreased to 0.170 mm at an acceleration of 0.05g (values can be seen in the Table 6.22).

Table 6.21: Experimental results for each layer of the model retaining wall of Local sand (Kobe-Acceleration amplification)

Test Name	**Parameters**	**Layer of sand layer/Location**	**Experimental Results**
KLT1	Accelaration	A3	1.21
		A6	1.37
KLT2		A3	1.34
		A6	1.51
KLT3		A3	1.39
		A6	1.57
KLT4		A3	1.43
		A6	1.71
KLT1	Surcharge	A3	1.21
		A6	1.37
KLT5		A3	1.33
		A6	1.47
KLT9		A3	1.47
		A6	1.56

Effect of Surcharge

The normalized displacement profile for tests KLT1, KLT5 and KLT9 which were conducted at 0.05g base acceleration were providing an insight into the effect of different surcharge loadings of 1.72 kPa, 1.12kPa and 0.7kPa as shown in Figure 6.66. It was observed that the displacement response against surcharge variation was inversely proportional at all elevations. Moreover, this observation was concurrent with the test performed by Krishna and Latha (2007). The maximum displacement of the wall was ($\delta h/H$=1.48%) at a surcharge pressure of 0.7 kPa, whereas it was decreased to ($\delta h/H$=0.43%) at a surcharge pressure of 1.72 kPa. From the same figure, it can also be observed that the maximum displacement was 0.590 mm at a surcharge of 0.7 kPa, whereas it decreased to 0.170 mm at a surcharge of 1.72 kPa (values can be seen in the Table 6.22).

Table 6.22: Experimental results for each layer of the model retaining Wall of Local sand (Kobe-Displacement)

Test Name	Parameters	Layer of sand layer/Location	Experimental Results (mm)
KLT1	Accelaration	2nd Layer (2nd Bottom)	0.051
		3rd Layer (Mid)	0.081
		4th Layer (Top)	0.170
KLT2		2nd Layer (2nd Bottom)	0.071
		3rd Layer (Mid)	0.091
		4th Layer (Top)	0.210
KLT3		2nd Layer (2nd Bottom)	0.170
		3rd Layer (Mid)	0.230
		4th Layer (Top)	0.410
KLT4		2nd Layer (2nd Bottom)	0.310
		3rd Layer (Mid)	0.410
		4th Layer (Top)	0.500
KLT1	Surcharge	2nd Layer (2nd Bottom)	0.051
		3rd Layer (Mid)	0.081
		4th Layer (Top)	0.170
KLT5		2nd Layer (2nd Bottom)	0.200
		3rd Layer (Mid)	0.330
		4th Layer (Top)	0.410
KLT9		2nd Layer (2nd Bottom)	0.350
		3rd Layer (Mid)	0.510
		4th Layer (Top)	0.590

6.3.2.3 Pore water pressure response

Typical pore water pressure variations obtained from the tests are presented in Figures 6.67 and 6.70. The height of Clayey soil layer (S) was taken as 300 mm in the case of pore water pressure.

Effect of Input Acceleration

The variations of the pore water pressure from model tests KLT1, KLT2, KLT3, and KLT4 with base accelerations 0.05g, 0.10g, 0.15g and 0.20g, respectively for surcharge load of 1.72

kPa is shown in Figure 6.67. The pore water pressure response against base acceleration variation was directly proportional at z/S=0.84 it can be seen from the figure. The maximum pore water pressure was 0.147 kPa at a base acceleration of 0.20g. The maximum pore water pressure for model tests KLT1, KLT2, KLT3, and KLT4 was 0.13 kPa, 0.20 kPa, 0.37 kPa, and 0.41 kPa, respectively. From the same figure, it can also be observed that the pore water pressure was 0.41 kPa at an acceleration of 0.2g, whereas it decreased to 0.13 kPa at an acceleration of 0.05g (values can be seen in the Table 6.23).

Effect of Surcharge

Variations of the pore pressure from model tests KLT1, KLT5 and KLT9 with of surcharge 1.72kPa, 1.12 kPa and 0.7 kPa, respectively for the base acceleration of 0.05g is presented in Figure 6.68. From the figure, it is observed that pore water pressure response against surcharge variation was inversely proportional at all elevations. The maximum pore water pressure was 0.45 kPa at a surcharge load of 0.7 kPa. The maximum pore water pressure for model tests KLT1, KLT5 and KLT9 was 0.13 kPa, 0.31 kPa and 0.45 kPa respectively. From the same figure, it can also be observed that the maximum pore water pressure was 0.45 kPa at a surcharge of 0.7 kPa, whereas it decreased to 0.13 kPa at a surcharge of 1.72 kPa (values can be seen in the Table 6.23).

Table 6.23: Experimental results for each layer of the model retaining Wall of Local sand (Kobe-Pore water pressure)

Test Name	Parameters	Layer of sand layer/Location	Experimental Results (kPa)
KLT1	Accelaration	P2 Location	0.13
KLT2		P2 Location	0.20
KLT3		P2 Location	0.37
KLT4		P2 Location	0.41
KLT1	Surcharge	P2 Location	0.13
KLT5		P2 Location	0.31
KLT9		P2 Location	0.45

6.3.2.4 Strain response

The Strain profiles from various tests after 20 cycles of sinusoidal motion are presented in Figures 6.69 to 6.70.

Effect of Input Acceleration

Figure 6.69 depicts the strain (%) profile for different base accelerations of 0.05g, 0.10g, 0.15g and 0.20g from tests KLT1, KLT2, KLT3, and KLT4 respectively. From the figure, it was observed that the strain (%) was relatively high at higher base accelerations at the normalized elevation of z/H= 0.75. From the Figure, a maximum strain (%) of 4.50 of the total wall height (H), for 0.20g, was observed compared with 1.20 for 0.05g base accelerations. From the same figure, it can also be observed that the maximum strain (%) was 4.50 at an acceleration of 0.2g, whereas it decreased to 1.20 at an acceleration of 0.05g (values can be seen in the Table 6.24). The strains of the bottom-layer were the smallest, and the strains of the top-layer were the largest, which indicates that the geotextiles located in the top layers play important roles in the seismic stability of the wrap faced reinforced retaining walls. The strains obtained in the present study are in close agreement with the results presented by Wang et al. (2015).

Effect of Surcharge

The strain (%) profile for tests KLT1, KLT5 and KLT9 which were conducted at 0.05g base acceleration, where providing an insight into the effect of different surcharge loadings of 1.72 kPa, 1.12kPa and 0.7kPa as shown in Figure 6.70. It was observed that the strain (%) response against surcharge variation was inversely proportional at all elevations. The maximum strain (%) of the wall was 3.20 at a surcharge pressure of 0.7 kPa, whereas it was decreased to 2.10 at a surcharge pressure of 1.72 kPa. From the same figure, it can also be observed that the maximum strain (%) was 3.20 at a surcharge of 0.7 kPa, whereas it decreased to 2.10 at a surcharge of 1.72 kPa (values can be seen in the Table 6.24).

6.3.2.5 Effect of relative density within the geotextile sand filling

In this section, the effect of backfill densities has been discussed for Local Sand. The backfill relative densities are 27%, 41%, and 55% for earthquake loading (Kobe) with base acceleration (0.1g) and surcharge (1.72 kPa). The face displacement, pore water pressure, strain and acceleration amplification responses have been described in Figures 6.71 to 6.74.

Face Displacement Response

Figure 6.71 presents the displacement profile for tests KLT1, KLT13 and KLT25 providing an insight into the effect of surcharge loading of 1.72kPa and acceleration of 0.1g with different relative densities (27%, 41% and 55%). Displacements at all elevations decreased with an increase in relative densities. From the same figure/Table, it can also be observed that the maximum displacement of the wall was 0.170 mm ($\delta h/H = 0.43\%$) at a relative density 27%, whereas it decreased to 0.080 mm ($\delta h/H = 0.20\%$) at a relative density 55% (values can be seen in the Table 6.25). The displacements obtained in the present study are in close agreement with the results presented by Latha et al. (2008) corresponding to the relative density levels used in the present study. Table 6.25 shows the Experimental results for each layer of the model retaining Wall.

Table 6.24: Experimental results for each layer of the model retaining Wall of Local sand (Kobe-Strain)

Test Name	**Parameters**	**Layer of sand layer/Location**	**Experimental Results (%)**
KLT1	Acceleration	Sg1 (Bottom)	1.20
		Sg4(Top)	3.20
KLT2		Sg1 (Bottom)	1.70
		Sg4(Top)	3.70
KLT3		Sg1 (Bottom)	2.10
		Sg4(Top)	4.30
KLT4		Sg1 (Bottom)	2.70
		Sg4(Top)	4.50
KLT1	Surcharge	Sg1 (Bottom)	1.20
		Sg4(Top)	3.20
KLT5		Sg1 (Bottom)	1.00
		Sg4(Top)	2.90
KLT9		Sg1 (Bottom)	0.80
		Sg4(Top)	2.10

Porewater Pressure Response

Figure 6.72 presents the pore water pressure profile for tests KLT1, KLT13 and KLT25 providing an insight into the effect of surcharge loading of 1.72 kPa and acceleration of 0.10g with different relative densities (27%, 41% and 55%). Pore water pressure at all elevations decreased with an increase in relative densities. From the same figure/Table, it can also be observed that the maximum pore water pressure of the wall was 0.130 kPa at a relative density of 27%, whereas it decreased to 0.032 kPa at a relative density of 55% (values can be seen in the Table 6.25).

<u>Strain Response</u>

Figure 6.73 presents the Strain profile for tests KLT1, KLT13 and KLT25 providing an insight into the effect of surcharge loadings of 1.72 kPa and acceleration of 0.10g with different relative densities (27%, 41% and 55%). Strain at all elevations decreased with an increase in relative densities. From the same figure/Table, it can also be observed that the maximum Strain (%) was 3.20 at a relative density of 27%, whereas it decreased to 2.10 at a relative density of 41% (values can be seen in the Table 6.25). The strains of the bottom-layer were the smallest, and the strains of the top-layer were the largest, which indicated that the geotextiles located in the top layers play important roles in the seismic stability of the wrap faced reinforced retaining walls. The strains obtained in the present study are in close agreement with the results presented by Wang et al. (2015).

<u>Acceleration Amplification Response</u>

Figure 6.74 presents the Acceleration amplification for tests KLT1, KLT13 and KLT25 providing an insight into the effect of surcharge loadings of 1.72 kPa and acceleration of 0.10g with different relative densities (27%, 41% and 55%). Acceleration amplification at all elevations decreased with an increase in relative densities. From the same figure/Table, it can also be observed that the maximum Acceleration amplification was 1.37 at a relative density of 27%, whereas it decreased to 1.21 at a relative density of 55% (values can be seen in the Table 6.25). The Acceleration amplification obtained in the present study is in close agreement with the results presented by Latha et al. (2008) corresponding to the relative density levels used in the present study.

6.3.3 Loma Prieta earthquake

The variation of the different soil parameters like acceleration amplification, displacement, pore water pressure and strain (LLT1, LLT2, LLT3, LLT4, LLT5 and LLT9) with respect to height for various Loma Prieta Earthquakes are presented in this section.

6.3.3.1 Acceleration response

Acceleration amplification for earthquake excitation was utilized to rearrange the introduction of acceleration response at various elevations of the wall. Acceleration amplification is the proportion of maximum peak to peak acceleration value in the soil to that of the corresponding value of the base motion. The acceleration amplification profile along with the height of the wall for various inputs of base motion after each test of 20 cycles of sinusoidal motion. However, the elevation (z) was represented in a non-dimensional shape subsequent to normalizing by the full height (T). Maximum acceleration amplification was observed at the top of the wall in all the tests.

Table 6.25: Experimental results of the model wall (Kobe- Relative density)

Test Name (Dr)	Dynamic properties	Layer of sand layer/Location	Experimental Results
KLT1 (27%)	Deformation (mm)	2^{nd} Layer (2^{nd} Bottom)	0.051
		3^{rd} Layer (Mid)	0.081
		4^{th} Layer (Top)	0.170
KLT13 (41%)		2^{nd} Layer (2^{nd} Bottom)	0.031
		3^{rd} Layer (Mid)	0.051
		4^{th} Layer (Top)	0.120
KLT25 (55%)		2^{nd} Layer (2^{nd} Bottom)	0.015
		3^{rd} Layer (Mid)	0.031
		4^{th} Layer (Top)	0.080
KLT1 (27%)	Pore water Pressure (kPa)	P2 location	0.130
KLT13 (41%)			0.011
KLT25 (55%)			0.032
KLT1 (27%)	Strain (%)	Sg1 (Bottom)	1.20
		Sg4(Top)	3.20
KLT13 (41%)		Sg1 (Bottom)	1.00
		Sg4(Top)	2.90
KLT25 (55%)		Sg1 (Bottom)	0.80
		Sg4(Top)	2.10
KLT1 (27%)	Accelaration Amplification	A3	1.21
		A6	1.37
KLT13 (41%)		A3	1.14
		A6	1.30
KLT25 (55%)		A3	1.05
		A6	1.21

Effect of Input Acceleration

The acceleration amplifications from along the height of the wall for different base accelerations of 0.05g, 0.10g, 0.15g, and 0.2g from LLT1, LLT2, LLT3 and LLT4 tests, respectively, which was conducted at 1.72 kPa surcharge pressure and 48% relative density is presented in Figure 6.75. Acceleration amplifications were increased with increased base accelerations. However, from the tests was conducted, later it was observed that acceleration amplifications shake table testing (LLT1, LLT2, LLT3 and LLT4) at the top of the wall (z/T = 0.93) for 0.05g base accelerations were very close to 1.52, whereas it was 1.57, 1.59 and 1.63 for 0.1g, 0.15g, and 0.20g base acceleration, respectively. From the same figure, it can also be observed that the maximum acceleration amplification was 1.63 at an acceleration of 0.2g, whereas it decreased to 1.52 at an acceleration of 0.05g (values can be seen in the Table 6.26).

Effect of Surcharge

Acceleration response against different surcharge pressures was presented from tests LLT1, LLT5 and LLT9 are depicted in Figure 6.76. These tests were conducted with 1.72 kPa, 1.12 kPa and 0.7 kPa surcharge pressures at 0.05g base acceleration. Accelerations at the top of the wall were inversely proportional to the surcharge pressures from the range of tests that were conducted. It is observed from the figure that, the acceleration amplification values were 1.52, 1.69 and 1.78 for 1.72 kPa, 1.12 kPa and 0.7 kPa, surcharge pressures, respectively. From the same figure, it can also be observed that the maximum acceleration amplification was 1.78 at a surcharge of 0.7 kPa, whereas it decreased to 1.52 at a surcharge of 1.72 kPa (values can be seen in the Table 6.26).

6.3.3.2 Displacement response

Horizontal face displacement along the height of the wall was monitored using three LVDTs positioned is shown in Figure 5.1. The displaced face profiles from various tests after 20 cycles of sinusoidal motion are presented in Figures 6.77 to 6.78. Here elevation (z) and horizontal displacements (δh) are presented in non-dimensional form after normalizing them by the height of the wall (H).

Table 6.26: Experimental results for each layer of the model retaining wall of Local sand (Loma Prieta-Acceleration amplification)

Test Name	**Parameters**	**Layer of sand layer/Location**	**Experimental Results**
LLT1	Accelaration	A3	1.27
		A6	1.52
LLT2		A3	1.32
		A6	1.57
LLT3		A3	1.41
		A6	1.59
LLT4		A3	1.47
		A6	1.63
LLT1	Surcharge	A3	1.27
		A6	1.52
LLT5		A3	1.31
		A6	1.69
LLT9		A3	1.41
		A6	1.78

Effect of Input Acceleration

Figure 6.77 depicts the normalized displacement profile for different base accelerations of 0.05g, 0.10g, 0.15g and 0.20g from tests LLT1, LLT2, LLT3 and LLT4 respectively. From the figure, it was observed that the normalized displacements were relatively high at higher base accelerations at the normalized elevation of z/H= 0.875. This phenomenon had similarities to the test results of Sakaguchi et al. (1992) and Krishna and Latha (2007). From the Figure, a maximum horizontal displacement of 1.10% of the total wall height (H), for 0.20g, was observed compared with 0.33% for 0.05g base accelerations. From the same figure, it can also be observed that the maximum displacement was 0.440 mm at an acceleration of 0.2g, whereas it decreased to 0.130 mm at an acceleration of 0.05g (values can be seen in the Table 6.27).

Effect of Surcharge

The normalized displacement profile for tests LLT1, LLT5 and LLT9 which were conducted at 0.05g base acceleration were providing an insight into the effect of different surcharge loadings of 1.72 kPa, 1.12 kPa and 0.7 kPa as shown in Figure 6.78. It was observed that the displacement response against surcharge variation was inversely proportional at all elevations. Moreover, this observation was concurrent with the test performed by Krishna and Latha (2007). The maximum displacement of the wall was ($\delta h/H$=1.68%) at a surcharge pressure of 0.7 kPa, whereas it was decreased to ($\delta h/H$=0.33%) at a surcharge pressure of 1.72 kPa. From the same figure, it can also be observed that the maximum displacement was 0.67 mm at a surcharge of 0.7 kPa, whereas it decreased to 0.13 mm at a surcharge of 1.72 kPa (values can be seen in the Table 6.27).

6.3.3.3 Pore water pressure response

Typical pore water pressure variations obtained from the tests are presented in Figures 6.79 and 6.82. The height of Clayey soil layer (S) was taken as 300 mm in the case of pore water pressure.

Effect of Input Acceleration

The variations of the pore water pressure from model tests LLT1, LLT2, LLT3, and LLT4 with base accelerations 0.05g, 0.10g, 0.15g and 0.20g, respectively for surcharge load of 1.72 kPa is shown in Figure 6.79. The pore water pressure response against base acceleration variation was directly proportional at z/S=0.84 it can be seen from the figure. The maximum pore water pressure was 0.34 kPa at a base acceleration of 0.20g. The maximum pore water pressure for model tests LLT1, LLT2, LLT3, and LLT4 was 0.11 kPa, 0.19 kPa, 0.25 kPa, and 0.34 kPa, respectively. From the same figure, it can also be observed that the pore water pressure was 0.34 kPa at an acceleration of 0.2g, whereas it decreased to 0.11 kPa at an acceleration of 0.05g (values can be seen in the Table 6.28).

Effect of Surcharge

Variations of the pore pressure from model tests LLT1, LLT5 and LLT9 with of surcharge 1.72kPa, 1.12 kPa and 0.7 kPa, respectively for the base acceleration of 0.05g is presented in Figure 6.80. From the figure, it is observed that pore water pressure response against surcharge variation was inversely proportional at all elevations. The maximum pore water pressure was 0.333 kPa at a surcharge load of 0.7 kPa. The maximum pore water pressure for model tests LLT1, LLT5 and LLT9 was 0.11 kPa, 0.21 kPa and 0.35 kPa respectively. From the same figure, it can also be observed that the maximum pore water pressure was 0.35 kPa at a surcharge of 0.7 kPa, whereas it decreased to 0.11 kPa at a surcharge of 1.72 kPa (values can be seen in the Table 6.28).

6.3.3.4 Strain response

The Strain profiles from various tests after 20 cycles of sinusoidal motion are presented in Figures 6.81 to 6.82.

Effect of Input Acceleration

Figure 6.81 depicts the strain (%) profile for different base accelerations of 0.05g, 0.10g, 0.15g and 0.20g from tests LLT1, LLT2, LLT3, and LLT4 respectively. From the figure, it was observed that the strain (%) was relatively high at higher base accelerations at the normalized elevation of z/H= 0.75. From the Figure, a maximum strain (%) of 3.30 of the total wall height (H), for 0.20g, was observed compared with 1.97 for 0.05g base accelerations. From the same figure, it can also be observed that the maximum strain (%) was 3.30 at an acceleration of 0.2g, whereas it decreased to 1.97 at an acceleration of 0.05g (values can be seen in the Table 6.29). The strains of the bottom-layer were the smallest, and the strains of the top-layer were the largest, which indicated that the geotextiles located in the top layers play important roles in the seismic stability of the wrap faced reinforced retaining walls. The strains obtained in the present study are in close agreement with the results presented by Wang et al. (2015).

Effect of Surcharge

The strain (%) profile for tests LLT1, LLT5 and LLT9 which were conducted at 0.05g base acceleration, were providing an insight into the effect of different surcharge loadings of 1.72 kPa, 1.12kPa and 0.7kPa as shown in Figure 6.82. It was observed that the strain (%) response against surcharge variation was inversely proportional at all elevations. The maximum strain (%) of the wall was 3.10 at a surcharge pressure of 0.7 kPa, whereas it was decreased to 1.97 at a surcharge pressure of 1.72 kPa. From the same figure, it can also be observed that the maximum strain (%) was 3.10 at a surcharge of 0.7 kPa, whereas it decreased to 1.97 at a surcharge of 1.72 kPa (values can be seen in the Table 6.29).

Table 6.27: Experimental results for each layer of the model retaining wall of Local sand (Loma Prieta-Displacement)

Test Name	Parameters	Layer of sand layer/Location	Experimental Results (mm)
LLT1	Acceleration	2nd Layer (2nd Bottom)	0.041
		3rd Layer (Mid)	0.061
		4th Layer (Top)	0.130
LLT2		2nd Layer (2nd Bottom)	0.061
		3rd Layer (Mid)	0.081
		4th Layer (Top)	0.250
LLT3		2nd Layer (2nd Bottom)	0.090
		3rd Layer (Mid)	0.120
		4th Layer (Top)	0.310
LLT4		2nd Layer (2nd Bottom)	0.100
		3rd Layer (Mid)	0.170
		4th Layer (Top)	0.440
LLT1	Surcharge	2nd Layer (2nd Bottom)	0.041
		3rd Layer (Mid)	0.061
		4th Layer (Top)	0.130
LLT5		2nd Layer (2nd Bottom)	0.150
		3rd Layer (Mid)	0.210
		4th Layer (Top)	0.510
LLT9		2nd Layer (2nd Bottom)	0.270
		3rd Layer (Mid)	0.410
		4th Layer (Top)	0.670

6.3.3.5 Effect of relative density within the geotextile sand filling

In this section, the effect of backfill densities has been discussed for Sylhet Sand. The backfill relative densities are 27%, 41%, and 55% for earthquake loading (Loma Prieta) with base acceleration (0.1g) and surcharge (1.72 kPa). The face displacement, pore water pressure, strain and acceleration amplification responses have been described in Figures 6.83 to 6.86.

Table 6.28: Experimental results for each layer of the model retaining wall of Local sand (Loma Prieta-Pore water pressure)

Test Name	Parameters	Layer of sand layer/Location	Experimental Results (kPa)
LLT1	Accelaration	P2 Location	0.11
LLT2		P2 Location	0.19
LLT3		P2 Location	0.25
LLT4		P2 Location	0.34
LLT1	Surcharge	P2 Location	0.11
LLT5		P2 Location	0.21
LLT9		P2 Location	0.35

Table 6.29: Experimental results for each layer of the model retaining Wall of Local sand (Loma Prieta-Strain)

Test Name	Parameters	Layer of sand layer/Location	Experimental Results (%)
LLT1	Acceleration	Sg1 (Bottom)	1.60
		Sg4(Top)	1.97
LLT2		Sg1 (Bottom)	1.95
		Sg4(Top)	2.51
LLT3		Sg1 (Bottom)	2.10
		Sg4(Top)	3.10
LLT4		Sg1 (Bottom)	2.50
		Sg4(Top)	3.30
LLT1	Surcharge	Sg1 (Bottom)	1.60
		Sg4(Top)	1.97
LLT5		Sg1 (Bottom)	2.11
		Sg4(Top)	2.90
LLT9		Sg1 (Bottom)	2.21
		Sg4(Top)	3.10

<u>Face Displacement Response</u>

Figure 6.83 presents the displacement profile for tests LLT2, LLT14 and LLT26 providing an insight into the effect of surcharge loading of 1.72kPa and acceleration of 0.1g with different

relative densities (27%, 41% and 55%). Displacements at all elevations decreased with an increase in relative densities. From the same figure/Table, it can also be observed that the maximum displacement of the wall was 0.130 mm (δh/H = 0.33%) at a relative density 27%, whereas it decreased to 0.090 mm (δh/H = 0.23%) at a relative density 55% (values can be seen in the Table 6.30). The displacements obtained in the present study are in close agreement with the results presented by Latha et al. (2008) corresponding to the relative density levels used in the present study. Table 6.30 shows the Experimental results for each layer of the model retaining Wall.

Porewater Pressure Response

Figure 6.84 presents the pore water pressure profile for tests LLT2, LLT14 and LLT26 providing an insight into the effect of surcharge loading of 1.72 kPa and acceleration of 0.10g with different relative densities (27%, 41% and 55%). Pore water pressure at all elevations decreased with an increase in relative densities. From the same figure/Table, it can also be observed that the maximum pore water pressure of the wall was 0.110 kPa at a relative density of 27%, whereas it decreased to 0.0.020 kPa at a relative density of 55% (values can be seen in the Table 6.30).

Strain Response

Figure 6.85 presents the Strain profile for tests LLT2, LLT14 and LLT26 providing an insight into the effect of surcharge loadings of 1.72 kPa and acceleration of 0.10g with different relative densities (27%, 41% and 55%). Strain at all elevations decreased with an increase in relative densities. From the same figure/Table, it can also be observed that the maximum Strain (%) was 1.97 at a relative density of 27%, whereas it decreased to 1.57 at a relative density of 41% (values can be seen in the Table 6.30). The strains of the bottom-layer were the smallest, and the strains of the top-layer were the largest, which indicates that the geotextiles located in the top layers play important roles in the seismic stability of the wrap faced reinforced retaining walls. The strains obtained in the present study are in close agreement with the results presented by Wang et al. (2015).

Table 6.30: Experimental results of the model wall (Loma Prieta-Relative density)

Test Name (Dr)	**Dynamic properties**	**Layer of sand layer/Location**	**Experimental Results**
LLT1 (27%)	Deformation (mm)	2nd Layer (2nd Bottom)	0.041
		3rd Layer (Mid)	0.061
		4th Layer (Top)	0.130
LLT13 (41%)		2nd Layer (2nd Bottom)	0.011
		3rd Layer (Mid)	0.031
		4th Layer (Top)	0.110
LLT25 (55%)		2nd Layer (2nd Bottom)	0.008
		3rd Layer (Mid)	0.021
		4th Layer (Top)	0.090
LLT1 (27%)	Pore water Pressure (kPa)	P2 location	0.110
LLT13 (41%)			0.090
LLT25 (55%)			0.020
LLT1 (27%)	Strain (%)	Sg1 (Bottom)	1.60
		Sg4(Top)	1.97
LLT13 (41%)		Sg1 (Bottom)	1.40
		Sg4(Top)	1.77
LLT25 (55%)		Sg1 (Bottom)	1.10
		Sg4(Top)	1.57
LLT1 (27%)	Accelaration Amplification	A3	1.27
		A6	1.52
LLT13 (41%)		A3	1.17
		A6	1.41
LLT25 (55%)		A3	1.11
		A6	1.35

Acceleration Amplification Response

Figure 6.86 presents the Acceleration amplification for tests LLT2, LLT14 and LLT26 providing an insight into the effect of surcharge loadings of 1.72 kPa and acceleration of 0.10g with different relative densities (27%, 41% and 55%). Acceleration amplification at all elevations decreased with an increase in relative densities. From the same figure/Table, it can also be observed that the maximum Acceleration amplification was 1.52 at a relative density of 27%, whereas it decreased to 1.35 at a relative density of 55% (values can be seen in the Table 6.30). The Acceleration amplification obtained in the present study is in close agreement with the results presented by Latha et al. (2008) corresponding to the relative density levels used in the present study.

6.4 Summary

The parameters varied in the tests were base acceleration, frequency, and surcharge pressure. The base acceleration was kept as 0.05g, 0.1g, 0.15g, and 0.2g in different tests. The range of frequency was varied from 1 Hz to 5 Hz. The surcharge pressure was kept as 0.70 kPa, 1.12 kPa, and 1.72 kPa. The relative densities of wrap faced embankment were 48%, 64%, & 80% for Sylhet sand and 27%, 41%, & 55% for Local sand. The model was also subjected to earthquake load (Kobe and Loma Prieta). The model used in the shake table was analyzed numerically using software PLAXIS 3D. The important observations from the experimental study using the shake table tests can be summarized as follows.

- ☐ Acceleration amplifications were increased with increased base accelerations. Accelerations at the top of the wall were inversely proportional to the surcharge pressures from the range of tests that were conducted. On the other hand, the acceleration response against frequency variation was not directly proportional.

- ☐ The normalized displacements were relatively high at higher base accelerations. The displacement response against surcharge variation was inversely proportional to all elevations. On the other hand, the displacement response against frequency variation was inversely proportional.

- ☐ There was no water table above the base of the shake table. The porewater pressure generated was only due to the entrapped water remaining within the Clay sample [water has been added to the dry Clay powder during the Clay sample preparation], which was not squeezed out during the one-dimensional consolidation process. The pore water pressure was relatively high within the Clay mass and will be low at the boundary.

- ☐ Excess pore water pressure increased with increased base accelerations. Pore water pressure at the top of the wall was inversely proportional to the surcharge pressures from the range of tests that were conducted. On the other hand, the pore water pressure against frequency variation was directly proportional.
- ☐ The strains of the bottom-layer were the smallest, and the strains of the top-layer were the largest, which indicated that the geotextiles located in the top layers play important roles in the seismic stability of the wrap faced reinforced retaining walls.
- ☐ The walls constructed with higher backfill relative density showed less face displacements, pore water pressure, strain and acceleration amplification compared to the walls constructed with lower densities when tested at higher base excitation.

CHAPTER 7
CONCLUSIONS AND RECOMMENDATIONS

7.1 General

The widespread use of reinforced-soil walls, especially in seismic regions, has led to extensive studies on seismic behavior of this soil structure. It is used to analyze the behavior of full-scale reinforced soil wrap faced retaining walls, wrap-faced cement-treated reinforced Clayey soil retaining walls, and vertical-faced wrap-around reinforced soil walls, and so on. The shake table test on the wrap faced embankment on the Clay soil foundation is new all over the world. In our country, the embankment on soft Clay soil is common and seismic analysis of this wrap faced embankment is important.

Shaking table studies were carried out on a wrap-faced reinforced soil wall to obtain apparent insight into their behavior under harmonic sinusoidal, Kobe and Loma Prieta earthquake input motions. A series of seven hundred and twenty shaking table tests were performed with variations in the acceleration and frequency of base sinusoidal and earthquake shaking. It was observed that the seismic response of the embankment was significantly affected by changes in frequency, surcharge, and acceleration of base shaking.

In this research, the wrap faced embankment constructed by Sylhet and Local sand, was analyzed for sinusoidal, Kobe and Loma Prieta earthquake input motions. From the results, it was observed that the dynamic parameters (acceleration amplifications, displacement, pore water pressure and strain) increased with increased base accelerations. On the other hand, dynamic parameters (acceleration amplifications, displacement, pore water pressure and strain) at the top of the wall were inversely proportional to the surcharge pressures and against frequency variation those were not directly proportional. From the test results, it was also found that the face displacements increased with a rise in elevation. At the higher elevations and high-frequency, pore water pressure was high.

The backfill relative densities of the embankment used in this study were 48%, 64%, and 80% for Sylhet sand and 27%, 41%, and 55% for local sand. The response of backfill relative density on the seismic response of reinforced soil retaining walls were studied by conducting shaking table tests on model walls. The wall constructed with higher backfill relative density showed lesser face displacements, pore water pressure, strain and acceleration amplification compared to the walls constructed with lower densities when tested at higher base excitation. These results were also found from the PLAXIS 3D analysis. Moreover, in all cases, numerically obtained values were slightly higher than the experimental results. The experimental result was found to be lower than the numerical result for all parameters, though the deviation was less than 15% in all cases. These results are helpful to observe the dynamic behavior of the wrap faced soil retaining wall on the soft Clay layer, which is usefull for updating (incorporating dynamic loading considering) design specification of this type of retaining wall (Railway and Road embankment).

7.2 Conclusions

The major findings from the experimental and numerical modeling of the wrap faced embankment on soft clay are listed below.

Dynamic Response of Sylhet Sand

Various dynamic soil parameters like acceleration amplification, displacement, pore water pressure and strain were summarized below:

- Maximum acceleration amplification was observed at the top of the wall in all the tests. Acceleration amplifications were increased with increased base accelerations for both experimental and numerical analysis.
- Accelerations at the top of the wall were inversely proportional to the surcharge pressures from the range of tests that were conducted. On the other hand, the acceleration response against frequency variation is not directly proportional. The differences in acceleration amplification for various frequencies were increased with an increase in wall height.
- The displacement response against acceleration variation was directly proportional to all elevations both of experimental and numerical analysis.
- The displacement response against surcharge variation was inversely proportional to all elevations. The normalized displacements were relatively high at higher base

accelerations at the highest normalized elevation. On the other hand, the displacement response against frequency variation was inversely proportional.

- The pore water pressure response against base acceleration variation was directly proportional both of experimental and numerical analysis.
- The pore water pressure response against surcharge variation was inversely proportional at all elevations. On the other hand, the pore water pressures response against frequency variation was directly proportional.
- Strain (%) was relatively high at higher base accelerations at the highest elevation. The strains of the bottom-layer were the smallest, and the strains of the top-layer were the largest, which indicated that the geotextiles located in the top layers play important roles in the seismic stability of the wrap faced reinforced retaining walls.
- The strain (%) response against surcharge variation was inversely proportional at all elevations. On the other hand, the strain (%) response against frequency variation was directly proportional.
- The different soil dynamic parameters (displacement, pore water pressure, strain and acceleration amplification) for seismic loading at all elevations decreased with an increase in relative densities.

Dynamic Response of Local Sand

Various dynamic soil parameters like acceleration amplification, displacement, pore water pressure and strain were summarized below.

- Acceleration amplifications were increased with increased base accelerations.
- Accelerations at the top of the wall were inversely proportional to the surcharge pressures from the range of tests that were conducted. On the other hand, the acceleration response against frequency variation was not directly proportional.
- The normalized displacements were relatively high at higher base accelerations at the normalized higher elevation.
- The displacement response against surcharge variation was inversely proportional to all elevations. On the other hand, the displacement response against frequency variation was inversely proportional.

- The pore water pressure response against base acceleration variation was directly proportional.
- The pore water pressure response against surcharge variation was inversely proportional at all elevations. On the other hand, the pore water pressures response against frequency variation was directly proportional.
- The strain (%) was relatively high at higher base accelerations at the normalized elevation. The strain (%) also at all elevations strain (%) variation against acceleration was directly proportional.
- The strain (%) response against surcharge variation was inversely proportional at all elevations. On the other hand, the strain (%) response against frequency variation was directly proportional.
- The different soil dynamic parameters (displacement, pore water pressure, strain and acceleration amplification) for seismic loading at all elevations decreased with an increase in relative densities.

7.3 Recommendations

The research conducted in the testing program and numerical analysis has led to many questions and subsequent future research interests. The areas of future research were listed below, followed by brief comments:

a) Study may be conducted to prepare specifications and guidelines for road and railway embankment on soft Clay to avoid failure or damage due to seismic load.

b) Study may be conducted to determine the suitable ground improvement techniques considering seismic load for such areas.

c) Modeling of the wrap faced wall with saturated backfill on soft Clay.

d) Study may be conducted on wrap faced wall in consideration with the stability of reinforced wall on soft Clay.

References:

Ali, M. H. (1998). Earthquake database and seismic zoning of Bangladesh, proceedings of International Symposium-Information Technology tools for Natural Disaster Risk Management, INCEDE report 11, pp. 59-73.

Adachi, T., Oka, F. (1982). Constitutive equation for normally consolidated Clays based on elasto-viscoplasticity. Soils and Foundations, 22, 57-70.

ASTM D4595. Standard Test Method for Tensile Properties of Geotextiles by the Wide Width Strip Method. ASTM International, West Conshohocken, PA, USA.

Atkinson, J.H., Sallfors, G. (1991). Experimental determination of soil properties. In Proc. 10th ECSMFE, 3, 915-956.

Bathurst, R.J., Hatami, K. (1998). Seismic response analysis of a geosynthetic reinforced soil retaining wall. *Geosynthetics International* 5 (1–2), 127–166.

Bathurst, R. J., El-Emam, M., Mashhour, M. M. (2002a). Shaking table model study on the dynamic response of reinforced soil walls. Proceedings of the *7th International Geosynthetics Conference*, Nice, France, September 2002, Vol. 1, pp. 99–102.

Benjamim, C. V. S., Bueno, B. S., Zornberg, J. G. (2007). Field monitoring and evaluation of geotextile-reinforced soil-retaining walls. *Geosynthetics International*, 14, No. 2, 100–118.

Benz, T., Schwab, R., Vermeer, P.A., Kauther, R.A. (2007). A hoek-brown criterion with intrinsic material strength factorization. Int.J. of Rock Mechanics and Mining Sci., 45(2), 210-222.

Bjerrum, L. (1967). Engineering geology of norwegian normally-consolidated marine Clays as related to settlements of buildings. Seventh Rankine Lecture, Geotechnique 17, 81-118.

BNBC (1993), Bangladesh National Building Code, HBRI-BSTI.

Borja, R.I., Kavaznjian, E. (1985). A constitutive model for the a-e-t behaviour of wet Clays. Geotechnique, 35, 283-298.

Brinkgreve, R.B.J. and Broere, W. (2006). Plaxis 3D Foundation Version 1.5, Delft University of Technology & PLAXIS bv, The Netherlands.

Brinkgreve, R.B.J. (2004). Time-dependent behaviour of soft soils during embankment construction - a numerical study. Proc. NUMOG IX, 631-637.

Burland, J. B. (1990). On the Compressibility and Shear Strength of Natural Clays. Geotechnique 40 (3): 329–78.

Buisman, K. (1936). Results of long duration settlement tests. Proceedings 1st International Conference on Soil Mechanics and Foundation Engineering, Mass. Vol. 1, 103-107.

Cai, W., Yu, B, Kaewunruen, S. (2019). "Shaking table tests of suspended structures equipped with viscous dampers," Applied Sciences, vol. 9, no. 13, pp. 1-16.

Carrion, J. and Spencer, B. F. (2007). Model-based strategies for real-time hybrid testing. Technical Report NSEL-006, University of Illinois at Urbana-Champaign.

Carrion, J. E., Spencer, B. F., and Phillips, B. M. (2009). Real-time hybrid simulation for structural control performance assessment. Earthquake Engineering and Engineering Vibration, 29(8):481–492.

CDMP (2009), Report on time predictable fault modeling.

Çelebi, E., Göktepe, F., Omid, A. J. (2019). "Seismic soil response of scaled geotechnical test model on small shaking table," Arabian Journal of Geosciences, vol. 12, no. 2, pp. 44.

Chen, C. and Ricles, J. (2009). Analysis of actuator delay compensation methods for real-time testing. Engineering Structures, 31(11):2643–2655. doi:10.1016/j.engstruct.2009.06.012.

Choi, S. K., Lee, M. J., Choo, H., Tumay, M. T., Lee, W. (2010). Preparation of a large size granular specimen using a rainer system with a porous plate. *Geotech Test J ASTM* 33(1):1–10.

Christenson, R., Lin, Y., Emmons, A., and Bass, B. (2008). Large-scale experimental verification of semiactive control through real-time hybrid simulation 1. Journal of Structural Engineering, 134(4):522–534.

Collin, J. G., Chouery-Curtis, V. E., Berg, R. R., (1992). Field observations of reinforced soil structures under seismic loading. In: Proc. Int. Symp. *Earth Reinforcement*, 223-228.

Conte, J. and Trombetti, T. (2000). Linear dynamic modeling of a uni-axial servo hydraulic shaking table system. Earthquake Engineering and Structural Dynamics, 29:1375–1404.

Conte, J. P., Luco, J. E., Restrepo, J. I., Seible, F., and Van Den Einde, L. (2004). UCSD-NEES large high performance outdoor shake table. In Proceedings of the 17-th ASCE Engineering Mechanics Conference, Newark, DE.

Dave T. N., Dasaka S. M. (2012). Assessment of portable traveling pluviator to prepare reconstituted sand specimens. *GeomechEngInt J* 4(2):79–90.

Deierlein, G. G., Krawinkler, H., Ma, X., Eatherton, M., Hajjar, J. F., Takeuchi, T., Kasai, K., and Midorikawa, M. (2011). Earthquake resilient steel braced frames with controlled rocking and energy dissipating fuses. Steel Construction: Design and Research, 4(3):171–175.

Doyle, J. and Stein, G. (1981). Multivariable feedback design: concepts for a classical modern synthesis. IEEE Transactions on Modern Control, AC-26(1):4–16.

Duncan, J.M., Chang, C.Y. (1970). Nonlinear analysis of stress and strain in soil. ASCE J. of the Soil Mech. and Found. Div., 96, 1629-1653.

Dyke, S., Spencer, B., Quast, P., and Sain, M. (1995). Role of control-structure inter- action in protective system design. Journal of Engineering Mechanics, 121(2):322– 338.

Edgar, T. V., Puckett, J. A., D'Spain, R. B., (1989). Effect of geotextiles on lateral pressure and displacement in highway embankments. *Geotextile and Geomembranes* 8, 275-292.

El-Emam, M. M., Bathurst, R. J. (2005). Facing contribution to seismic response of reduced-scale reinforced soil walls. *Geosynthetics International* 12 (5), 215–238.

El-Emam, M. M., Bathurst, R. J. (2007). Influence of reinforcement parameters on the seismic response of reduced-scale reinforced soil retaining walls. *Geotextiles and Geomembranes* 25 (1), 33–49.

Elwood, K. and Moehle, J. (2003). Shake table tests and analytical studies on the gravity load collapse of reinforced concrete frame. Technical Report PEER 2003/01, University of California, Berkeley.

Filiatrault, A., Fischer, D., Folz, B., and Uang, C. (2001). Shake table testing of a full- scale two story woodframe house. In Proceeding of the 2001 Structures Congress, Washington, D.C.

Fretti C., Lo Presti D. C. F., Pedroni S. (1995) A pluvial deposition method to reconstitute specimens well graded sand. *Geotech Test J ASTM* 18(2):292–298.

Gade V. K., Dasaka S. M. (2016). Development of a mechanized travelling pluviator to prepare reconstituted uniform sand specimens. J Mater Civ Eng.

Garlanger, J.E. (1972). The consolidation of soils exhibiting creep under constant effective stress. Geotechnique, 22, 71-78.

Gao, X., Castaneda, N., and Dyke, S. (2013). Real time hybrid simulation: from dynamic system, motion control to experimental error. Earthquake Engineering and Structural Dynamics, 42(6):322–338. doi: 10.1002/eqe.2246.

Goktepe, F., Celebi, E., Omid, A. J. (2019). "Numerical and experimental study on scaled soil-structure model for small shaking table tests," Soil Dynamics and Earthquake Engineering, vol. 119, pp. 308-319.

Hatami, K., Bathurst, R.J. (2000). Effect of structural design on fundamental frequency of reinforced-soil retaining walls. *Soil Dynamics and Earthquake Engineering* 19, 137–157.

Hoek, E., Carranza-Torres, C., Corkum, B. (2002). Hoek-brown failure criterion - 2002 edition, volume 1, 267-273.

Hoek, E., Diederichs, M.S. (2006). Empirical estimation of rock mass modulus, volume 43, 203-215

Huang, C. C., Chou, L. H., Tatsuoka, F. (2003). Seismic displacements of geosynthetic-reinforced soil modular block walls. *Geosynthetics International*, 10, No. 1, 2–23.

Huang, C. -C., Wu, S.-H. (2006). Simplified approach for assessing seismic displacements of soil-retaining walls. Part I: Geosynthetic reinforced modular block walls. *Geosynthetics International*, 13, No. 6, 219–233.

Ho. S. K., Rowe, R. K., (1996). Effect of wall geometry on the behavior of reinforced soil walls. *Geotextile and Geomembranes* 14 (10), 521-541.

Horiuchi, T., Inoue, M., Konno, T., and Namita, Y. (1999). Real-time hybrid exper- imental system with actuator delay compensation and its application to a piping system with energy absorber. Earthquake Engineering and Structural Dynamics, 28(10):1121–1141.

Horiuchi, T. and Konno, T. (2001). A new method for compensating actuator delay in real-time hybrid experiments. Philosophical Transactions of the Royal Society of London Series A: Mathematical Physical and Engineering Sciences, 359:1893–1909.

Hossain, M. Z., Ansary, M. A. (2018). Development of a portable traveling pluviator device and its performance to prepare uniform sand specimens. *Innovative Infrastructure Solutions*. 3(1), 53.

Hore, R., Arefin, M. R. and Ansary, M. A. (2019).Development of Zonation map based on soft Clay for Bangladesh. Journal of Engineering Science, vol. 10, no1, pp.13-18.

Igarashi, A., Iemura, H., and Suwa, T. (2000). Development of substructured shaking table test method. In Proceedings of the 12th World Conference on Earthquake Engineering, Auckland, New Zealand.

Igarashi, A., Sanchez-Flores, F., Iemura, H., Fujii, K., and Toyooka, A. (2009). Real- time hybrid testing of laminated rubber dampers for seismic retrofit of bridges. In 3rd International Conference on Advances in Experimental Structural Engineering. San Francisco, USA.

lizuka, A., Ohta, H. (1987). A determination procedure of input parameters in elasto-viscoplastic finite element analysis. Soils and Foundations, 27, 71-87.

Jacobsen, S. (1930). Experimental study of the dynamic behavior of models of timber walls. Bulletin of the Seismological Society of America, 20:115–146.

Janbu, N. (1985). Soil models in offshore engineering (25th rankine lecture). Geotechnique, 35, 241-280

Ji, X., Kajiwara, K., Nagae, T., Enokida, R., and Nakashima, M. (2009). A sub-structure shaking table test for reproduction of earthquake responses of high-rise buildings. Earthquake Engineering and Structural Dynamics, 38:1381–1399.

Kamal and Midorikawa (2004). GIS-based geomorphological mapping using remote sensing data and supplementary geoinformation: A case study of the Dhaka city area, Bangladesh. International Journal of Applied Earth Observations and Geoinformation, 6/2, 111-125.

Kondner, R.L. (1963). A hyperbolic stress strain formulation for sands. 2. Pan. Am. ICOSFE Brazil, 1, 289-324.

Kokusho, T., (1980). Cyclic triaxial test of dynamic soil properties for wide strain range. Soils and foundations 20, 45–60.

Koerner, R. M. (1999). Designing with Geosynthetics, 4th edition, Prentice Hall, NJ, 761.

Koseki, J., Bathurst, R. J., Gu ̈ler, E., Kuwano, J., Maugeri, M. (2006). Seismic stability of reinforced soil walls: Keynote paper. CD *Proceedings of the 8th International Conference on Geosynthetics*, Yokohama, Japan, 18–22 September 2006, 28.

Kramer, S. L. (1996). Geotechnical Earthquake Engineering, Prentice Hall, Upper Saddle River, NJ, 653.

Krishna, A. M.,Latha, G. M. (2007). Seismic response of wrap-faced reinforced soil-retaining wall models using shaking table tests. *Geosynthetics International*, 14(6), 355-364.

Kuehn, J., Epp, D., and Patten, W. (1999). High fidelity control for a seismic shake table. Earthquake Engineering and Structural Dynamics, 28(11):1235–1254.

Latha, G. M., Krishna, A. M. (2006). Shaking table studies on reinforced soil retaining walls. *Indian Geotechnical Journal*, 36(4), 321-333.

Latha, G. M., Krishna, A. M. (2008). Seismic response of reinforced soil retaining wall models: influence of backfill relative density. *Geotextiles and Geomembranes*, 26(4), 335-349.

Latha, G. M., NandhiVarman, A. M. (2014). Shaking table studies on geosynthetic reinforced soil slopes. *International Journal of Geotechnical Engineering*, 8(3), 299-306.

Latha, G. M., Manju, G. S. (2016). Seismic Response of Geocell Retaining Walls Through Shaking Table Tests. *International Journal of Geosynthetics and Ground Engineering*, 2(1), 7.

Leroueil, S. (1977). Quelques considerations sur le comportement des argiles sensibles. Ph.d. thesis, Laval University, Quebec.

Ling, H. I., Mohri, Y., Leshchinsky, D., Perry, E. B., (1997). Seismic design and performance of geosynthetic-reinforced soil structures. Geotechnique 47 (5), 933-952.

Ling, H.I., Leshchinsky, D., Chou, N. N. S., (2001). Post-earthquake investigation on sevealgeosynthetic-reinforced soil retaining walls and slopes during1999 Ji-Ji earthquake of Taiwan. *Soil Dynamics and Earthquake Engineering* 21(4), 297-313.

Ling, H. I., Mohri, Y., Leshchinsky, D., Christopher, B., Matsushima, K., Liu, H., (2005). Large- scale shaking table tests on modular-block reinforced soil retaining walls. *Journal of Geotechnical and Geoenvironmental Engineering* 131 (4), 465-476.

Lo Presti, D. C. F., Berardi, R., Pedroni, S., Crippa, V. (1993) A new traveling sand pluviator to reconstitute specimens of well graded silty sand. Geotech Test J ASTM 16(1):18–26.

Lee, S., Parka, E., Mina, K., and Park, J. (2007). Real-time substructuring technique for the shaking table test of upper substructures. Engineering Structures, 29:2219– 2232.

Mesri, G., Godlewski, P.M. (1977). Time and stress-compressibility inter-relationship. Journal of the Geotechnical Engineering Division, ASCE, 103(GT5), 417-430.

Murayama, S., Shibata, T. (1966). Flow and stress relaxation of Clays. In I.U.T.A.M. Symp. on Rheology and Soil Mechanics. Grenoble, 99-129.

Miura, S., Toki, S. (1982). A sample preparation method and its effect on static and cyclic displacement strength properties of sand. *Soils Found* 22(1):61–77.

Murata, O., Tateyama, M., Tatsuoka, F. (1994). Shaking table tests on a large geosynthetic-reinforced soil retaining wall model. *Recent Case Histories of Permanent Geosynthetic-Reinforced Soil Retaining Walls*, Tatsuoka, F., &Leshchinsky, D., Editors, Balkema, Rotterdam, The Netherlands, 259–264.

Matsuo, O., Tsutsumi, T., Yokoyama, K., Saito, Y., (1998). Shaking table tests and analysis of geosynthetic-reinforced soil retaining walls. *Geosynthetics International* 5 (1–2), 97–126.

Mahin, S. and Shing, P. (1985). pseudodynamic method for seismic testing. Journal of Structural Engineering, 111(7):1482–1503.

Matlab (2011). The Math Works, Inc. Natick, Massachusetts. Merritt, H. (1967). Hydraulic Control Systems. John Wiley and Sons.

Mosalam, K. M. and Gu¨nay, S. (2013). Seismic performance evaluation of high voltage disconnect switches using real-time hybrid simulation: I. system development and validation. Earthquake Engineering and Structural Dynamics, pages 1786–1893. doi:10.1002/eqe.2395.

Nova-Roessing, L., Sitar, N. (1999). Centrifuge Studies of the Seismic Performance of Reingorced Soil Structures. Ph.d. dissertation, University of California, Berkeley.

Nimbalkar, S. S., Choudhury, D., Mandal, J. N. (2006). Seismic stability of reinforced-soil wall by pseudo-dynamic method. *Geosynthetics International*, 13, No. 3, 111–119.

Nakashima, M., Kato, H., and Takaoka, E. (1992). Development of real-time pseudo dynamic testing. Earthquake Engineering and Structural Dynamics, 21(11):79–92.

Nakashima, M. and Masaoka, N. (1999). Real-time on-line test for mdof systems. Earthquake Engineering and Structural Dynamics, 28(4):393–420.

Nakata, N. (2010). Acceleration trajectory tracking control for earthquake simulators. Engineering Structures, 32:2229–2236.

Nakata, N. (2011). A multi-purpose earthquake simulator and a flexible development platform for actuator controller design. Journal of Vibration and Control. doi: 10.1177/107754631142194.

Nakata, N. (2012). Effective force testing using a robust loop shaping con- troller. Earthquake Engineering and Structural Dynamics, 42(2):261–275. doi: 10.1002/eqe.2207.

Nakata, N. and Krug, E. (2013). Multidegrees-of-freedom effective force testing: a feasibility study and robust stability assessment. Earthquake Engineering and Structural Dynamics, 42(13):1985–2002. doi: 10.1002/eqe.2308.

Nakata, N. and Stehman, M. (2012). Substructure shake table test method using a controlled mass: formulation and numerical simulation. Earthquake Engineering and Structural Dynamics, 41:1977–1988.

Nakata, N. and Stehman, M. (2014a). Compensation techniques for experimental errors in real-time hybrid simulation using shake tables. Smart Structures and Systems: Special Issue on Real-Time Hybrid Simulation. In Press.

Nakata, N. and Stehman, M. (2014b). Substructure shake table testing of 10-story RTHS structure. Network for Earthquake Engineering Simulation (NEES)(distributor). Dataset. DOI: 10.4231/D3ST7DX1R.

Nakata, N. and Stehman, M. (2014c). Substructure shake table testing with force controlled actuators. In ASCE 2014 Structures Congress, pages 1197–1208. Boston, USA.

Neild, S. A., Stoten, D. P., Drury, D., and Wagg, D. (2005). Control issues relating to real-time substructuring experiments using a shaking table. Earthquake Engi- neering and Structural Dynamics, 34:1171–1192.

Nowak, R. F., Kusner, D. A., Larson, R. L., and Thoen, B. K. (2000). Utilizing modern digital signal processing for improvement of large scale shaking table per- formance. In Proceedings of the 12th World Conference on Earthquake Engineering, Auckland, New Zealand.

Ogawa, N., Ohtani, K., Katayama, T., and Shibata, H. (2001). Construction of a three-dimensional, large-scale shaking table and development of core technology. Philosophical Transactions of the Royal Society, 359:1725–1751.

Ohta, H., Hata, S. (1973). Immediate and consolidation displacements of Clay. In 8th. Int. Conf. S.M.F.E. volume 1, 193-196.

Paulsen, S. B. (2002). *A Numerical model for estimating seismic displacements of reinforced steep slopes* (Doctoral dissertation, University of Washington).

Pan, P., Nakashima, M., and Tomofuji, H. (2005). Online test using displacement- force mixed control. Earthquake Engineering and Structural Dynamics, 34(8):869– 888.

Phillips, B. and Spencer, B. F. (2011). Model-based feedforward-feedback actuator control for real-time hybrid simulation. Journal of Structural Engineering, 139(7):1205–1214. doi: 10.1061/(ASCE) ST.1943-541X.0000606.

Phillips, B., Wierschem, N. E., and Spencer, B. F. (2013). Model-based multi-metric control of uni-axial shake tables. Earthquake Engineering and Structural Dynamics. doi: 10.1002/eqe.2366.

Perez, A., Holtz, R. D. (2004). Seismic response of reinforced steep soil slopes: results of a shaking table study. GeoTrans 2004, *Proceedings of Geotechnical Engineering for Transportation Projects*, 27–31 July, Los Angeles, CA, Yegian, M. K. and Kavazanjian, E., Editors, *ASCE Geotechnical Special PublicationNo. 126*, 1664–1672.

Richardson, G. N., Lee, K. L. (1975). Seismic design of reinforced earth walls. *Journal of the Geotechnical Engineering Division, ASCE*, 101, No. 2, 167–188.

Richardson, G. N., Feger, D., Fong, A., Lee, K. L. (1977). Seismic testing of reinforced earth walls. *Journal of the Geotechnical Engineering Division*, *ASCE*, 103, No. 1, 1–17.

Rad, N. S., Tumay, M. T. (1987). Factors affecting sand specimen preparation by raining. *Geotech Test J ASTM* 10(1):31–37.

Roscoe, K.H., Schofield, A.N., Thurairajah, A. (1963). Yielding of Clays in states wetter than critical. Geotechnique, 13(3), 211-240.

Reinhorn, A. M., Bruneau, M., Whittaker, A. S., Constantinou, M. C., The- vanayagam, S., Sivaselvan, M., Shao, X., Hanley, J., Pitman, M., and T., A. (2004). The UB-NEES versatile high performance testing facility. In Proceedings of the 13th World Conference on Earthquake Engineering, Vancouver, B.C.

Roessing L.N., Sitar N., (1998). Centrifuge studies of the seismic Response of Reinforced soil slopes. *Third Geotechnical Engineering and soil Dynamic conference*, Geotechnical special publication No. 75, ASCE, Pp.458-468, Seattle, Washington,

Sakaguchi, M., Muramatsu, M., Nagura, K. (1992). A discussion on reinforced embankment structures having high earthquake resistance. *Proceedings of the International Symposium on Earth Reinforcement Practice, IS-Kyushu '92*, Fukuoka, Japan, Vol. 1, pp. 287–292.

Sakaguchi, M. (1996). A study of the seismic behaviour of geosynthetic reinforced walls in Japan. *Geosynthetics International*. 3 (1), 13–30.

Sabermahani, M., Ghalandarzadeh, A., Fakher, A. (2009). Experimental study on seismic displacement modes of reinforced-soil walls. *Geotextiles and Geomembranes*, 27(2), 121-136.

Srilatha, N., Latha, G. M., Puttappa, C. G. (2013). Effect of frequency on seismic response of reinforced soil slopes in shaking table tests. *Geotextiles and Geomembranes*, 36, 27-32.

Srilatha, N., Latha, G. M., Puttappa, C. G. (2014). Shaking Table Studies on Geotextile Reinforced Soil Slopes, Golden Jubilee Conference of the IGS Bangalore Chapter, *Geo-Innovations*, 30-31 October 2014, 1-8.

Srinivasan, V., Srivastava, S., Ghosh, P. (2016). Optimization and parametrical investigation to assess the reconstitution of different types of Indian sand using portable travelling pluviator. *GeotechGeolEng* 34(1):59–73.

Schellenberg, A., Becker, T. C., and Mahin, S. A. (2013). Hybrid shake table for the testing of midlevel seismic isolation systems. In Proceedings of the 13th World Conference on Seismic Isolation, Energy Dissipation and Active Vibration Control of Structures, Sendai, Japan.

Schanz, T., Vermeer, P.A. (1998). Special issue on pre-failure displacement behaviour of geomaterials. Geotechnique, 48, 383-387.

Severn, R. T. (2011). The development of shaking tables-a historical note. Earthquake Engineering and Structural Dynamics, 40(2):195–213.

Shao, X., Reinhorn, A., and Sivaselvan, M. (2011). Real-time hybrid simulation using shake tables and dynamic actuators. Journal of Structural Engineering, 137:748– 760.

Shi, Y., Masahiro, K., and Nakshima, M. (2014). Disorder and damage of base-isolated medical facilities when subjected to near-fault and long-period ground motions. Earthquake Engineering and Structural Dynamics. doi: 10.1002/eqe.2417.

Spencer, B. and Yang, G. (1998). Earthquake simulator control by transfer function iteration. In Proceeding of the 12th ASCE Engineering Mechanics Conference, San Diego, C.A.

Sekiguchi, H. (1977). Rheological characteristics of Clays. In Proceedings of the 9th ICSMFE. Tokyo, volume 1, 289-292.

Sekiguchi, H., Ohta, H. (1977). Induced anisotropy and time dependency in Clays. In Proceedings of the 9th ICSMFE. Tokyo, volume 3, 542-544.

Stehman, M. and Nakata, N. (2013). Direct acceleration feedback control of shake tables with force stabilization. Journal of Earthquake Engineering, 17(5):736–749.

Stehman, M. and Nakata, N. (2014). IIR compensation in real-time hybrid simu- lation using shake tables with complex control-structure-interaction. Journal of Earthquake Engineering. Under Peer Review.

Stoten, D. P. and G´omez, E. (2001). Adaptive control of shaking tables using the min- imal control synthesis algorithm. Philosophical Transactions of the Royal Society A: Mathematical, Physical and Engineering Sciences, 359:1697–1723.

Tatsuoka, F., Tateyama, M., Koseki, J., (1995). Behavior of geogrid-reinforced soil retainng walls during the great Hanshin-Awaji earthquake. In: Proc. *1st Int. Symp. Eathquake Geotechnical Eng*., vol.2, 55-60.

Telekes, G., Sugimoto, M., Agawa, S. (1994). Shaking table tests on reinforced embankment models. Proceedings of the *13th International Conference on Soil Mechanics and Foundation Engineering*, New Delhi, India, Vol. 2. 649–654.

Tatsuoka, F., Koseki, J., Tateyama, M., (1997). Performance reinforced soil structures during the 1995 Hyogo-ken Nambu earthquake. In: Ochiai H., Yasufuku, N., Omine, K. (Eds.), *Earthquake Reinforcement*. Balkema, Rotterdam, 979-1008.

Tagawa, Y. and Kajiwara, K. (2007). Controller development for the e-defense shaking table. In Proceedings of the Institution of Mechanical Engineers, Part 1: Journal of Systems and Control Engineering, volume 221, pages 1697–1723.

Trombetti, T. L. and Conte, J. P. (2002). Shaking table dynamics: results from a test-analysis comparison study. Journal of Earthquake Engineering, 6(4):736–749.

Wang, L., Chen, G., Chen, S. (2015). Experimental study on seismic response of geogrid reinforced rigid retaining walls with saturated backfill sand. Geotextiles and Geomembranes, 43, 35-45.

White, D., Holtz, R. D., (1997). Performance o geosynthetic reinforced slopes and walls during the Nothridge California earthquake of January 17, 1994. In: Ochiai, H., Yasufuku, N., Omine, K. (Eds.), *Earth Reinforcement*. Balkema, Rotterdam, 965-972.

USGS (2011). Earthquake facts and statistics. accessed: September 24, 2013. http://earthquake.usgs.gov/earthquakes/eqarchives/year/eqstats.php.

Vermeer, P.A., Neher, H. (1999). A soft soil model that accounts for creep. In R.B.J. Brinkgreve, Beyond 2000 in Computational Geotechnics, Balkema, Rotterdam. 249-261.

Vermeer, P.A., Stolle, D.F.E., Bonnier, P.G. (1998). From the classical theory of secondary compression to modern creep analysis. Proc. 9th Int. Conf. Comp. Meth. and Adv. Geomech. , Wuhan, China, 4, 2469-2478.

Viswanadham, B. V. S., Mahajan, R. R. (2007). Centrifuge model tests on geotextile-reinforced slopes. Geosynthetics International. Volume 14 Issue 6, pp. 365-379.

Xiao, M., Ledezma, M., Hartman, C. (2014). Shake Table Test to Investigate Seismic Response of a Slurry Wall. In Geo-Congress 2014: *Geo-characterization and Modeling for Sustainability* (pp. 1234-1243).

Yazdandoust, M. (2017). Investigation on the seismic performance of steel-strip reinforced-soil retaining walls using shaking table test. *Soil Dynamics and Earthquake Engineering*, 97, 216-232.

Ye J., Jiang, L. (2018). “Simplified analytical model and shaking table test validation for seismic analysis of mid-rise cold-formed steel composite shear wall building,” Sustainability, vol. 10, no. 9, pp. 1-18,.

Yunus, N. Z. M., Wanatowski, D., Hassan, N. A., Marto, A. (2019). “Shear strength and compressibility behavior of lime-treated organic Clay,” KSCE Journal of Civil Engineering, vol. 20, no. 5, pp. 1721-1727.

Yu, P., Richart, F.E. (1984). Stress ratio effects on shear modulus of dry sands. *Journal of Geotechnical Engineering*, ASCE 110 (GT3), 331–345.

Zahid et al (2004). Groundwater Level Declining Trend in Dhaka City Aquifer. In: Water Resource Management in Dhaka City, Hassan, M.Q. (Ed.). Goethe-Institute, Dhaka, pp: 17-32.

Zapateiro, M., Karimi, H. R., Luo, N., and Spencer, B. (2010). Real-time hybrid testing of semiactive control strategies for vibration reduction in a structure with mr damper. Structural Control and Health Monitoring, 17(4):427–451.

Zhao, Y., Gafar, K., Elshafie, M. Z. E. B., Deeks, A. D., Knappett, J. A., Madabushi, S. P. G. (2006). Calibration and use of new automatic sand pourer. In: *Sixth international conference on physical modeling in geotechnics*. Hong Kong. Taylor and Francis. London, 265–270. 4–6 Aug 2006.

Zhang, Z., Cho, C., Pan, Q., Lu, X. (2009). Experimental Investigation on Excess Pore Water Pressure in Soft Soil-Foundations under Minor Shocks. *International Journal of Engineering and Applied Sciences*, 5(4), 259-263.

Zhou, Z., Lei, J. Shi, S. and Liu, T. (2019). “Seismic response of aeolian sand high embankment slopes in shaking table tests,” Applied Sciences, vol. 9, no. 8, pp. 1677.

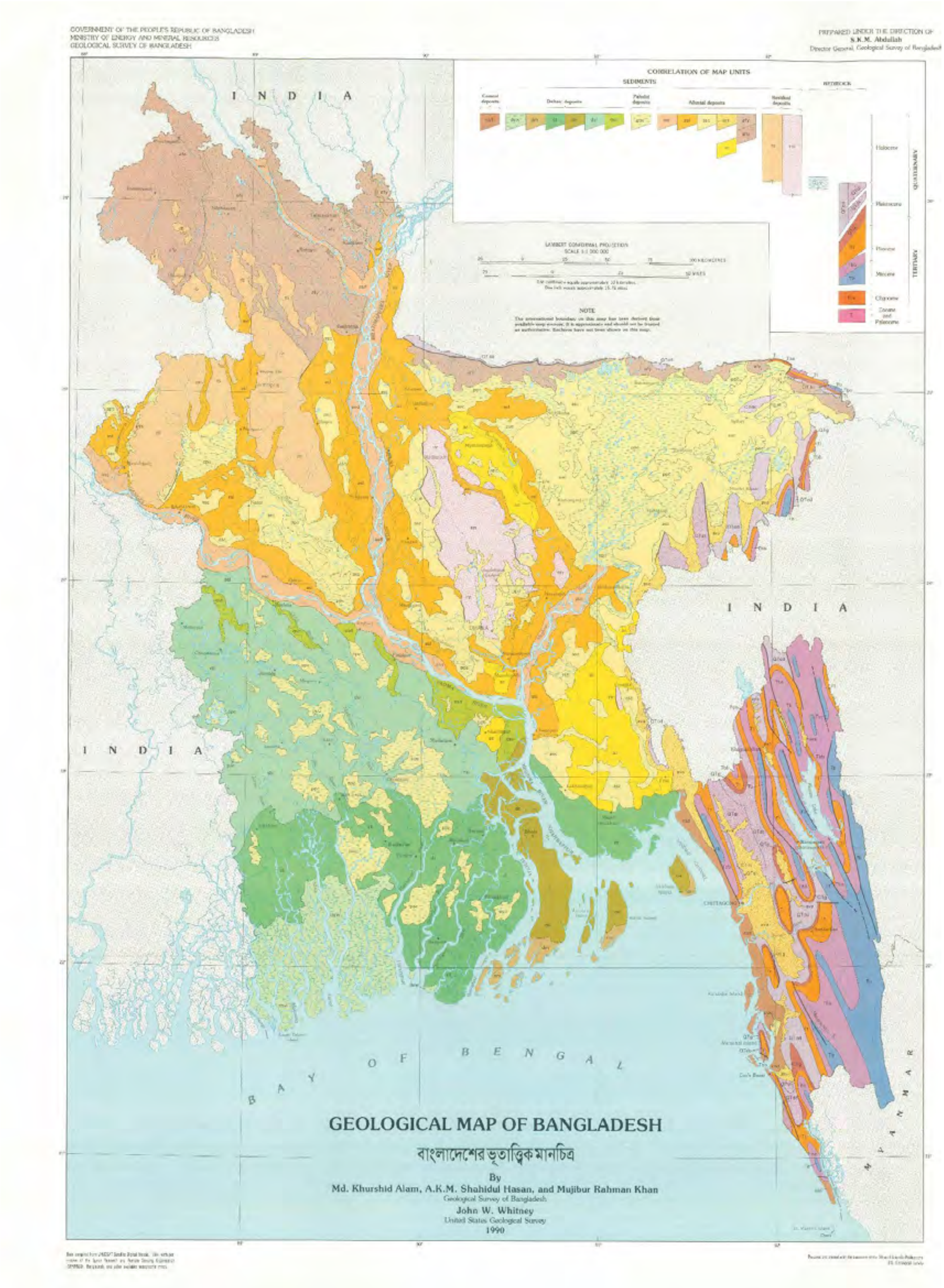

Figure 1.1: Geological map of Bangladesh (Geological survey of Bangladesh)

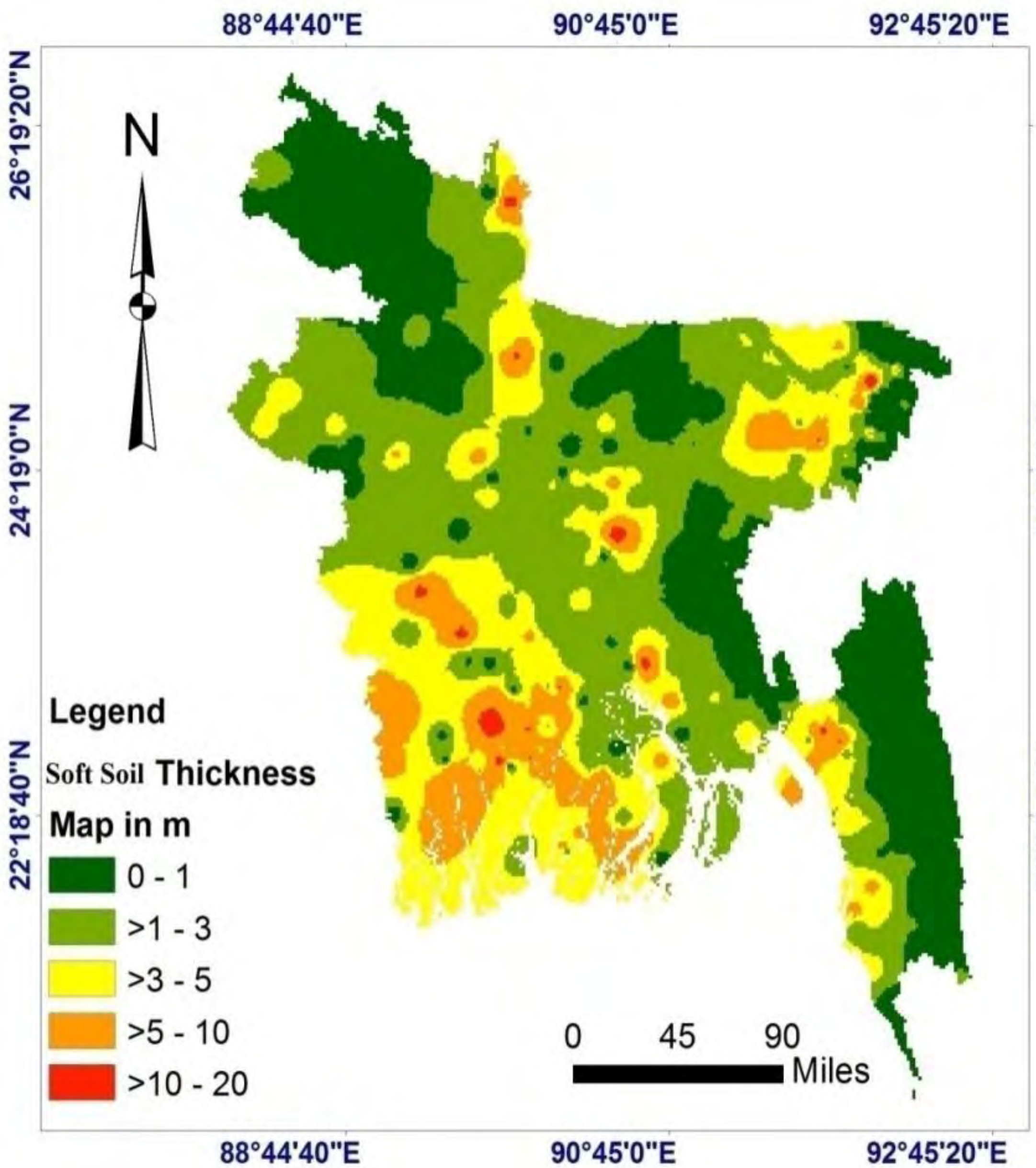

Figure 1.2: Thickness map for Soft soil (After Hore, R. et al.2019)

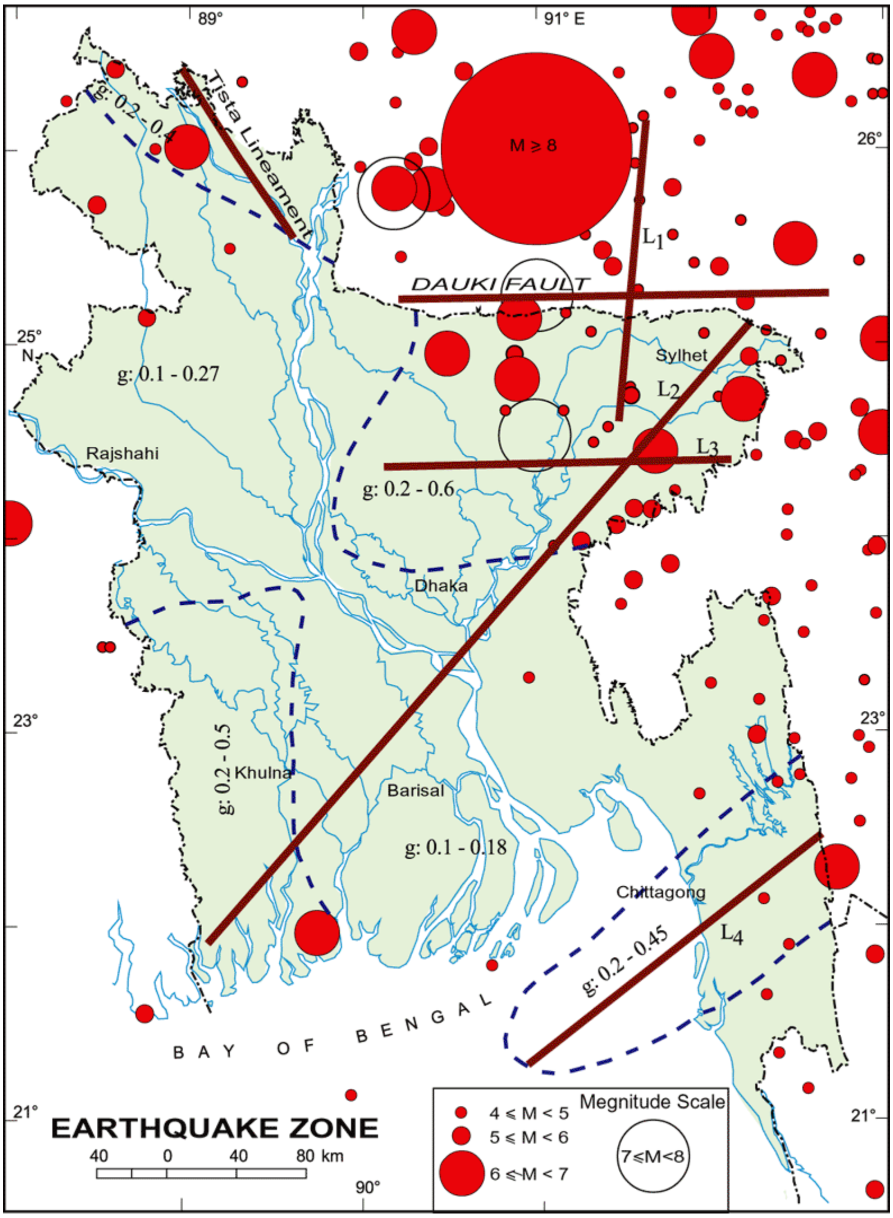

Figure 2.1: Seismo-tectonic lineaments capable of producing damaging earthquakes

(Source: www.banglapedia.com)

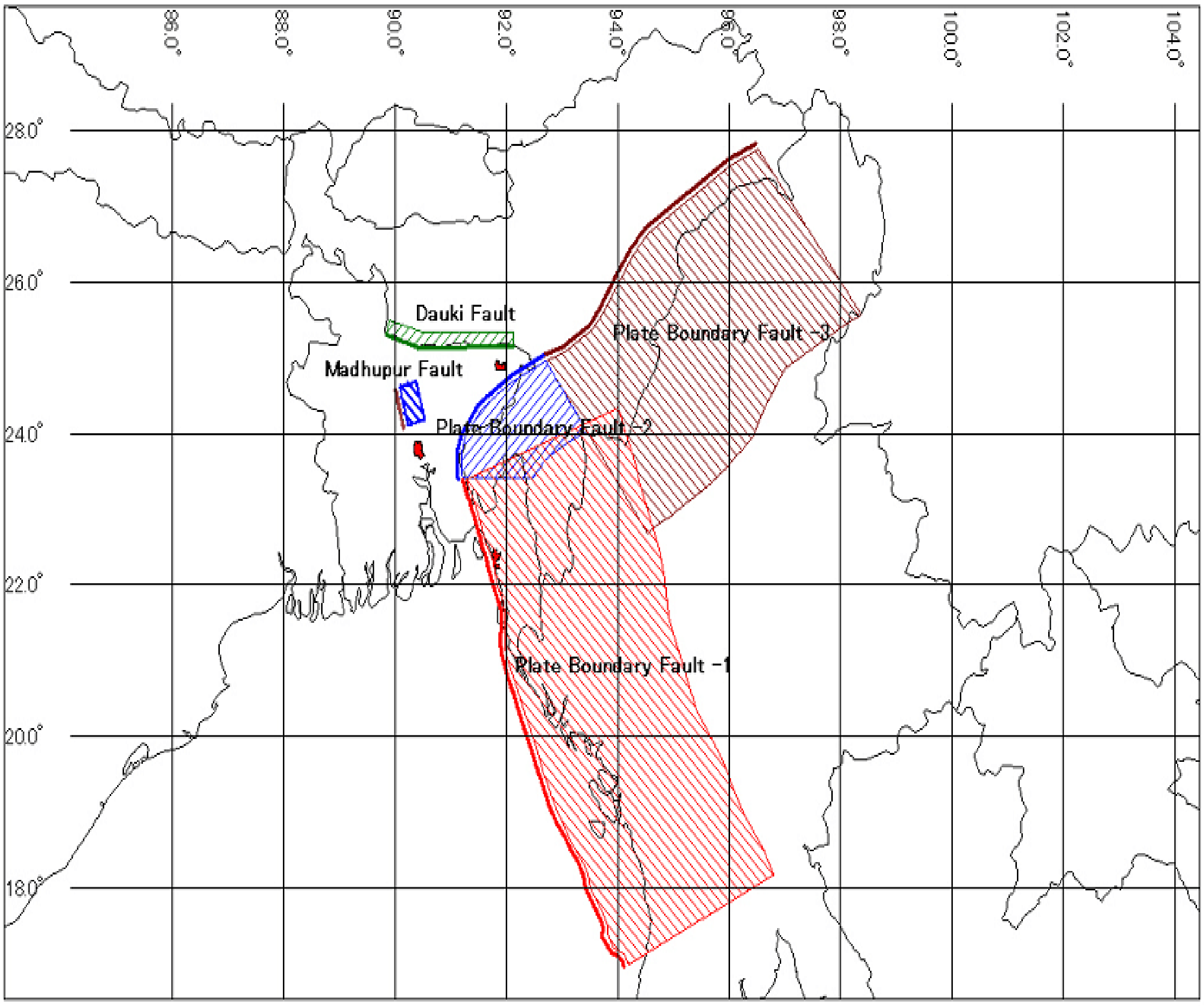

Figure 2.2: The major fault lines which affect seismicity in Bangladesh

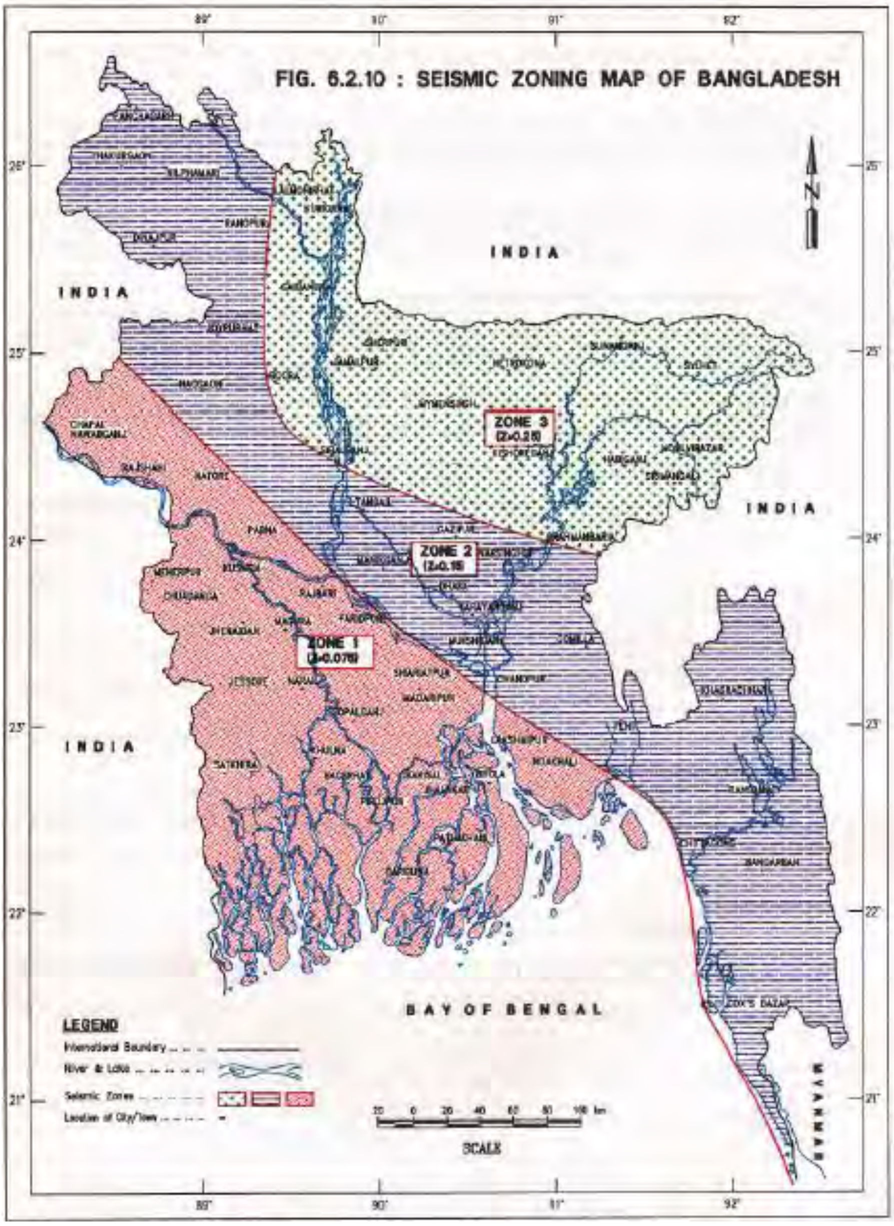

Figure 2.3: Seismic Zoning Map of Bangladesh (After BNBC, 1993)

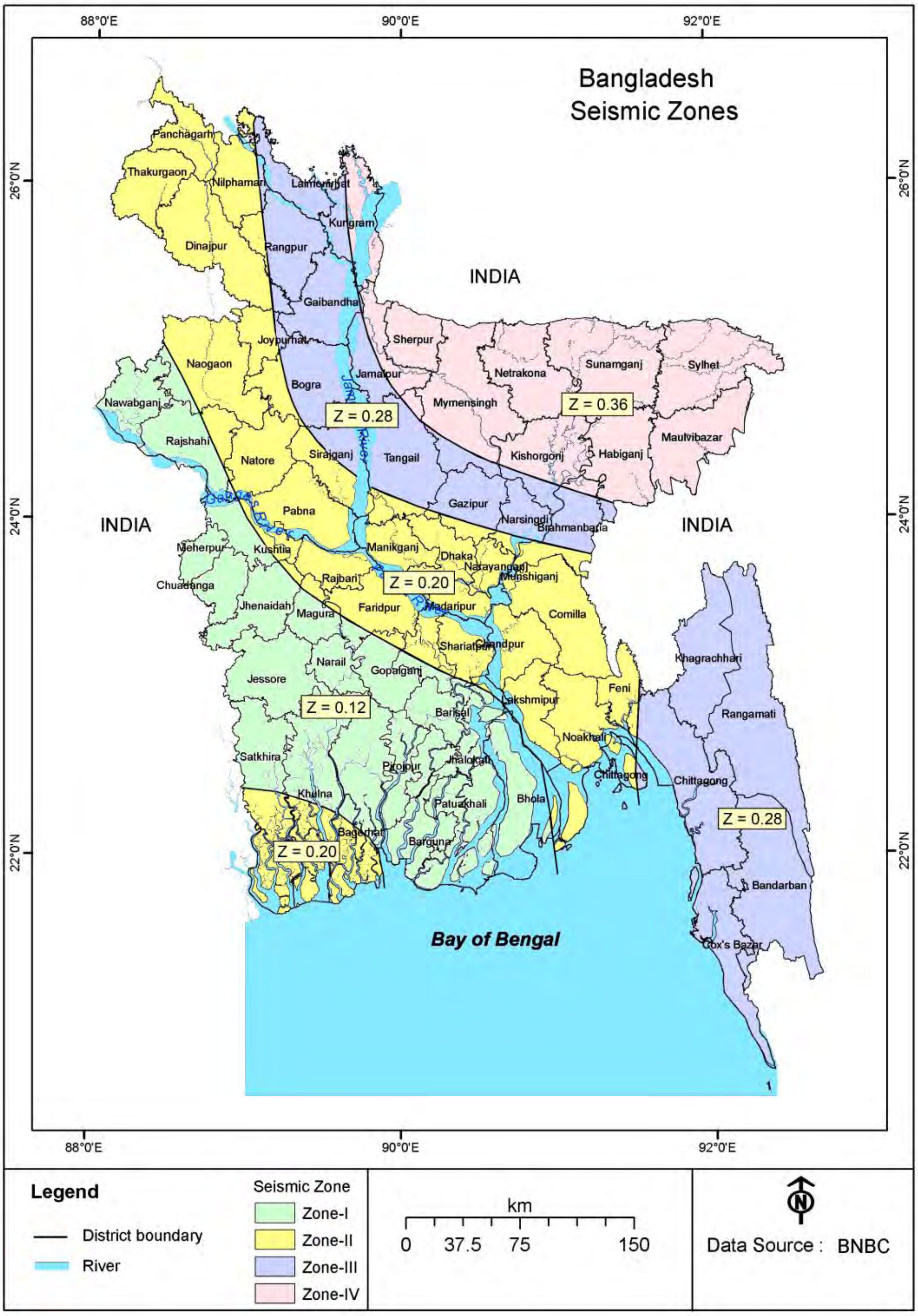

Figure 2.4 : Proposed Seismic Zoning Map of Bangladesh (Proposed BNBC, 2020)

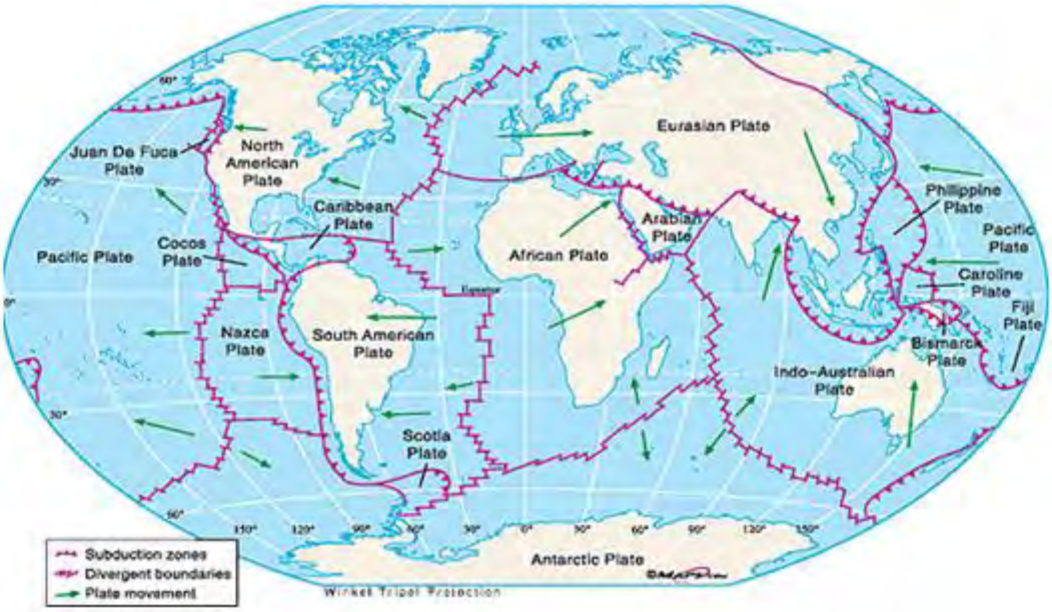

Figure 2.5: Tectonic plates

Figure 2.6: Damage of different infrastructures due to Kobe earthquake

Figure 2.7 : Damage of different infrastructures due to Loma earthquake

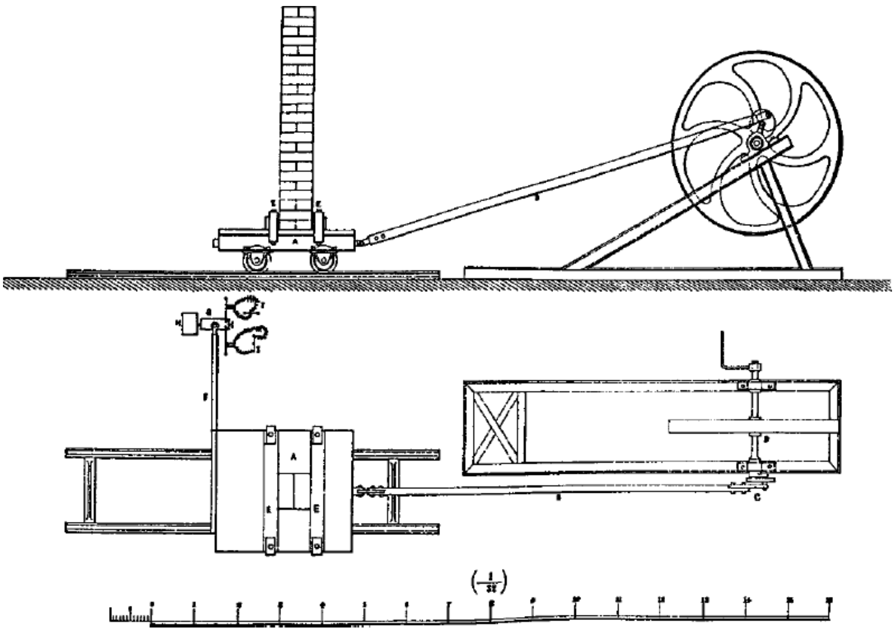

Figure 2.8: Schematic of an early stage hand powered shake table, CREDIT: Severn (2011).

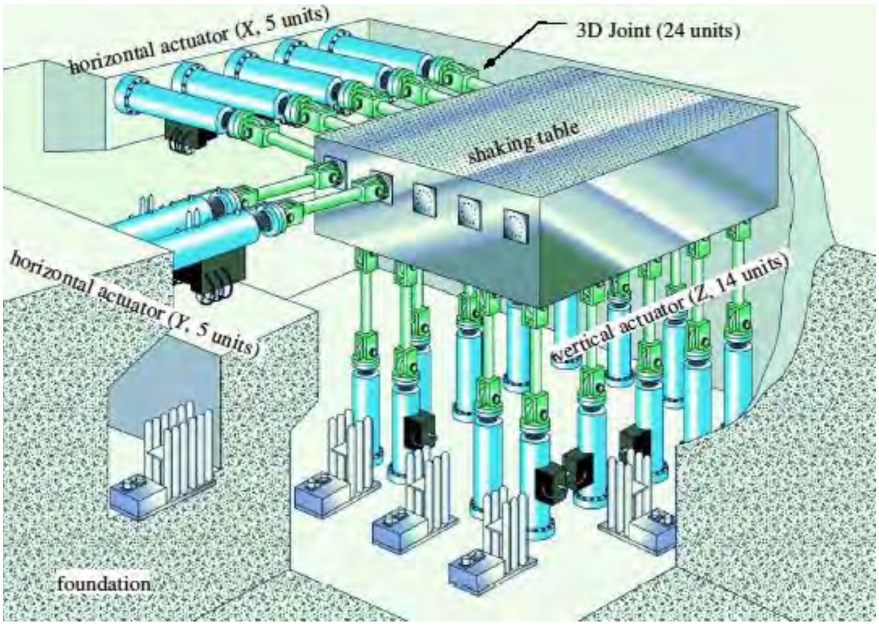

Figure 2.9: Schematic of the E-Defense shake table system, CREDIT: Ogawa et al. (2001).

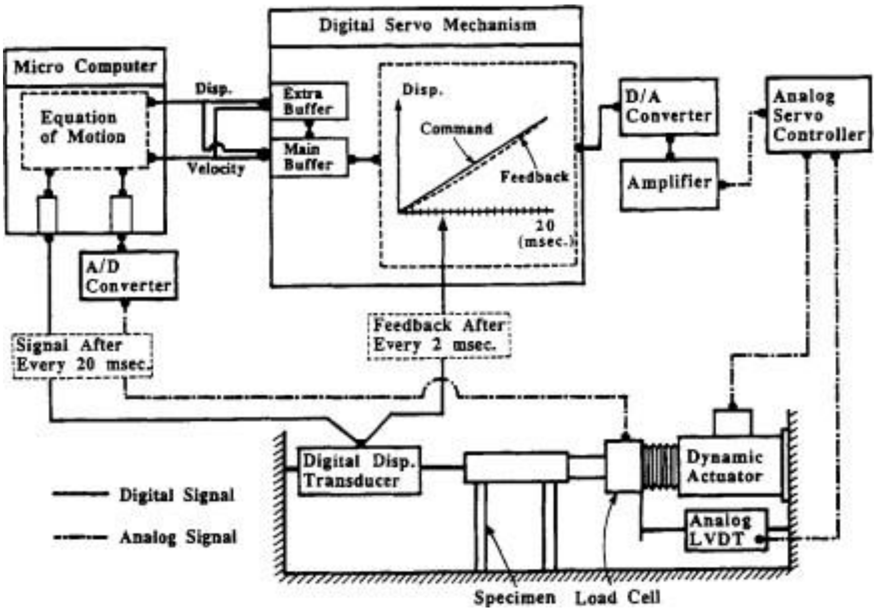

Figure 2.10: Early implementation of pseudo-dynamic testing, CREDIT: Nakashima et al. (1992).

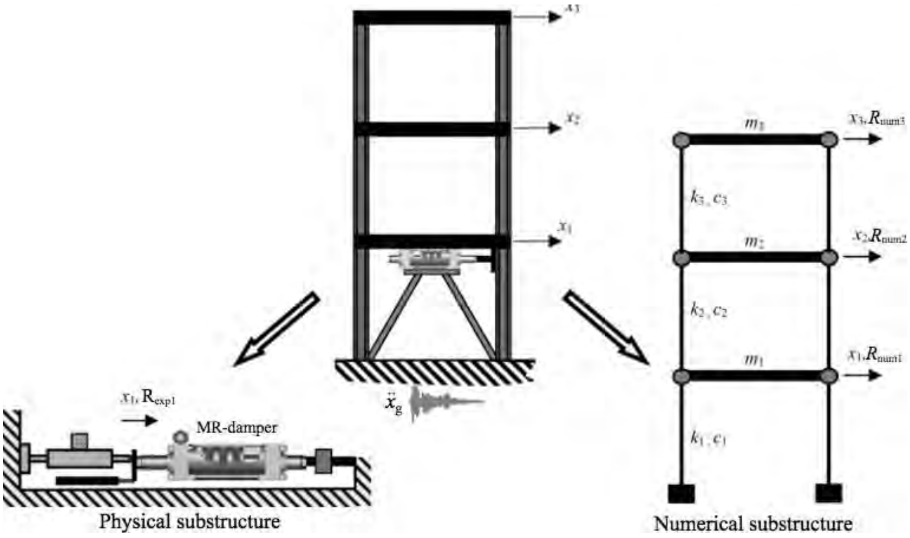

Figure 2.11: Implementation of RTHS where the experimental substructure is a single damper, CREDIT: Carrion et al. (2009).

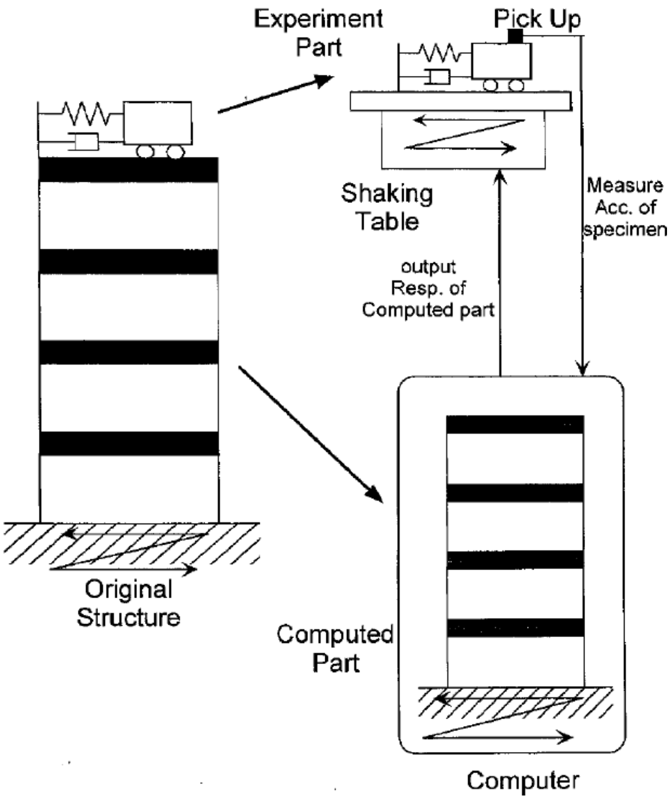

Figure 2.12: Concept of substructure shake table testing including a tuned mass damper, CREDIT: Igarashi et al. (2000).

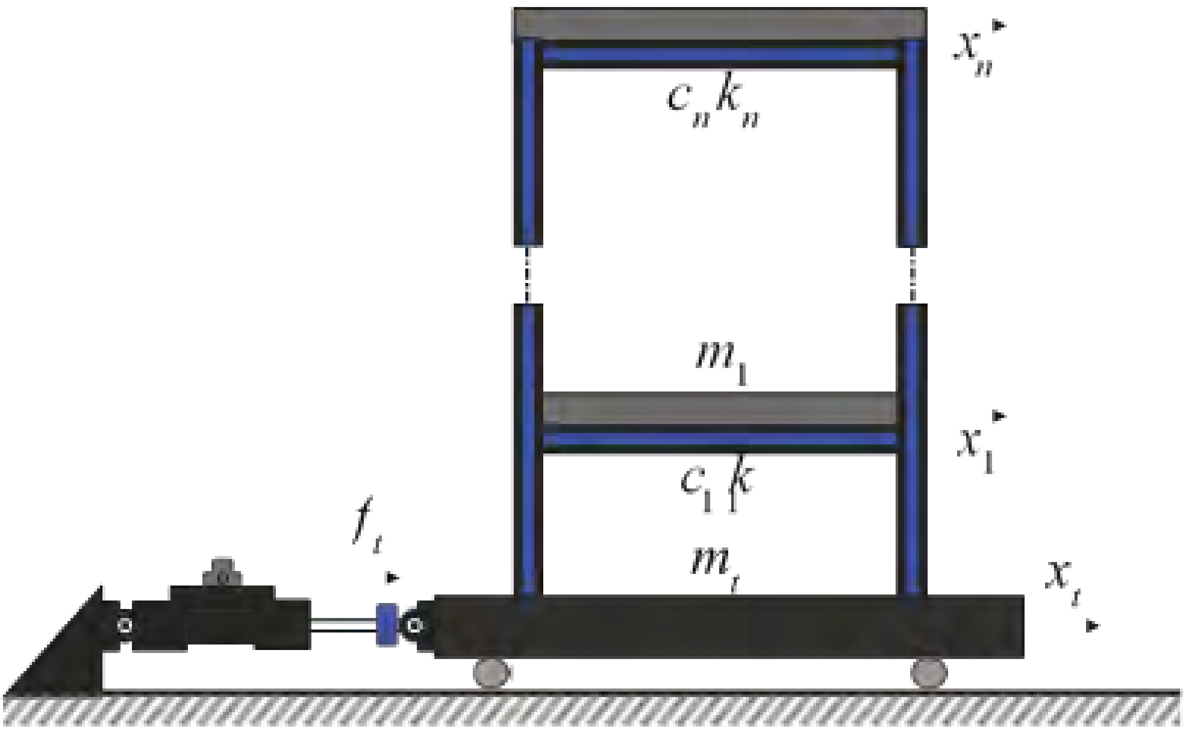

Figure 2.13: Schematic of a uni-axial shake table with linear structure.

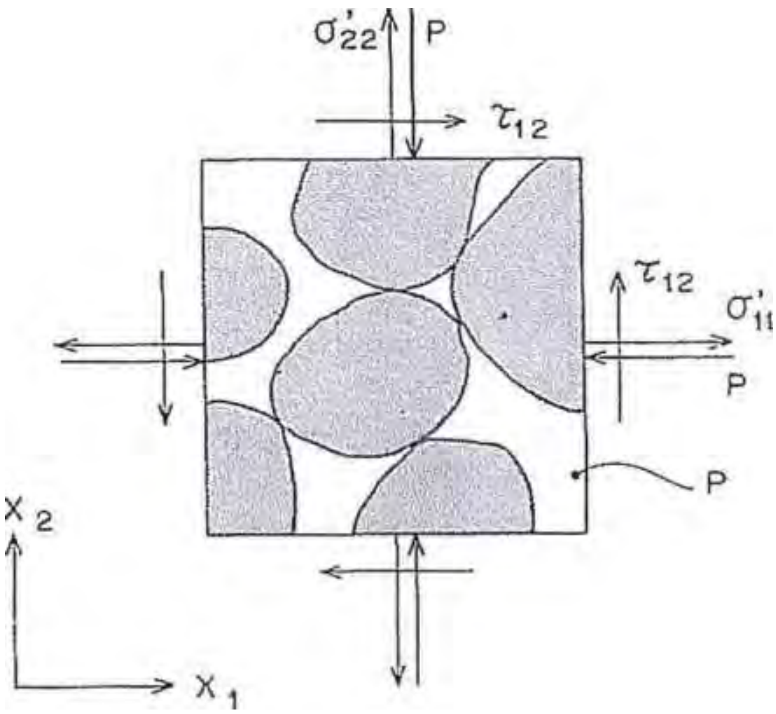

Figure. 2.14 Effective stress a' of soil and pore water pressure p in an element of porous material

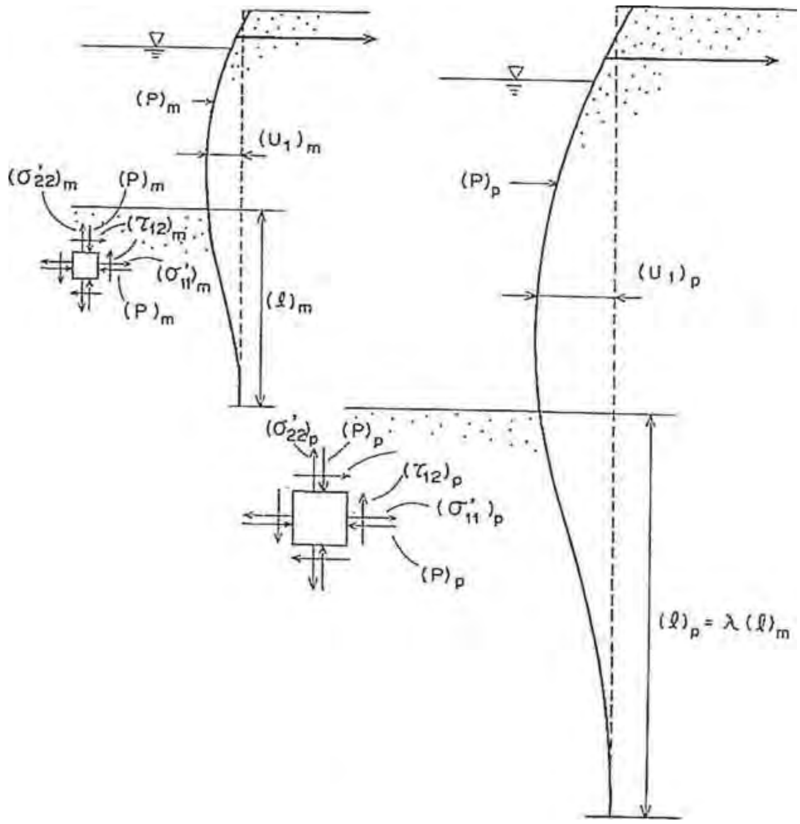

Figure 2.15 The displacements u, effective stresses σ' and pressures of pore water and external water p in the model and the prototype

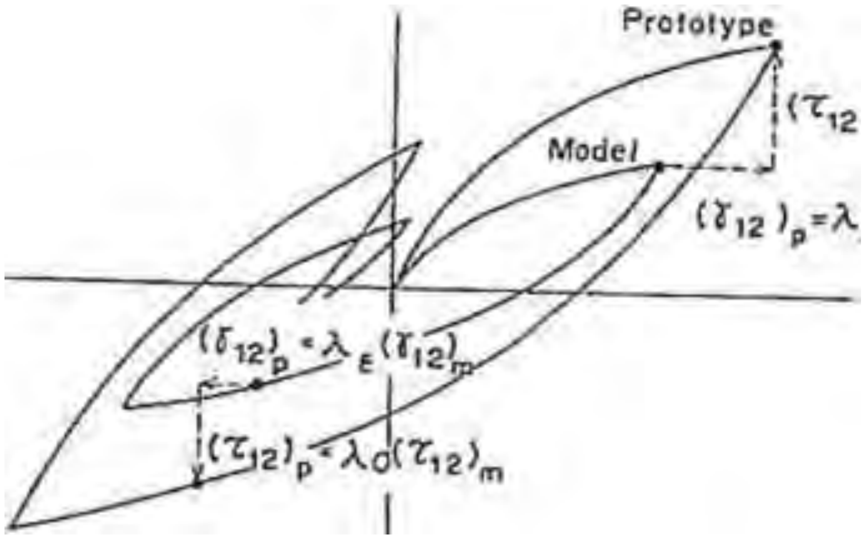

Figure 2.16 Stress-strain relations of soils in the model and the prototype

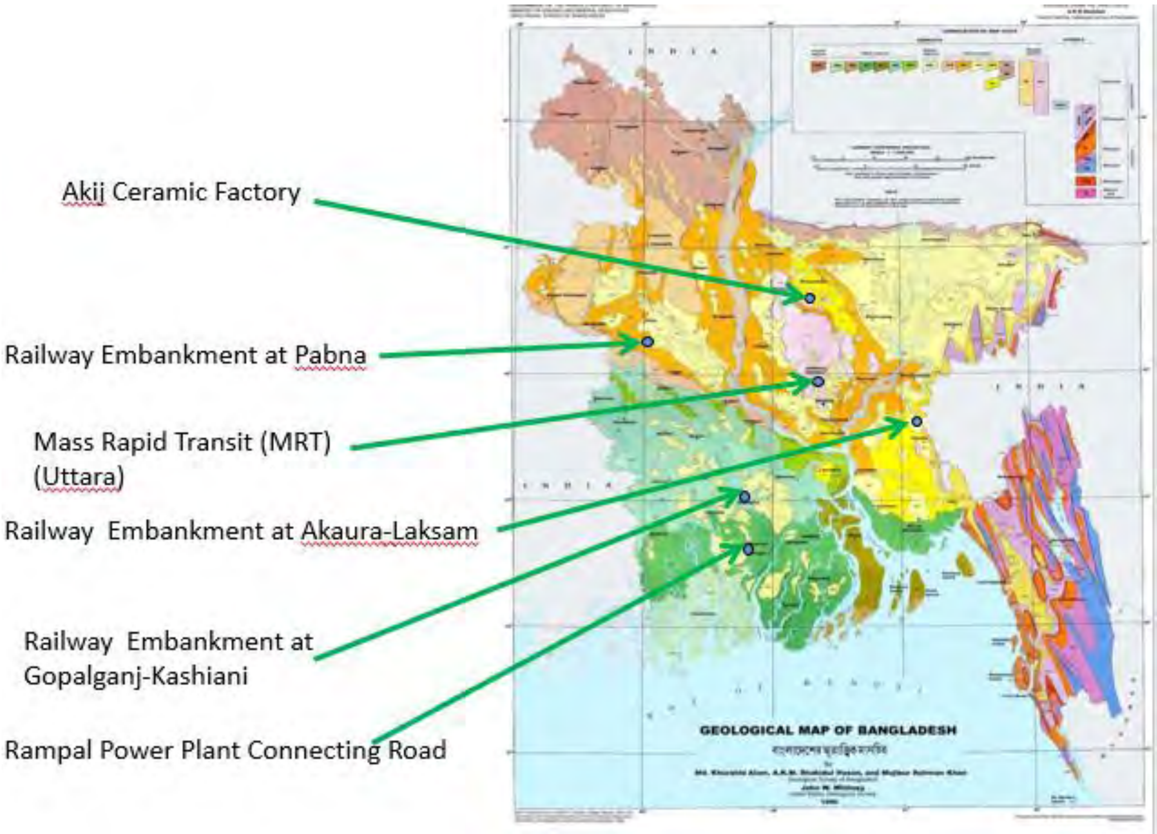

Figure 2.17: Few Soft Clay Improved Sites Reviewed

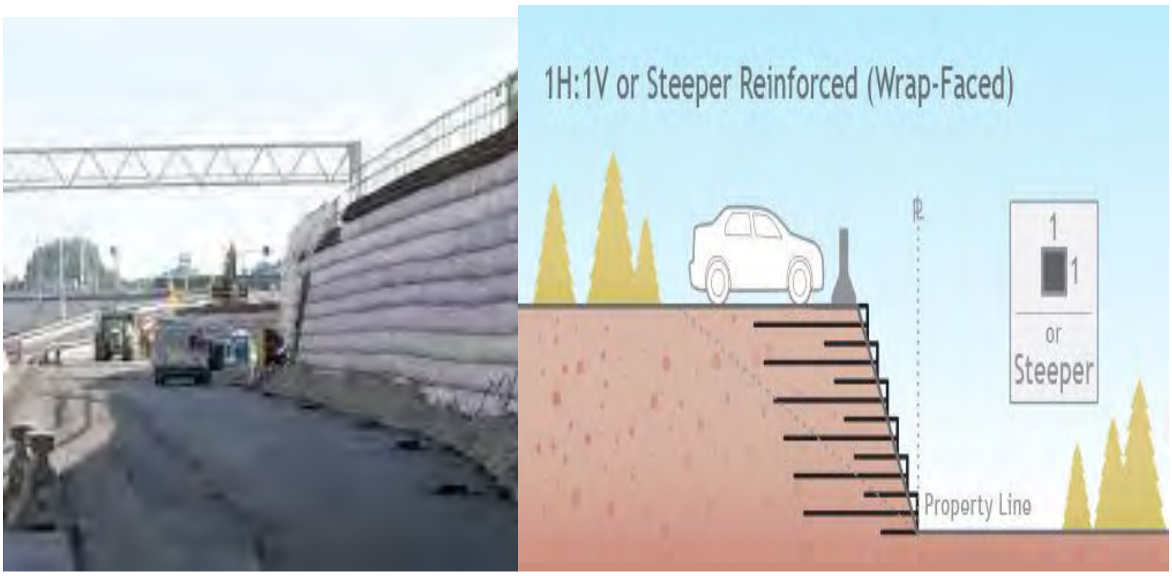

Figure 2.18. Example of a wrap faced geotextile wall

E	:	Young's modulus	[kN/m^2]
ν	:	Poisson's ratio	[-]
c	:	Cohesion	[kN/m^2]
φ	:	Friction angle	[°]
ψ	:	Dilatancy angle	[°]
σ_t	:	Tension cut-off and tensile strength	[kN/m^2]

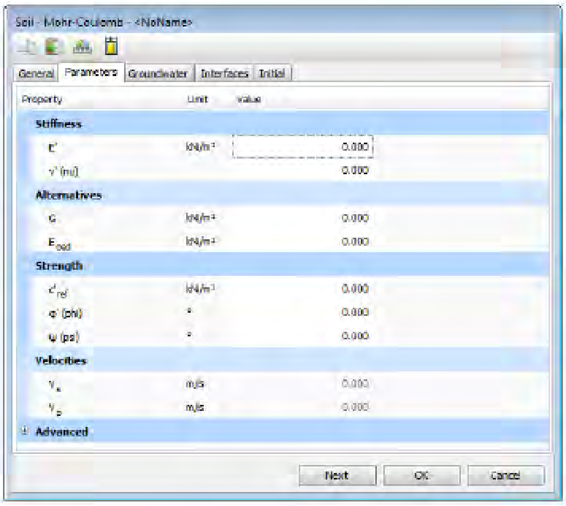

Figure 2.19 Parameter tabsheet for Mohr-Coulomb model

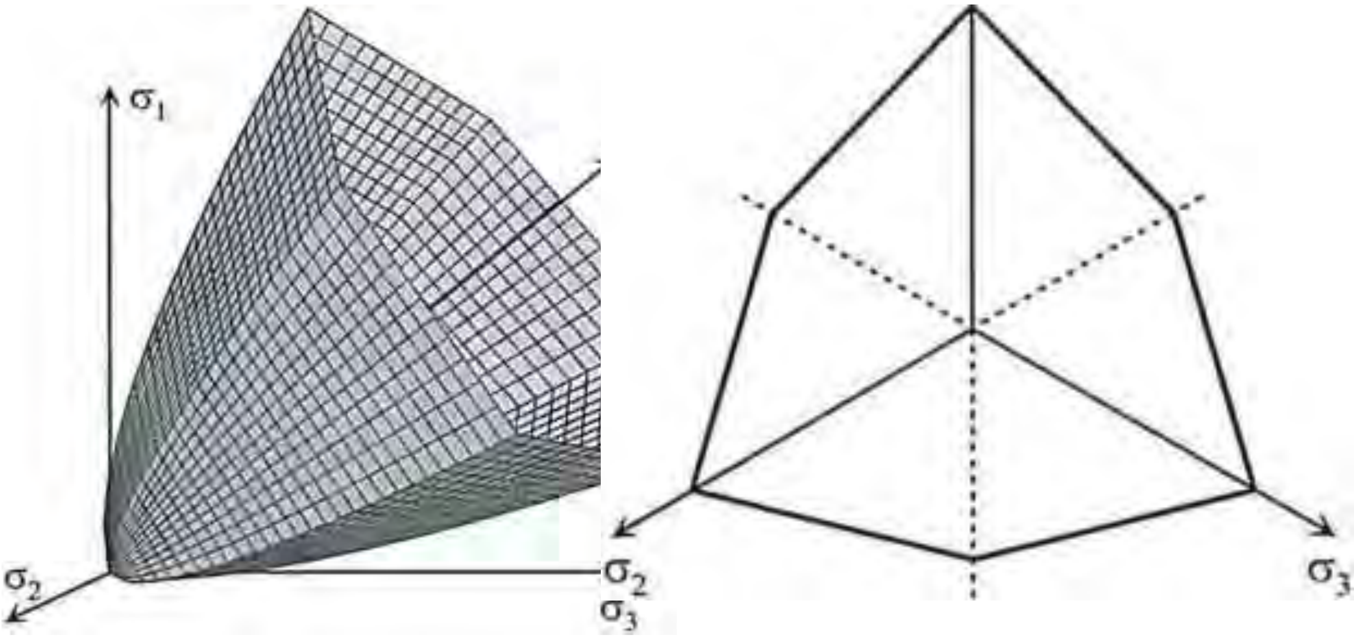

Figure 2.20 The Hoek-Brown failure contour in principal stress space

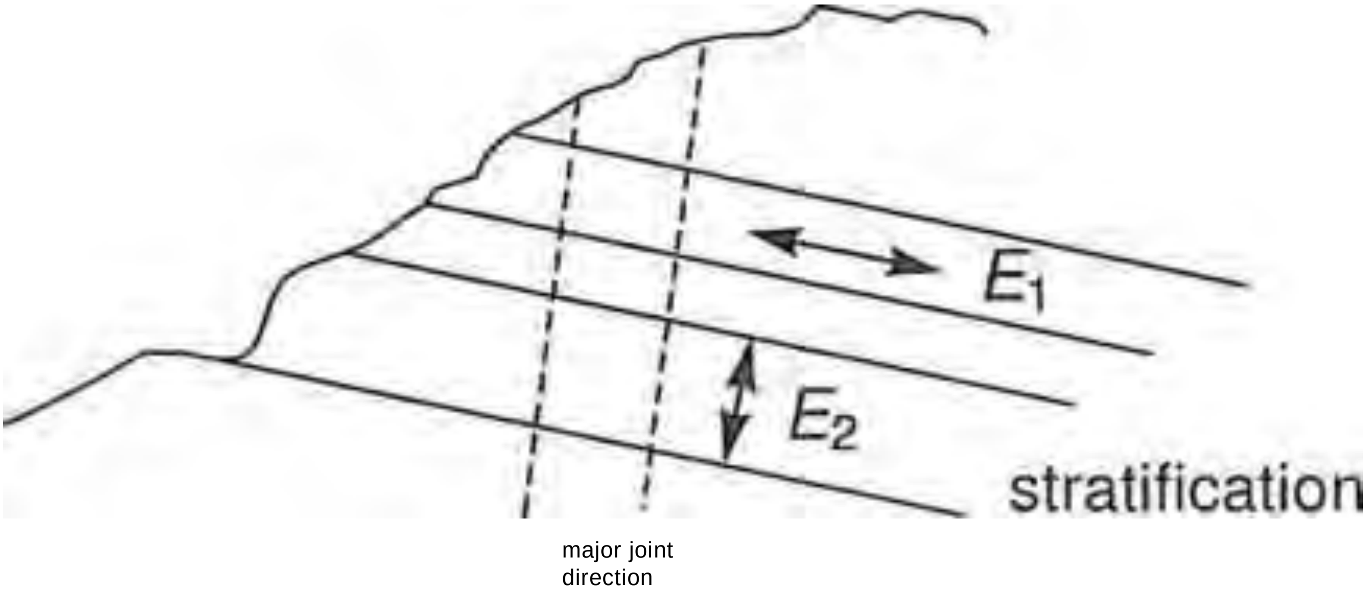

Figure 2.21 Visualization of concept behind the Jointed Rock model

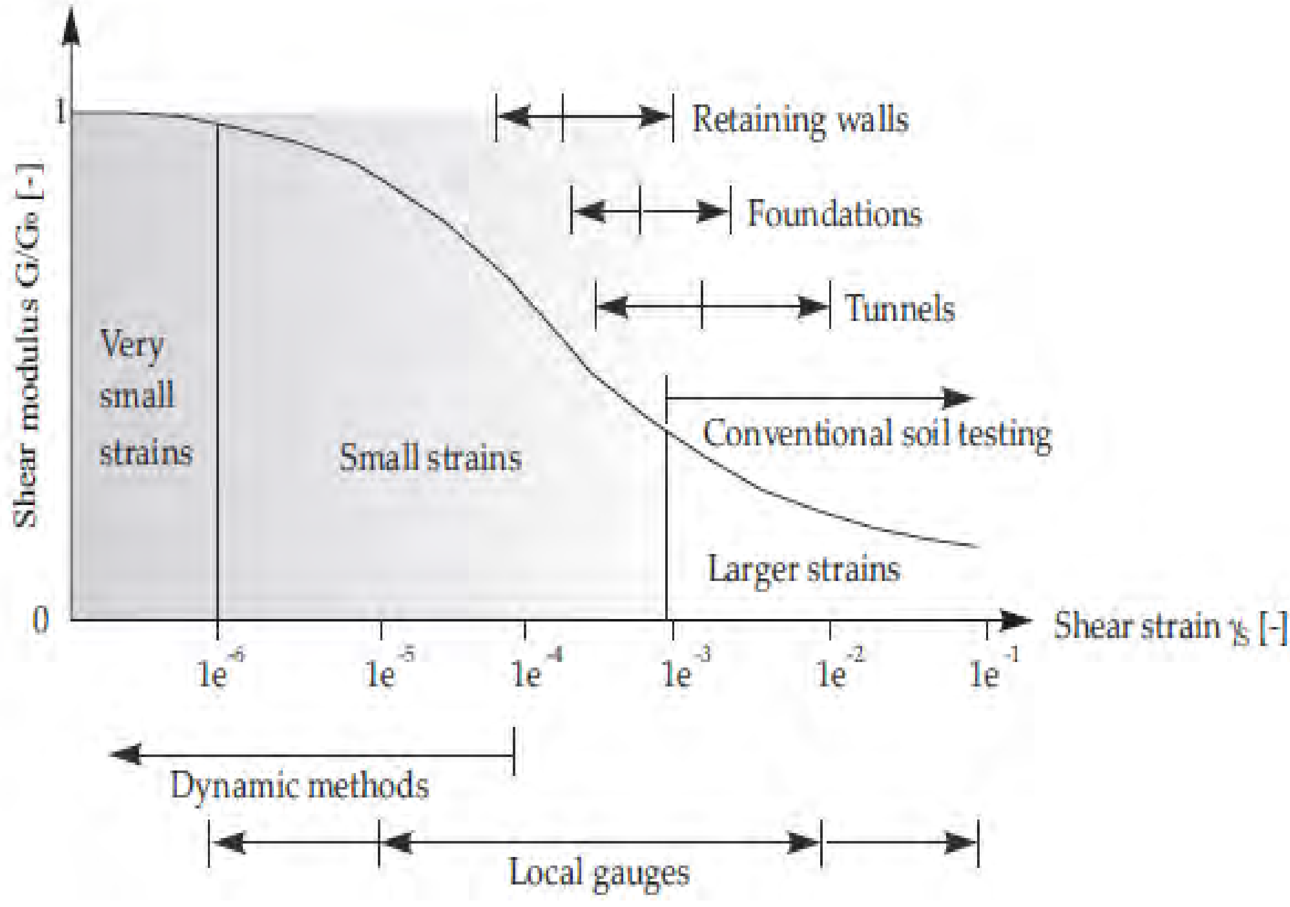

Figure 2.22 Characteristic stiffness-strain behaviour of soil with typical strain ranges for laboratory tests and structures (after Atkinson & Sallfors (1991))

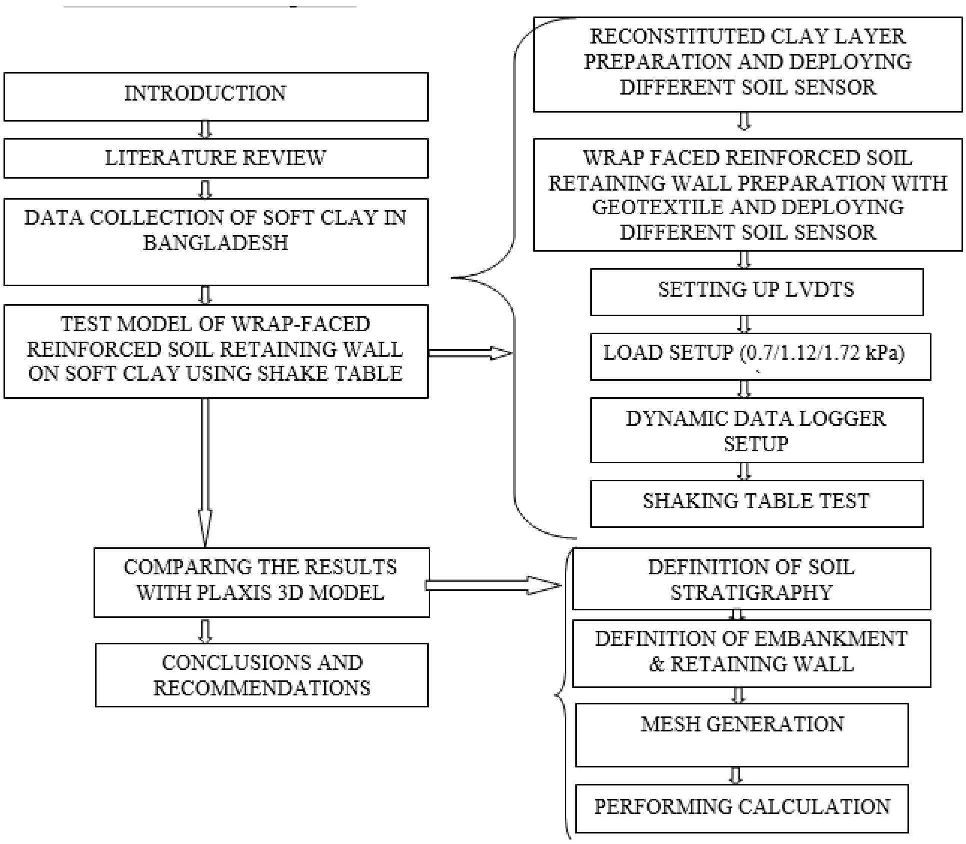

Figure 3.1: The Study layout at a Glance

Figure 4.1 a) The testing platform

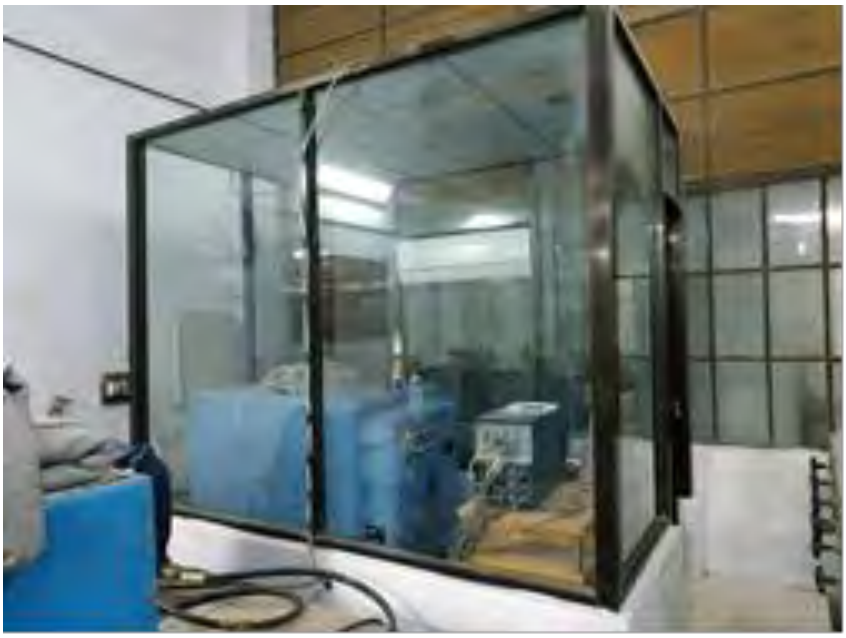

Figure 4.1 b) The control room.

Figure 4.2a: Laminar box mounted on the shaking platform.

Figure 4.2b: Membrane inside the laminar box

Figure 4.2 c: Portable pluviator for construction of the model wall.

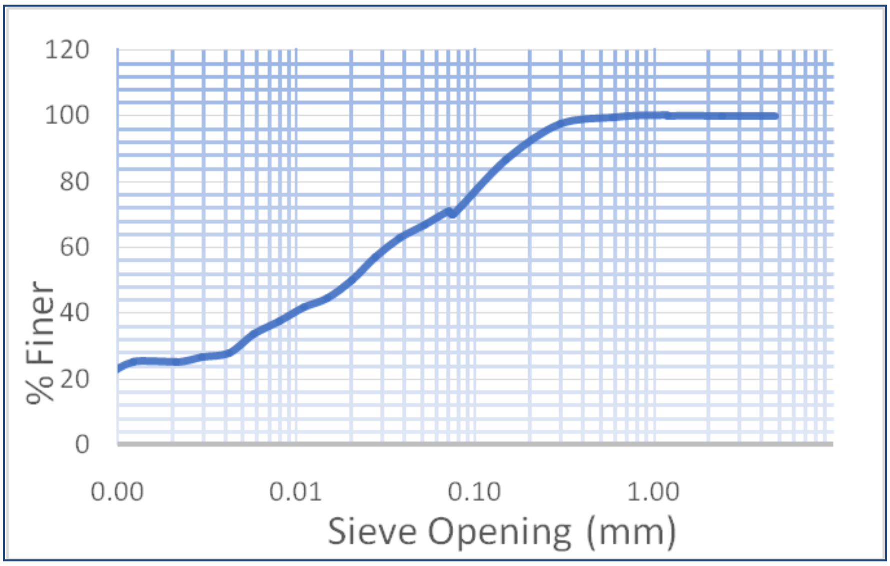

Figure 4.3. a) The grain size distribution of clay soil

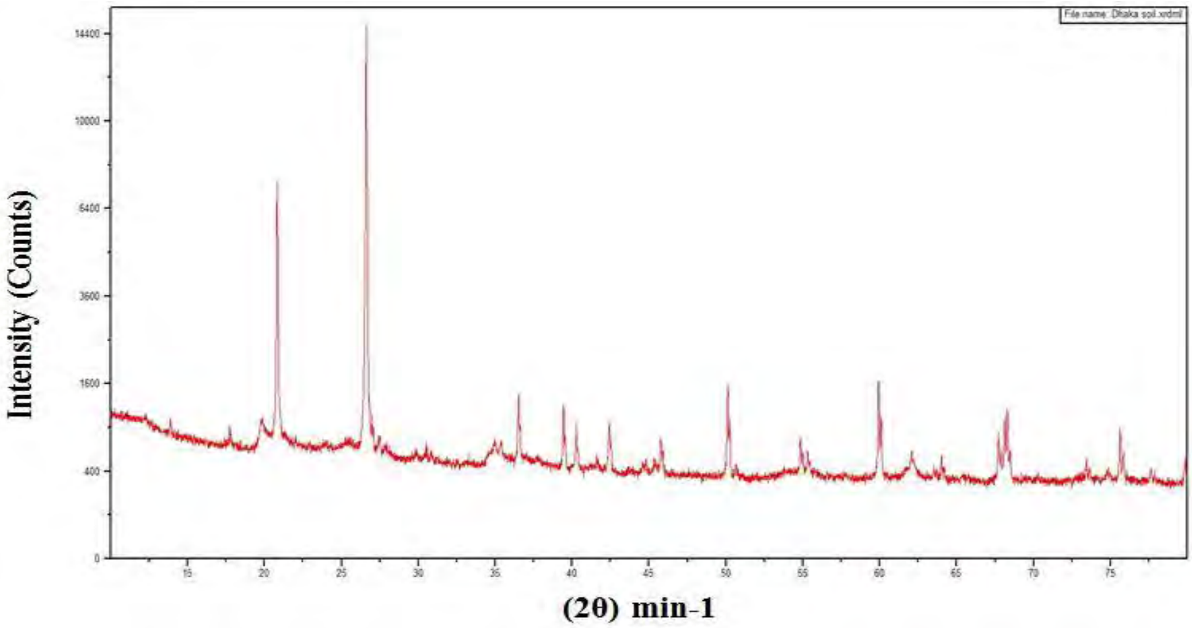

Figure 4.3. b) The Intensity versus (2θ) min-1 curve

Figure 4.4. a) The mixing process of slurry with Hobart rotary mixer

Figure 4.4 b): Isotropic condition at loads

Figure 4.4 c): Sensor Arrangement

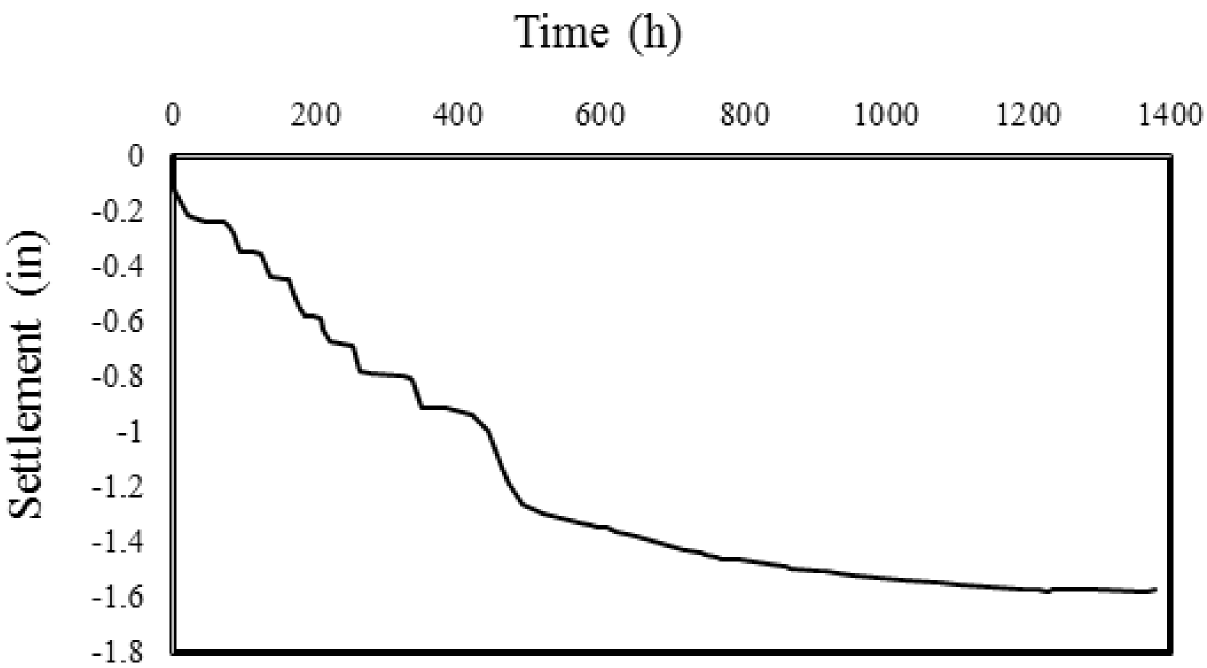

Figure 4.4. d) The average settlement curve

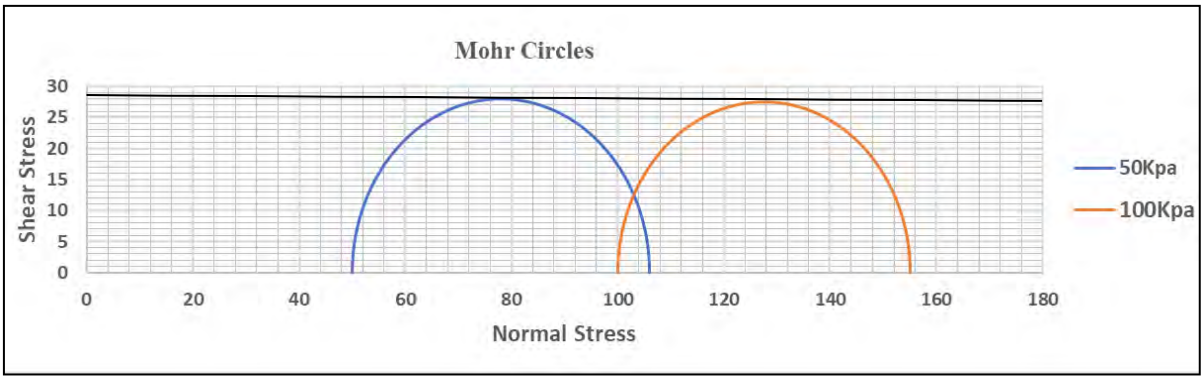

Figure 4.4. e) The undrained strength of Clay soil

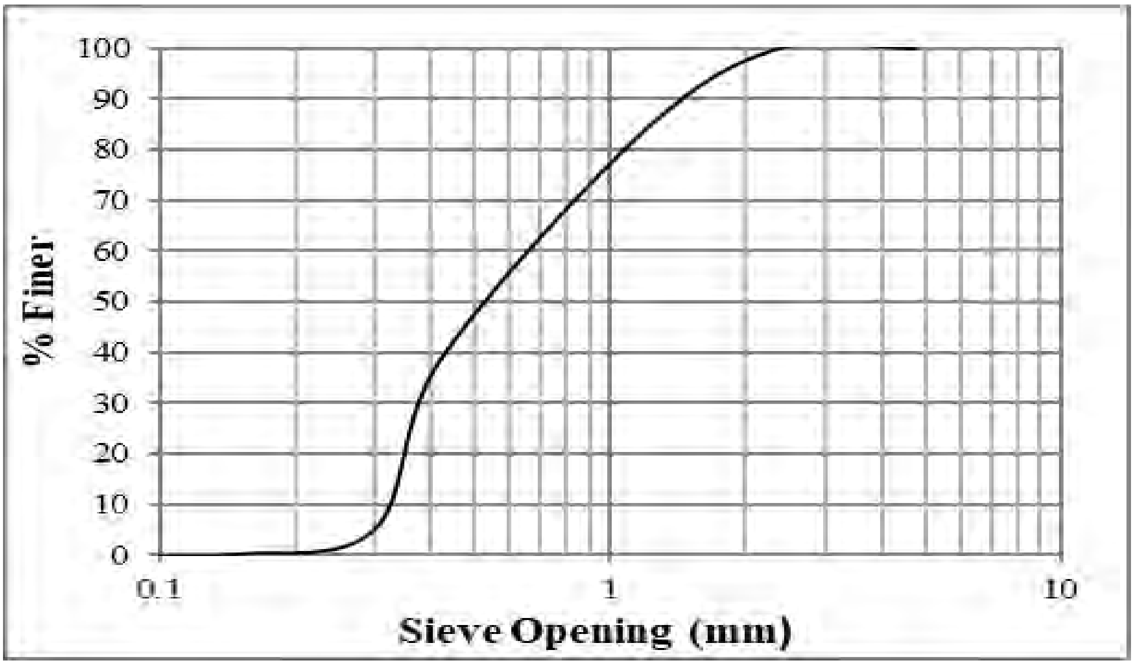

Figure 4.5. a) The grain size distribution of sylhet sand

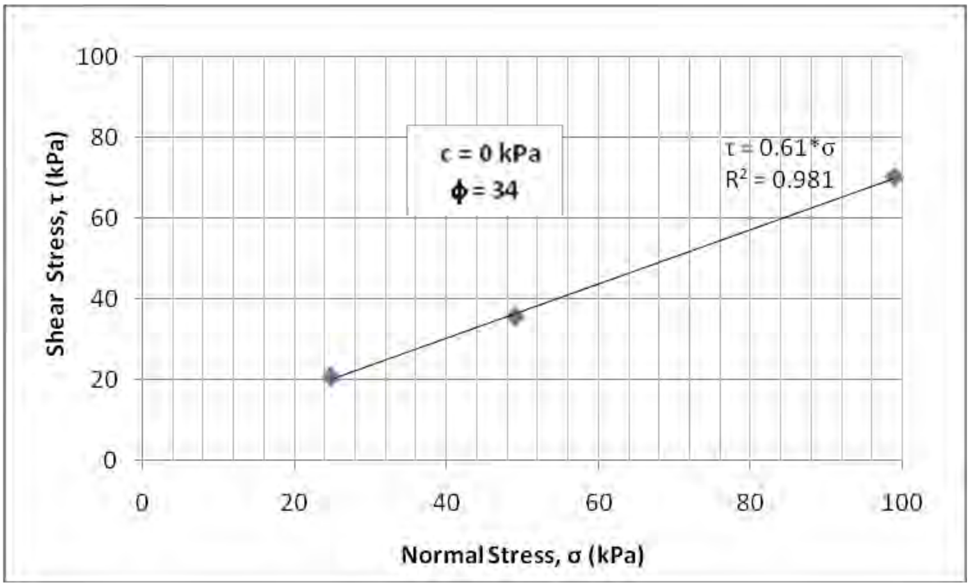

Figure 4.5. b) The Normal stress versus shear stress curve of sylhet sand

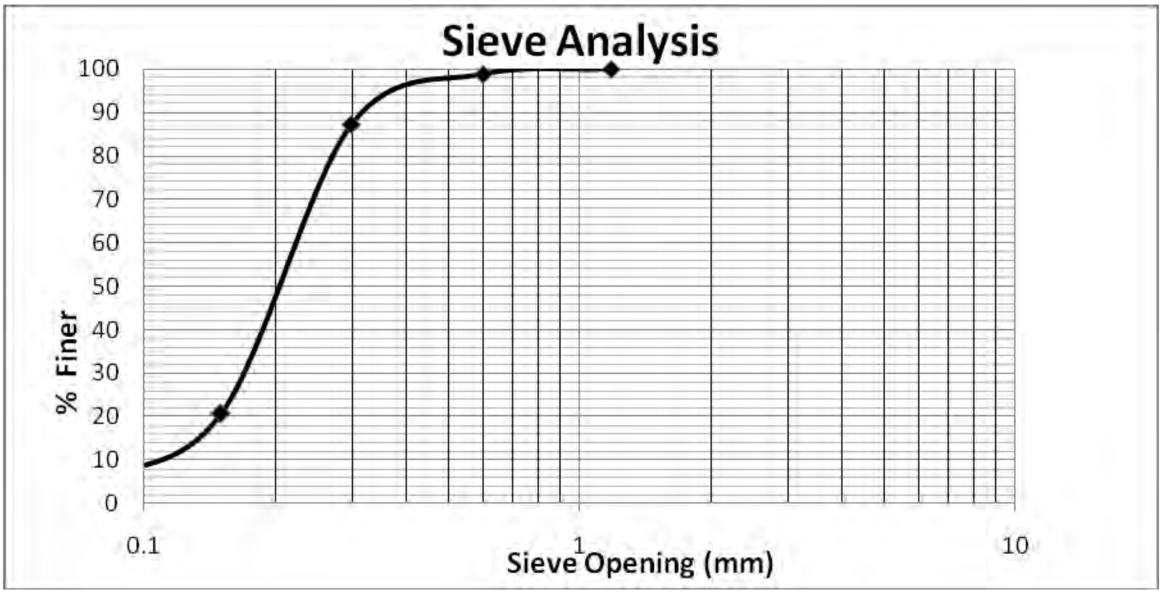

Figure 4.5. c) The grain size distribution of local sand

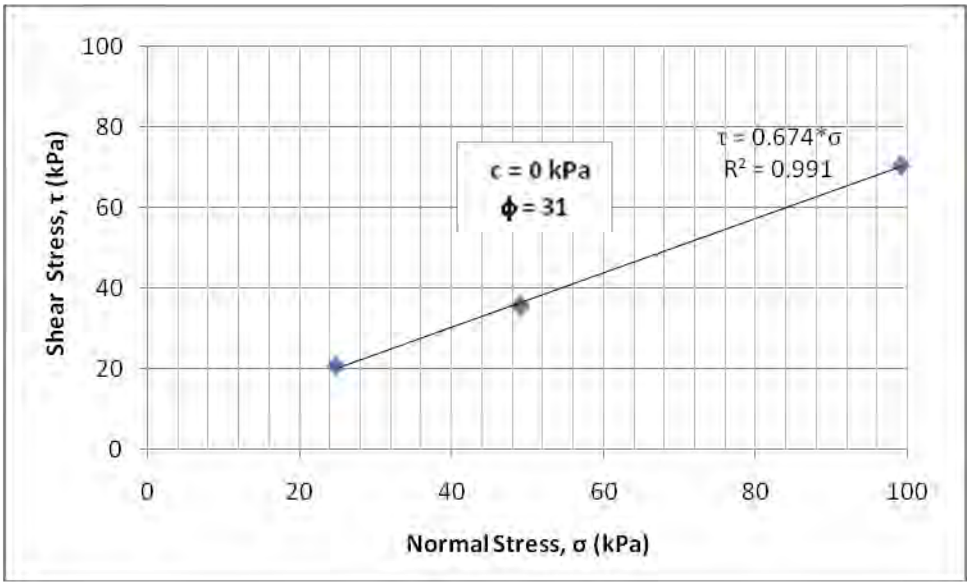

Figure 4.5. d) The Normal stress versus shear stress curve of Local sand

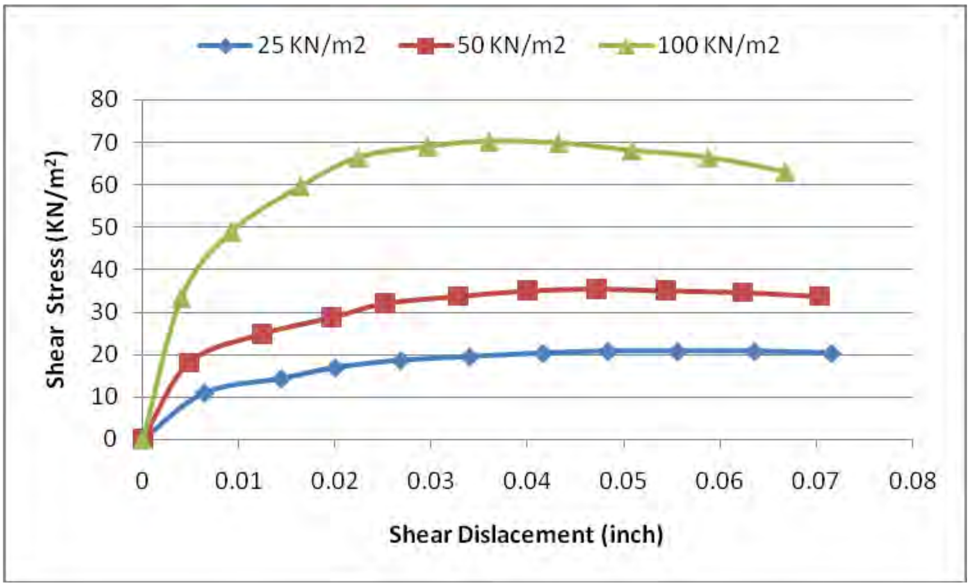

Figure 4.5. e) The Shear Stress versus shear displacement curve of sylhet sand

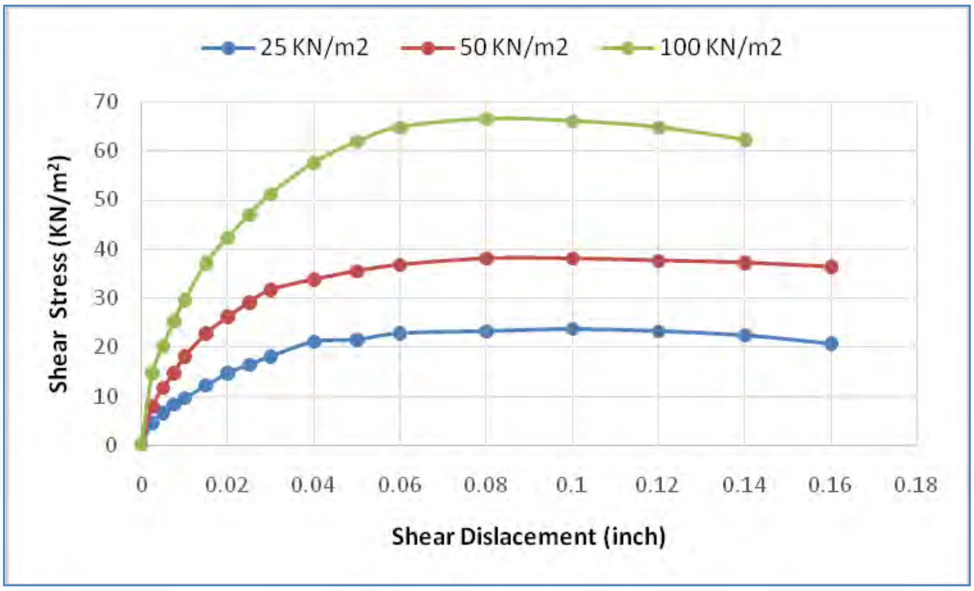

Figure 4.5. f) The Shear Stress versus shear displacement curve of local sand

a) b)

Figure 4.6. a) The Universal tensile testing machine and b) shows the geotextile sample

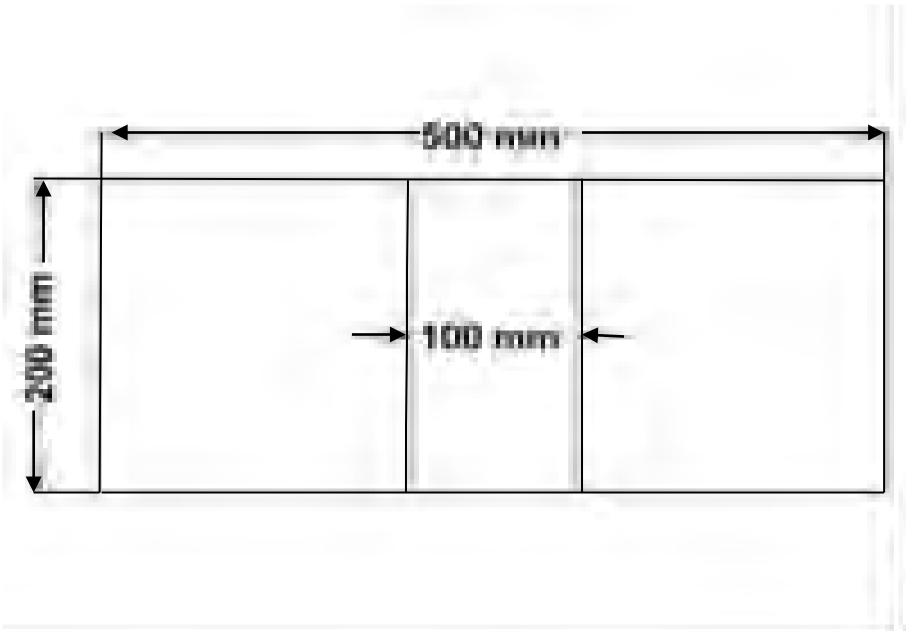

Figure 4.6. c) The dimension of geotextile for wide-width test

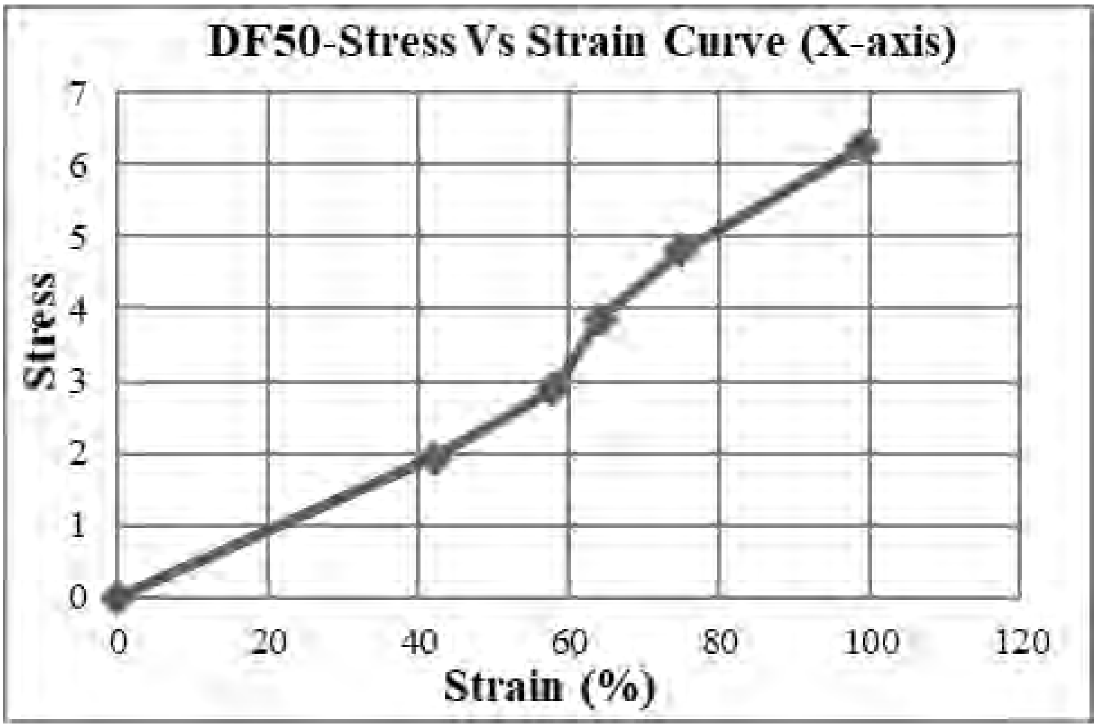

Figure 4.7.a) The Load-elongation response of X direction of geotextile sample.

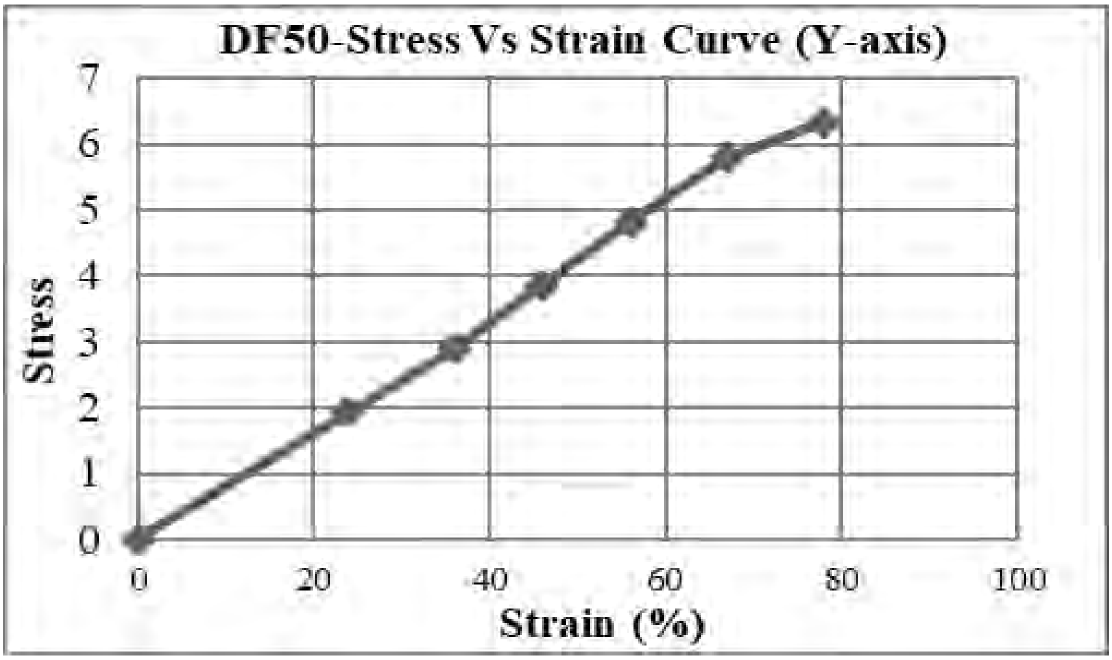

Figure 4.7. b) The Load-elongation response of Y direction of geotextile sample.

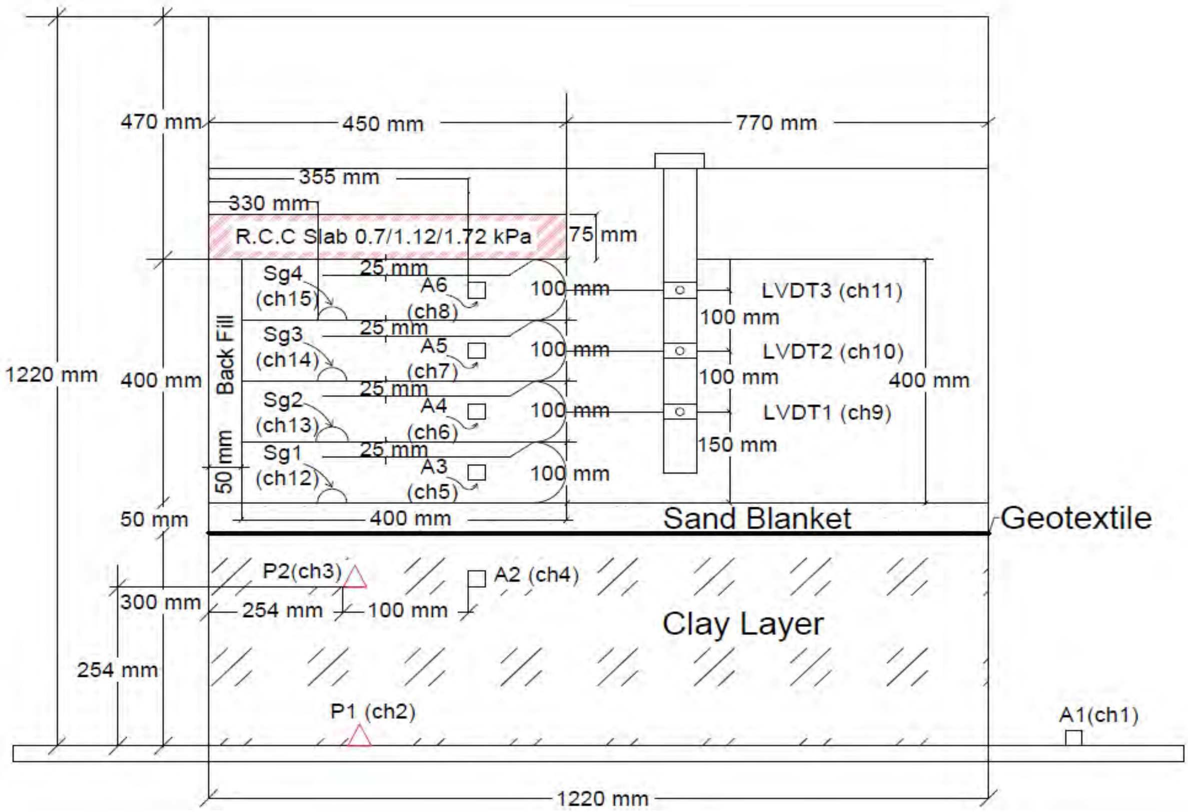

Figure 4.8. Schematic diagram of the scaled model of a wrap faced geotextile wall

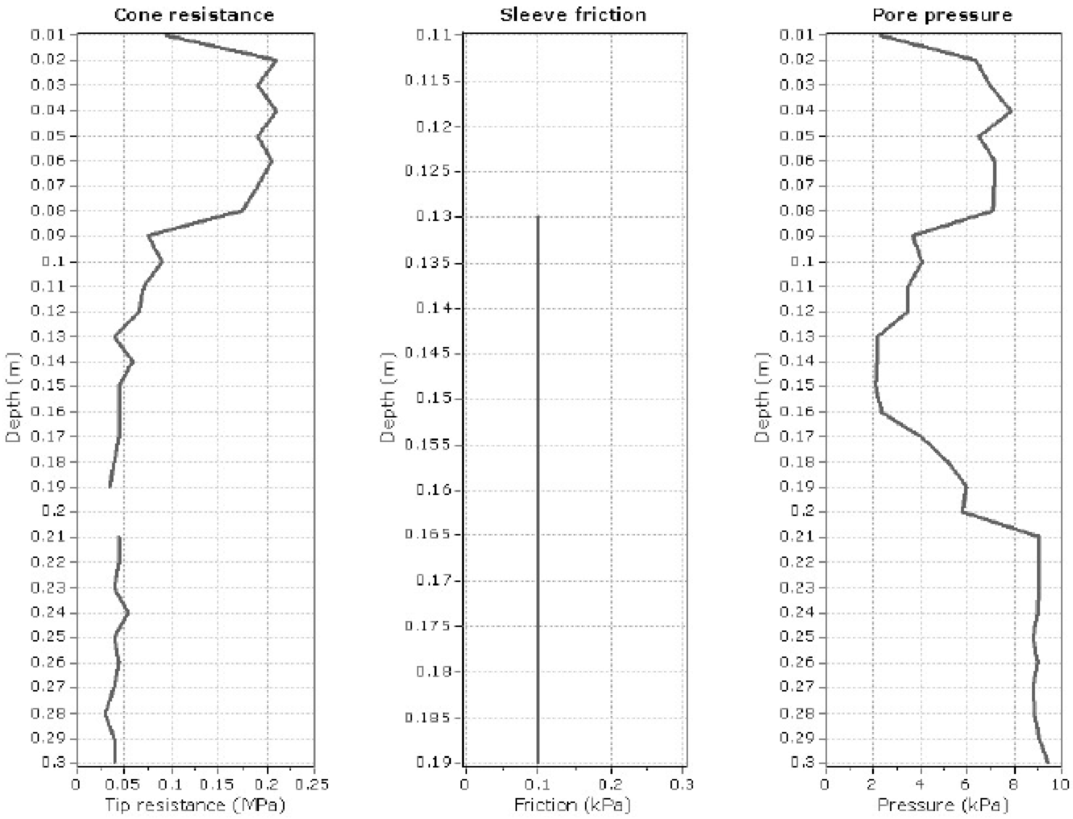

Figure 4.9 (a): CPT test on Reconstitute soil sample layer

Figure 4.9 (b): conducting CPT test on Reconstitute soil sample

Figure 4.10: Placement of third layer of clayey soil.

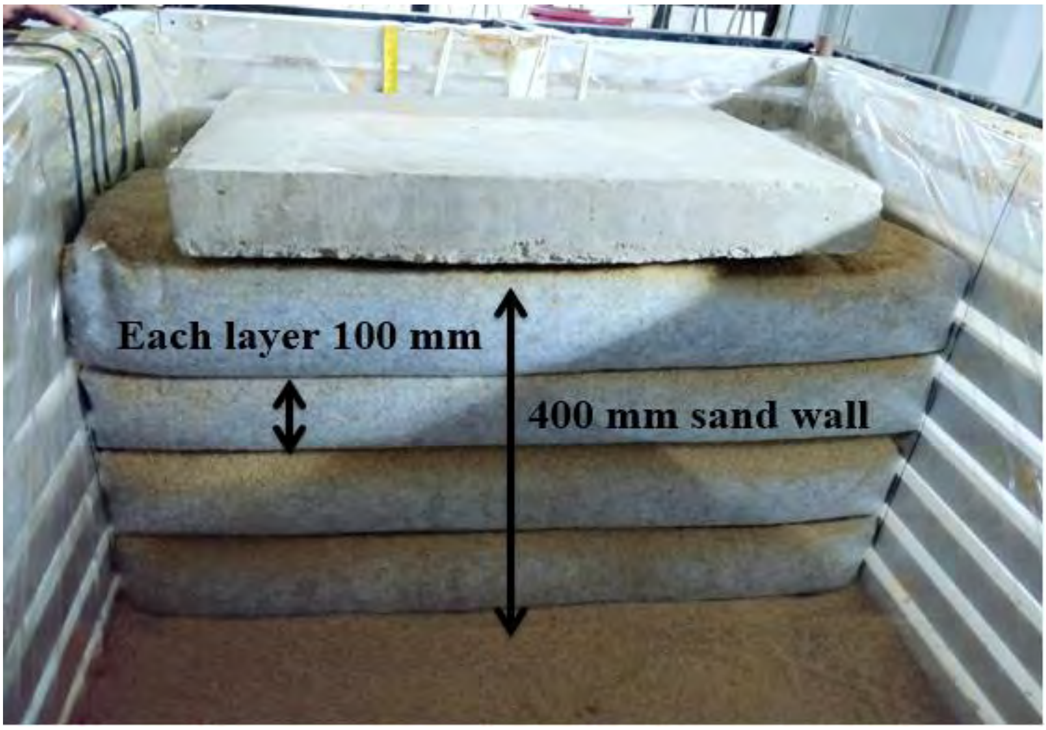

Figure 4.11: Accomplished wrap-faced wall.

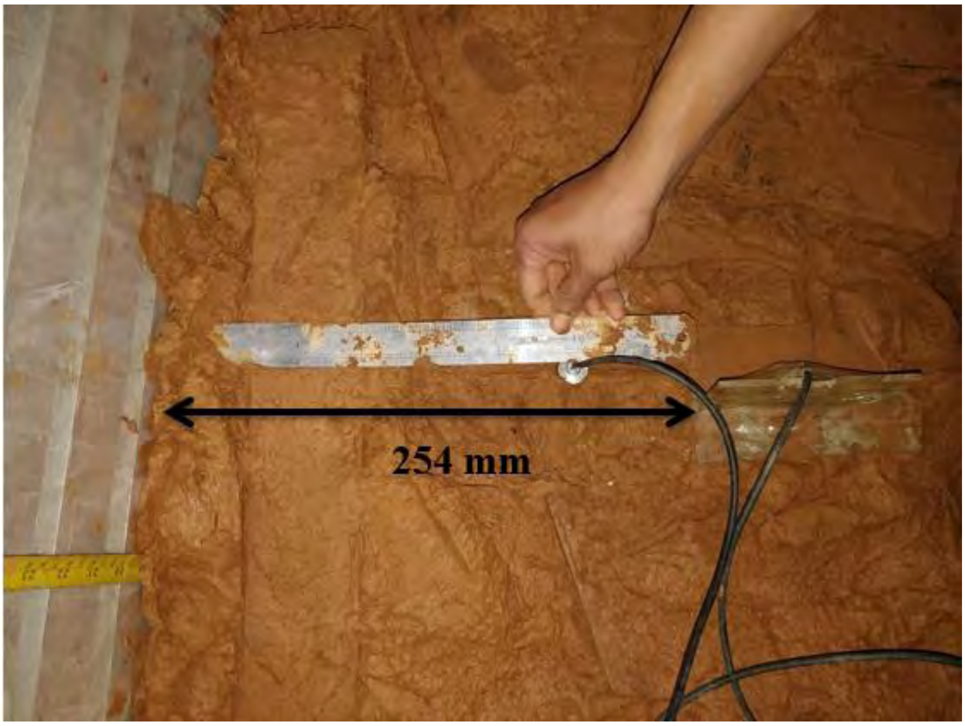

Figure 4.12: Positioning the pore pressure sensor (P2) at desired location.

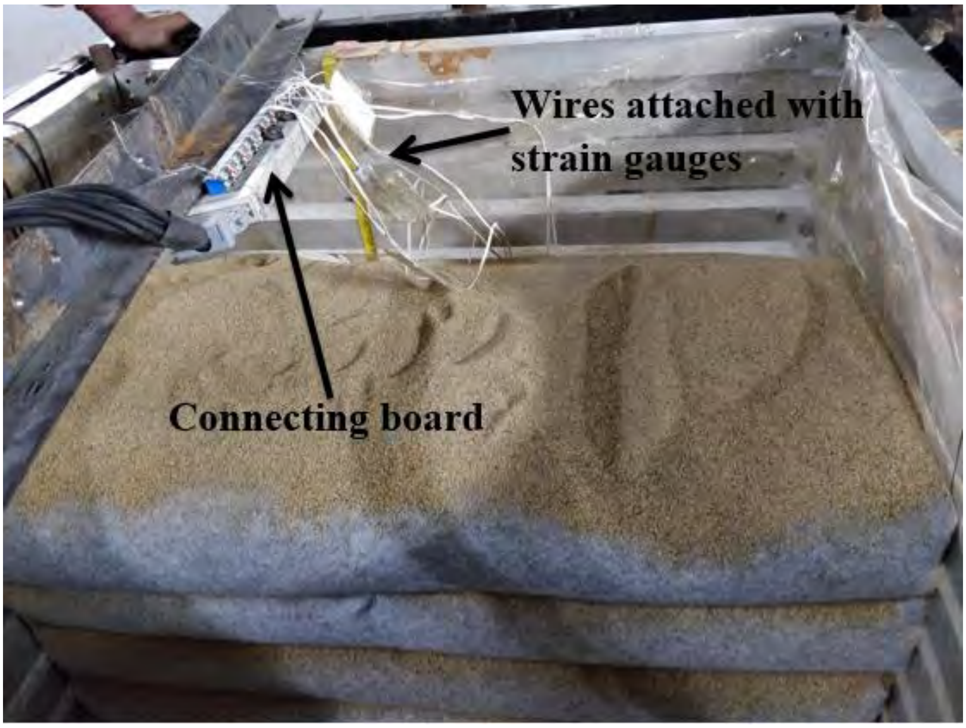

Figure 4.13:Connection board of all strain gauges.

Figure 4.14: Three allocated LVDTs.

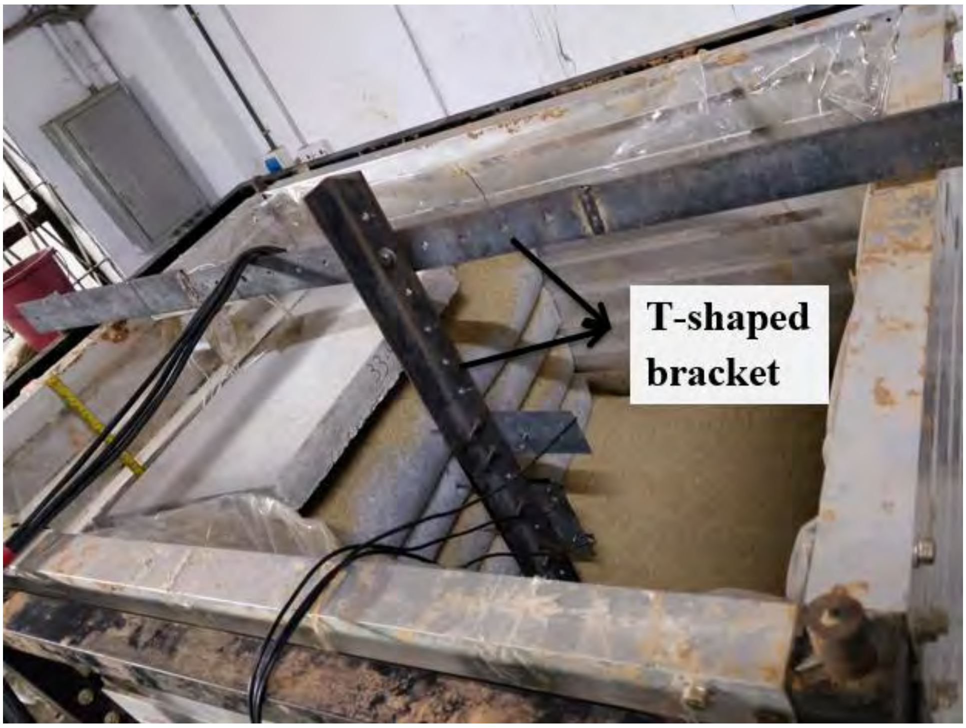

Figure 4.15: T-shaped bracket for supporting LVDTs.

Figure 4.16: R.C.C. slab as surcharge load.

Figure 4.17: Attached scale with diffuser to maintain accurate height of fall.

Figure 4.18: Construction of third layer of model wall with pluviator.

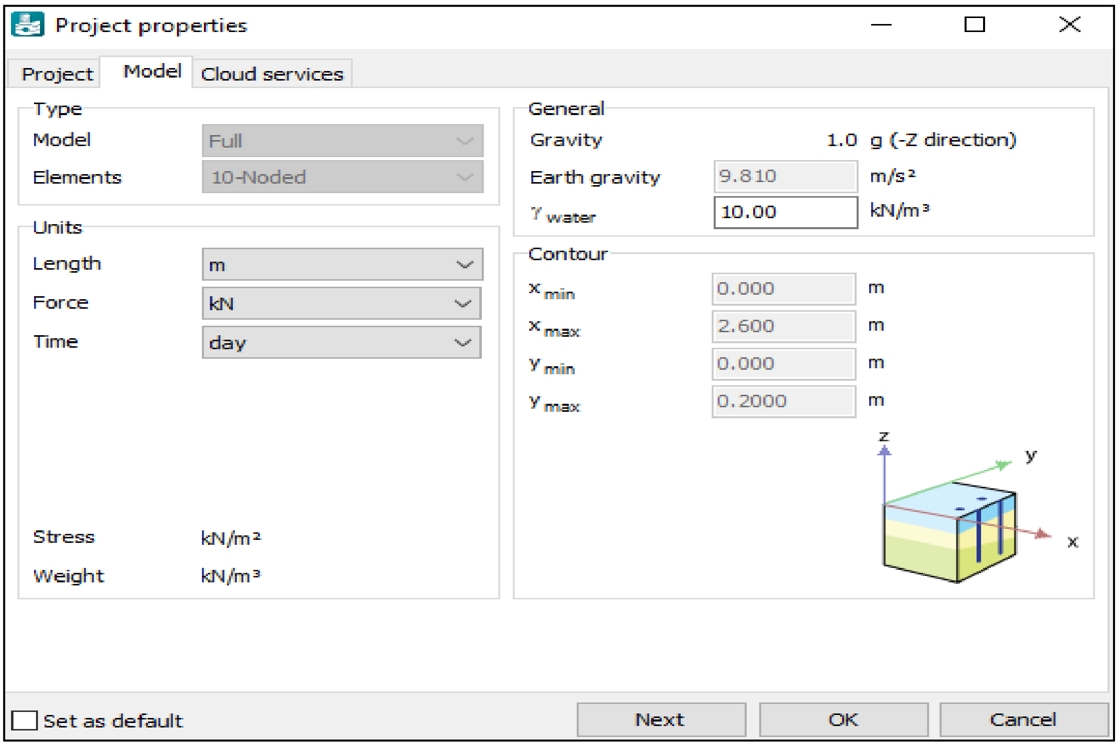

Figure 5.1 Model tabsheet of the project properties window

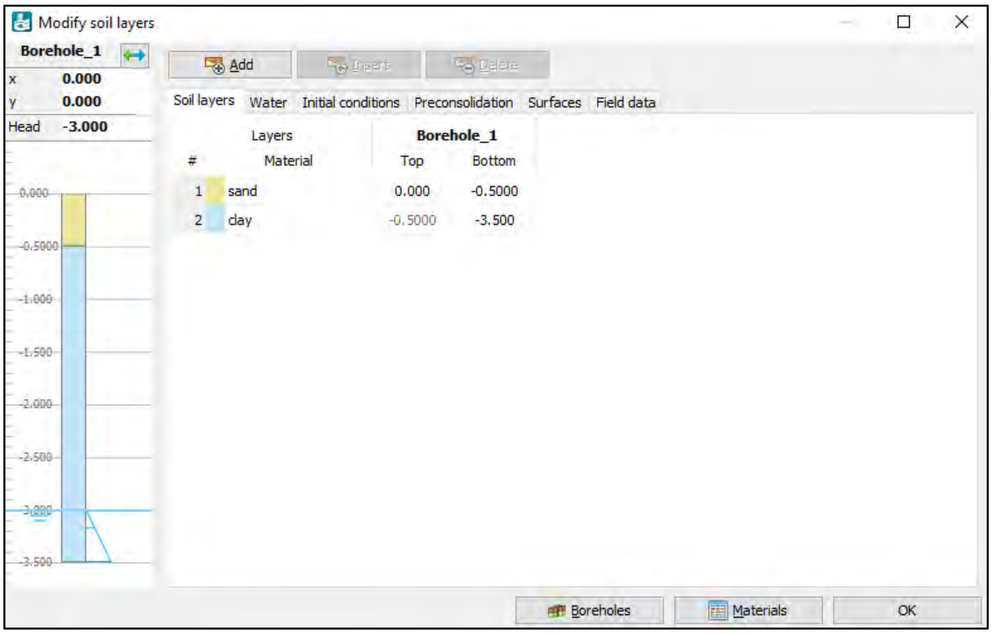

Figure 5.2: Two soil layers

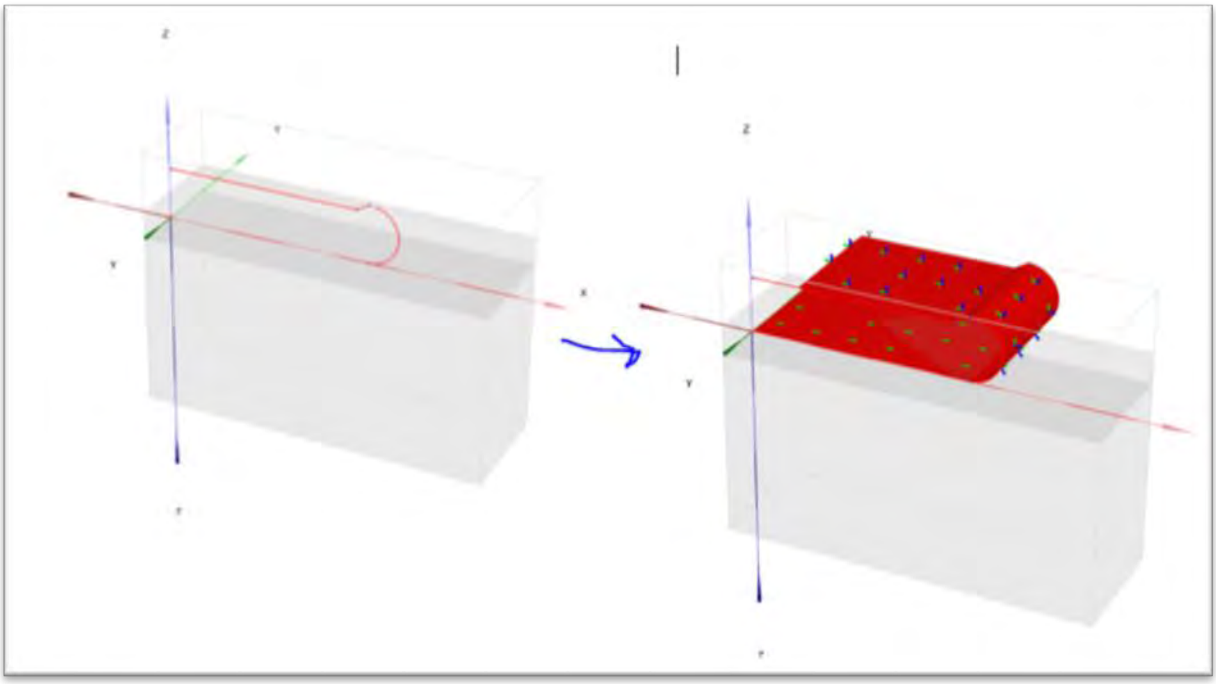

Figure 5.3: Created geotextile layer

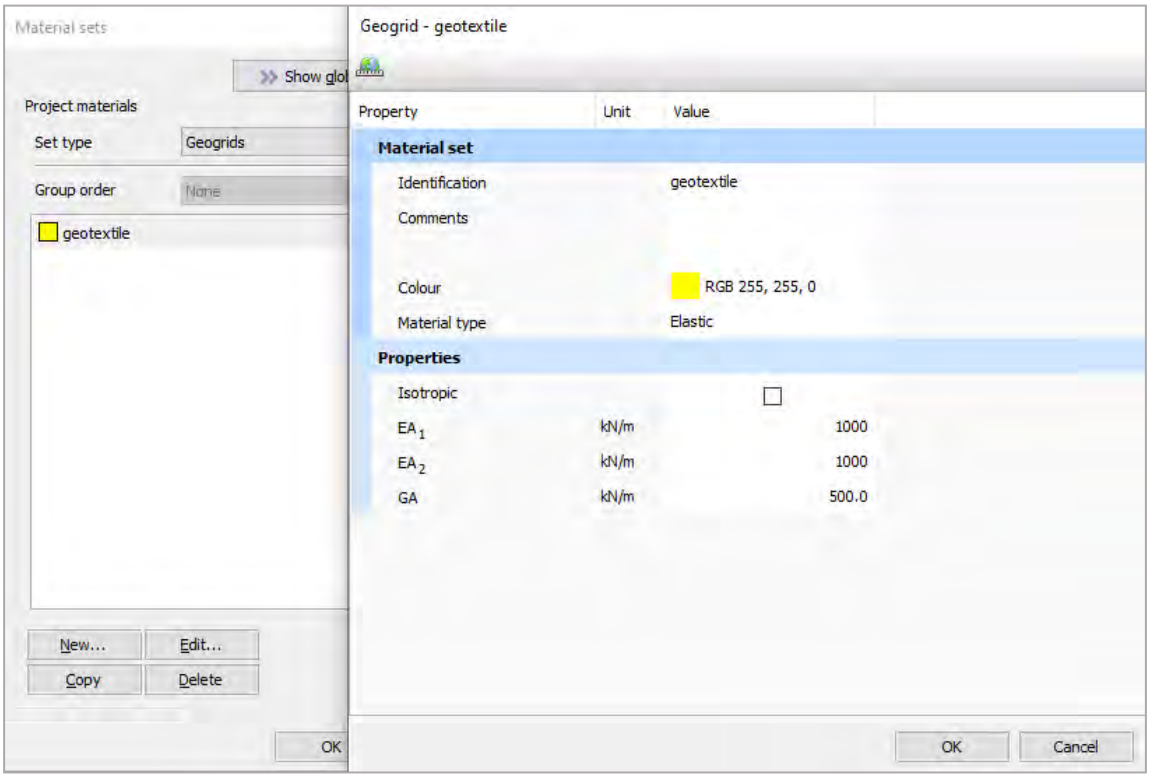

Figure 5.4:The properties of geotextile layer

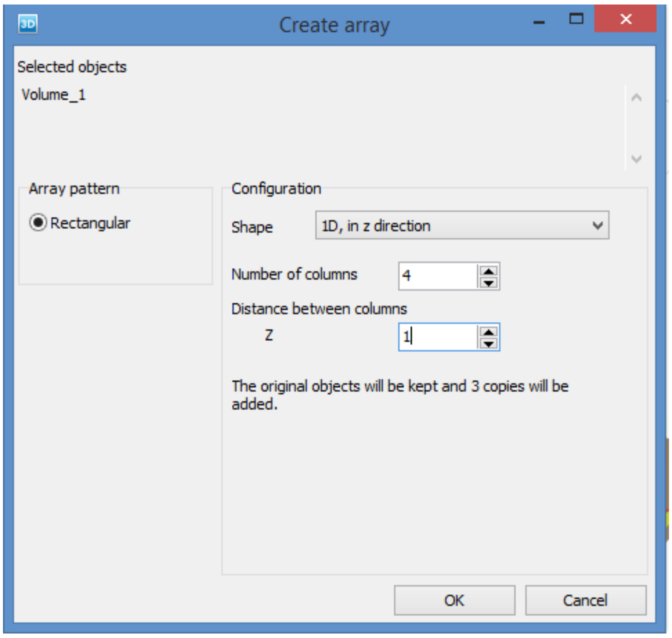

Figure 5.5 : Creation of array

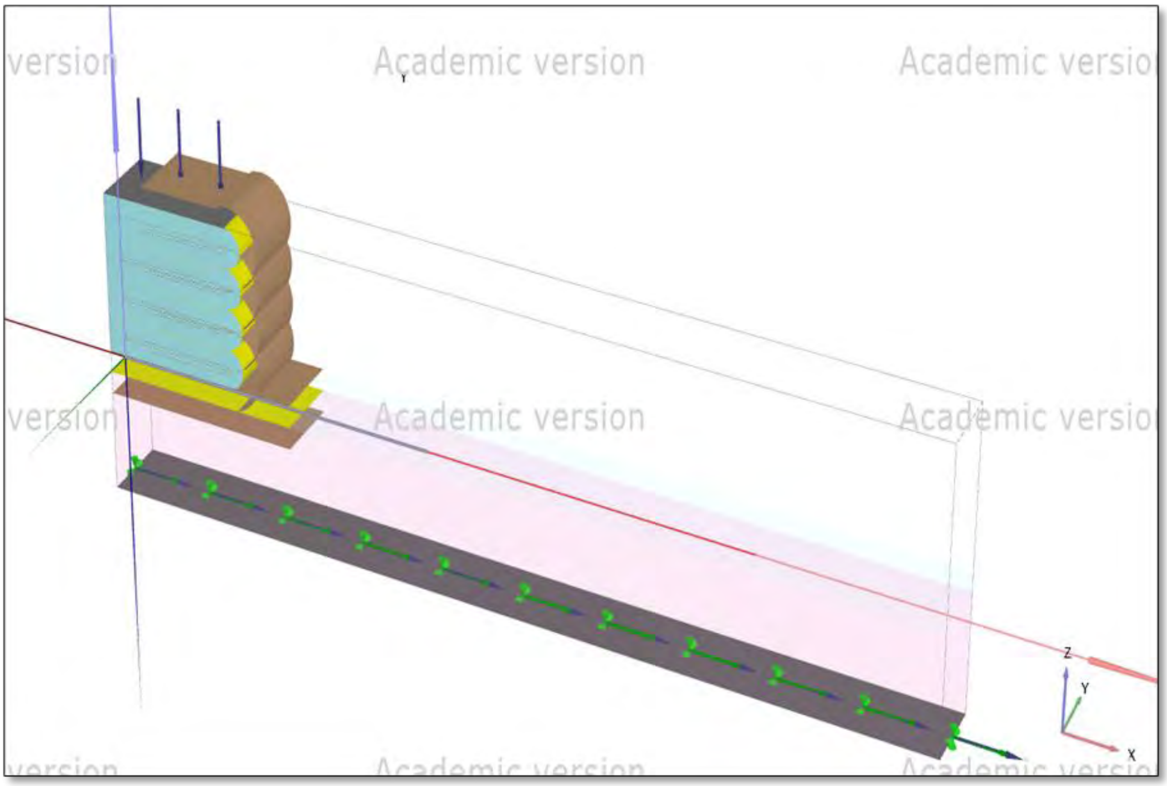

Figure 5.6: Whole diagram of the model

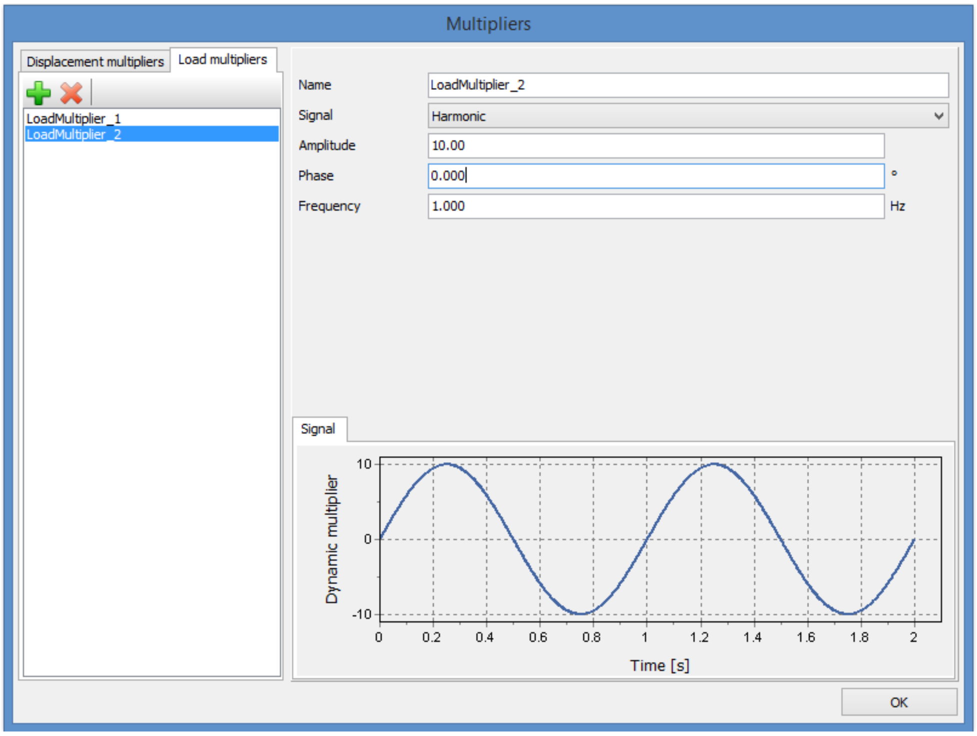

Figure 5.7 Definition of dynamic propertie

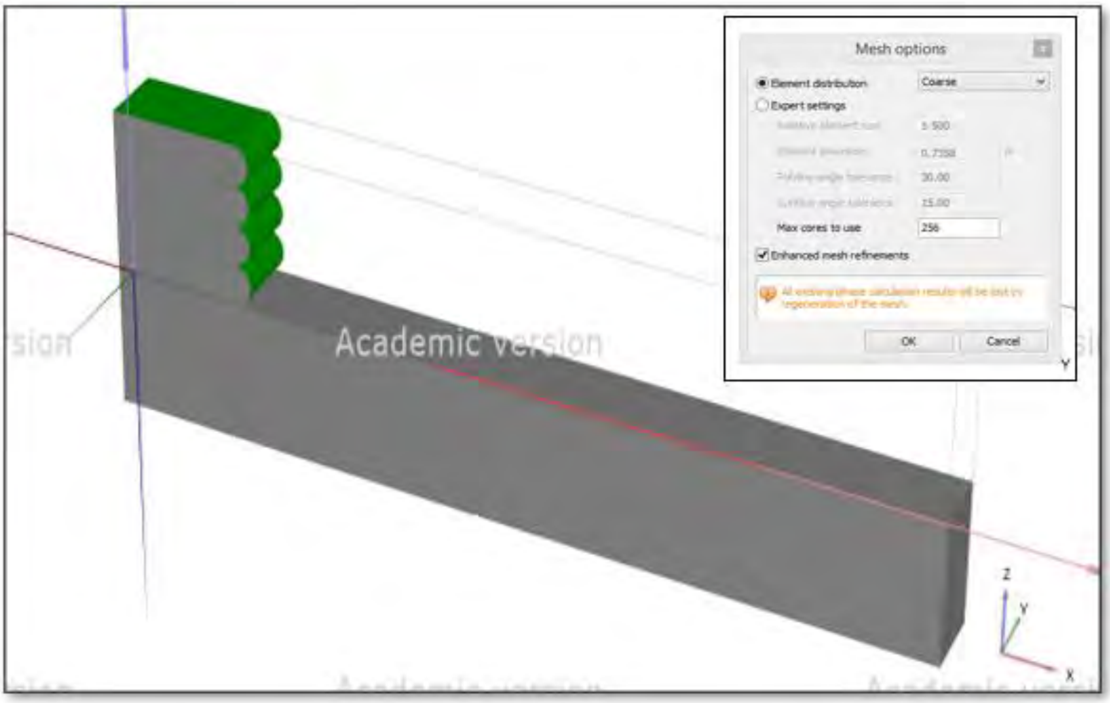

Figure 5.8 Mesh generation

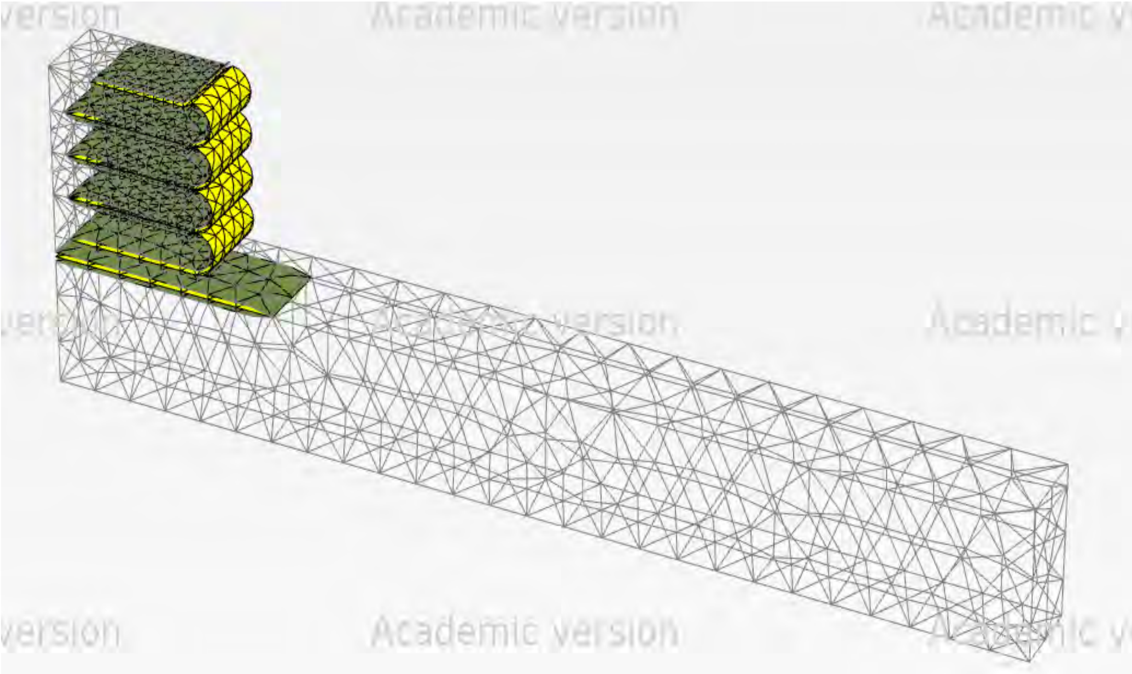

Figure 5.9: The Generated Mesh

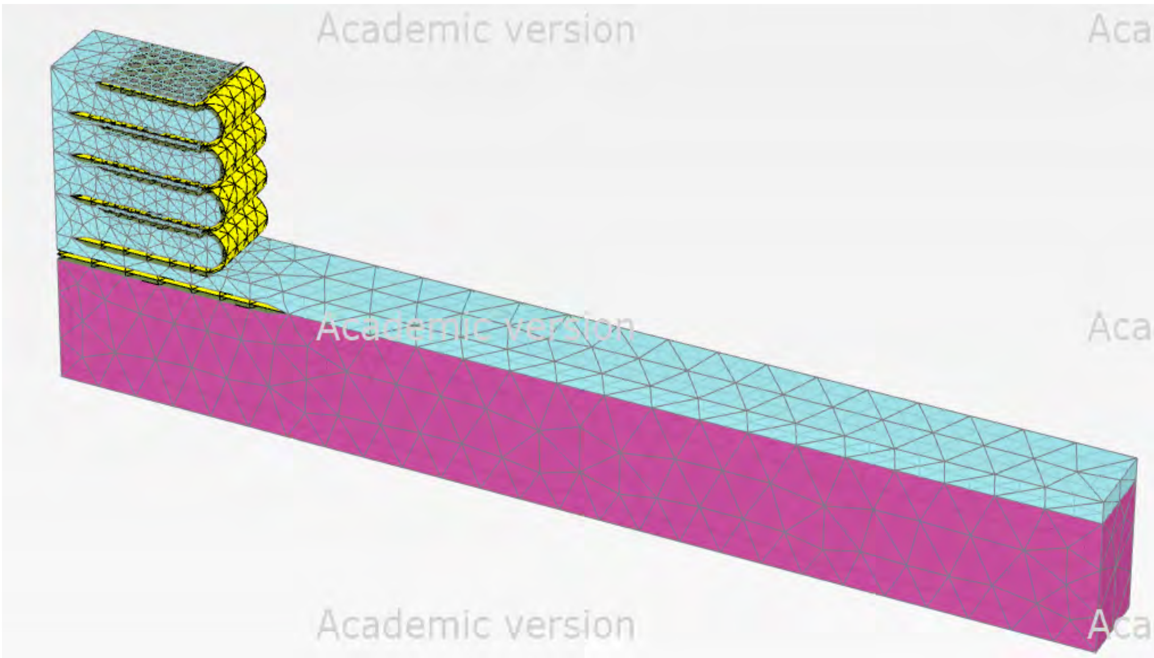

Figure 5.10: The resulting mesh

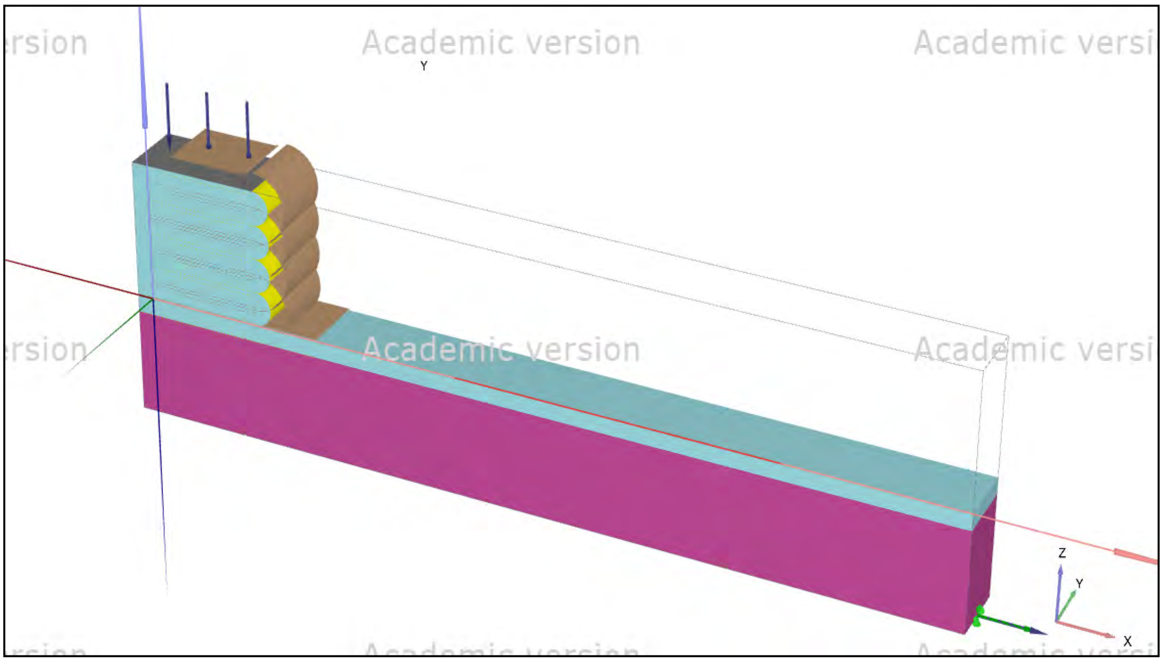

Figure 5.11: Profile of construction

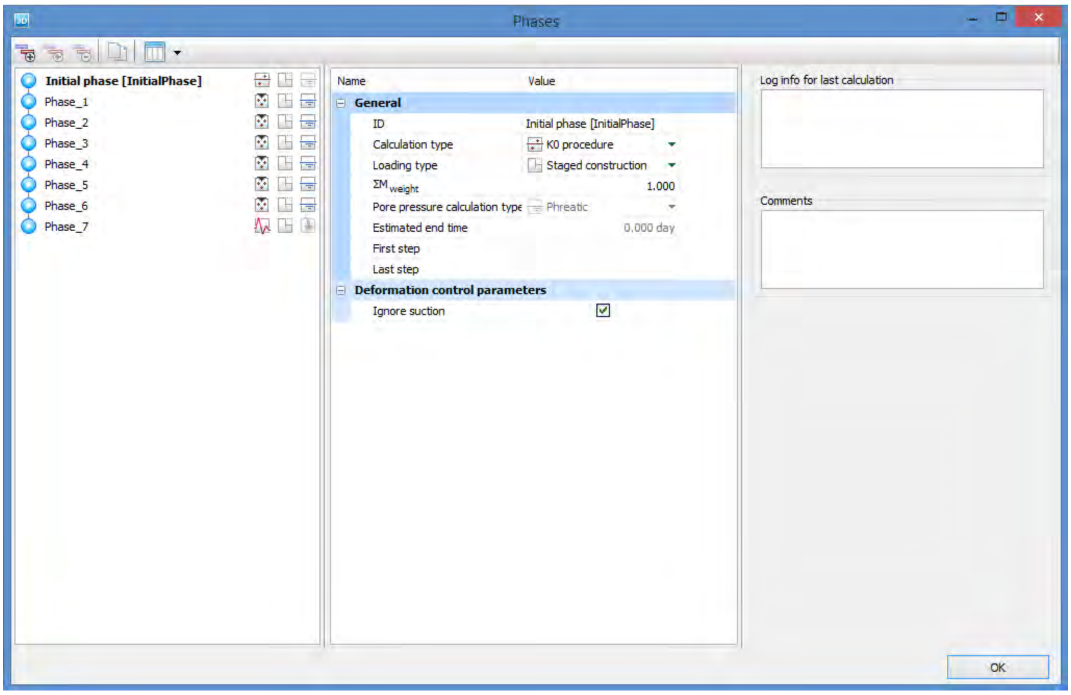

Figure 5.12: Defining the initial phase.

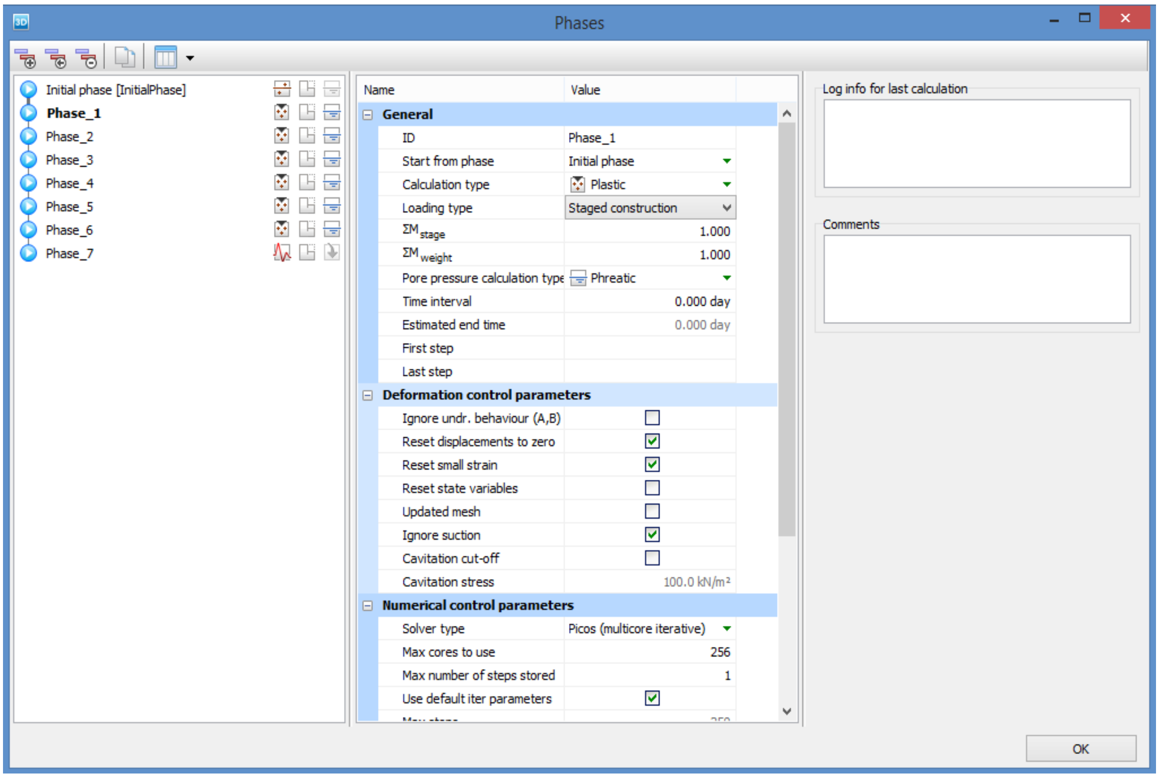

Figure 5.13: Defining the structural element at phase 1

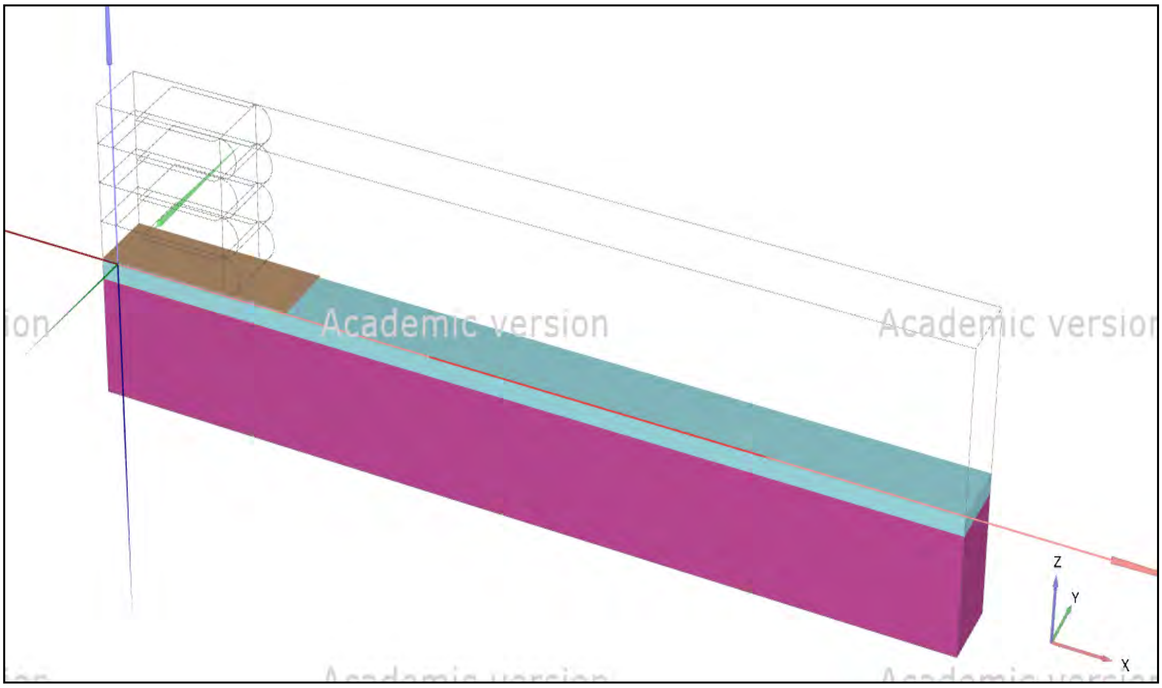

Figure 5.14 : The structural element at phase 1

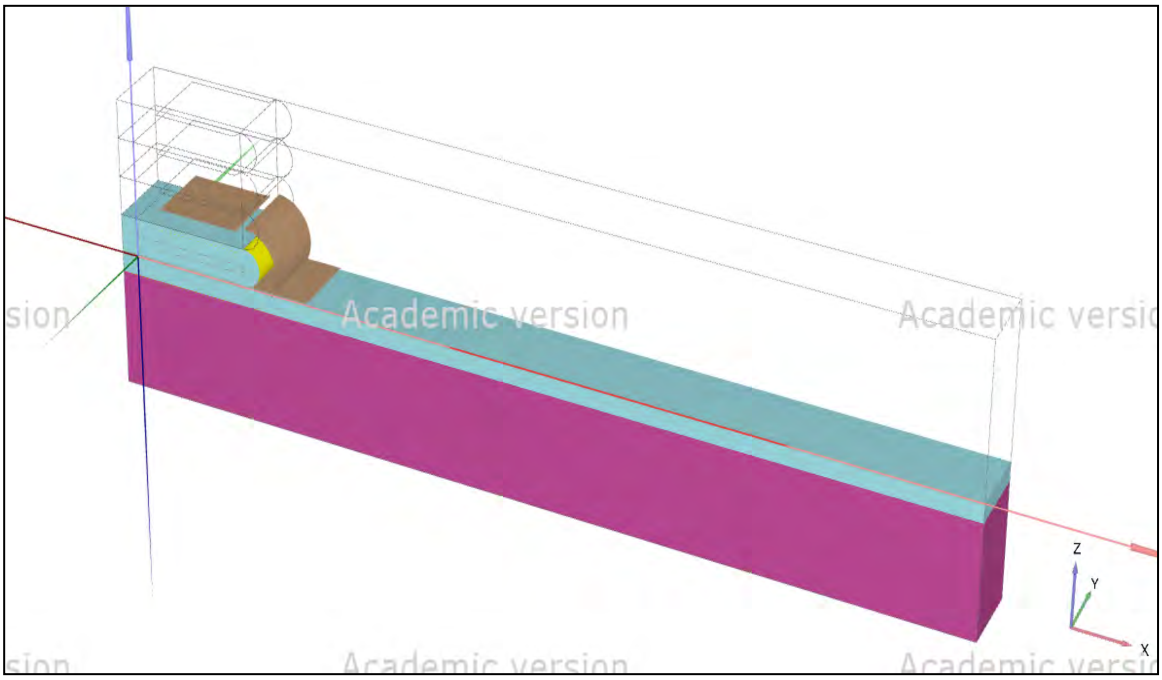

Figure 5.15 : The structural element at phase 2

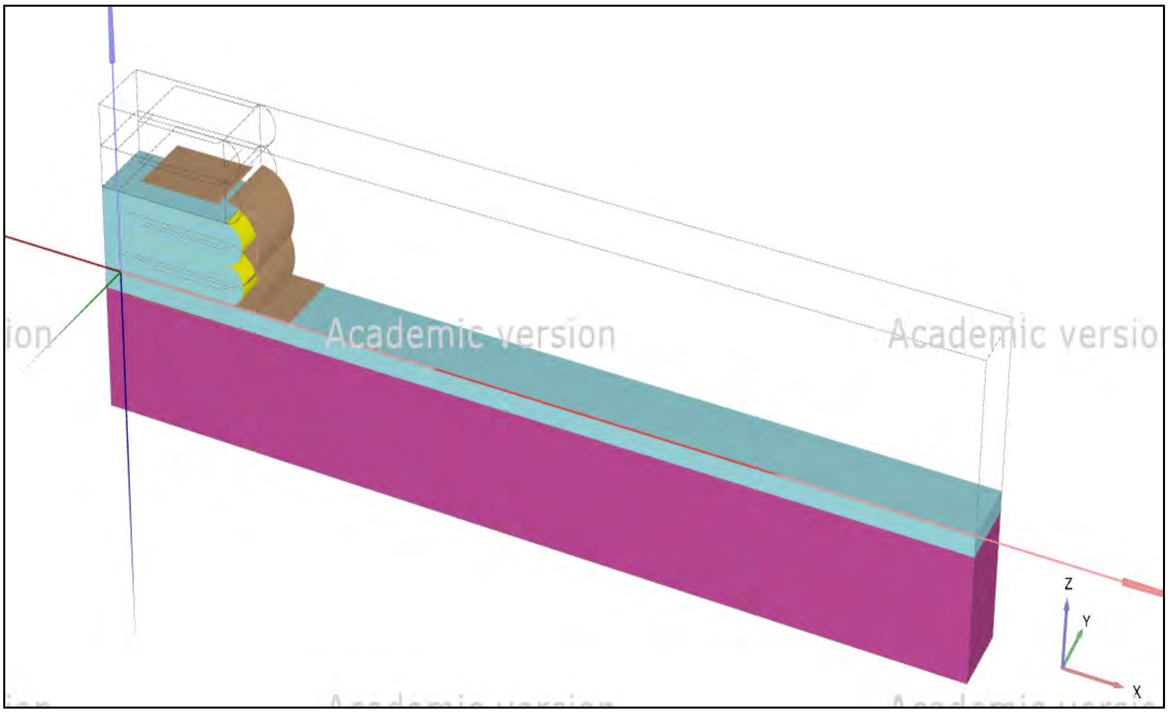

Figure 5.16: The structural element at phase 3

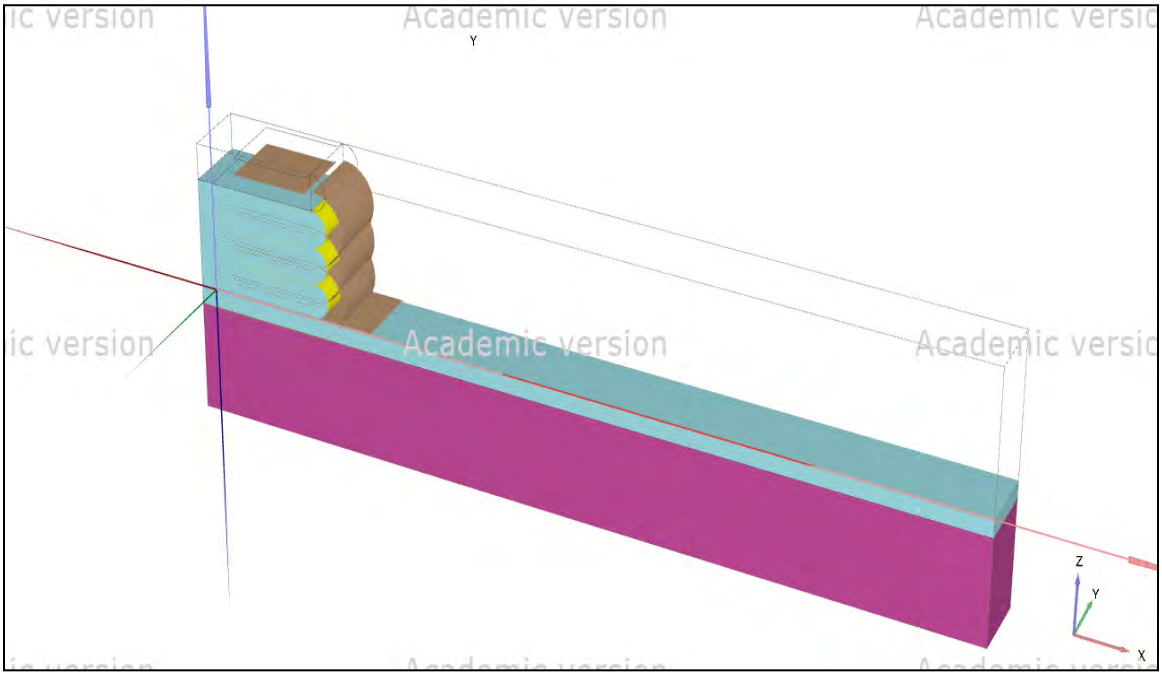

Figure 5.17 The structural element at phase 4

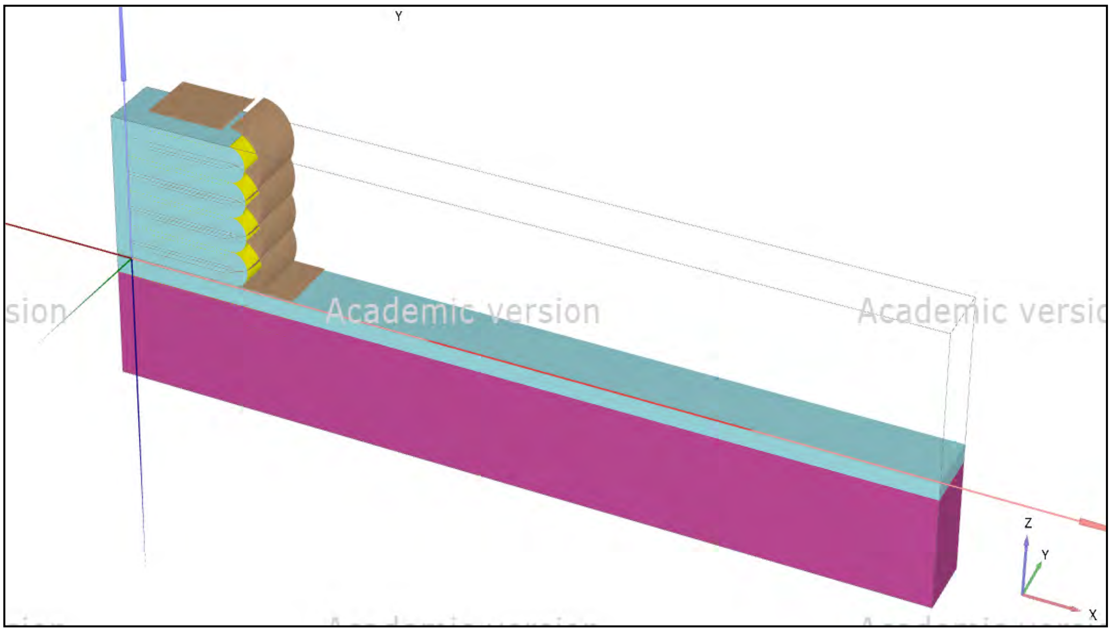

Figure 5.18 The structural element at phase 5

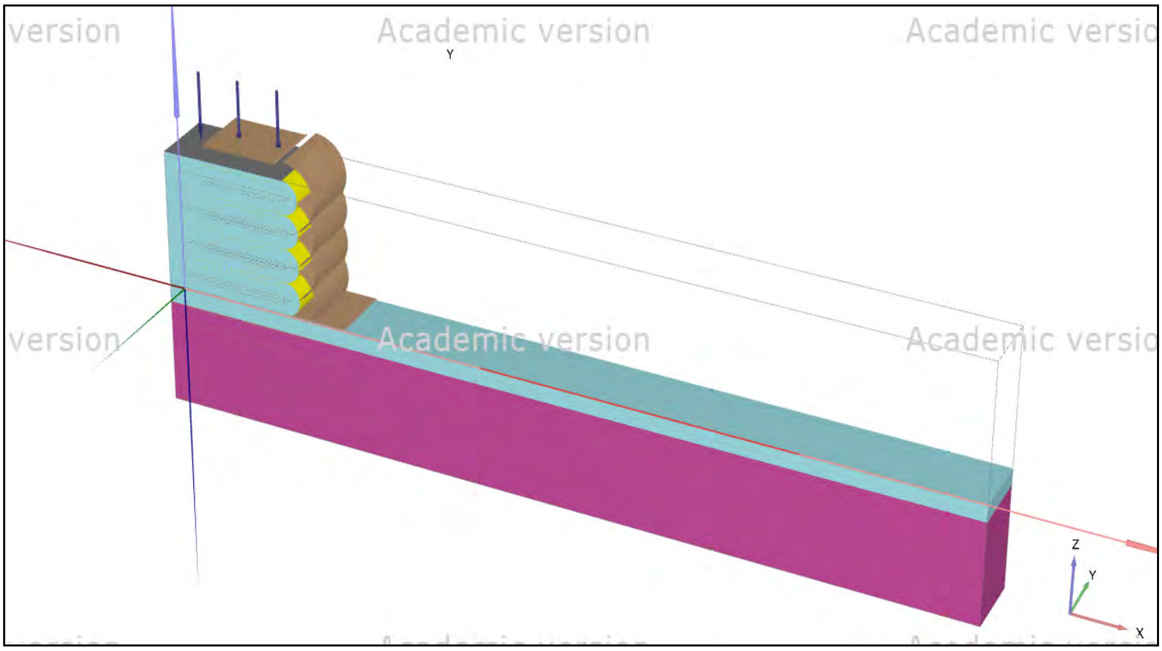

Figure 5.19: The structural element at phase 6

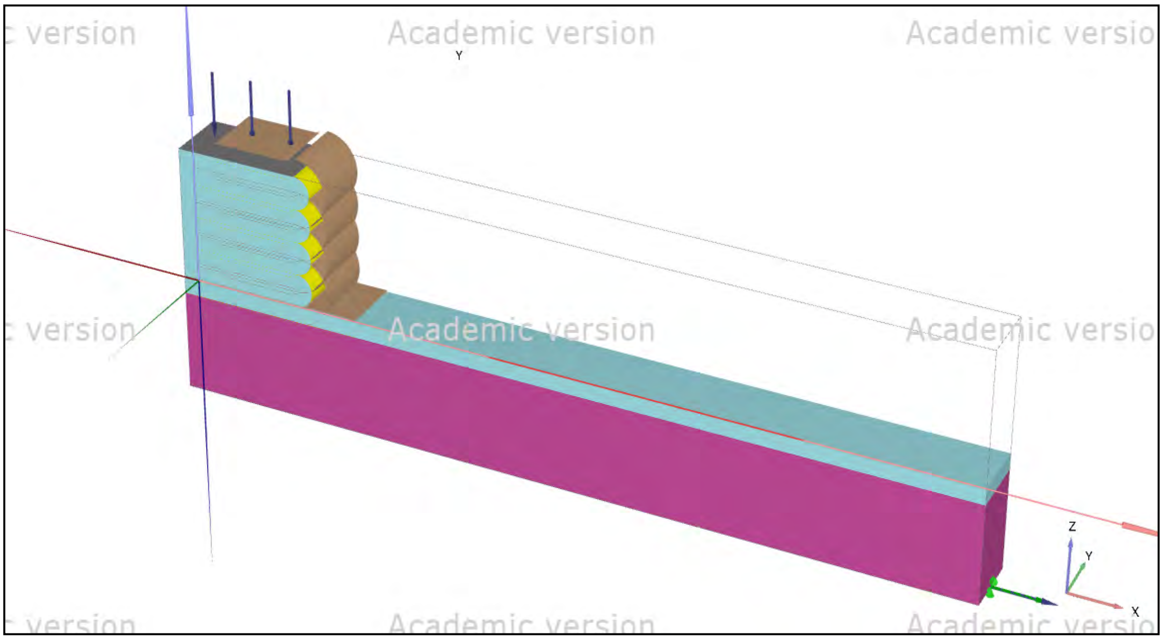

Figure 5.20 The structural element at phase 7

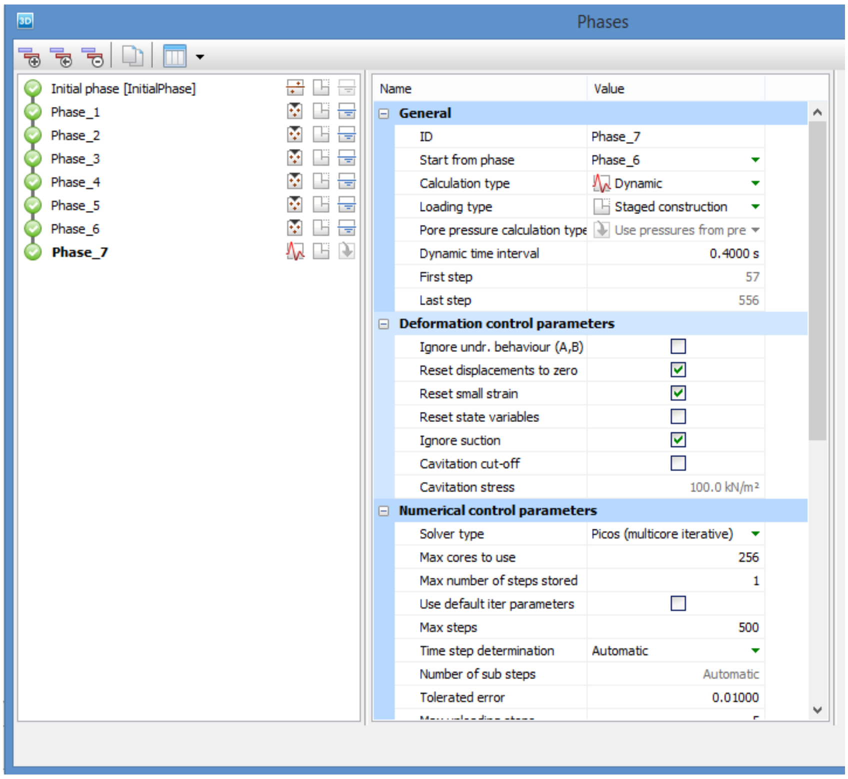

Figure 5.21(a) : Defining the structural element at phase 7

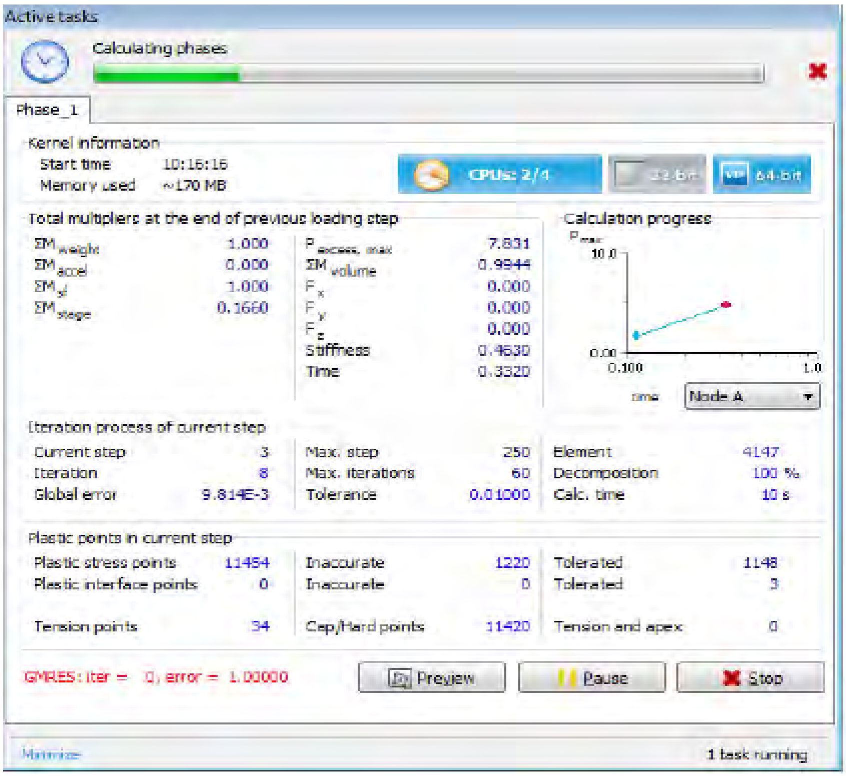

Figure 5.21(b): Calculating phases

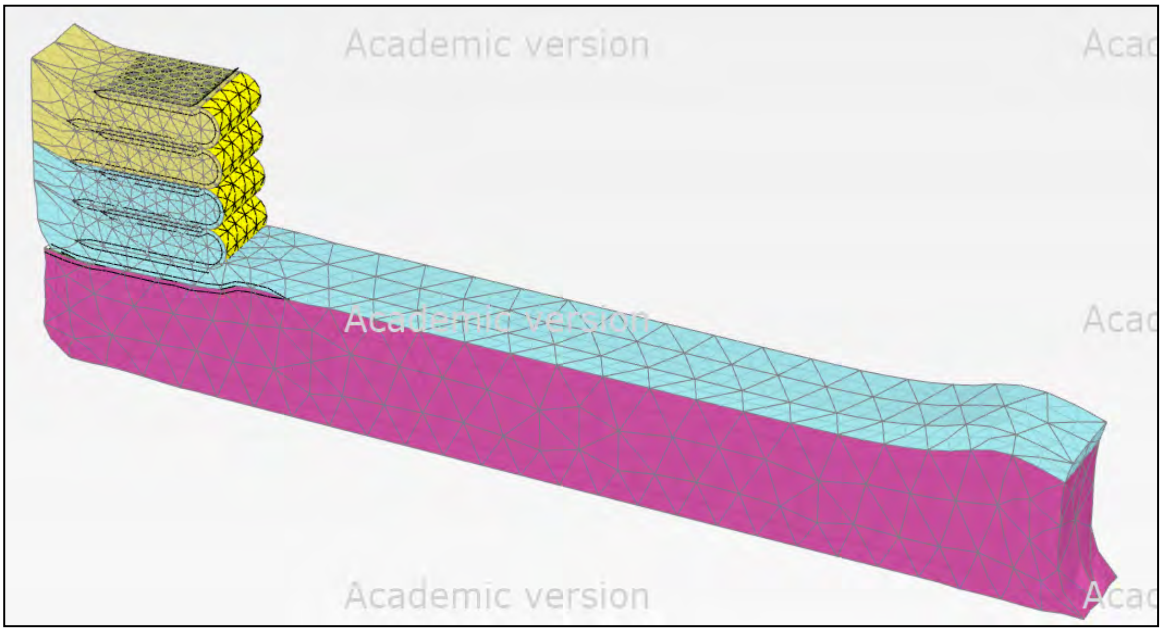

Figure 5.22: Deformed mesh after undrained construction of embankment (phase 7)

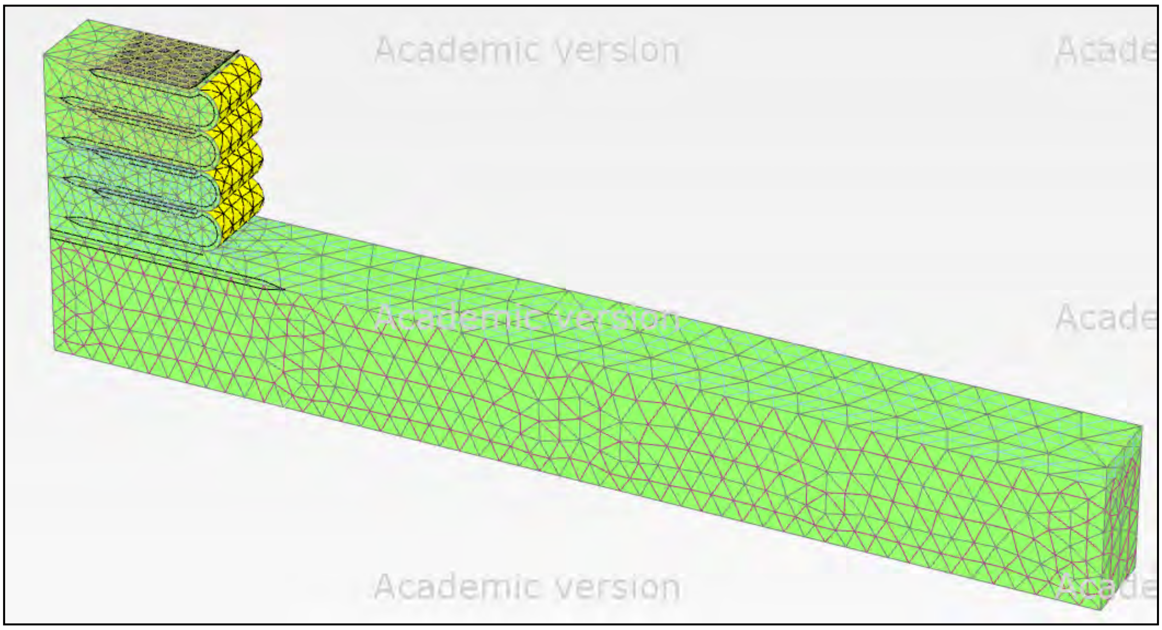

Figure 5.23: Displacement increments after undrained construction of embankment

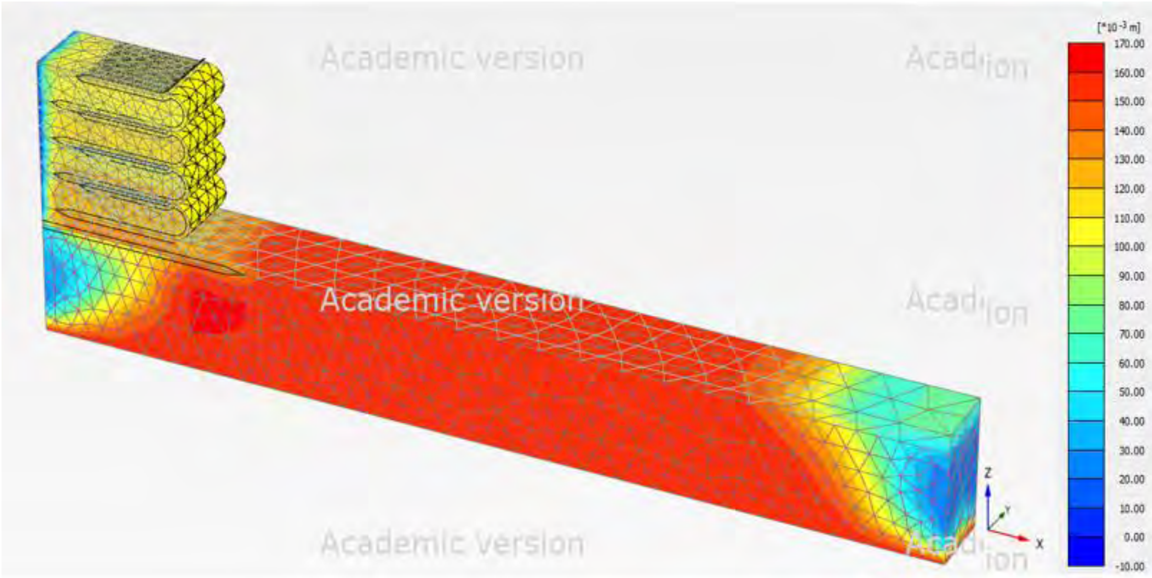

Figure 5.24 (a): Structural element (Shading)

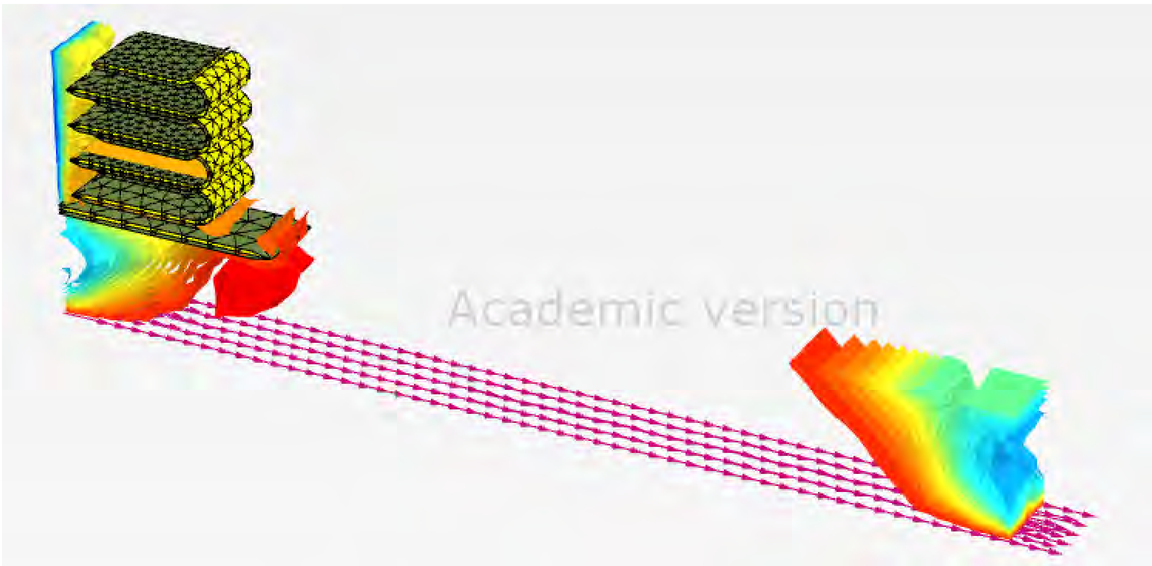

Figure 5.24 (b): Structural element (ISO surface)

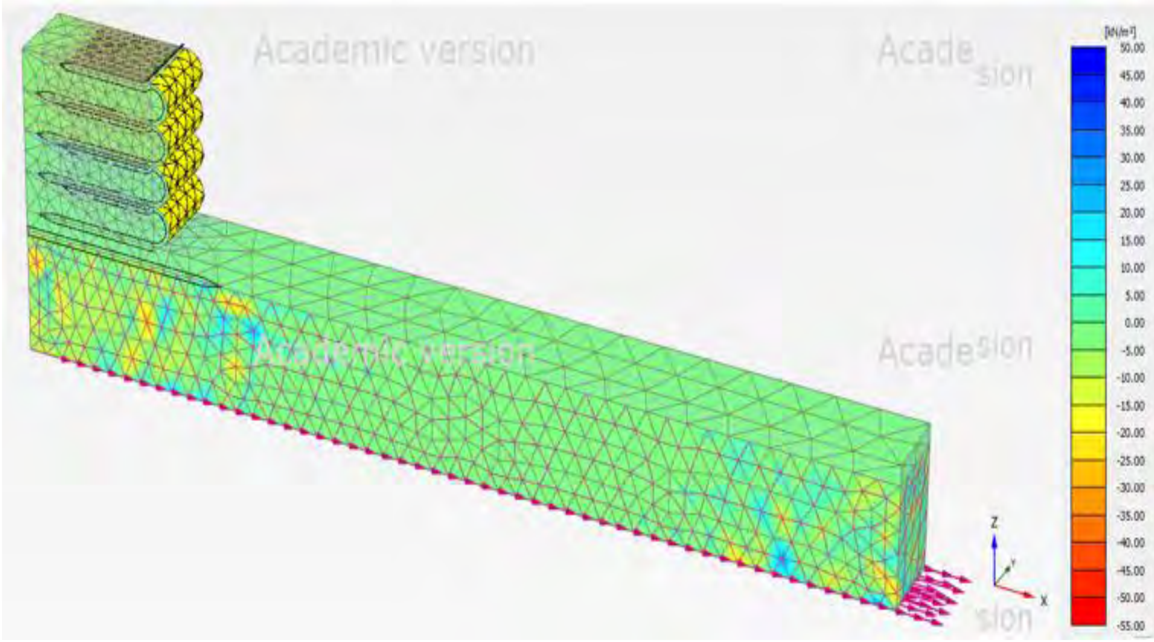

Figure 5.25: Excess pore water pressure after undrained construction of embankment (Phase 7)

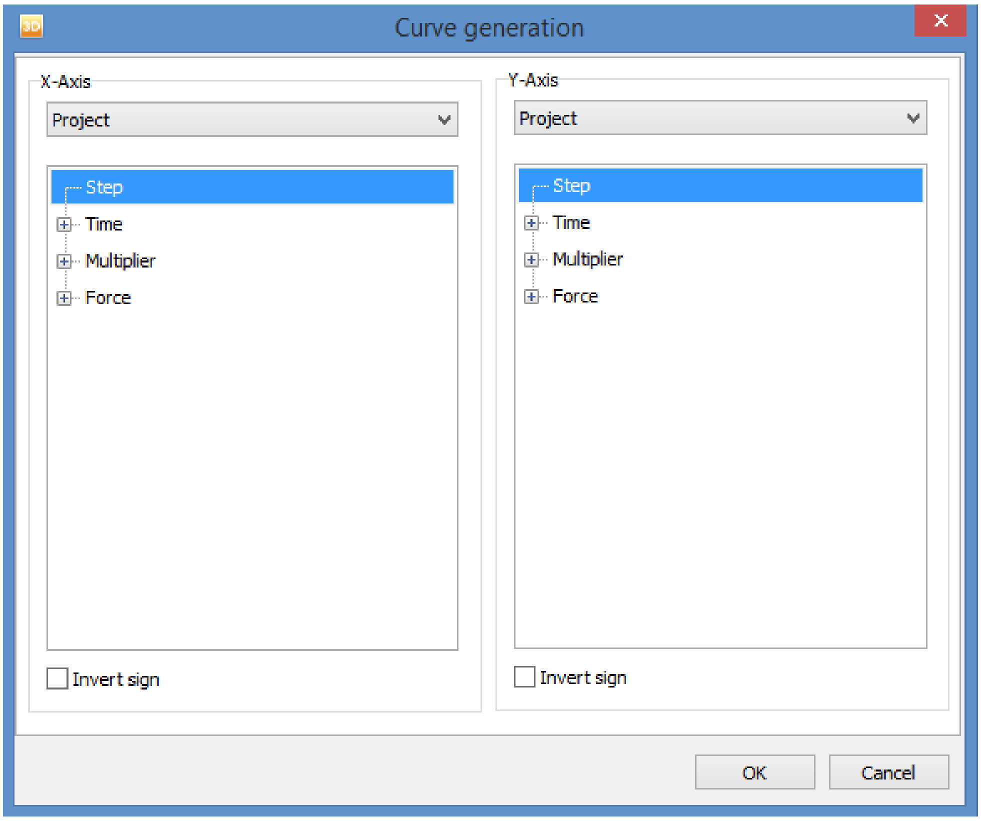

Figure 5.26: Curve Generation process

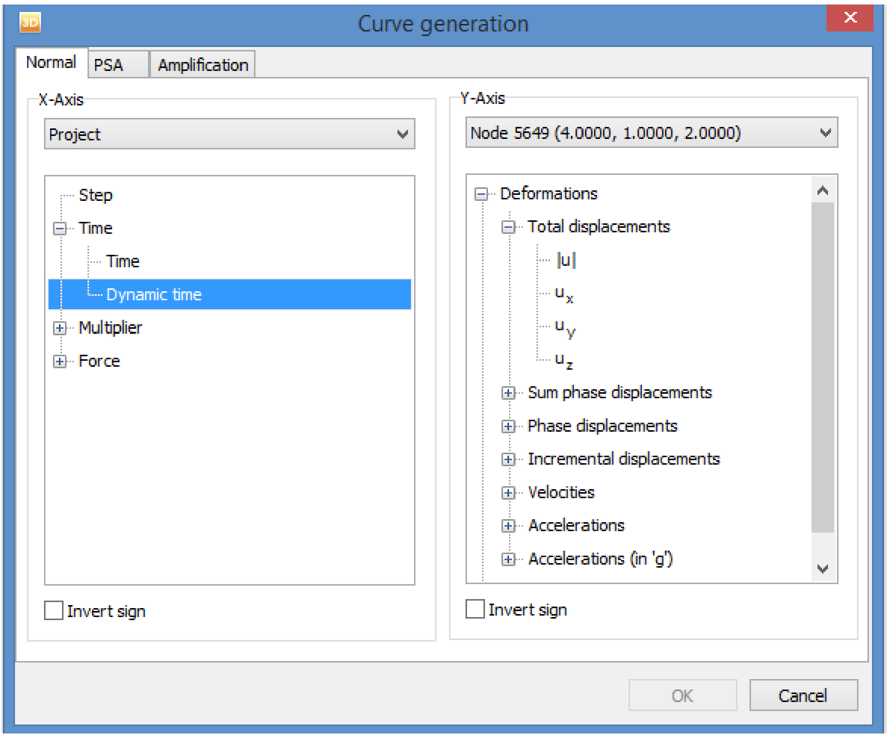

Figure 5.27:curve Generation

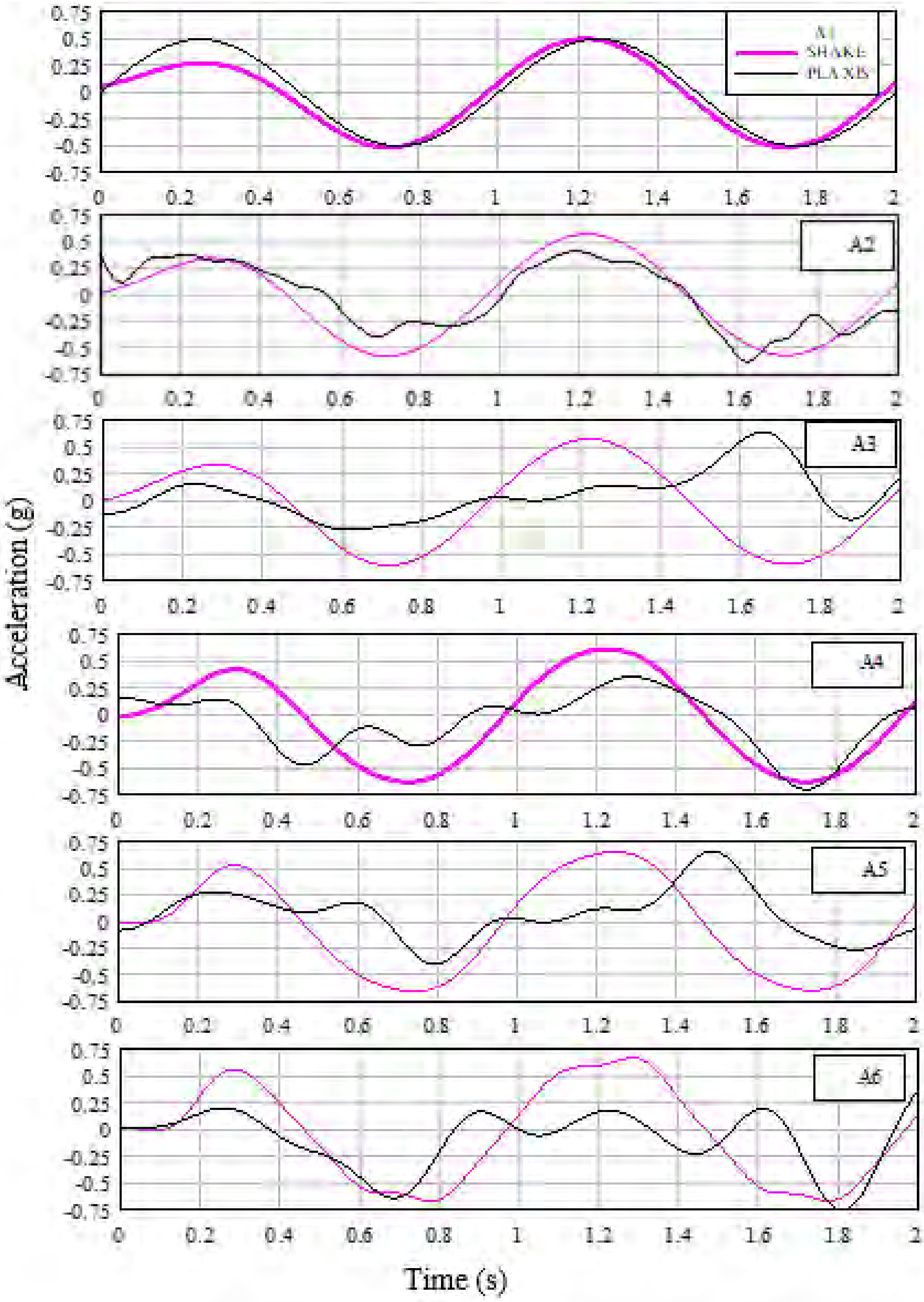

Figure 6.1 (a): Acceleration responses (Model ST1- Frequency 1 Hz, Acceleration-0.05g, Relative density 48% and surcharge 1.72 kPa)

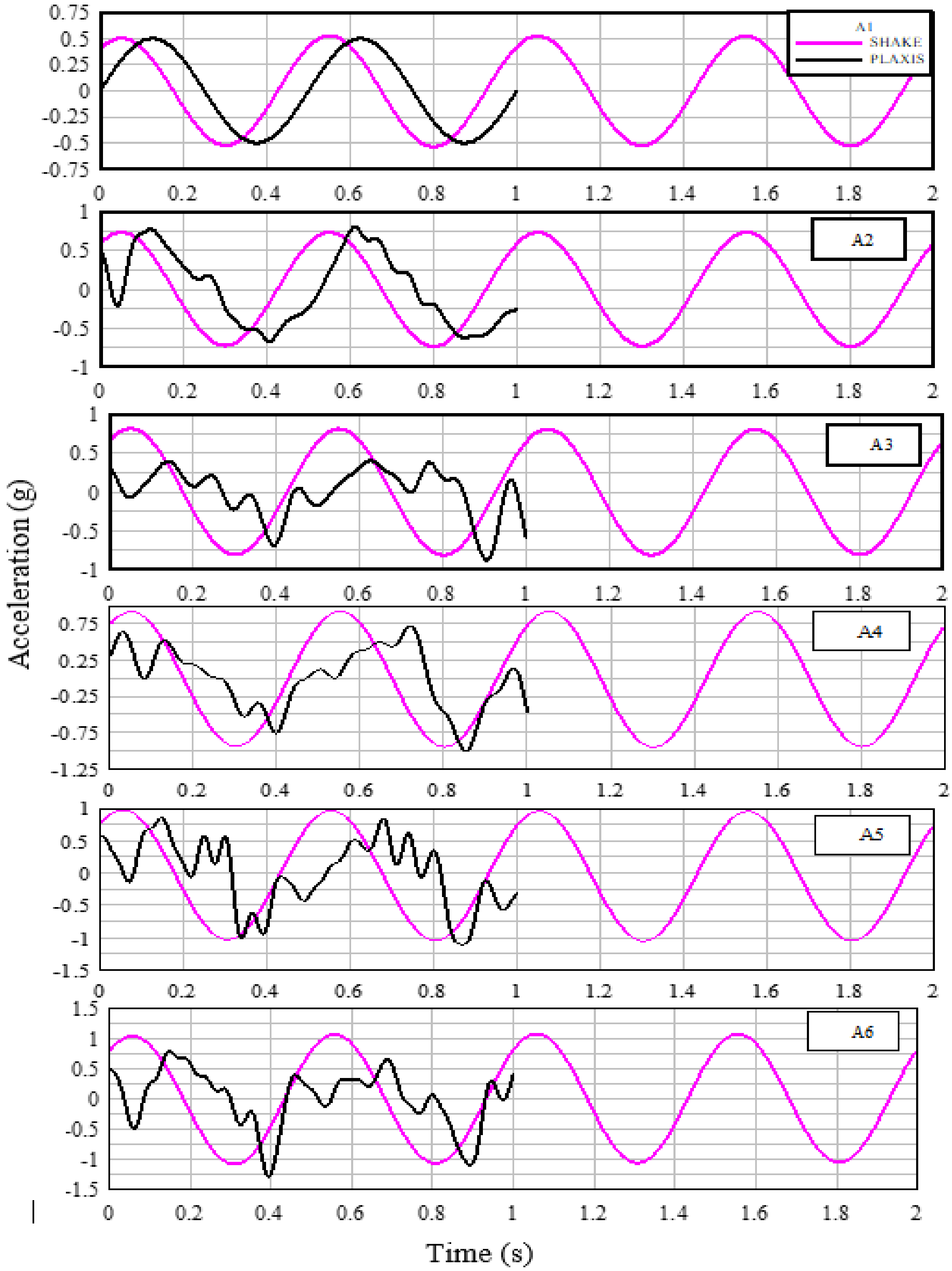

Figure 6.1 (b): Acceleration responses (Model ST2- Frequency 2 Hz, Acceleration- 0.05g, Relative density 48% and surcharge 1.72 kPa)

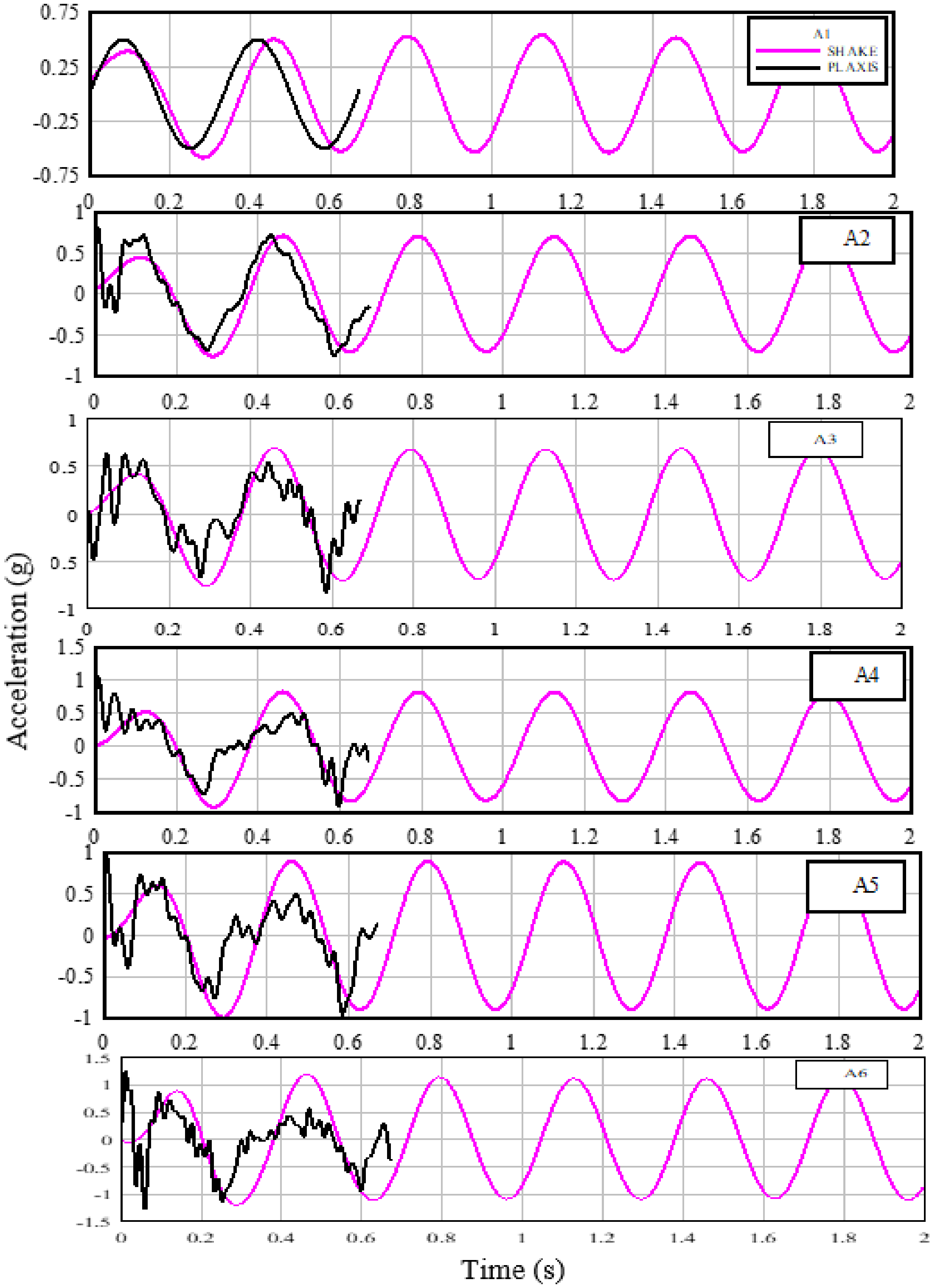

Figure 6.1 (c): Acceleration responses (Model ST3- Frequency 3 Hz, Acceleration-0.05g, Relative density 48% and surcharge 1.72 kPa)

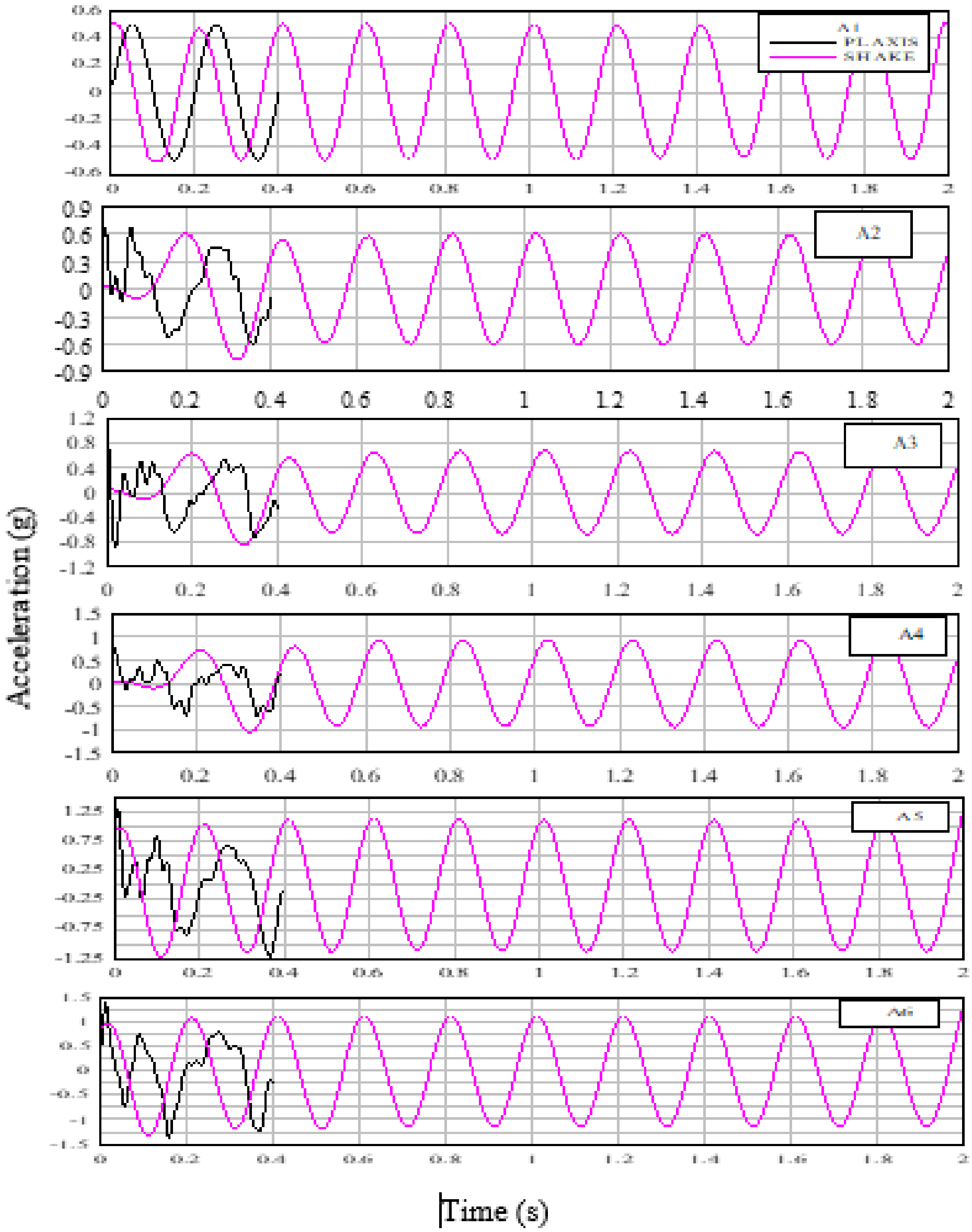

Figure 6.1(d): Acceleration responses (Model ST4- Frequency 5 Hz, Acceleration-0.05g, Relative density 48% and surcharge 1.72 kPa)

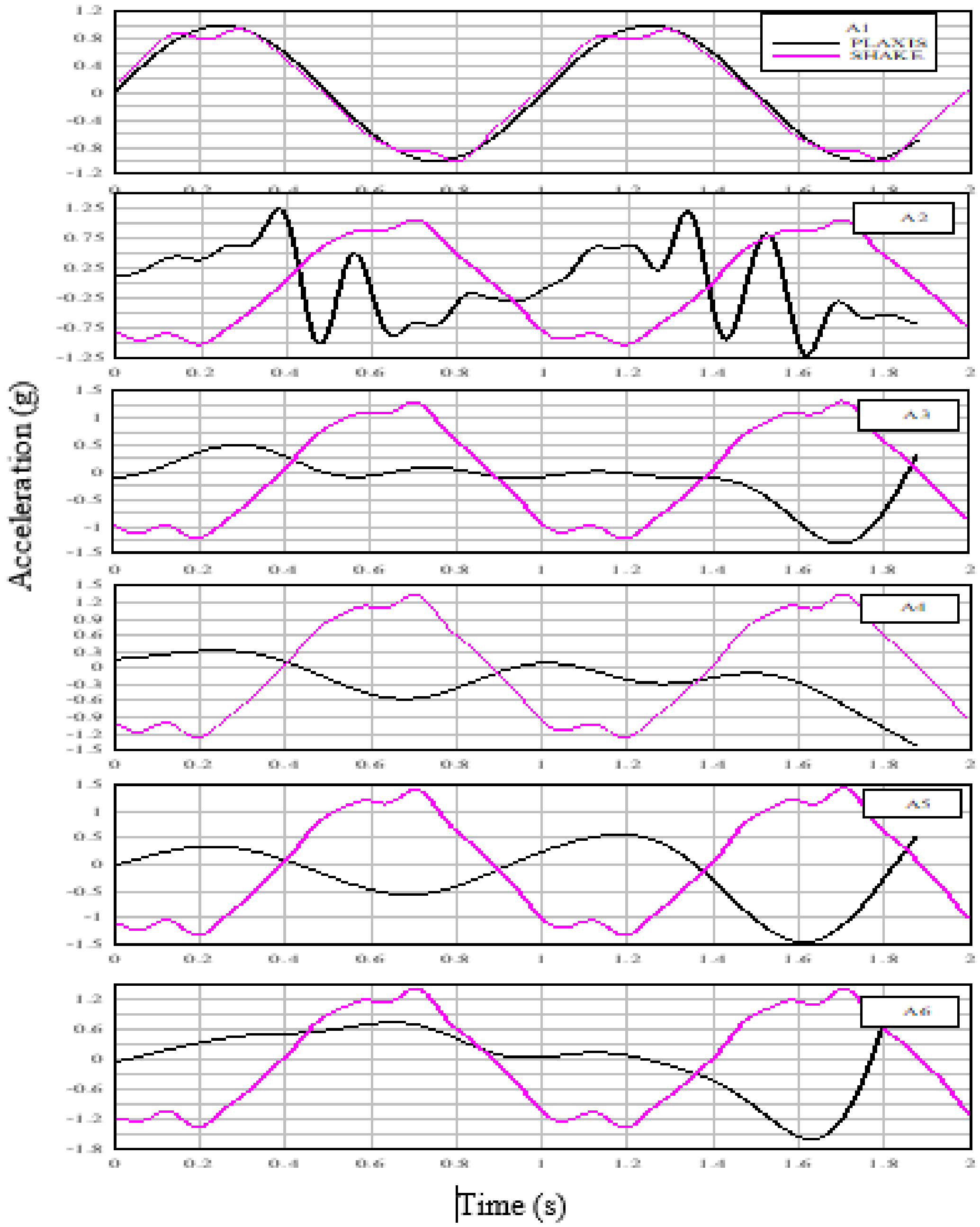

Figure 6.1 (e): Acceleration responses (Model ST9- Frequency 1 Hz, Acceleration- 0.10g, Relative density 48% and surcharge 1.72 kPa)

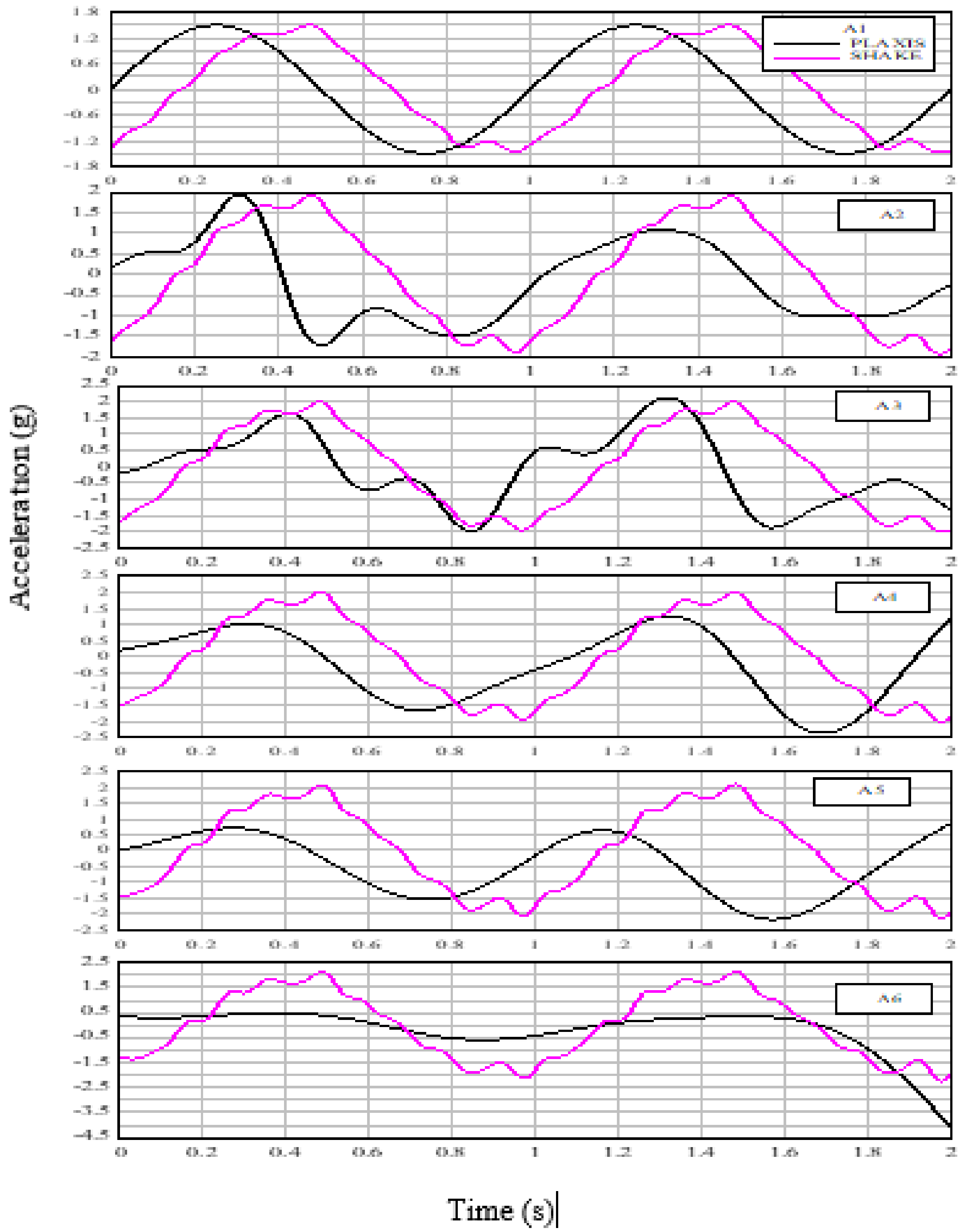

Figure 6.1 (f): Acceleration responses (Model ST19- Frequency 1 Hz, Acceleration- 0.15g, Relative density 48% and surcharge 1.72 kPa)

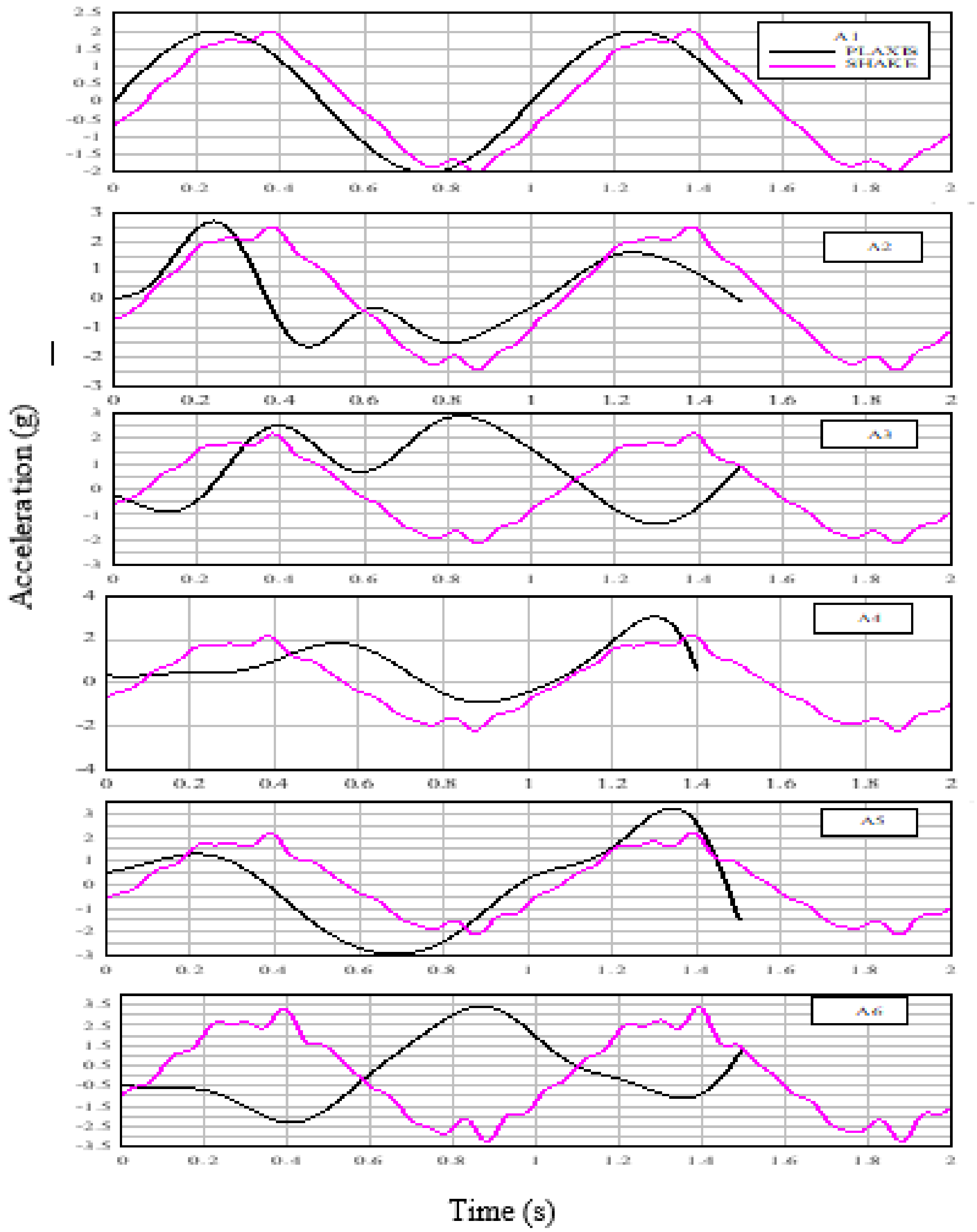

Figure 6.1 (g): Acceleration responses (Model ST27- Frequency 1 Hz, Acceleration- 0.20g, Relative density 48% and surcharge 1.72 kPa)

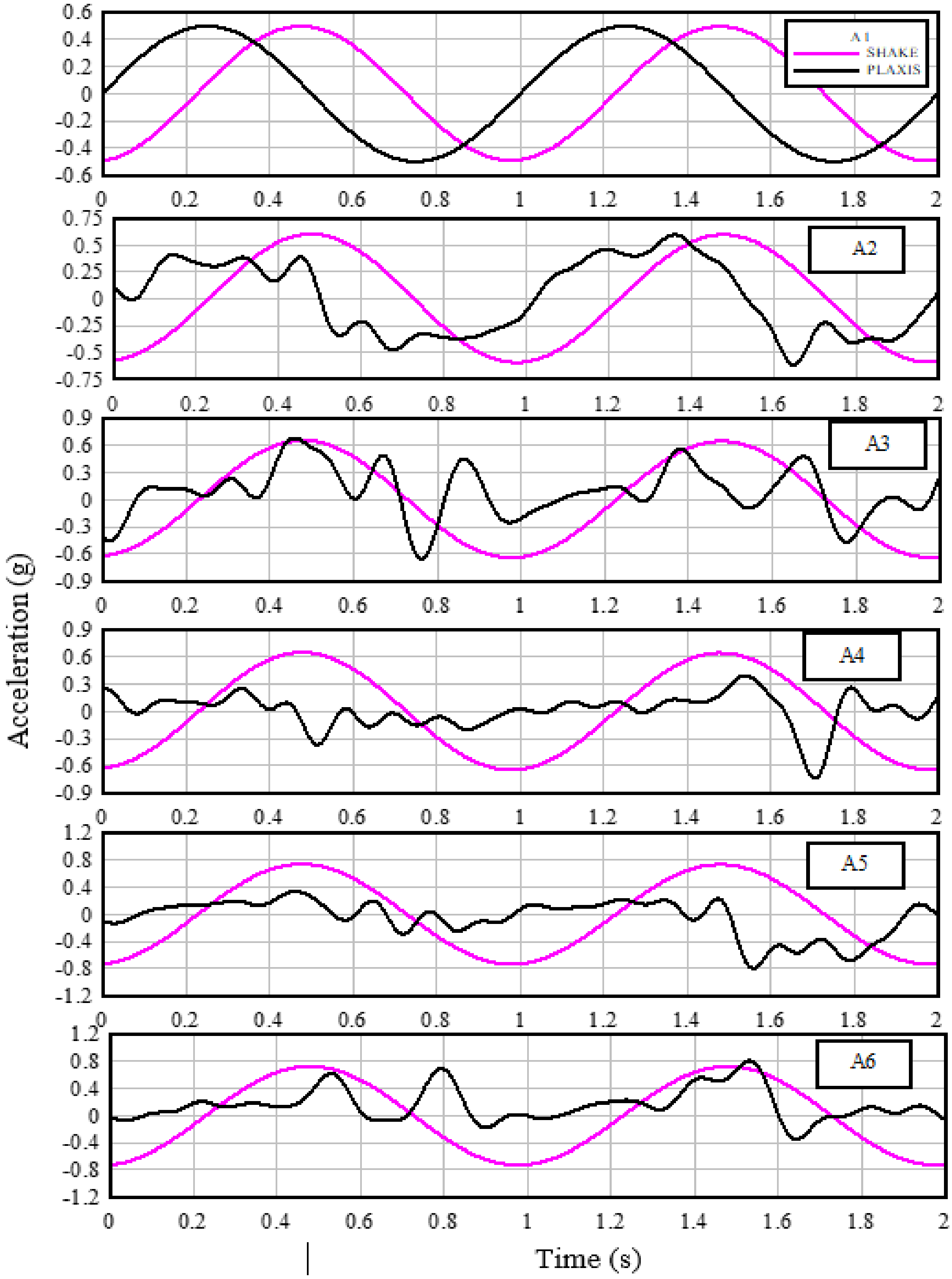

Figure 6.1 (h): Acceleration responses (Model ST35- Frequency 1 Hz, Acceleration- 0.05g, Relative density 48% and surcharge 1.12 kPa)

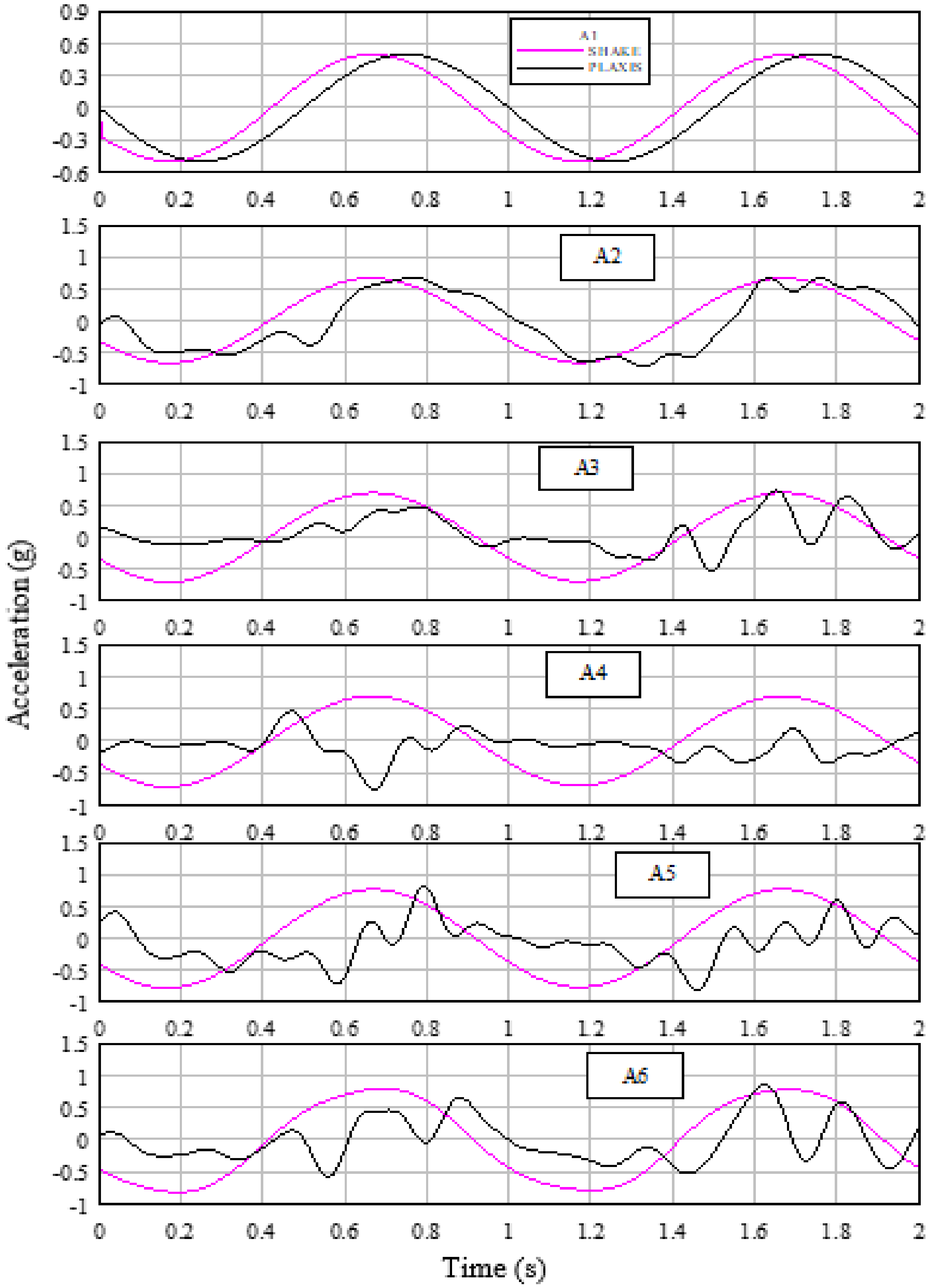

Figure 6.1 (i): Acceleration responses (Model ST67- Frequency 1 Hz, Acceleration- 0.05g, Relative density 48% and surcharge 0.70 kPa)

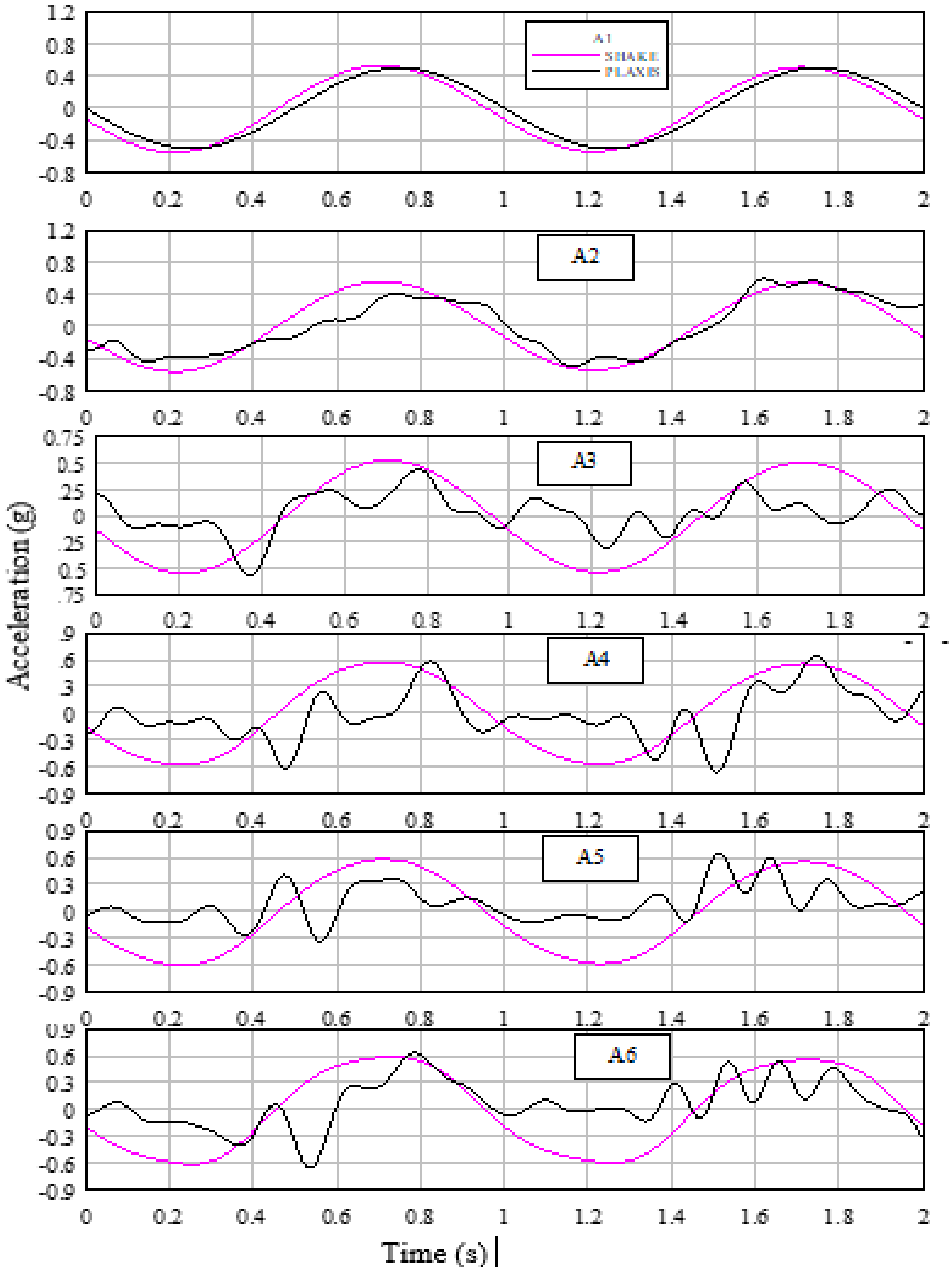

Figure 6.1(j): Acceleration responses (Model ST99- Frequency 1 Hz, Acceleration- 0.05g, Relative density 64% and surcharge 1.72 kPa)

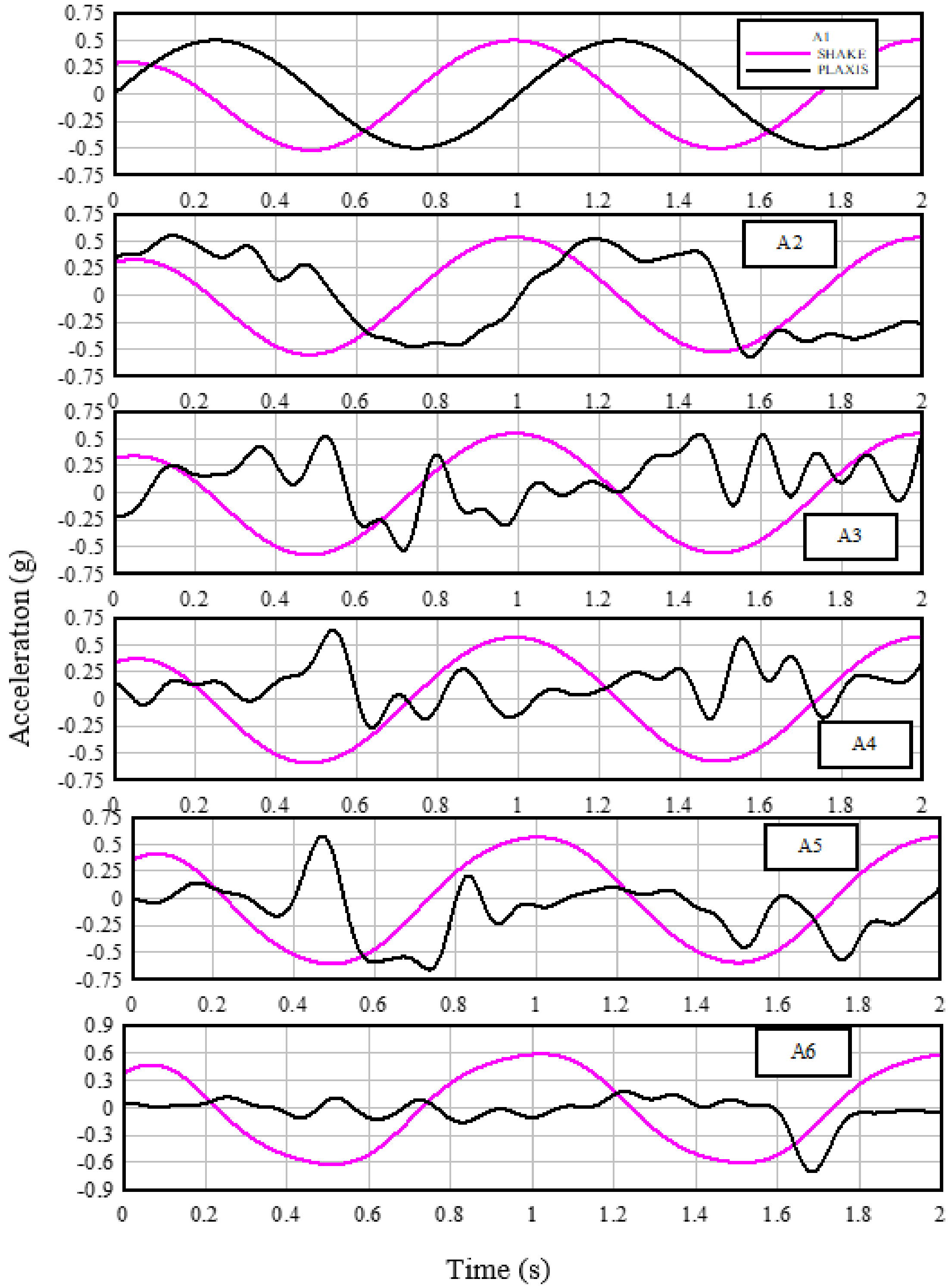

Figure 6.1(k): Acceleration responses (Model ST193- Frequency 1 Hz, Acceleration-0.05g, Relative density 80% and surcharge 1.72 kPa)

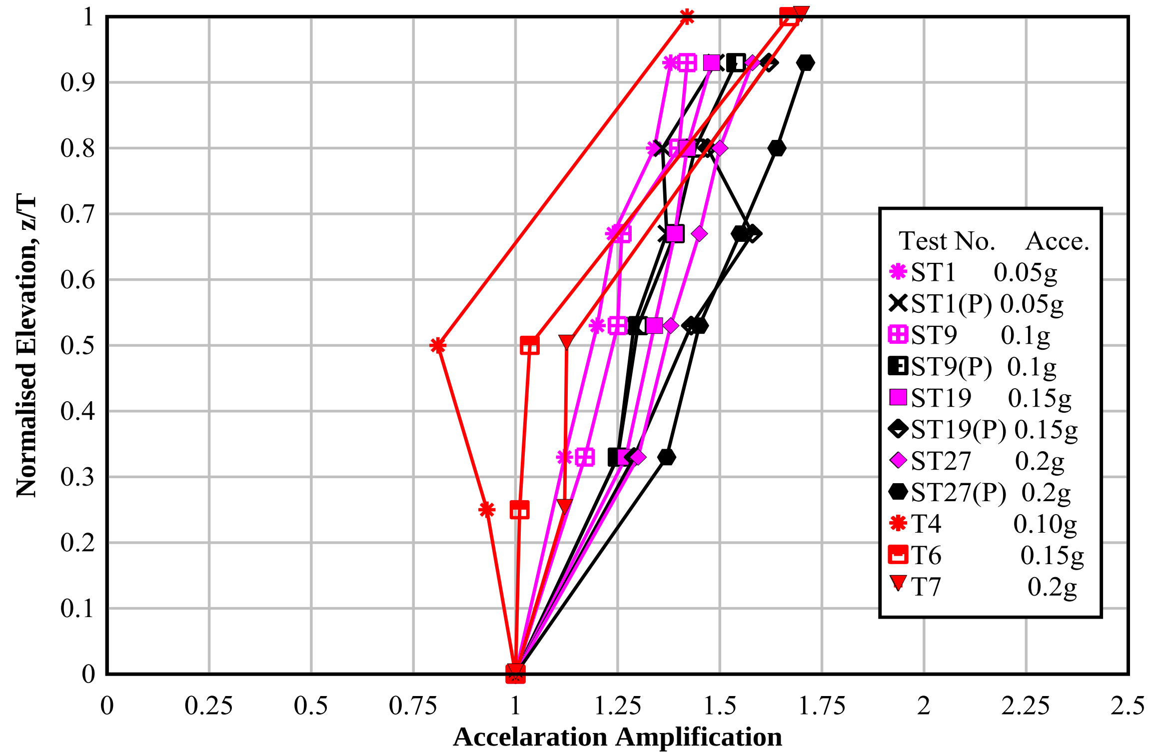

Figure 6.2: Effect of base acceleration on acceleration amplification(ST1, 9, 19 and 27) aa.grf

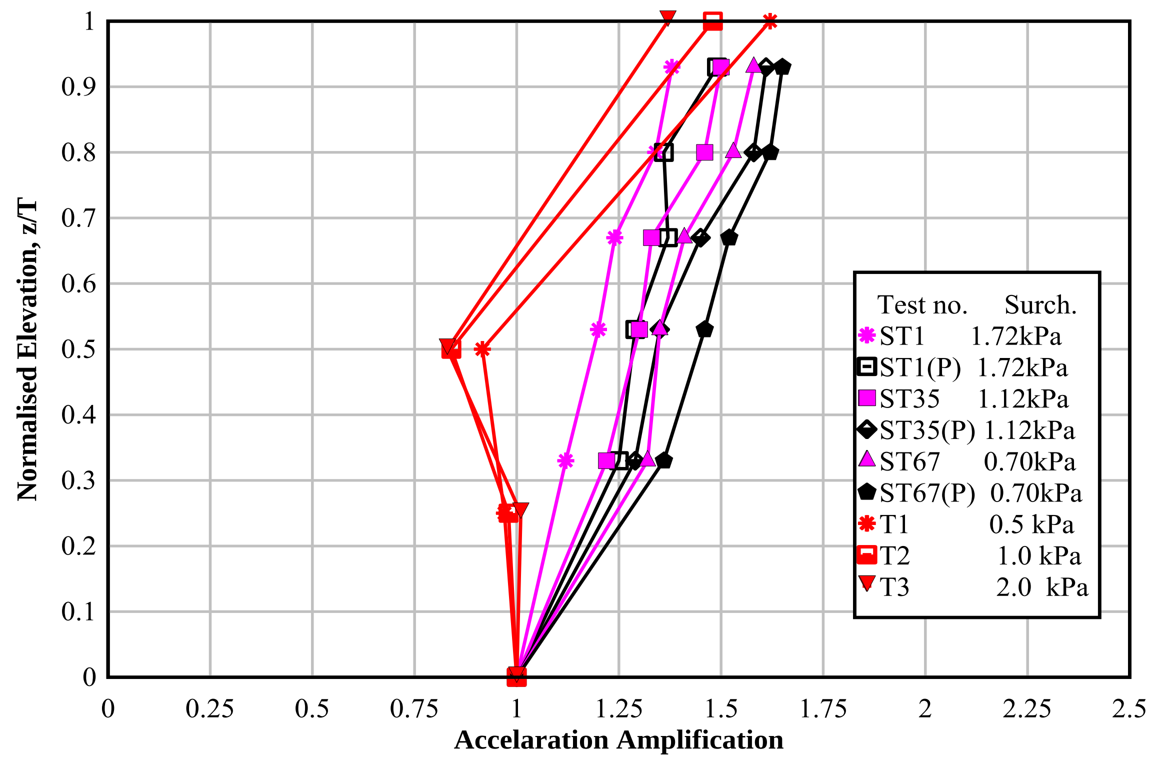

surch.grf

Figure 6.3: Effect of surcharge on acceleration amplification (ST1, 35 and 67)

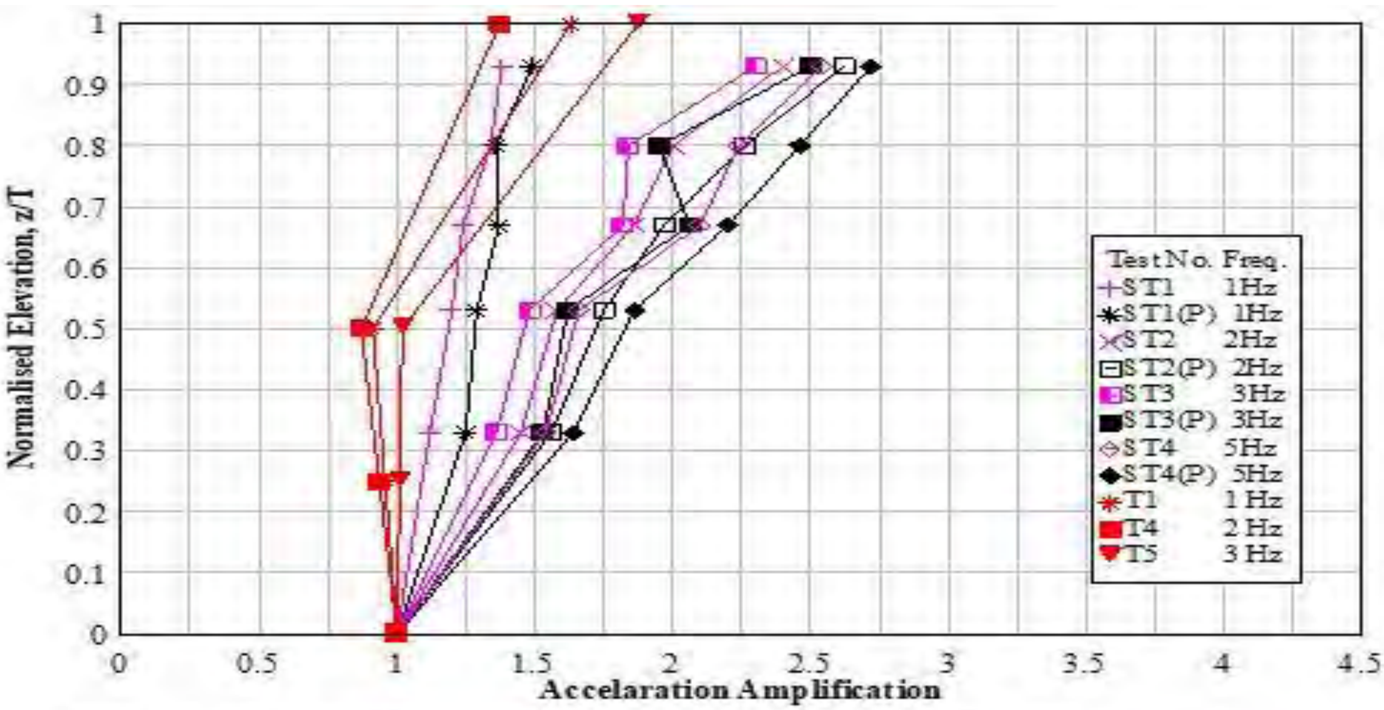

Figure 6.4: Effect of frequency on acceleration amplification (ST1-ST4)

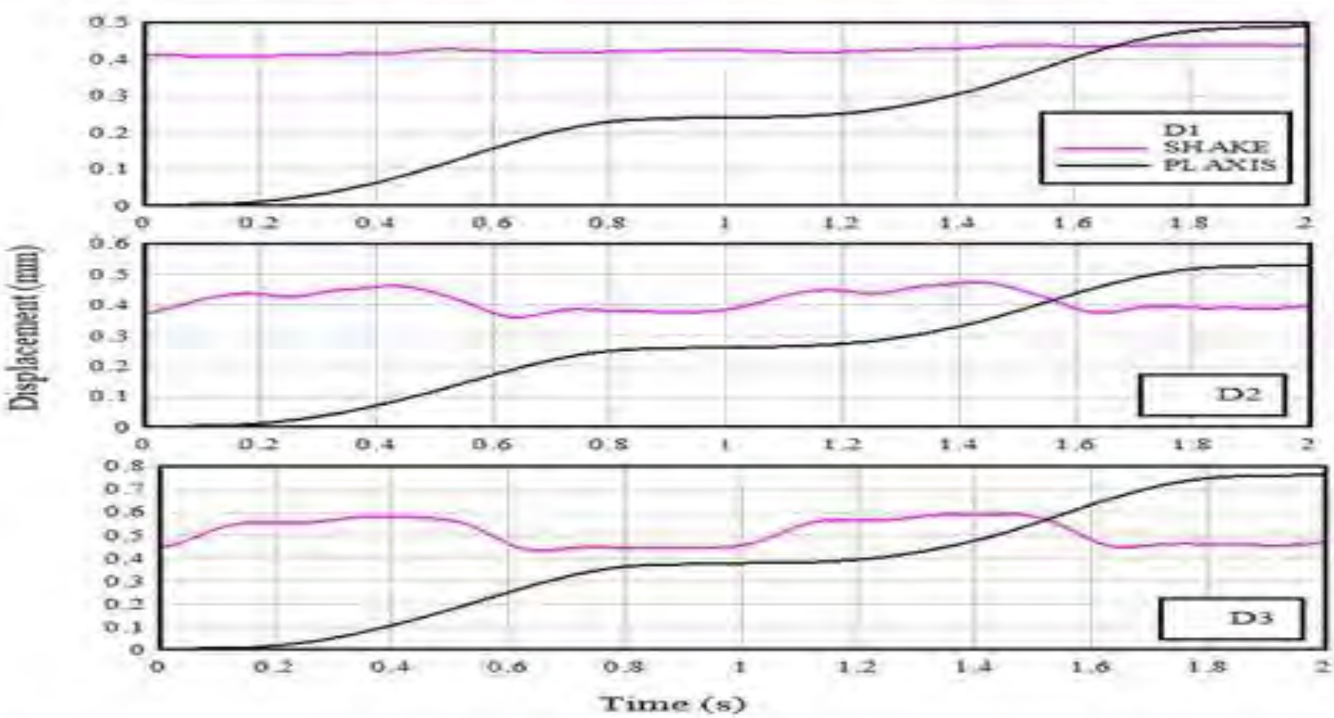

Figure 6.5 (a): Displacement response (Model ST1-Frequency 1 Hz, Acceleration- 0.05g, Relative density 48% and surcharge 1.72 kPa)

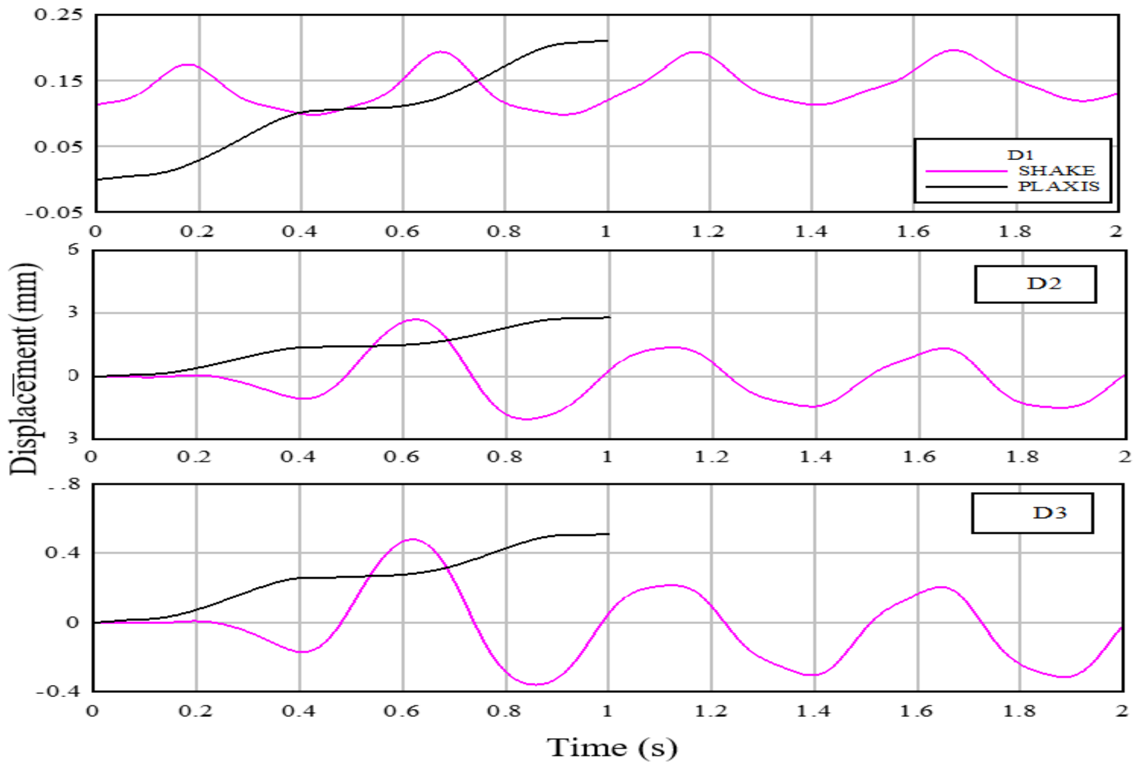

Figure 6.5 (b): Displacement response (Model ST2-Frequency 2 Hz, Acceleration- 0.05g, Relative density 48% and surcharge 1.72 kPa)

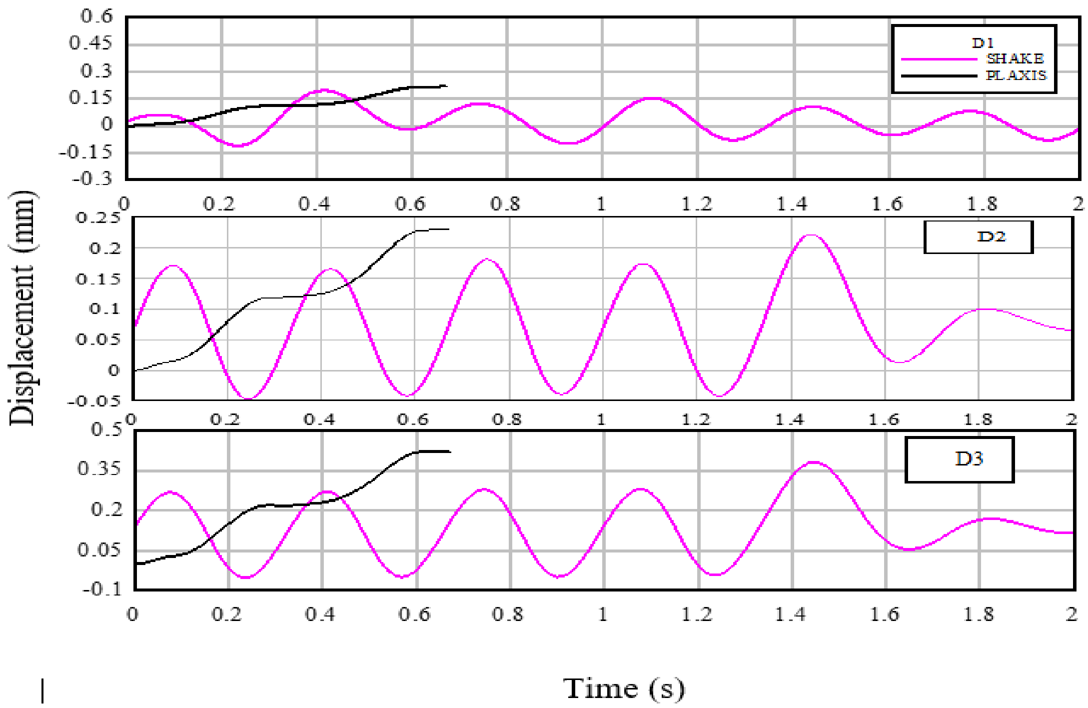

Figure 6.5 (c): Displacement response (Model ST3-Frequency 3 Hz, Acceleration- 0.05g, Relative density 48% and surcharge 1.72 kPa)

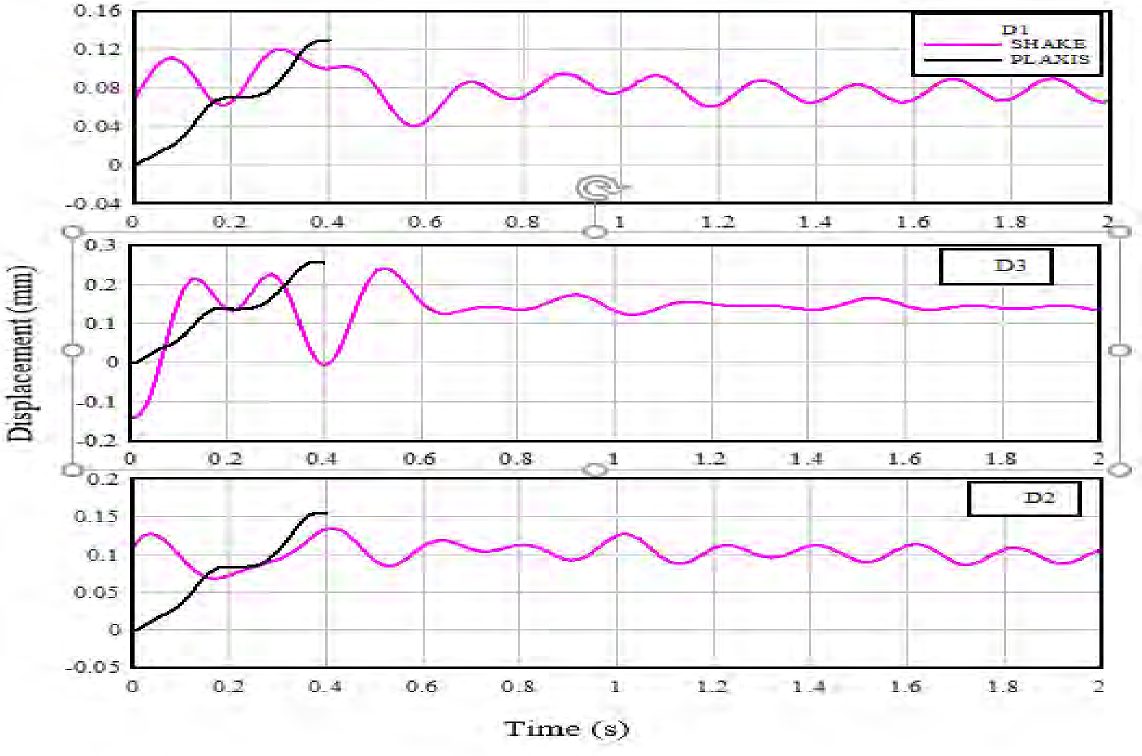

Figure 6.5 (d): Displacement response (Model ST4-Frequency 5 Hz, Acceleration- 0.05g, Relative density 48% and surcharge 1.72 kPa)

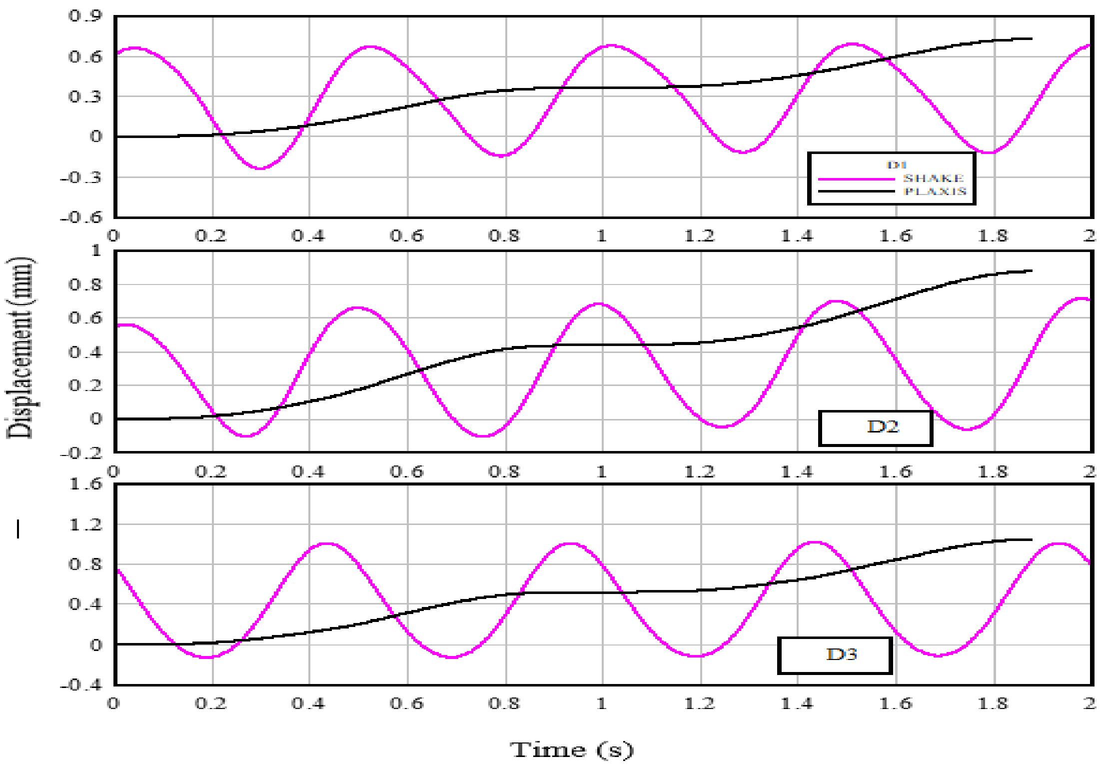

Figure 6.5 (e): Displacement response (Model ST9-Frequency 1 Hz, Acceleration- 0.10g, Relative density 48% and surcharge 1.72 kPa)

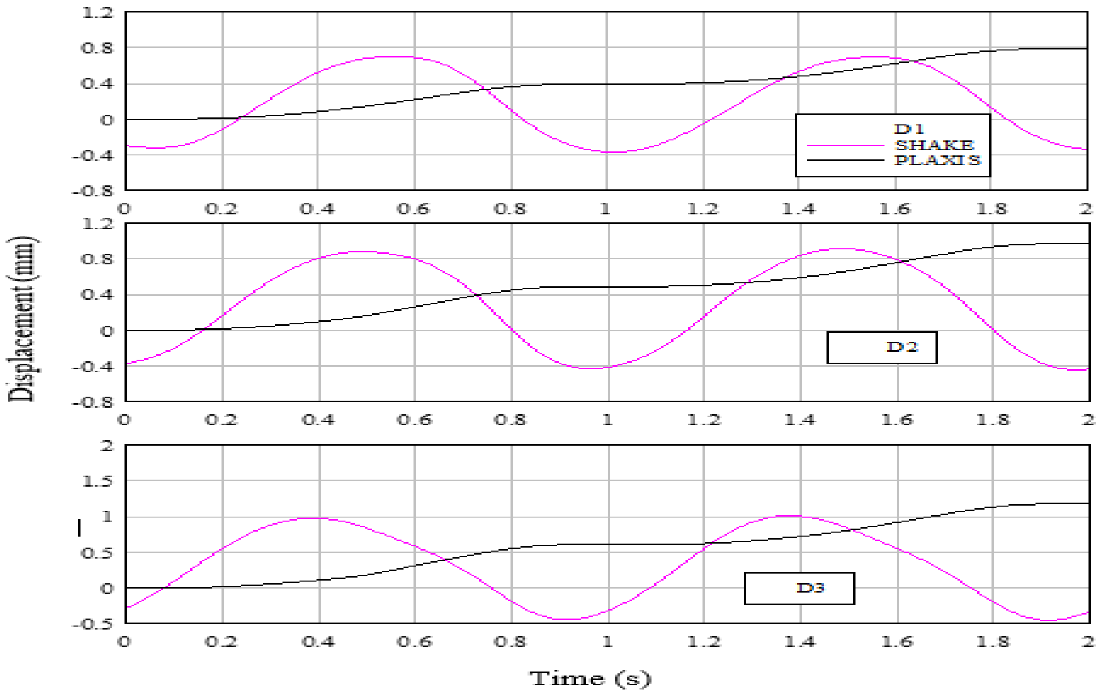

Figure 6.5 (f): Displacement response (Model ST19-Frequency 1 Hz, Acceleration- 0.15g, Relative density 48% and surcharge 1.72 kPa)

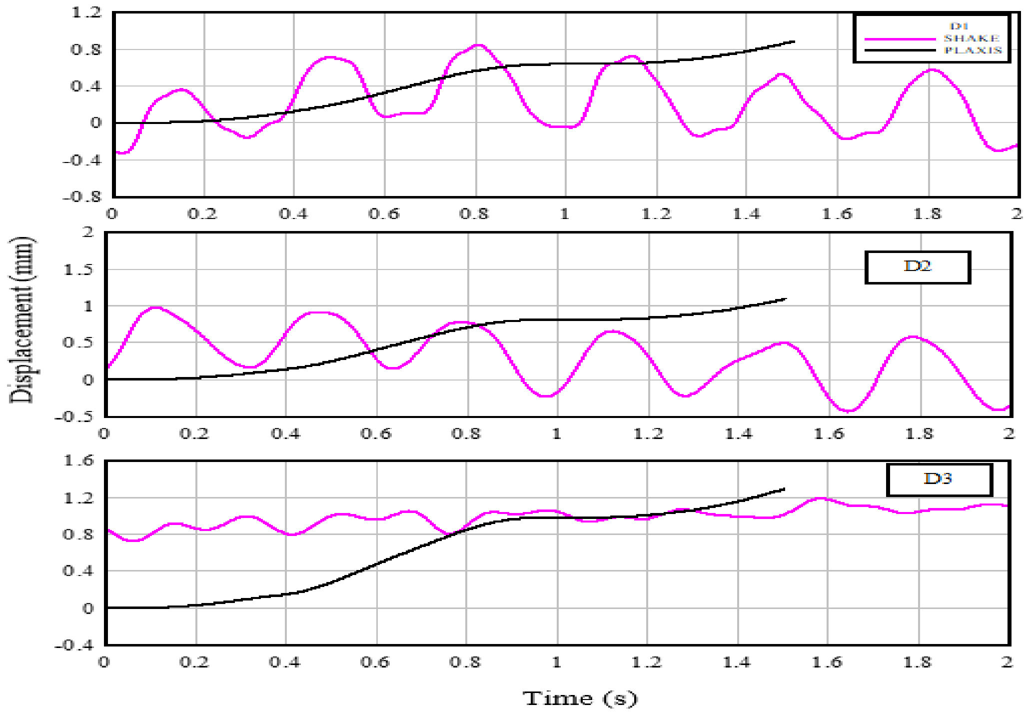

Figure 6.5 (g): Displacement response (Model ST27-Frequency 1 Hz, Acceleration- 0.20g, Relative density 48% and surcharge 1.72 kPa)

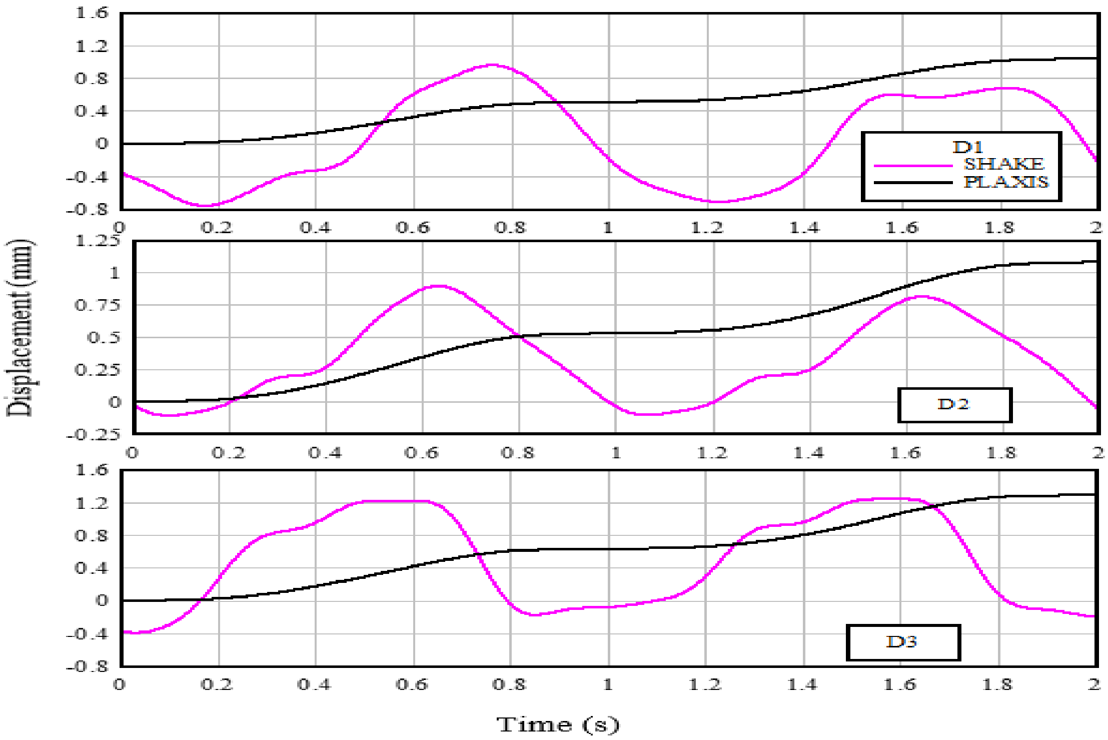

Figure 6.5 (h): Displacement response (Model ST35-Frequency 1 Hz, Acceleration- 0.05g, Relative density 48% and surcharge 1.12 kPa)

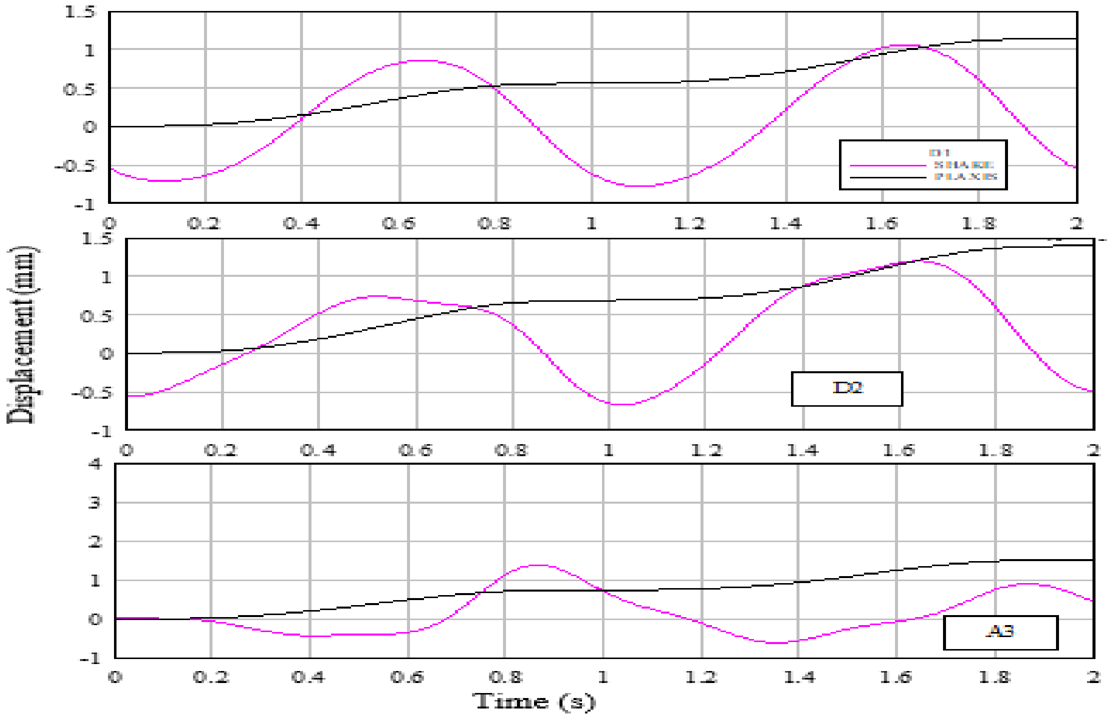

Figure 6.5 (i): Displacement response (Model ST67-Frequency 1 Hz, Acceleration- 0.05g, Relative density 48% and surcharge 0.70 kPa)

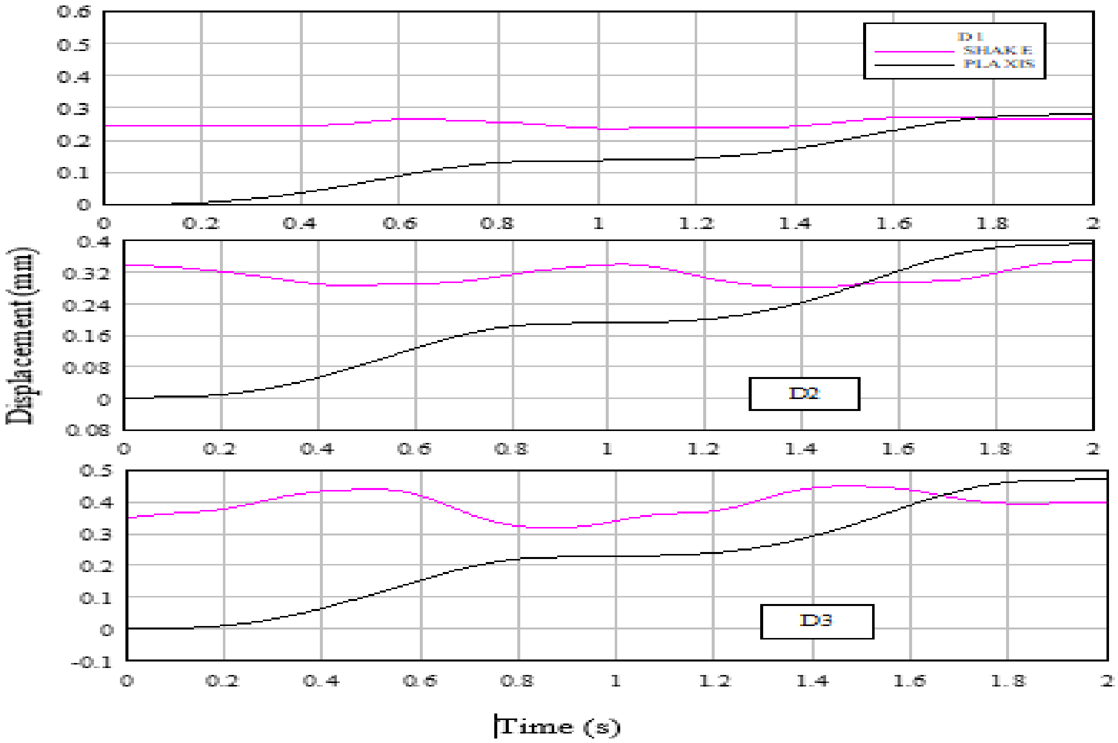

Figure 6.5 (j): Displacement response (Model ST99-Frequency 1 Hz, Acceleration- 0.05g, Relative density 64% and surcharge 1.72 kPa)

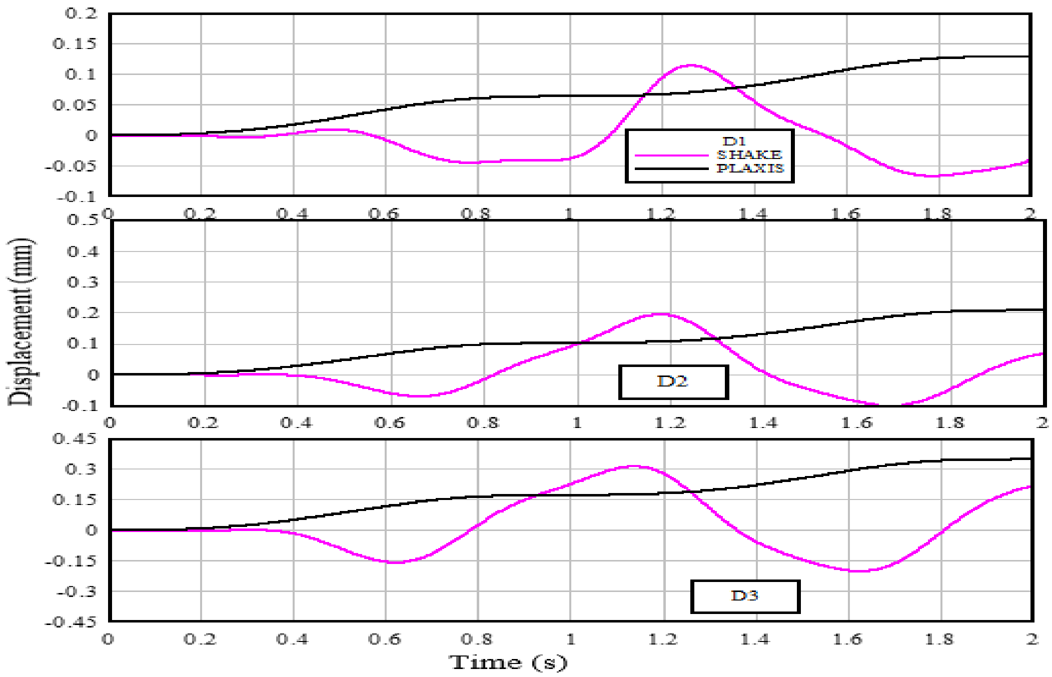

Figure 6.5 (k): Displacement response (Model ST193-Frequency 1 Hz, Acceleration- 0.05g, Relative density 80% and surcharge 1.72 kPa)

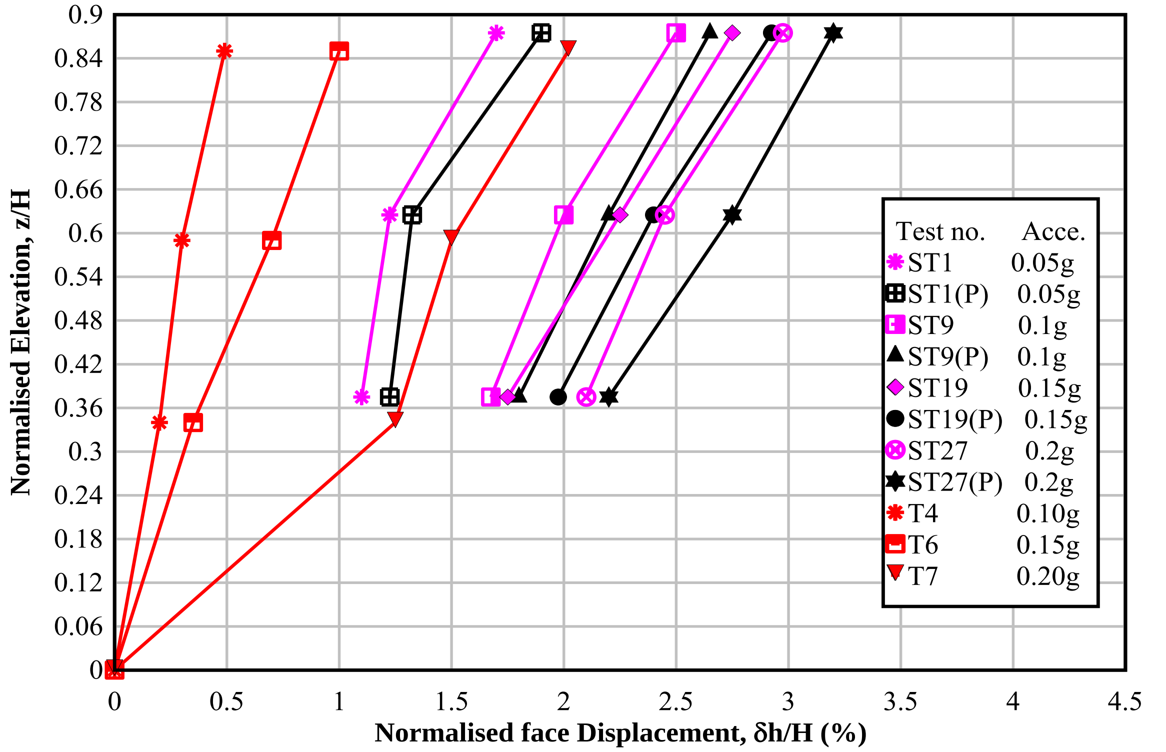

Figure 6.6:Effect of base acceleration on displacement profile (ST1, 9, 19 and 27)

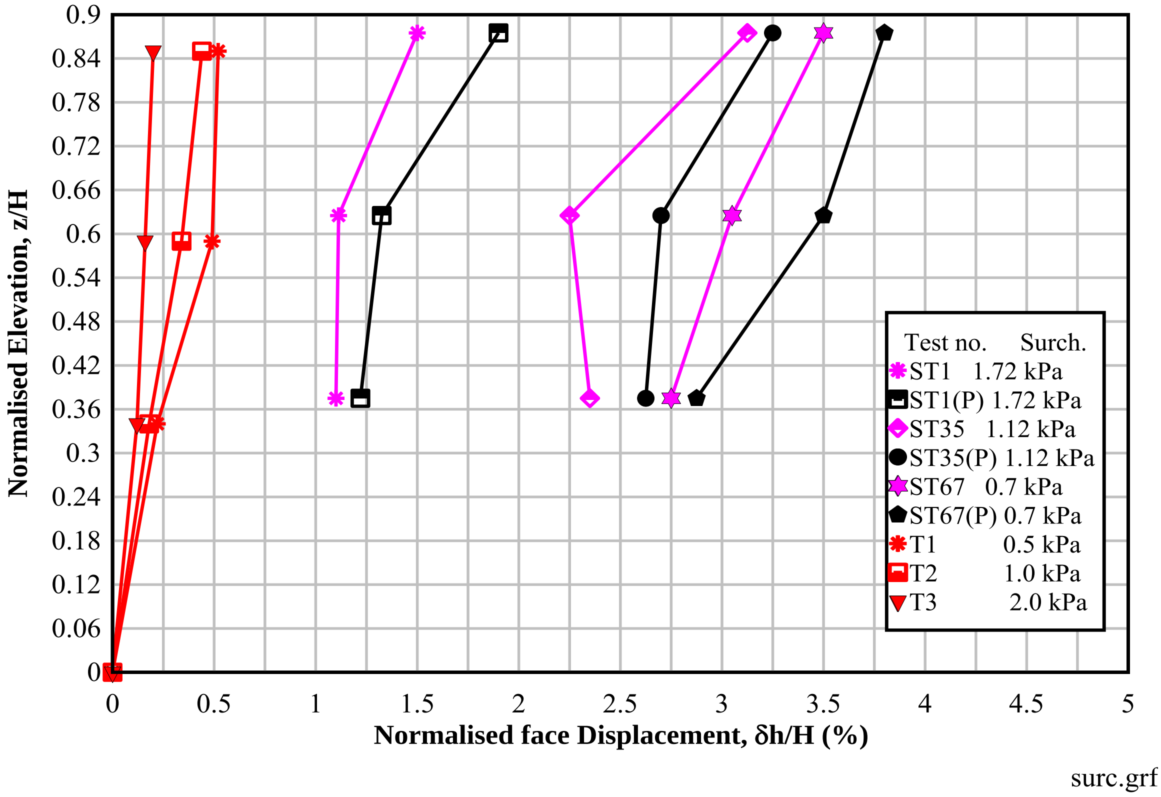

Figure 6.7: Effect of surcharge on displacement profile (ST1, 35 and 67)

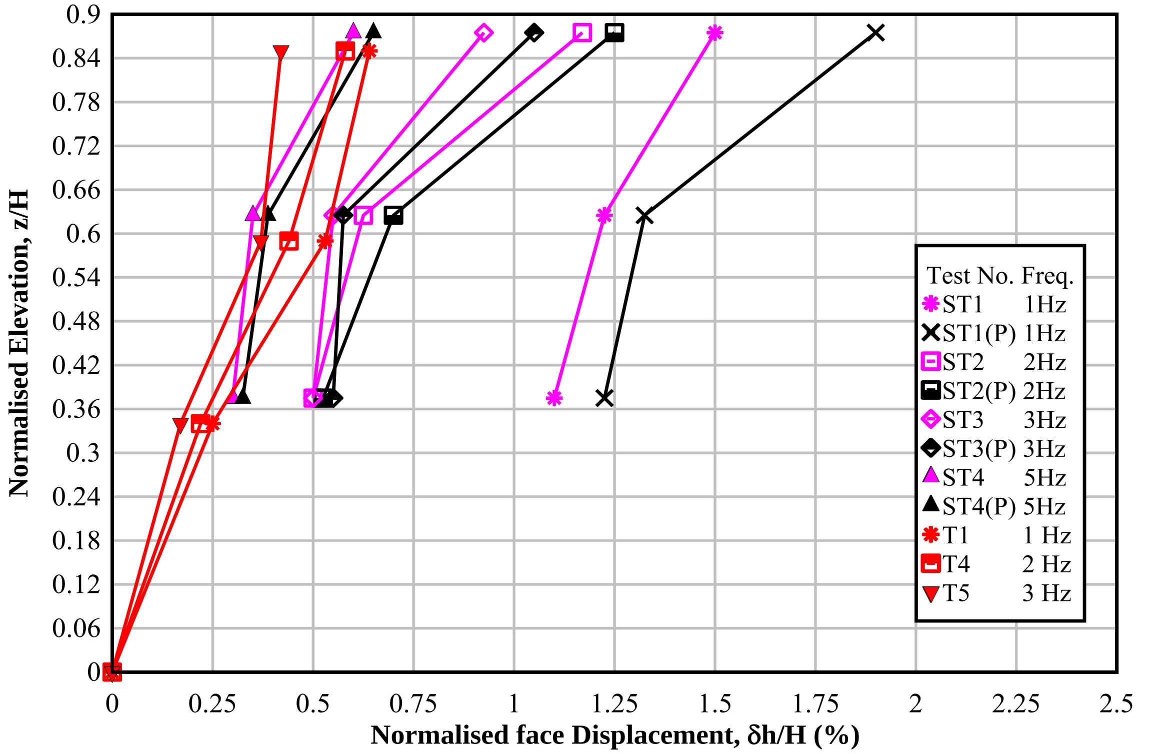

Figure 6.8: Effect of frequency on displacement profile (ST1-ST4)

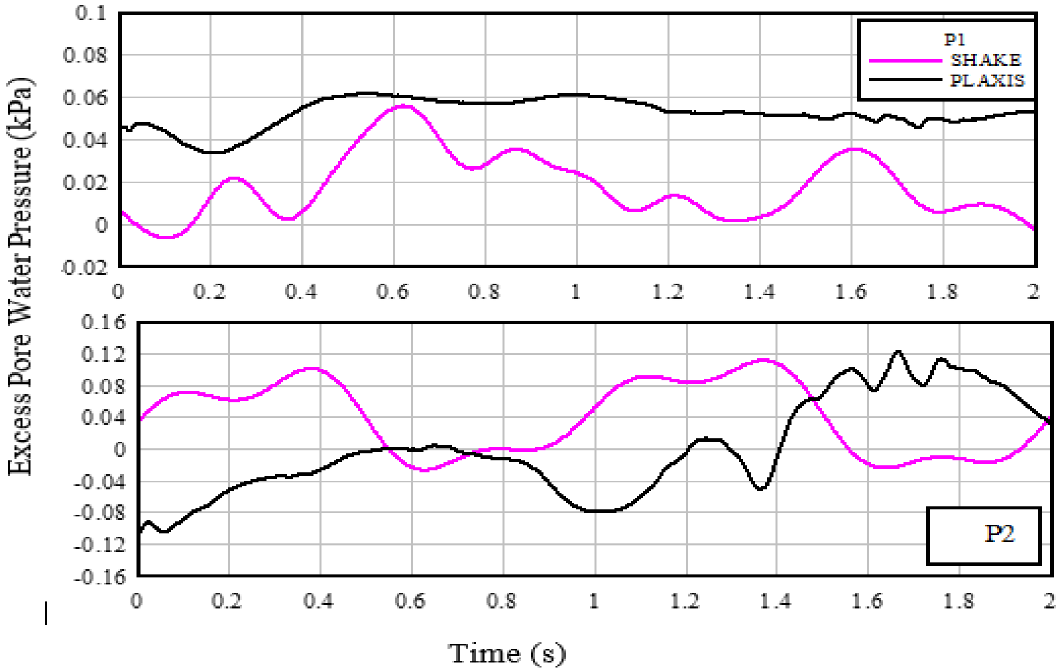

Figure 6.9 (a): Excess Pore water Pressure response (Model ST1-Frequency 1 Hz, Acceleration- 0.05g, Relative density 48% and surcharge 1.72 kPa)

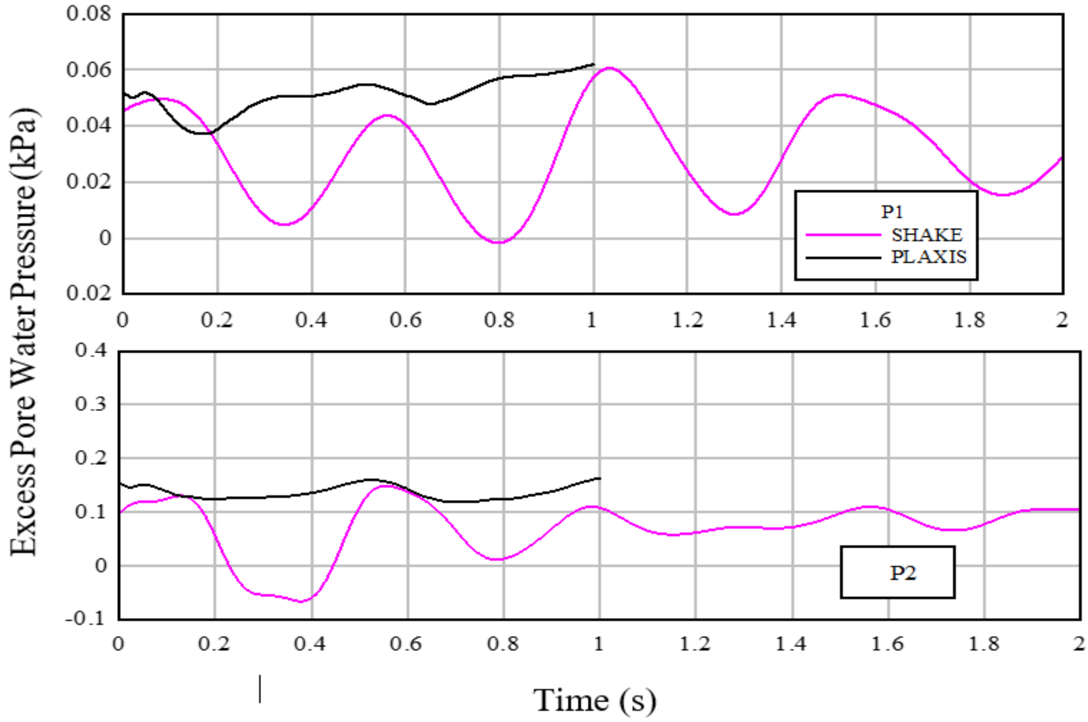

Figure 6.9 (b): Excess Pore water Pressure response (Model ST2-Frequency 2 Hz, Acceleration- 0.05g, Relative density 48% and surcharge 1.72 kPa

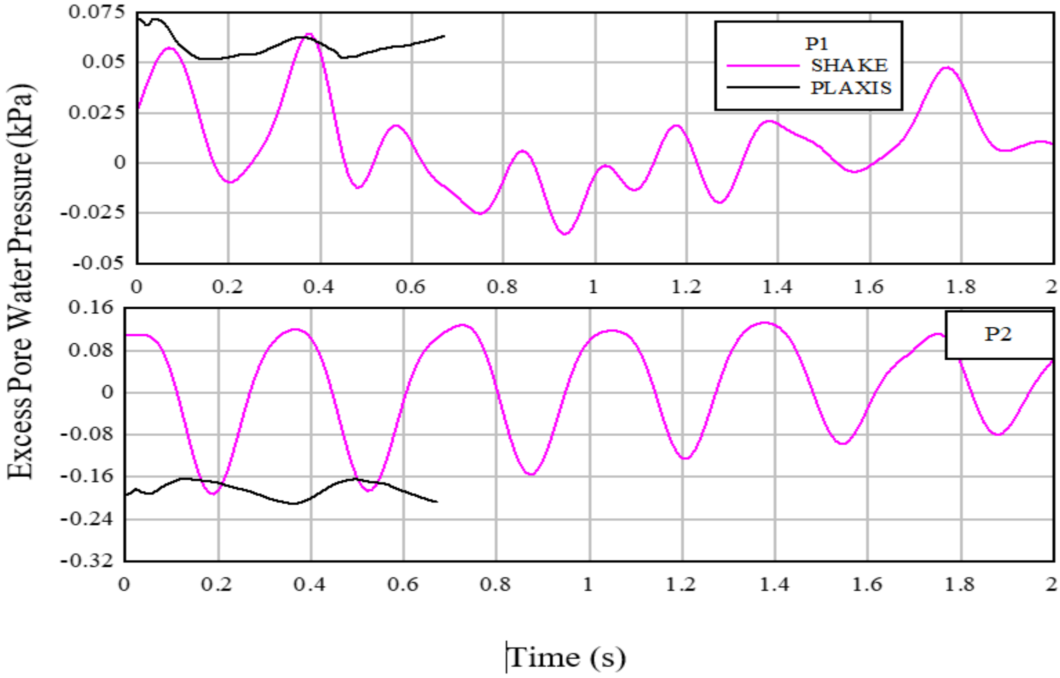

Figure 6.9 (c): Excess Pore water Pressure response (Model ST3-Frequency 3 Hz, Acceleration- 0.05g, Relative density 48% and surcharge 1.72 kPa)

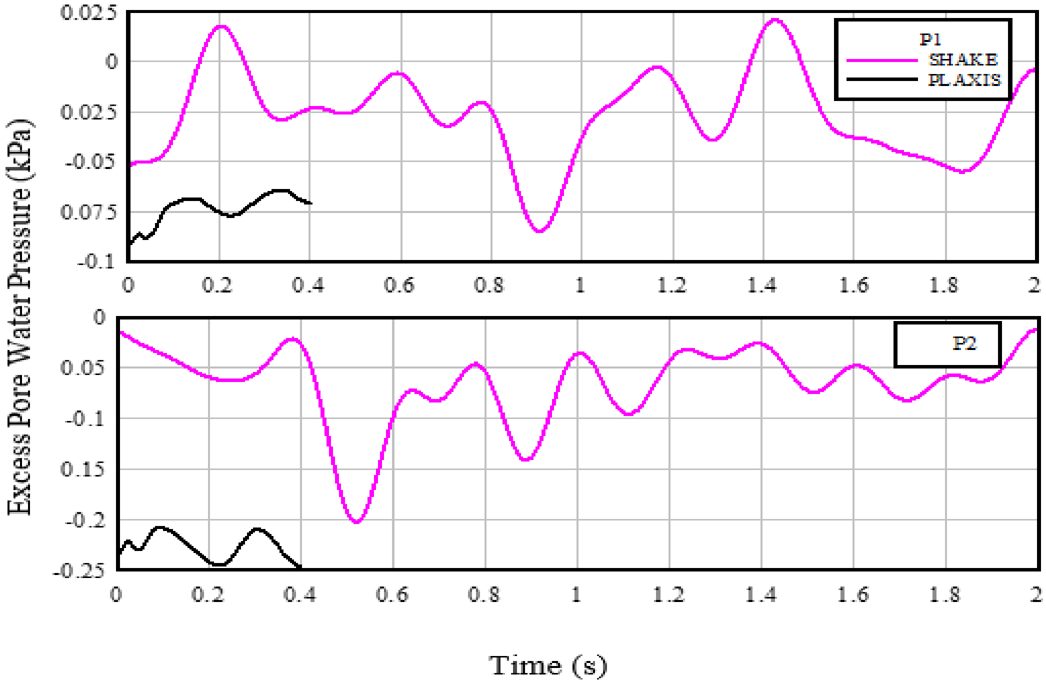

Figure 6.9 (d): Excess Pore water Pressure response (Model ST4-Frequency 5 Hz, Acceleration- 0.05g, Relative density 48% and surcharge 1.72 kPa)

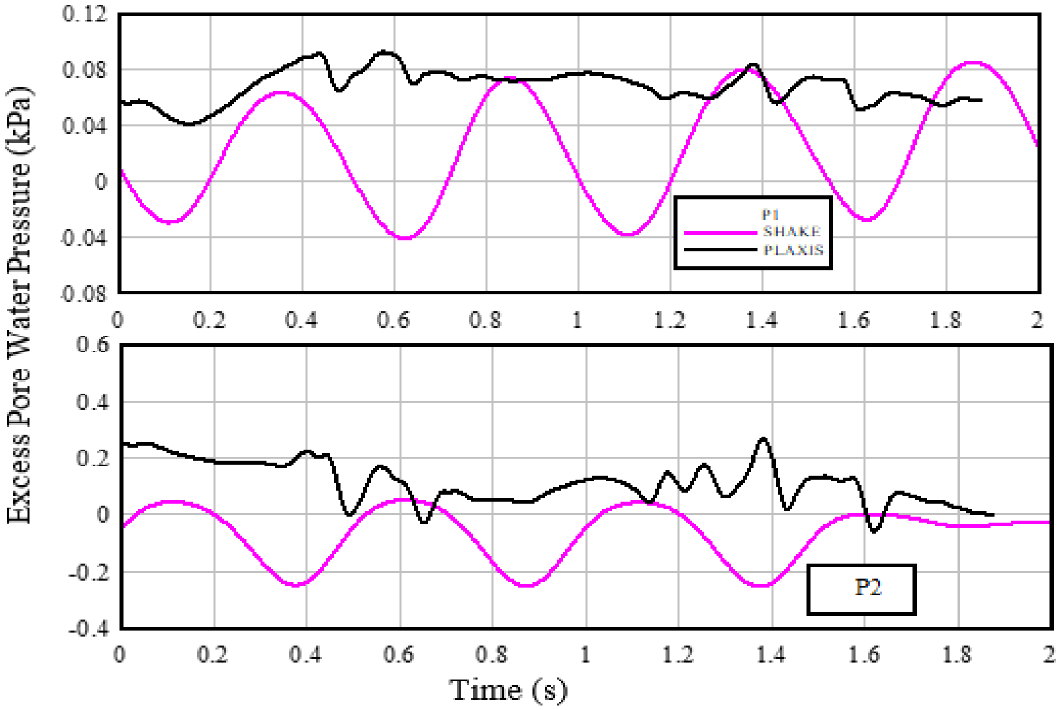

Figure 6.9 (e): Excess Pore water Pressure response (Model ST9-Frequency 1 Hz, Acceleration- 0.10g, Relative density 48% and surcharge 1.72 kPa)

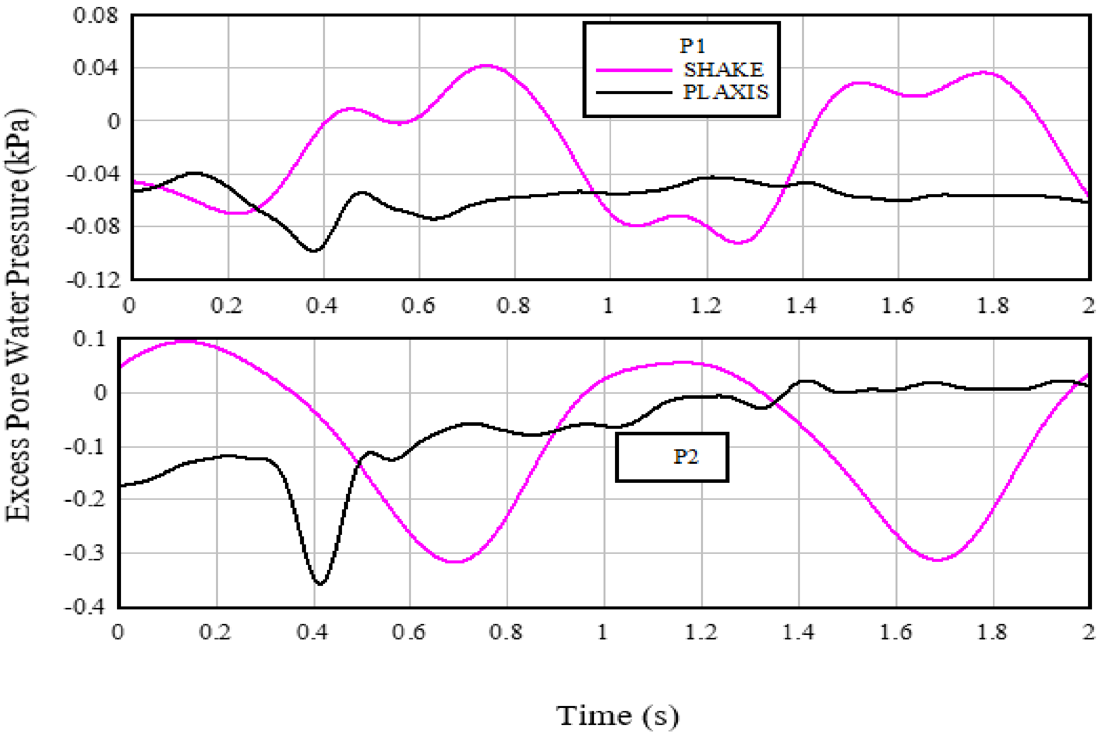

Figure 6.9 (f): Excess Pore water Pressure response (Model ST19-Frequency 1 Hz, Acceleration- 0.15g, Relative density 48% and surcharge 1.72 kPa)

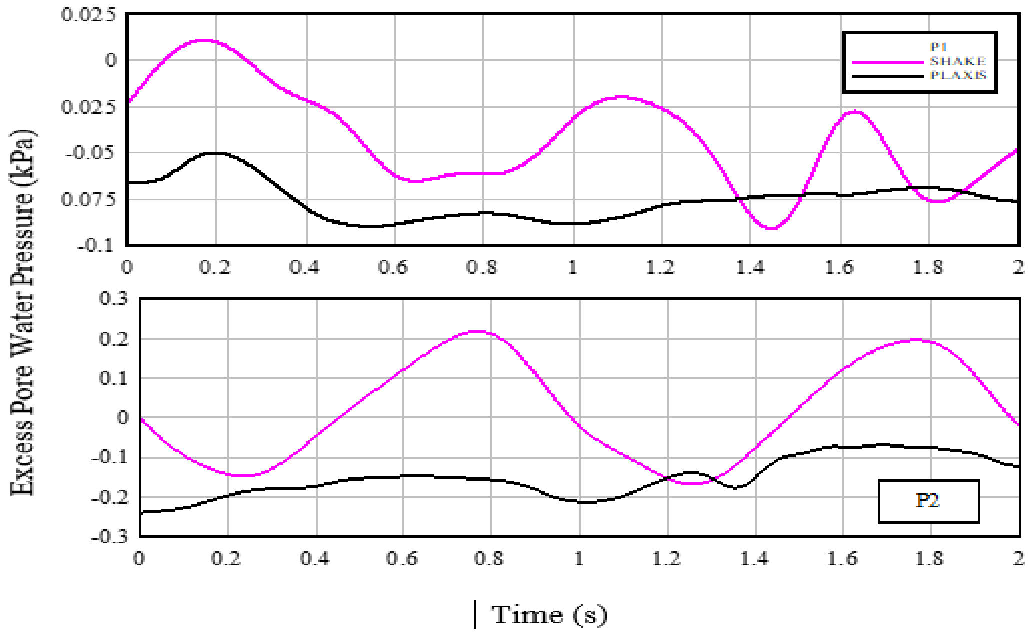

Figure 6.9 (g): Excess Pore water Pressure response (Model ST27-Frequency 1 Hz, Acceleration- 0.20g, Relative density 48% and surcharge 1.72 kPa)

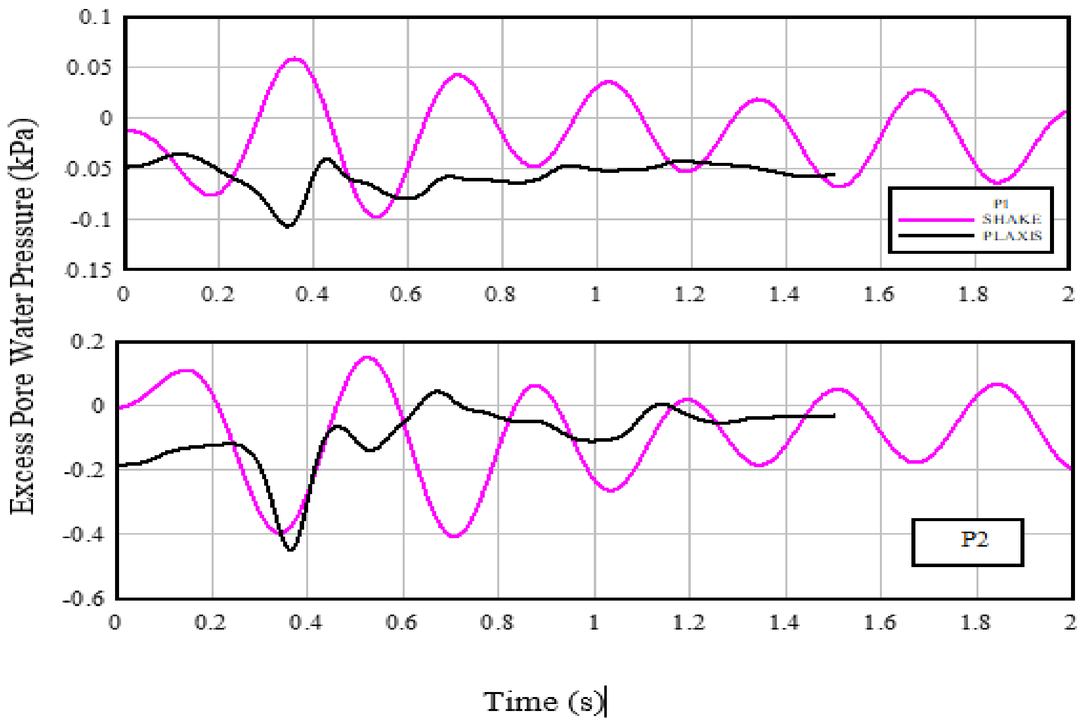

Figure 6.9 (h): Excess Pore water Pressure response (Model ST35-Frequency 1 Hz, Acceleration- 0.05g, Relative density 48% and surcharge 1.12 kPa)

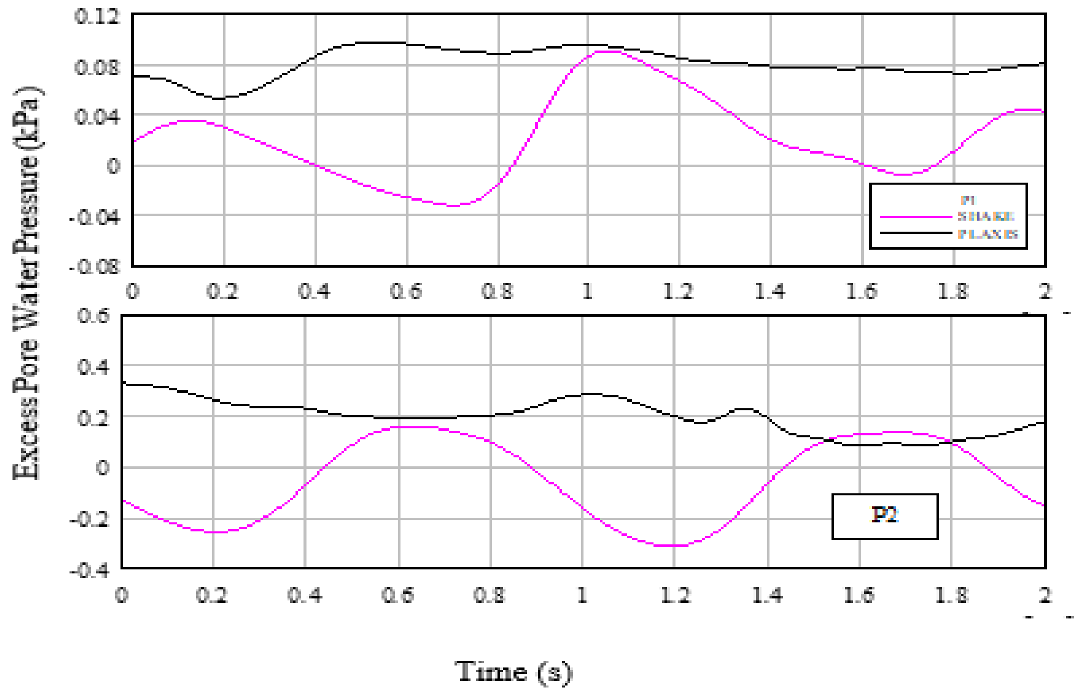

Figure 6.9 (i): Excess Pore water Pressure response (Model ST67-Frequency 1 Hz, Acceleration- 0.05g, Relative density 48% and surcharge 0.70 kPa)

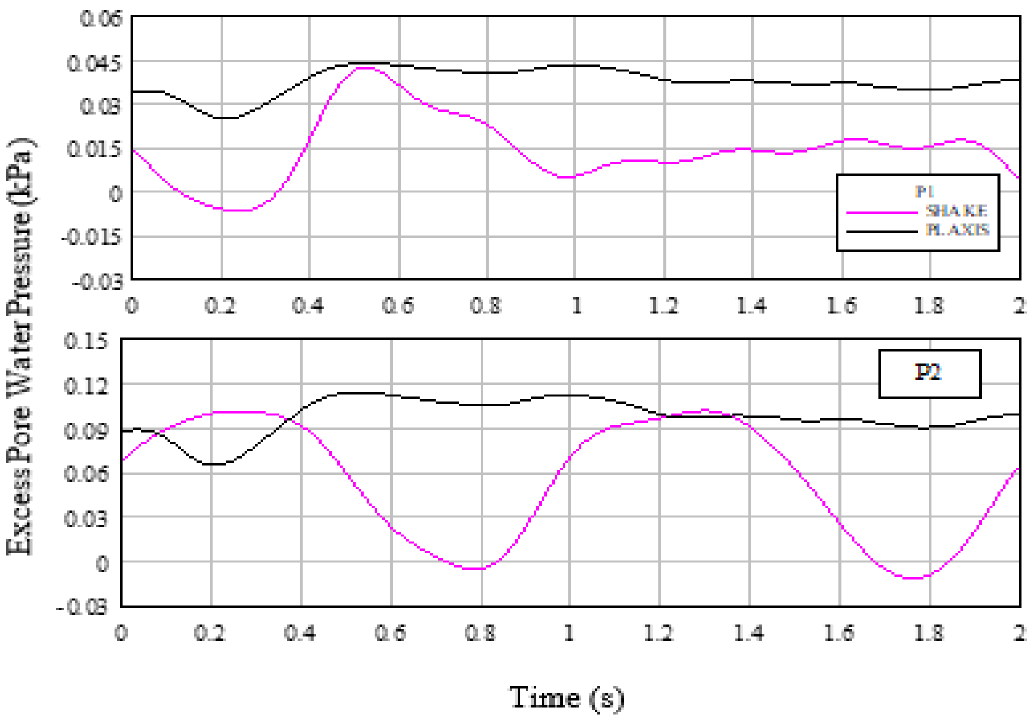

Figure 6.9 (j): Excess Pore water Pressure response (Model ST99-Frequency 1 Hz, Acceleration- 0.05g, Relative density 64% and surcharge 1.72 kPa)

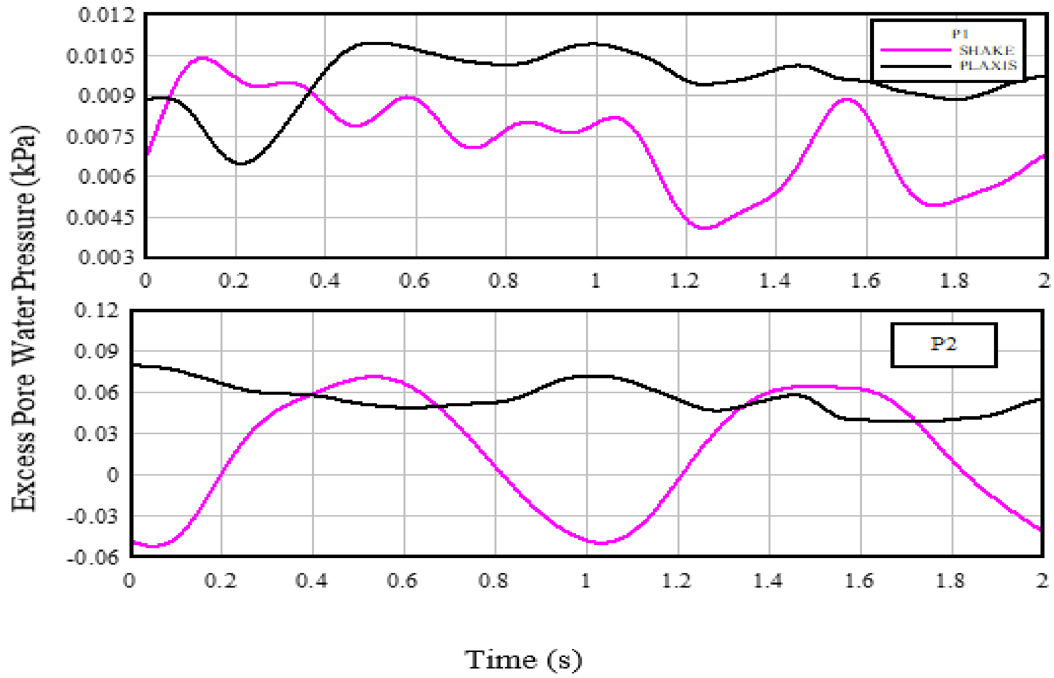

Figure 6.9 (k): Excess Pore water Pressure response (Model ST35-Frequency 1 Hz, Acceleration- 0.05g, Relative density 80% and surcharge 1.72 kPa)

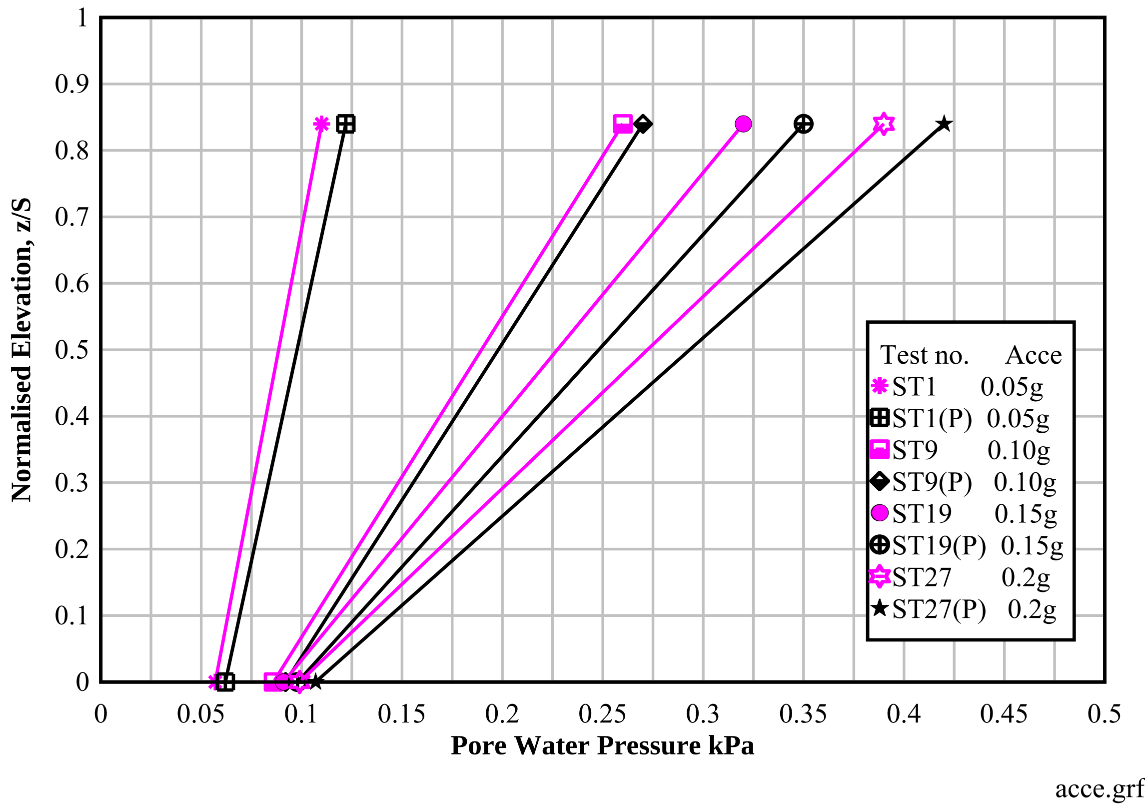

Figure 6.10: Effect of base acceleration on pore water pressure (ST1, 9, 19 and 27).

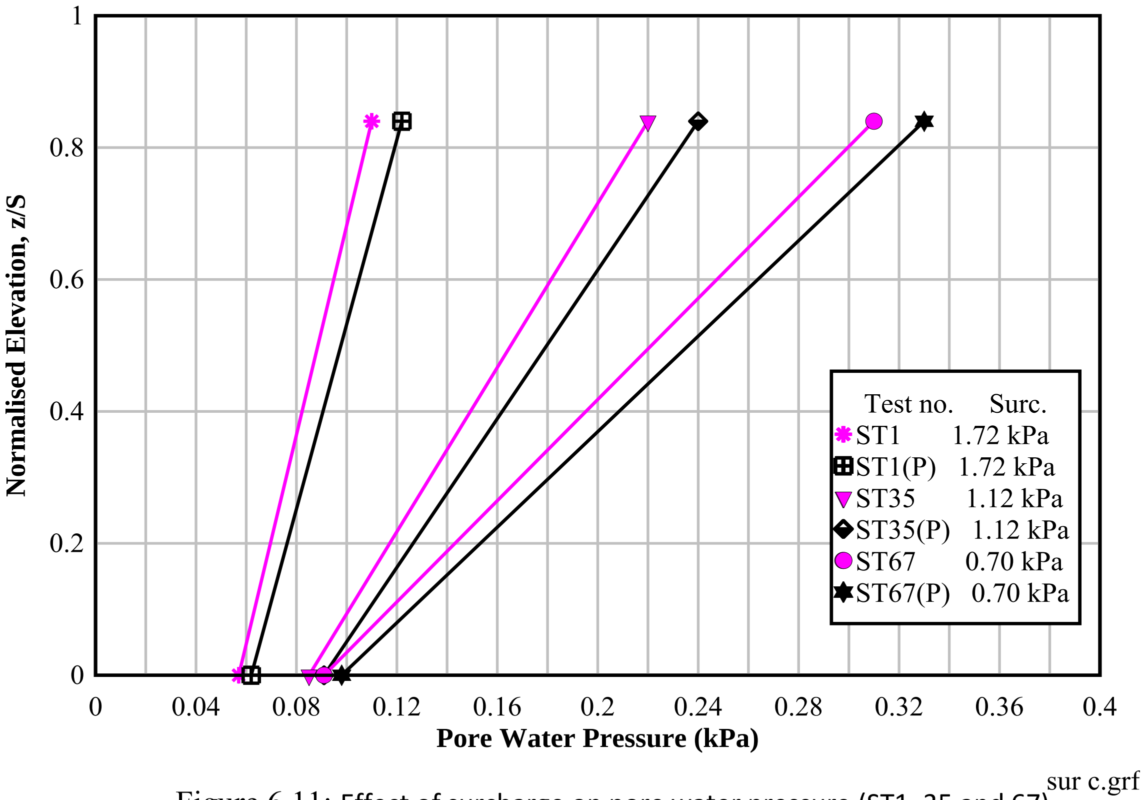

Figure 6.11: Effect of surcharge on pore water pressure (ST1, 35 and 67)

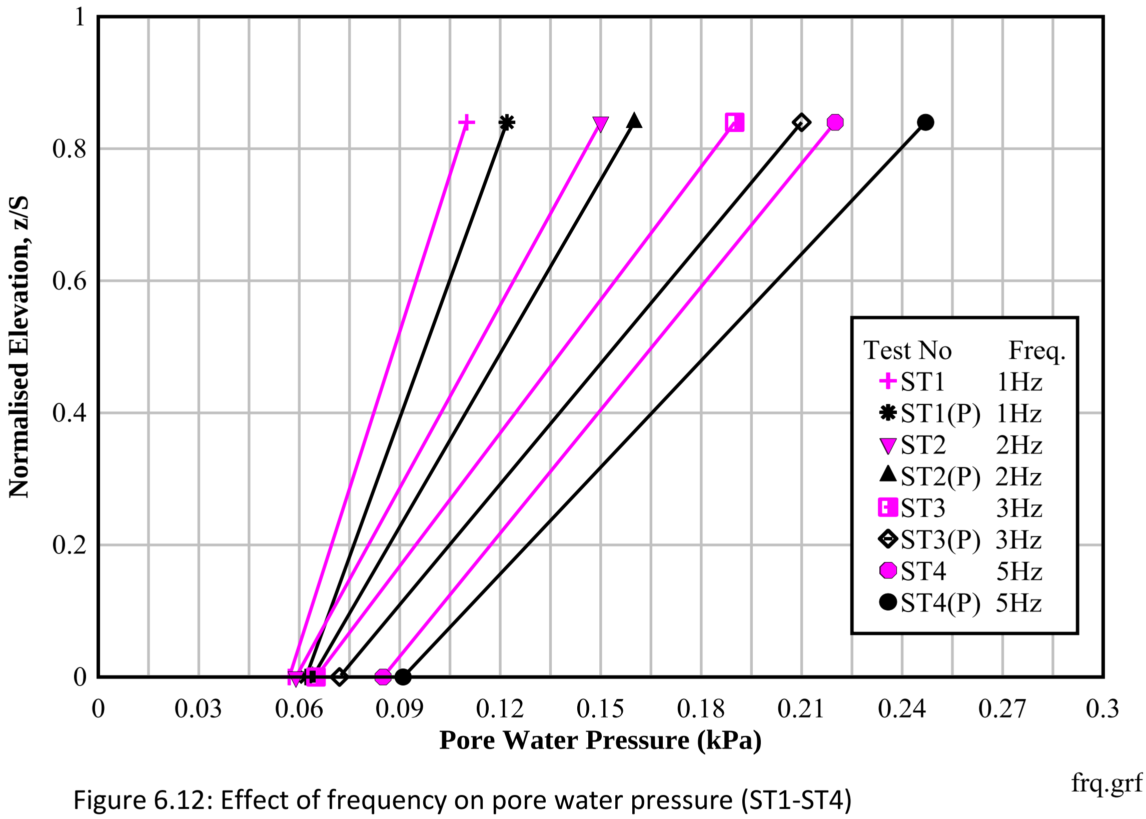

Figure 6.12: Effect of frequency on pore water pressure (ST1-ST4)

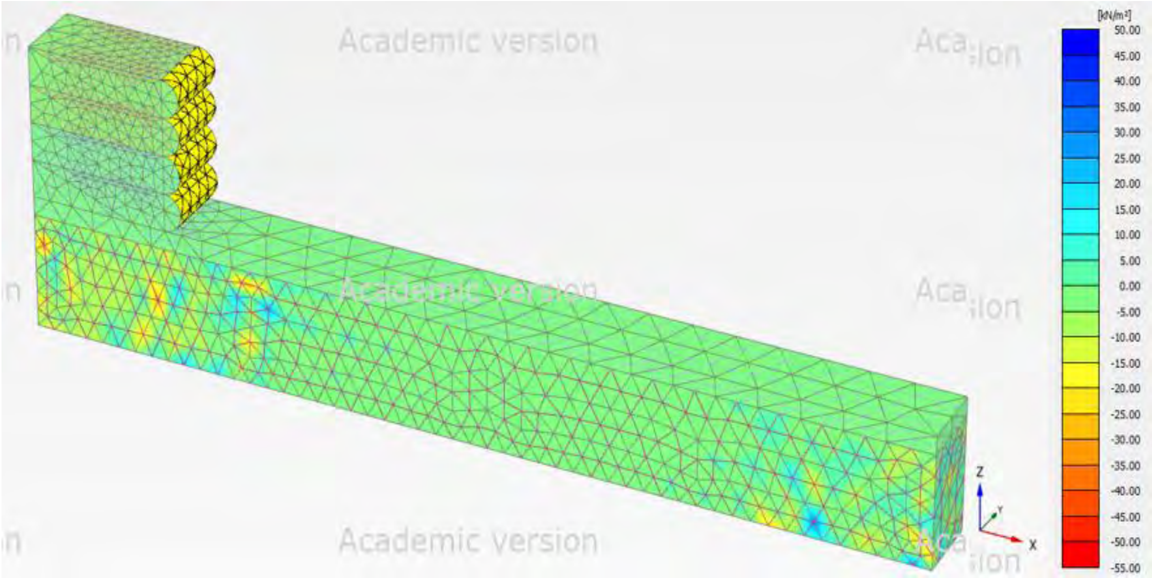

Figure 6.13 (a) Pore water pressure response (ST1)

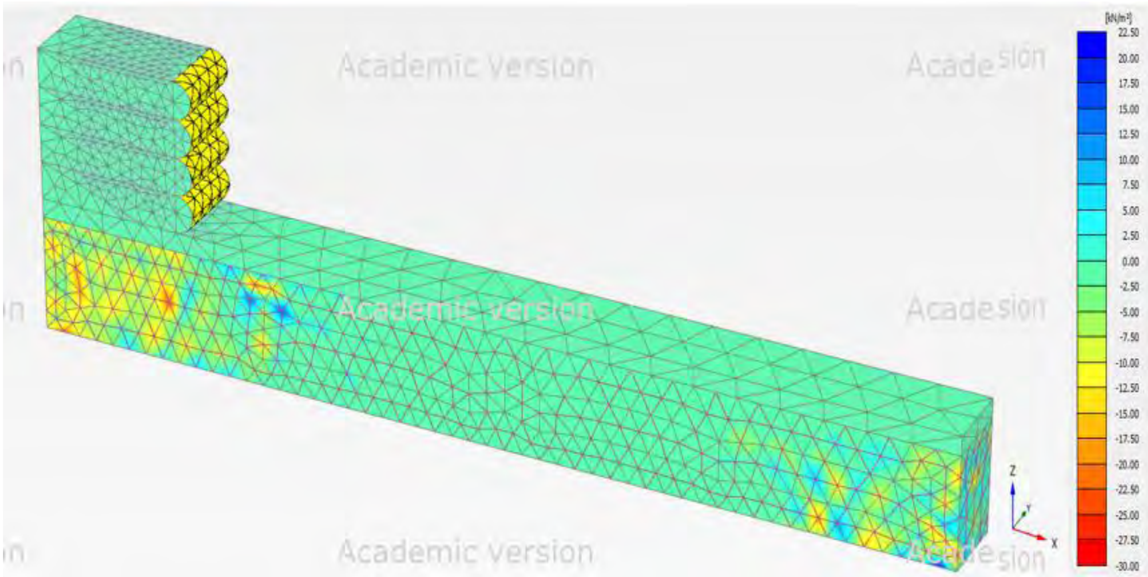

Figure 6.13 (b) Pore water pressure response (ST2)

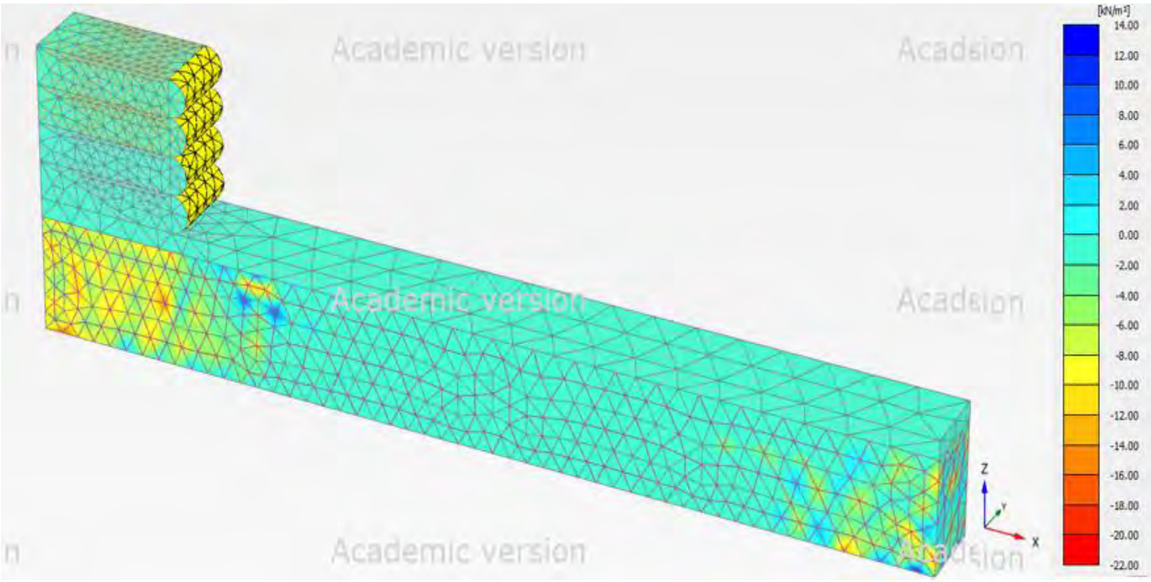

Figure 6.13 (c) Pore water pressure response (ST3)

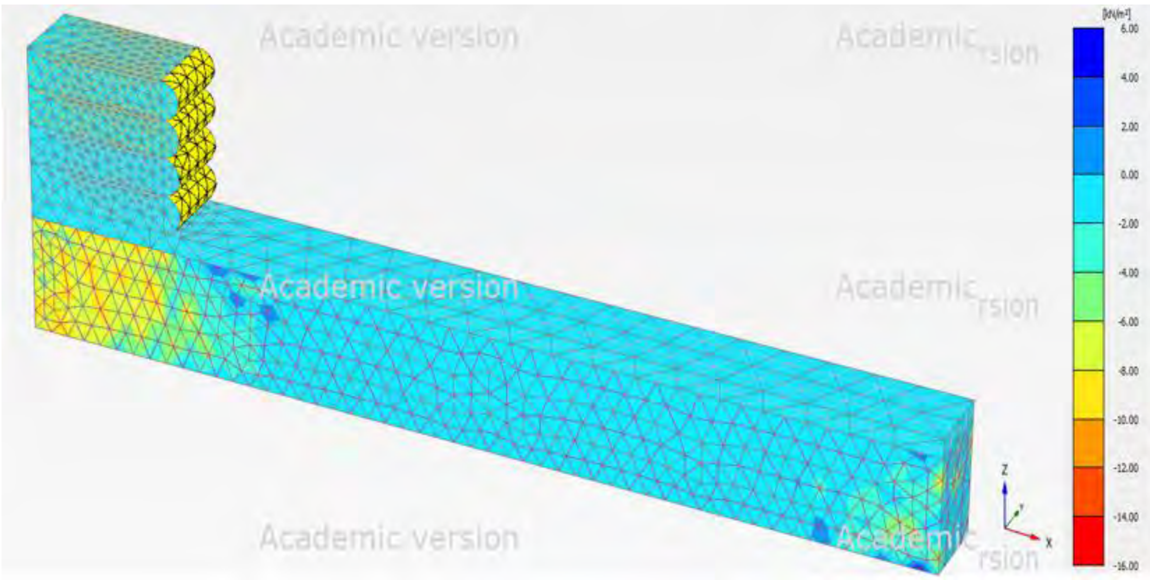

Figure 6.13 (d) Pore water pressure response (ST4)

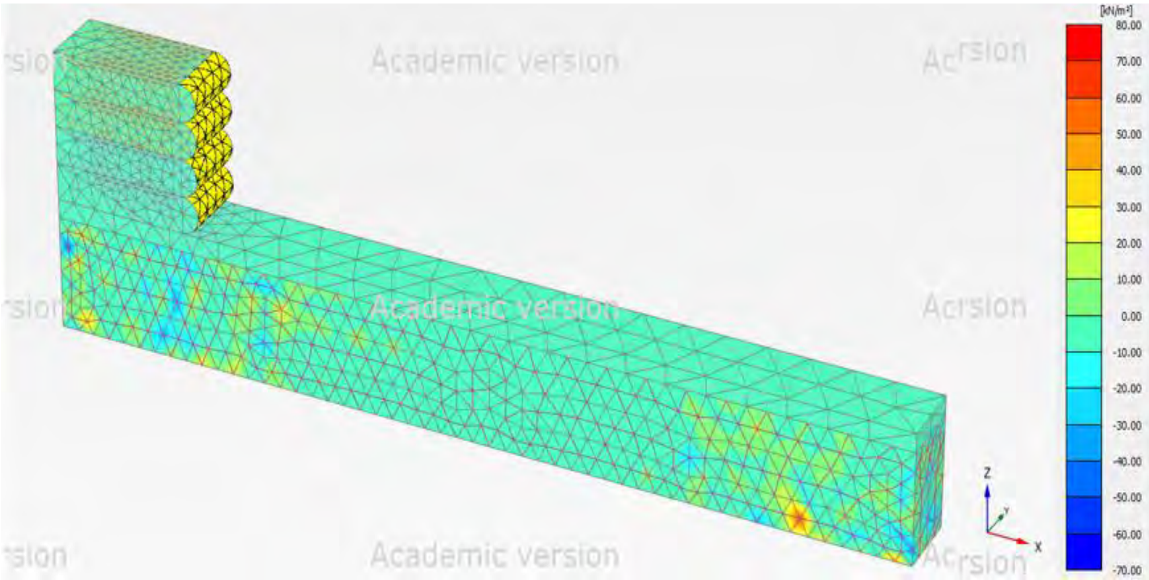

Figure 6.13 (e) Pore water pressure response (ST9)

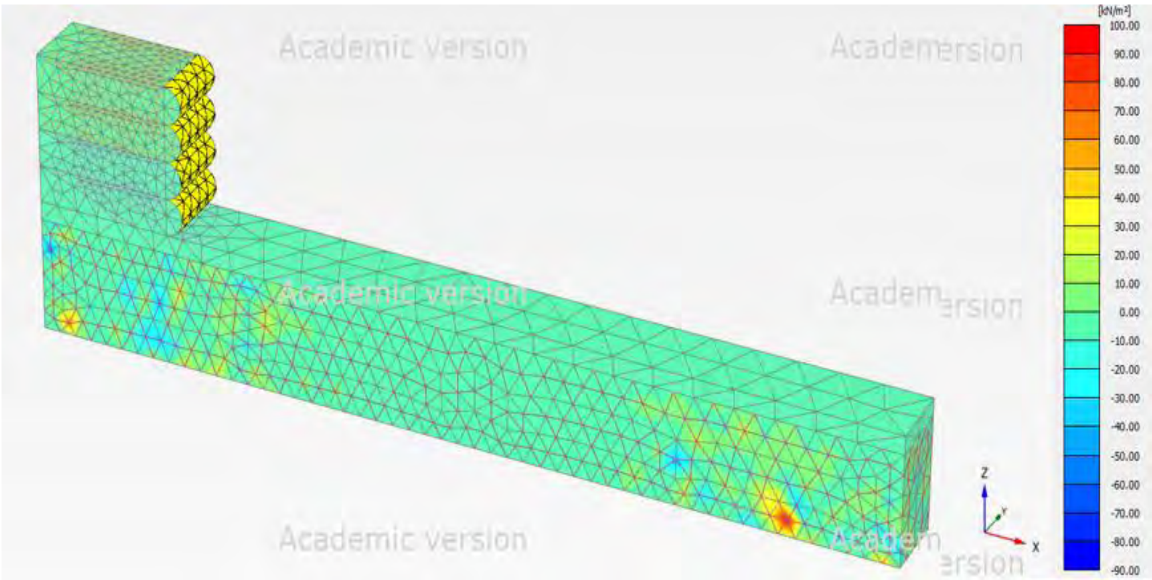

Figure 6.13 (f) Pore water pressure response (ST19)

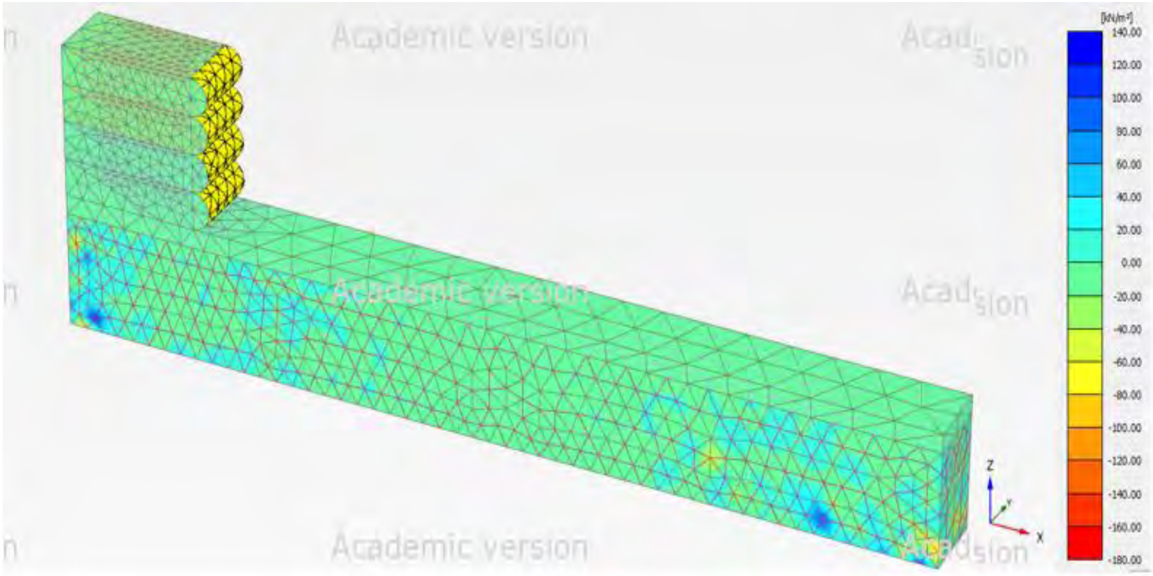

Figure 6.13 (g) Pore water pressure response (ST27)

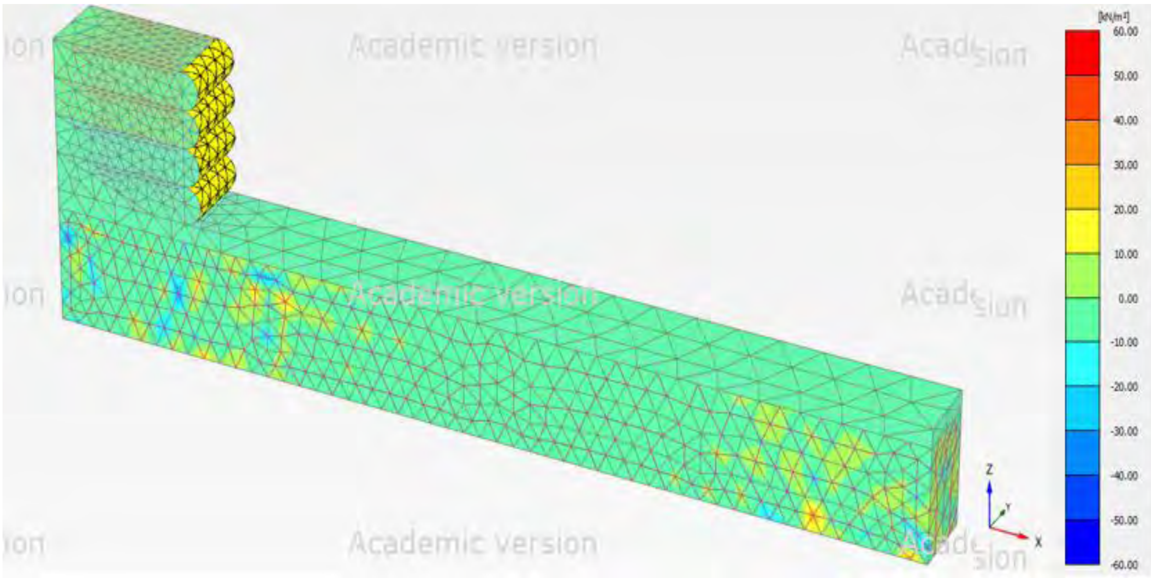

Figure 6.13 (h) Pore water pressure response (ST35)

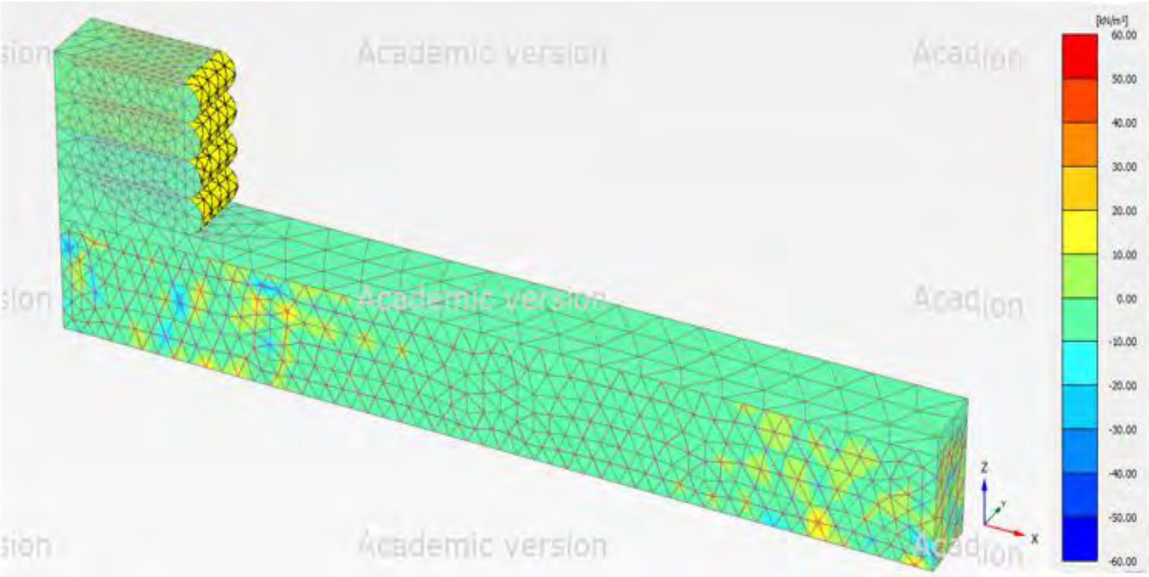

Figure 6.13 (i) Pore water pressure response (ST67)

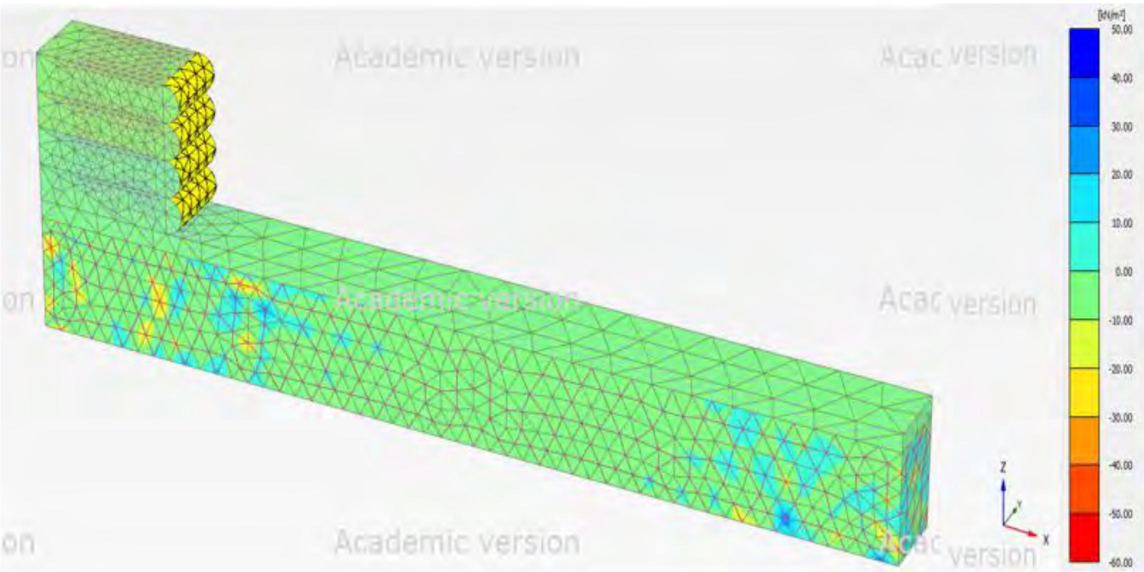

Figure 6.13 (j) Pore water pressure response (ST102)

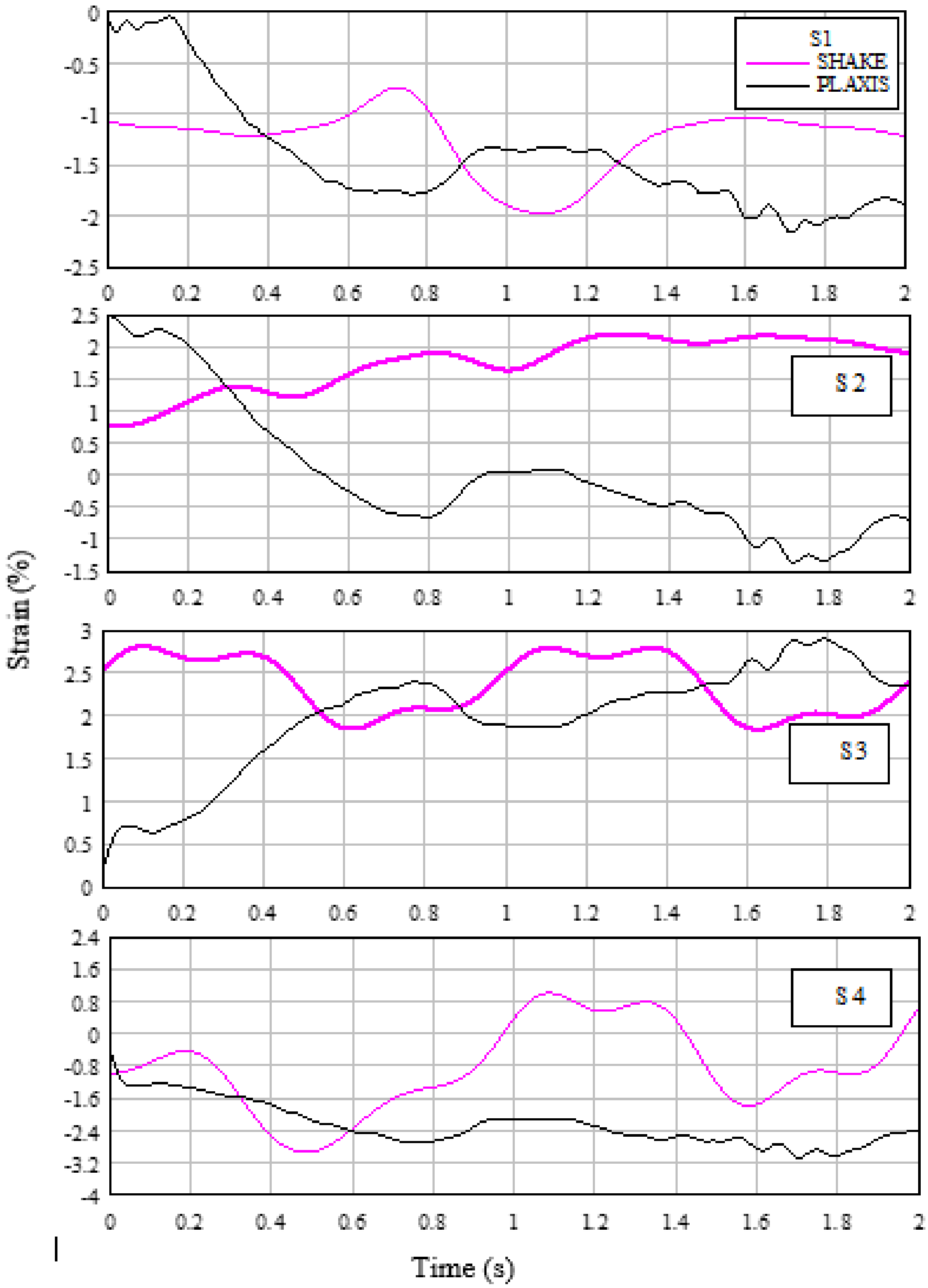

Figure 6.14 (a): Strain Response (Model ST1-Frequency 1 Hz, Acceleration- 0.05g, Relative density 48% and surcharge 1.72 kPa)

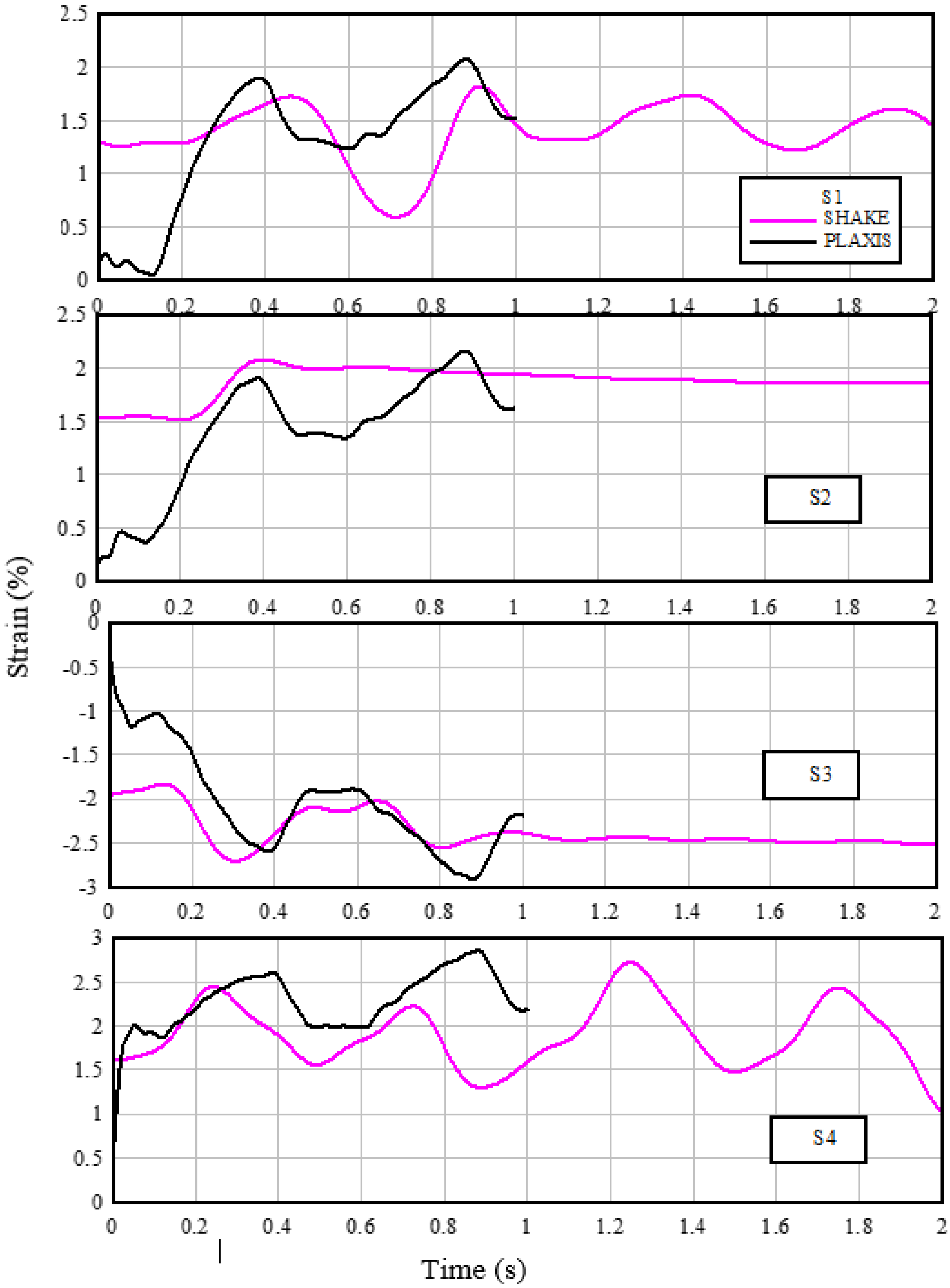

Figure 6.14 (b): Strain Response (Model ST2-Frequency 2 Hz, Acceleration- 0.05g, Relative density 48% and surcharge 1.72 kPa)

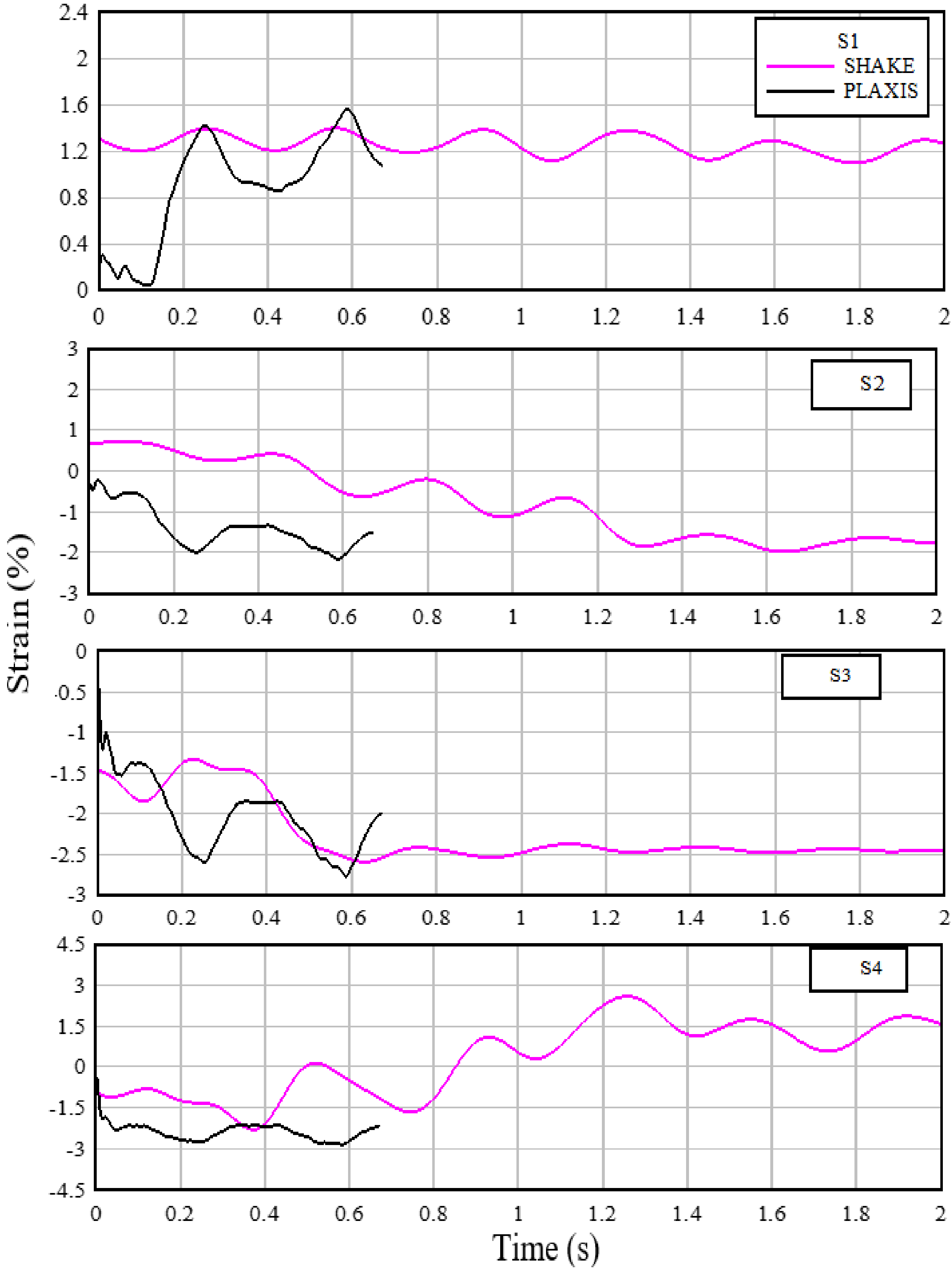

Figure 6.14 (c): Strain Response (Model ST3-Frequency 3 Hz, Acceleration-0.05g, Relative density 48% and surcharge 1.72 kPa)

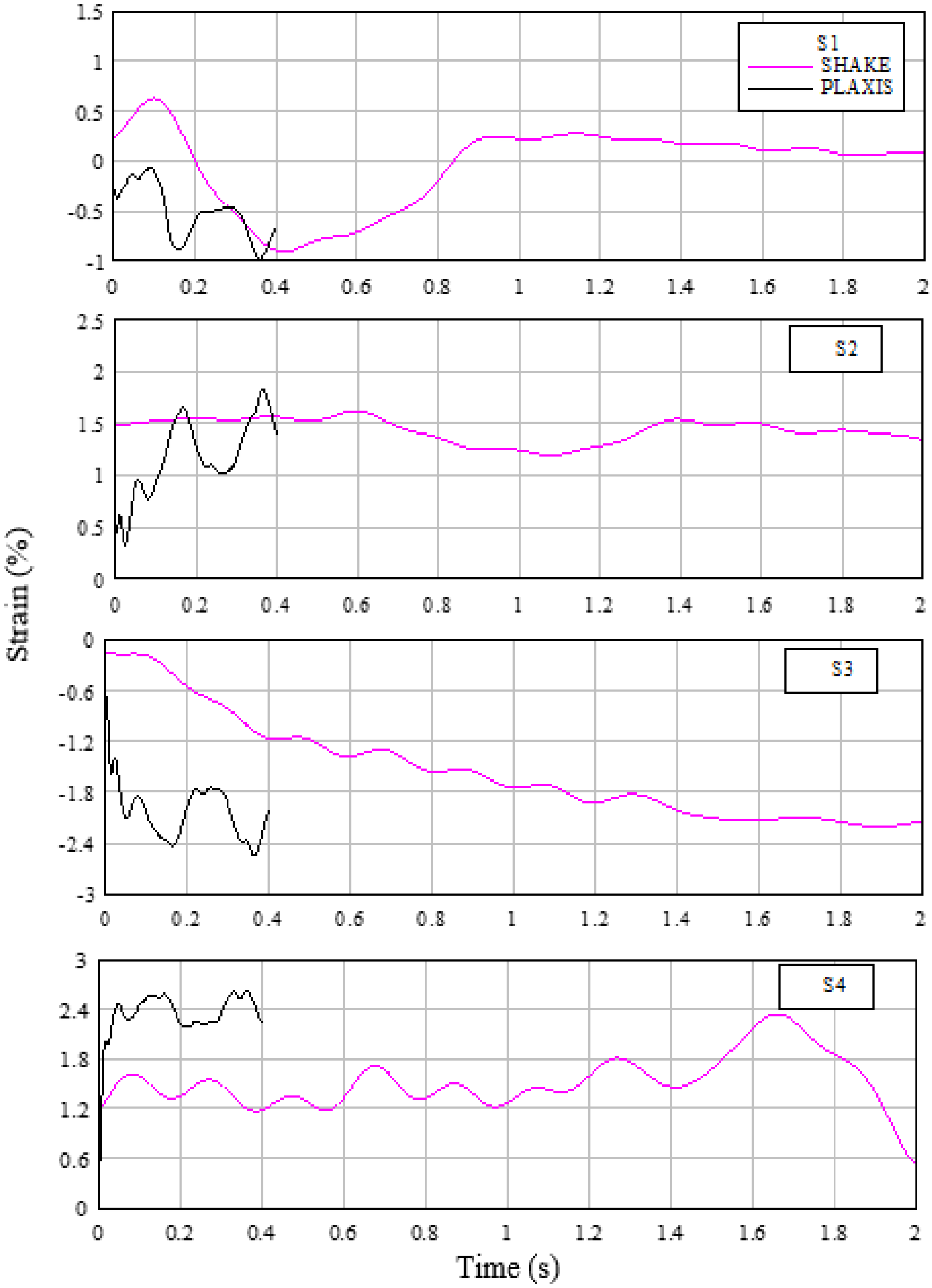

Figure 6.14 (d): Strain Response (Model ST4-Frequency 5 Hz, Acceleration- 0.05g, Relative density 48% and surcharge 1.72 kPa)

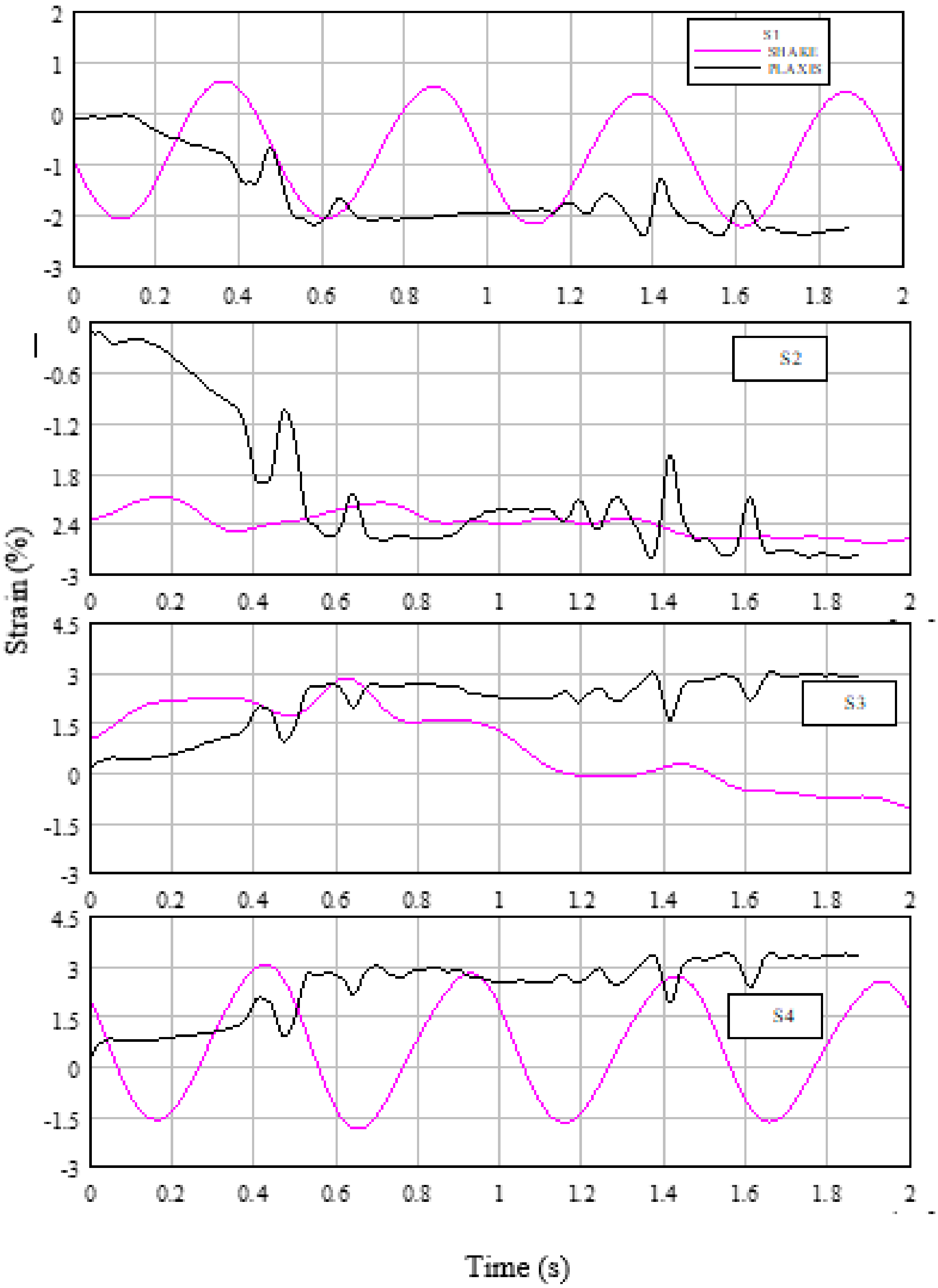

Figure 6.14 (e): Strain Response (Model ST9-Frequency 1 Hz, Acceleration- 0.10g, Relative density 48% and surcharge 1.72 kPa)

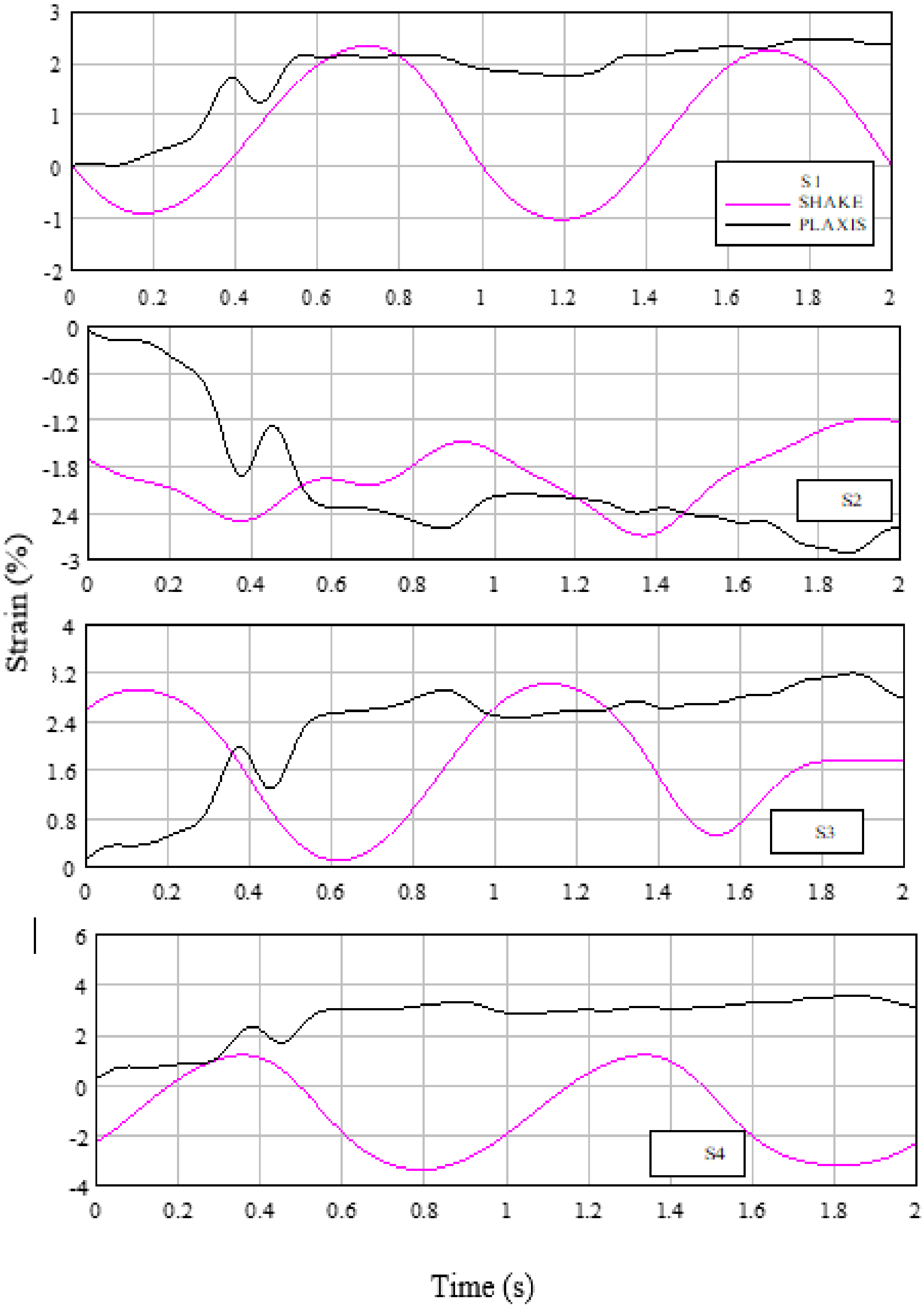

Figure 6.14 (f): Strain Response (Model ST19-Frequency 1 Hz, Acceleration- 0.15g, Relative density 48% and surcharge 1.72 kPa)

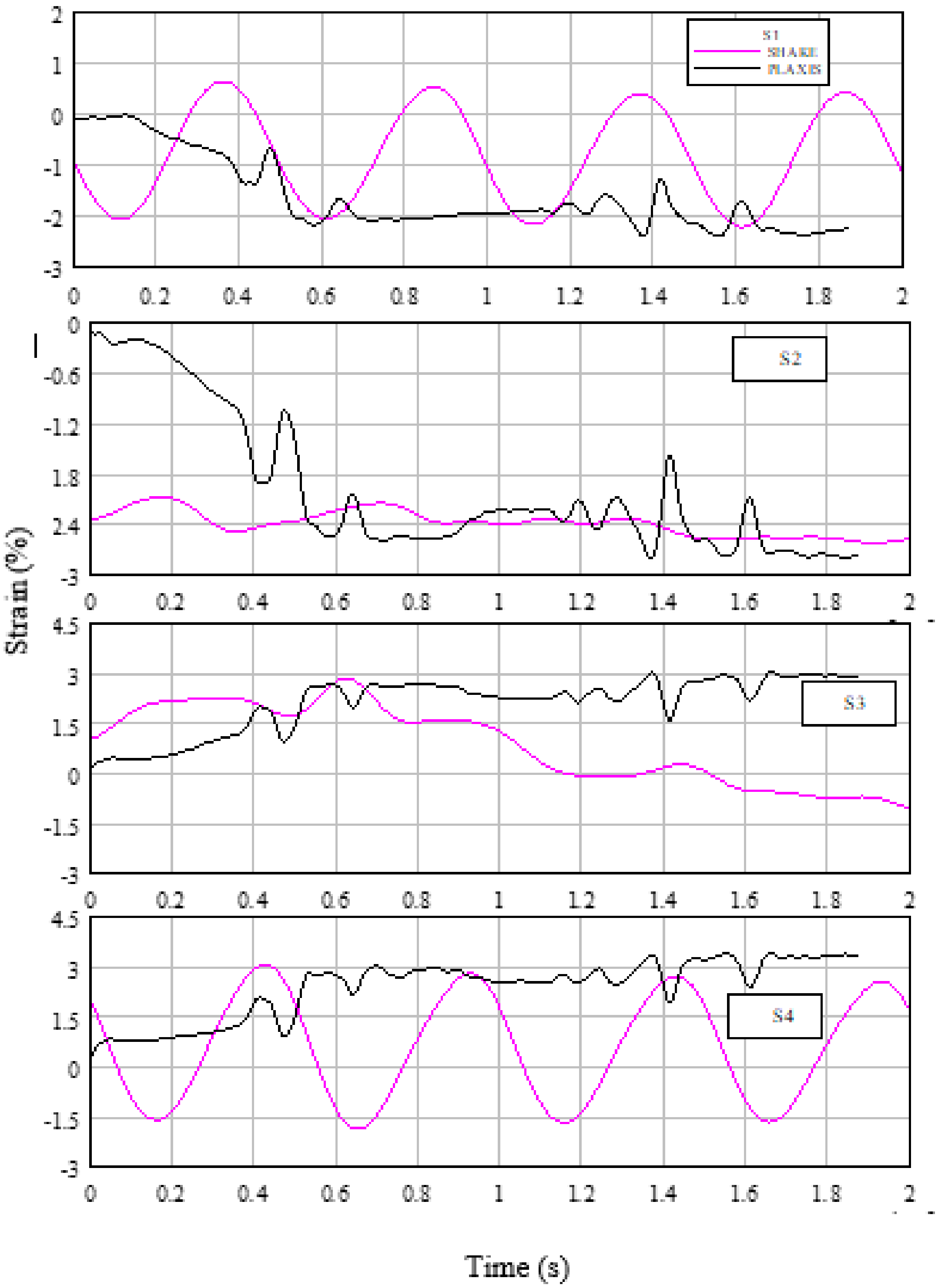

Figure 6.14 (g): Strain Response (Model ST27-Frequency 1 Hz, Acceleration-0.20g, Relative density 48% and surcharge 1.72 kPa)

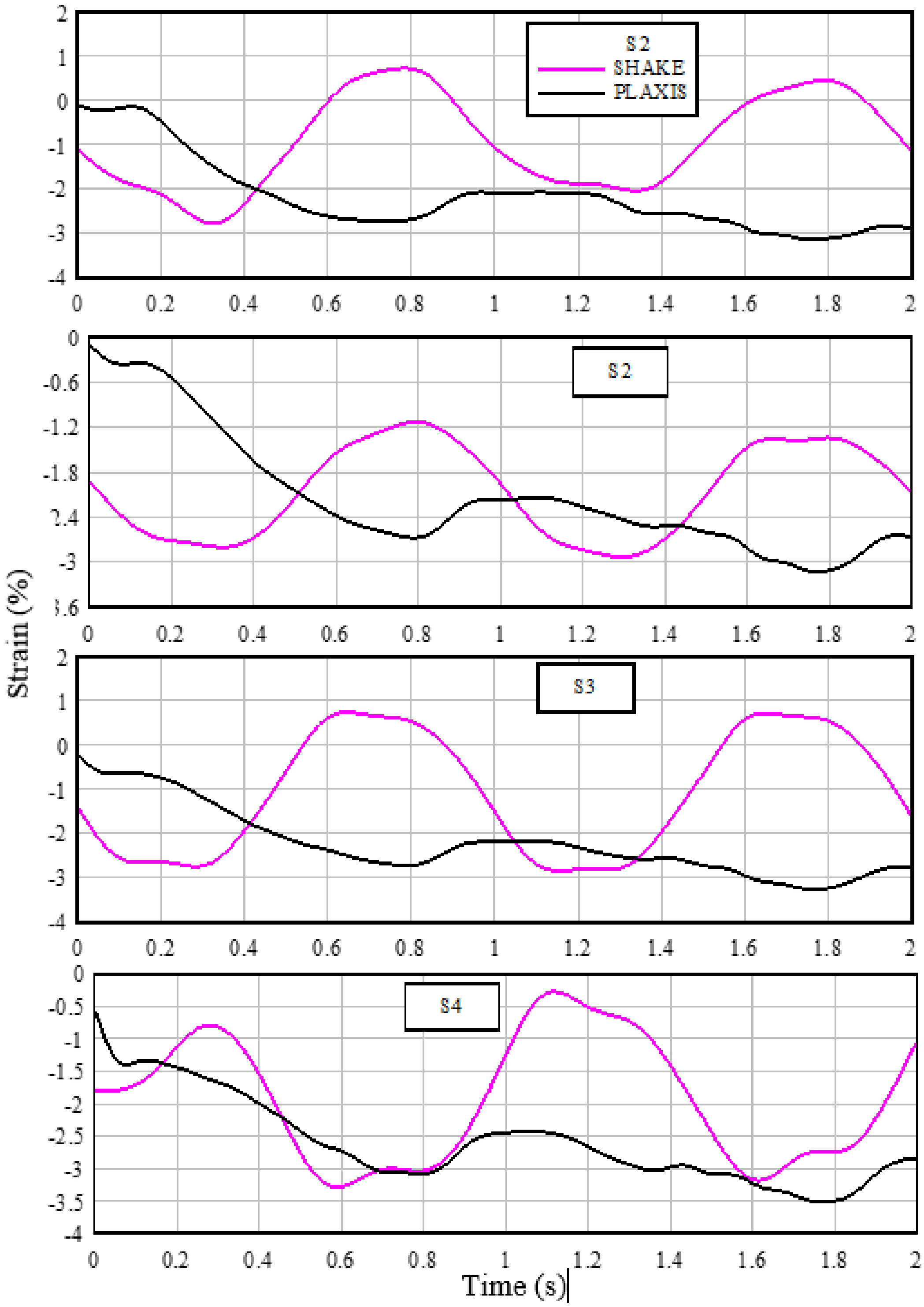

Figure 6.14 (h): Strain Response (Model ST35-Frequency 1 Hz, Acceleration-0.05g, Relative density 48% and surcharge 1.12 kPa)

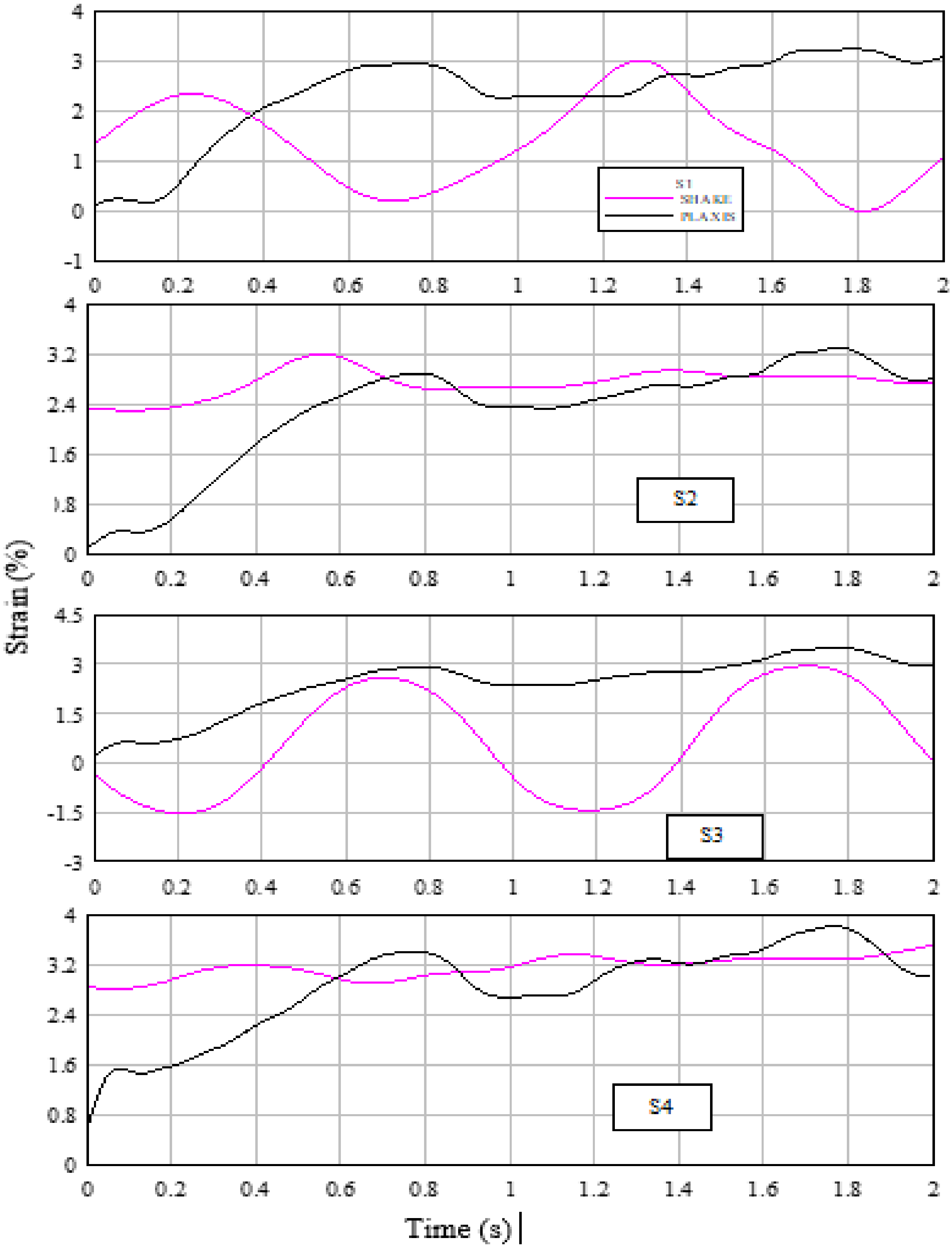

Figure 6.14 (i): Strain Response (Model ST67-Frequency 1 Hz, Acceleration- 0.05g, Relative density 48% and surcharge 0.70 kPa)

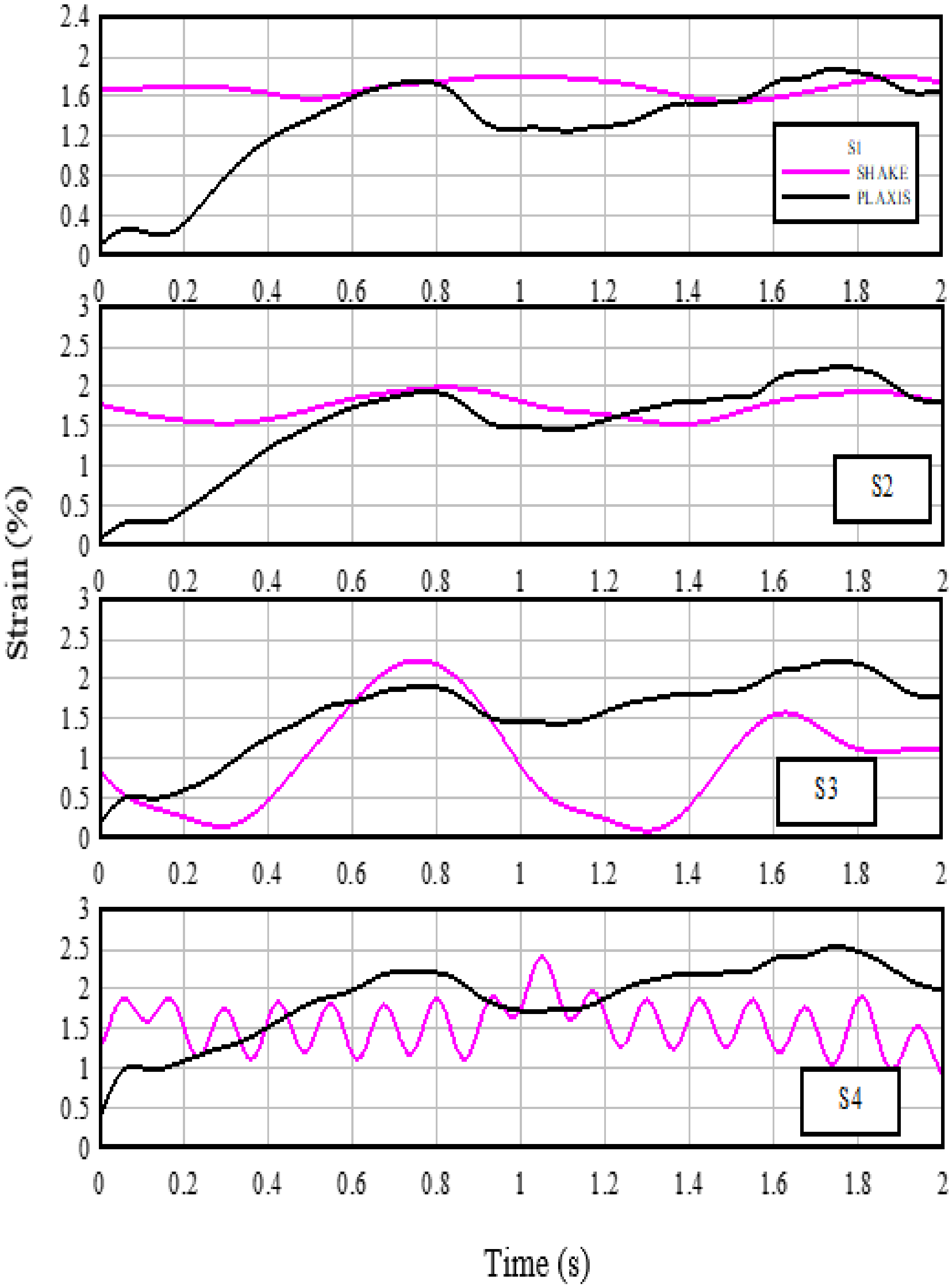

Figure 6.14 (j): Strain Response (Model ST1-Frequency 1 Hz, Acceleration- 0.05g, Relative density 64% and surcharge 1.72 kPa)

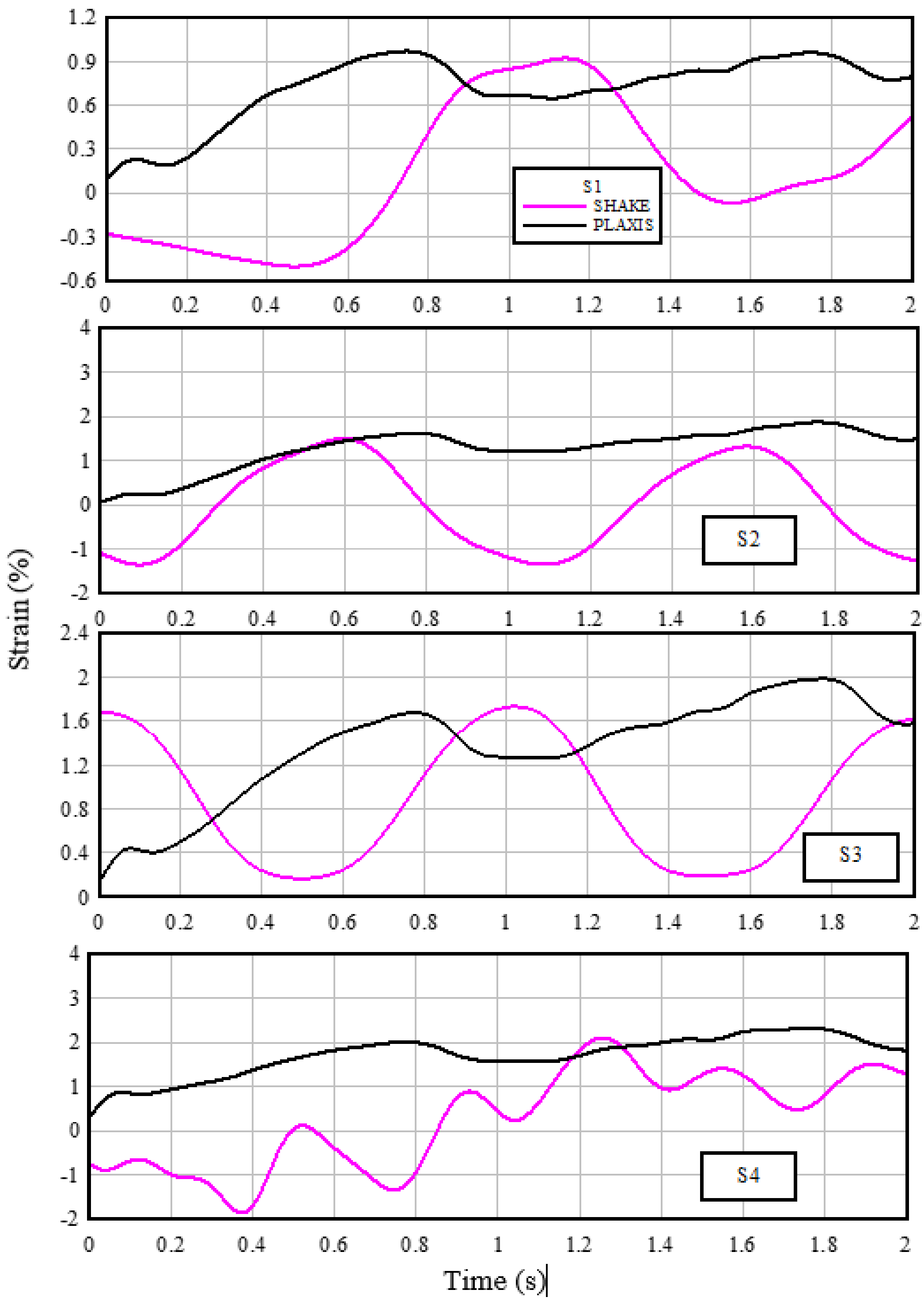

Figure 6.14 (k): Strain Response (Model ST1-Frequency 1 Hz, Acceleration- 0.05g, Relative density 80% and surcharge 1.72 kPa)

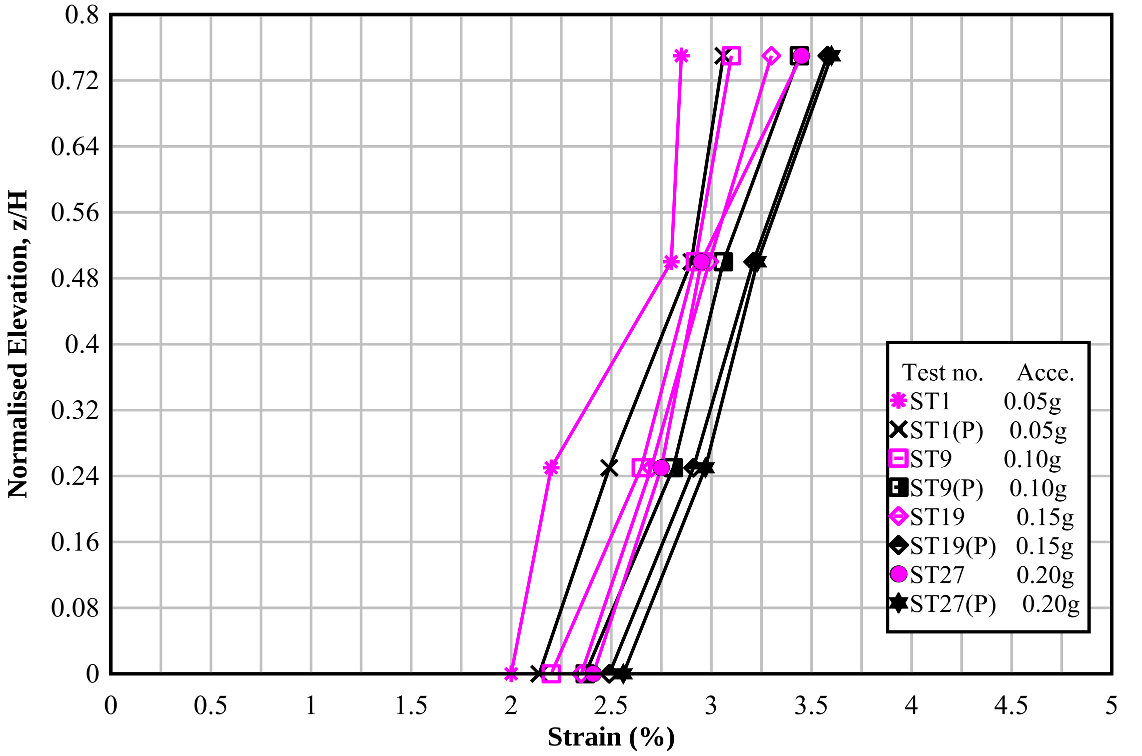

Figure 6.15: Effect of base acceleration on strain (ST1, 9, 19 and 27)

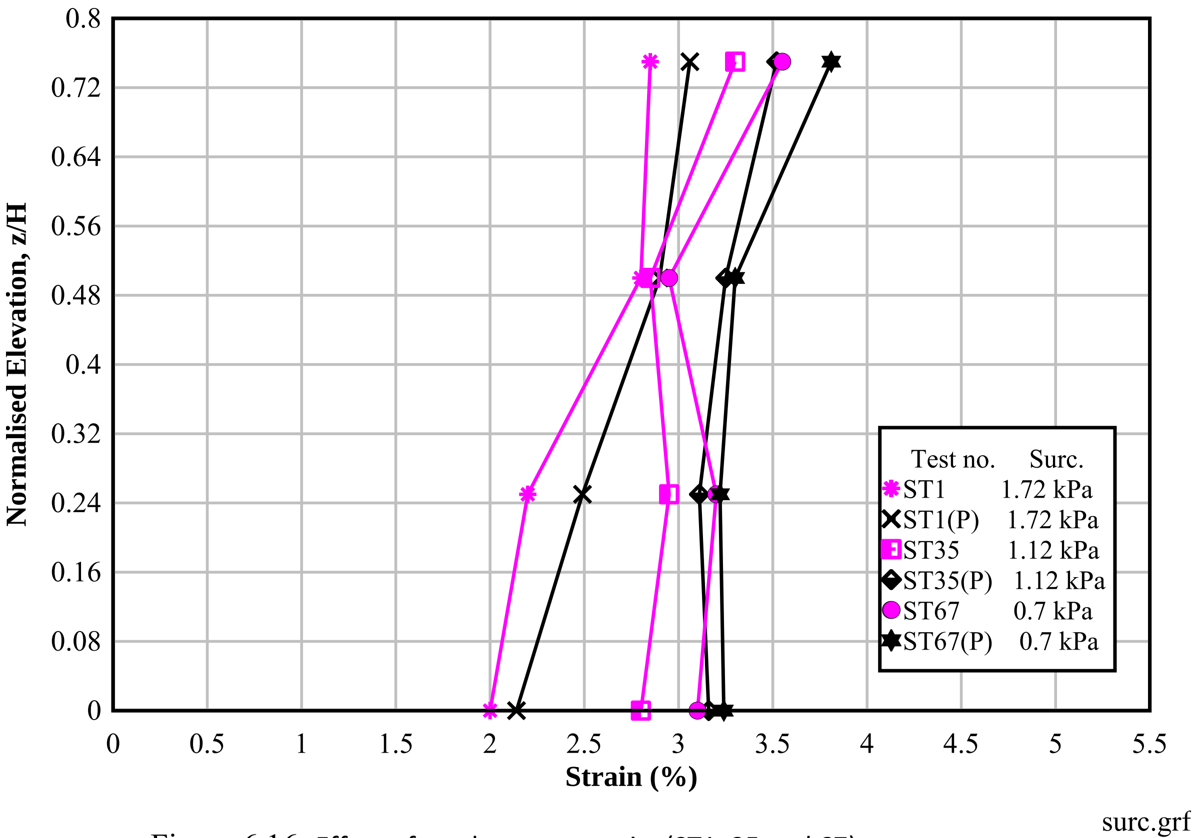

Figure 6.16: Effect of surcharge on strain (ST1, 35 and 67)

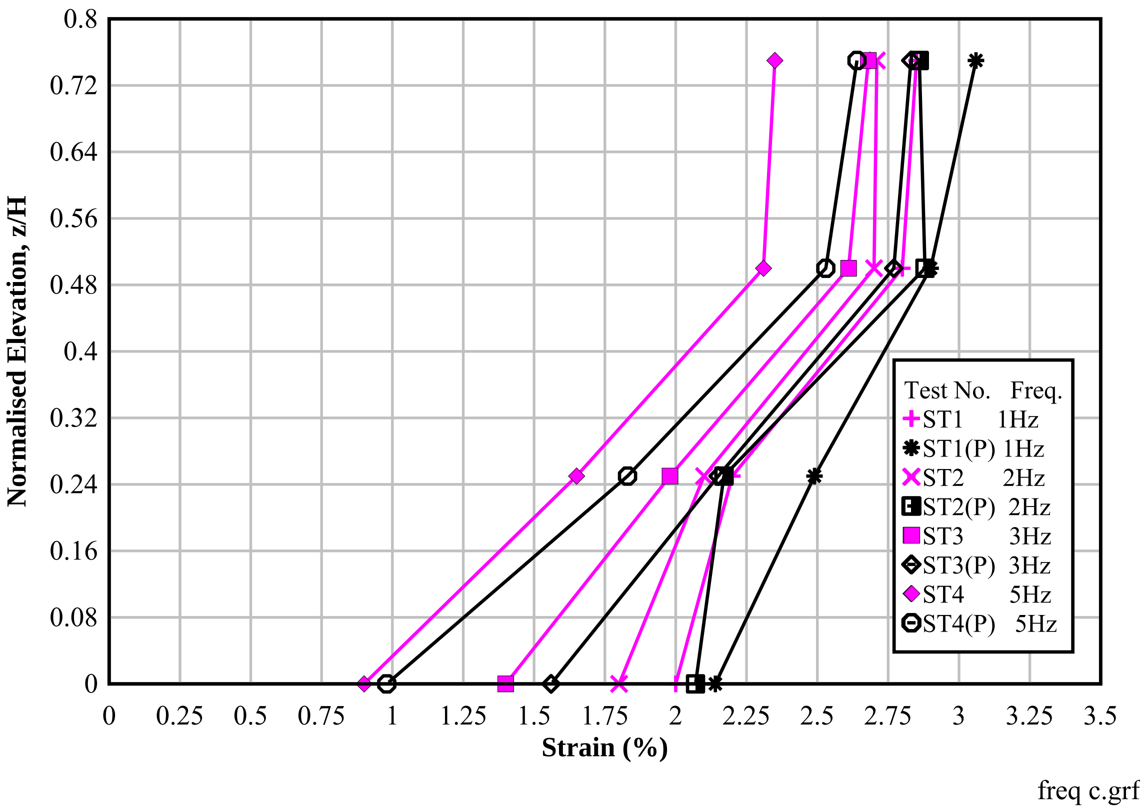

Figure 6.17: Effect of frequency on strain (ST1-ST4)

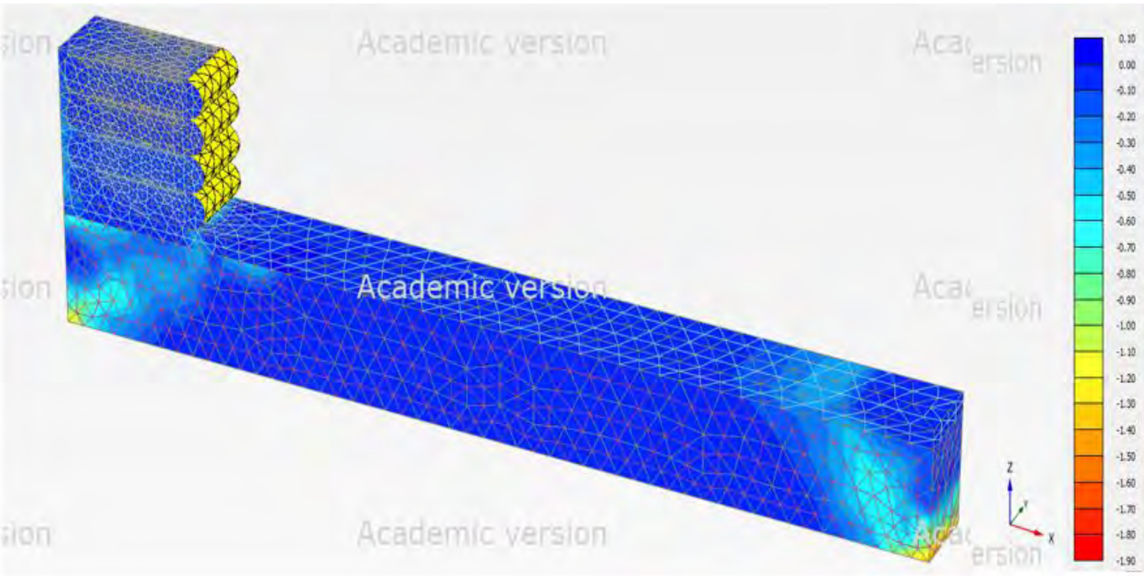

Figure 6.18 (a) Strain Contour at end (ST1)

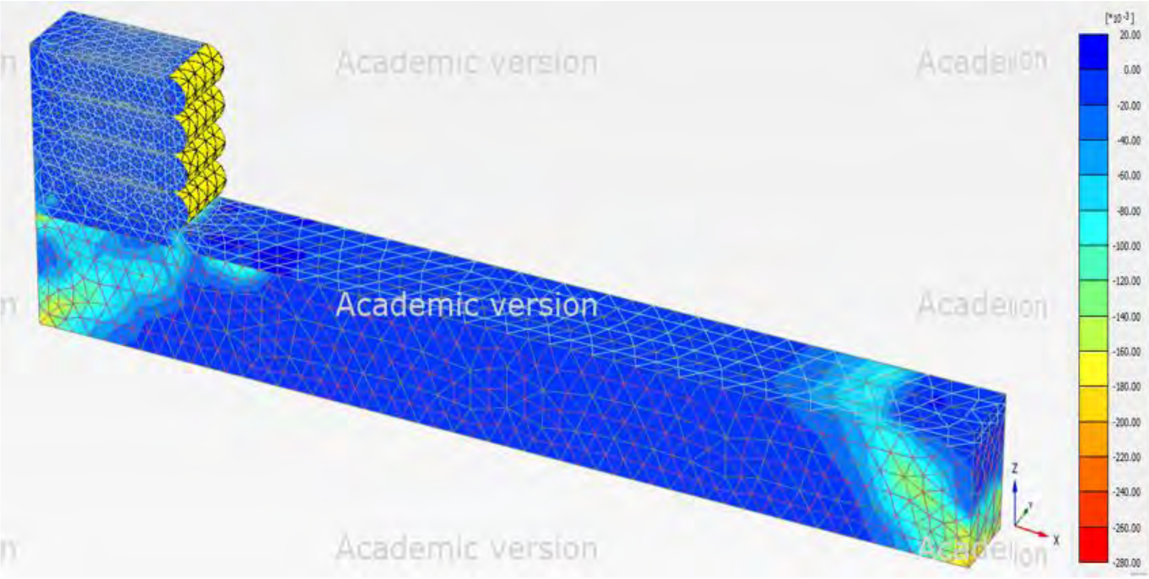

Figure 6.18 (b) Strain Contour at end (ST2)

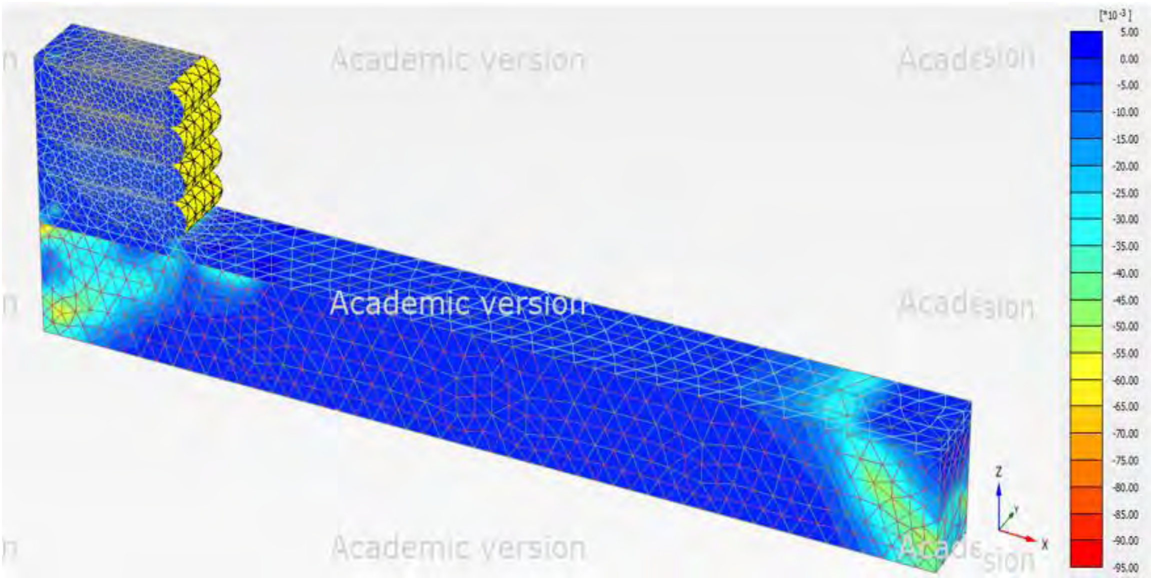

Figure 6.18 (c) Strain Contour at end (ST3)

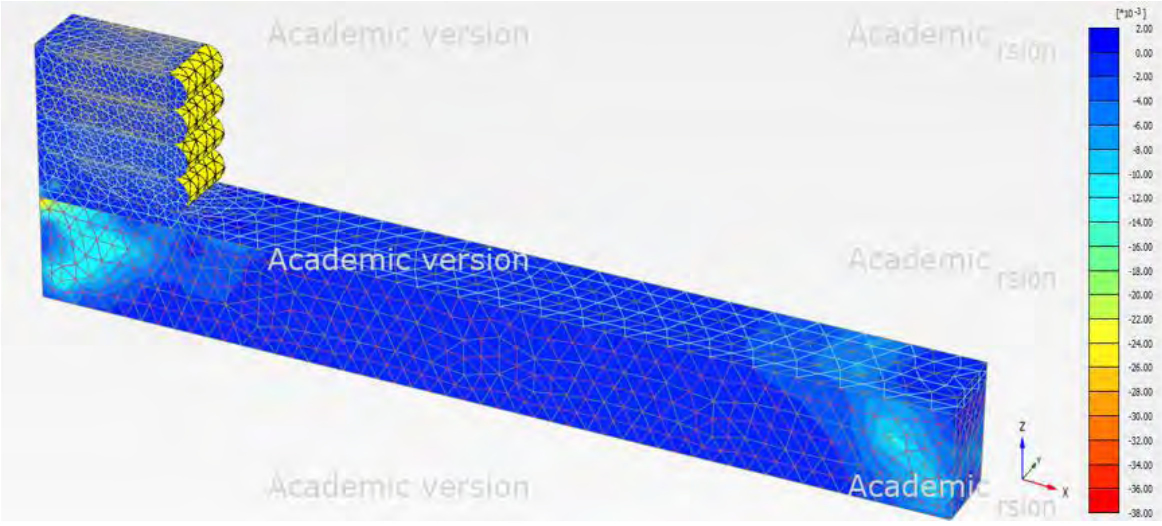

Figure 6.18 (d) Strain Contour at end (ST4)

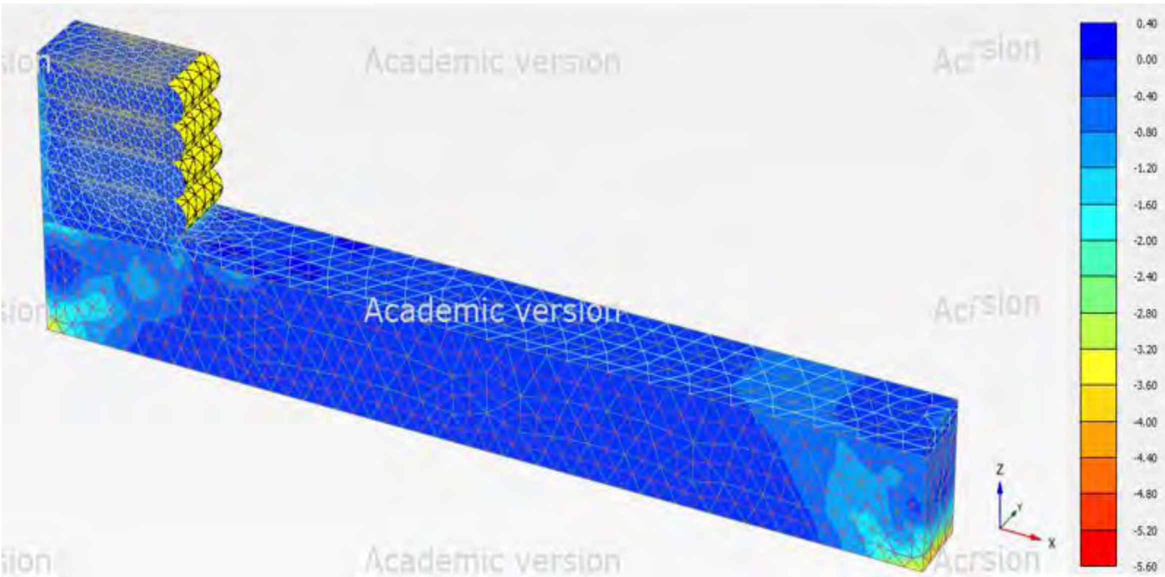

Figure 6.18 (e) Strain Contour at end (ST9)

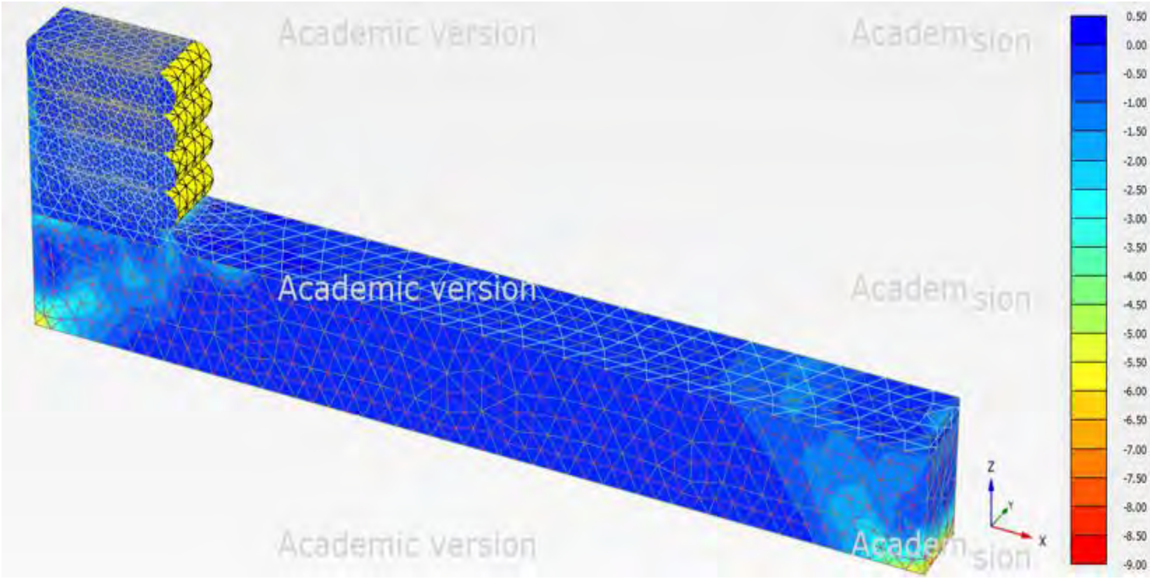

Figure 6.18 (f) Strain Contour at end (ST19)

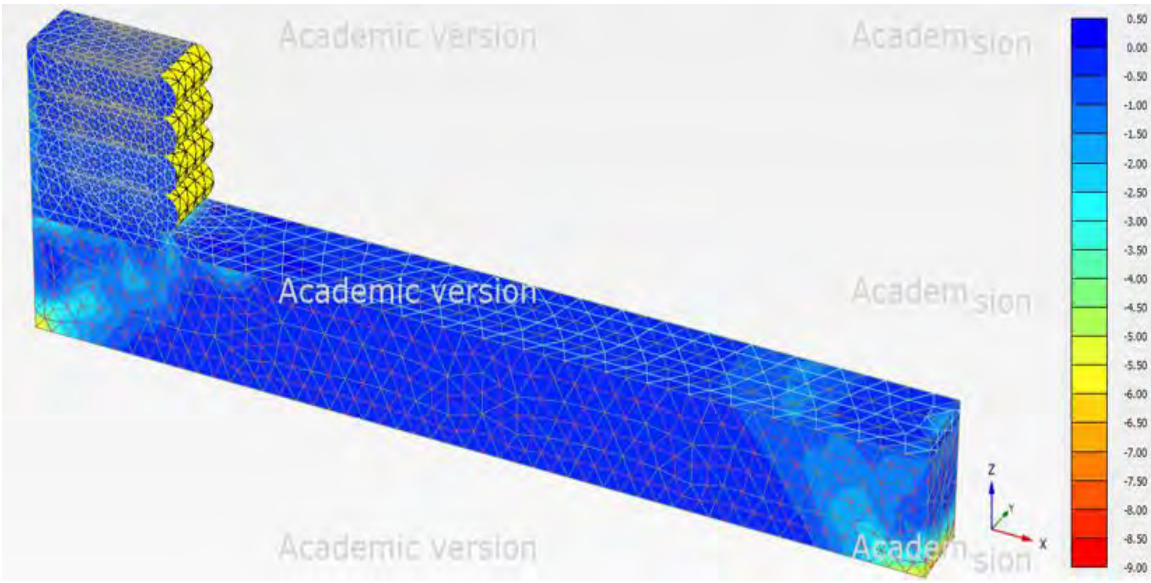

Figure 6.18 (g) Strain Contour at end (ST27)

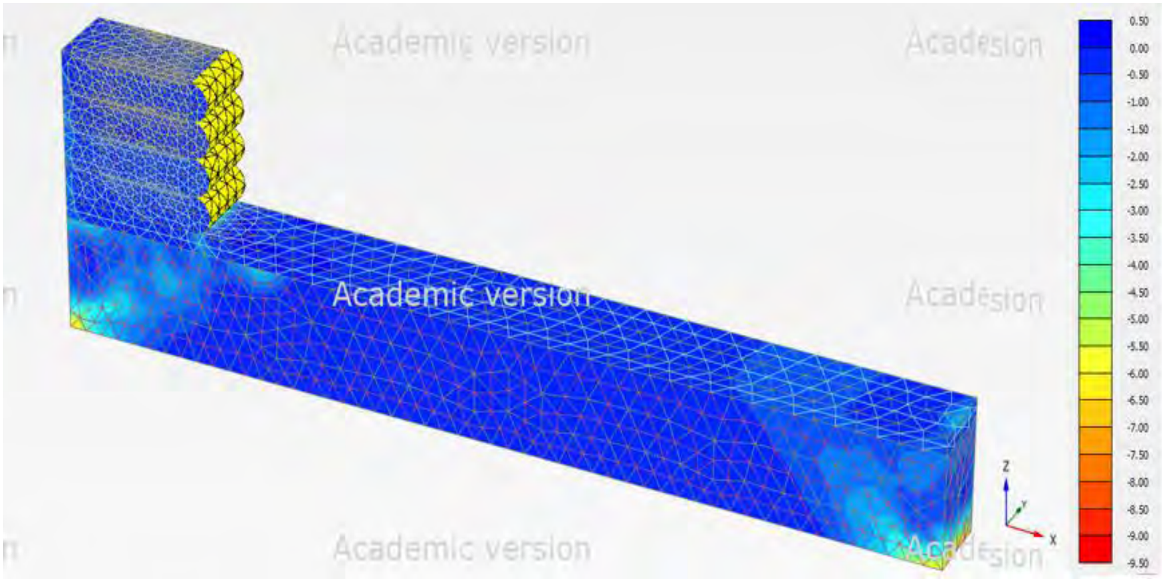

Figure 6.18 (h) Strain Contour at end (ST35)

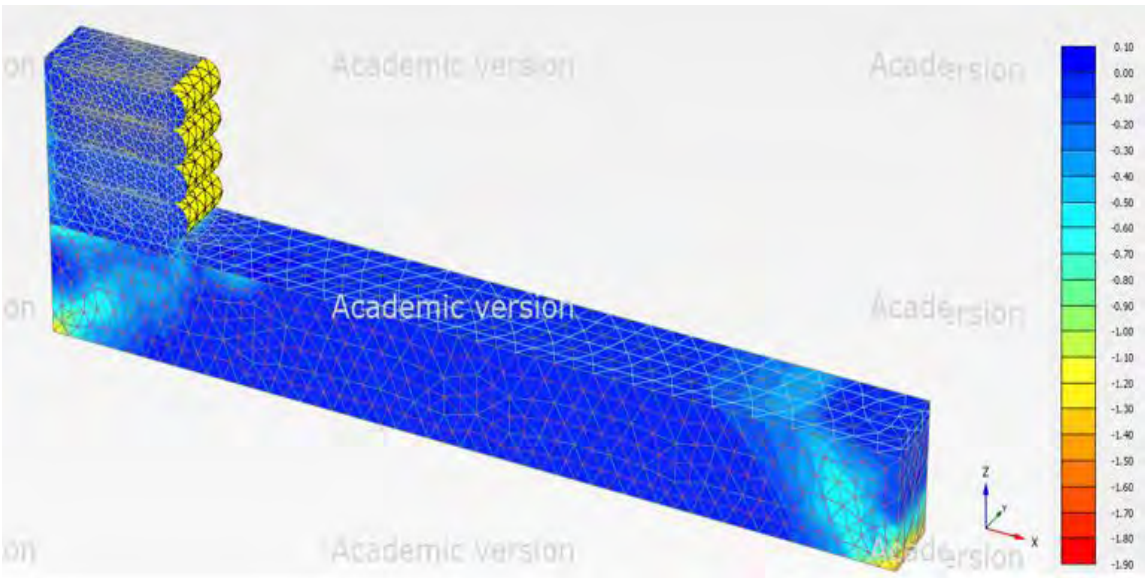

Figure 6.18 (i) Strain Contour at end (ST67)

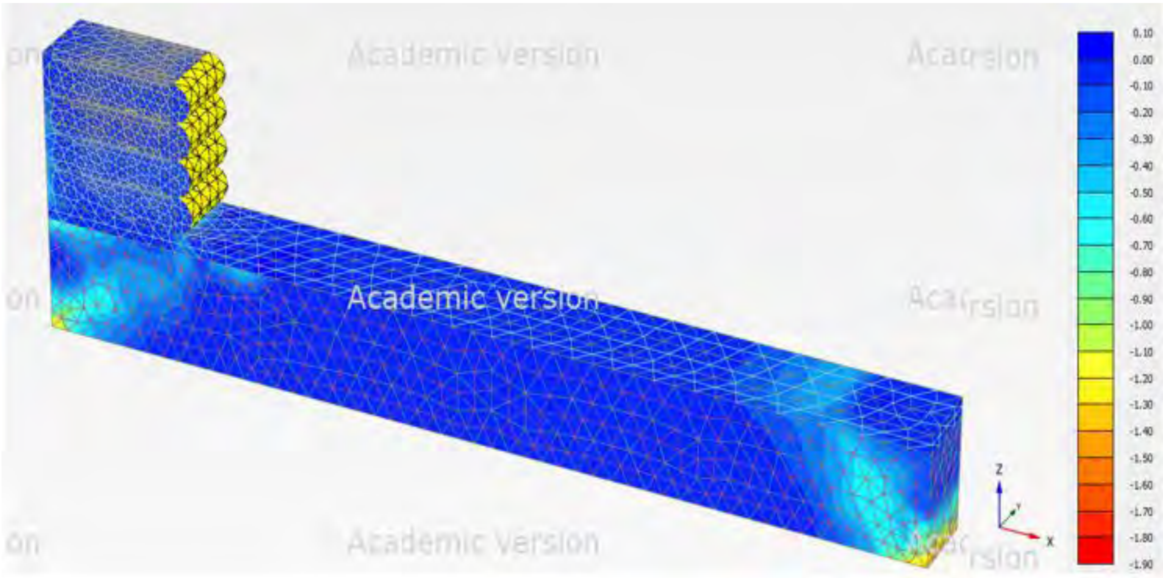

Figure 6.18 (j) Strain Contour at end (ST99)

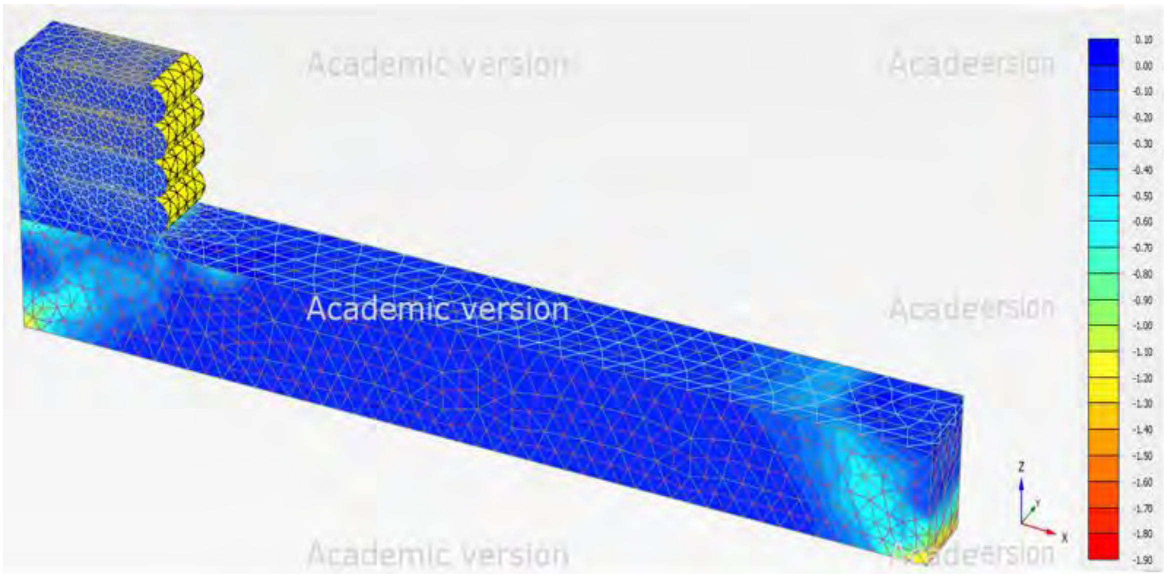

Figure 6.18 (k) Strain Contour at end (ST193)

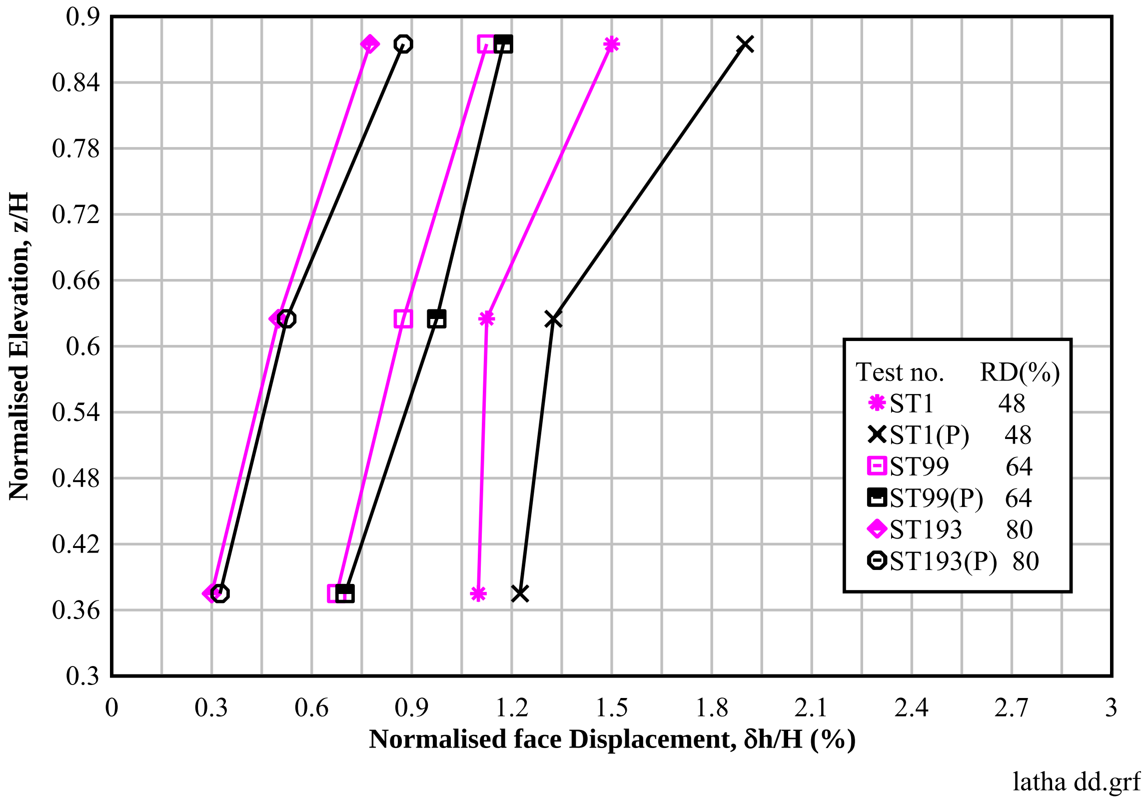

Figure 6.19: Displacement Response (ST1, 99 and 193)

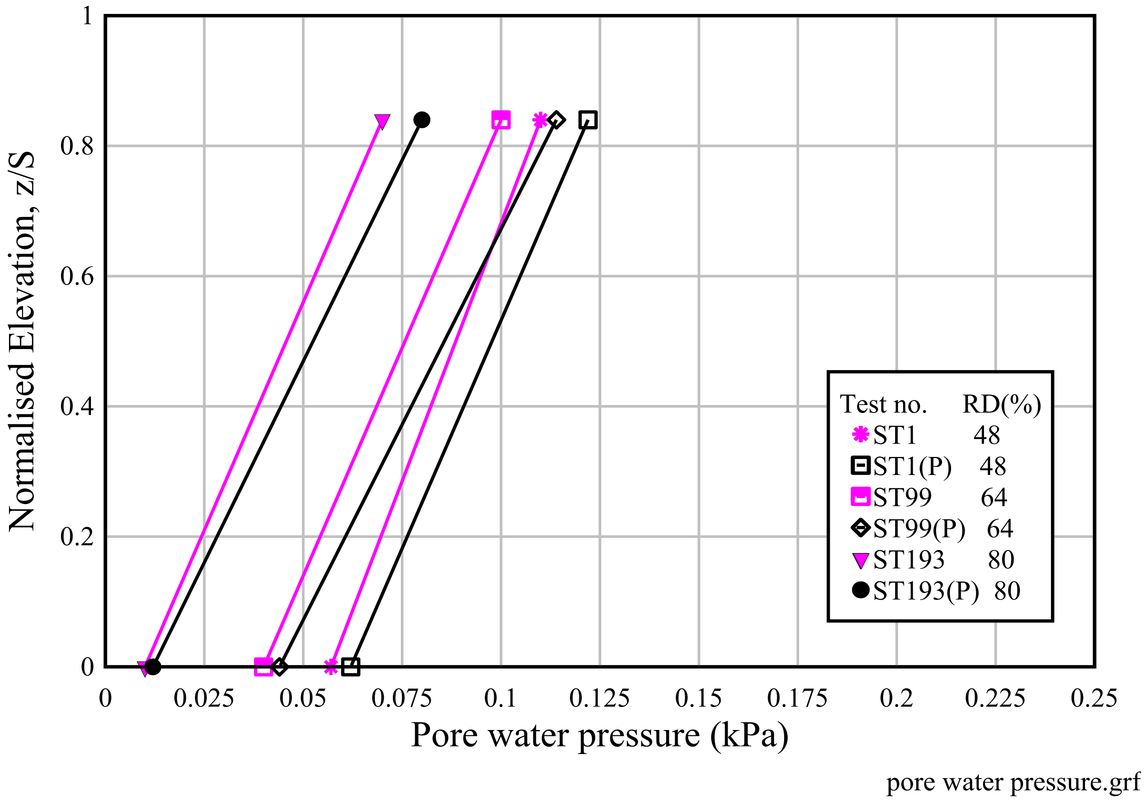

Figure 6.20: Pore Water Pressure Response (ST1, 99 and 193)

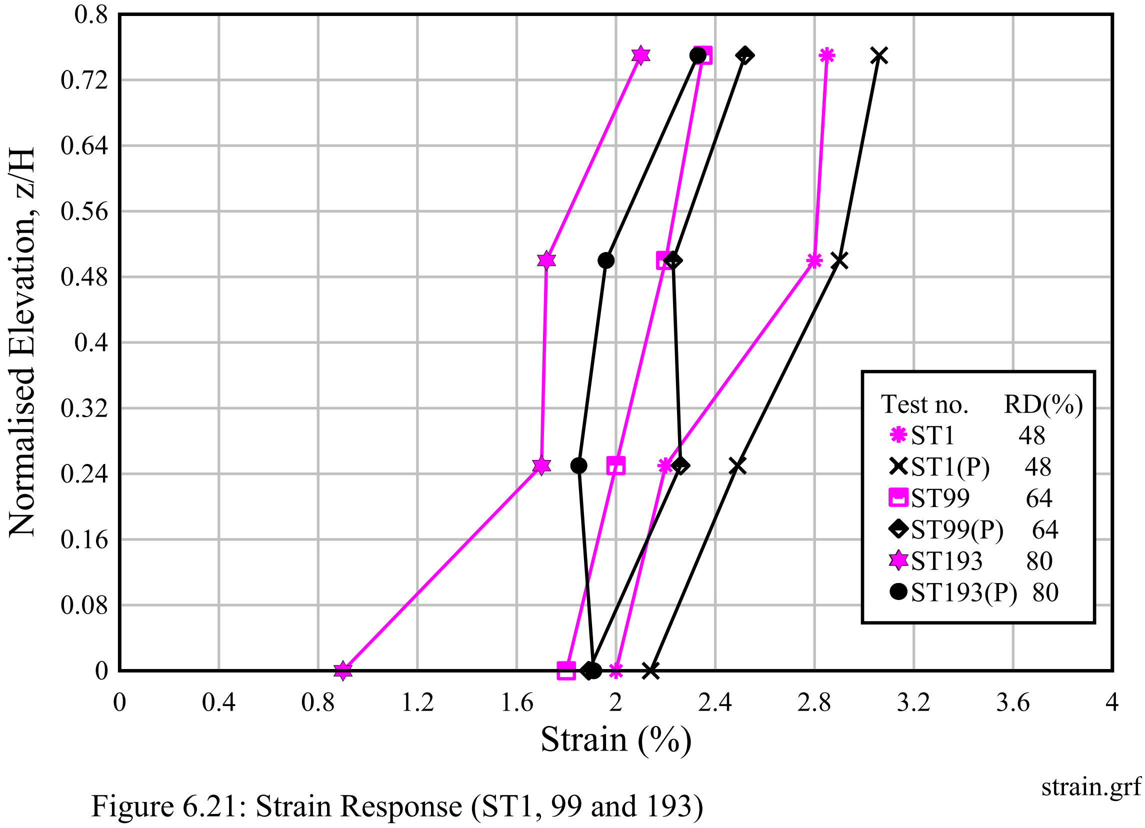

Figure 6.21: Strain Response (ST1, 99 and 193)

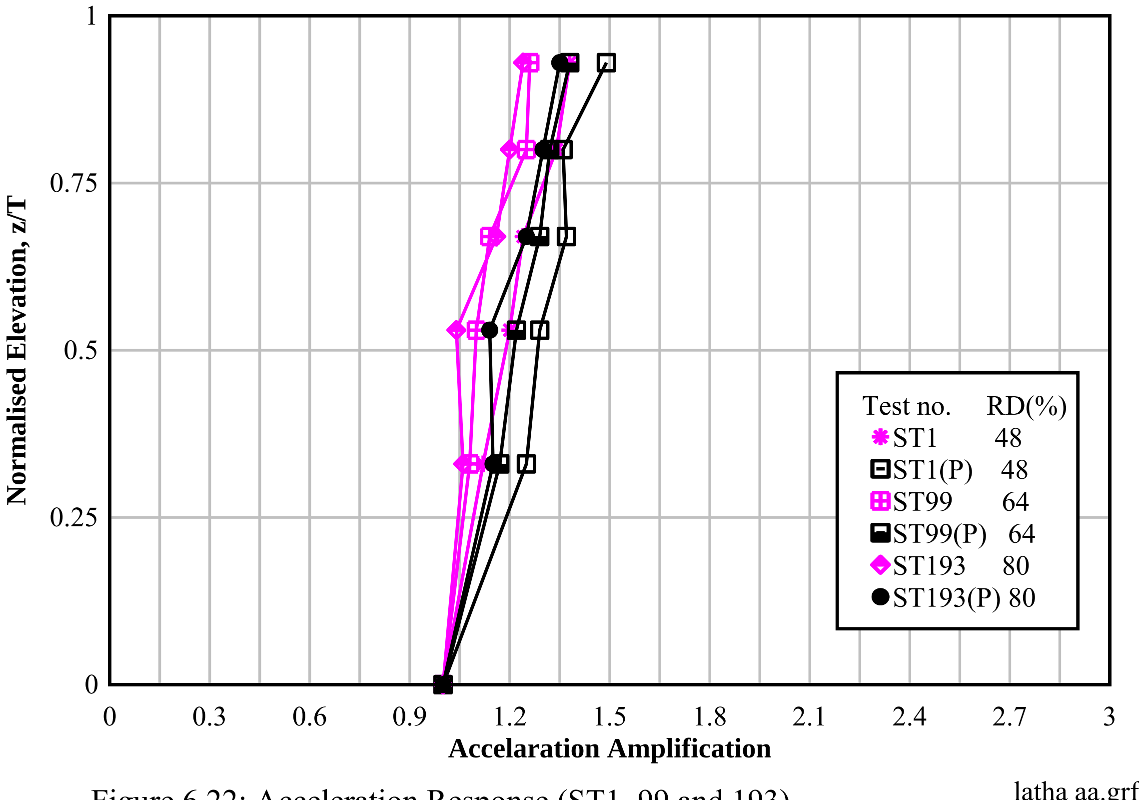

Figure 6.22: Acceleration Response (ST1, 99 and 193)

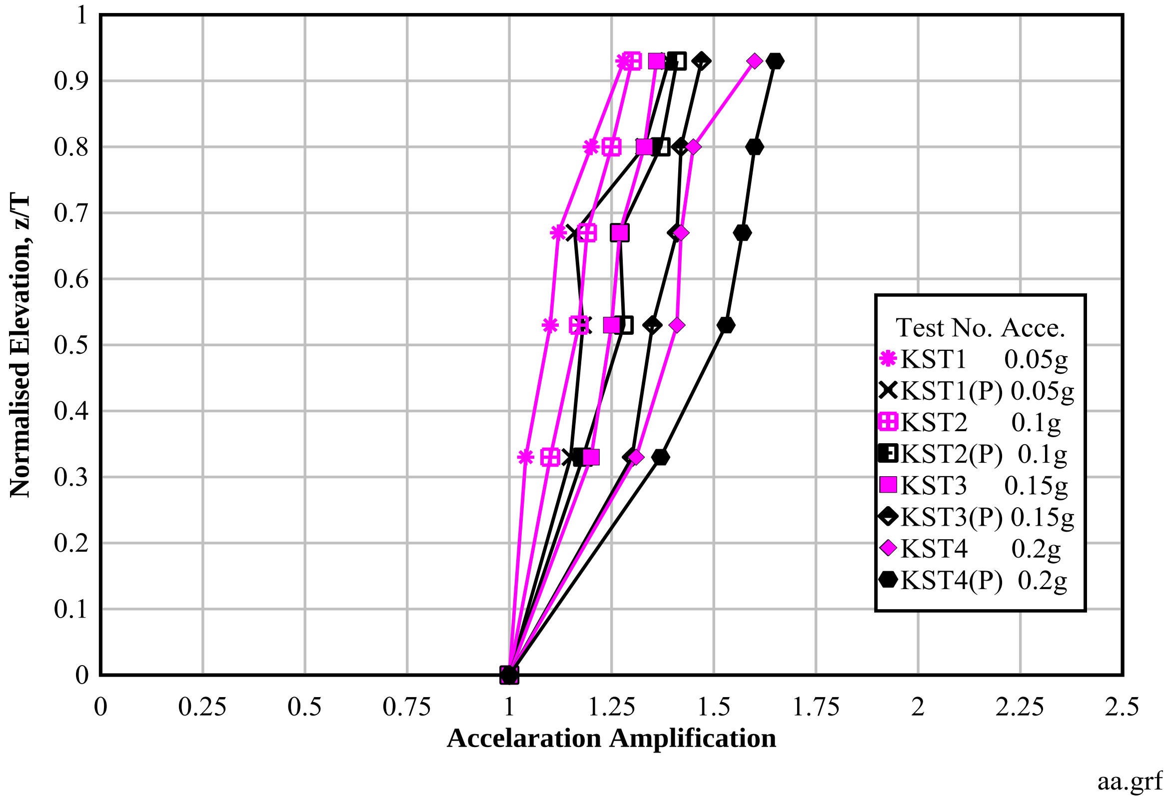

Figure 6.23: Effect of base acceleration on acceleration amplification (KST1-KST4)

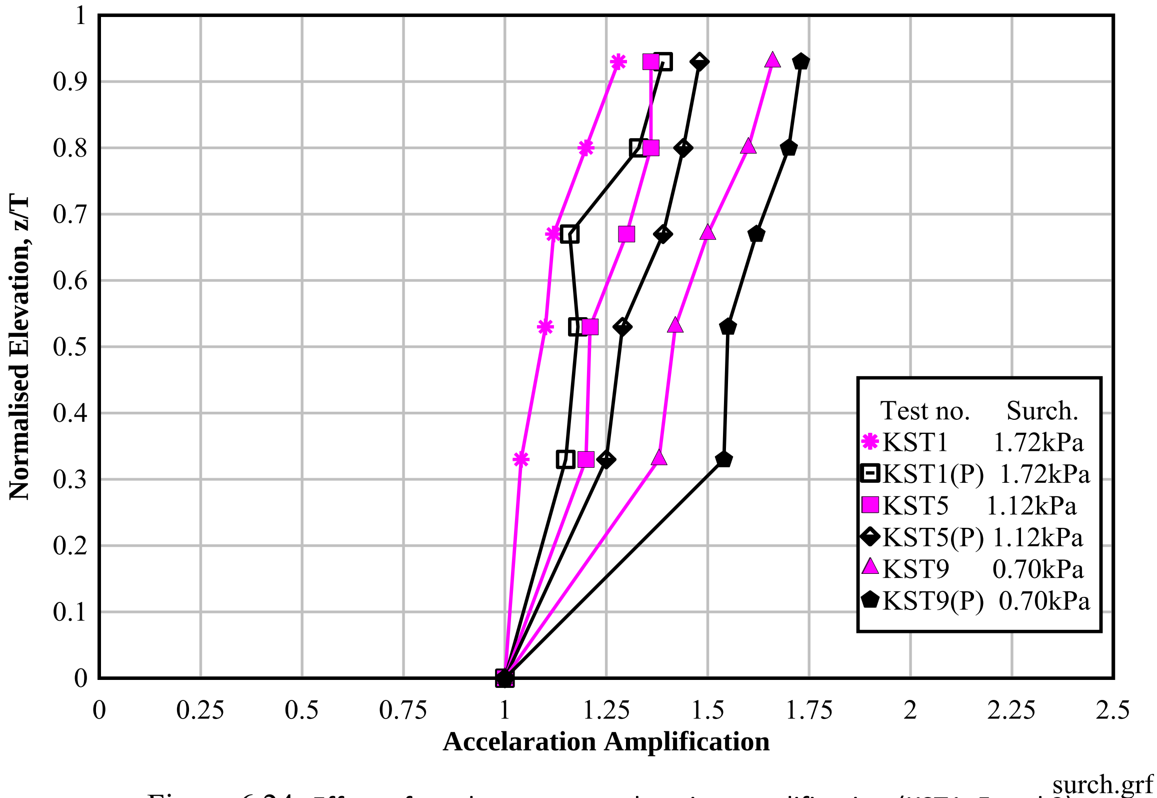

Figure 6.24: Effect of surcharge on acceleration amplification (KST1, 5 and 9)

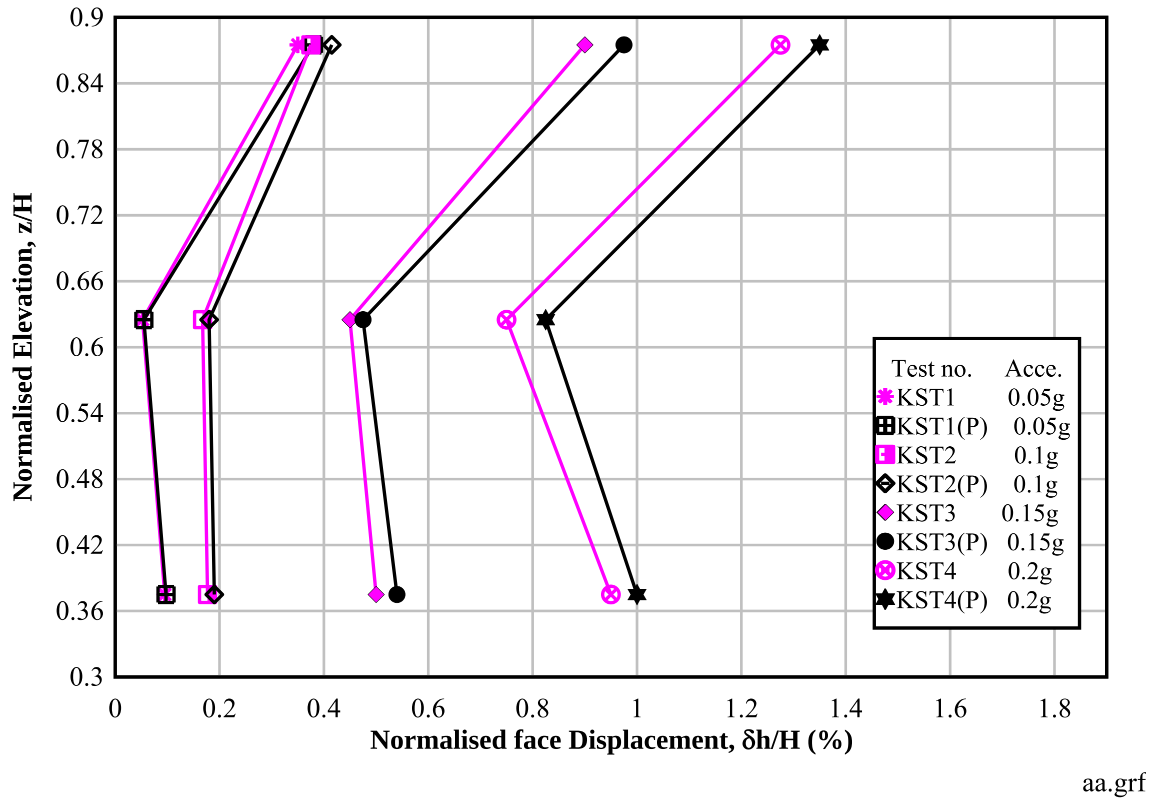

Figure 6.25: Effect of base acceleration on displacement profile (KST1-KST4)

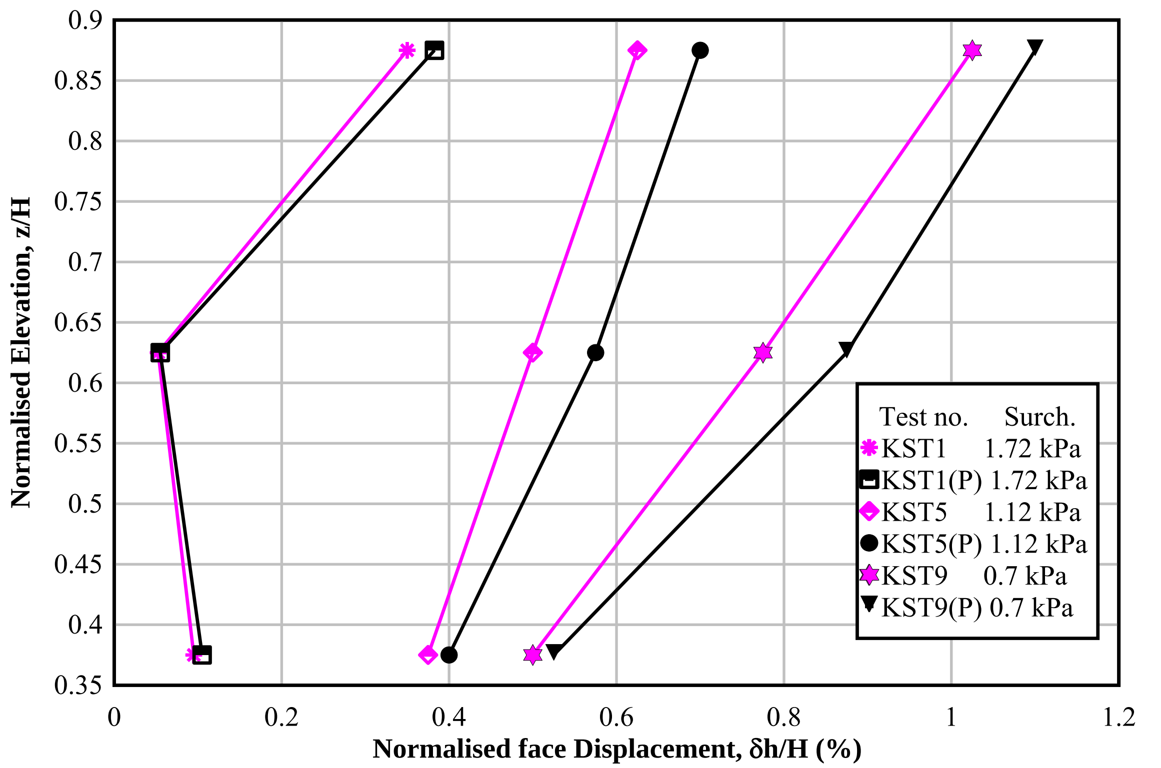

Figure 6.26: Effect of surcharge on displacement profile (KST1, 5 and 9)

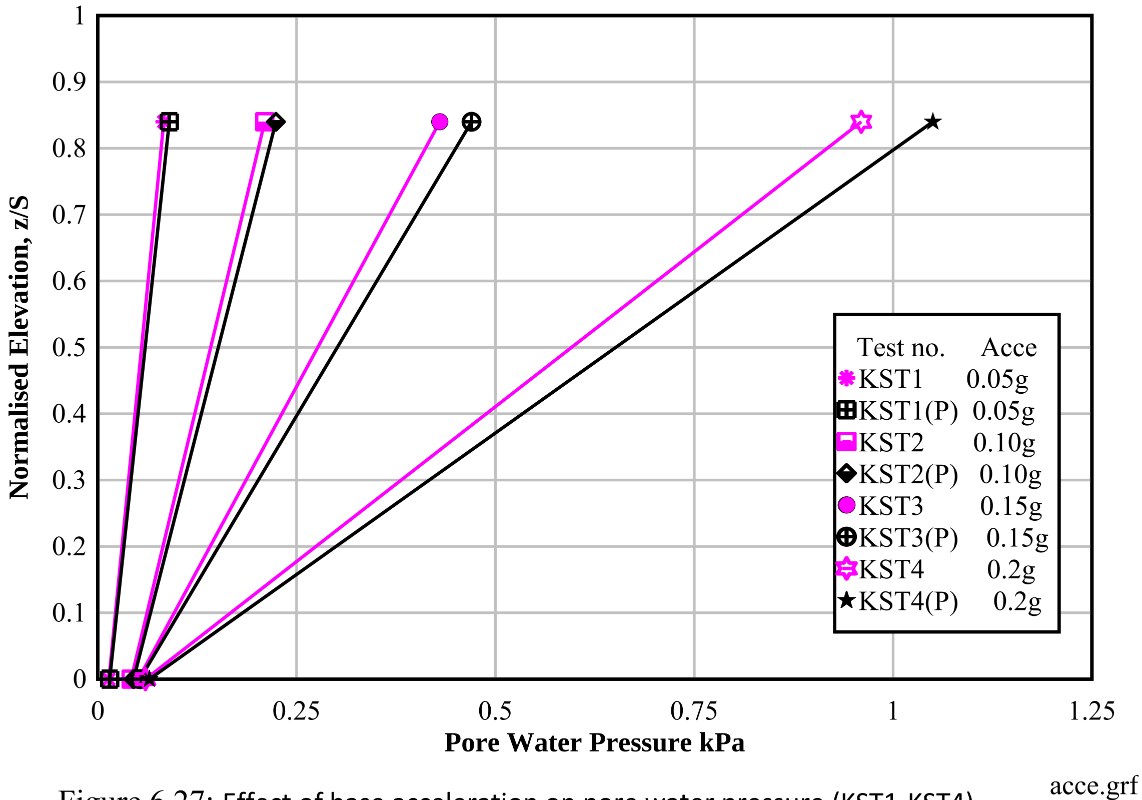

Figure 6.27: Effect of base acceleration on pore water pressure (KST1-KST4)

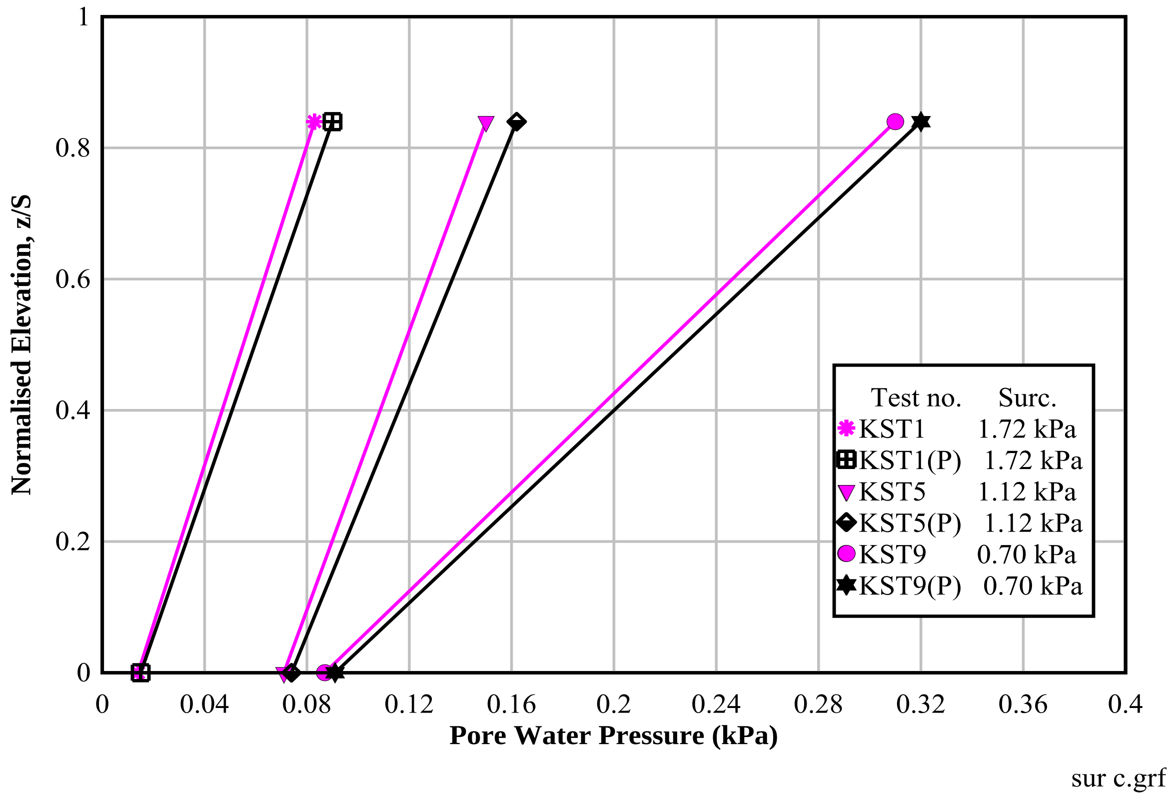

Figure 6.28: Effect of surcharge on pore water pressure (KST1, 5 and 9)

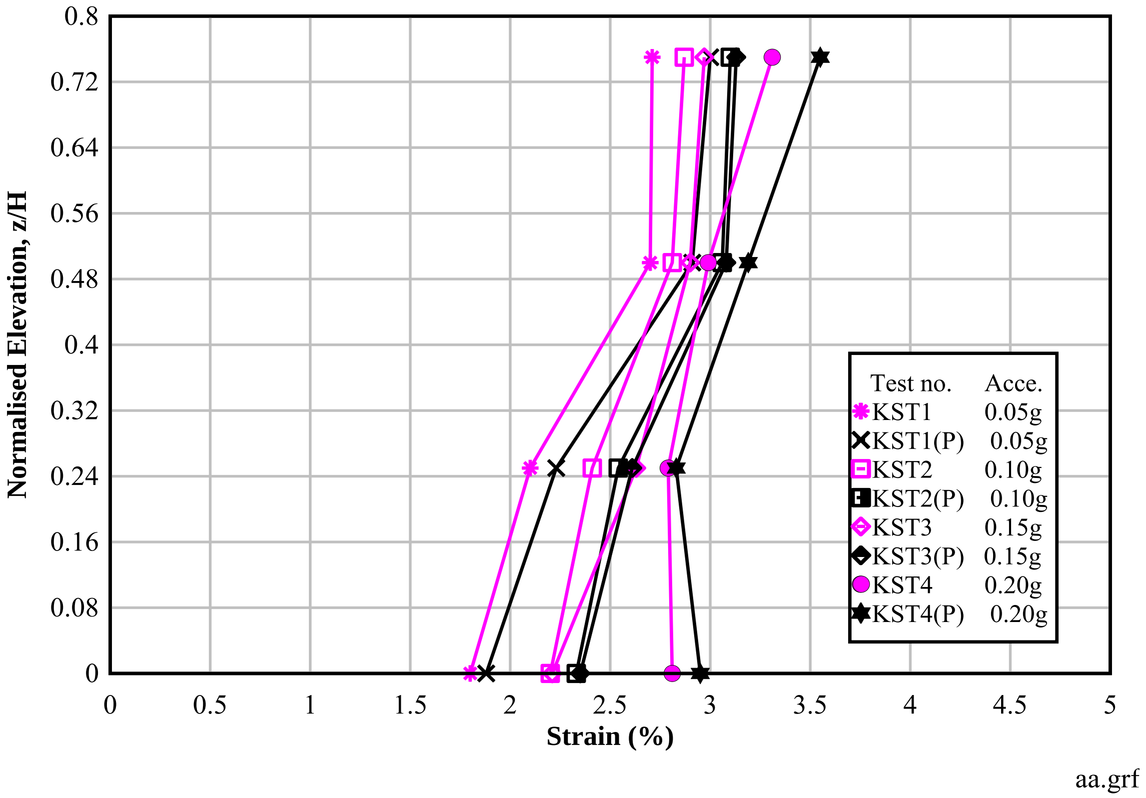

Figure 6.29: Effect of base acceleration on strain (KST1-KST4)

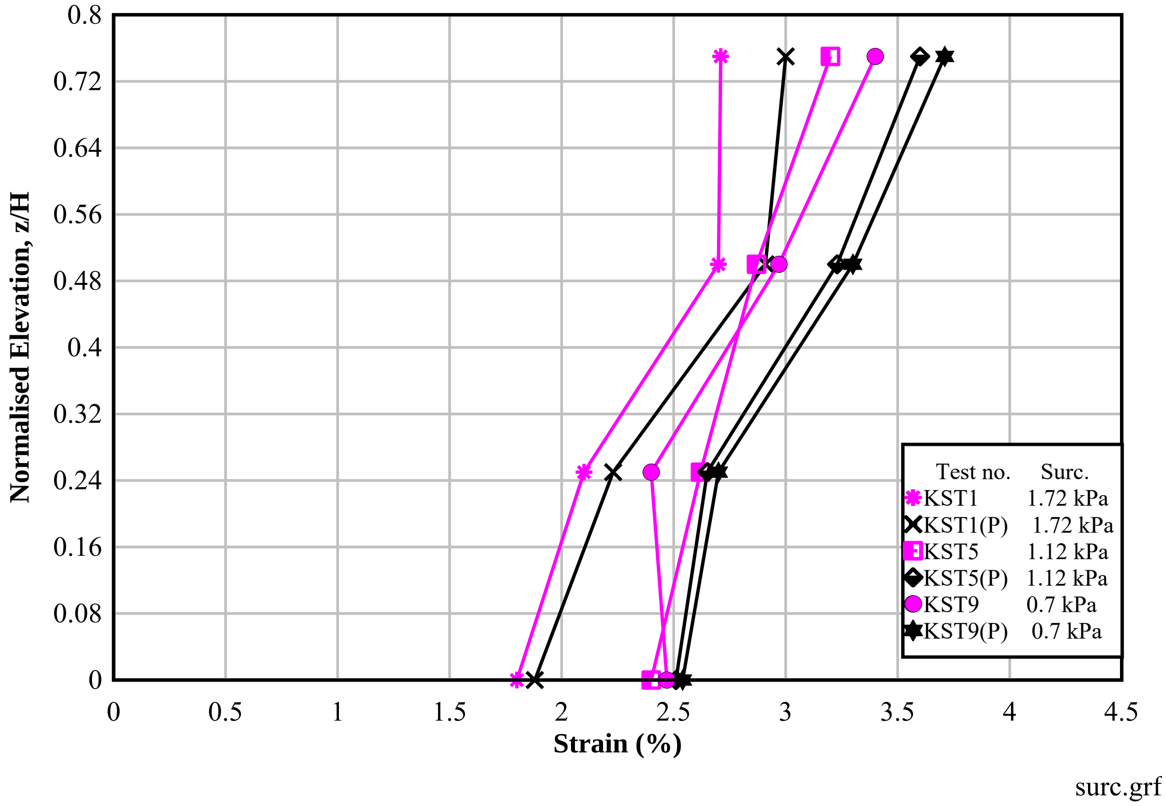

Figure 6.30: Effect of surcharge on strain (KST1, 5 and 9)

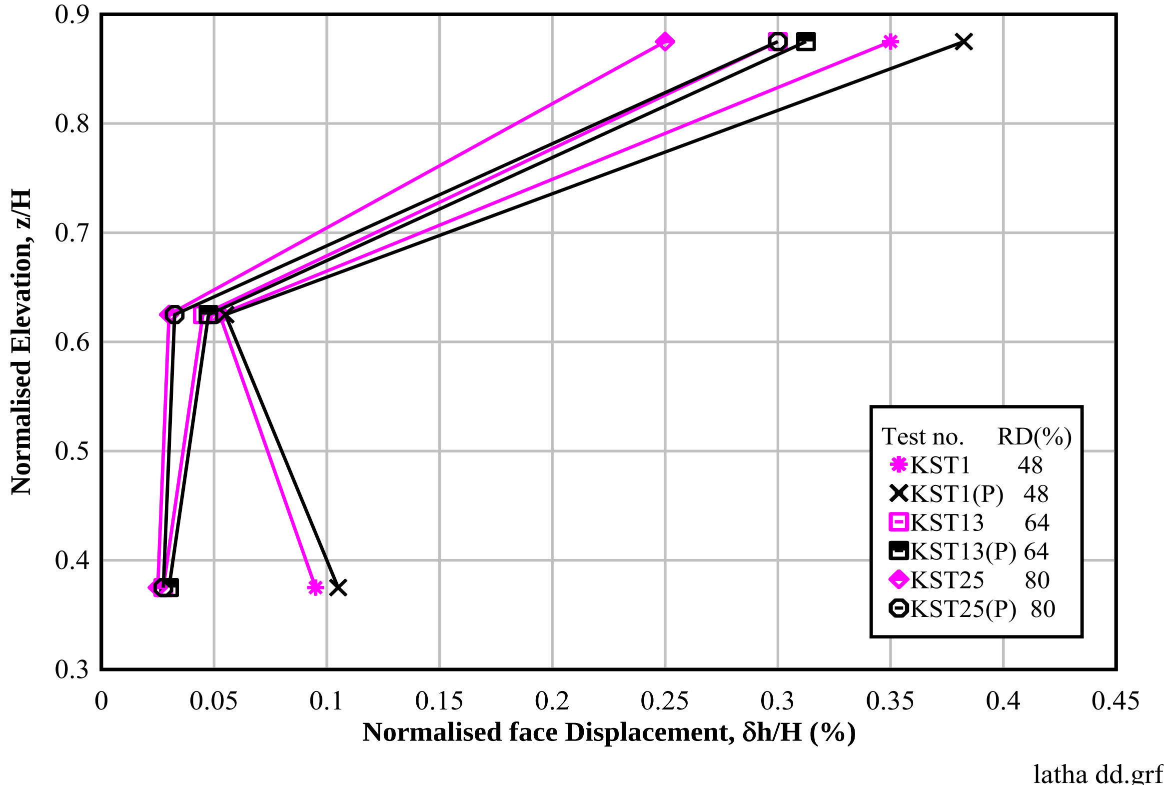

Figure 6.31: Displacement Response (KST1, 13 and 25)

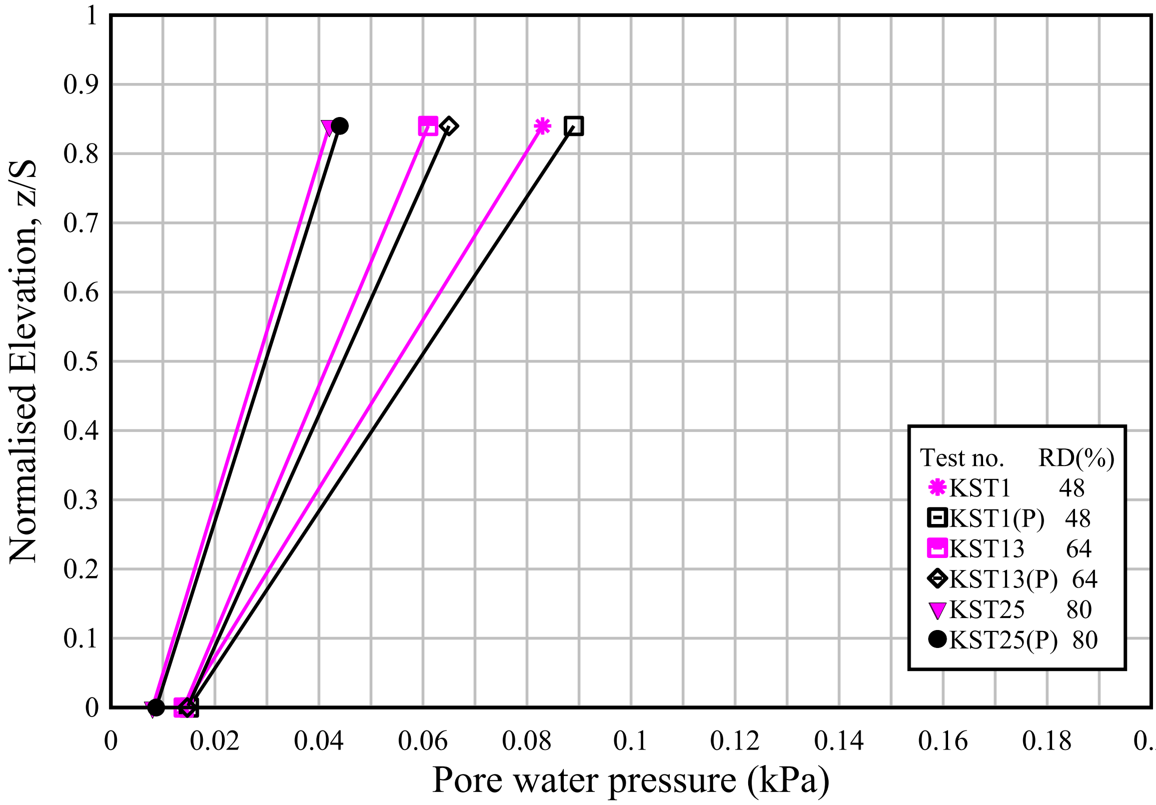

pore water pressure.grf

Figure 6.32: Pore Water Pressure Response (KST1, 13 and 25)

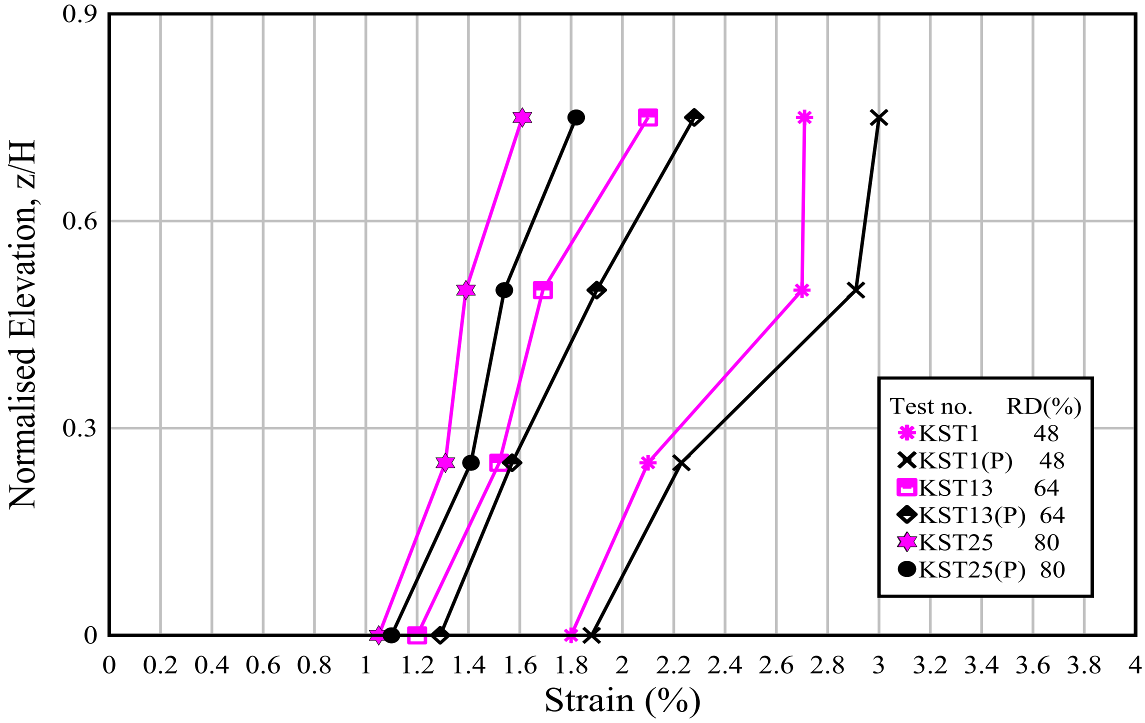

strain.grf

Figure 6.33: Strain Response (KST1, 13 and 25)

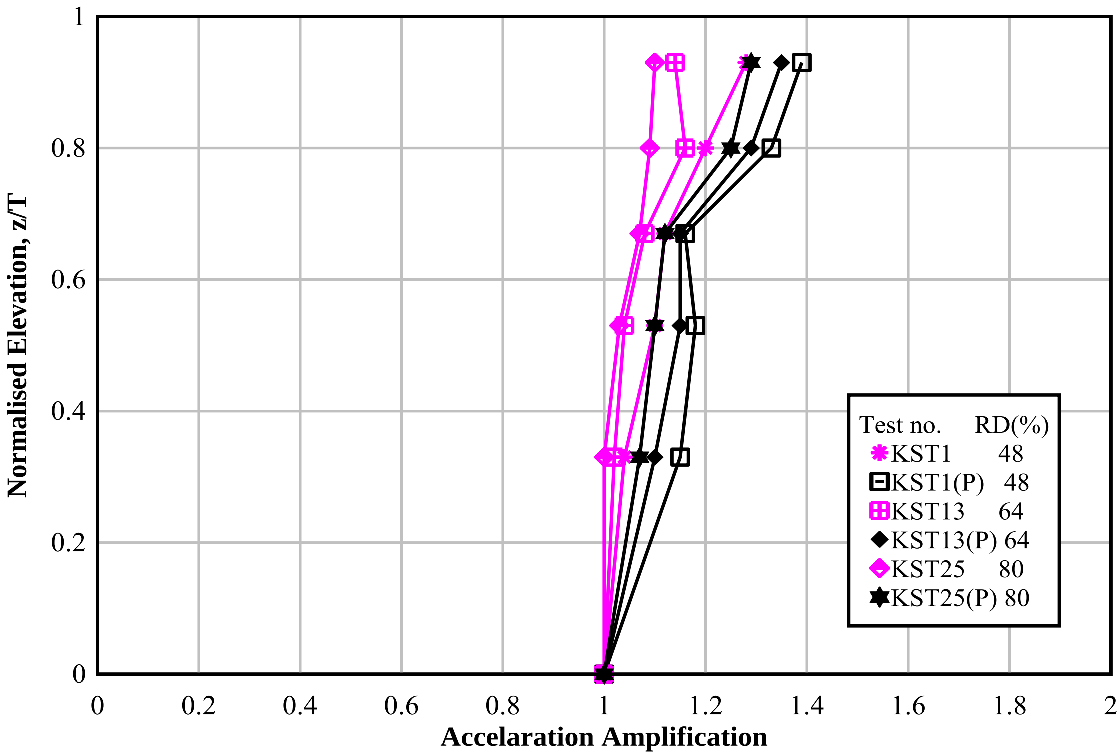

Figure 6.34: Acceleration Response (KST1, 13 and 25) latha aa.grf

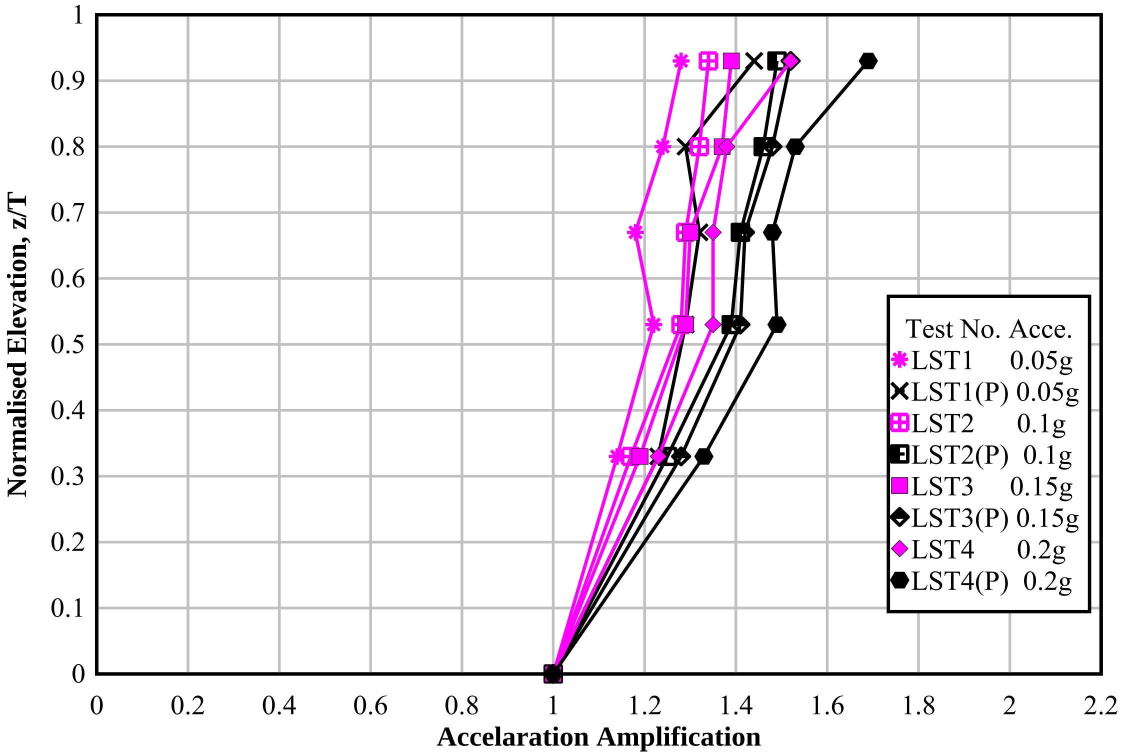

Figure 6.35: Effect of base acceleration on acceleration amplification (LST1-LST4) aa.grf

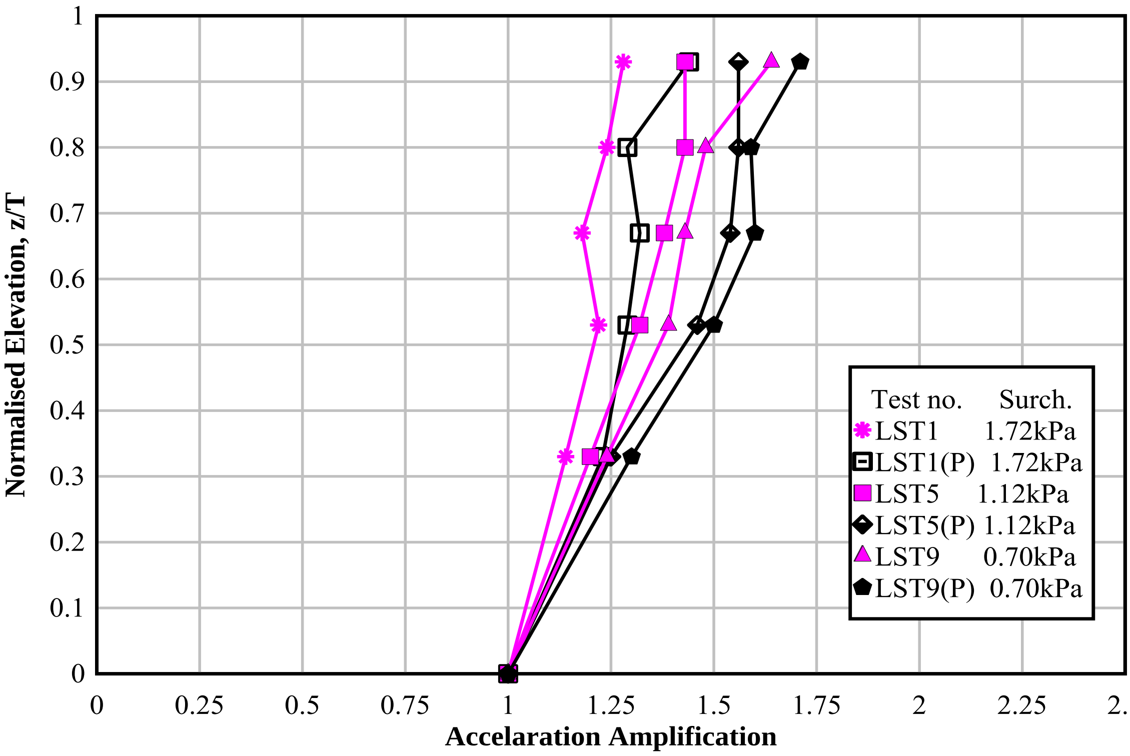

Figure 6.36: Effect of surcharge on acceleration amplification (LST1, 5 and 9) surch.grf

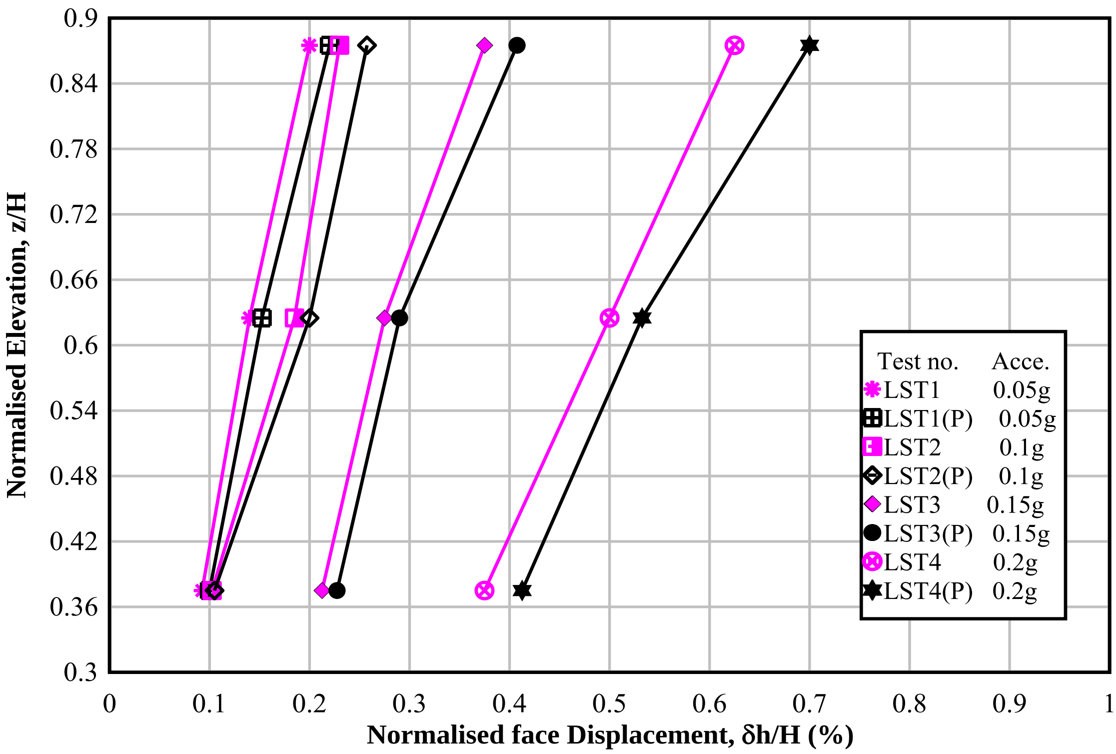

aa.grf

Figure 6.37: Effect of base acceleration on displacement profile (LST1- LST4)

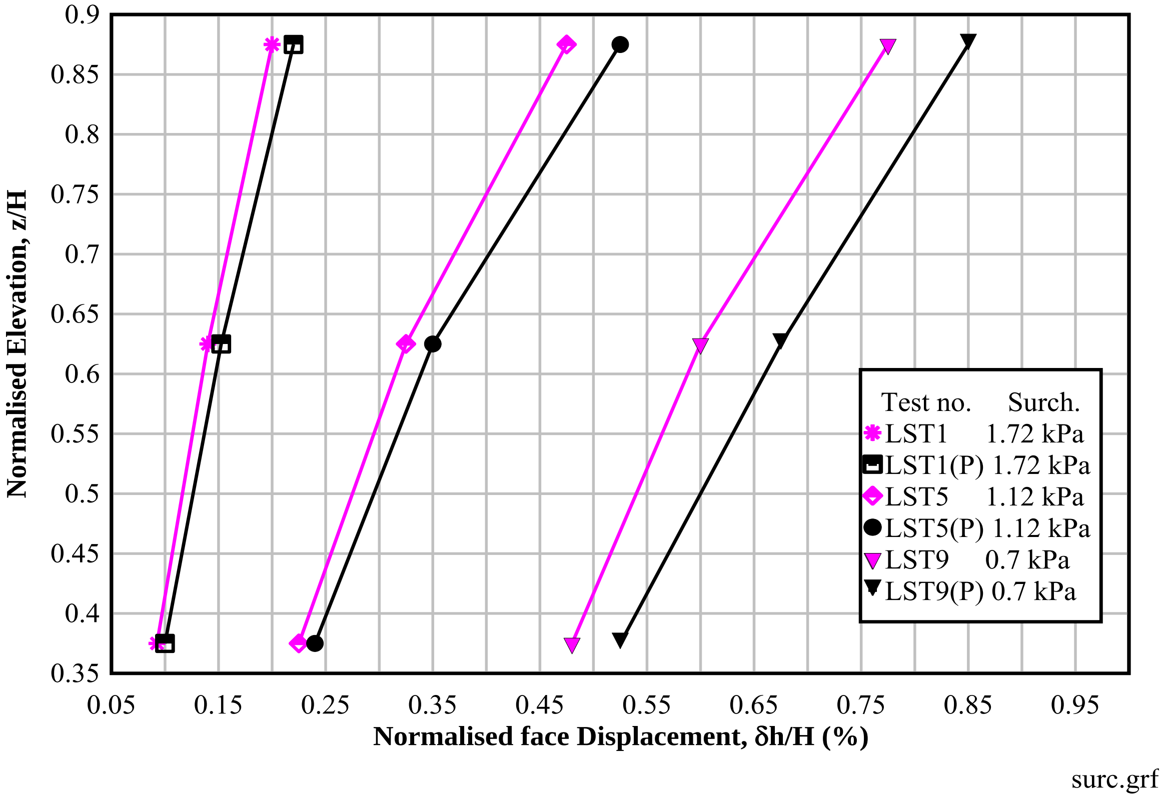

Figure 6.38: Effect of surcharge on displacement profile (LST1, 5 and 9)

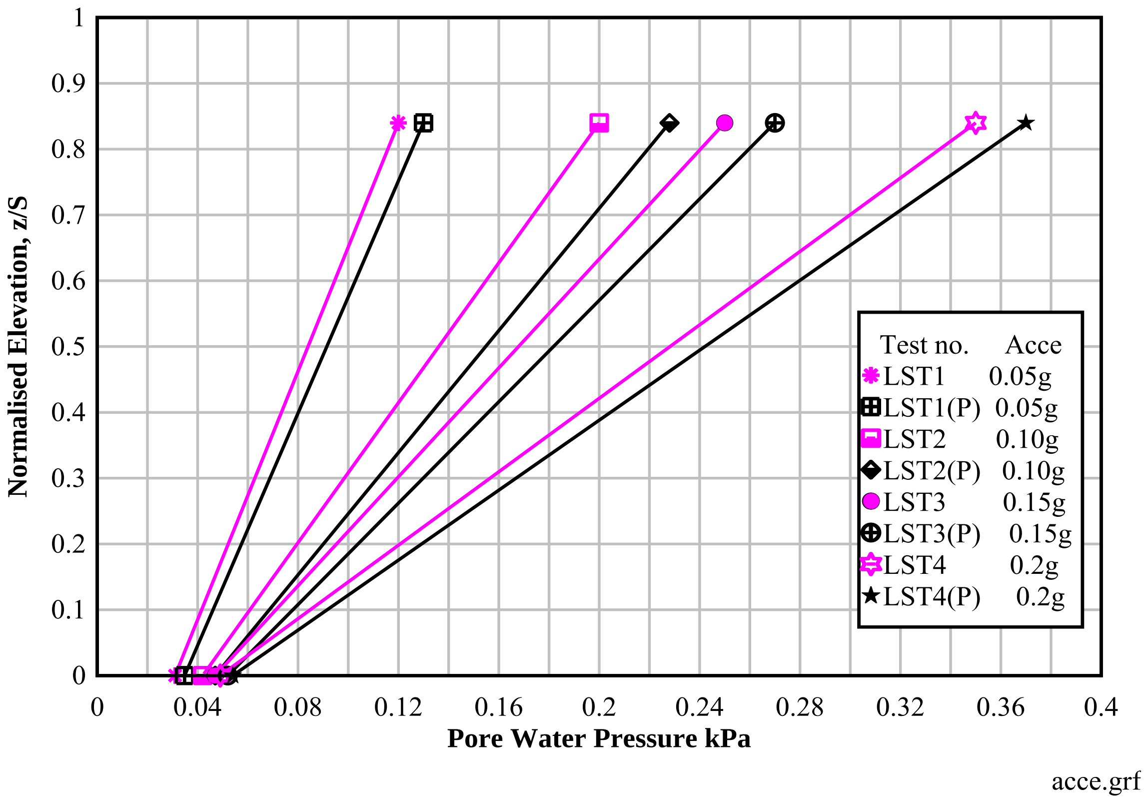

Figure 6.39: Effect of base acceleration on pore water pressure (LST1-LST4)

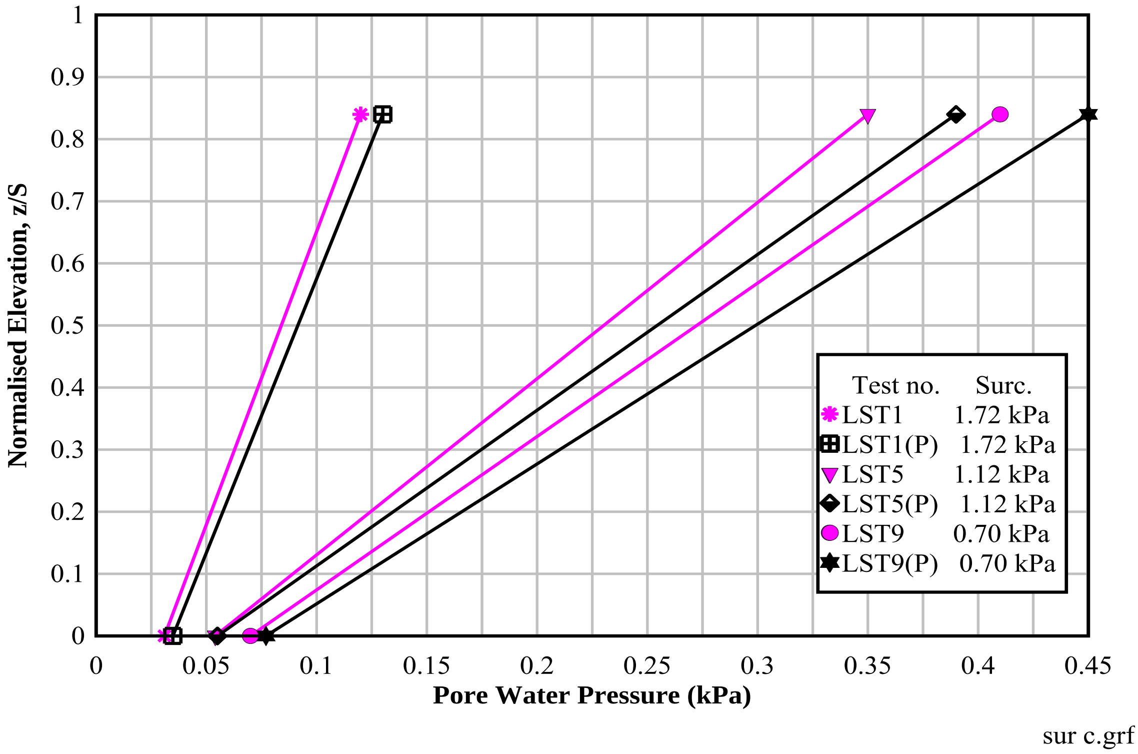

Figure 6.40: Effect of surcharge on pore water pressure (LST1, 5 and 9)

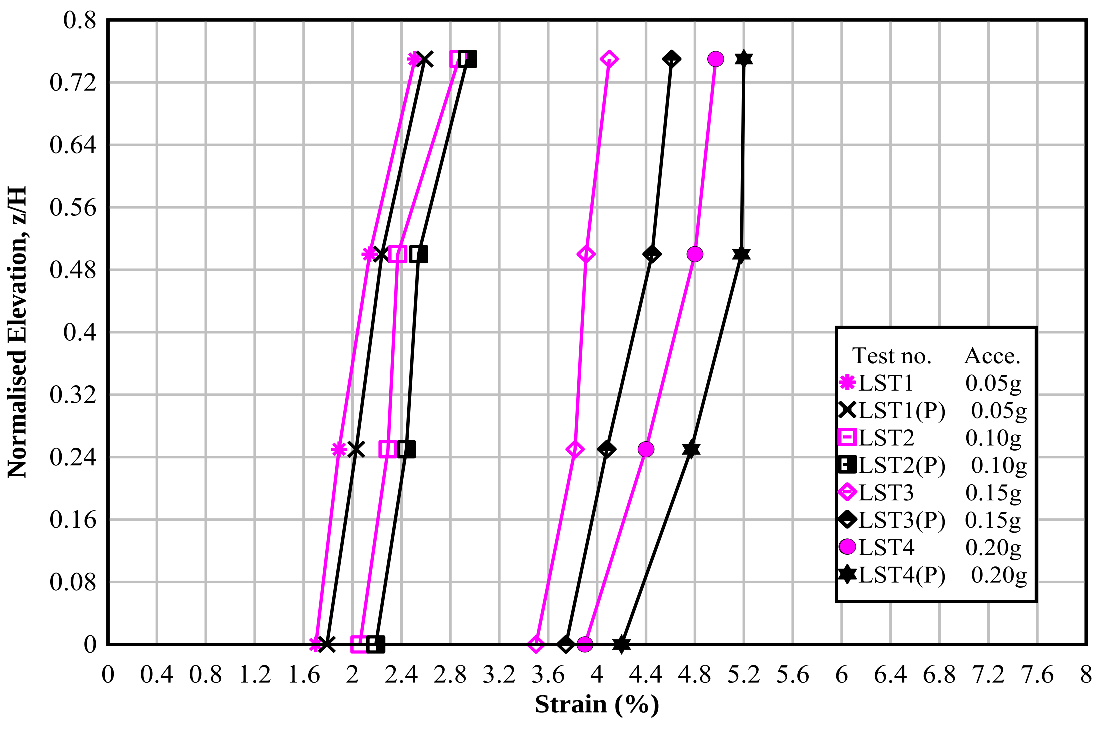

Figure 6.41.: Effect of base acceleration on strain (LST1-LST4)

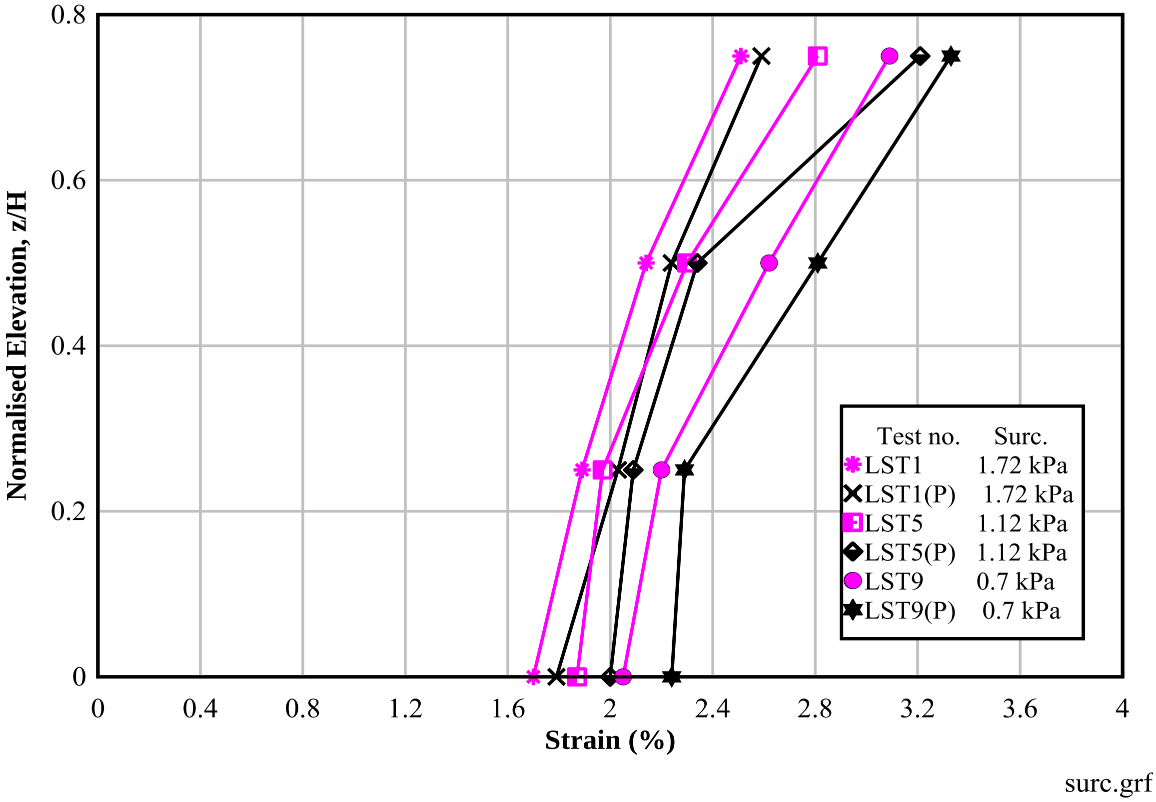

Figure 6.42: Effect of surcharge on strain (LST1, 5 and 9)

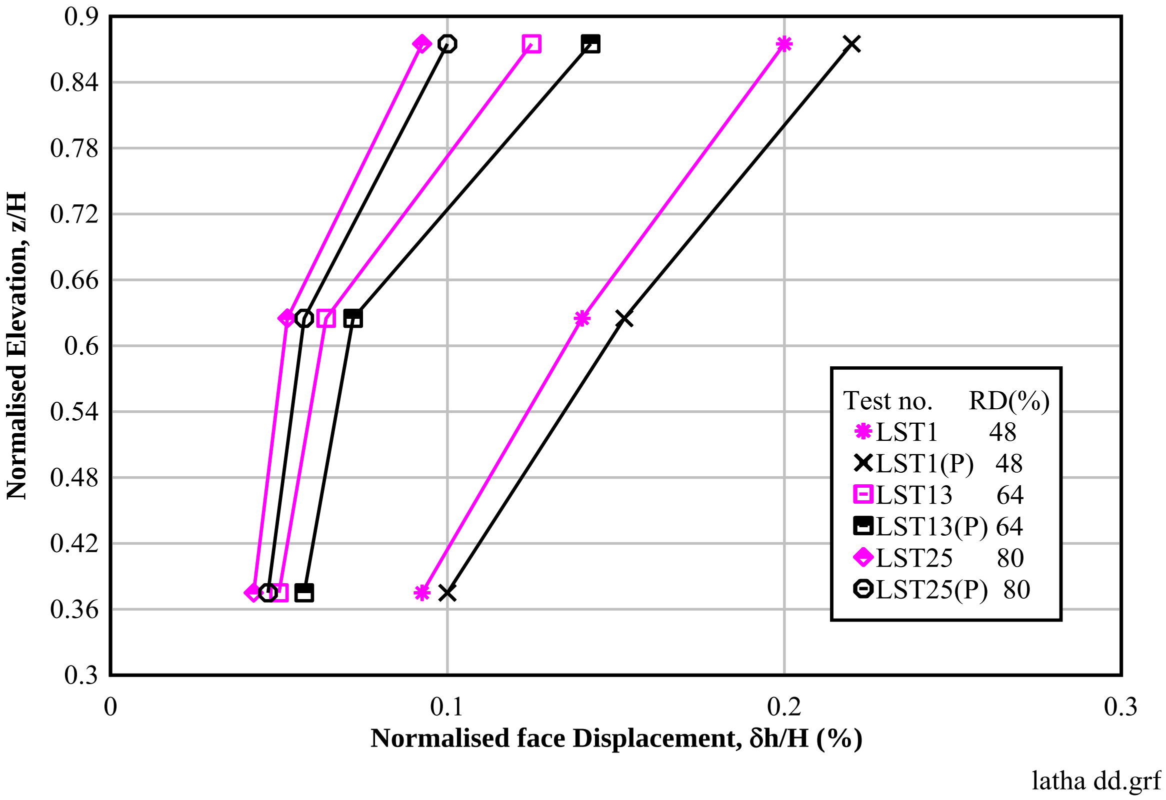

Figure 6.43: Displacement Response (LST1, 13 and 25)

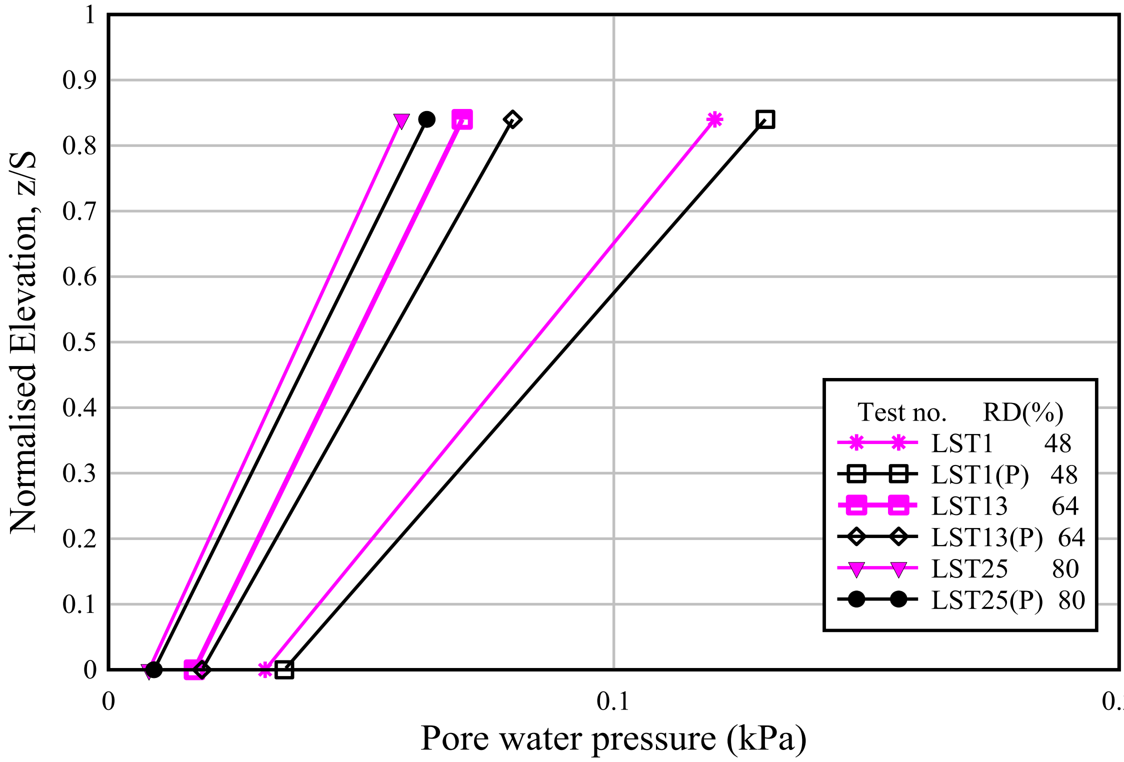

Figure 6.44: Pore Water Pressure Response (LST1, 13 and 25) pore water pressure.grf

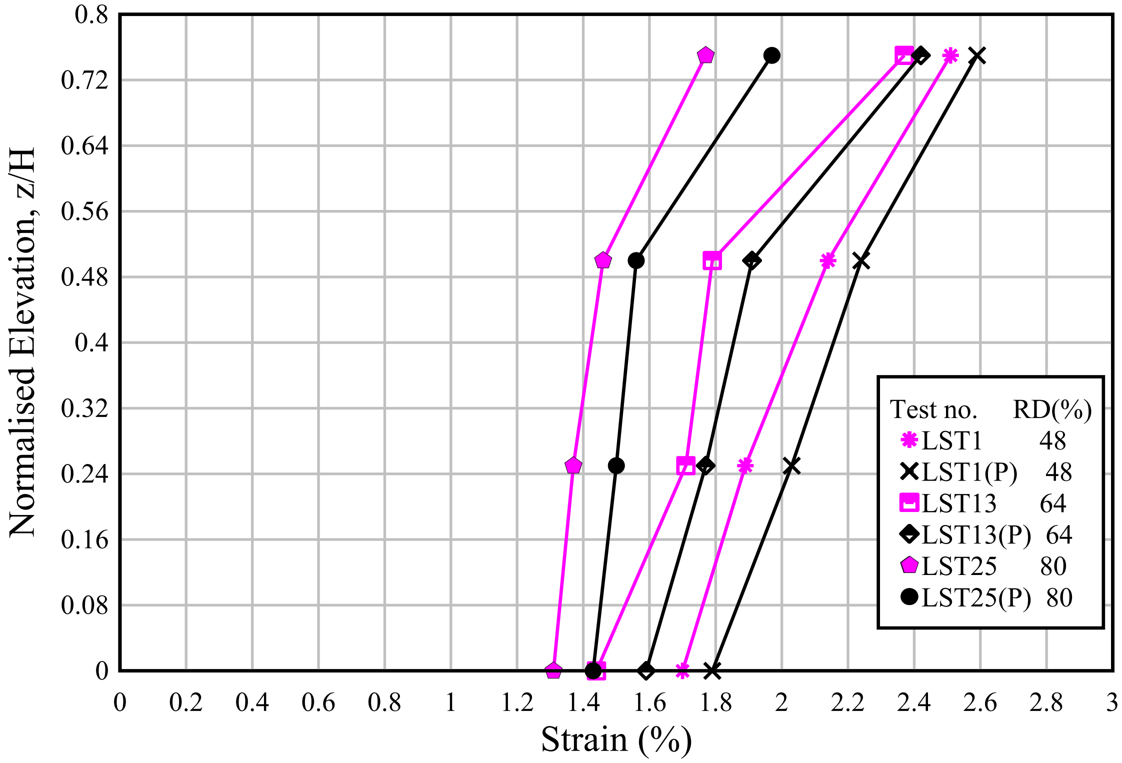

strain.grf

Figure 6.45: Strain Response (LST1, 13 and 25)

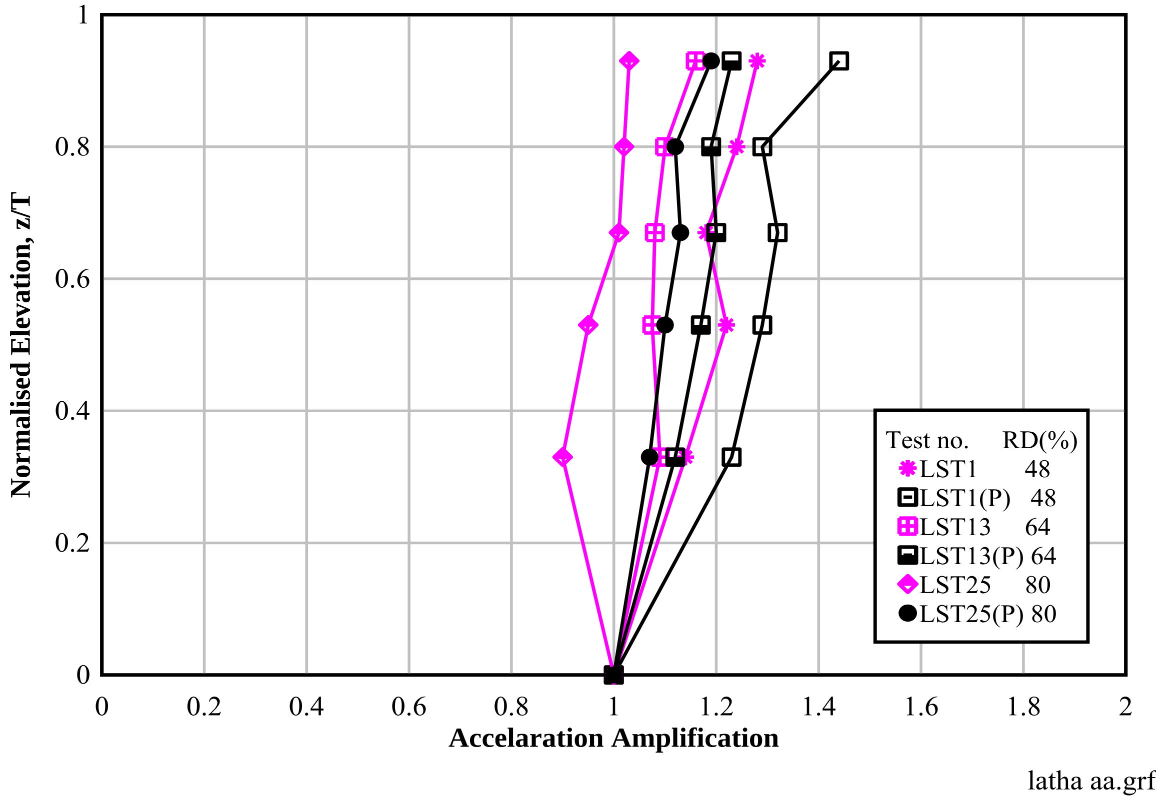

Figure 6.46: Acceleration Response (LST1, 13 and 25)

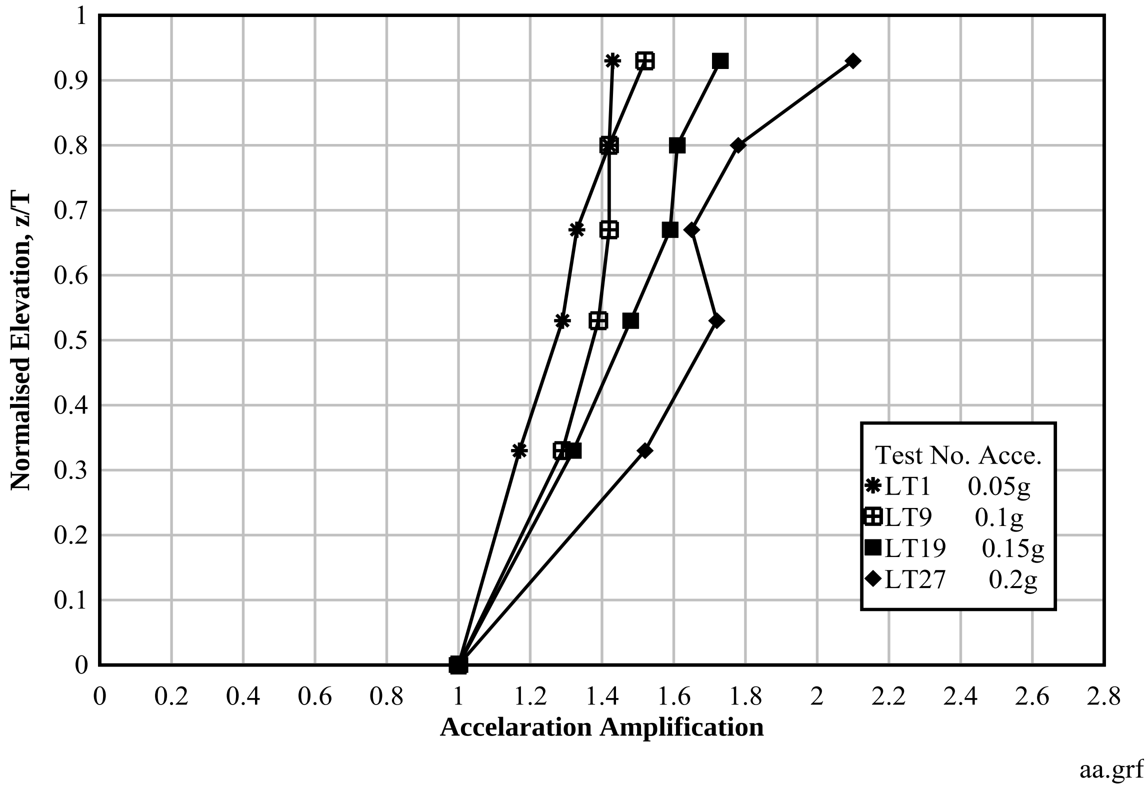

Figure 6.47: Effect of base acceleration on acceleration amplification (LT1, 9, 19 and 27)

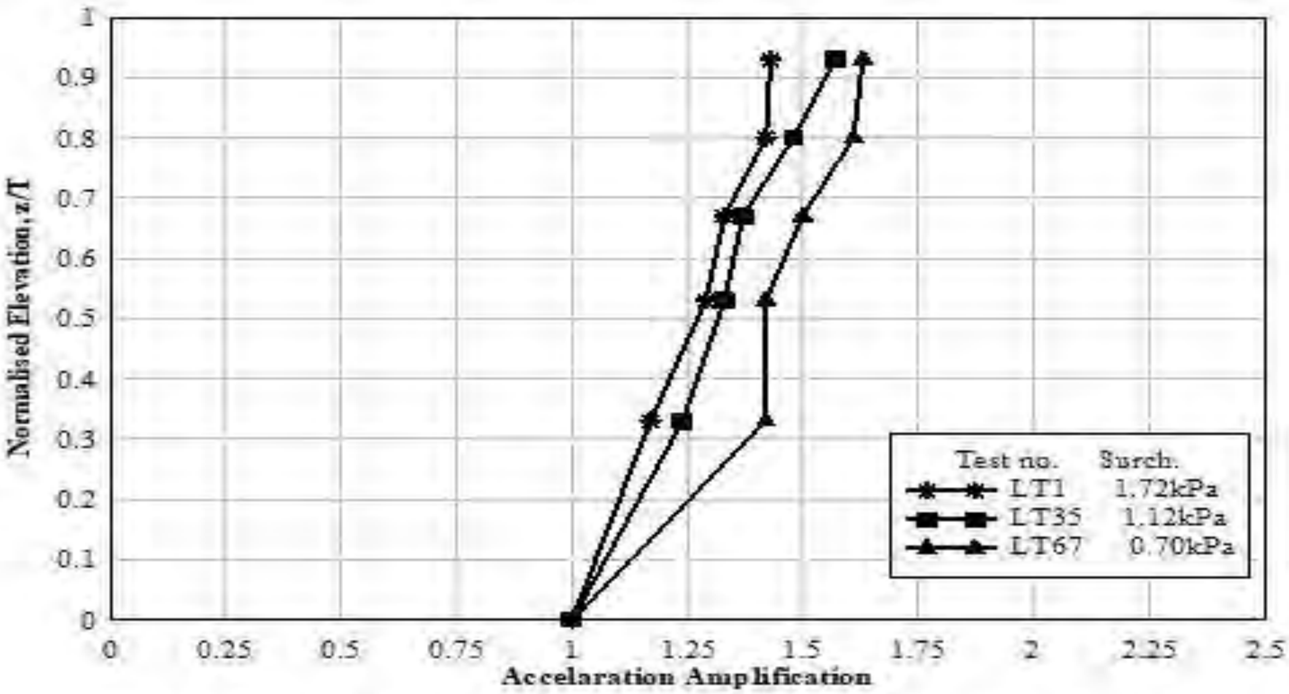

Figure 6.48: Effect of surcharge on acceleration amplification (LT1, 35 and 67)

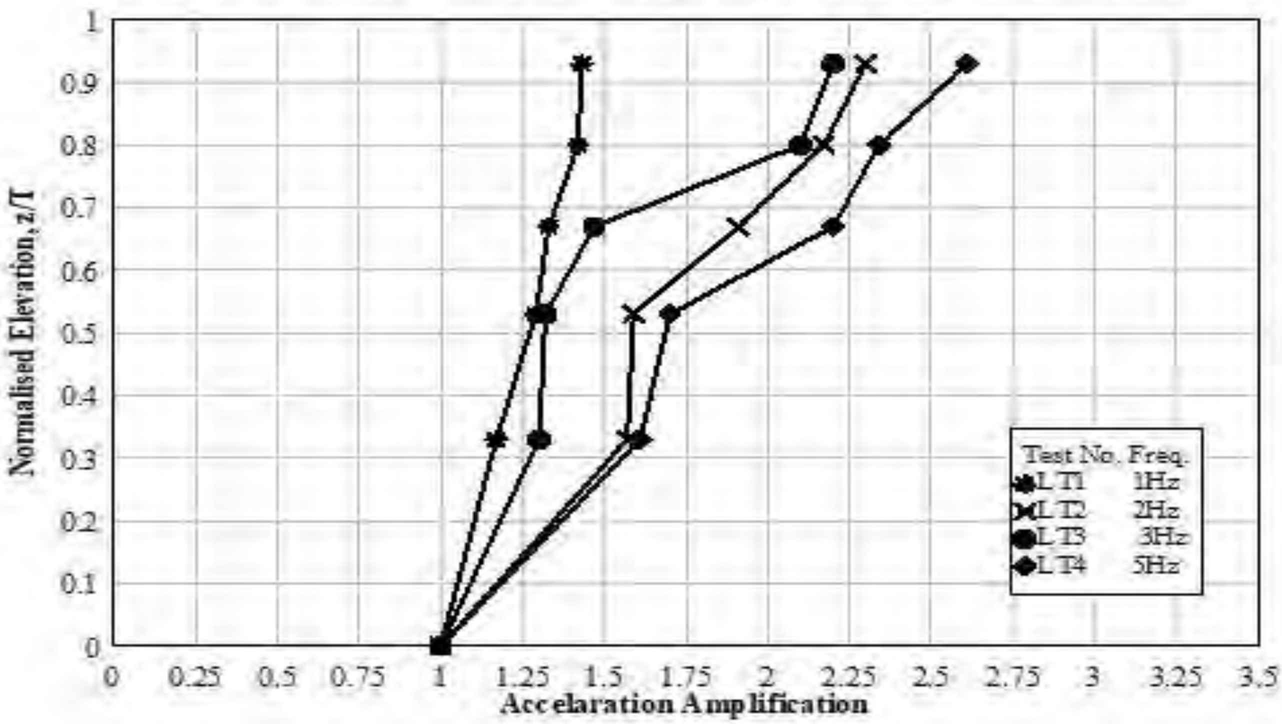

Figure 6.49: Effect of frequency on acceleration amplification (LT1-LT4)

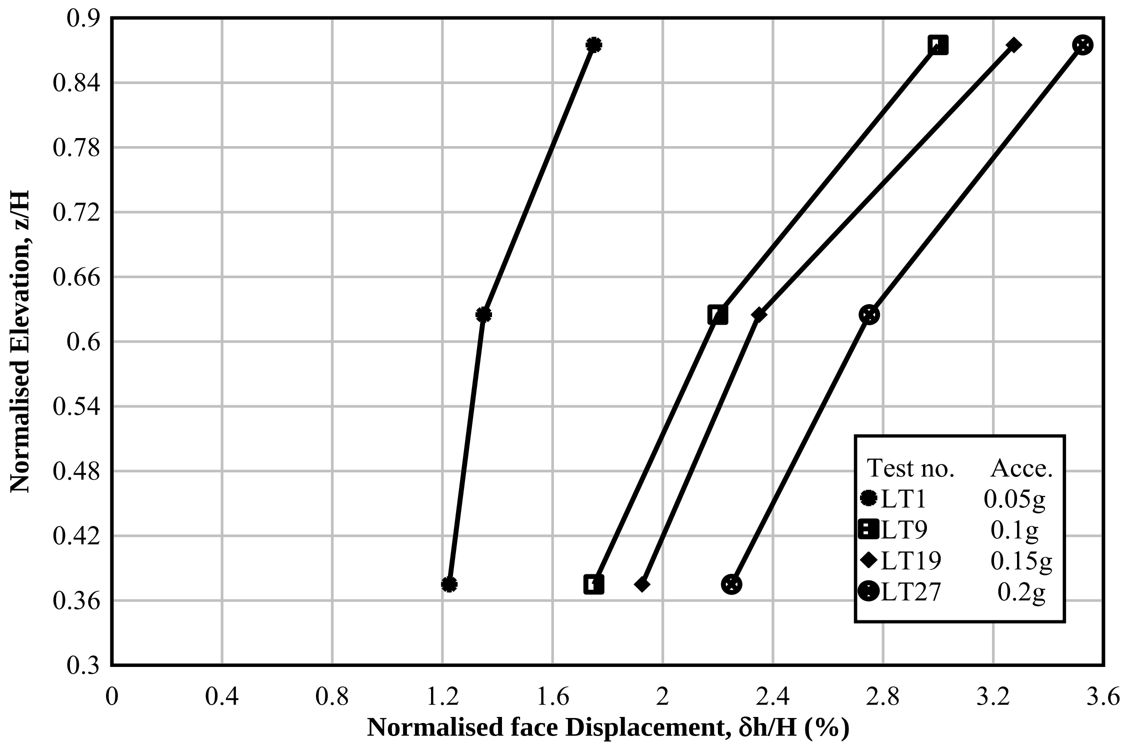

Figure 6.50: Effect of base acceleration on displacement profile (LT1, 9, 19 and 27) aa.grf

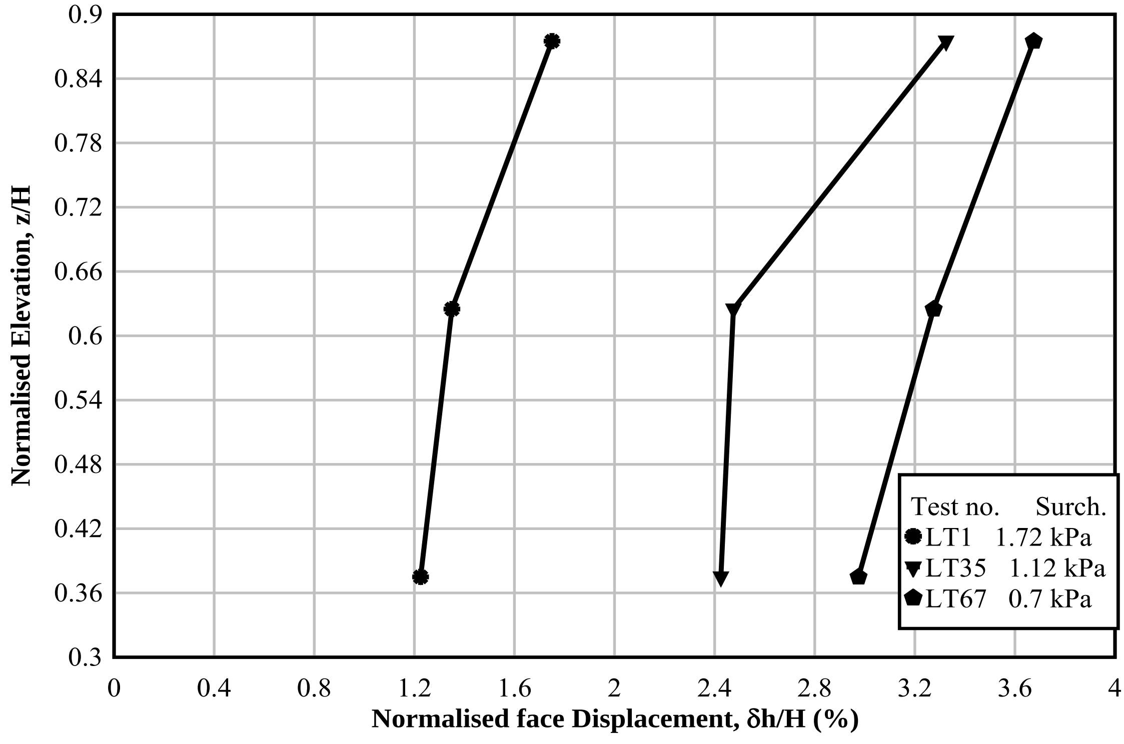

surc.grf

Figure 6.51: Effect of surcharge on displacement profile (LT1, 35 and 67)

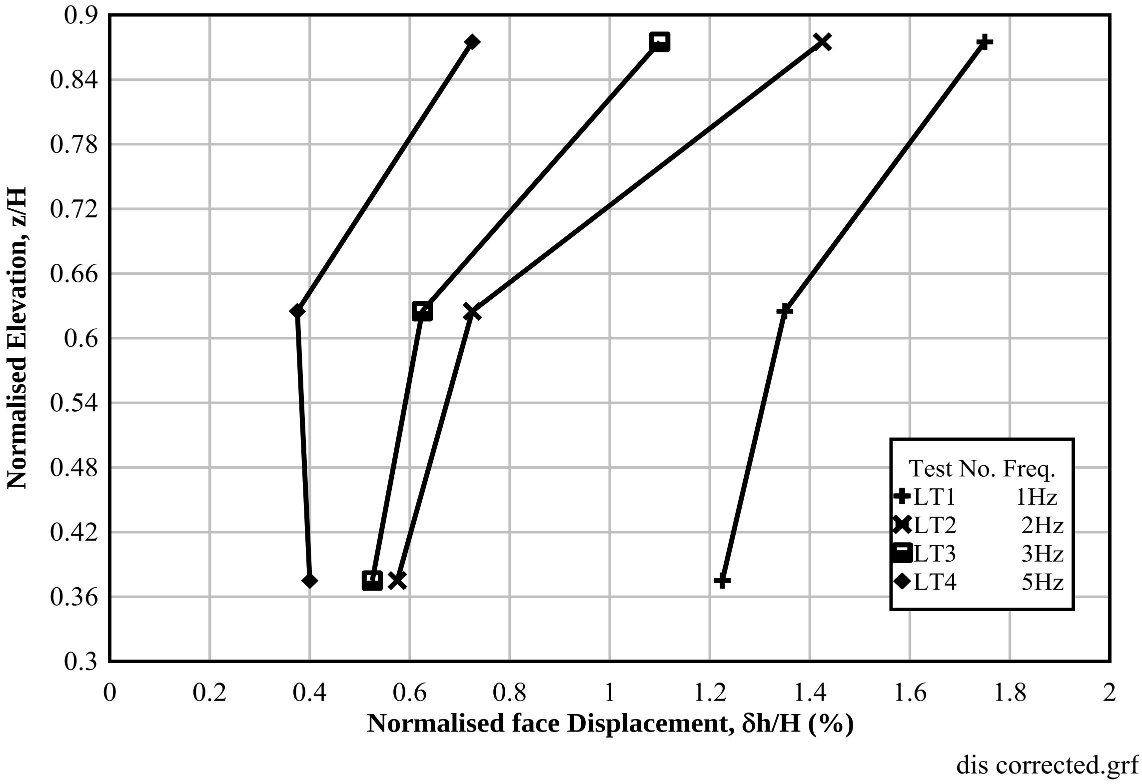

Figure 6.52: Effect of frequency on displacement profile (LT1-LT4)

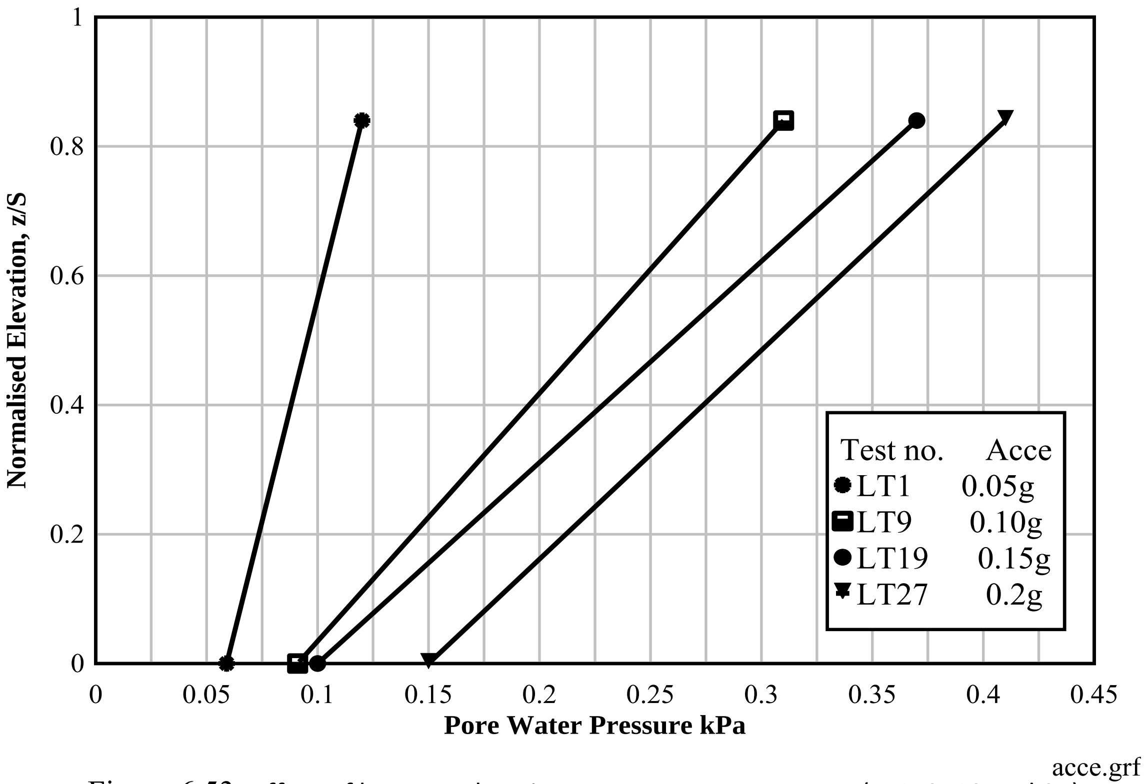

Figure 6.53: Effect of base acceleration on pore water pressure (LT1, 9, 19 and 27)

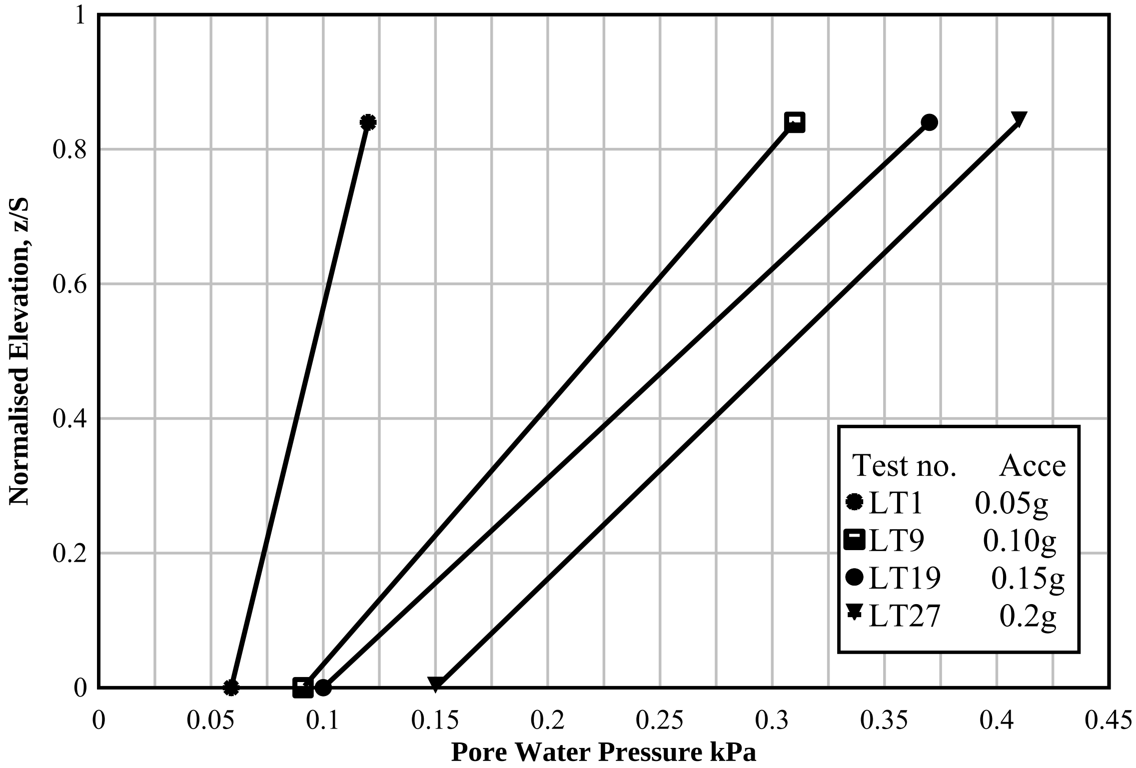

acce.grf

Figure 6.54: Effect of surcharge on pore water pressure (LT1, 35 and 67)

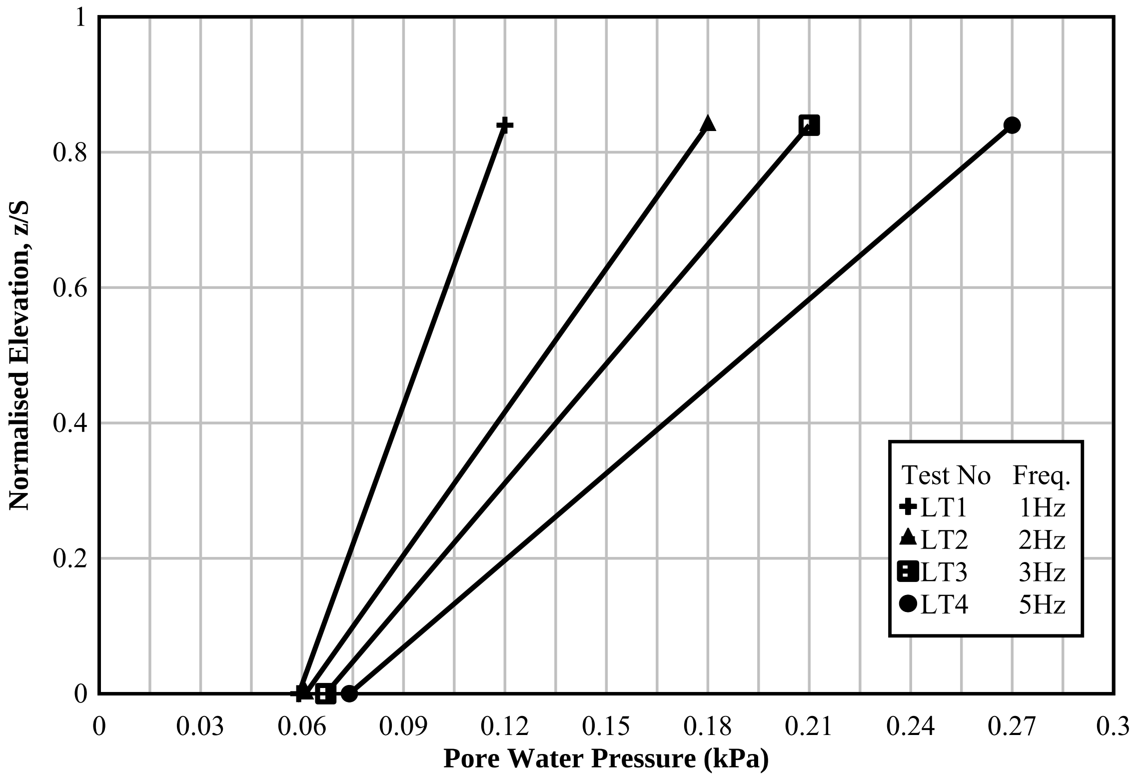

Figure 6.55: Effect of frequency on pore water pressure (LT1-LT4)

frq.grf

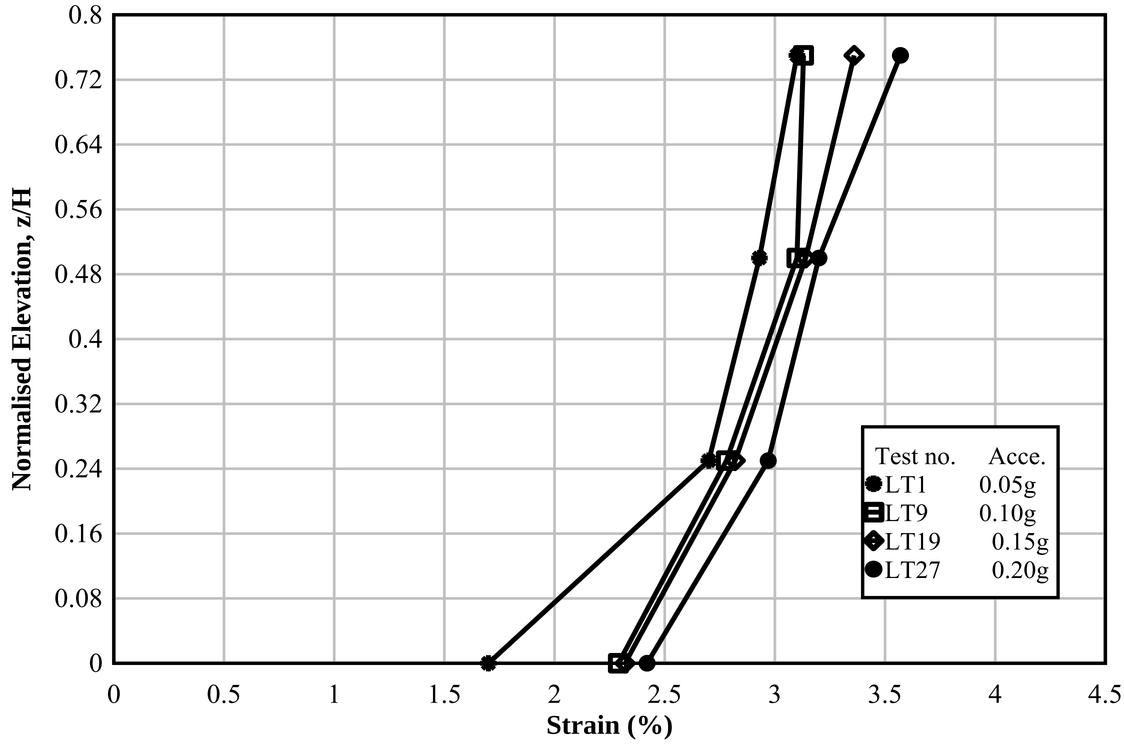

Figure 6.56: Effect of base acceleration on strain (LT1, 9, 19 and 27)

aa.grf

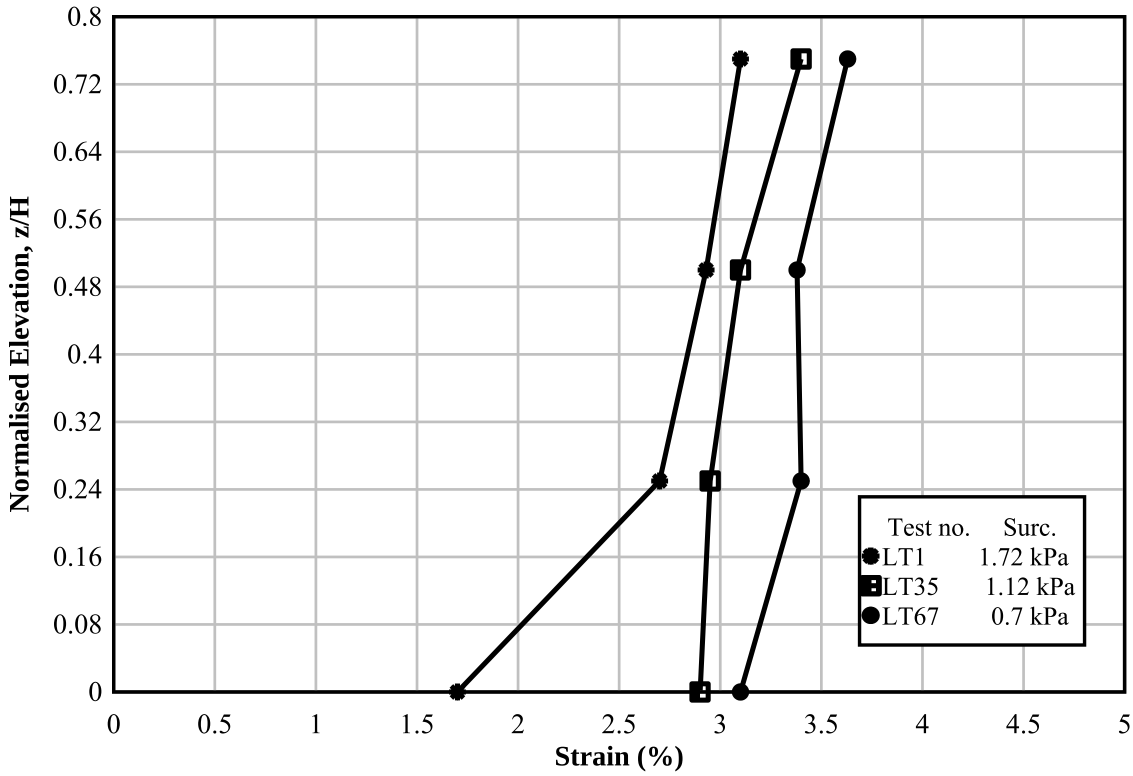

Figure 6.57: Effect of surcharge on strain (LT1, 35 and 67)

surc.grf

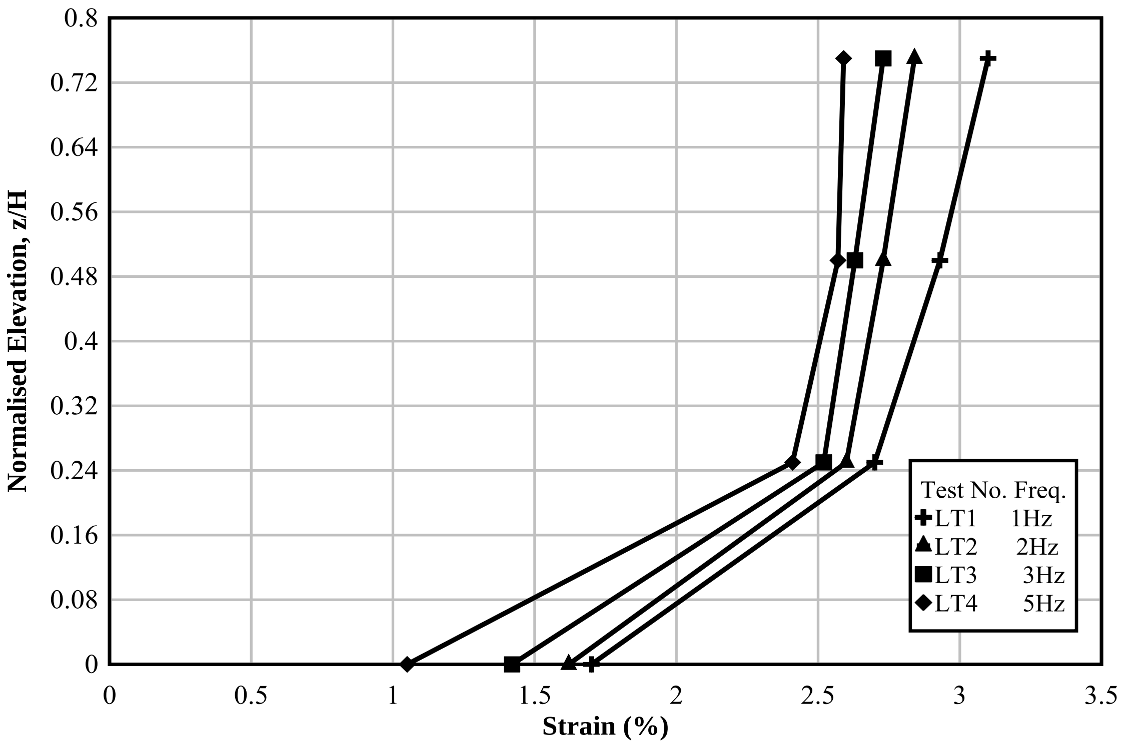

Figure 6.58: Effect of frequency on strain (LT1-LT4)

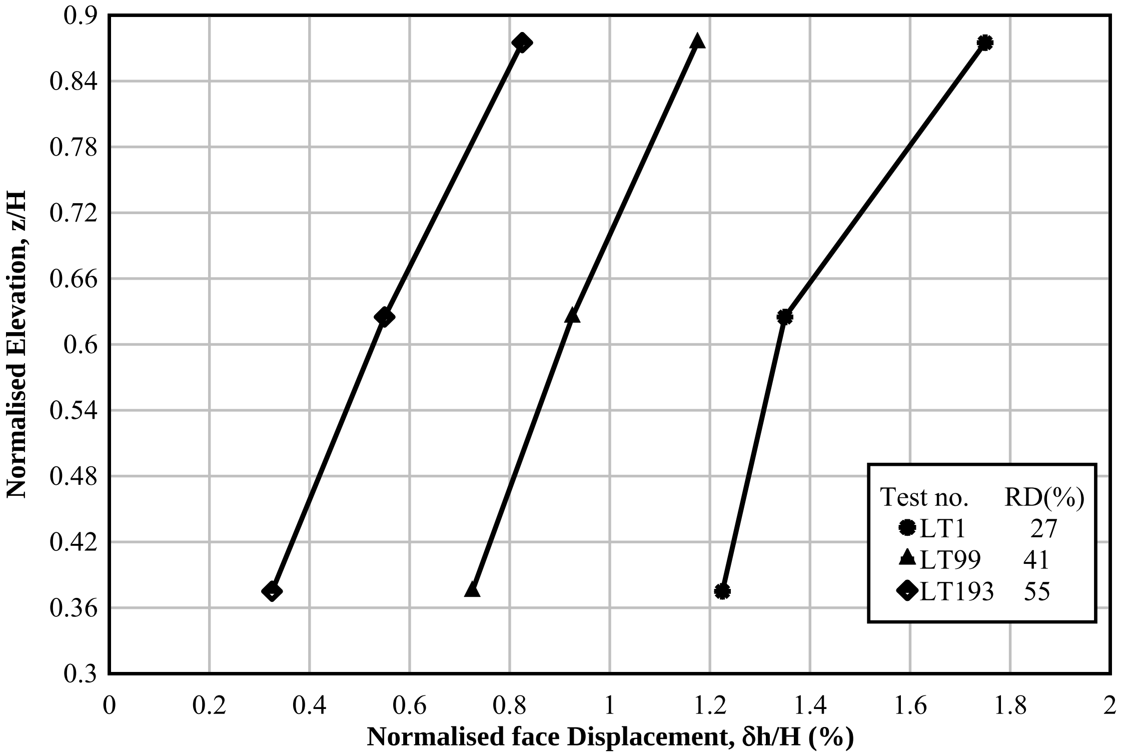

Figure 6.59: Displacement Response (LT1, 99 and 193)

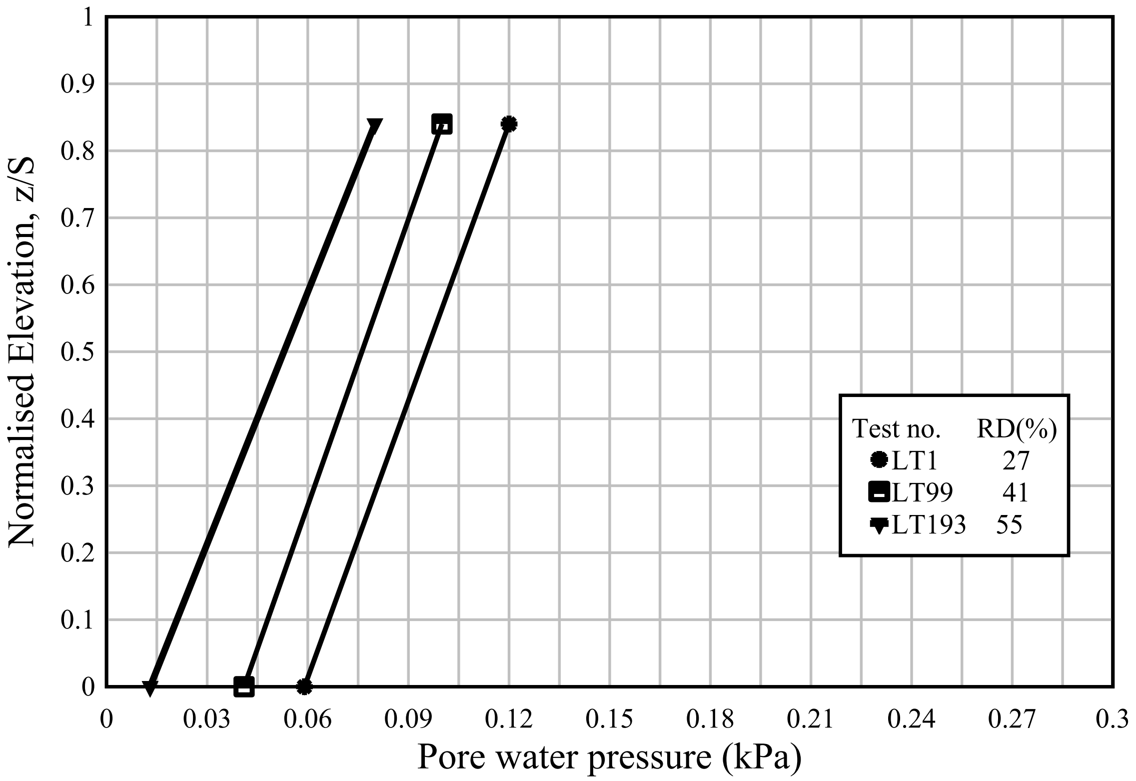

pore water pressure.grf

Figure 6.60: Pore Water Pressure Response (LT1, 99 and 193)

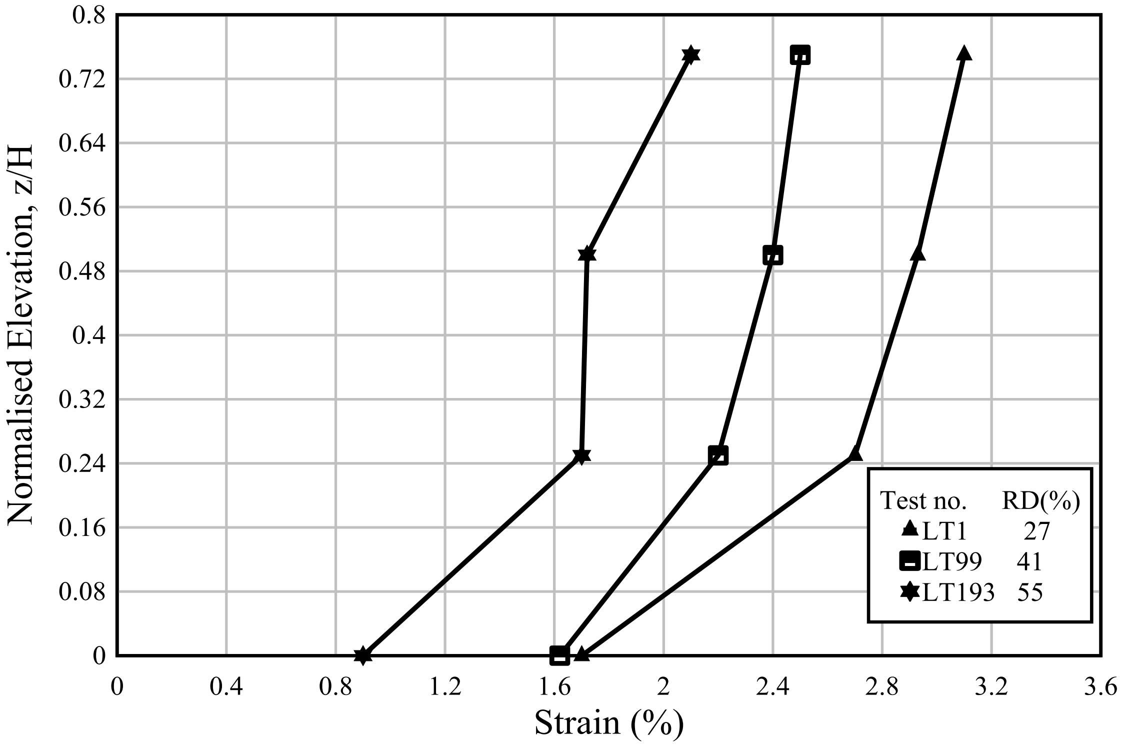

strain.grf

Figure 6.61: Strain Response (LT1, 99 and 193)

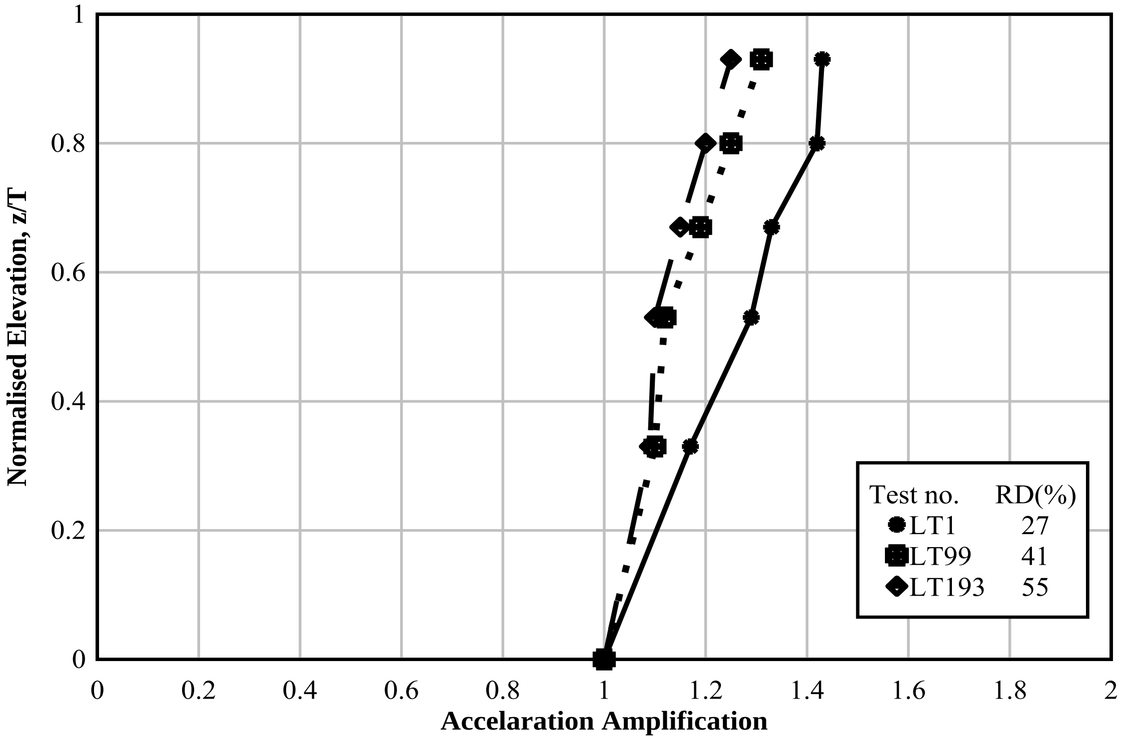

Figure 6.62: Acceleration Response (LT1, 99 and 193)

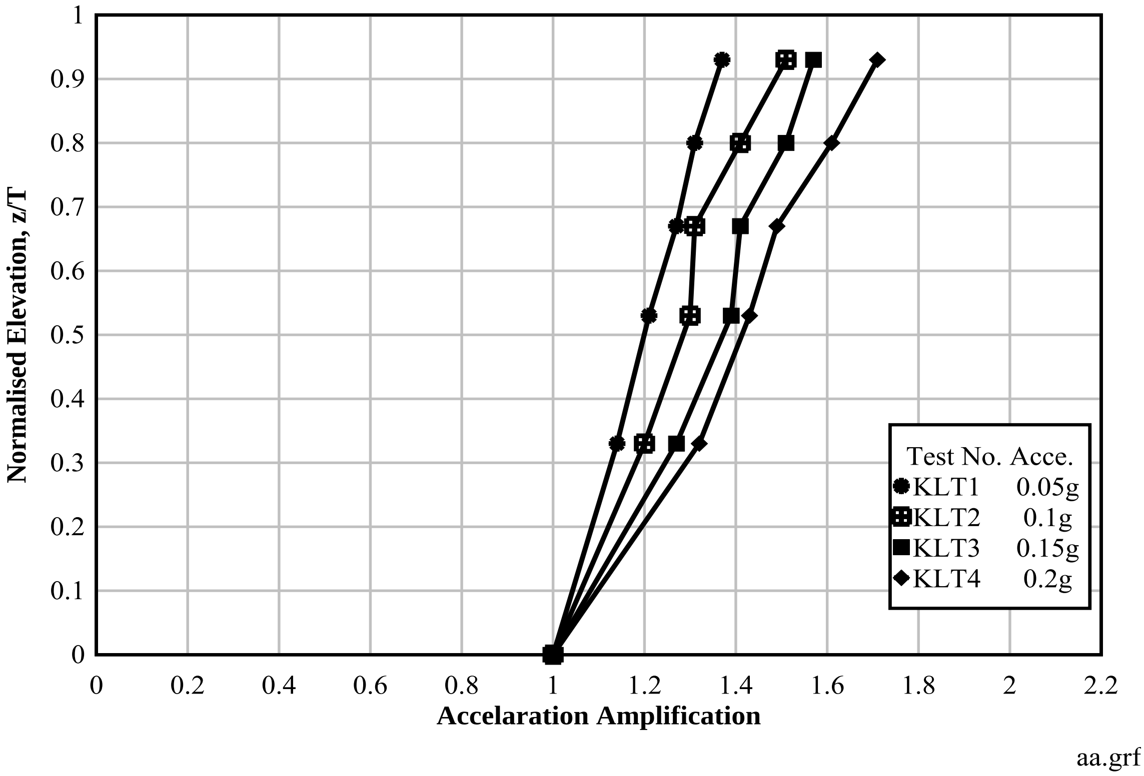

Figure 6.63: Effect of base acceleration on acceleration amplification (KLT1-KLT4)

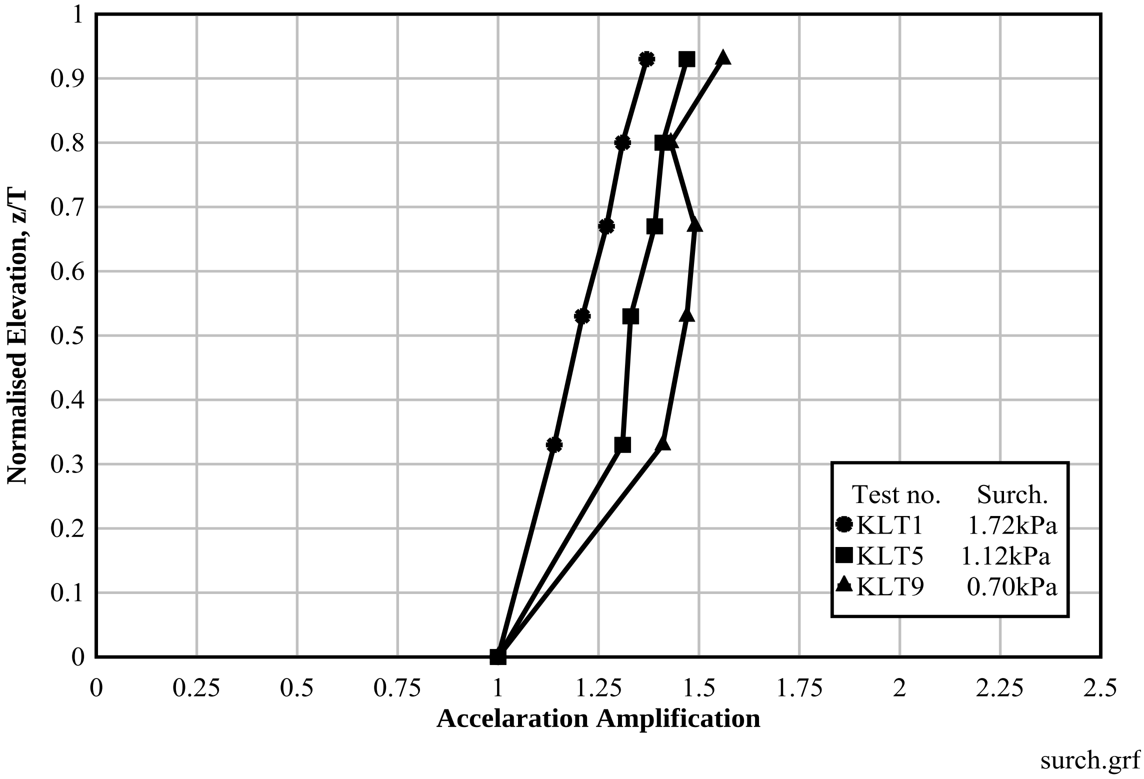

Figure 6.64 Effect of surcharge on acceleration amplification (KLT1, 5 and 9)

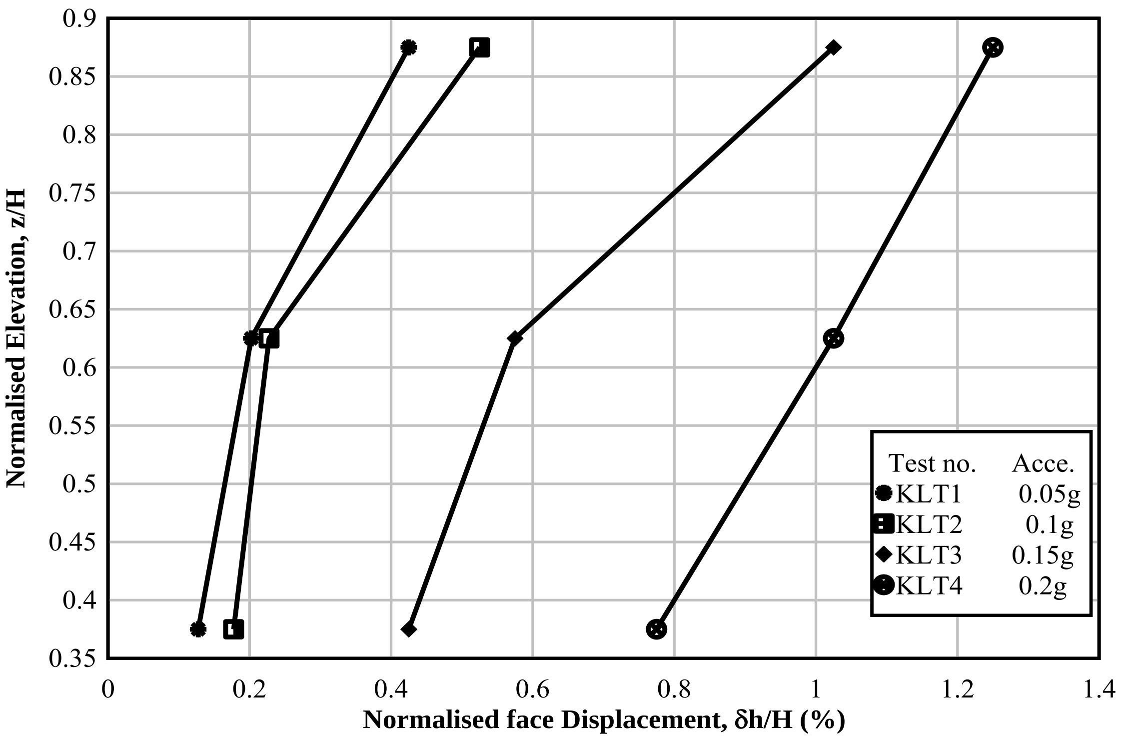

Figure 6.65: Effect of base acceleration on displacement profile (KLT1-KLT4)

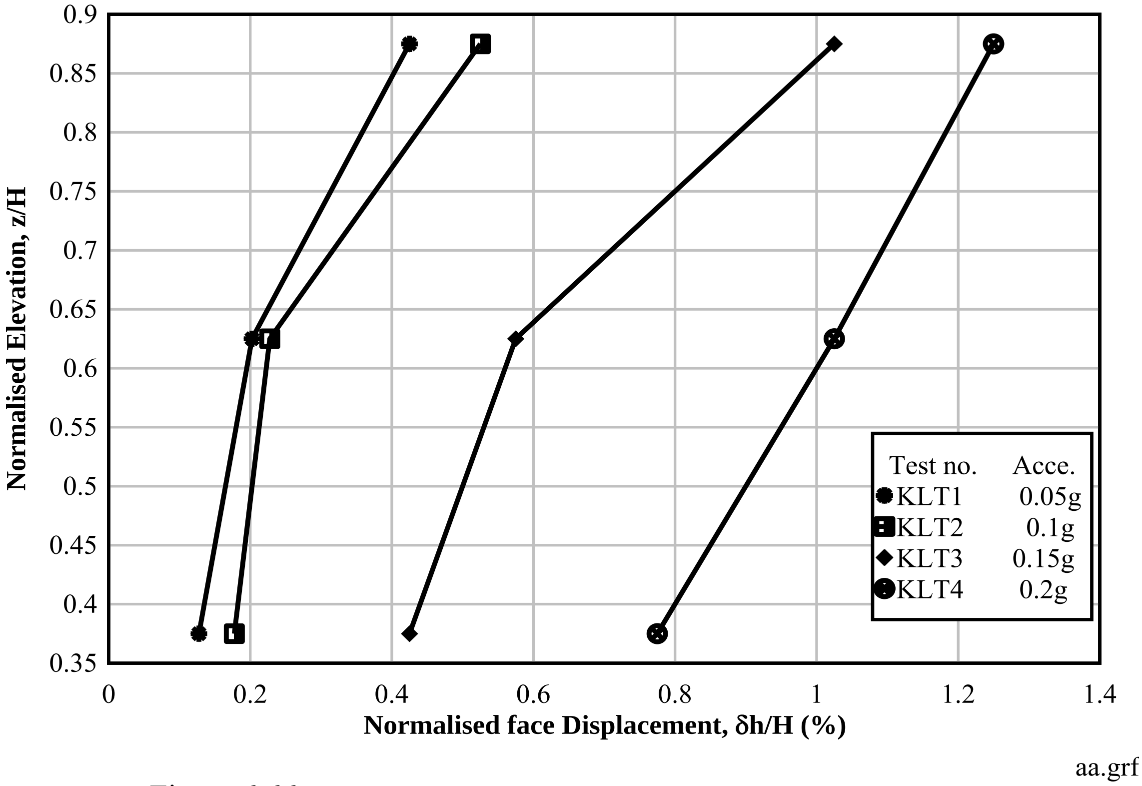

Figure 6.66: Effect of surcharge on displacement profile (KLT1, 5 and 9)

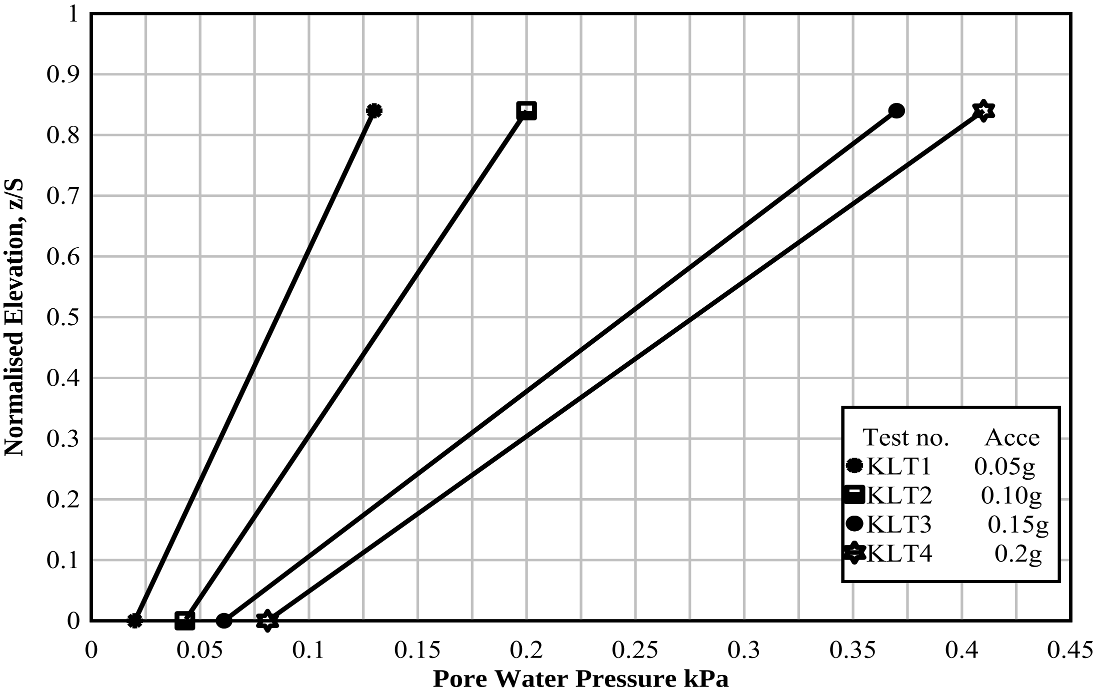

Figure 6.67: Effect of base acceleration on pore water pressure (KLT1-KLT4) acce.grf

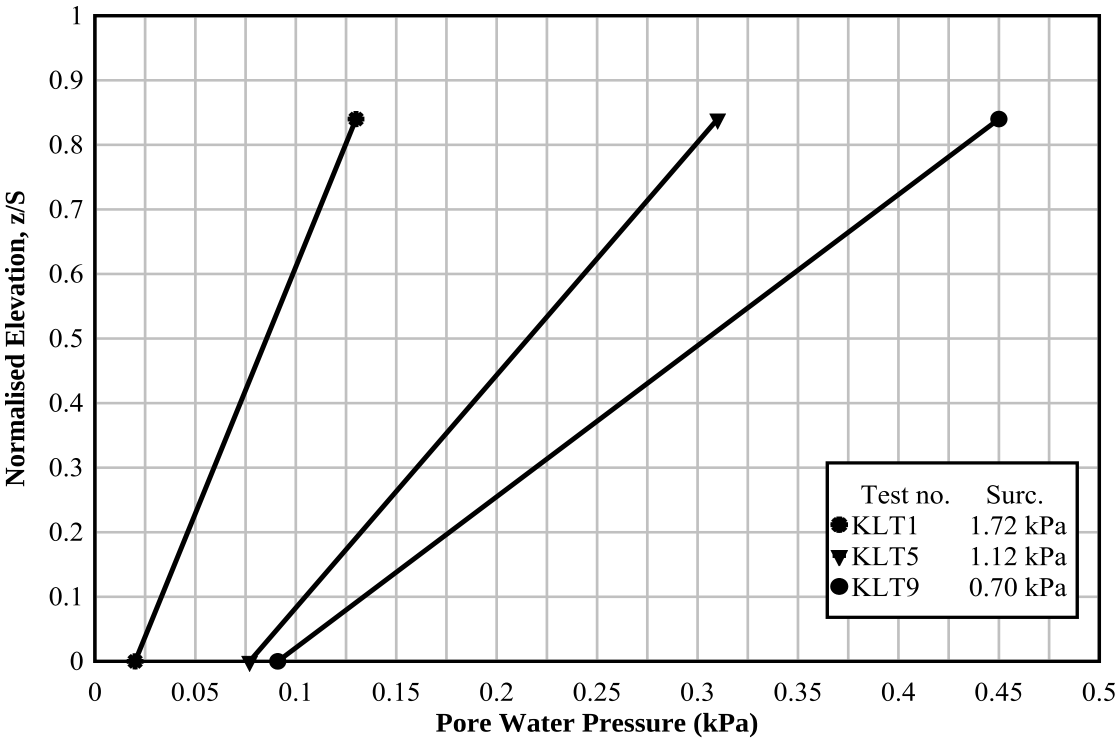

Figure 6.68: Effect of surcharge on pore water pressure (KLT1, 5 and 9)

sur c.grf

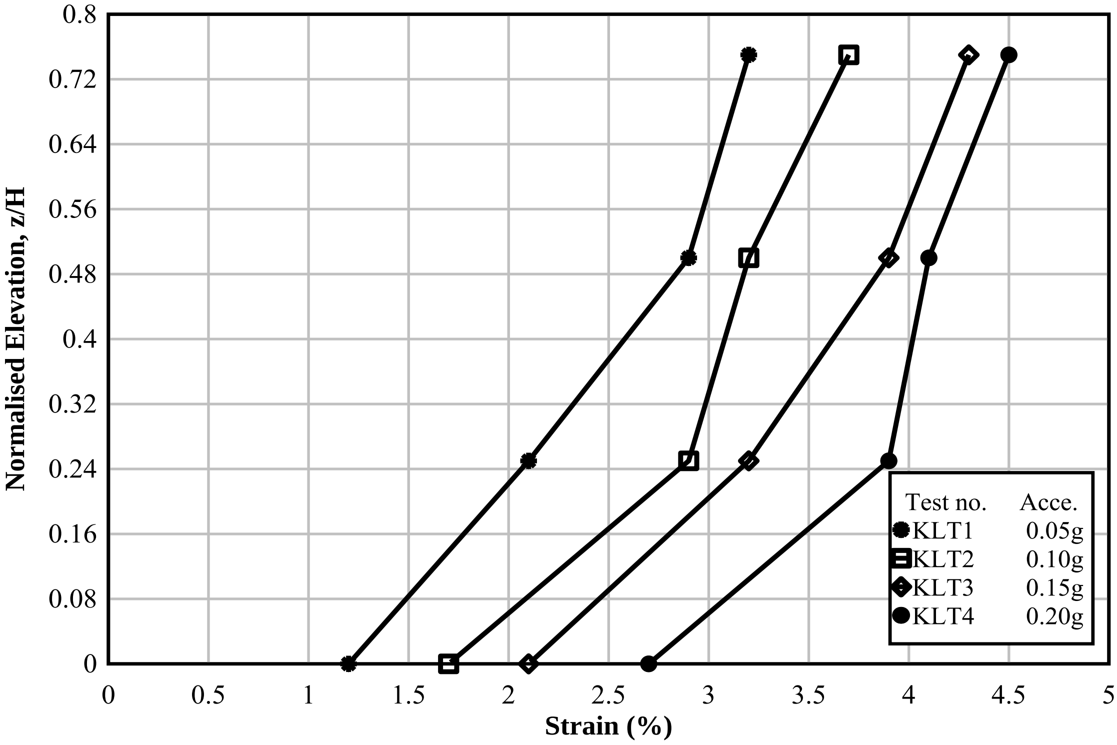

Figure 6.69: Effect of base acceleration on strain (KLT1-KLT4)

aa.grf

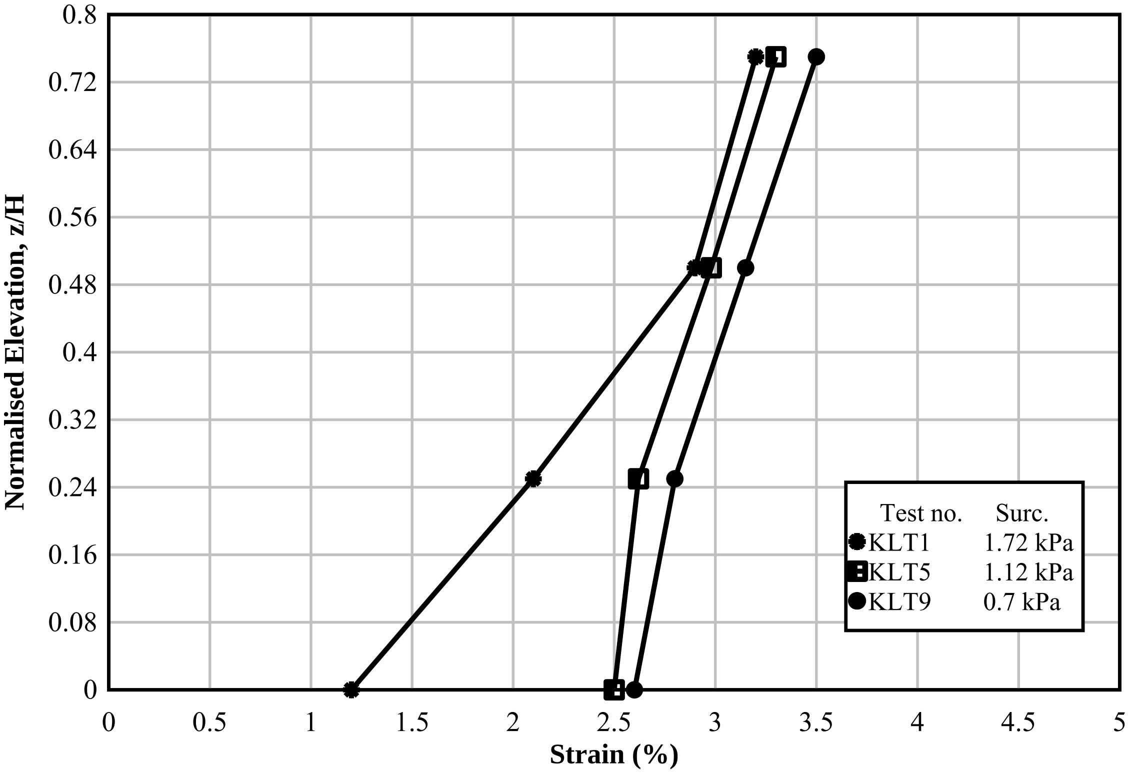

Figure 6.70: Effect of surcharge on strain (KLT1, 5 and 9)

surc.grf

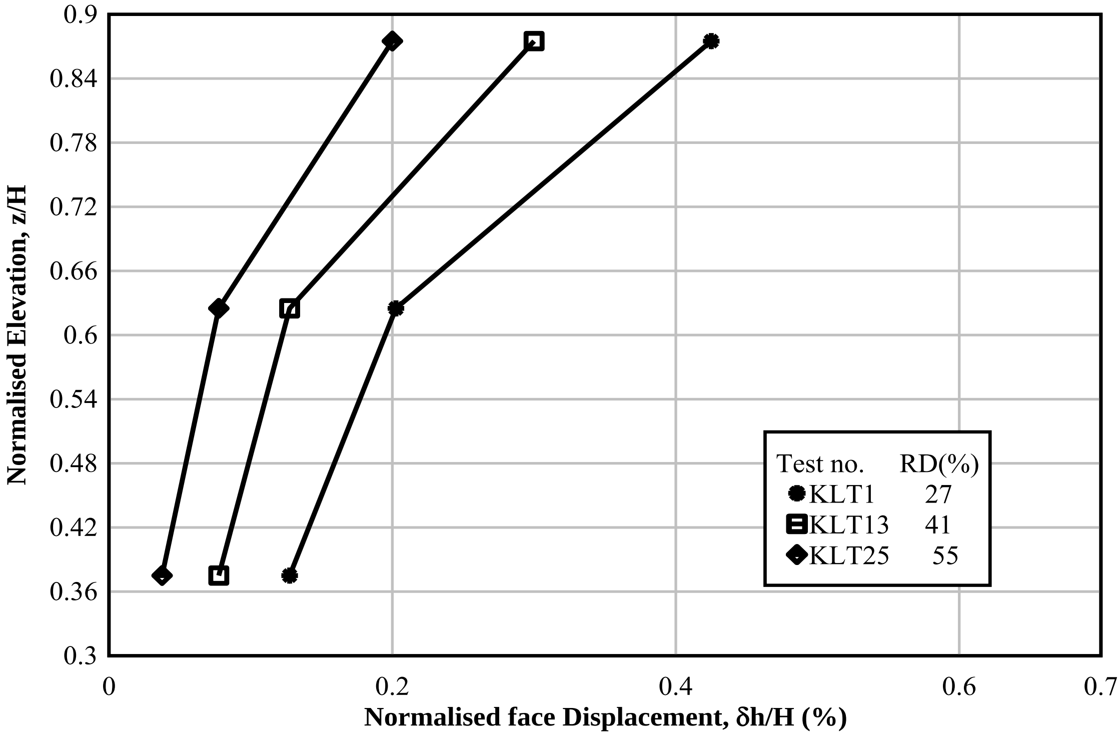

latha dd.grf

Figure 6.71 : Displacement Response (KLT1, 13 and 25)

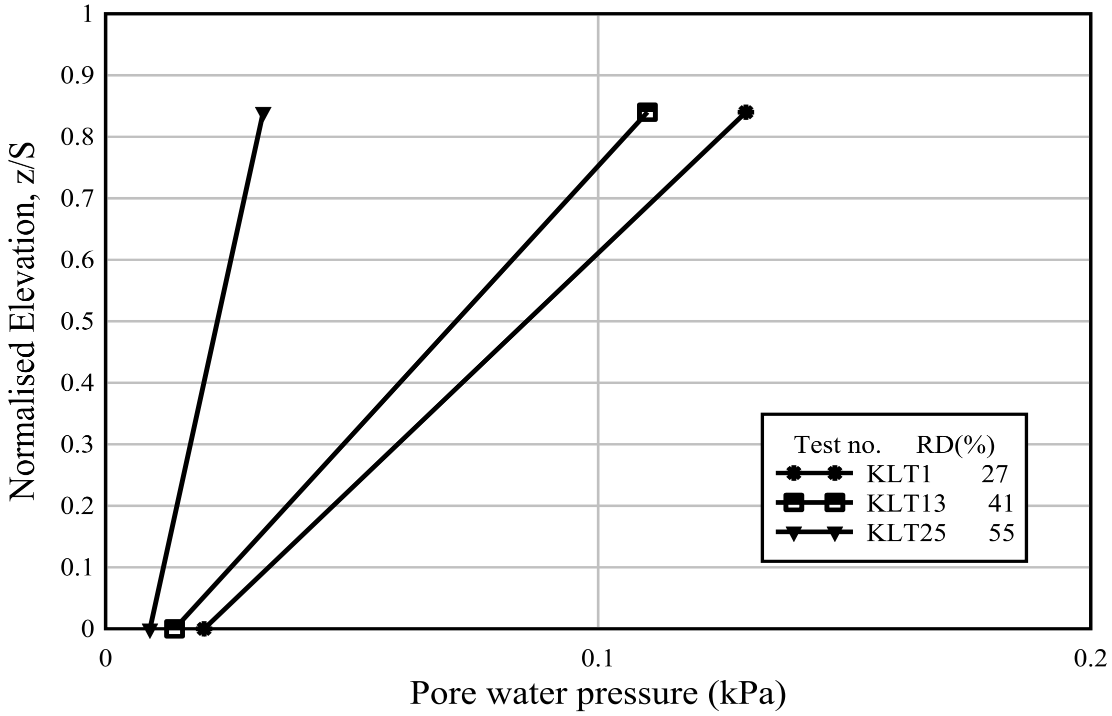

Figure 6.72: Pore Water Pressure Response (KLT1, 13 and 25)pore water pressure.grf

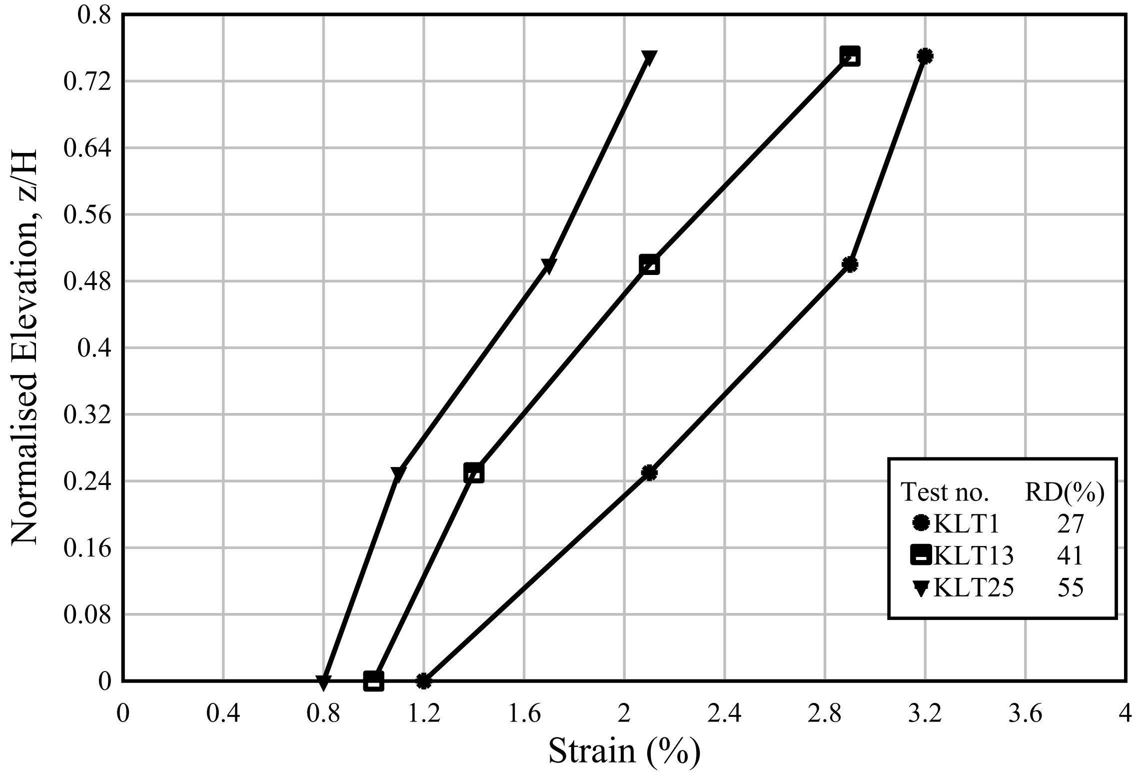

Figure 6.73: Strain Response (KLT1, 13 and 25) strain.grf

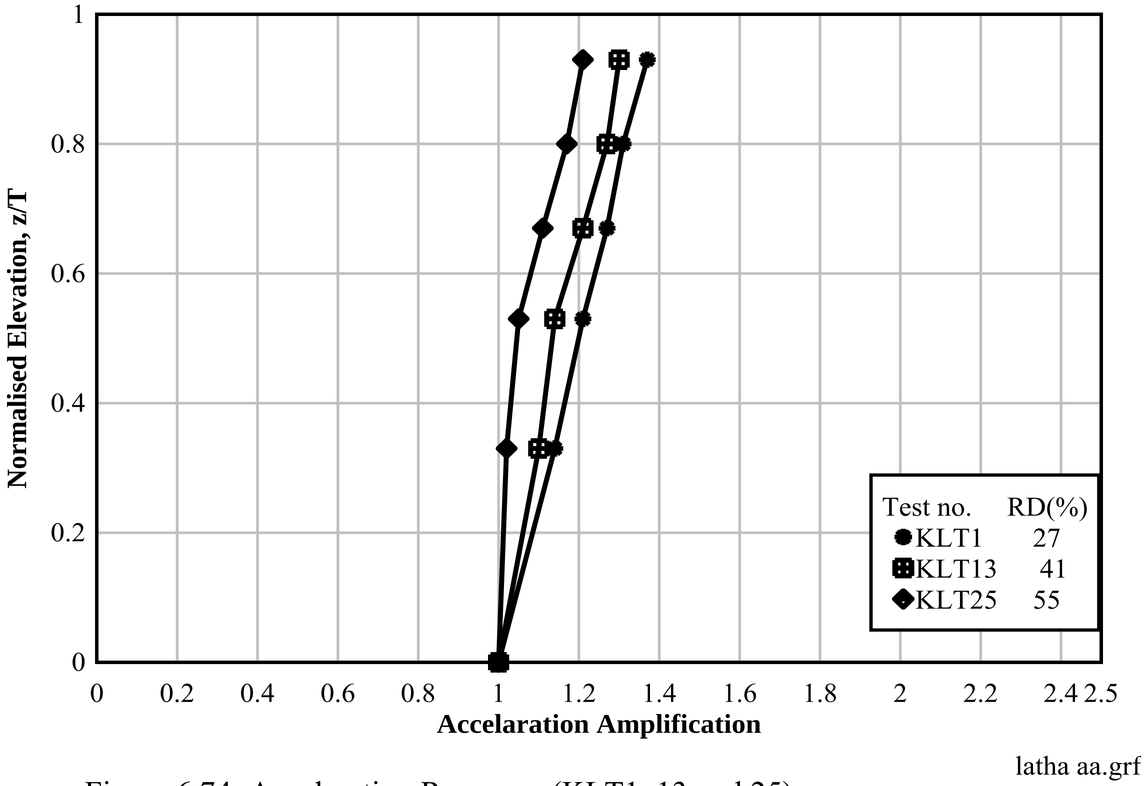

Figure 6.74: Acceleration Response (KLT1, 13 and 25)

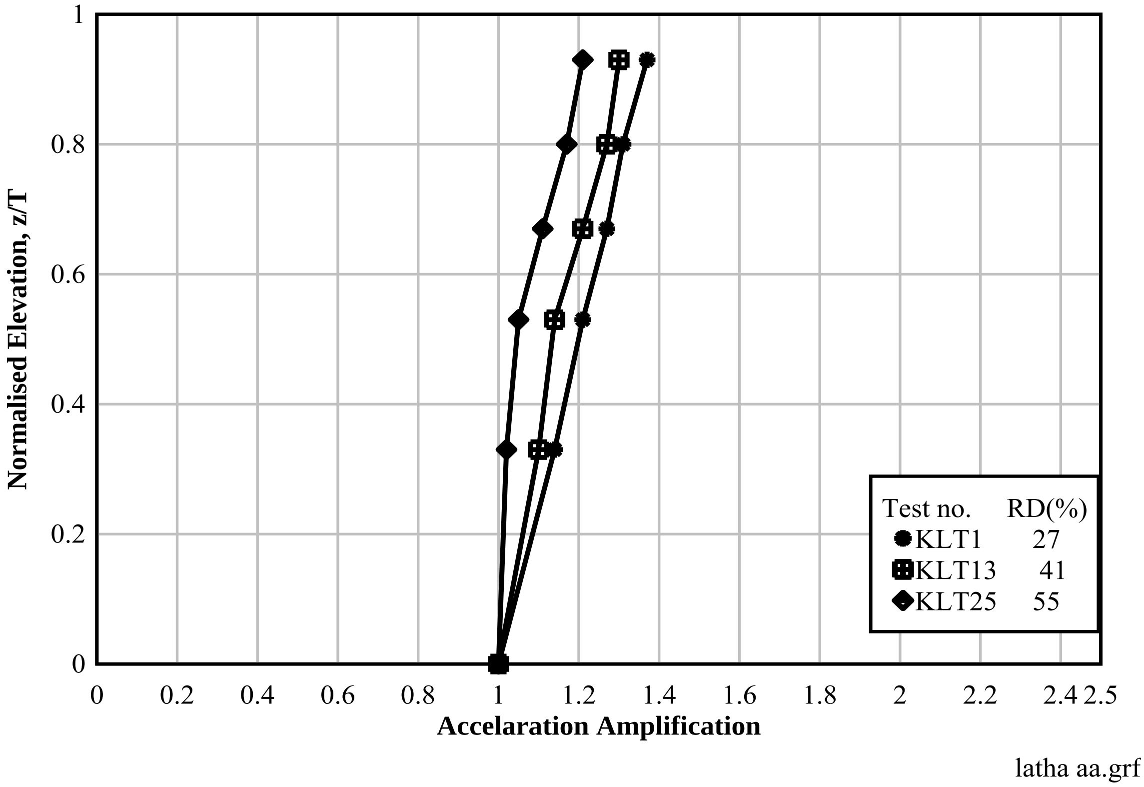

Figure 6.75: Effect of base acceleration on acceleration amplification (LLT1-LLT4)

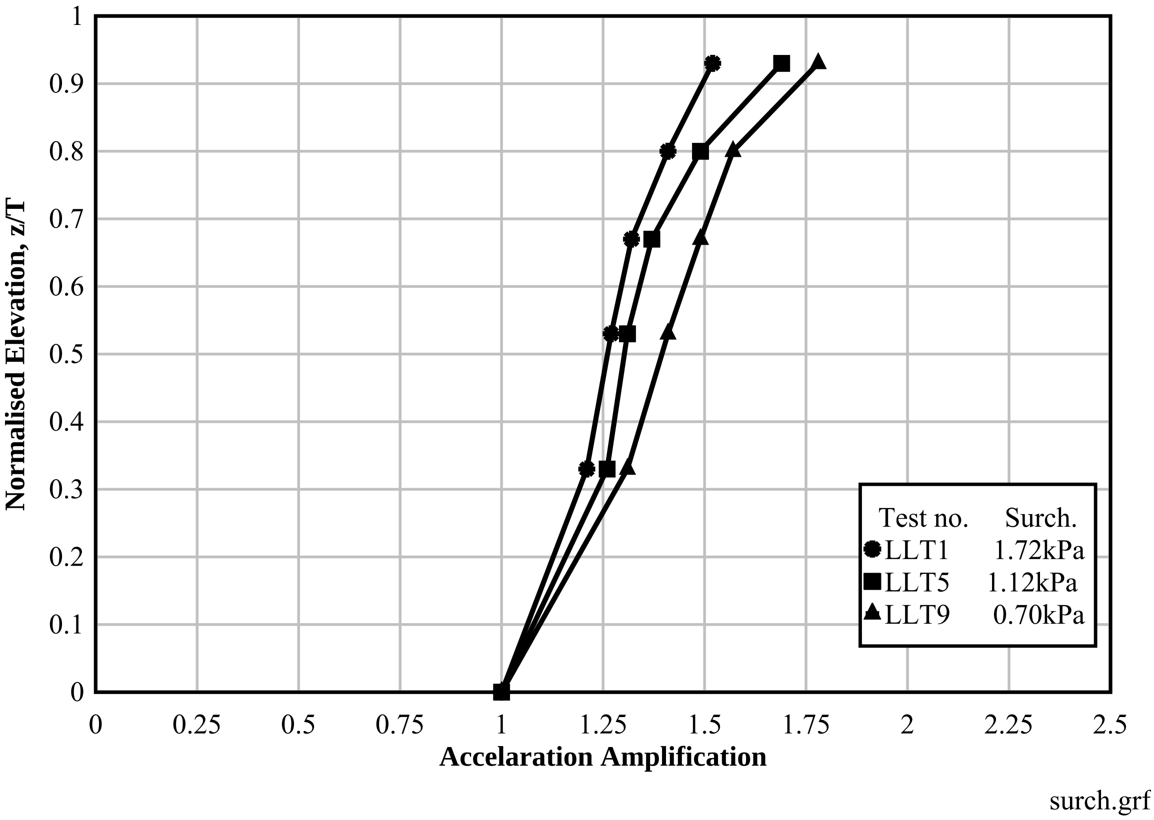

Figure 6.76: Effect of surcharge on acceleration amplification (LLT1, 5 and 9)

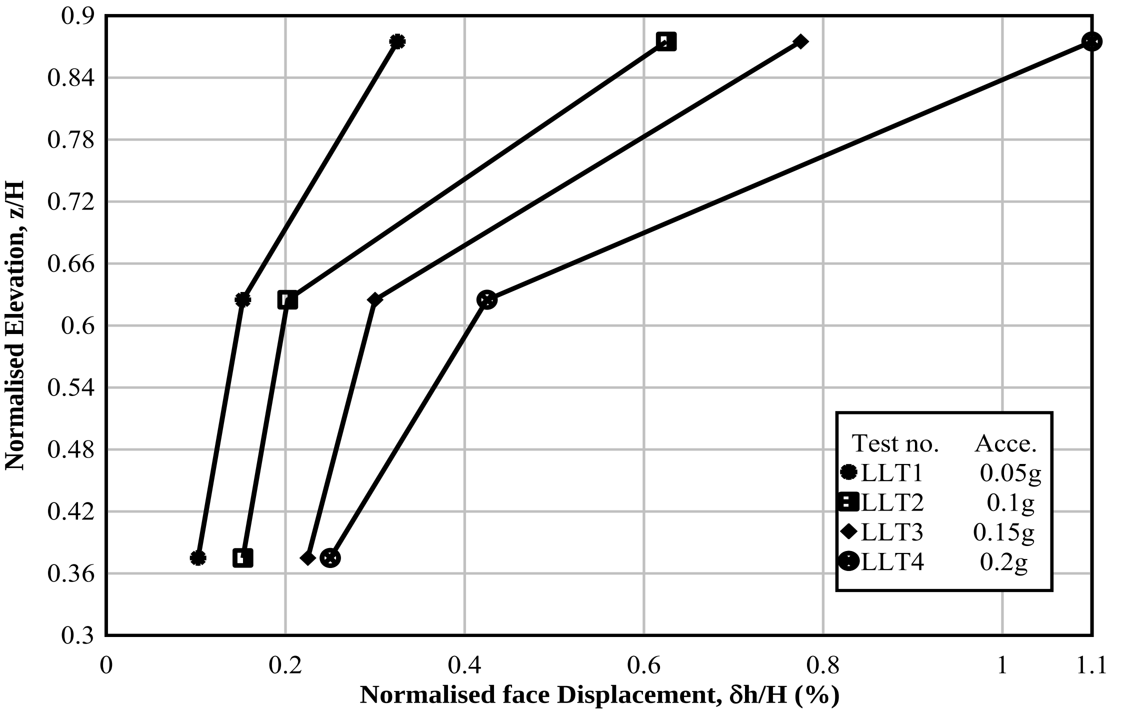

Figure 6.77: Effect of base acceleration on displacement profile (LLT1-LLT4)

aa.grf

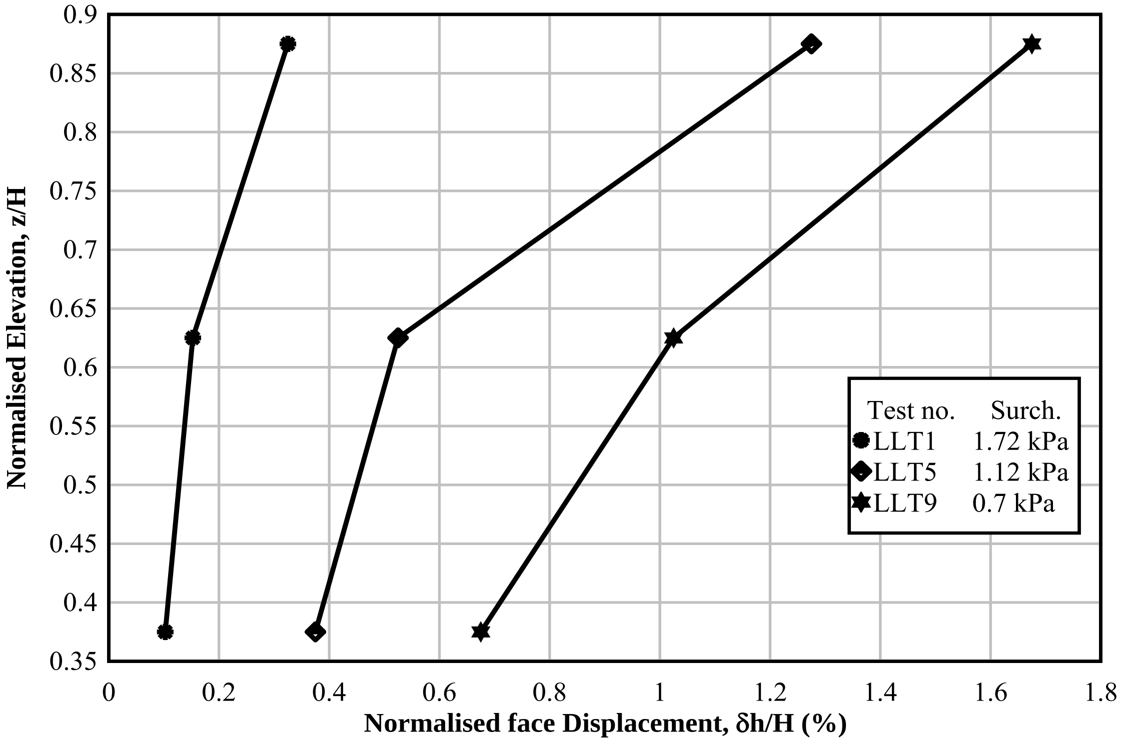

Figure 6.78: Effect of surcharge on displacement profile (LLT1, 5 and 9)

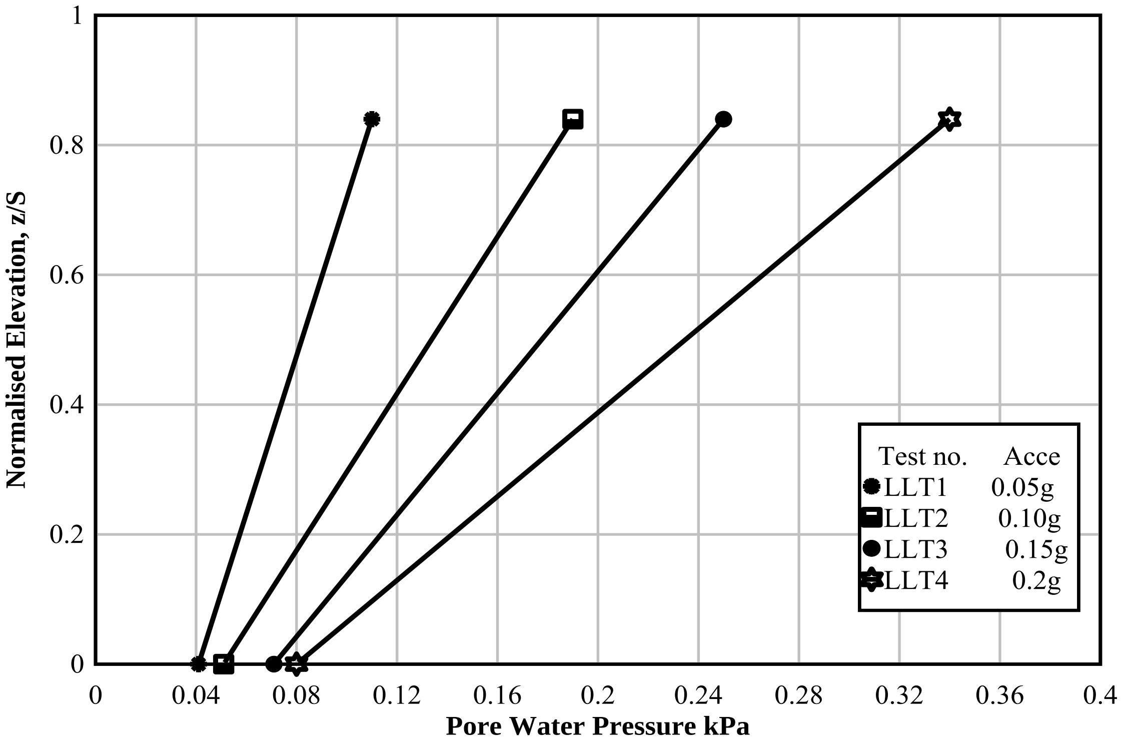

Figure 6.79: Effect of base acceleration on pore water pressure (LLT1-LLT4)

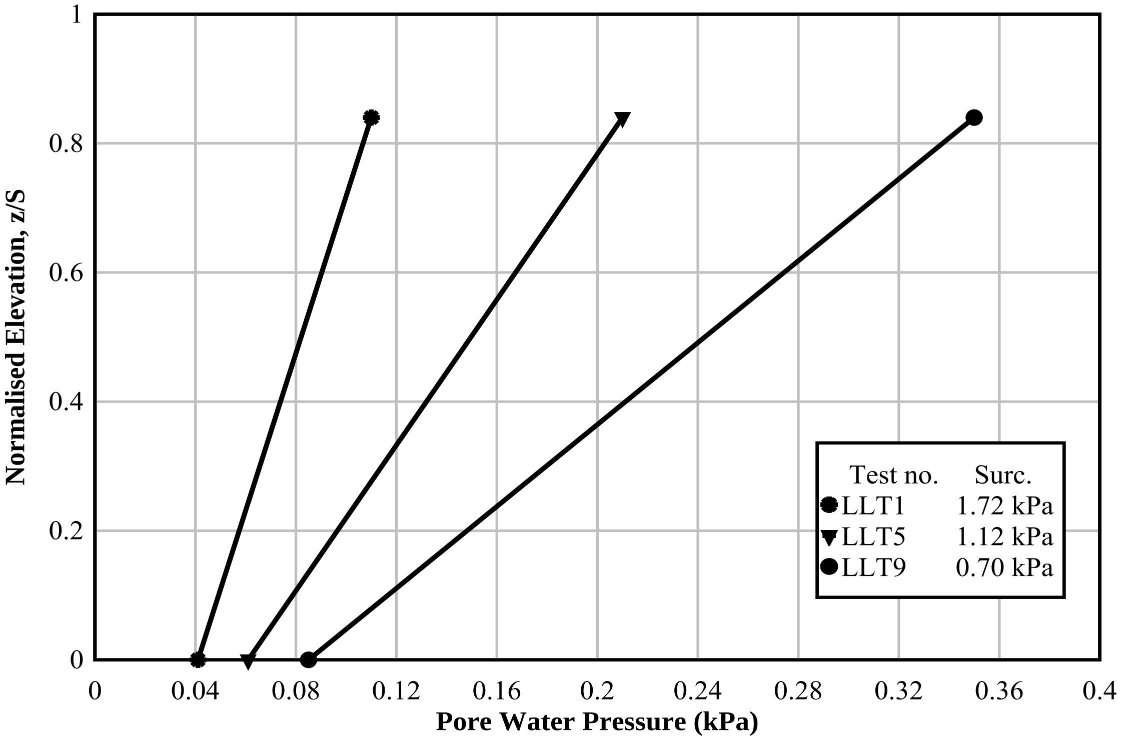

Figure 6.80: Effect of surcharge on pore water pressure (LLT1, 5 and 9)

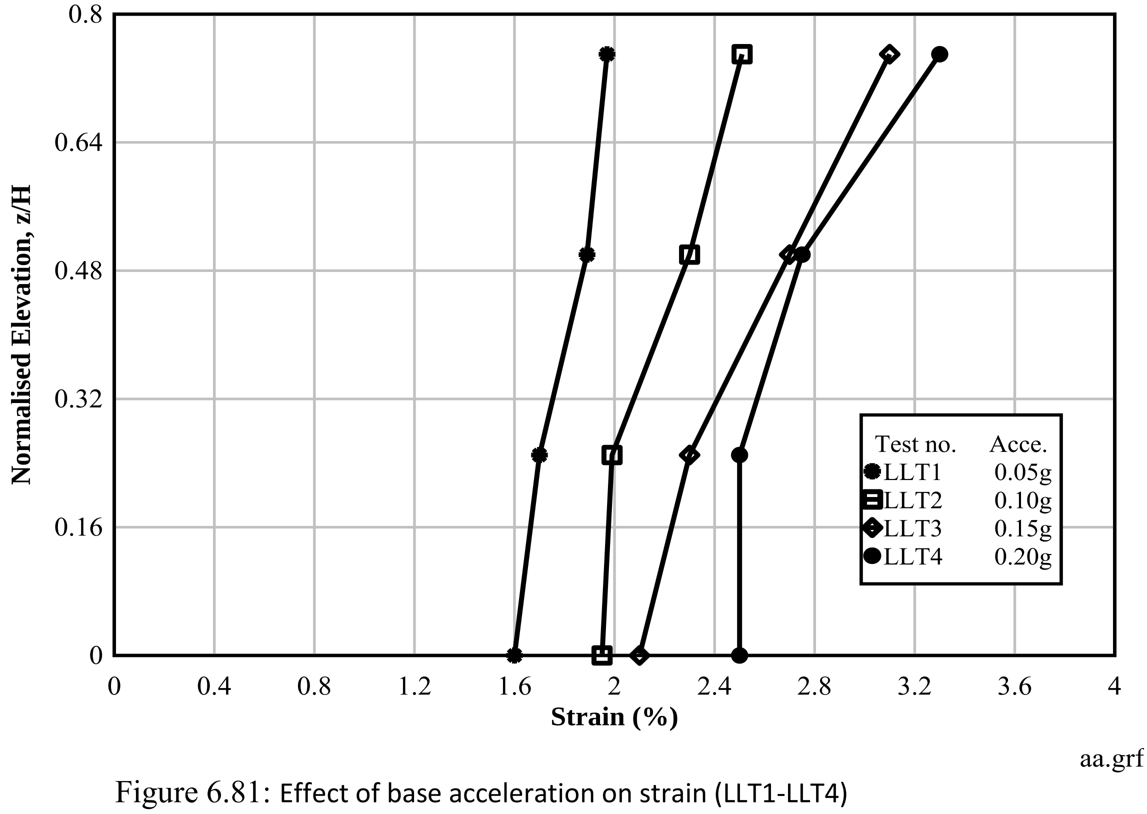

Figure 6.81: Effect of base acceleration on strain (LLT1-LLT4)

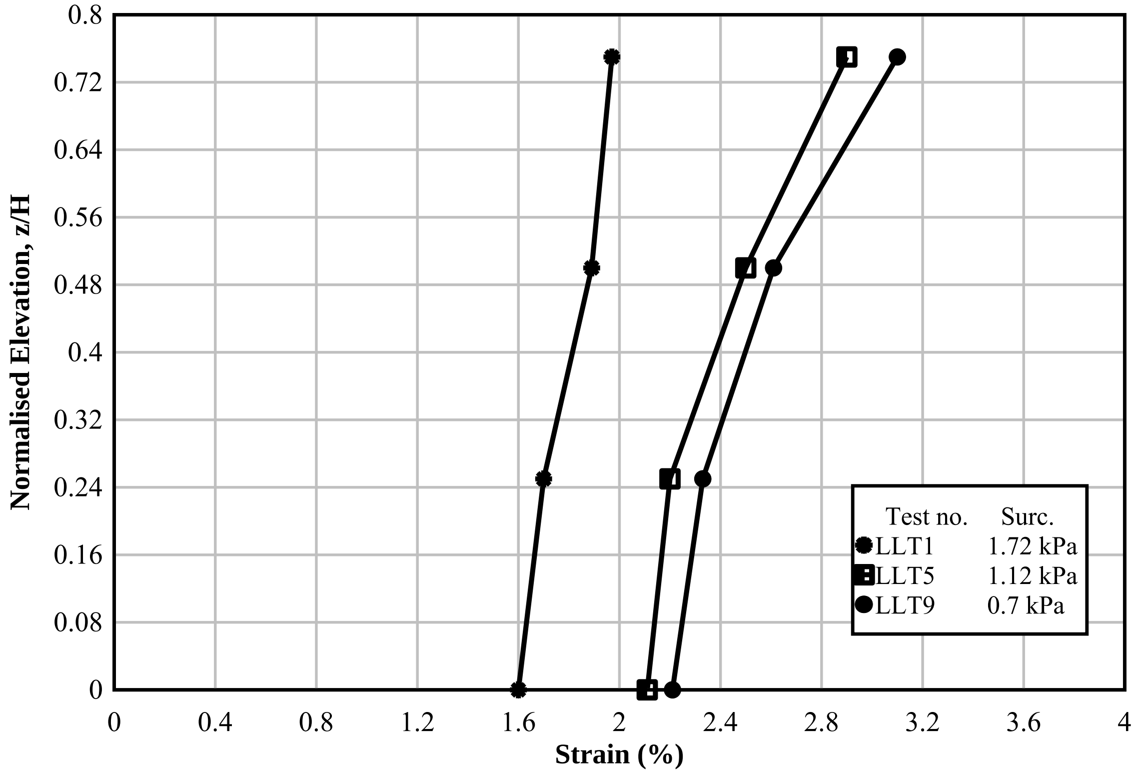

Figure 6.82: Effect of surcharge on strain (LLT1, 5 and 9) surc.grf

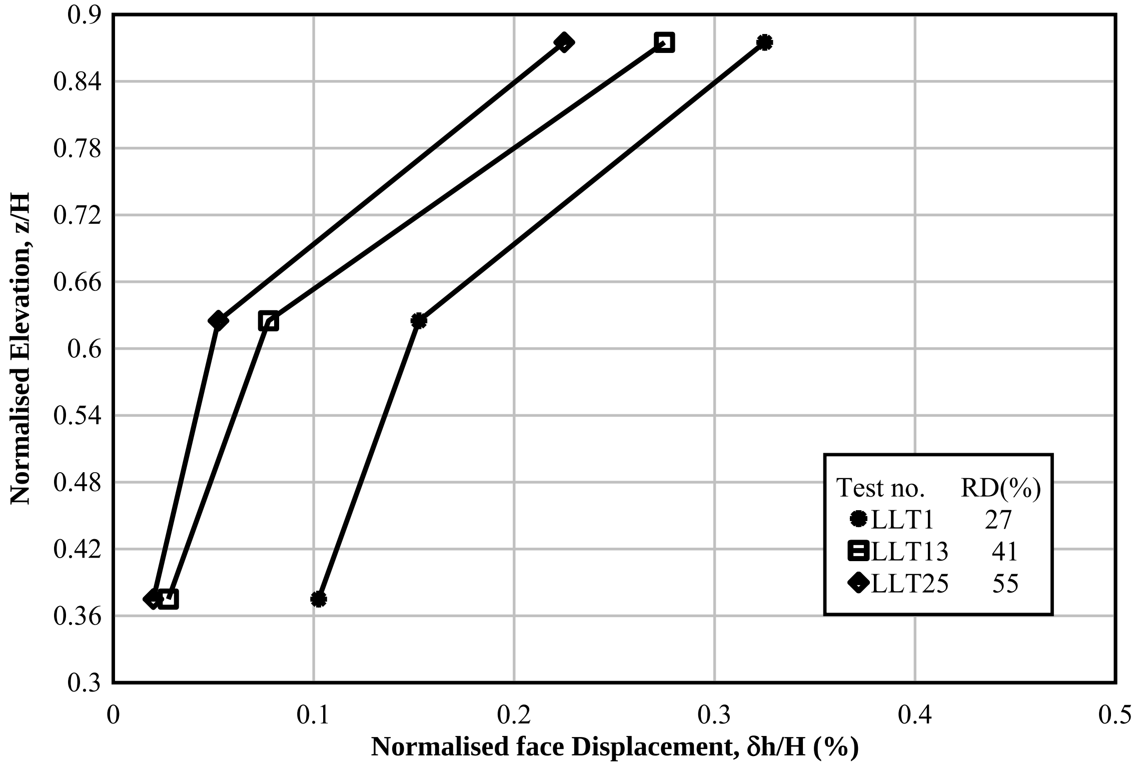

Figure 6.83: Displacement Response (LLT1, 13 and 25) latha dd.grf

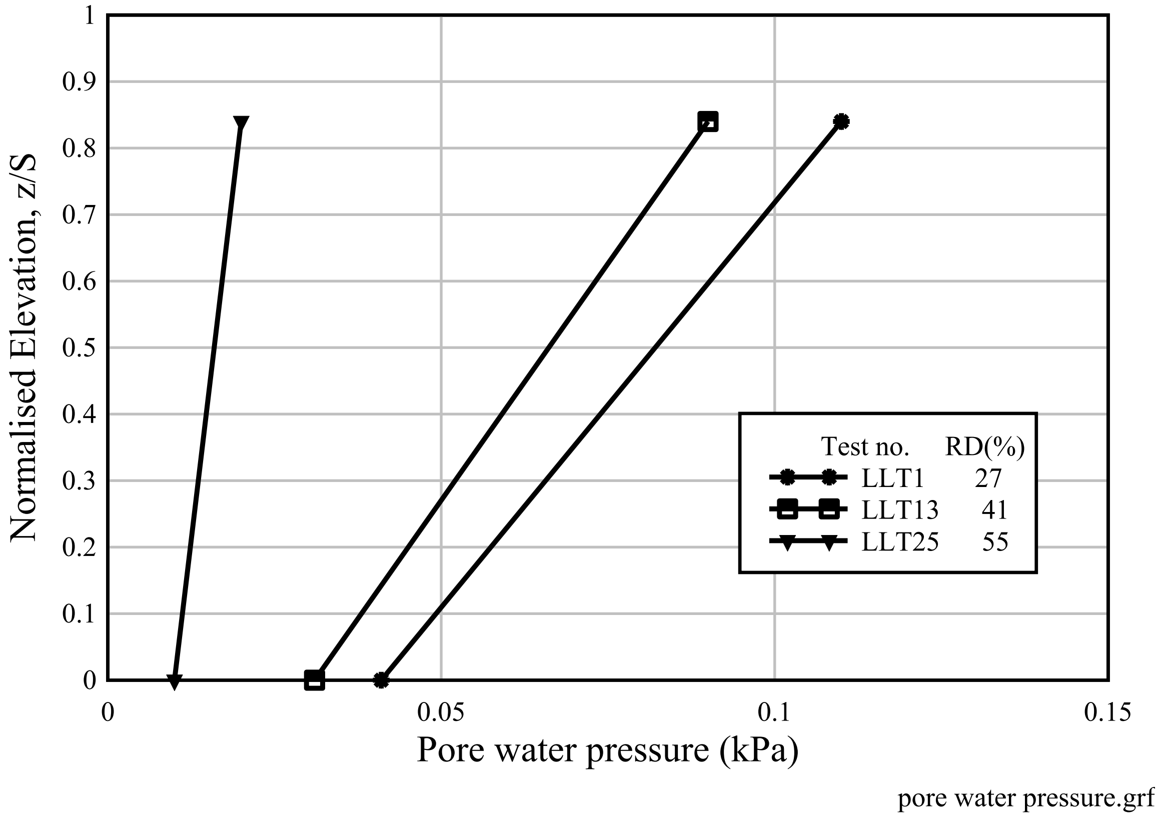

Figure 6.84: Pore Water Pressure Response (LLT1, 13 and 25)

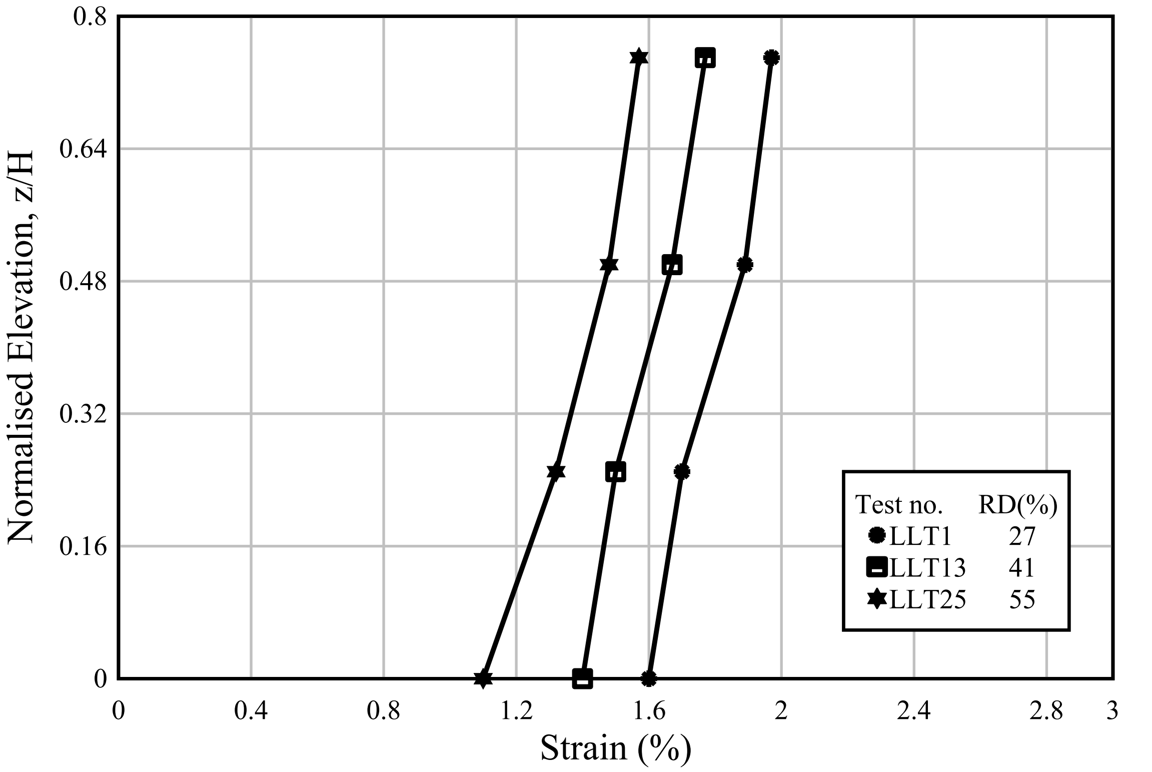

Figure 6.85: Strain Response (LLT1, 13 and 25)

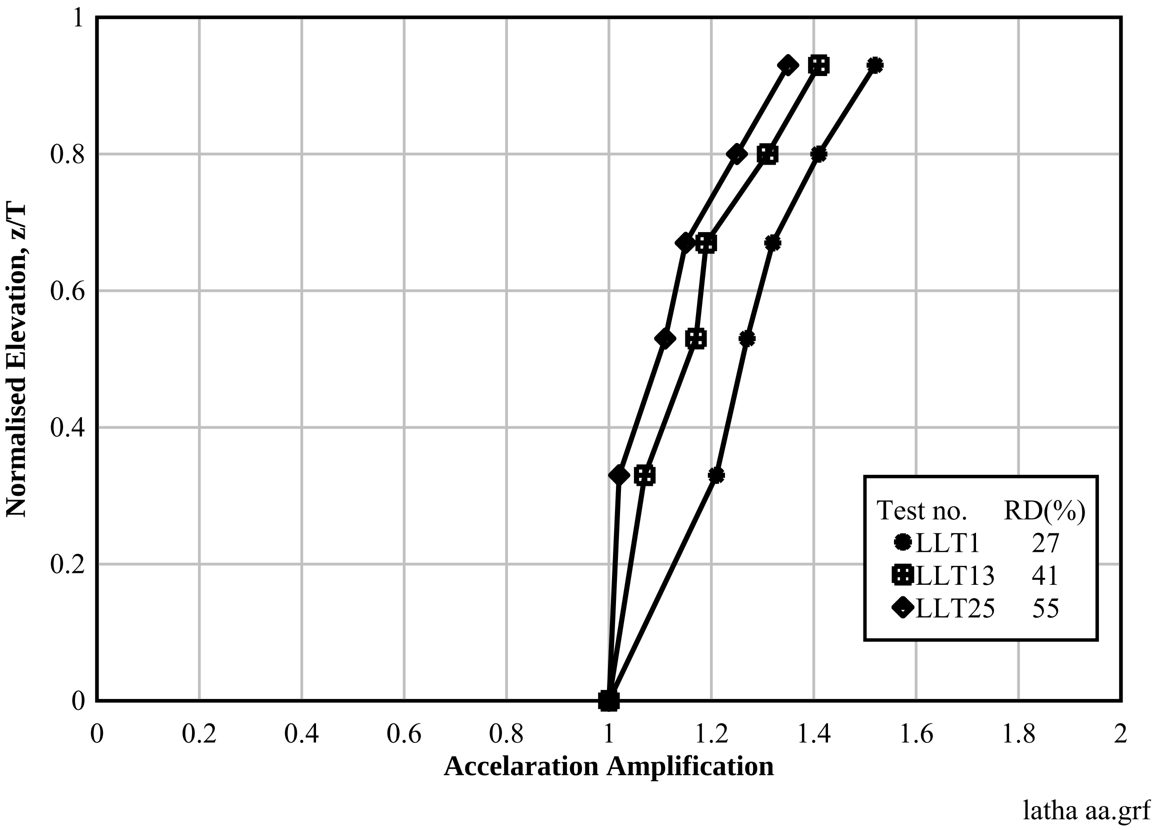

Figure 6.86: Acceleration Response (LLT1, 13 and 25)